The synthesis and luminescence properties of platinum, palladium and iridium complexes featuring multidentate ligands

Melissa Teresa Walden

A thesis submitted for the degree of Doctor of Philosophy

Department of Chemistry

September 2018

Abstract

Luminescent metal complexes have seen great success in many applications from bio-sensing to display technology and lighting. A range of different Pt, Pd and Ir complexes featuring multidentate ligands have been synthesised in this work with the aim of incorporation into organic light emitting diodes (OLEDs).

Chapter 2 focuses on Pt complexes containing bidentate 1,2,4-triazole ligands. Homoleptic complexes exhibit red emission that is concentration-dependent, showing excimeric emission at higher concentrations. Impressive quantum yield (ϕ) values ranging from 21 to 48 % have been obtained in degassed solution. Consequently, both solution-processed and vacuum thermally evaporated devices of these complexes were fabricated and a maximum EQE of 14.9 % was obtained for a thermally evaporated device.

Chapter 3 describes the synthesis and photophysical properties of Ir^{III} complexes featuring tridentate N^C^N ligands in combination with 1,2,4-triazole ligands of bidentate and tridentate denticity. Some isoelectronic Pt^{IV} analogues were also synthesised for comparison. The Pt^{IV} complexes display superior photophysical properties in comparison to the Ir complexes. Indeed, the Pt complex containing dipyridylbenzene (dpyb) as the N^C^N ligand in combination with a bidentate 1,2,4-triazole ligand has a ϕ of 5.9 % and a lifetime of 3.1 µs. On increasing the denticity of the triazole ligand from bidentate to tridentate in a bis-tridentate Pt complex, an improved ϕ of 28 % and a lifetime of 11 µs were obtained.

In Chapter 4, Pt and Pd analogues containing C^N^N^C ligands were synthesised and probed for their excimeric emission. Increased complex rigidity was observed for these compounds due to the incorporation of tetradentate ligands about the metal centre. The Pt compounds generally displayed more impressive photophysical properties compared to their Pd analogues, but a Pd complex containing a thiophene tetradentate ligand was incorporated into a solution-processed OLED to give a respectable EQE of 3.17 %.

Finally, in Chapter 5 the foundations for future work to achieve highly efficient NIR OLEDs were laid via the synthesis of dinuclear complexes containing Pt(N^C^N) units rigidly linked by a xanthene core in a face-to-face conformation. These complexes displayed visible and NIR emission with high efficiencies in both solution (ϕ = 5-35 %) and in films (ϕ up to 57 %). The NIR emission emanates from excimer-like excited states in each case, probably involving a varying mixture of face-to-face intra- and intermolecular interactions.

Declaration

The research described herein was undertaken at the Department of Chemistry at Durham University between October 2014 and September 2018. All of the work is my own, except where specifically stated otherwise. No part of it has previously been submitted for a degree at this or any other university.

Statement of copyright

Acknowledgements

I have had a fantastic few years doing my PhD. I have learned so much, met so many amazing people and travelled to some incredible places. Of course, this would not have been possible without the funding bodies that have supported me during my studies. These include the EPSRC, the Durham University CDT in Energy and the JSPS.

A huge thank you must then go to Professor Gareth Williams for allowing me the opportunity to work in his group on such a *bright* and varied area of Chemistry. I respect him so much for being fair, thorough and always asking our opinion (even when he definitely knows best!). A lovely man and a great supervisor, so thanks Gareth!

The JAGW group has been at the heart of my everyday life for the past four years and I couldn't have asked for a more unique, kind and hilarious group of people to work with. First and foremost is Emma, not only because she would be annoyed if I didn't put her first (only joking!), but because she was the one to show me the ropes in the lab, to give me a hug when I was down, was my conference buddy and my partner in crime when it came to everything else (banana in the coffee is all I'm saying). I still miss Eddy's whistling to all the latest Radio 1 hits and Raminder's encyclopaedic knowledge of pretty much everything from Chemistry to Kylie Minogue. Thank you to David for putting up with me in the last few months and for introducing me to the Arriva bus app! Thanks also go to all of our MChem students who have been incredible to work with and who remain excellent friends not least Elizabeth, Jack, Rebecca, Chris and Ben.

Thank you to everyone in the department including all service staff who work so hard to ensure we can get our results and who keep the place ticking over. I would especially like to mention Miriam, Tavleen and Vicki for always being there to have a chat with. There are so many fantastic people in the department and I feel lucky to have been able to work in such a friendly environment. I have also enjoyed working in collaboration with the Physics department and special thanks goes to Piotr for all of his efforts on making the devices, even if it was sometimes with less material than he would have liked!

Outside of Chemistry I have some truly amazing people in my life and I am so glad to have met a lot of them through my PhD. Jasmine, Carl, Eddy, Chris and Kirstyn you have all been amazing housemates over the years and I can't wait to make more funny memories with you all post-Durham!

Finally, I would like to thank all of my family and friends who have supported me so much, I'm so lucky to have you.

Mum and Dad, you've been there since day one and have done everything for me. You have always gone out of your way to make things work for me and I just can't express how much that means. As long as I don't ask you any Chemistry questions, you will always do everything you can to find an answer, thanks a million.

Jack, you're my calming influence and you can read me like a book. You know everything I like and exactly how I work. You're amazing and where would I be without you? Thank you.

Abbreviations

26mCPy	2,6-bis(N-carbazolyl)pyridine
2-MeTHF	2-methyltetrahydrofuran
3TPYMB	Tri[3-(3-pyridyl)mesityl]borane
AcOH	Acetic acid
ada	Adamantyl
ASAP	Atmospheric solids analysis probe
B_2pin_2	Bis(pinacolato)diboron
B3LYP	Becke, 3-parameter, Lee-Yang-Parr hybrid exchange-correlation energy functional
B3PymPm	4,6-Bis(3,5-di(pyridin-3-yl)phenyl)-2-methylpyrimidine
BAlq	Bis(8-hydroxy-2-methylquinoline)-(4-phenylphenoxy)aluminum
bbtxH	1,3-bis(2-benzothiazolyl)-4,6-dimethylbenzene
BCPO	9,9'-(4,4'-(Phenylphosphoryl)bis-(4,1-phenylene))bis(9H-carbazole)
bhq	Benzo(h)quinoline
BmPyPb	1,3-Bis(3,5-dipyrid-3-yl-phenyl)benzene
bpy	2,2'-Bipyridine
BPyTP	2,7-di(2,2'-bipyridin-5-yl)triphenylene
CBP	4,4'-Bis-(carbazol-9-yl)biphenyl
CIE	Commission internationale de l'Eclairage
COSY	Correlation spectroscopy
CRI	Colour rendering index
CuAAC	Copper-catalysed azide-alkyne cycloaddition
dba	bis(dibenzylideneacetone)
DCM	Dichloromethane
DFT	Density functional theory
DME	Dimethoxyethane
DMF	Dimethylformamide
DPEPO	Bis[2-(diphenylphosphino)phenyl] ether oxide
dppf	1,1'-bis(diphenylphosphino)ferrocene
DPPS	Diphenyl-bis[4-(pyridin-3-yl)phenyl]silane
$dppyH_2$	Diphenylpyridine
dpybH	Dipyridylbenzene
EBL	Electron-blocking layer
EGL	Energy gap law
EL	Electroluminescence
EML	Emitting layer
en	Ethylenediamine
EPA	Diethylether/isopentane/ethanol
EQE/ η_{ext}	External quantum efficiency
ES-MS	Electrospray mass spectrometry
et al.	et alia (and others)
Et_2O	Diethyl ether
FIrpic	Bis[2-(4,6-difluorophenyl)pyridinato-C2,N](picolinato)iridium(III)
FPT	Freeze-pump-thaw
HATCN	1,4,5,8,9,11-Hexaazatriphenylenehexacarbonitrile

HBL	Hole-blocking layer
HMBC	Heteronuclear multiple-bond correlation spectroscopy
HOMO	Highest occupied molecular orbital
$HP(^tBu)_3{}^+BF_4{}^-$	Tri-*tert*-butylphosphonium tetrafluoroborate
HRMS	High resolution mass spectrometry
HSQC	Heteronuclear single-quantum correlation spectroscopy
IC	Internal conversion
IQE/η_{in}	Internal quantum efficiency
ISC	Inter-system crossing
ITO	Indium tin oxide
k_{ISC}	Rate of intersystem crossing
k_{nr}	Non-radiative rate constant
k_p	rate constant of phosphorescence
k_r	Radiative rate constant
k_{sq}	Self-quenching rate constant
LANL2DZ	Los Alamos National Laboratory 2-double-zeta basis set
LC	Ligand-centred
LEEC	Light-emitting electrochemical cell
LMCT	Ligand to metal charge transfer
L_P	Luminous power
LUMO	Lowest unoccupied molecular orbital
MC	Metal-centred
mCBP	3,3-di(9H-carbazol-9-yl)biphenyl
mCP	1,3-Bis(N-carbazolyl)benzene
Mebib	1,3-bis(1-methyl-benzimidazol-2-yl)benzene
Mebip	2,6-bis(1-methyl-benzimidazol-2-yl)pyridine
MeCN	Acetonitrile
MLCT	Metal to ligand charge transfer
MMLCT	Metal-metal to ligand charge transfer
NaO^tBu	Sodium-*tert*-butoxide
NBu_4Br	Tetra-n-butylammonium bromide
NEt_3	Triethylamine
NHC	N-heterocyclic carbon
NIR	Near-infrared
NOESY	Nuclear overhauser effect spectroscopy
NPB	N,N'-Di(1-naphthyl)-N,N'-diphenyl-(1,1'-biphenyl)-4,4'-diamine
OLED	Organic light emitting diode
OTf	Triflate
OXD-7	1,3-bis[2-(4-tert-butylphenyl)-1,3,4-oxadiazo-5-yl]benzene
$Pd(PPh_3)_2Cl_2$	Bis(triphenylphosphine)palladium(II) dichloride
$Pd(PPh_3)_4$	Tetrakis(triphenylphosphine)palladium(0)
PDT	Photodynamic therapy
phen	Phenanthroline
$PhICl_2$	Iodobenzenedichloride
PL	Photoluminescence
PLQY	Photoluminescence quantum yield
PMMA	Poly(methylmethacrylate)

PO15	2,8-bis(diphenylphosphoryl)dibenzothiophene
PO-T2T	2,4,6-Tris[3-(diphenylphosphinyl)phenyl]-1,3,5-triazine
PPh_3	Triphenylphosphine
ppy	Phenylpyridine
PS	Polystyrene
PVK	Poly(9-vinylcarbazole)
RISC	Reverse intersystem crossing
RT	Room temperature
S_0	Singlet ground state
sh	shoulder
S_n	N^{th} singlet excited state
S_N2	Nucleophilic substitution
SOC	Spin-orbit coupling
T_0	Triplet ground state
T2T	2,4,6-Tris(biphenyl-3-yl)-1,3,5-triazine
TADF	Thermally activated delayed fluorescence
TAPC	4,4’-Cyclohexylidenebis[N,N-bis(4-methylphenyl)benzenamine]
TAZ	3-(Biphenyl-4-yl)-5-(4-tert-butylphenyl)-4-phenyl-4H-1,2,4-triazole
^tBu	*tert*-butyl
TCTA	4,4’,4”-tris(N-carbazolyl)triphenylamine
TD-DFT	Time-dependent density functional theory
TFA	Trifluoroacetic acid
THF	Tetrahydrofuran
thpy	2-(2-thienyl)pyridine
TmPyPB	1,3,5-Tri(m-pyridin-3-ylphenyl)benzene
T_n	Nth triplet excited state
TPBI	2,2’,2”-(1,3,5-benzenetriyl)tris(1-phenyl-1-H-benzimidazole)
TPBP	Tetraphenyltetrabenzoporphyrin
TPD	N,N’-Bis(3-methylphenyl)-N,N’-diphenylbenzidine
TrisPCZ	9-Phenyl-3,6-bis(9-phenyl-9Hcarbazol-3-yl)-9H-carbazole
TSBPA	4,4'-(Diphenylsilanediyl)bis(N,N-diphenylaniline)
TTA	Triplet-triplet annihilation
VTE	Vacuum thermal evaporation
WOLED	White organic light emitting diode
η_C	Viewing direction efficiency
η_p	Luminous power efficiency/luminosity
λ_{max}	Wavelength maximum
λ-NPD	λ-N,N'-Bis- (1-naphthalenyl)-N,N'-bis-phenyl-(1,1'-biphenyl)-4,4'-diamine
τ_{aer}	Aerated lifetime
τ_{deg}	Degassed lifetime

Table of contents

1. General Introduction

The role of transition metals such as Pt^{II} and Ir^{III} in luminescent complexes for applications such as OLEDs[1,2,3,4,5], photodynamic therapy (PDT) agents[6,7,8,9,10] and sensors[11,12,13,14] has gained significant standing in the past few years. Perhaps the most widely recognised luminescent Ir complex is $Ir(ppy)_3$, where ppy is 2-phenylpyridine, which was discovered to have excellent photoluminescent properties in dilute solution.[15] Pt compounds have been rather less well studied but offer a range of intriguing properties owing to their d^8 electron configuration which can result in square planar geometries. This can allow for structural distortion, as well as intermolecular interactions which can impact upon the subsequent luminescence properties of Pt^{II} complexes, opening up a vast array of exciting structure-property relationships.

1.1 Luminescence in metal complexes

1.1.1 What is luminescence?

Luminescence describes the excitation and subsequent relaxation of electrons in molecules back to the ground state to give out radiation in the form of light. The two main classes of photoluminescence are fluorescence and phosphorescence.

Fluorescence occurs when an excited state of a molecule returns rapidly to the ground state with emission of a photon via a spin-allowed transition i.e. $\Delta S = 0$. This could for example be the transition from the first excited singlet state to the ground state ($S_1 \rightarrow S_0$). Fluorescence usually occurs when higher vibrational excited states of either S_1 or S_2 are populated followed by internal conversion (IC) and subsequent rapid relaxation to the lowest vibrational level of S_1. This process of IC is non-radiative and usually takes place in 10^{-12} s or less.[10] Emission may occur to a higher vibrational level of the electronic ground state, which then quickly reaches thermal equilibrium.

Phosphorescence, on the other hand, is the emission of light via a non-spin-allowed transition, i.e. $\Delta S \neq 0$. In organic molecules for example, transitions from the triplet excited state to the ground state are formally spin-forbidden. Consequently, emission rate constants are low and radiative lifetimes are typically on the order of milliseconds to seconds.

A Jablonski diagram, first proposed in 1935 by Alexander Jablonksi, is used to represent the radiative and non-radiative processes through absorption and emission via either

fluorescence or phosphorescence.[16] A typical Jablonski diagram is shown in Figure 1.1. The ground, first and second electronic singlet states are depicted by S_0, S_1 and S_2, respectively. At each electronic energy level, the fluorophores can exist in several vibrational energy levels. Transitions between states are depicted as vertical lines to illustrate the instantaneous nature of light absorption, dashed lines are used to represent non-radiative processes such as IC, inter-system crossing (ISC) and vibrational relaxation.

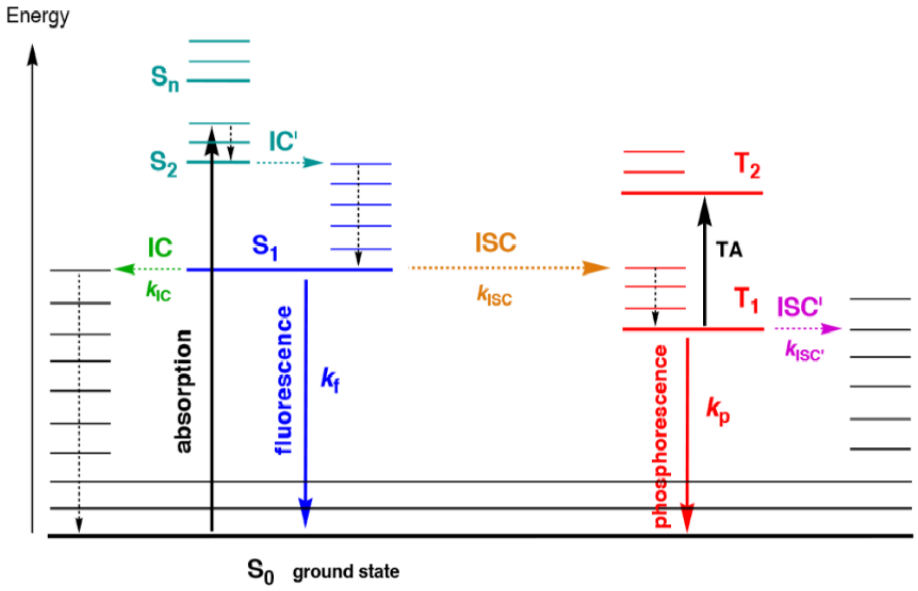

Figure 1.1: *A Jablonksi diagram showing the vibrational levels for absorption, non-radiative decay and luminescence via either fluorescence or phosphorescence.*

The molecular orbitals in metal complexes are described loosely as metal-centred or ligand-centred. There are four main electronic transitions to describe the excited state: metal-centred (MC), ligand-to-metal charge transfer (LMCT), metal-to ligand charge transfer (MLCT) and ligand-centred (LC) (Fig. 1.2). The relative energies of the orbitals within the complex and hence the energies of the transitions will depend greatly on the identity of the metal, its oxidation state and the identity of the ligands. Density functional theory (DFT) is often employed to calculate the energies of the highest occupied molecular orbital (HOMO) and lowest unoccupied molecular orbital (LUMO) levels within complexes to determine the energies of each transition, in addition to predicting the contribution of each ligand and metal to these transitions.

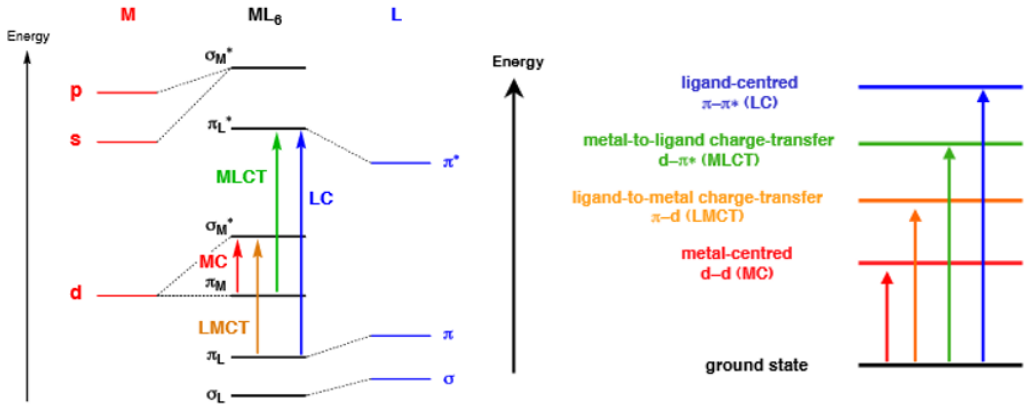

Figure 1.2: *Diagrams showing the energy levels of molecular orbitals between which the excitations occur for an arbitrary metal complex (left) and the relative energies of these resulting transitions on an energy level diagram in which the ground state is represented as having E=0 (right).*

1.1.2 The efficiency of luminescence in metal complexes

The efficiency of luminescence is quantified by the quantum yield, ϕ_{lum}, or the ratio between the number of photons absorbed versus those emitted in a molecule. This can also be referred to as the photoluminescence quantum yield (PLQY). The assumption that the emissive state is formed with unitary efficiency leads to the PLQY being determined by equation 1. Luminescence in metal complexes is favoured by a high radiative rate constant, k_r, of the emissive state and by a low rate of non-radiative decay, k_{nr}, which are also defined below (equations 2 and 3). The luminescence lifetime, τ, is defined as the reciprocal of the experimentally determined rate constant of decay.

$$\varphi_{lum} = \frac{k_r}{k_r + k_{nr}} \qquad (1)$$

$$k_r = \varphi\tau^{-1} \qquad (2)$$

$$k_{nr} = k_r(\varphi^{-1} - 1) \qquad (3)$$

Suppression of k_{nr} is key to achieving efficient phosphorescence and there are two main strategies to achieve this.

1. Decreasing the degree of structural distortion in the excited state relative to the ground state.
2. Destabilisation of potentially deactivating MC excited states.

Pt^{II} complexes with d^8 electron configuration normally adopt a square planar arrangement. This geometry offers the greatest stabilization according to the ligand field theory, since the highest energy orbital d_{x2-y2} remains unoccupied. However, this vacant coordination site renders the excited state more flexible and prone to reorganisation which can promote k_{nr}.

The Huang-Rhys factor *S* quantifies the structural distortion of a molecule in going from its ground to excited state.[17] When *S*=0 there is no structural distortion and a sharp single peak is observed in the emission spectrum corresponding to the 0-0 transition. With increasing structural distortion, a vibronic progression is observed in the emission spectrum (Fig. 1.3). The relative intensities of the 0-0 transition and the first vibronic peak 1-0 are given by the equation below.

$$S = \frac{I_{1-0}}{I_{0-0}} \qquad (4)$$

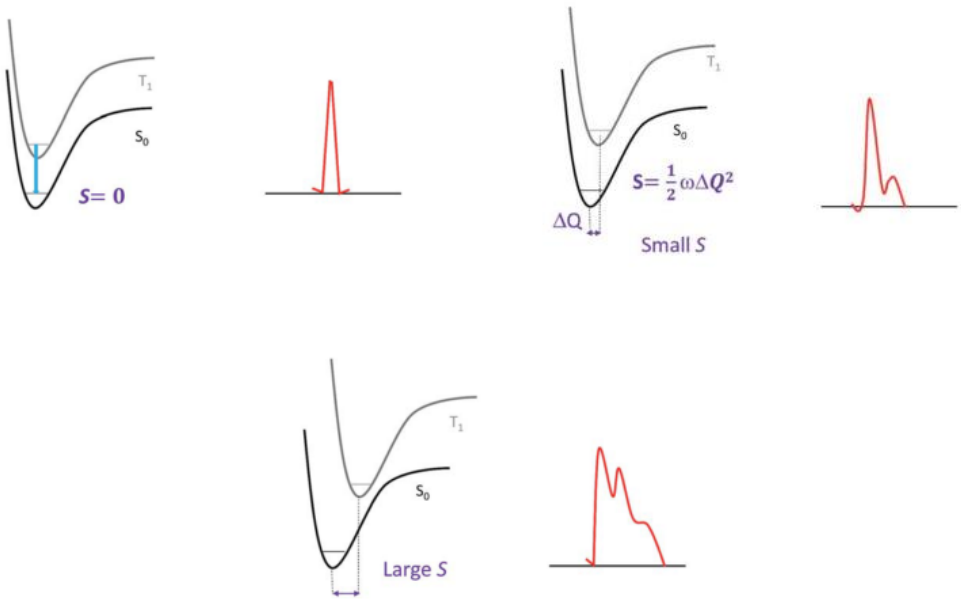

Figure 1.3: *Correlations between the structural distortion of the triplet excited state with respect to the ground state and the emission spectrum. Reproduced from Li et al. by permission of the Royal Society of Chemistry.* [18]

Another approach to reduce k_{nr} comes from increasing the energy of the MC ^{3}d-d states to well above that of the emitting triplet excited state. These MC d-d states contain antibonding orbitals and serve to decrease the Pt-L bonding character which allows non-radiative decay via severe distortion in the excited state. The use of strong field ligands such as C-deprotonated cyclometallated ligands can help to achieve this.

1.1.3 Effect of cyclometallation on excited states

Cyclometallation involves the binding of a polydentate ligand to a metal via a covalent metal–carbon bond, whilst other bonds to the metal from heteroatoms such as nitrogen can be classed as being of a more coordinate nature. There is a net deprotonation of the aromatic C–H upon binding, hence cyclometallating ligands are anionic. Examples include the bidentate 2-phenylpyridine (ppyH) and tridentate 1,3-di(2-pyridyl)benzene (dpybH). The C^- ligating ion is a very strong σ-donor whereas the pyridyl group is a good π-acceptor. As a result, these ligands offer the metal ion a very strong ligand-field. They cause large d orbital splitting and raise the d_{x2-y2} orbitals to higher energy than the anti-bonding ligand π* orbital(s).[19] This minimises the undesirable non-radiative d-d transition and improves the phosphorescence quantum efficiency. The involvement of the metal in the electronic transitions is essential in promoting the formally forbidden phosphorescent emission where the excited states are classified as having MLCT character.[20] Usually in cyclometallating complexes, however, the ligand and metal are heavily mixed in the HOMO hence they are assigned a more mixed MLCT/LLCT character.

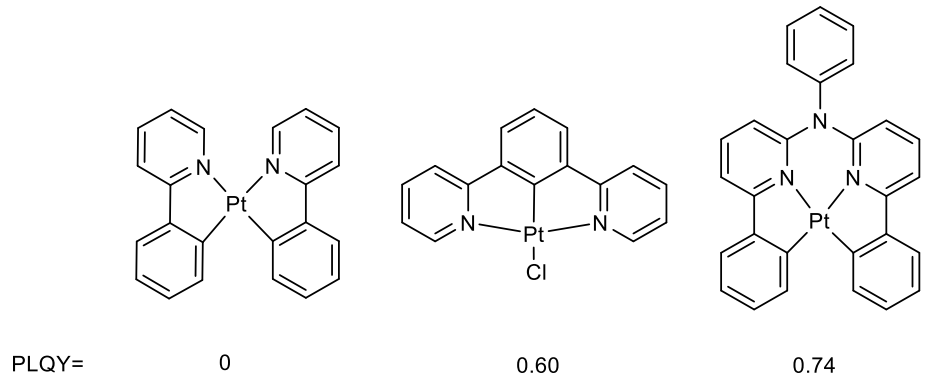

Figure 1.4: *Increasing rigidity across complexes of bidentate,[21] tridentate[20] and tetradentate[22] ligands (left to right) and their corresponding φ values.*

Generally, an increase in complex rigidity might be expected to arise from an increase in the number of binding sites in the cyclometallating ligand from bidentate to tetradentate (Fig. 1.4). This increase in rigidity helps to inhibit non-radiative decay such as vibrational deactivation and promote efficient luminescence. For example, rigidity usually increases in the order of bidentate < tridentate < tetradentate complexes. Hence, there are many examples of cyclometallated tetradentate ligands in different transition metal complexes which are currently under investigation for use within OLEDs owing to their impressive

photophysical properties, a result of strongly rigidified complex structures with high energy d-d states.[22, 23, 24,25,26]

On the contrary, investigation into many bis-cyclometallated platinum complexes with bidentate ligands has shown that their potential for application in OLED devices is rather limited owing to their poor photophysical characteristics and inadequate thermal stability.[21,27] The complex *cis*-Pt(ppy)$_2$ was found to be nearly non-emissive at room temperature (RT) whilst Pt(thpy)$_2$ (Hthpy = 2-(2-thienyl)pyridine) was emissive at RT yet was unstable toward sublimation and consequently unsuitable for the vapour deposition process used in OLED manufacture.

The lack of RT phosphorescence and thermal stability for these bis-bidentate complexes is at least partially attributed to the lack of rigidity and D_{2d} distortion.[28,29,30] The design of a more rigid complex structure could help to improve the emission efficiency and for this reason tri- and tetradentate ligands are potentially highly attractive.

1.2 *Inter*- and *intra*molecular interactions in Pt^{II} complexes

As mentioned previously, one of the ways in which Pt^{II} complexes differ from those of other metals such as Ir^{III} is that they are normally 4-coordinate square-planar as opposed to 6-coordinate octahedral. Aside from the structural distortion which can negatively impact upon the luminescence of the compound, this geometry can also introduce the possibility of interactions between complexes which often play an important role in their photophysical behaviour. These interactions may involve π-π stacking between ligands, π-d interactions between one filled $5d_{z2}$ Pt orbital and a π orbital on the ligand, d-d interactions between $5d_{z2}$ orbitals on the metal, or a combination of these.

In terms of Pt···Pt interactions, for complexes containing only one metal centre (mononuclear Pt^{II} complexes) interactions are present between individual molecules and so are classed as *intermolecular* interactions. In complexes containing two or more distinct Pt^{II} units that are covalently bound (multinuclear Pt^{II} complexes), some interactions can potentially also occur between the units within the molecule and are classed as *intramolecular*. For complexes containing two metals of the same type, the term dinuclear is used, whilst if two different metal sites are present, these complexes are classed as bimetallic.

These interactions can occur in the ground state, leading to dimers or aggregates, or in the excited state, leading to excimers, or both. Aggregates and excimers may display different

emission properties. They are typically red-shifted from those of the isolated monomers, due to the stabilisation that arises when two Pt^{II} units are brought into close contact.

The face-to-face interaction between two Pt^{II} atoms splits the occupied $5d_{z2}$ and unoccupied $6p_z$ atomic orbitals to give filled dσ and dσ* and unfilled pσ and pσ* molecular orbitals.[31] Configuration interaction with MOs of the same symmetry formed by overlap of the vacant 6_{pz} orbitals results in stabilisation of the $5d_{z2}$ MOs, decreasing the total energy leading to a red-shift in energy (Fig. 1.5).[32]

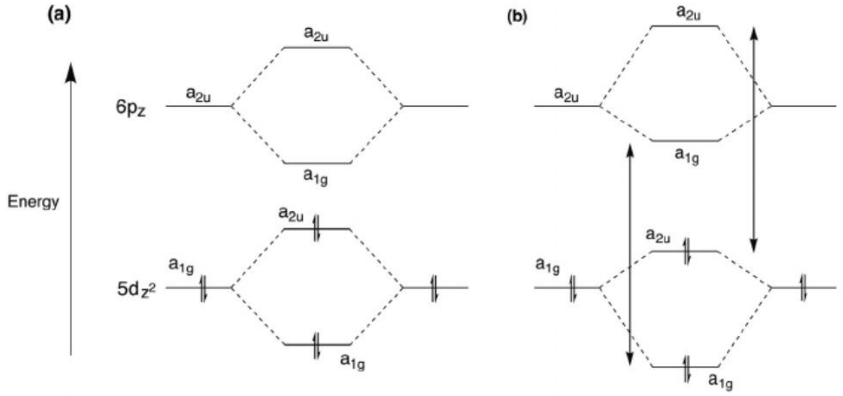

Figure 1.5: *a) MO diagram showing the occupation of the $5d_{z2}$ orbitals without considering the configuration interaction and b) stabilisation of the $5d_{z2}$ orbitals due to the configuration interaction. Reproduced from Puttock et al. by permission of Elsevier.*[32]

When aromatic ligands are involved, they provide additional π and π* orbitals which allow electronic transitions of MMLCT (metal-metal to ligand charge transfer) character. These transitions are seen to have a smaller HOMO-LUMO gap and hence can explain why the absorption and emission are typically red-shifted. Moreover, it also gives the possibility of π→π* transitions which could also account for the lower energy emission (Fig. 1.6).

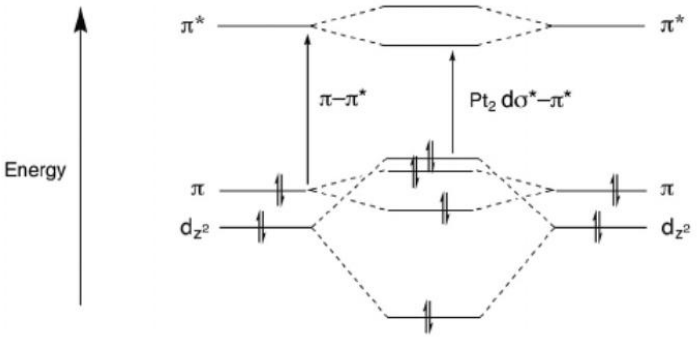

Figure 1.6: *MO diagram to show the involvement of aromatic ligands with π orbitals. Reproduced from Puttock et al. by permission of Elsevier.*[32]

1.3 Organic light emitting diodes (OLEDs)

As alluded to earlier, one of the main applications in which luminescent Pt^{II} complexes have been used is OLEDs. OLEDs have become of increasing interest since the first report of such a device in 1987 by Tang and Van Slyke.[33] They have potential applications as a new generation of display and lighting technology. The energy efficiency of traditional light bulbs and lighting devices is very low. Lighting accounts on average for over 20 % of the world's electricity consumption, giving rise to high carbon emissions.[34] OLEDs are much more energy efficient than traditional light sources such as incandescent bulbs and could consequently reduce the world's carbon emissions significantly. Moreover, for display technologies, they do not require a backlight, give higher colour purity and offer improved viewing angles in comparison to LED TVs.[35,36]

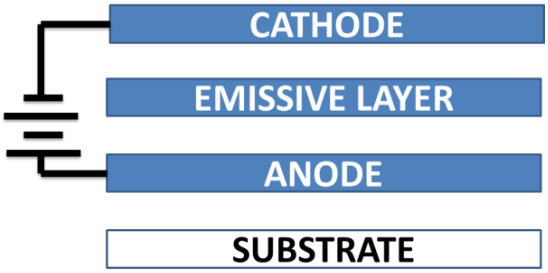

***Figure 1.7**: Simplified schematic of a single-layer OLED.*

OLEDs can be in single-layer or multi-layer devices. In a single-layer device, OLEDs contain two electrodes with a single emitting layer (EML) sandwiched in between (Fig. 1.7). The EML is usually made up of an organic material such as a polymer e.g. poly(p-phenylenevinylene) or a small molecule such as tris(8-hydroxyquinolinato)aluminium (Alq_3).[37,38,39] A voltage is applied across the device making the anode positive with respect to the cathode. A current of electrons flows through the device from cathode to anode and electrons are injected into the LUMO of the organic layer at the cathode and withdrawn from the HOMO at the anode. The resulting holes and electrons that are formed can recombine through electrostatic forces to form an exciton. The decay of this exciton results in a relaxation of the energy levels, accompanied by emission of radiation via *electroluminescence* whose frequency depends on the HOMO-LUMO gap of the material (Fig. 1.8).

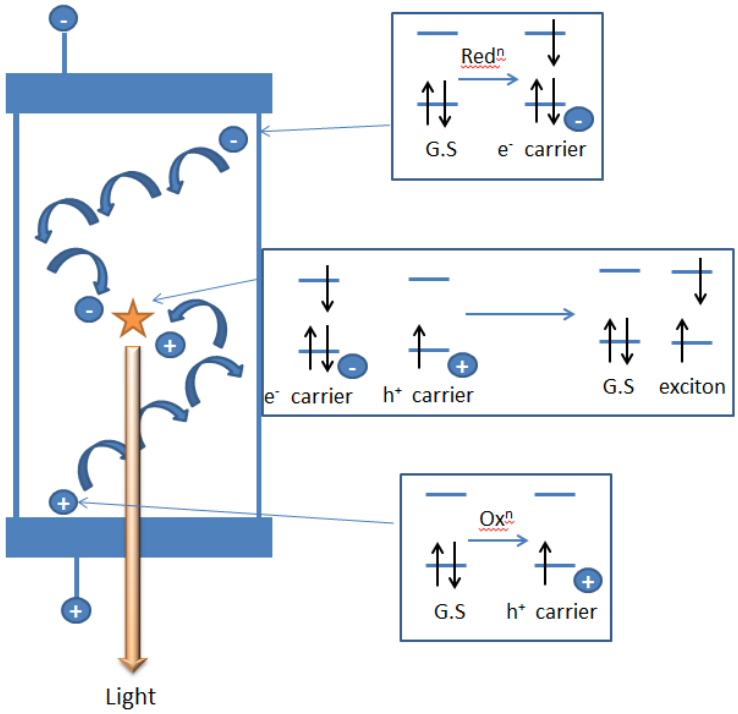

***Figure 1.8**: Schematic representation of electroluminescence where G.S represents the ground state.*

These excitons can emit from either the singlet or triplet state. Statistically, in electroluminescence the triplet to singlet exciton formation is 3:1, irrespective of spin orbit coupling (SOC) and the rate of intersystem crossing (k_{ISC}). Electroluminescence thus differs from photoluminescence, where the amount of triplet excited state formation in a molecule can be anything from 0 to 100 % according to the magnitude of k_{ISC} versus other processes open to the singlet state (i.e. non-radiative decay etc.).

Transitions from triplet excited states to the singlet ground state are formally spin-forbidden, therefore only the singlet states, about 25 % of total excitons generated in the OLED during electroluminescence, can be harvested with the use of a fluorescent emitter (excluding thermally activated delayed fluorescence (TADF) emitters). Phosphorescent emitters such as Pt^{II} complexes, on the other hand, can harness both singlet and triplet excitons and theoretically maximise the internal quantum efficiency (IQE) of devices to 100 % when incorporated into an EML.[11] RT phosphorescence emitted from many transition metal complexes is attributed to the large SOC constants of these metals, which enables an efficient singlet-triplet ISC and promotes the rate constant of phosphorescence (k_p).

Exciton-quenching processes close to the electrodes or non-radiative recombination of charges at the electrodes can occur and reduce the efficiency of devices. To combat this,

other layers are introduced to form a multi-layer device. In these devices incorporation of hole- and electron-transport and blocking layers facilitate charge injection and enhanced recombination of electrons and holes in the EML to improve the efficiency of devices.[40,41,42]

1.3.1 Efficiencies

The efficiency of an OLED is defined by both the internal and external quantum efficiencies, IQE and EQE respectively. The IQE (η_{int}) can theoretically reach up to 100 % and is defined as the ratio of the total number of photons produced within the device to the number of electrons injected.[43] Similarly, but with a subtle key difference, the EQE (η_{ext}) is defined as the ratio of the number of photons emitted by the OLED into the viewing direction, or the viewing direction efficiency (η_C), to the number of electrons injected. The two parameters can thus be connected by the equation given below:[44]

$$\eta_{ext}(\lambda) = \eta_{int}(\lambda)\eta_C \quad (5)$$

The luminous efficiency measured in cd/A is a key term used to describe the efficiency of an OLED for display applications. It is very similar to η_{ext} but differs as the incident photons from the device are weighted according to the *photopic* response from the eye i.e. how sensitive the eye is to certain colours, whilst η_{ext} counts all photons as equal. The luminous efficiency is given by the following equation:

$$\eta_L = \frac{AL}{I_{OLED}} \quad (6)$$

where L is the luminance of the OLED in cd/m^2 and A is the device active area (not always equal to the area of light emission, owing again to the photopic response factor).

The luminous power efficiency or luminosity (η_p) is measured in lm/W. It is defined as the ratio of the luminous power emitted in the forward direction (L_P) to the total electrical power required to drive the OLED at a given voltage. The equation below shows the relationship between these variables:

$$\eta_P = \frac{L_P}{I_{OLED}V} \quad (7)$$

1.3.2 Processing methods

The processing methods for OLED fabrication have developed significantly over the past few years and range from physical vapour deposition methods to condensed phase techniques.[45] The processing methods are tailored to the type of device structure i.e. multi-layer/single-layer devices and to the types of polymer/small molecules within these layers. The two main processing techniques that will be discussed in this thesis are limited to vacuum thermal evaporation (VTE) and solution-processing, but many other techniques including inkjet printing and organic vapour phase deposition are also currently employed in many commercial OLED fabrications.[46]

VTE involves heating the compounds for deposition under vacuum to temperatures ranging from 100 to 500 °C in crucibles (Fig. 1.9). This induces evaporation of the compounds onto substrates. The material must pass through a shadow mask which protects the substrate and allows one third of all pixels to be deposited before it moves and allows deposition of the next set of pixels. VTE enables the formation of homogeneous layers, promoting ease of multi-layer device fabrication. The main drawback with this technique is the high cost of vacuum equipment and the shadow masks which are heavy, hard to clean and sometimes hard to obtain precise alignment for the deposition of pixels.

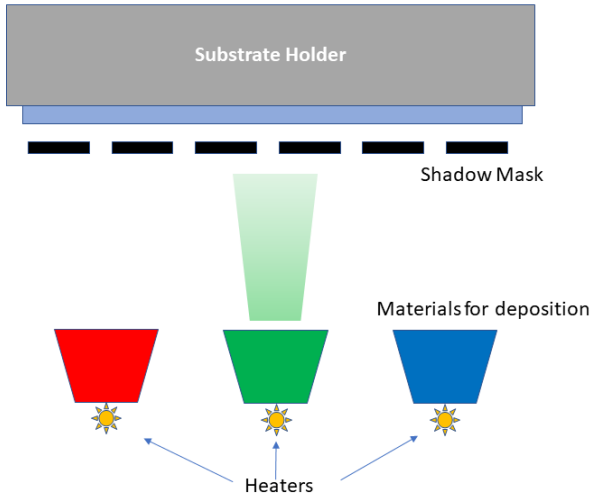

Figure 1.9: *Schematic of VTE in OLED fabrication.*

Solution-processing utilises volatile solvents such as chlorobenzene to apply the material to a substrate. The solvent evaporates and leaves behind a thin film of material via techniques such as spin-coating. Solution-processing is becoming more widely used but is still limited by the lower control over film quality and more complicated route to multi-layer devices in comparison to VTE.

1.3.3 OLED development

The development and efficiency of OLEDs has increased significantly over the years for both purely organic and heavy metal-doped devices. TADF molecules were first put to use in OLEDs by Adachi *et al*. in 2012.[47] They removed the maximum barrier for η_{int} of 25 % for purely organic devices via reverse intersystem crossing (RISC) from the lowest energy triplet excited state to the lowest energy singlet excited state which enables utilisation of 100 % of excitons. This has led to a surge of research in the area with multiple papers reporting high EQEs of over 30 % for purely organic TADF molecule-containing devices.[48,49,50]

Consequently, there has been a remarkable effort to improve the efficiency of heavy metal-based devices and a push to achieve purer colour emission for deep blue[51,52] and red colours[53,54], as well as huge efforts towards efficient white organic light emitting diodes (WOLEDs)[55,56,57] which could dramatically reduce the energy consumption for lighting worldwide.

Of particular interest in this thesis is the advancement of red and near-infrared (NIR) emission in Pt^{II} complexes. This has many potential applications including bio-imaging[58,59,60], since skin transparency is at its highest at these wavelengths[61], and OLED lighting where highly efficient OLEDs in the NIR region are currently scarce. This lack of efficient red and NIR emitters mainly stems from the consequences of the energy gap law (EGL) which describes how the deactivation pathway between the lowest lying singlet (S_1) or triplet (T_1) states and the ground state (S_0) can occur by coupling between the zero vibration level of the S_1 (or T_1) state and the higher vibration levels of the S_0 state.[62,63] The smaller the energy gap, the larger this non-radiative process is and consequently red and NIR emission are particularly vulnerable when it comes to poorer efficiencies. One way of achieving deep red and NIR emission is via the formation of Pt excimers as alluded to earlier, and this will be covered in greater detail in the chapters that follow.

A large area of interest to improve efficiency in phosphorescent OLEDs of all emission colours has been in orientation of the emitting dipole[64,65] to surpass the theoretical limit of 25-30 % EQE. The design criteria for horizontally oriented molecules parallel to the substrate has two main points[66,67]:

1) the molecule should be linear
2) the molecule must have bulky terminal units to suppress intermolecular interactions other than crystallisation

It has subsequently been found that highly oriented emitting dipoles (parallel to the substrate) in purely crystalline layers of Pt and Ir complexes can lead to high EQEs of up to 45 %. [68,69,70] Many other research efforts are taking place to improve the design of OLEDs to make them more commercially accessible and the investigation of heavy metal complexes is at the forefront of this research.

2. Pt complexes featuring bidentate triazole and tetrazole ligands

2.1 Introduction

2.1.1 Synthesis of triazole and tetrazole ligands

Azole ligands are increasingly popular in luminescent metal complexes.[71,72,73,74] They can be combined with a heterocycle such as pyridine to give ligands with synergistic strong σ-donating and π-accepting character.[75] Triazoles and tetrazoles are the main focus of this section.

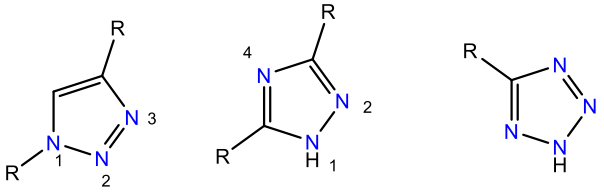

***Figure 2.1**: 1,2,3-triazole, 1,2,4-triazole and tetrazole structures.*

Triazoles are defined as any five-membered ring containing three nitrogen atoms and can exist as either 1,2,3-triazoles or 1,2,4-triazoles as shown in Fig. 2.1. They were first discussed by Bladin in 1895[76] and have since made significant contributions in agriculture[77,78,79], medicine[80,81,82] and, as will be discussed, photoactive devices. In tetrazoles there are four nitrogen atoms in the five-membered ring. They have similar attributes to triazoles but are more prone to instability as they are more electron rich and can generate two moles of N_2 per molecule. This can subsequently limit their usage in many applications.

1,2,3-Triazoles are typically accessed via either the Huisgen azide-alkyne 1,3-dipolar cycloaddition[83] or the copper-catalysed azide-alkyne cycloaddition (CuAAC) (Scheme 2.1).[84] The CuAAC method is favourable as it utilises click chemistry first pioneered by Sharpless in 2001[85] which makes these types of ligands easily accessible with high purity. The 1,2,3-triazole ligands can exist in two main forms: regular and inverse (Fig. 2.2). The regular form is more common and allows coordination to a metal centre via the more electron rich N^3 atom whereas the inverse form is more synthetically challenging and 1,2,3-triazoles coordinate through the less electron rich N^2 position.[86]

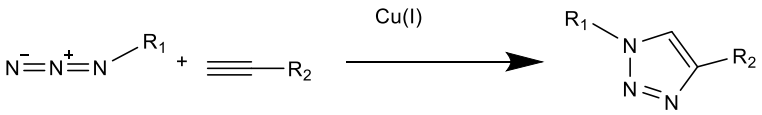

Scheme 2.1: *Copper-catalysed azide-alkyne cycloaddition synthesis.*

1,2,4-Triazoles substituted at the 3 and 5 positions are of particular interest due to the functionality that can be incorporated into the ring which can aid in solubility and influence the luminescent properties of the subsequent complexes that are formed. They can be synthesised via a variety of different methods.[87] During their first years of synthesis, fusion of an aromatic cyanide with an acid hydrazide benzenesulfonate or *p*-toluenesulfonate at 200-250 °C was a popular method.[88] This was succeeded by distillation of an acid hydrazide with an acid amide, known as the *Pellizzari* reaction.[89] Now more modern methods of synthesis are used which include oxidative cyclization of amidines with nitriles or acylhydrazines.[90] One example is from De Cola *et. al.*[91] shown in Scheme 2.2 where formation of the 1,2,4-triazole takes place in three main steps:

1. initial reaction of 2-pyridinecarbonitrile with hydrazine monohydrate
2. attack of the resulting amidrazone on an acyl chloride
3. condensation reaction in ethylene glycol at 185 °C to form the triazole

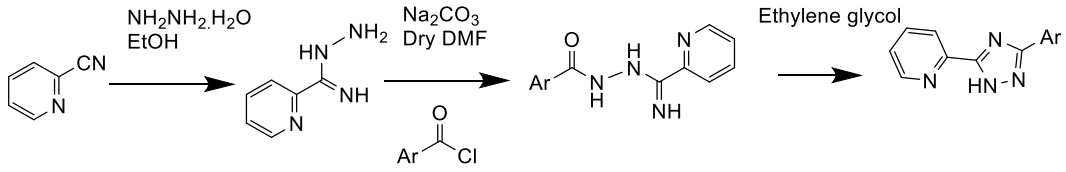

Scheme 2.2: *Three-step synthesis of 1,2,4-triazoles adapted from De Cola et al.*

Tetrazoles are commonly synthesised via the 1,3-dipolar cycloaddition of a carbonitrile with sodium azide (NaN_3) in the presence of ammonium chloride (NH_4Cl) as a buffer (Scheme 2.3).[92] This is another example of click chemistry and is followed in this project.

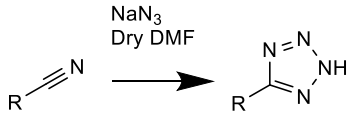

Scheme 2.3: *Tetrazole synthesis via 1,3-dipolar cycloaddition.*

2.1.2 Binding modes of bidentate triazole and tetrazole ligands in complexes

Both classes of triazole, and the tetrazoles, can be combined with pyridine to form bidentate ligands for metals such as Pt^{II}. Depending upon the coordination mode, these ligands can be analogous to the archetypal bipyridine (bpy) ligand via binding through both

neutral N atoms or they can bind via a neutral N atom on the pyridine and a deprotonated N atom on the triazole/tetrazole to form a *pseudo-cyclometallating* ligand like the archetypal phenyl pyridine (ppy) (Fig. 2.2).

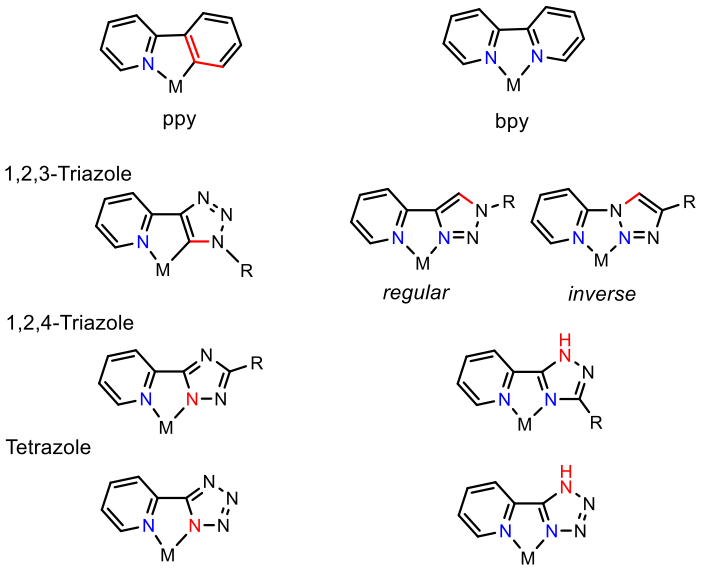

Figure 2.2: *Different modes of coordination in 1,2,3-triazole, 1,2,4-triazole and tetrazole complexes where blue indicates neutral coordination and red indicates anionic/potentially anionic coordination.*

Many examples of bidentate luminescent azolate complexes have been synthesised in the past few decades and this review will focus primarily on triazole and tetrazole Pt^{II} complexes, together with some examples that combine these ligands with Ir^{III}.

2.1.3 Pt complexes containing bidentate cyclometallating ligands

2.1.3.1 Pt(N^C)$_2$ complexes

Firstly, it is important to set the scene with the development and current standing of cyclometallated Pt(N^C)$_2$ complexes containing bidentate ligands which can be used as a platform for comparison with triazole and tetrazole pseudocyclometallating analogues that will be discussed. Homoleptic complexes, namely *cis*-[Pt(ppy)$_2$], *cis*-[Pt(thpy)$_2$] and *cis*-[Pt(bhq)$_2$], (where ppy= 2-phenylpyridine, thypy= 2-(2-thienyl)pyridine and bhq= benzo(h)quinoline), were first prepared over 20 years ago (Fig. 2.3).[21,27] It was only *cis*-[Pt(thpy)$_2$] that showed any RT emission, giving an impressive PLQY of 36 % whilst the others were virtually non-emissive at RT and only displayed emission at 77 K with lifetimes on the µs timescale.

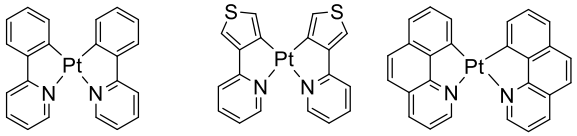

1 **2** **3**

Figure 2.3: *Structures of cis-[Pt(ppy)$_2$] (**1**), cis-[Pt(thpy)$_2$] (**2**) and cis-[Pt(bhq)$_2$] (**3**).*

2.1.3.2 Pt[(N^C)(HC^N)(Cl)] Complexes.

Complexes containing chloride ligands are expected to be only weakly emissive at RT due to their low ligand field strength. This was demonstrated through the photophysical properties of $[Pt(ppy)Cl_2]^-$ investigated by Kvam *et al*. which showed no emission at RT but highly structured emission at 77 K with a quantum yield of 0.9 and lifetime of 15.2 µs in MeOH/H_2O (1:1).[93] It was found that the weak-field splitting of the chloride ligand causes a small energy gap between the lowest emitting ^{3}MLCT state and the upper lying d-d states, which can be thermally populated at RT, and thus quenches the emission. Through the attempted synthesis of many other homoleptic Pt(N^C)$_2$ complexes, came heteroleptic complexes with the general structure Pt[(N^C)(HC^N)(Cl)].[94] These complexes contain one cyclometallating unit, a terminal chloride and neutral N donor ligand.

The structures and luminescence spectra of complexes **4-7** of the form Pt[(N^C)(HC^N)(Cl)] are shown below (Fig. 2.4). Complex **4** emission was studied in detail in an earlier paper and was seen to give emission in solution with λ_{max} of 489, 523 and 555 nm. Lifetimes in toluene solution at 298 K and at 77 K were 640 ns and 11 µs respectively.[95] On comparing complexes **4**-**7** there was an obvious red-shift in the λ_{max} of emission from **6** > **7** > **5** > **4**. Emission from **6** and **7**, which contain electron-donating groups and extended conjugation, was red-shifted significantly in comparison to that from complexes **4** and **5** which contained no substitution or electron-withdrawing substituents on the phenyl rings.

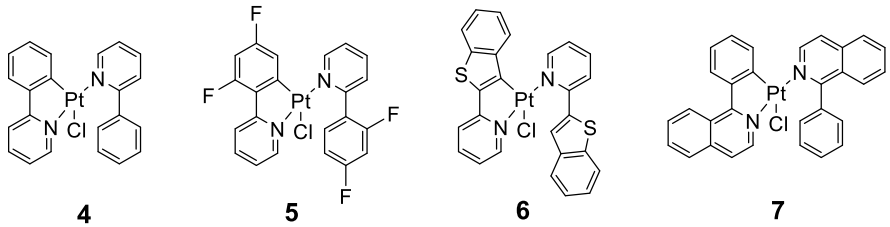

4 **5** **6** **7**

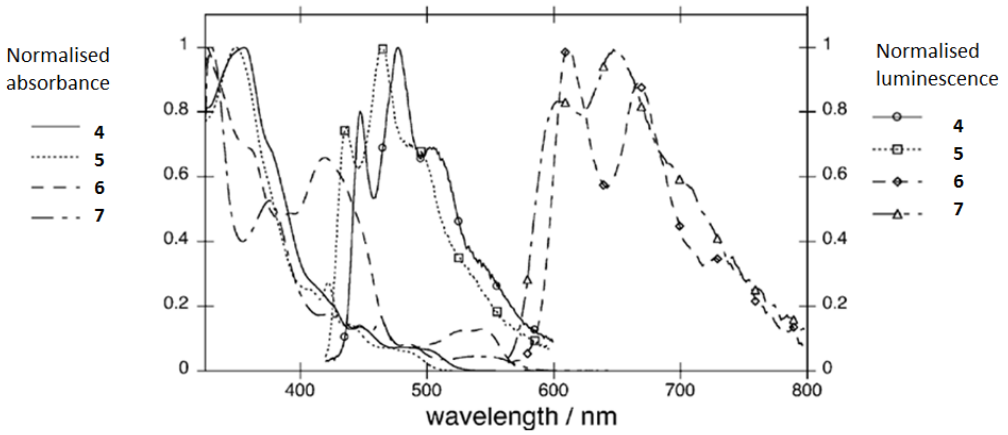

Figure 2.4: *Structures of complexes **4**-**7** and their normalised absorbance and luminescence in DCM. Reproduced from Cho et al. by permission of Elsevier.*[95]

2.1.3.3 $[Pt(N^C)L]^+$ Complexes

Kvam also investigated the photophysical properties of charged heteroleptic complexes; $[Pt(ppy)(en)]^+$ (**8**), $[Pt(ppy)(bpy)]^+$ (**9**) and $[Pt(phen)(bpy)]^+$ (**10**).[93] These complexes contain a cyclometallating unit and a neutral ligand of the form N^N which results in an overall positive charge on the complex. These complexes were found to be emissive at RT where **8**, **9** and **10** had lifetimes and quantum yields of 1.7, 4.0 and 3.5 µs and 5.8, 1.7 and 1.3 % respectively in dimethylformamide (DMF) solution. The combination of strong σ-donating cyclometallating ligands with strong-field bpy and ethylenediamine (en) ligands in these complexes helps to increase the energy gap between MLCT and MC states, giving efficient emission.

2.1.4 Pt complexes containing bidentate azole ligands

The photophysical properties of the Pt complexes containing bidentate azole ligands that are discussed in the following sections are summarised in Table 2.1 at the end of the introductory section of this chapter.

2.1.4.1 1,2,3-Triazole complexes

Despite an increasing amount of research interest on 1,2,3-triazole-containing complexes of transition metals including Ir, Re and Os,[96,97,98] there is very little literature on the photophysical properties of Pt complexes containing 1,2,3-triazoles as bidentate ligands. Kilpin *et al.* synthesised regular and inverse Pt and Pd 1,2,3-triazole complexes **11**-**14** with chloride ancillary ligands (Fig. 2.5). The only electronic spectroscopic data provided was the UV-Vis absorption of the *regular* complexes **11** and **12** which showed LC π-π^* transitions at

279 nm for the Pd complex and 294 nm for the Pt complex. MLCT transitions were observed at 376 and 330 nm for the Pd and Pt complexes respectively.[99]

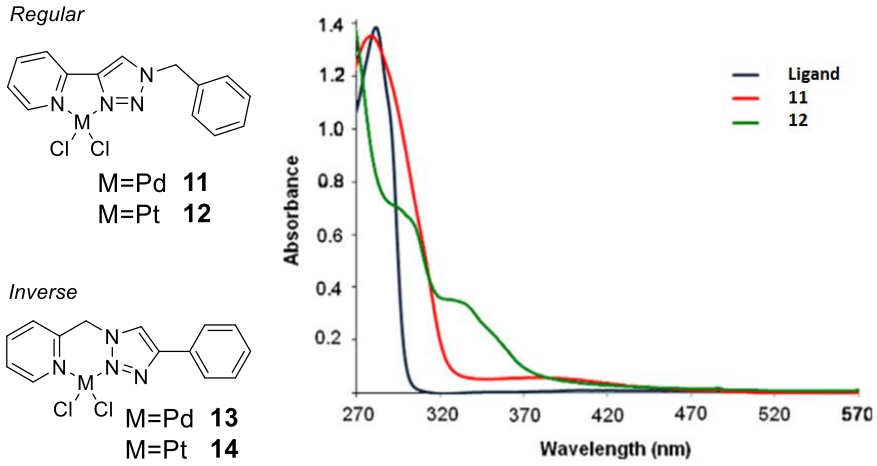

Figure 2.5: *Absorption spectra of regular 1,2,3-triazole complexes **11** and **12** and the corresponding ligand in DMF solution. Reproduced from Kilpin et al. by permission of Elsevier.*[99]

As previously alluded to, work on luminescent Ir complexes containing 1,2,3-triazoles has been more prevalent. Felici *et al.* synthesised a series of luminescent ionic iridium complexes of the form [Ir(X)(Y)(Z)]Cl where X, Y and Z represent different bidentate 1-substituted-4-phenyl-1*H*-1,2,3-triazole cyclometallating ligands (Fig. 2.6).[100] Quantum yields ranged from 7.1 to 25 % and lifetimes ranged from 18 to 34 ns in degassed solutions. The broad emission was assigned as an MLCT excited state of the HOMO-LUMO transition. The figure below shows complex **15** where X = 1-methyl-4-phenyl-1*H*-1,2,3-triazole, Y = 1-adamantyl-4-phenyl-1*H*-1,2,3-triazole and Z = 1-adamantyl-4-pyridyl-1*H*-1,2,3-triazole and it displayed a PLQY of 11 % in acetonitrile (MeCN).

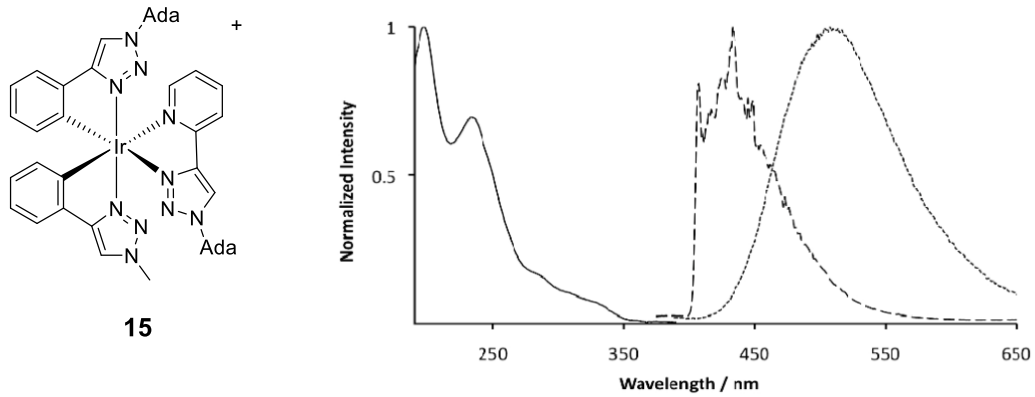

Figure 2.6: *UV-Vis absorption spectrum (solid), RT emission spectrum (dotted) in MeCN of **15** and 77 K emission spectrum (dashed) in glassy butyronitrile matrix (λ_{exc}= 335 nm) where ada = adamantyl. Reproduced from Felici et al. by permission of MDPI.*[100]

2.1.4.2 1,2,4-triazole complexes

Interestingly, there are also relatively few examples of Pt^{II} complexes containing bidentate 1,2,4-triazole ligands that are strongly luminescent in solution and there are fewer examples of these 1,2,4-triazole-containing complexes that have been incorporated into devices.[101] Examples of some Pt^{II} complexes containing bidentate 1,2,4-triazole ligands were prepared by Chang *et al.* in 2006 (Fig. 2.7).[102] The luminescence spectra of **16** and **17** were measured in a degassed tetrahydrofuran (THF) solution at RT; however, the emission was extremely weak with PLQYs lower than 10^{-3} and phosphorescence lifetimes of <10 ns. It was postulated this was due to self-quenching because of the strong tendency for Pt···Pt units to aggregate. Due to the poor solubility of these compounds, concentration-dependent studies could not be performed to elucidate this further, but in vacuum-deposited thin films, moderate to highly intense luminescence was obtained with λ_{max} values of 564 and 544 nm for complexes **16** and **17** respectively.

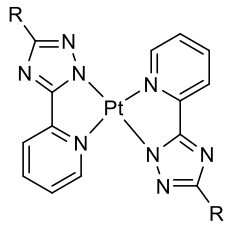

R= ^{t}Bu (**16**); C_3F_7 (**17**)

Figure 2.7: *Structure of Pt^{II} 1,2,4-triazole complexes **16** and **17**.*

Indeed, even changing the binding mode of the ligand does not seem to improve the solution-state properties of these 1,2,4-triazole Pt^{II} bidentate complexes. For example, Strassner *et al*. have recently returned to their investigations on the 'Enders triazole', previously reported by Enders *et al.* in 2003.[103] This compound contains a 1,2,4-triazole ligand which binds through the carbon, as opposed to any of the available nitrogens, as an N-heterocyclic carbene (NHC). The Pt complexes **18** and **19** shown in Figure 2.8 display no observable emission in degassed DCM, but when doped at 2 wt. % into a PMMA film give highly efficient sky blue emission with quantum yields of over 80 %.[104] These are rare examples of a 1,2,4-triazole binding as a C^C^{-} ligand and, as of yet, there is no data referring to the electroluminescent performance of these complexes.

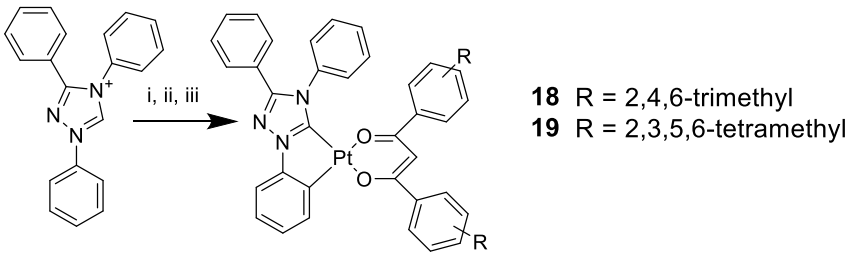

Figure 2.8: *Synthesis of complexes **18** and **19** using the Enders triazole ligand, i) Ag_2O, DMF, 40 °C; ii) Pt(COD)Cl_2, DMF, 3 h at RT, 21 h at 125 °C; and iii) KO^{t}Bu, β-diketone, DMF, 21 h at RT, 6 h at 100 °C.*

In 2009 Li *et al.*[105] reported the Pt^{II} bis[3,5-bis(2-pyridyl)-1,2,4-triazolato] complex (**20**) which remains as one of the few strongly luminescent and soluble examples of a 1,2,4-triazole Pt complex containing bidentate ligands that is suitable for OLED incorporation in the literature to date (Fig 2.9). It was synthesised by refluxing two equivalents of 3,5-bis(2-pyridyl)-1,2,4-triazole with one equivalent of *cis*-bis(benzonitrile)$PtCl_2$ in pyridine/acetone under nitrogen for three days. The crystal structure of the complex showed columnar stacks stabilized via strong intermolecular interactions with Pt···Pt distances of 3.289 Å. These short distances could help to explain the formation of excimers which were present in both the photoluminescence (PL) and electroluminescence (EL) spectra. The amount of excimer formation was dependent upon either the concentration of the thin film or the dopant concentration within the EML of the OLED. OLEDs were fabricated by sequential thermal evaporation with the device structure of: glass / ITO / NPB (40 nm) / x % **20** : CBP (25 nm) / TPBI (30 nm) / Mg:Ag, 1:10 (200 nm) (Table 2.1). Doping levels of x = 5–10 % gave optimal EL efficiency and white colour coordinates resulting from simultaneous monomer and excimer emissions. The peak power and luminous efficiencies obtained were 9.8 lm/W and 14 cd/A, respectively, whilst the peak EQE was 6.6 %.

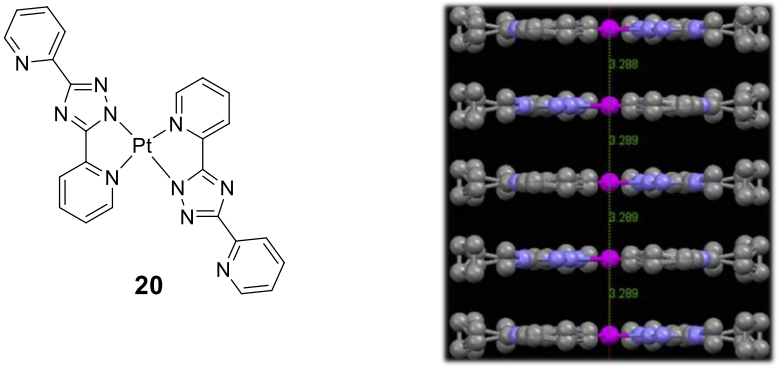

Figure 2.9: *Molecular structure of **20** and the columnar stacks formed, stabilised by strong intermolecular interactions. Reproduced from Li et al. by permission of Elsevier.*[105]

As implied earlier, there are also examples of Ir complexes with azole ligands giving different properties to those offered by Pt. A detailed study into Ir^{III} complexes containing (4'-substituted-2'-pyridyl)-1,2,4-triazole ligands has been conducted by Park *et al.* to obtain highly desirable deep blue emission.[106] The synthesis of the 1,2,4-triazole ligands was achieved by a [2 + 3] cycloaddition reaction of substituted 2-pyridylnitriles where R=CH_3 and OCH_3 with trifluoroacetic acid hydrazide (Scheme 2.4). Subsequent reactions to afford complexes **21** and **22** (Fig. 2.10) included formation of the Ir chloro-bridged dimer which was then cleaved with the appropriate triazole ligand.

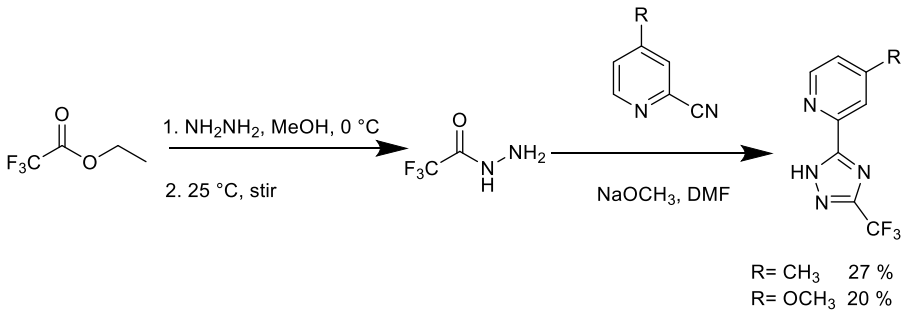

Scheme 2.4: *Synthesis of selected 1,2,4-triazole ligands used in the synthesis of complexes* ***21*** *and* ***22****.*

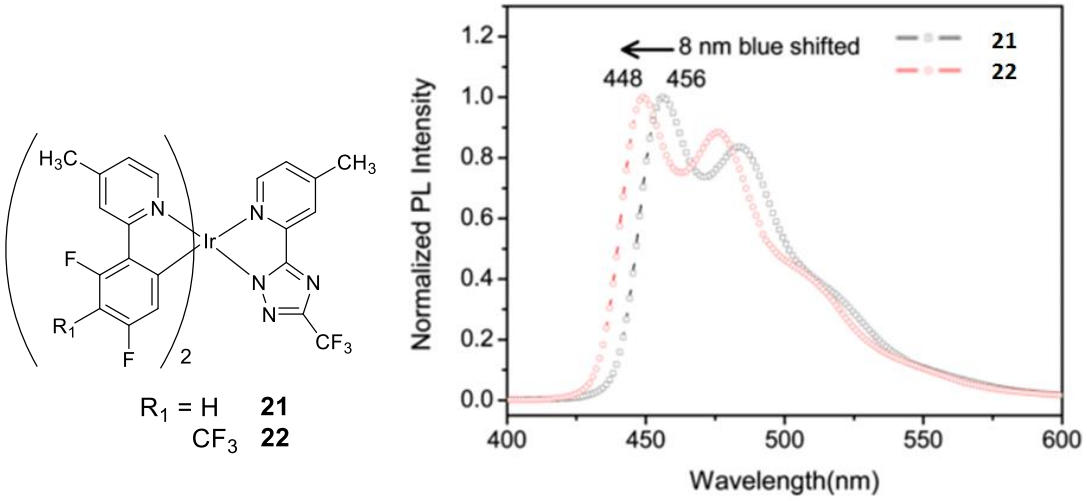

Figure 2.10: *Emission of complexes* ***21*** *and* ***22.*** *Reprinted with permission from Park et al.*[106] *Copyright 2013 American Chemical Society.*

Depending upon the R groups on both the N^C ligand and the triazole ligand, the emission maxima ranged from 448 to 464 nm with quantum yields of between 0.20 and 0.42 either in DCM solution or thin film (5 wt. % in PMMA). Electron-donating substituents on the pyridine of the triazole ligand and electron-withdrawing substituents on the difluorophenyl

of the N^C ligand proved to give the bluest emission and complex **22** was thus chosen to be tested in an OLED device (λ_{max} of 448 nm, PLQY= 42 %). This device gave commission internationale de l'Eclairage (CIE) coordinates of (0.15, 0.18) which is extremely close to the 'perfect' deep blue coordinates of (0.15, 0.15) and thus shows the potential of 1,2,4-triazole Ir complexes for colour purity in deep blue OLEDs.

Despite some impressive photophysical properties in the solid-state for some Pt^{II} complexes containing bidentate triazole complexes, solubility issues and poor luminescence efficiency in the solution-state has led to these complexes taking a back seat in terms of OLED fabrication. The current leaders in the field for bidentate Pt^{II} azole complexes as potential OLED dopants are in fact those containing pyrazole ligands. These are seen to show impressive PL and EL properties, a few of which are outlined here.

2.1.4.3 Pyrazole complexes

Kim *et al.* optimised the orientation of the molecular dipole in OLEDs containing the Pt pyrazole complexes **23**-**25** (based on the work by Chang *et al.* in 2006[102]) to give very high EQE values (Fig. 2.11).[107] The maximum EQE obtained was 38.8 % for complex **23** which was incorporated as a neat film for the EML of an OLED.

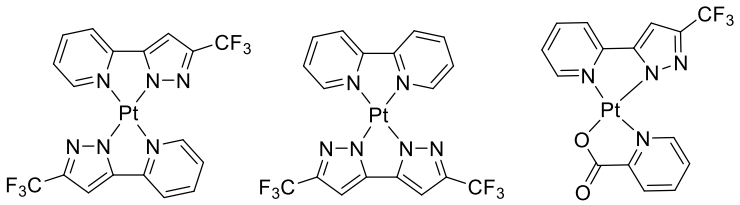

23 **24** **25**

Figure 2.11: *Structures of Pt pyrazole complexes **23**, **24**, and **25**.*

Interestingly, the PL intensities of these complexes in solution were very low, showing largely monomer emission at 10^{-5} M concentrations, however, when measured in a neat thin film, the emission was purely excimeric and gave PLQYs of 96, 43 and 56 % for **23**, **24** and **25** respectively. The emitting dipole orientation of the crystal emitting layers was also found to be largely affected by the position of the CF_3-substituted pyrazolate units in these Pt complexes and complex **23** gave the best arrangement for molecular orientation.

As mentioned earlier, devices with deep-red emission are highly sought after for their biological applications, but the number of highly efficient devices remains relatively low. New research pushes these boundaries every day where, for example, Ly *et al.* synthesised three new homoleptic 2-pyrazinyl pyrazolate Pt^{II} complexes in 2016 (**26**-**28**, Fig. 2.12).[108]

They have very similar structures to the ones made by Kim's group but incorporate pyrazine groups to replace pyridine moieties, giving impressive results.

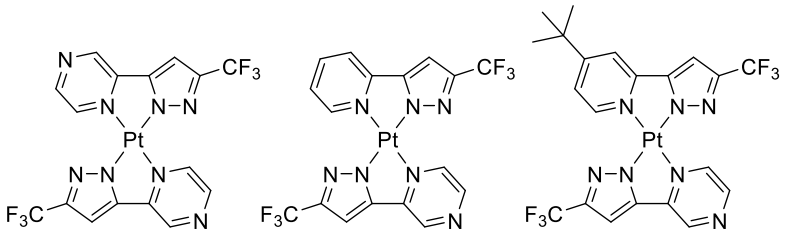

26 **27** **28**

Figure 2.12: *Structures of homoleptic 2-pyrazinyl pyrazolate Pt^{II} complexes **26, 27** and **28**.*

Quantum yields of the complexes ranged from 55 to 82 % with complex **26** displaying the most impressive EQE of 24 % in the device emitting at 740 nm in the NIR. This impressive device performance was attributed to the high thin-film PLQY of 81 %, as well as the horizontal orientation of the emission dipoles. Indeed, it surpassed any other NIR OLED efficiency prior to it, the closest of which had an EQE of 14.5 % with emission at 700 nm based upon a tridentate Pt(NCN)Cl complex synthesised by our group in 2008.[109]

2.1.4.4 Tetrazole complexes

The number of tetrazole complexes in OLEDs is significantly fewer than many other azole complexes due to their instability stemming from the extremely electron rich heterocycle containing four nitrogen atoms. They do, however, show some promising photophysical attributes. For instance, MaGee *et al.* investigated Pt^{II} complexes with 2-pyridyltetrazolate and *ortho*-xylene-linked bis(NHC)cyclophane (cyph) ligands (**29** and **30**, Fig. 2.13).[110] Complex **29** was synthesised by reaction of Pt(cyph)Cl_2 with the 2-pyridyltetrazole ligand in DMSO with triethylamine (NEt_3) base and subsequent anion exchange with potassium hexafluorophosphate (KPF_6) in water. Complex **30** was then afforded by reaction of **29** with a solution of methyl triflate in dichloromethane (DCM) at −50 °C. Complex **29** displayed a quantum yield of 14 % and had deep blue emission with λ_{max} of 436 nm whilst complex **30** had slightly red-shifted emission at 448 nm and a reduced quantum yield of 2 %.

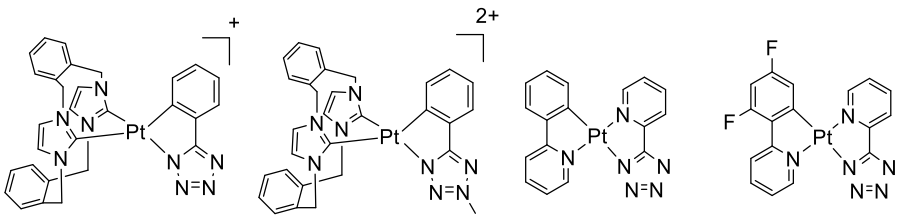

29 **30** **31** **32**

Figure 2.13: *Structures of Pt tetrazole complexes **29, 30, 31** and **32**.*

These compounds were not incorporated into devices, but efforts have been made by Brulatti *et al.* to include similar 2-pyridyl tetrazolate Pt^{II} complexes, **31** and **32** (Fig. 2.13), into VTE OLEDs.[111] Synthesis of these complexes was conducted by cleavage of the corresponding $[Pt(N^C)(\mu\text{-}Cl)]_2$ dimer with the 2-pyridyltetrazole ligand in methoxyethanol at reflux for 10 hours. The effect of complex concentration in the device was probed and showed that higher concentrations of the complex dopant in 4,4',4"-tris(N-carbazolyl)triphenylamine (TCTA) films gave red excimeric emission whilst at low concentrations blue-green emission was observed for the monomer, and this was reflected in their CIE coordinates (Fig. 2.14 and 2.15). The neat films that were studied were polycrystalline, in comparison to the amorphous films which resulted at lower weight concentrations of the Pt emitter in TCTA. The best performing device was found to have 15 wt. % of **31** in the TCTA host giving an EQE of 10 %. For Pt complexes containing bidentate tetrazole ligands this is the highest recorded EQE in the literature (see Table 2.1 for device information).

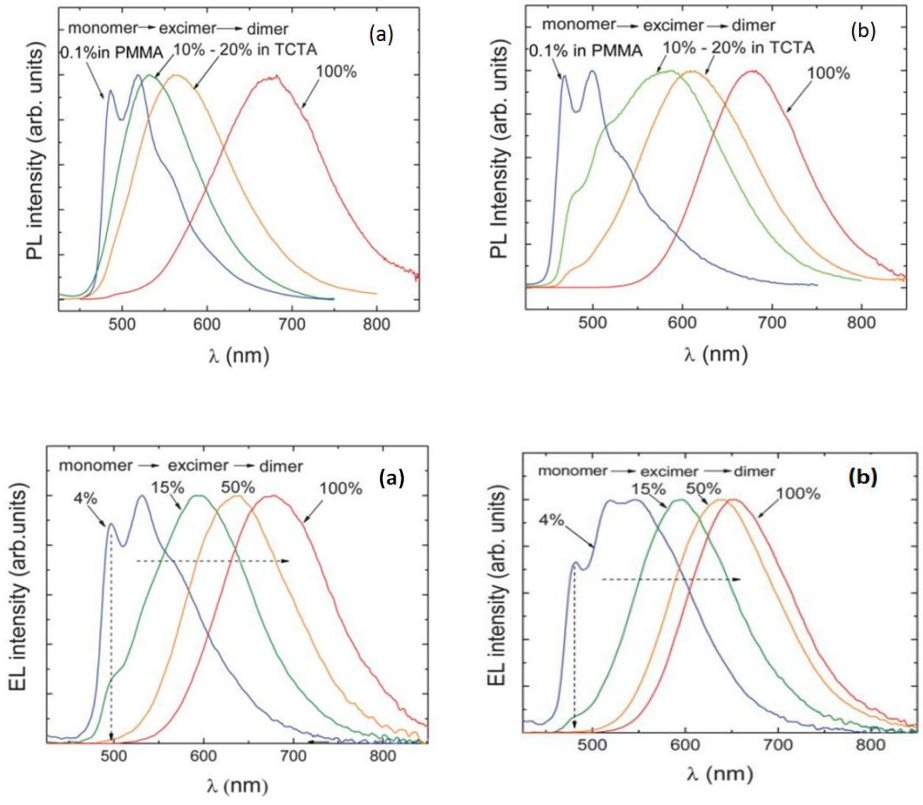

Figure 2.14: *Top: Solid-state PL spectra of (a)* ***31*** *and (b)* ***32*** *and bottom: EL spectra of (a)* ***31*** *and (b)* ***32*** *with different dopant concentrations in the TCTA host. Reproduced from Brulatti et al. by permission of the Royal Society of Chemistry.*[111]

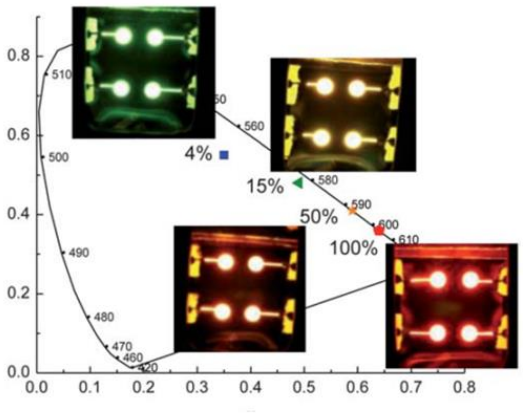

Figure 2.15: *CIE coordinates for complex* ***31*** *in different devices demonstrating effective colour tuning abilities. Reproduced from Brulatti et al. by permission of the Royal Society of Chemistry.*[111]

Although the focus of this work is on complexes containing *bidentate* triazole and tetrazole ligands, one cannot ignore the huge development in highly rigidified *tridentate* and *tetradentate* complexes with impressive photophysical properties that in many, but not all, cases outperform bidentate analogues, and these will be discussed in the chapters that follow.

Table 2.1: *PL and EL data of Pt azole complexes containing bidentate ligands. All EL data given is for the maximum values obtained. Please refer to the list of abbreviations for the device architecture column.*

Complex no. & reference	*Device Architecture*	*PL performance*			*EL performance*				
		λ_{max} (nm) [soln/film]	*PLQY (%) [soln/film]*	*Lifetime (ns) [soln/film]*	*λ_{max}(nm) [mono/exc]*	*CE (cd A^{-1})*	*PE (lm W^{-1})*	*Brightness (cd m^{-2})*	*EQE (%)*
Triazole									
16 [102]	-	[482, 512, 540 / 564]	[2/16]	[400/400]	-	-	-	-	-
17 [102]	-	[-/544]	[-/33]	[-/300]	-	-	-	-	-
18 [104]	-	[-/470]	[-/82]	[-/7200]	-	-	-	-	-
19 [104]	-	[-/467]	[-/87]	[-/8500]	-	-	-	-	-
20 [105]	ITO / NPB (40 nm) / 10 wt. % **20** : CBP (25 nm) / TPBI (30 nm) / Mg:Ag, 1:10 (200 nm)	-	-	-	[480/575]	14	9.8	6130	6.6
22 [106]	ITO / NPB (500 nm) / TAPC (350 nm) / CDBP (100nm) / CDBP: 10 wt. % **22** (500 nm) / $Me_2Si(TAZ)_2$ (600 nm) / LiF : Al	[448/448]	[42-/]	[3600/-]	-	7	-	4	-
Pyrazole									
23 [107]	ITO (100 nm) / TAPC (80 nm) / TCTA (10 nm)/ **23/24** (30 nm) / BmPyPb (15 nm) / BmPyPb: 1 wt. % Rb_2CO_3 (40 nm) / Al (100 nm).	[407/625]	[- / 96]	[- /380]	[-/625]	62	53.8	-	38.8
24 [107]		[403/622]	[- / 43]	[- /480]	[-/622]	22.4	8.4	-	15.7
25 [107]	ITO (100nm) / mCP: 5wt. % ReO_3 (60 nm) / mCP (10 nm) / **25** (30 nm) / B3PymPm (15 nm) / B3PYMPM: 1 wt. % Rb_2CO_3 (40 nm) / Al (100 nm).	[423/620]	[- / 56]	[- /490]	[-/620]	36.3	18.2	-	22.6
26 [108]	ITO (100 nm)/ HATCN (10 nm)/ NPB (50 nm)/ mCP (15 nm)/ **26/27/28** (20 nm) / TPBi (60 nm) / Liq (2 nm) / Al (100 nm).	[-/ 740]	[- / 81]	[- /310]	[-/740]	-	-	-	24
27 [108]		[-/ 703]	[- /55]	[- /370]	[-/683]	-	-	-	21
28 [108]		[-/ 673]	[- /82]	[- /310]	[-/669]	-	-	-	24
Tetrazole									
31[111]	ITO (20 nm) / TPD:PC (60 nm) / TCTA (10 nm)/ **31/32** (30 nm) / TAZ (10 nm) / LiF (0.5 nm)/ Al (100 nm).	[480/675]	[- /30]	[- /700]	[-/675]	-	-	-	2
32[111]		[460/678]	[- /75]	[- /500]	[-/655]	-	-	-	8
31[111]	ITO (20 nm) / TPD:PC (60 nm) / TCTA (10 nm) / TCTA : 15 wt. % **31** (30 nm) / TAZ (10 nm) / LiF (0.5 nm) / Al (100 nm).	-	-	-	[-/600]	-	-	-	10

2.2 Objectives

As can be seen from the literature review, there are a number of Pt^{II} azole complexes containing bidentate ligands which show potential application in OLED devices. However, specifically for triazole and tetrazole complexes, there are only limited examples showing the necessary attributes for OLED incorporation. This is due to several factors, but it has been identified that the main problems facing these types of complexes are associated with solubility and aggregation. It is also apparent that efficient deep blue and deep red/NIR emission are both highly sought after for many applications, although they remain a challenge to achieve.

Consequently, we aim to:

- Synthesise luminescent Pt^{II} complexes featuring bidentate 1,2,4-triazole and tetrazole ligands with high performance in both solution and solid-state photoluminescence.
- Tune the emission of these types of complexes to push for deep red/NIR emission via intermolecular interactions.
- Test these complexes for their electroluminescence behaviour in OLED devices.

To achieve these aims we have synthesised two main types of 1,2,4-triazole complex:

1. Homoleptic complexes containing two of the same bidentate ligand bound to a Pt^{II} centre.
2. Heteroleptic complexes which contained only one 1,2,4-triazole ligand bound to a Pt^{II} centre but with another ligand, including bipyridine (bpy), phenanthroline (phen), thienylpyridine (thpy) and phenylquinoline (pquin), to complete the coordination sphere.

In addition to this, we investigated some homoleptic Pt^{II} complexes containing bidentate tetrazole ligands of a similar nature for comparison.

2.3 Results and discussion: Triazole complexes

2.3.1 Homoleptic 1,2,4-Triazole complexes

2.3.1.1 Synthesis

Three groups of 1,2,4-triazole ligands were synthesised containing:

1. no functionality on the pyridine ring HL^{1-4},
2. a quinoline ring in place of the pyridine HL^{5-6},
3. functionality at the 4-position on the pyridine HL^{7-10}.

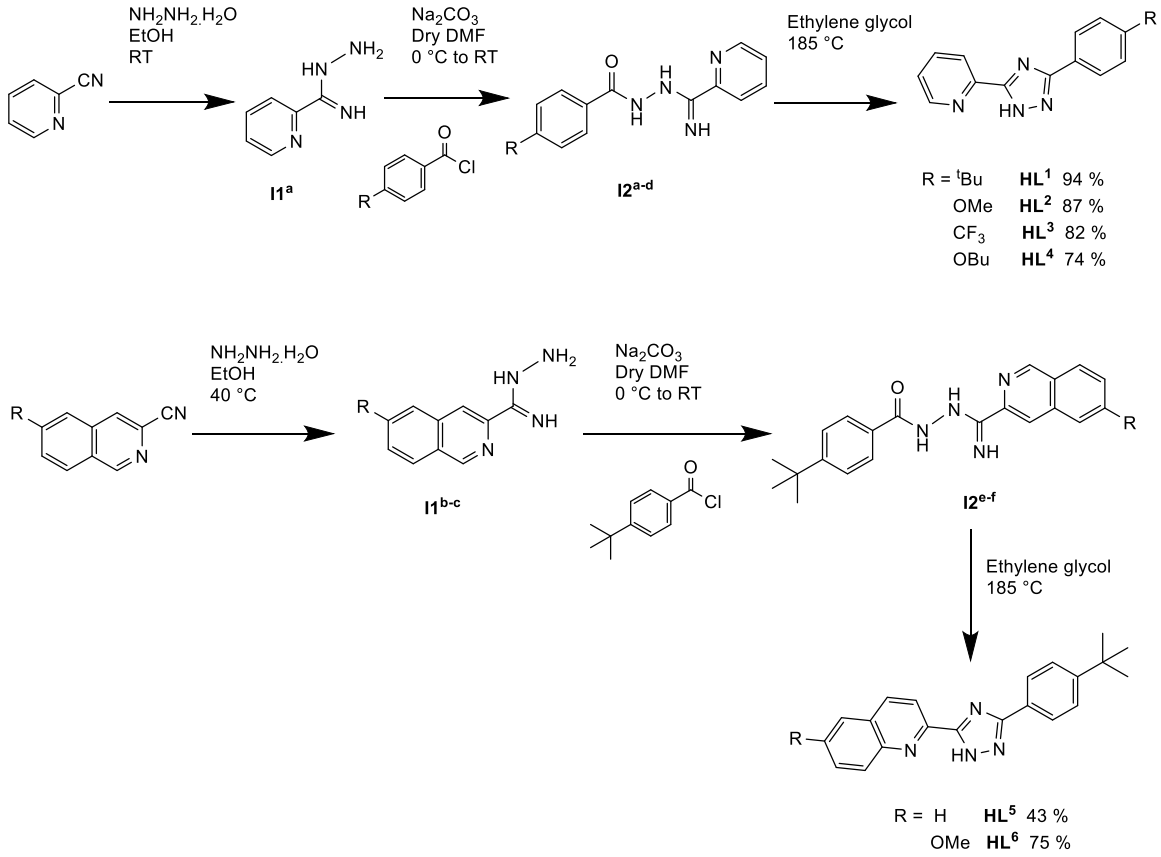

Scheme 2.5: *Synthesis of 1,2,4-triazole intermediates and resulting ligands HL^{1-6}.*

The synthesis of HL^{1-6} took place in a 3-step process adapted from De Cola's group[91] shown in Scheme 2.5:

1. Formation of intermediate 1 ($I1^{x}$) via reaction of the carbonitrile with hydrazine monohydrate.
2. Formation of intermediate 2 ($I2^{x}$) via reaction of $I1^{x}$ with the appropriate acyl chloride.
3. Formation of 1,2,4-triazole ligands (HL^{1-6}) via the condensation reaction of $I2^{x}$.

Respectable yields were achieved at each step and final-step yields ranged between 43 and 94 %. The triazole with R=NO_2 was also synthesised, but this gave a low yield as the ligand did not lead to a soluble complex so it is not discussed any further. Purification was achieved with water washes and recrystallization in hot EtOH for HL^{5-6}.

HL^{7-10} were synthesised in a similar manner to HL^{1-6} with a prior Suzuki cross-coupling to incorporate functionality at the 4-position on the pyridine ring in the formation of precursors (P^{1-4}, Scheme 2.6). The Suzuki step proceeded in good yields for all variants (50-90 %) and the presence of the aryl group at the 4-position did not hinder the subsequent steps, hence all the derivatives were obtained in good yield and with high purity.

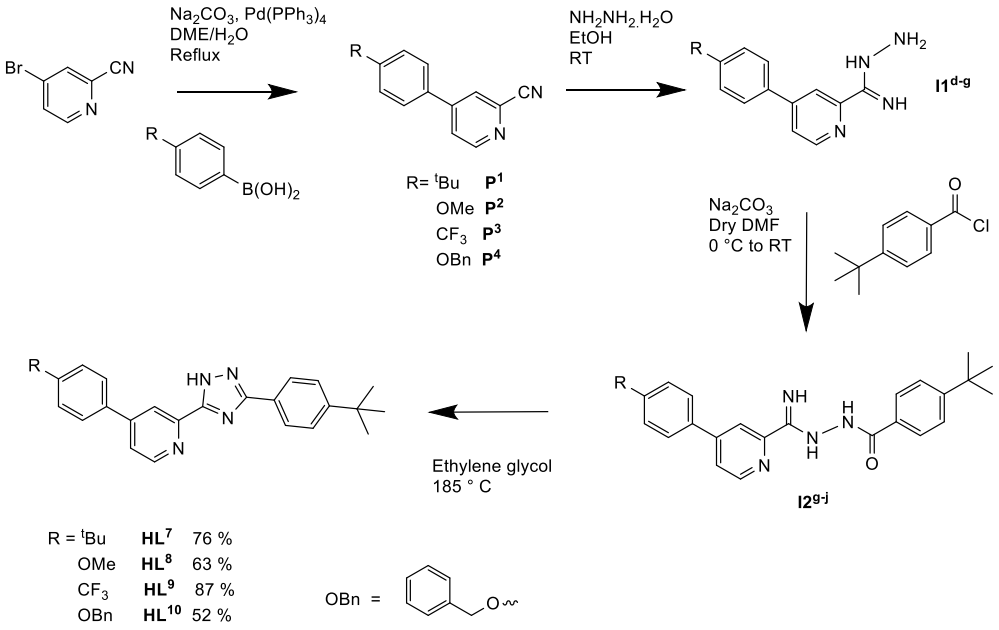

Scheme 2.6: *Synthesis of 1,2,4-triazole precursors, intermediates and ligands HL^{7-10}.*

Crystals suitable for X-ray diffraction analysis were obtained for HL^1 and HL^2 by slow evaporation from DCM solution (Figs. 2.16 and 2.17). HL^1 is close to linear with a torsion angle of 9.137 ° between the pyridyl ring and the triazole ring. HL^1 is arranged in dimers connected through hydrogen-bonding between the pyridine N and the triazole N—H. These dimers stack in an anti-parallel fashion which may arise from the ^{t}Bu groups that provide steric hindrance to parallel stacking. Similarly, HL^2 displays a structure close to linearity with a torsion angle between the pyridyl ring and the triazole ring of 7.572 °. Moreover, a similar packing arrangement is adopted in HL^2 with hydrogen bonding connecting the independent molecules, but in this case the OMe groups orient themselves facing towards each other.

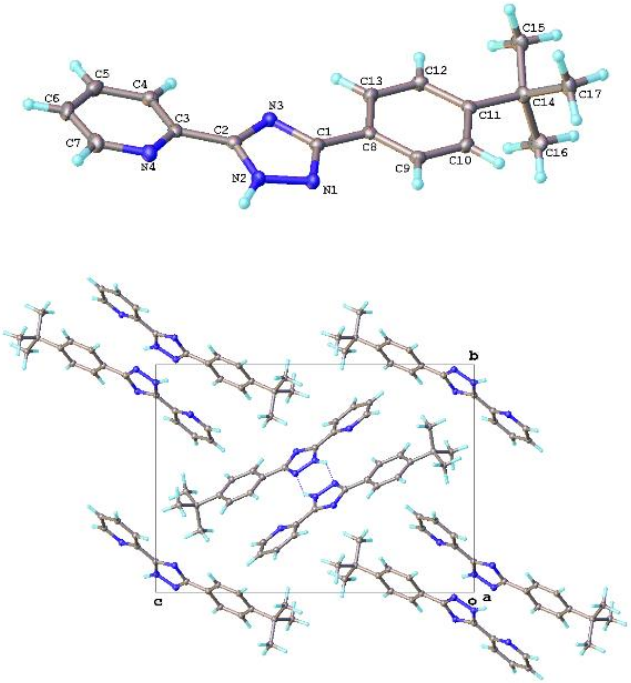

Figure 2.16: *Molecular structure and crystal packing of HL[1].*

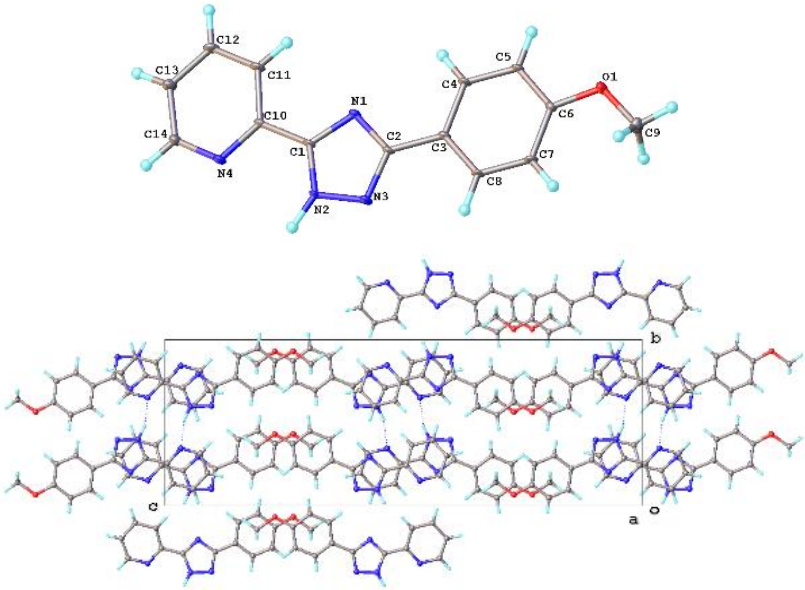

Figure 2.17: *Molecular structure and crystal packing of HL[2].*

Crystals suitable for X-ray diffraction were also obtained for HL[6] by slow evaporation from DCM solution (Fig. 2.18). The crystal structure revealed parallel sheets of dimers stacking in a staggered conformation alongside antiparallel stacked staggered sheets. The dimers in parallel sheets were connected though hydrogen bonding between the N—H and N atoms on opposite triazole rings. Interplanar distances in the parallel sheets were ca. 3.7 Å.

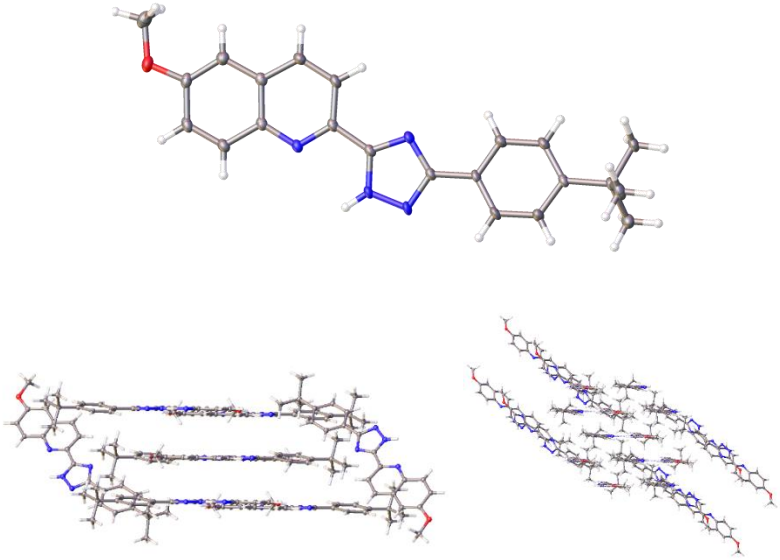

Figure 2.18: *Molecular structure and crystal packing of HL[6].*

Homoleptic Pt^{II} complexes of the form PtL^{1-4}_2 were synthesised by reaction of the proligands HL^{1-4} with potassium tetrachloroplatinate(II) (K_2PtCl_4) in EtOH/H_2O (3:1) under reflux for 18 hours (Scheme 2.7). The conditions are somewhat milder than those typically used for cyclometallation with platinum where higher boiling point solvents such as acetic acid (AcOH) at reflux are commonly used.[112,113,114]

The complexes were purified by recrystallization from hot DMF and yields varied from 17 to 67 %. Complexation was also attempted for HL^{5-6} and evidence of some product formation was observed by mass spectrometry (MS), but the products could not be successfully isolated due to low yields with a lot of starting material left over. This may perhaps be due to the steric hindrance of the 2 bulky quinoline ligands coming into contact with each other, disfavouring complexation.

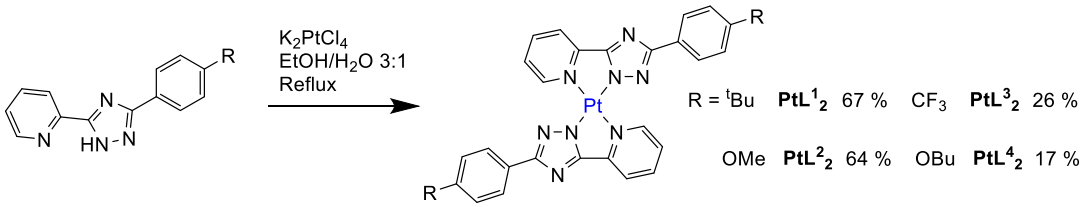

Scheme 2.7: *Synthesis of homoleptic 1,2,4-triazole complexes PtL^{1-4}_2.*

All complexes other than PtL^1_2 suffered from poor solubility in common organic solvents. It was found that the addition of trifluoroacetic acid (TFA) helped to solubilise PtL^{2-4}_2 in $CDCl_3$ for NMR analysis, presumably by protonation of the "exterior" N atom which is discussed later on.

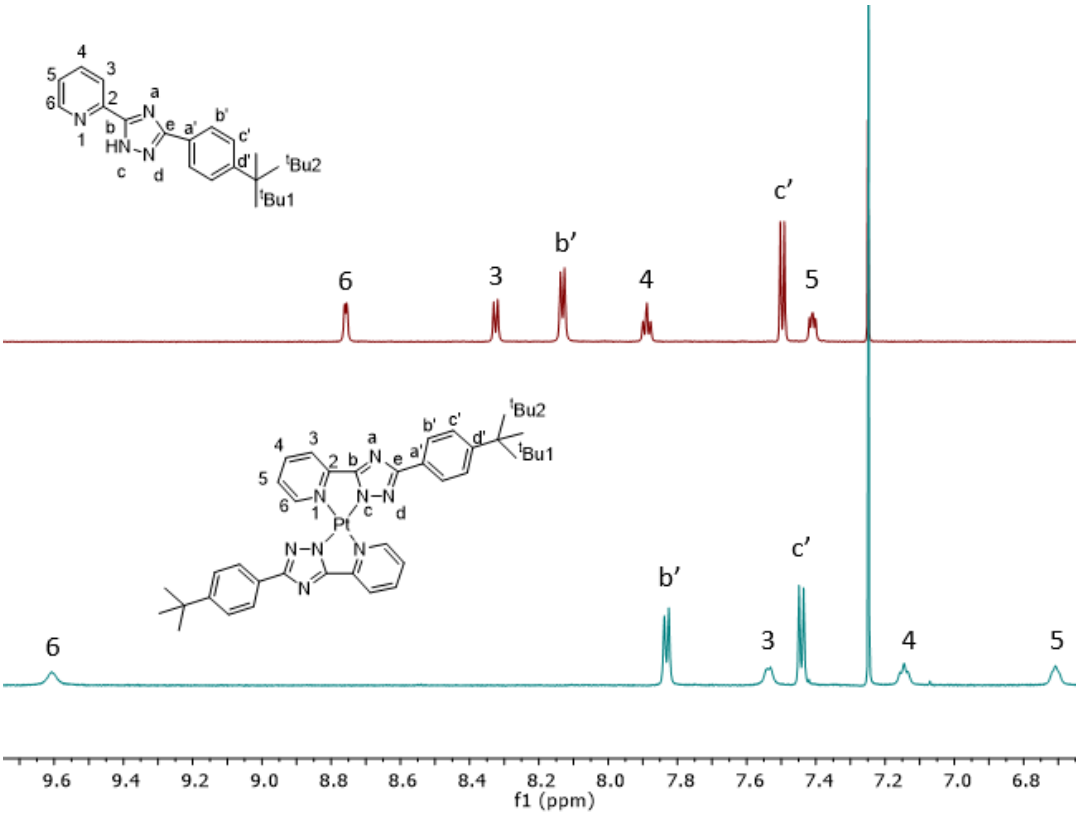

***Figure 2.19**: 400 MHz 298K ^{1}H NMR spectrum in $CDCl_3$ showing comparison between HL^1 (top) and PtL^1_2 (bottom).*

The complexes were analysed by ^{1}H NMR and Figure 2.19 shows the comparison of the free ligand HL^1 and the corresponding homoleptic complex PtL^1_2. The downfield shift of H^6 to higher ppm was indicative of complexation and this was accompanied by upfield shifts of the other signals.

Crystals suitable for X-ray diffraction were obtained for complexes PtL^1_2 and PtL^2_2 by hot recrystallization in DMF (Figs. 2.20 and 2.21). In all cases the triazole rings are *trans* to each other. This contrasts with bis-cyclometallated Pt complexes which normally have a *cis* relation between the pyridine N atoms and the C^- atoms owing to the strong *trans* influence of the σ-donating C^- atoms which makes them unfavourable to be placed opposite one another.[115] This suggests the N^- *trans* effect in these complexes is less important. Indeed, it is evident that the Pt1—N2 (triazole) distances are only slightly smaller than the Pt1—N1 (pyridine) distances in each complex (Tables 2.2 and 2.3).

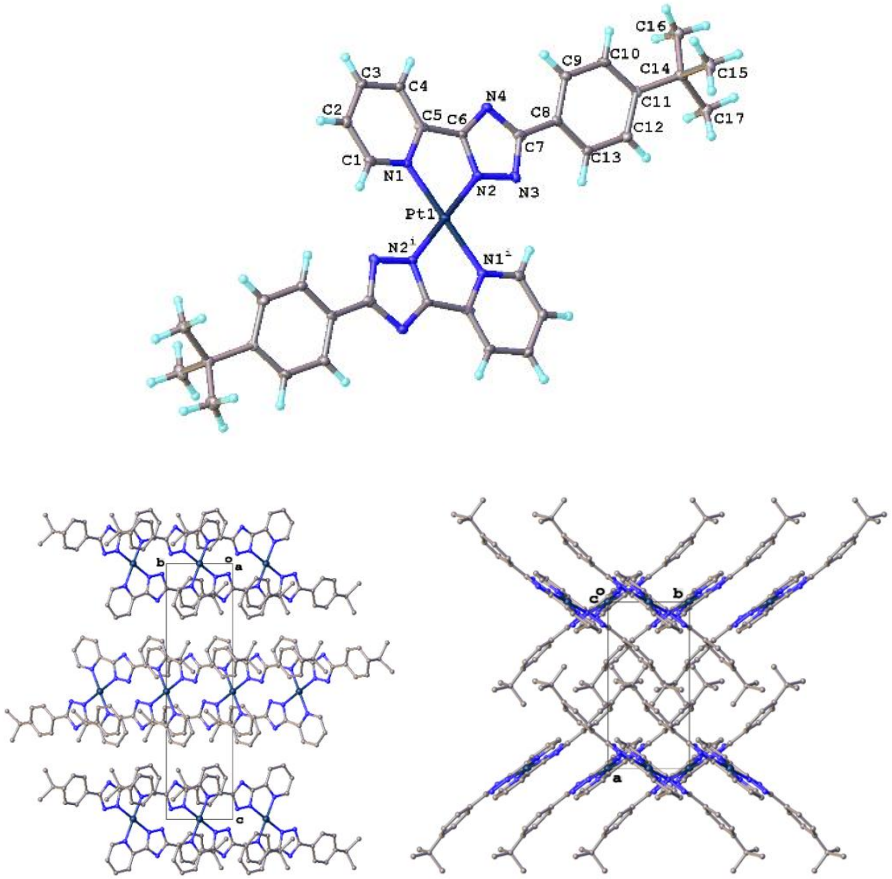

Figure 2.20: *Molecular structure and crystal packing of PtL^{1}_{2}.*

Table 2.2: *Selected bond lengths and angles for PtL^{1}_{2}.*

Bond Lengths/ Å		*Bond Angles / °*	
Pt1—N1	2.033(4)	$N1^{1}$-Pt1-N1	180.0
Pt1—N2	1.992(4)	N2-Pt1-$N1^{1}$	100.61(16)
		$N2^{1}$-Pt1-$N1^{1}$	79.39(16)

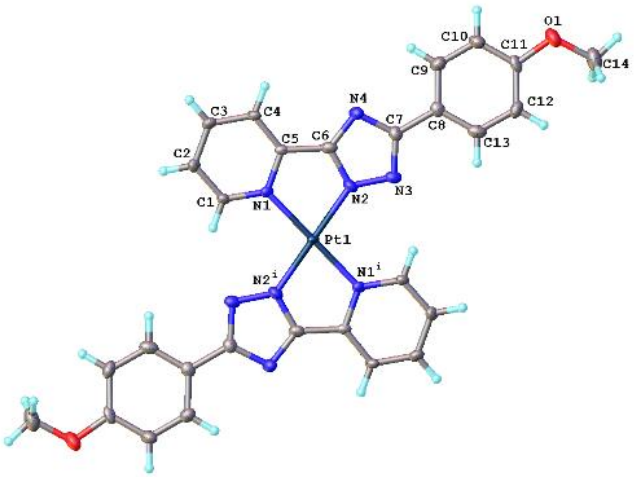

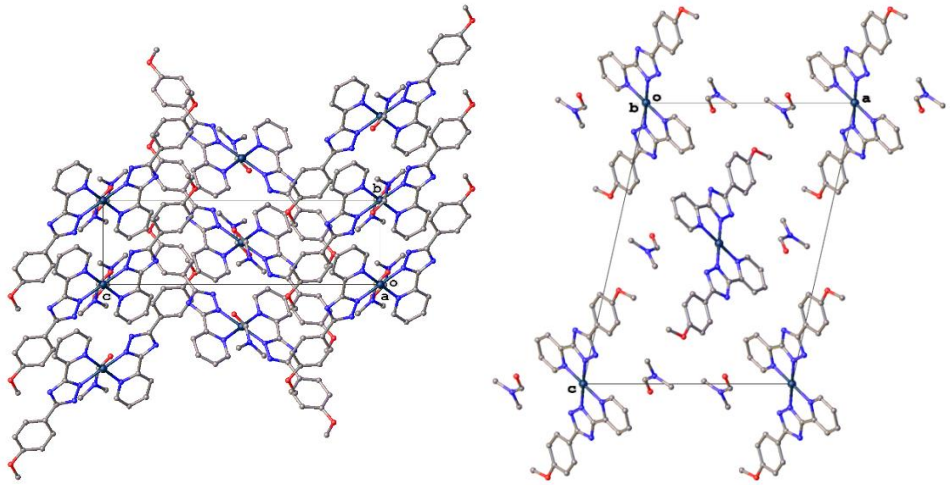

Figure 2.21: *Molecular structure and crystal packing of PtL^2_2.*

Table 2.3: *Selected bond lengths and angles for PtL^2_2.*

Bond Lengths/ Å		*Bond Angles / °*	
Pt1—N1	2.026(4)	$N1^1$-Pt1-N1	180.0
Pt1—N2	1.996(4)	N2-Pt1-$N1^1$	101.04(15)
		N2-Pt1-N1	78.97(15)

In $Pt(ppy)_2$ the bond distances are reported as being Pt—N = 2.13 Å and Pt—C = 1.99 Å.[115] In both PtL^1_2 and PtL^2_2, however, the Pt—N^- and Pt—N bond lengths are virtually identical, at 2.0 Å.

Due to solubility issues with complex PtL^2_2, the complex PtL^4_2 was synthesised containing an OBu chain instead of an OMe chain. Unfortunately, the solubility in common organic solvents was still not improved in the absence of TFA. Crystals of PtL^4_2 were easily obtained by leaving the complex to stand in $CDCl_3$ containing TFA overnight. This revealed the protonation of the exterior N atom, N4, which allowed a hydrogen bonding network to form between the N—H of the N4 on the triazole and the trifluoroacetate anions with a N—H···O distance of 2.71 Å (Fig. 2.22). The packing thus consisted of layers of π-π linked metal complexes with layers of acid molecules between both ligands.

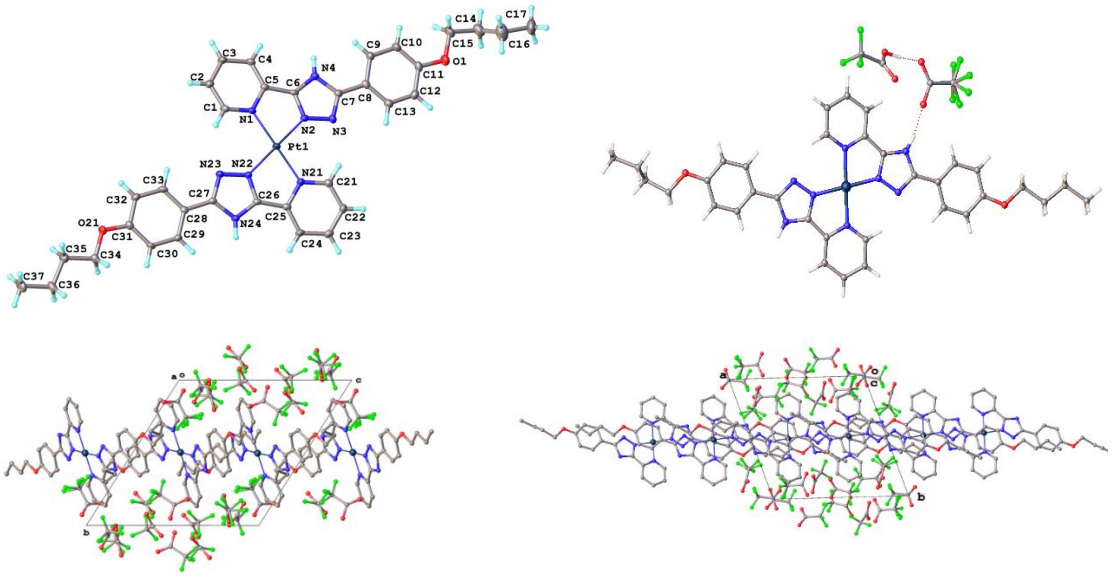

Figure 2.22: *Molecular structure, hydrogen bonding between TFA and crystal packing for protonated $PtL^4{}_2$.*

Bond lengths and angles between the Pt centre and the N atoms on both the triazole and the pyridine rings did not show any significant change in comparison to the non-protonated complexes discussed earlier (Table 2.4).

Table 2.4: *Selected bond lengths and angles for $PtL^4{}_2$.*

Bond Lengths/ Å		*Bond Angles / °*	
Pt1—N1	2.040(3)	N2-Pt1-N1	79.30(11)
Pt1—N2	1.995(3)	N2-Pt1-N21	100.78(11)
Pt1—N21	2.031(3)	N21-Pt1-N1	178.97(11)
Pt1—N22	1.984(3)		

Synthesis of complexes $PtL^{7\text{-}9}{}_2$ was attempted in the same solvents as before ($EtOH/H_2O$ 3:1) but was not successful. As a result, many other solvent combinations were attempted as well as using different sources of Pt including $Pt(DMSO)_2Cl_2$ and $Pt(COD)Cl_2$, but the highest yielding syntheses were achieved using K_2PtCl_4 in a $MeCN/H_2O$ (3:1) solvent system at reflux (Scheme 2.8). Syntheses of complexes $PtL^{7\text{-}9}{}_2$ proceeded in lower yields than those of $PtL^{1\text{-}4}{}_2$ and this was partly due to the more difficult purification of complexes which required column chromatography on alumina followed by recrystallization. Synthesis of $PtL^{10}{}_2$ was attempted and the complex was formed but could not be purified.

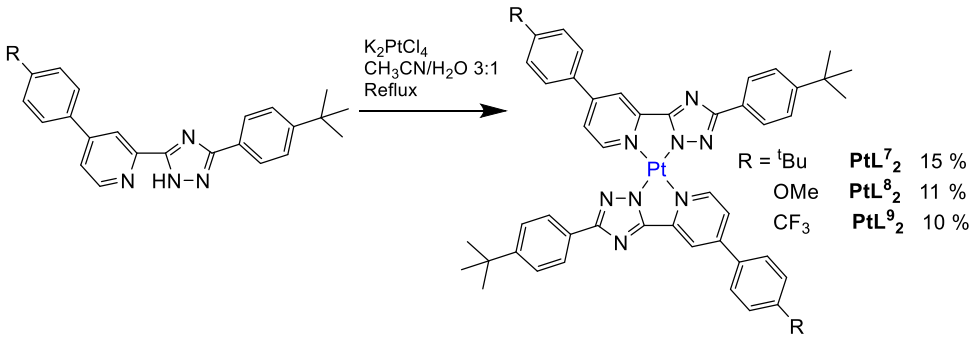

Scheme 2.8: *Synthesis of homoleptic 1,2,4-triazole complexes PtL^{7-9}_2*

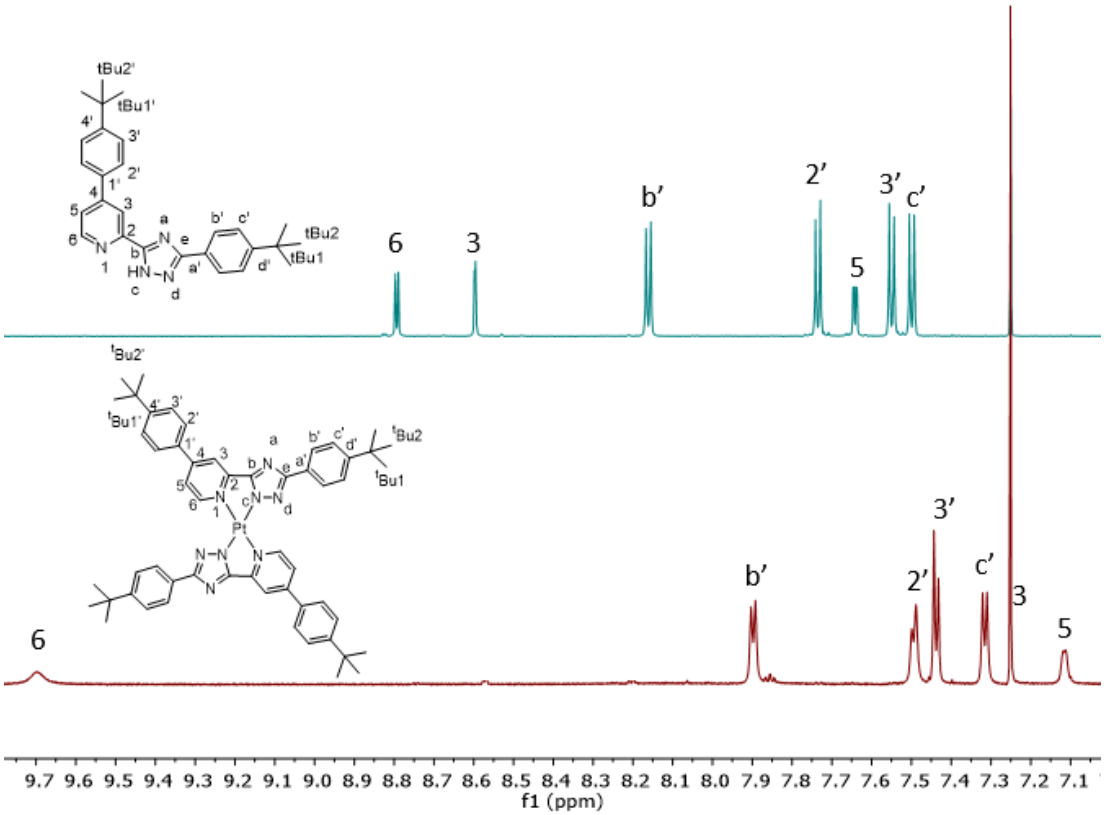

Figure 2.23: *400 MHz 298K ^{1}H NMR spectrum in $CDCl_3$ showing comparison between HL^7 (top) and PtL^7_2 (bottom).*

Similar to PtL^1_2, these complexes were analysed by ^{1}H NMR and Figure 2.23 shows the comparison of the free ligand HL^7 and the corresponding homoleptic complex PtL^7_2. The downfield shift of H^6 to higher ppm was indicative of complexation and this was accompanied by upfield shifts of the other signals. Signals for H^3 and H^5 were significantly shifted upfield (signal 3 is partially masked by the residual solvent peak at 7.25 ppm).

Crystals suitable for X-ray diffraction were obtained for complex PtL^7_2 by recrystallization from DCM/Hexane (Fig. 2.24). An off-centred stacking was displayed for this complex with

no close contacts between Pt centres. Bond lengths and angles were like those for PtL^1_2 (Table 2.5).

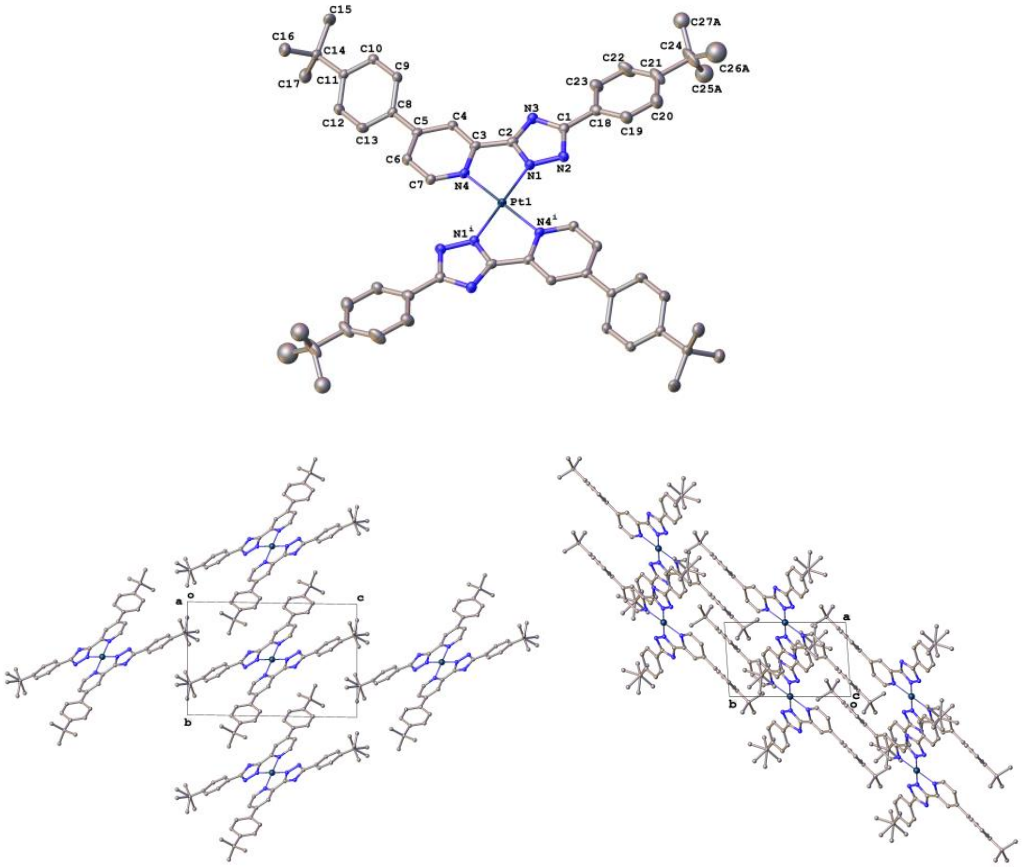

Figure 2.24: *Molecular structure and packing for PtL^7_2.*

Table 2.5: *Selected bond lengths and distances for PtL^7_2.*

Bond Lengths/ Å		*Bond Angles / °*	
Pt1—N1	1.996(3)	N1-Pt1-N1^1	180.00(11)
Pt1—N1^1	1.997(3)	N1^1-Pt1-N4^1	79.05(11)
Pt1—N4	2.024(3)	N1^1-Pt1-N4	100.95(11)
Pt1—N4^1	2.024(3)		

2.3.1.2 Photophysical properties

The absorption spectra of complexes PtL^1_2,PtL^2_4 and PtL^4_2 and $PtL^{7\text{-}9}_2$ were measured in DCM at RT unless otherwise stated (Fig. 2.25). PtL^3_2 was too insoluble to study in all common organic solvents. Bands with high extinction coefficients were observed at high energy between 250 and 325 nm which can be described as a spin-allowed transition, LC in nature, involving mainly the triazole ligand ($\pi\rightarrow\pi^*$) similar to other Pt-azolate complexes.[116,117] An additional band at lower energy (λ_{max} at ~425 nm) was assigned as the lowest-lying MLCT transition, in line with those already reported for comparable compounds. These bands are the $S_0\rightarrow S_1$ transitions and mainly involve the platinum d orbitals and π^* orbitals of the triazole ligand.

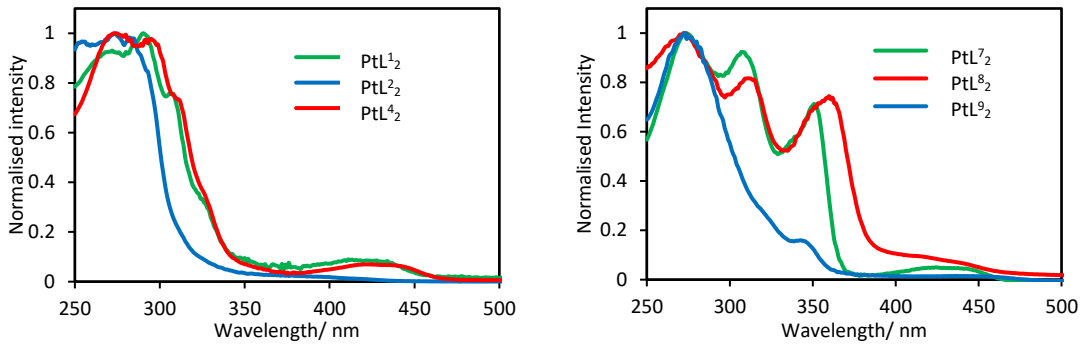

Figure 2.25: *UV-Vis absorption of complexes PtL^n_2 in DCM solution except PtL^2_2 which was in DMF due to its very poor solubility in DCM.*

For complexes PtL^{7-9}_2 a band and shoulder between approximately 350 and 370 nm are noticeable but are not present for PtL^{1-4}_2 which suggests that these may originate from a transition with mixed MLCT/LC character owing to the presence of the conjugated functionalisation on the pyridine of the ligand.

The complexes were luminescent with quantum yields ranging from 21 to 48 %. These are high efficiencies which are comparable with and exceed many cyclometallated $Pt(N\hat{}C)_2$ complexes. Emission profiles of complexes PtL^n_2 show a distinct band with vibrational structure (Fig. 2.26). This has been assigned as a HOMO→LUMO transition from TD-DFT data where the HOMO is mainly localised on the triazole and aryl rings and the LUMO on the pyridyl ring (see DFT section 2.3.3). The lowest energy emission is seen to emanate from PtL^9_2 which contains stabilising CF_3 groups on the LUMO to red-shift the emission relative to PtL^7_2 which contains slightly electron donating ^{t}Bu groups to destabilise the LUMO. Lifetimes of the complexes PtL^n_2 where n=1, 7, 8 and 9 were seen to range between 3.9 and 5.1 µs, whilst those with n= 2 and 4 were longer at 12 and 13 µs (Table 2.7).

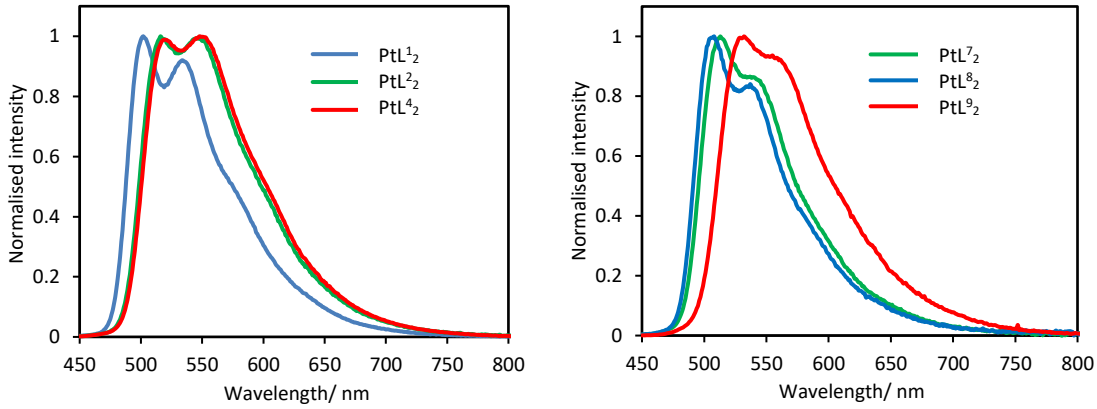

Figure 2.26: *Emission of complexes $Pt(L^n)_2$ in 1 x 10^{-6} M solution DCM at RT.*

Concentration-dependent emission spectra were run at RT on the most soluble complexes namely: PtL^1_2, PtL^7_2 and PtL^9_2. The spectra for complex PtL^1_2 revealed the formation and development of a broad and structureless band at λ_{max} 580 nm with a subsequent decrease in intensity of the monomer band (Fig. 2.27A). On the other hand, complexes PtL^7_2 and PtL^9_2 showed the development of red-shifted bands at 615 and 630 nm respectively, whilst the relative intensity of their monomer bands was retained (Figs 2.27B and C). The assignment of these red-shifted emission bands as excimeric is supported by the linear dependence of the decay rate upon concentration when fitted to the Stern-Volmer equation shown below, where k_{sq} is the self-quenching rate constant, [Pt] is the concentration of the platinum complex, and k_0 is the decay rate for the monomer complex obtained from lifetime data.[118]

$$k_{obs} = k_{sq}[Pt] + k_0 \qquad (8)$$

It was apparent that PtL^1_2 was the most susceptible to excimer formation from the intensity of the excimer band compared to PtL^7_2 and PtL^9_2. Indeed, the k_{sq} value for PtL^1_2 (5.1 x 10^8 mol^{-1} dm^3 s^{-1}) was higher than those of PtL^7_2 and PtL^9_2 (3.3 x 10^8 and 2.0 x 10^8 mol^{-1} dm^3 s^{-1}) which supports this.

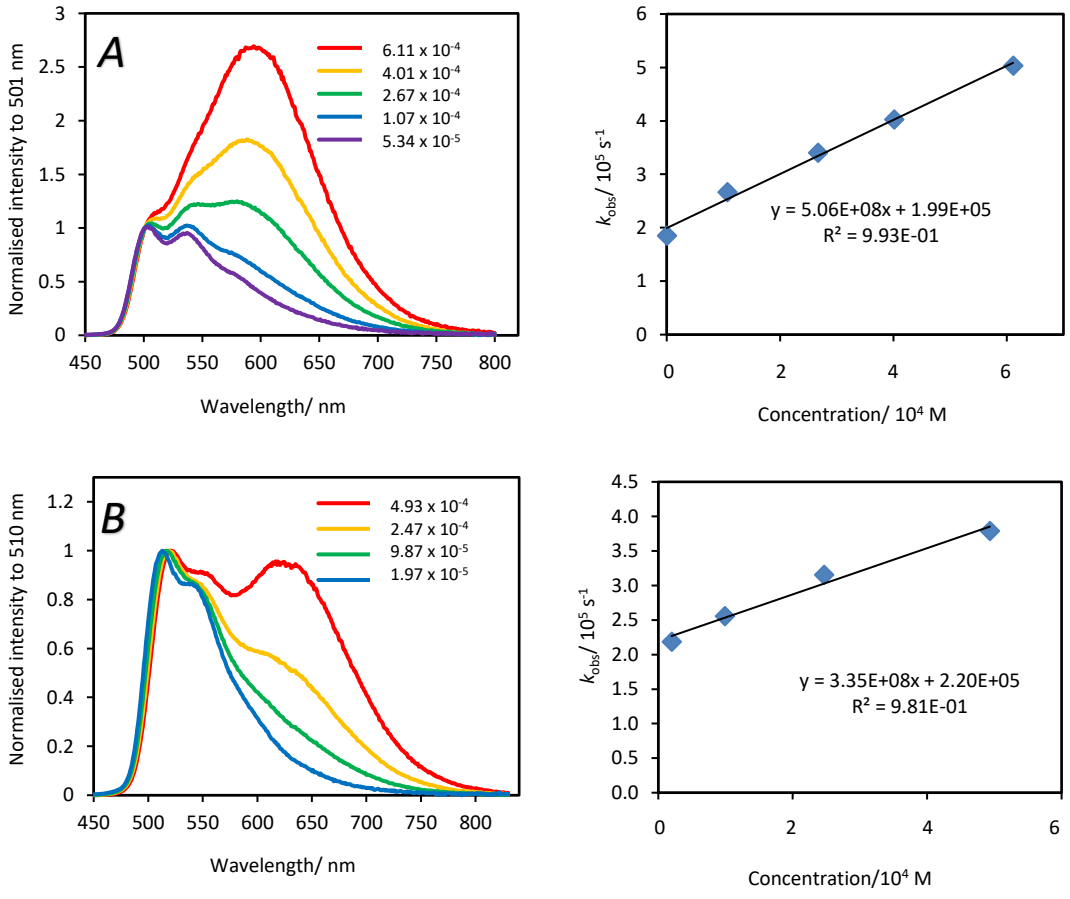

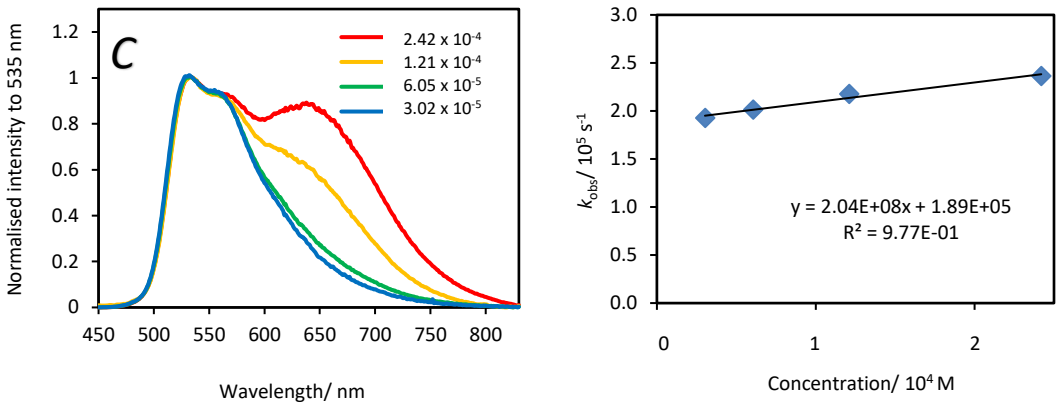

Figure 2.27: *Concentration-dependent emission and Stern-Volmer plots of: A) PtL^1_2 normalised to 501 nm, B) PtL^7_2 normalised to 510 nm and C) PtL^9_2 normalised to 535 nm.*

We attempted to record the low-temperature spectra at 77 K for all triazole complexes. Attempts were initially run in butryonitrile/EPA glass and these displayed broad emission peaks in the red-region with λ_{max} of over 600 nm in each case, independent of concentration. Using a 1:1 DCM/DMSO mixture, the emission was seen to be concentration-dependent. At very low concentrations ($<10^{-7}$ M), weak structured emission with λ_{max} of 491 and 495 nm for PtL^1_2 and PtL^7_2 respectively was observed (Fig. 2.28). In more concentrated solutions, red-shifted and structureless emission was observed with λ_{max} values of 615 and 675 nm for PtL^1_2 and PtL^7_2 respectively.

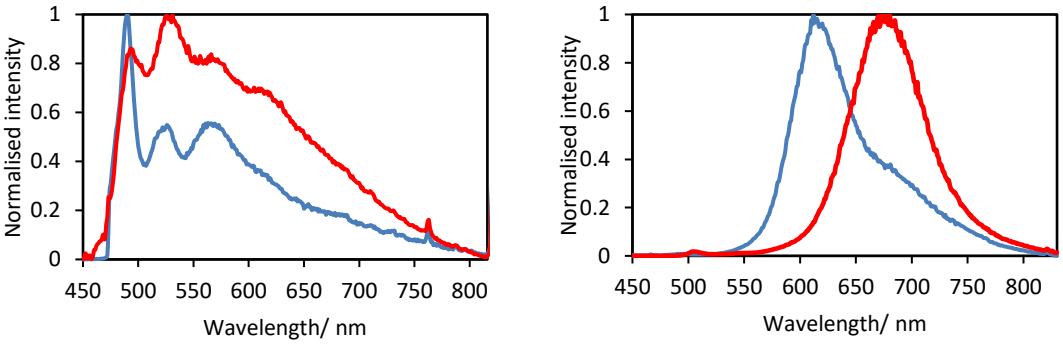

Figure 2.28: *77 K spectra of PtL^1_2 (blue) and PtL^7_2 (red) in DCM/DMSO at low concentration (left) and at high concentration (right).*

The structured emission observed at low-concentrations is assigned to monomer emission owing to the similarity of the emission peaks to the low-concentration RT emission. The emission at higher concentrations is ascribed to either aggregate or excimeric emission. The lifetimes of the 77 K emission were recorded for each complex where dilute solutions showed mono-exponential decay, indicative of one species, i.e. the monomer, in each case (Table 2.6). The concentrated solutions displayed a biexponential decay which was fitted to

obtain two lifetimes indicative of trace amounts of monomer and an aggregate/excimer in each case. The aggregate/excimer lifetimes were an order of magnitude smaller than the monomer lifetimes.

Table 2.6: *77 K lifetimes of PtL^1_2 and PtL^7_2 in DCM/DMSO (dilute and concentrated, the wavelengths of emission are given in the parentheses).*

Complex	τ_{77K} (dilute)/ μs	τ_{77K} (concentrated) /μs	
		τ_1	τ_2
PtL^1_2	12 (480 nm)	1.1 (625 nm)	12 (625 nm)
PtL^7_2	13 (490 nm)	1.4 (650 nm)	12 (650 nm)

At high concentrations, the λ_{max} values of the red-shifted bands at 77 K are seen to be considerably longer than those recorded at RT for PtL^1_2 (615 vs. 580 nm) and PtL^7_2 (675 vs. 615 nm). This possibly supports the formation of excimers in solution at RT and aggregates at 77 K, where the complexes exhibit reduced solubility at low-temperature.

Table 2.7: *Photophysical data for complexes PtL^n_2. Emission was run in degassed DCM at a concentration of 10^{-6} M and 77 K spectra were run in DCM/DMSO 1:1 v/v solutions.*

Complex	298 K										77 K	
	λ_{abs} (nm)	λ_{em} (nm)	τ_{deg} (µs)	τ_{aer} (ns)	τ_0 (µs)	φ (%)	k_r (10^3 s^{-1})	k_{nr} (10^5 s^{-1})	k_q (O_2) (10^8 M^{-1} s^{-1})	k_{sq} (M^{-1} s^{-1})	λ_{em} (nm)	τ (µs)
PtL^1_2	275 (79,880), 290 (86,260), 310 (58,870), 325 (27,240), 425 (4,050).	500, 532	5.1	300	5.0	21	41.2	1.55	14.3	5.1 x 10^8	491, 530, 568	12
PtL^2_2	275 (55840), 290 (55210), 310 (41020), 325 (52010), 425 (2770).	515, 547	12	260	/	41	35	0.5	17	/	500, 630	12
PtL^4_2	273 (19725), 295 (18221), 310 (13803), 425 (1018).	518, 552	13	280	/	35	28	0.5	16	/	514, 557, 610.	13
PtL^7_2	270 (117,767), 304 (110,242), 352 (85,109), 420 (5,868).	513, 539	4.6	500	4.5	48	100	1.1	8.1	3.3 x 10^8	495, 532, 570, 610	13
PtL^8_2	277 (63,070), 300 (43,124), 311 (35,892), 360 (31,997), 425 (5,551).	502, 531, 571sh	3.9	430	/	30	77	1.8	9.4	/	513, 547, 592sh	12
PtL^9_2	276 (26,256), 316 (20782), 341 (11,054), 430 (1,627).	528, 553	4.6	540	5.3	23	50	1.7	7.4	2.0 x 10^8	490, 532, 644	12

2.3.1.3 Investigation into OLED devices

The type of processing of an OLED determines which kinds of complexes are suitable for devices. For solution-processed devices, complexes must have good solubility in solvents which are readily vaporised e.g. chlorobenzene. For VTE devices, complexes must have high thermal stability and thus high degradation temperatures.

Thin-film photophysical characterisation

From the initial photophysical characterisation, PtL^1_2 was seen to have good attributes for both kinds of OLED testing and thus was studied for its photophysical properties in the solid-state when doped into OLED host materials. Two films were made with PtL^1_2 as the dopant:

1. 6 wt. % in an evaporated film with 3,3-di(9H-carbazol-9-yl)biphenyl (mCBP) as the host
2. 10 wt. % in a spin-coated film with poly(methyl methacrylate) (PMMA) as the host

Film **1** displayed a quantum yield of 72 %, whilst film **2** displayed a quantum yield of 92 %. The lifetime of the complex was the same in both films, as in solution, at 5 µs. The emission in film **1** shows two bands with λ_{max} of 502 nm and 580 nm which are consistent with the bands previously attributed to monomer and excimer in solution (Fig. 2.29). In film **2** the loading percentage of PtL^1_2 was higher than in film **1** and a narrower and mainly structureless emission profile was observed with λ_{max} of 610 nm. This is red-shifted by 30 nm relative to the excimer emission peak in solution and in film **1,** suggesting that the origin of this emission may be an aggregate rather than an excimer.

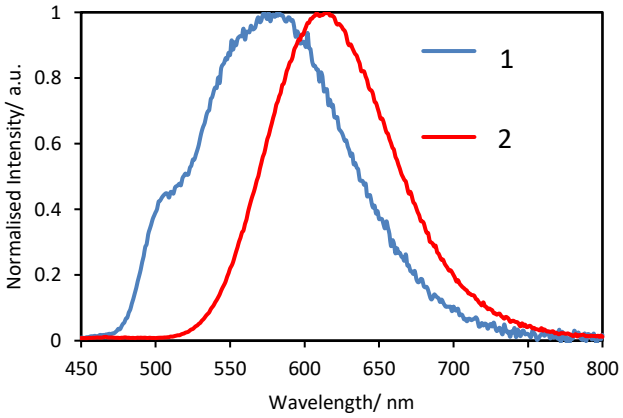

ϕ DCM (%)	21
τ DCM (µs)	5
ϕ powder (%)	5
ϕ Film 1 (%)	72
ϕ Film 2 (%)	92

***Figure 2.29**: Solid-state emission of PtL^1_2 in thin films 1 and 2 and photophysical properties in solution and in the solid-state.*

Device Fabrication

Vacuum thermal evaporation (VTE) devices

VTE OLED device fabrication was carried out for PtL^1_2 owing to its high quantum yield in the film. Two devices were fabricated with the aim of device optimisation to improve the EQE. The first device had an OLED architecture containing 6 wt. % PtL^1_2 doped in a mCBP EML with a 2,2',2"-(1,3,5-benzenetriyl)tris(1-phenyl-1-H-benzimidazole) (TPBi) electron transport layer (ETL) and a N,N'-Bis-(1-naphthalenyl)-N,N'-bis-phenyl-(1,1'-biphenyl)-4,4'-diamine (λ-NPD) hole transport layer (HTL) (Fig. 2.30). This gave a maximum EQE of 4.1 % (at 13.7 mA cm^{-2}) (Table 2.8). To try to improve this device by reducing the recombination of holes and electrons within the device, an electron-blocking layer (EBL) 1,3-Bis(N-carbazolyl)benzene (mCP) and hole-blocking layer (HBL) 2,4,6-Tris(biphenyl-3-yl)-1,3,5-triazine (T2T) were added. Unfortunately, this reduced the maximum EQE to 3.0 % (at 39.5 mA cm^{-2}). The performances of devices 1 and 2 are shown in Table 2.8 and 2.9 and reveal purely monomer-based emission in each device.

Table 2.8: *VTE device properties for PtL^1_2 (fabricated in the Adachi Lab by me).*

	Device architecture	*λ_{max}(nm)*	*Current density (mA cm^{-2})*	*EQE (%)*
1	Al (100nm) / LiF (0.8nm) / TPBI (40 nm)/ mCBP : 6 wt. % **PtL^1_2** (30 nm)/ λ-NPD (30 nm) / ITO.	503, 533	13.7	4.1
2	Al (100nm) / LiF (0.8nm) / TPBI (40 nm) / T2T (30nm) / mCBP : 6 wt. % **PtL^1_2** (30 nm / mCP (10nm) / λ-NPD (30 nm)/ ITO.	507, 542	39.5	3.0

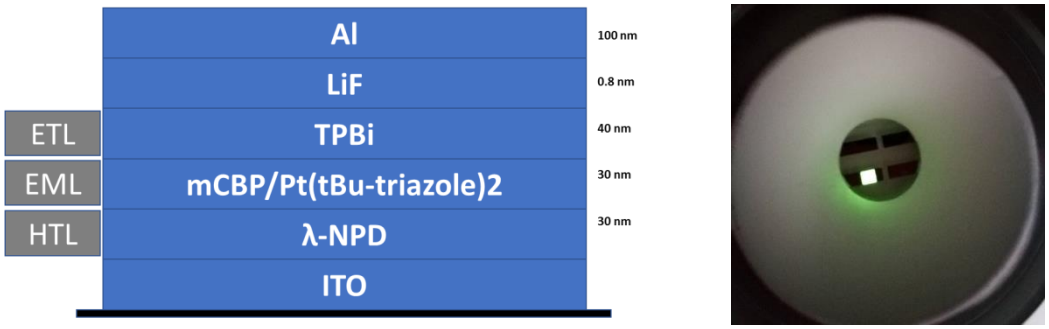

Figure 2.30: *Structure of device 1 (left) and picture of the device turned on with green emission (right).*

The properties displayed by these devices are not very impressive considering the high quantum yields of over 70 % that have been obtained in the film for this complex. The low EQEs displayed in these devices may be due to the mis-match in energy levels between the EML and the HTL/ETL. Fine-tuning of the device structure would need to be done to improve these properties.

Table 2.9: *EL at different current densities, voltage vs. current density and current density vs. EQE plots for PtL^1_2 in devices 1 and 2.*

1

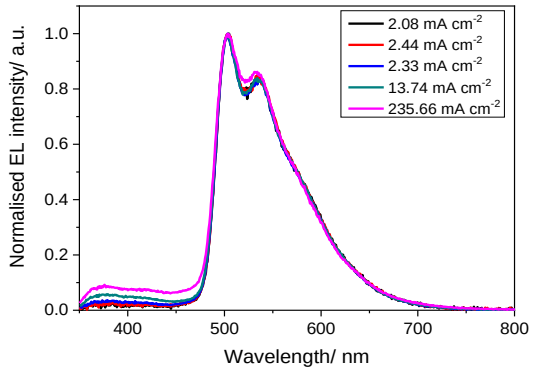

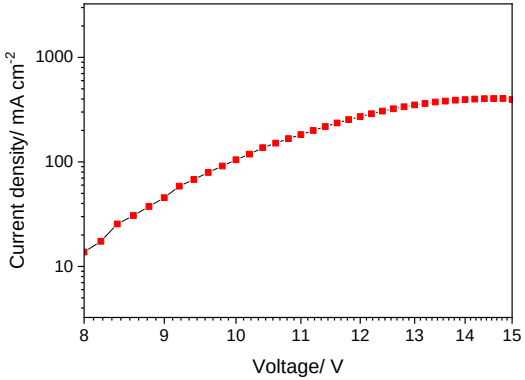

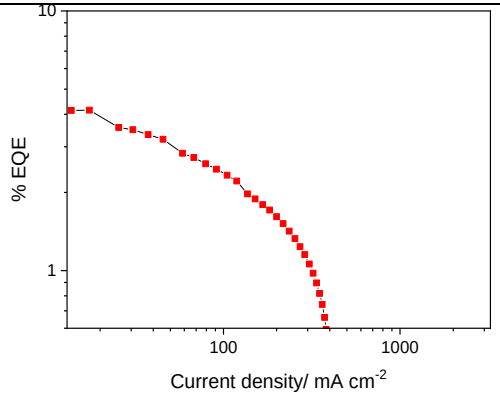

2

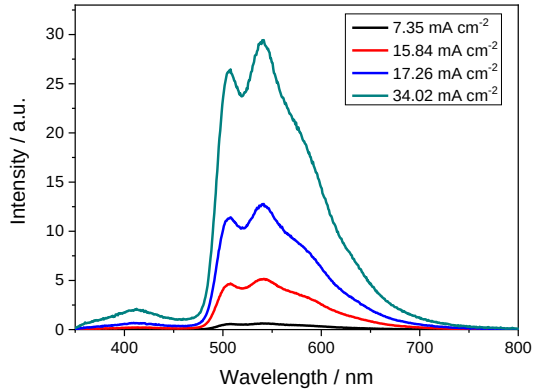

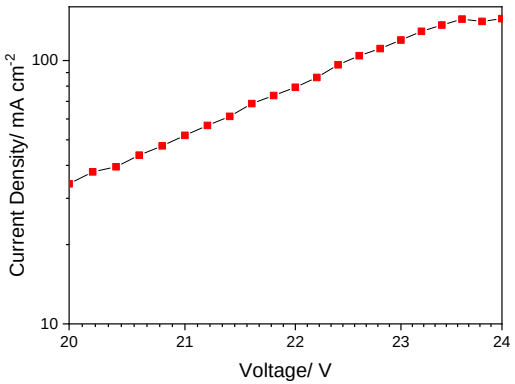

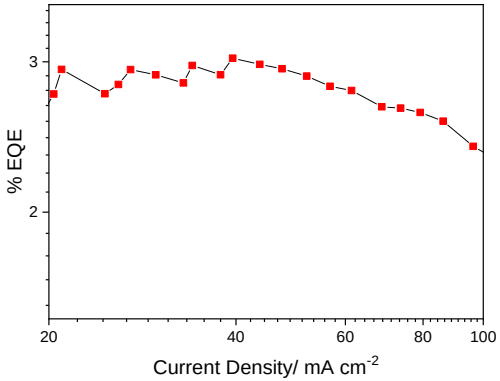

Solution-processed devices

PtL^1_2 and PtL^7_2 were selected for solution-processed OLED fabrication owing to their high solubility. These devices were fabricated by Piotr Pander (Durham University Physics Department) with the device structure of: ITO | HIL 1.3N (45 nm) | mCP : OXD7 (80 : 20) co. x % **PtL^1_2/PtL^7_2** (62 nm) | TPBi (50 nm) | LiF (0.8 nm) | Al (100 nm). PtL^1_2 was also incorporated into a VTE with the device architecture of ITO | NPB (35 nm) | TSBPA (10 nm) | mCP (5 nm) | mCP co. 30 % **PtL^1_2** (20 nm) | TPBi (50 nm) | LiF (0.8 nm) | Al (100 nm) at 30 wt. % for comparison with both the solution-processed devices and the previously synthesised VTE devices of different device architecture. The solution-processed devices showed maximum EQE values between 8.7 and 12.5 %, very low roll-off and high maximum brightness of up to 28620 cd m^{-2} (device 2, Table 2.10).

Table 2.10: *Solution-processed device properties for PtL^1_2 and PtL^7_2.* * Denotes VTE device.

Device No.	*Complex (wt. %)*	*EL λ_{max} (nm)*	*Current density (mA cm^{-2})*	*Brightness (cd m^{-2})*	*EQE (%)*
1	PtL^1_2 (5)	507, 542	61.68	10550	10.4
2	PtL^1_2 (20)	575	74.68	28620	12.5
3	PtL^1_2 (30)	585	107.6	17270	9.6
4	PtL^1_2(30)*	507(sh), 580	352.0	38750	14.9
5	PtL^7_2 (5)	512, 544	109.6	17777	9.9
6	PtL^7_2 (20)	533(sh), 587	110.2	20740	11.2
7	PtL^7_2 (30)	533(sh), 606	80.9	13200	8.7

At the lowest doping concentrations investigated, device 1 (5 wt. % PtL^1_2) was dominated by broad, red-shifted emission likely to be excimeric in nature. In contrast, device 5 (5 wt. % PtL^7_2) displayed structured emission reminiscent of the monomer seen in the PL spectra at low-concentrations (Table 2.11). The colour-tuning of these devices is evident from the EL spectra, particularly in the devices containing PtL^7_2 which exhibit yellow-green monomer emission at low doping concentrations and orange-red emission at higher doping concentrations. In comparison to the solution-processed devices, the VTE device 4 proved to be the most efficient device with an EQE of 14.9 % and high brightness of 38750 cd m^{-2}. The emission in this device displayed mostly excimeric emission with a small amount of monomer emission still present. The solution-processed devices 2 and 6 with dopant concentrations of 20 % for each complex were seen to be close contenders to this VTE with EQEs of 12.5 and 11.2 % respectively. These results highlight the value of solution-processing as an effective technique to produce high efficiency devices incorporating these soluble triazole complexes. In terms of large-scale production this is favourable owing to the ease of fabrication and ultimately lower cost of production in solution-processed devices compared to VTE devices.

Table 2.11: *EL spectra, brightness and current density vs. voltage and current density vs. EQE for solution-processed OLEDs containing PtL^1_2 and PtL^7_2 at different doping concentrations. Devices were fabricated by Piotr Pander (Durham University, Physics department).*

PtL^1_2	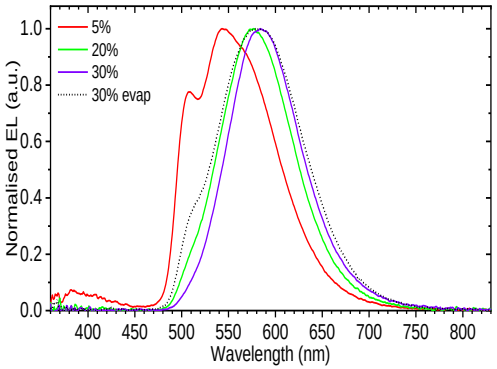	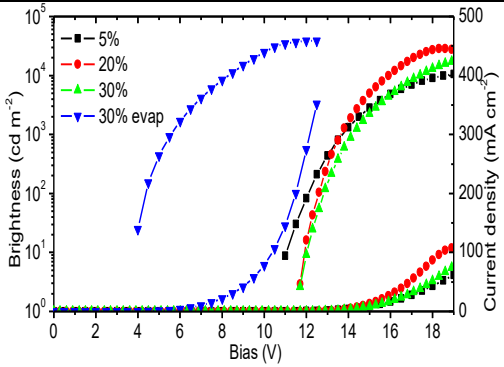	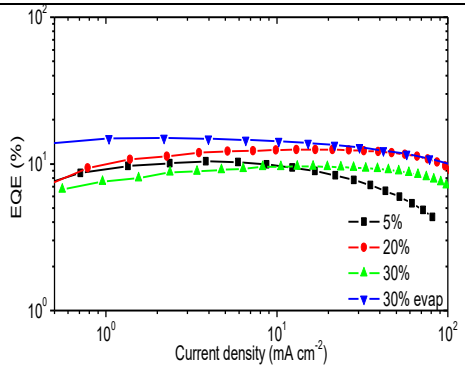
PtL^7_2	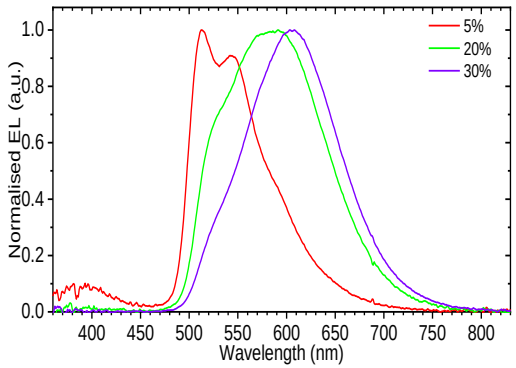	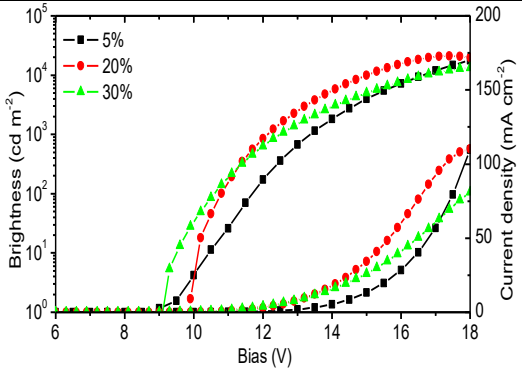	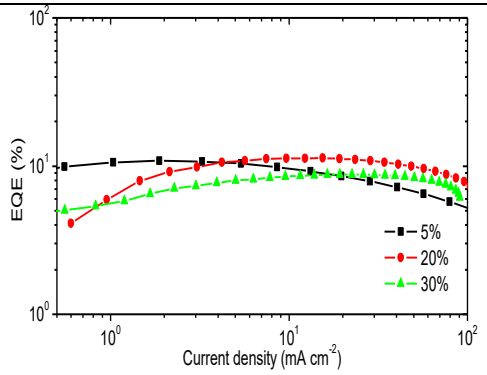

2.3.2 Heteroleptic 1,2,4-Triazole Complexes

Heteroleptic complexes featuring 1,2,4-triazole ligands in combination with N^C^{-} and N^N ligands were investigated to give both neutral and charged complexes respectively. Many typical synthesis routes for other heteroleptic neutral complexes involve the formation of a Pt(N^C) chloro-bridged dimer which is then cleaved by reaction with an appropriate ligand.[119] In this way, a range of Pt dimers were synthesised and cleaved with varying 1,2,4-triazole ligands to form neutral heteroleptic complexes. The cationic complexes on the other hand were formed via reaction of Pt(N^N)Cl_2 compounds with the triazole ligands (where N^N = bpy or phen).

2.3.2.1 Neutral Heteroleptic Complexes

Synthesis

Thienylpyridine complexes

Initially the [Pt(thpy)(μ-Cl)]$_2$ chloro-bridged dimer was formed and isolated in good yield. To afford a range of complexes, this dimer was subsequently cleaved with the 1,2,4-triazole ligands HL^n where n= 1,2,3,7,8,9 and 10 in DCM/MeOH (1:1) at 60 °C (Scheme 2.9). The complexes were purified by alumina column chromatography followed by recrystallization in DCM/Hexane. The yields of the final complexes varied widely from 22 to 95 %. The complexes with aryl substituents on the pyridyl ring, Pt(thpy)L$^{7\text{-}10}$, were formed in superior yields to those with no pyridyl substituent, Pt(thpy)L$^{1\text{-}3}$.

Phenylquinoline complexes

Initially the chloro-bridged [Pt(pquin)(μ-Cl)]$_2$ dimer was isolated and then cleaved with the 1,2,4-triazole ligand in DCM/MeOH (1:1) at 60 °C (Scheme 2.10). The complexes were purified by washing with MeOH and Et_2O followed by recrystallization from DCM/Hexane. Yields of the purified complexes ranged from 60 to 77 %.

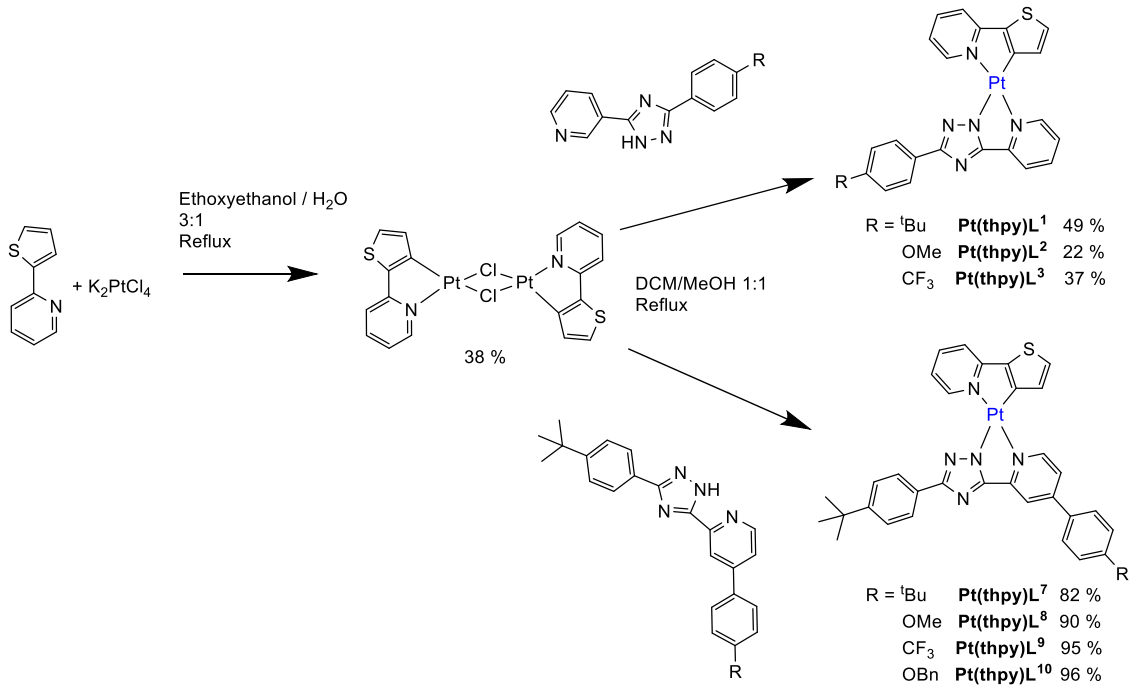

Scheme 2.9: *Synthesis of [Pt(thpy)(μ-Cl)]$_2$ dimer and subsequent cleavage with 1,2,4-triazole ligands to form Pt(thpy)L$^{1-3}$ and Pt(thpy)L$^{7-10}$.*

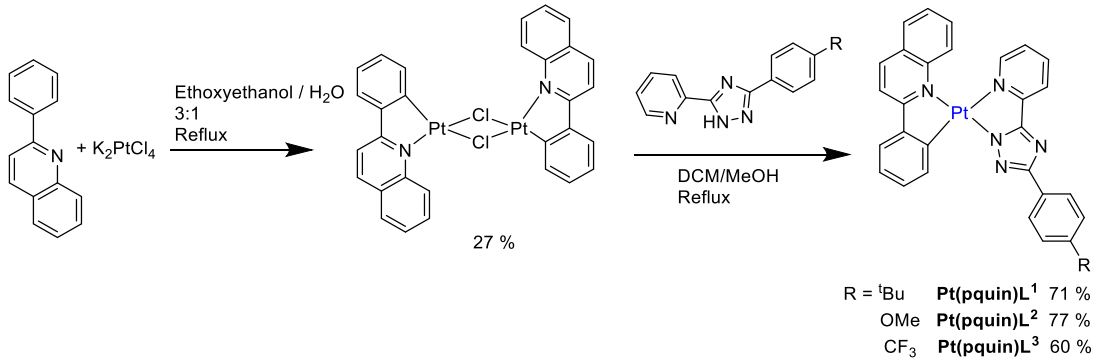

Scheme 2.10: *Synthesis of [Pt(pquin)(μ-Cl)]$_2$ dimer and subsequent cleavage with 1,2,4-triazole ligands to form Pt(pquin)L^n complexes.*

Characterisation

Thienylpyridine complexes

The ^{1}H NMR comparison of the of the free ligand HL^1 and the complex Pt(thpy)L^1 was a useful tool in confirming the identity of the thienylpyridine complexes (Fig. 2.31). The presence of signals at 10.5 and 9.3 ppm for Pt(thpy)L^1 show satellites for coupling to ^{195}Pt and were assigned as H^{6triz} and H^{6thpy} respectively after 2D NMR analysis.

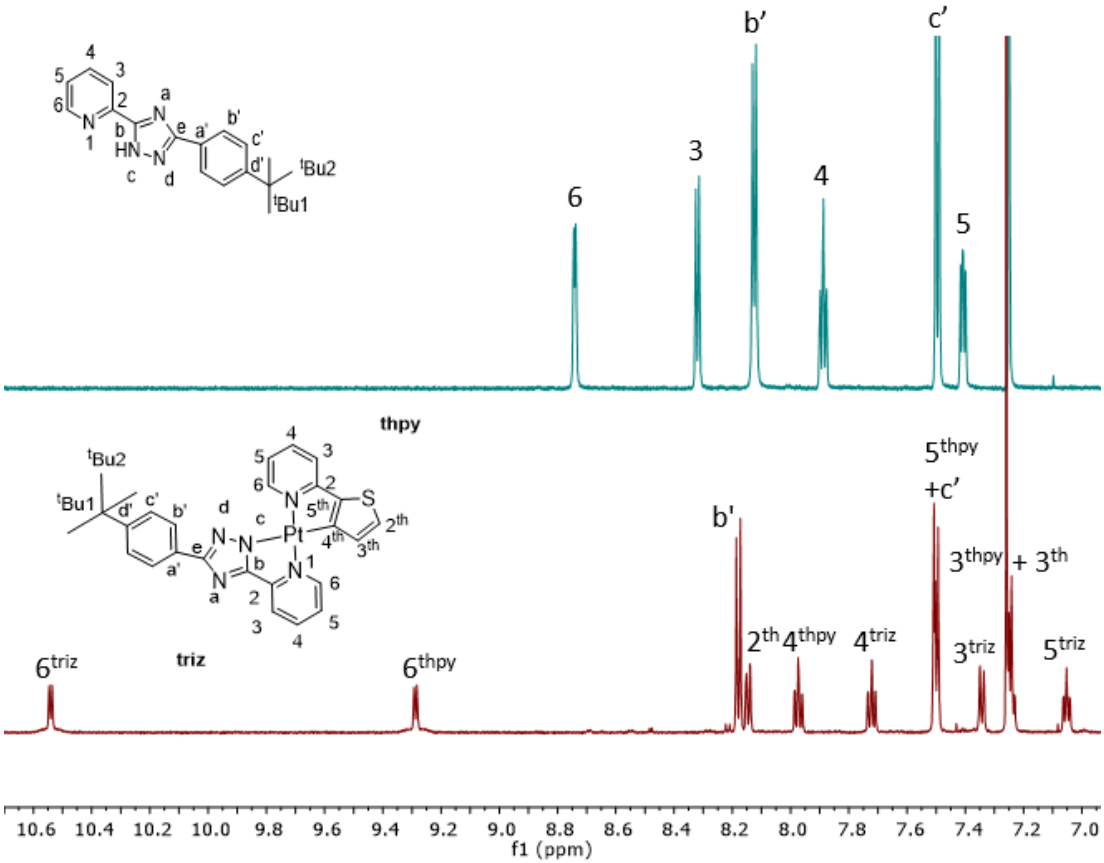

Figure 2.31: *700 MHz 298K ^{1}H NMR spectrum in $CDCl_3$ showing comparison between HL^1 (top) and Pt(thpy)L^1 (bottom).*

Phenylquinoline complexes

Crystals of Pt(pquin)L^3 were obtained by slow evaporation from a DCM solution (Fig. 2.32). The crystal structure revealed the presence of two molecules of the complex in the unit cell which differed only in the orientation of the CF_3 group in one complex relative to the other. These complexes were arranged in a head-to-tail conformation and displayed a nearest Pt···Pt distance of 3.734 Å. Interestingly, the structure is seen to be twisted away from planarity and the torsion angle between the planes of the two 5 membered rings Pt1-N3-C21-C20-N2 and Pt1-N1-C1-C10-C15 was found to be 20.3 ° owing to large steric hindrance This contrasts with the planarity of the homoleptic structures discussed previously in this chapter. The Pt1—C15 bond is the shortest at 1.975 Å owing to its cyclometallated nature and Pt1—N3, which involves the bonding of the N^- atom, is seen to be of a similar length at 2.002 Å (Table 2.12). Both Pt—N bonds, where N is a neutral N donor, are slightly longer.

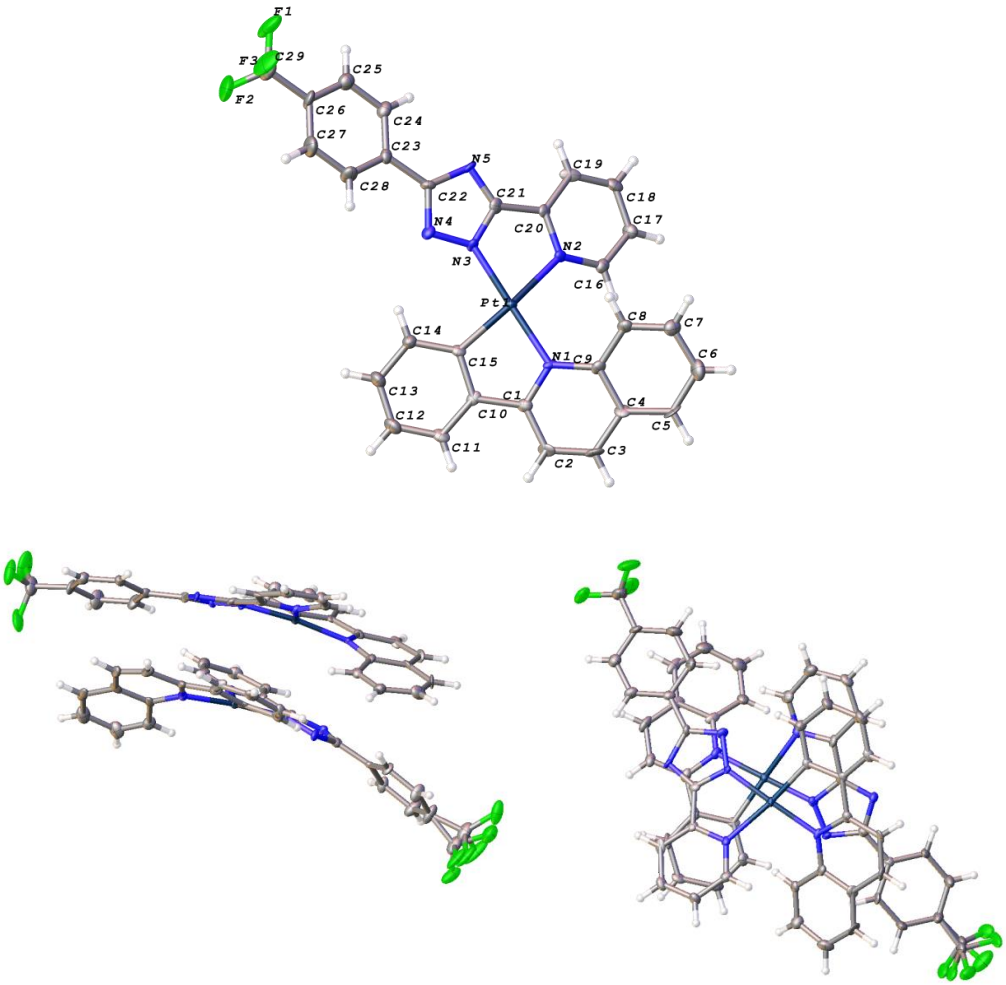

Figure 2.32: *Crystal structure and packing of Pt(pquin)L[3].*

Table 2.12: *Selected bond lengths and angles for Pt(pquin)L[3].*

Bond Lengths/ Å		*Bond Angles / °*	
Pt1—N1	2.037(6)	N1-Pt1-N2	103.9(2)
Pt1—N2	2.177(7)	N3-Pt1-N1	175.0(3)
Pt1—N3	2.002(6)	N3-Pt1-N2	76.9(3)
Pt1—C15	1.975(7)	C15-Pt1-N1	80.6(3)
		C15-Pt1-N2	166.7(3)
		C15-Pt1-N3	99.8(3)

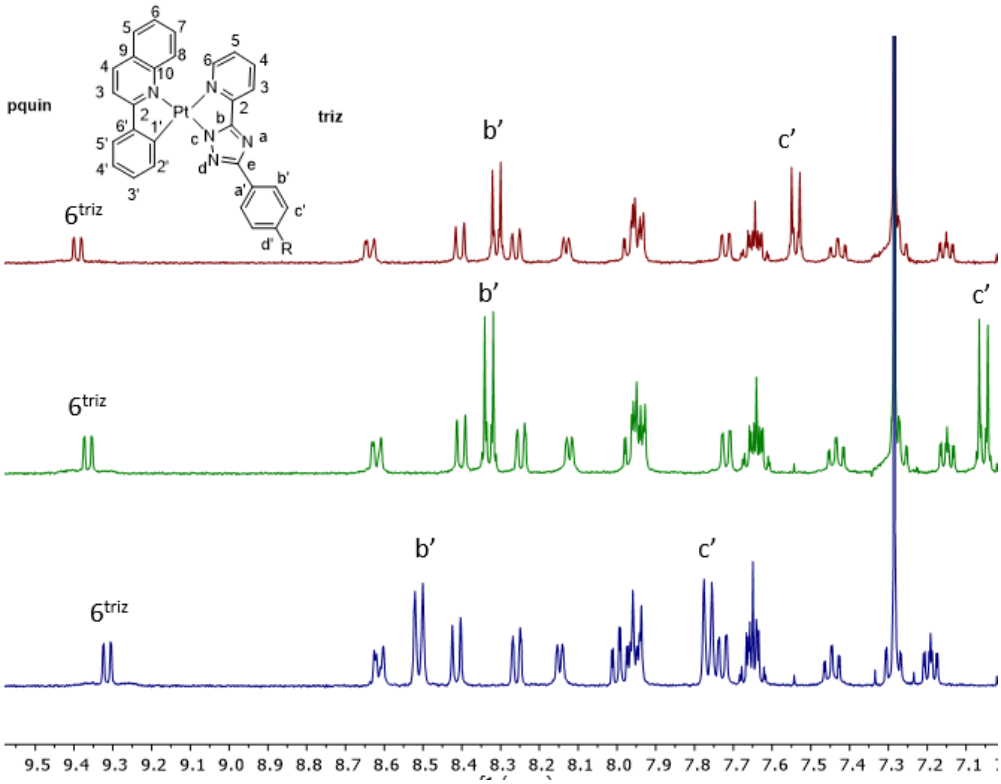

Figure 2.33: *Pt(pquin)L[1], Pt(pquin)L[2] and Pt(pquin)L[3] 400 MHz NMR in $CDCl_3$ from top to bottom.*

The ^{1}H NMR spectra were compared for Pt(pquin)L^n where n=1, 2 and 3 (Fig. 2.33). The chemical shifts of the H^{6triz} protons are not vastly different for the complexes, however, the most de-shielded proton is seen to be in Pt(pquin)L^1. The protons on the aromatic phenyl ring of the triazole ligand are most affected by the nature of the R group. In comparison to Pt(pquin)L^1 where R=^{t}Bu, the H$^{c'}$ proton in Pt(pquin)L^2 where R= OMe is shifted to a lower ppm value, whilst in Pt(pquin)L^3 it is shifted to a higher ppm value. This is due to the electron-donating nature of OMe and the electron-withdrawing nature of CF_3 which affect the shielding of the appropriate protons.

Photophysical properties

Thienylpyridine complexes

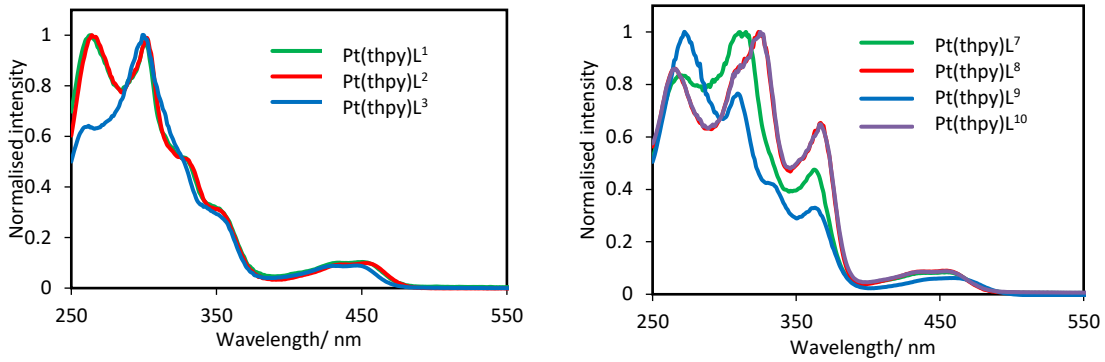

Figure 2.34: *Absorption spectra of Pt(thpy)L$^{1-3}$ and Pt(thpy)L$^{7-10}$ in DCM at RT.*

Pt(thpy)L$^{1-3}$ displayed absorption spectra with two main bands between 250-320 nm assigned as LC transitions (Fig. 2.34). Weaker bands/shoulders are present at ~350 nm and broader bands at longer wavelength centred at λ_{max} 440 nm are characteristic of MLCT transitions. For complexes Pt(thpy)L$^{7-10}$ similar absorption profiles were observed, but with more pronounced bands centred at 365 nm. Moreover, the absorption spectra are seen to be red-shifted in comparison to Pt(thpy)L$^{1-3}$, whereby the absorption extends to 490 nm (vs. 480 nm for Pt(thpy)L$^{1-3}$), owing to the extended conjugation offered by the phenyl groups on the pyridyl ring of the triazole ligand.

The emission of these complexes in degassed DCM at RT was studied and all complexes show similar vibrationally-resolved emission spectra to one another with bands at 570, 615 and a shoulder at 665 nm (Fig. 2.35).

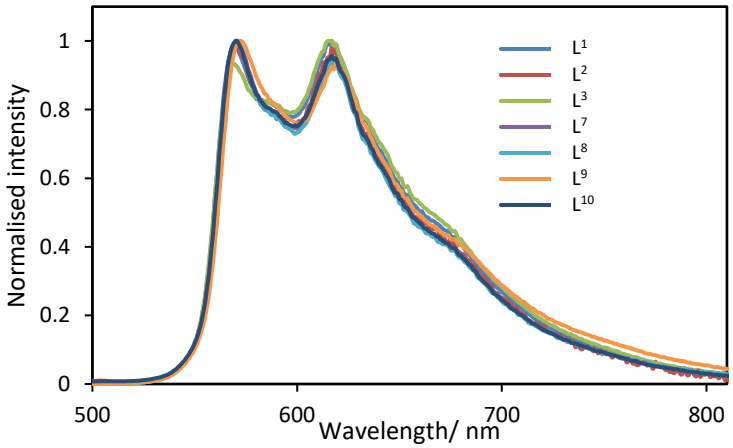

Figure 2.35: *Pt(thpy)L$^{1-3}$ and Pt(thpy)L$^{7-10}$ RT emission in 1 x 10^{-6} M degassed DCM solution.*

The PLQY values for Pt(thpy)L^{n} ranged from 30-37 % with lifetimes of 13 to 17 µs and thus all complexes displayed similar photophysical properties in degassed DCM solution (Table

2.13). The concentration-dependent emission spectra were measured for Pt(thpy)L[7-10] and are shown in Figure 2.36. As the concentration is increased, they show the introduction of a broad and structureless band with λ_{max} values of 740 nm for all complexes. These are likely to be excimeric in nature as Stern-Volmer plots show the correlation between the concentration and inverse of the lifetimes for each solution measured (Fig. 2.36). Pt(thypy)L[7] and Pt(thpy)L[8] were calculated as having larger k_{sq} values which is consistent with their concentration-dependent emission spectra which show more intense excimeric emission in comparison to Pt(thpy)L[9] and Pt(thpy)L[10].

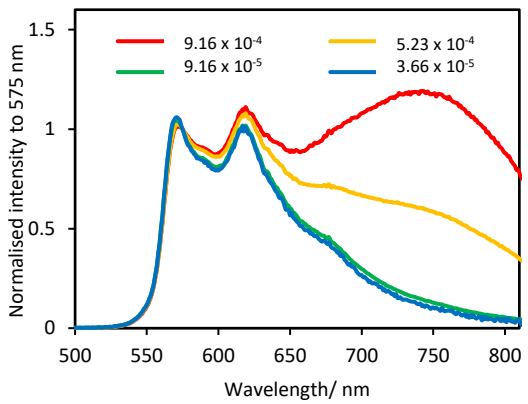

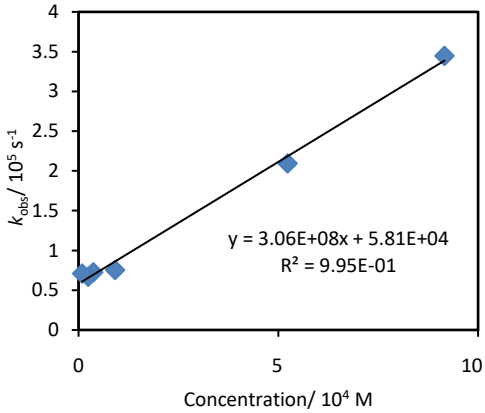

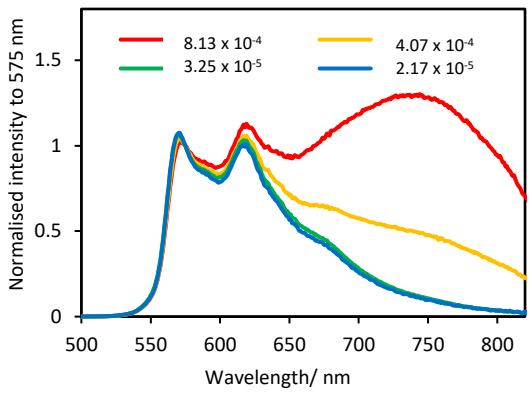

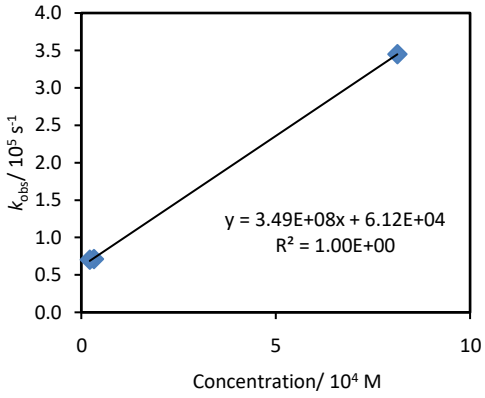

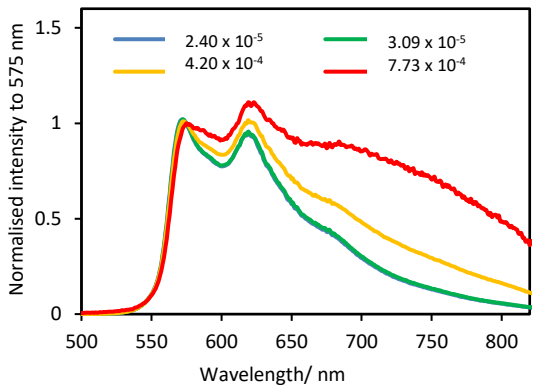

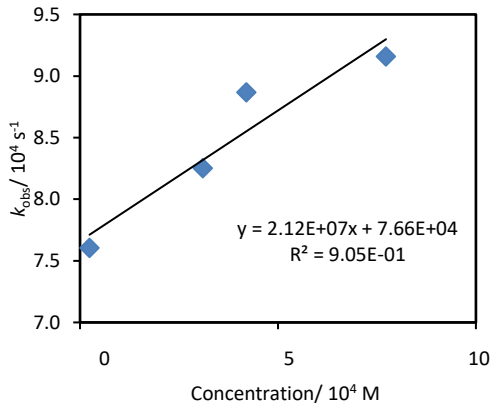

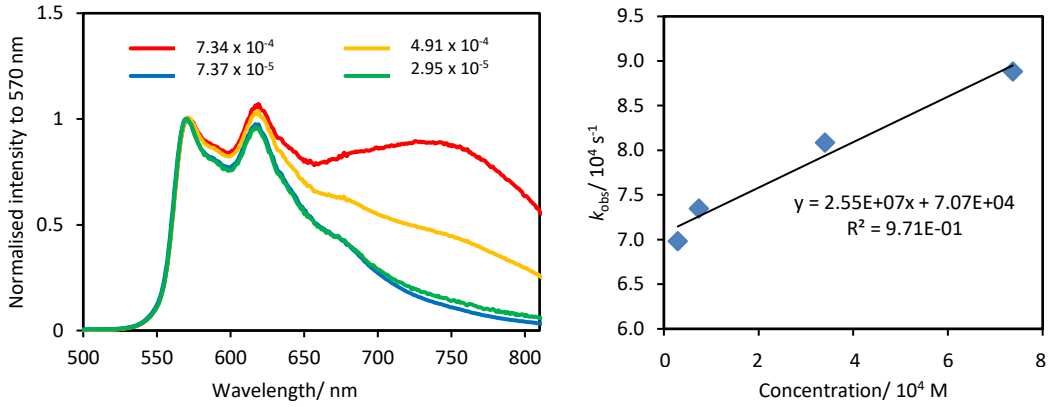

Figure 2.36: *From top to bottom: Pt(thpy)L[7], Pt(thpy)L[8], Pt(thpy)L[9] and Pt(thpy)L[10] concentration-dependent emission spectra in degassed DCM where concentrations are given in mol dm[-3] (left) and their corresponding Stern-Volmer plots (right).*

The 77 K emission spectra were recorded for each complex and show sharper peaks than the RT emission spectra with increased vibrational resolution (Fig. 2.37). The structure is particularly well-resolved for complexes Pt(thpy)L[7-10], presumably associated with the phenyl rings on the 4 positions of the pyridyl rings. Upon going from RT to 77 K there is virtually no change in the wavelength of the 0-0 transition for all complexes (Table 2.13), implying that there is little excited state distortion even at RT, which is also reflected in their high PLQY values.

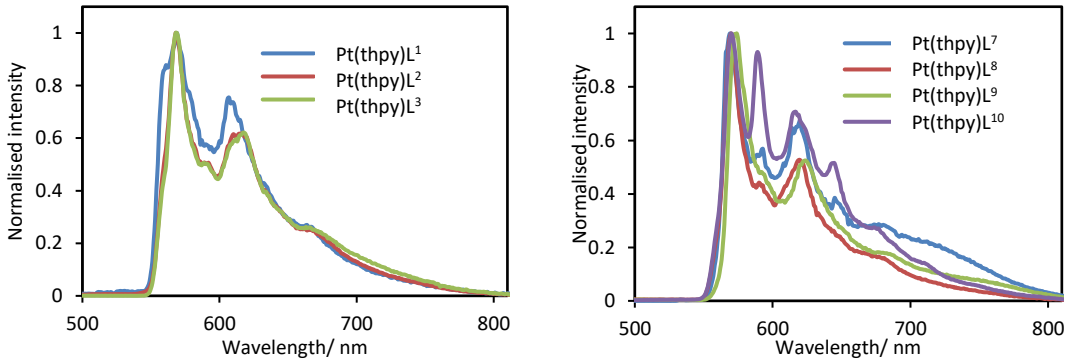

Figure 2.37: *Pt(thpy)L[1-3] (left) and Pt(thpy)L[7-10](right) 77 K emission spectra in butyronitrile.*

Table 2.13: *Photophysical data for complexes Pt(thpy)L[1-10]. Emission was run in degassed DCM at a concentration of 10^{-6} M and 77 K spectra were run in butyronitrile glass.*

Complex	298 K										77 K	
	λ_{abs} (nm)	λ_{em} (nm)	τ_{deg} (µs)	τ_{aer} (ns)	τ_0 (µs)	φ (%)	k_r (10^4 s^{-1})	k_{nr} (10^4 s^{-1})	k_q (O_2) (10^8 M^{-1} s^{-1})	k_{sq} (10^8 M^{-1} s^{-1})	λ_{em} (nm)	τ (µs)
Pt(thpy)L[1]	262 (60340), 301 (59057), 328 (31280), 352 (18975), 430 (5773), 451 (6200).	569, 585(sh), 616, 660(sh)	16	480	/	34	2.1	4.1	9.2	/	568, 593(sh), 606, 633(sh), 662.	18
Pt(thpy)L[2]	262 (42965), 301 (41898), 328 (22439), 351 (13754), 434 (4106), 455 (4325).	568, 581(sh), 615, 656(sh)	17	510	/	30	1.8	4.2	8.6	/	568, 590(sh), 614, 635(sh), 667.	15
Pt(thpy)L[3]	259 (48523), 298 (71486), 323 (41698), 345 (23526), 425 (6346), 448 (6793).	568, 587(sh), 615, 661(sh)	16	590	/	32	2.0	4.2	7.5	/	568, 588, 615, 638(sh), 663.	15
Pt(thpy)L[7]	284 (30241), 298 (37099), 362 (23434), 440 (3772).	570, 586(sh), 617, 668	15	700	17	37	2.5	4.2	6.2	3.1	568, 592, 619, 646, 674, 706(sh)	16
Pt(thpy)L[8]	268 (28801), 325 (39543), 368 (25650), 437 (3290).	568, 585(sh), 614, 662(sh)	14	610	16	37	2.6	4.4	7.2	3.5	569, 590, 617, 643, 673, 709(sh)	16
Pt(thpy)L[9]	270 (57790), 304 (42439), 329 (25902), 359 (19646), 450 (3990).	570, 587(sh), 617, 670(sh)	13	530	13	37	2.8	4.8	8.3	0.2	572, 591(sh), 622, 650(sh), 682(sh)	16
Pt(thpy)L[10]	283 (25621), 324 (49702), 367 (32393), 438 (4021).	568, 585(sh), 615, 664(sh)	14	520	14	36	2.5	4.5	8.5	0.3	570, 589, 615, 642, 673(sh), 706(sh).	14

Phenylquinoline complexes

The absorption spectra of the complexes Pt(pquin)L^1 and Pt(pquin)L^2 show three main peaks in the region of 250 to 300 nm (Fig. 2.38). For Pt(pquin)L^3, however, only one main peak is observed at 300 nm with a shoulder between 275 and 300 nm. For all complexes, vibronic bands are seen at 325 to 375 nm and the MLCT band is observed at λ_{max}~425 nm. Pt(pquin)L^3 has a slightly blue-shifted absorption in comparison to the other complexes, probably reflecting the stabilising effect of the electron-withdrawing CF_3 group on the HOMO.

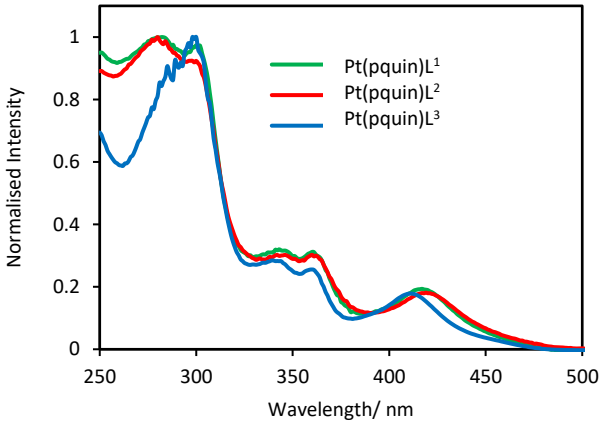

Figure 2.38: *Absorption spectra of Pt(pquin)L^{1-3} in DCM at RT.*

The complexes Pt(pquin)L^{1-3} were weakly emissive with similar PLQYs ranging between 3.4 and 3.7 % and lifetimes between 1.1 and 1.5 µs. The emission spectra of the complexes show very similar profiles to one another in DCM at RT (Fig. 2.39). Even at low concentrations (10^{-6} M) broad emission is observed with no defined peaks. As in the absorption spectra, there is a slight blue-shift in the emission of Pt(pquin)L^3, presumably stemming from the stabilisation of the HOMO via the CF_3 group.

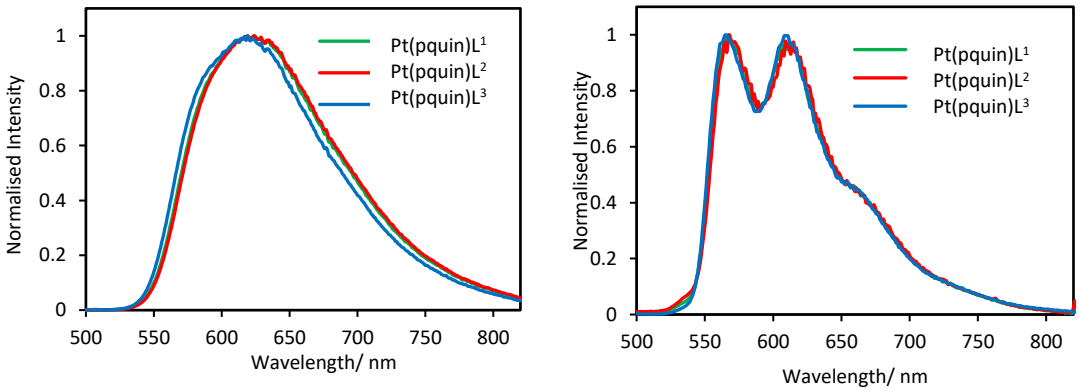

Figure 2.39: *Emission spectra of Pt(pquin)L^{1-3} in DCM at RT (left) and at 77 K in butyronitrile glass (right).*

The emission profile at 77 K for all three complexes clearly show vibrational components in defined peaks at ≈ 565 and 610 nm with a shoulder at 665 nm, in contrast to the emission in DCM at RT. This suggests that the excited state distortion is high at RT. Moreover, the luminescence lifetimes were seen to increase by an order of magnitude for these complexes on cooling to 77 K (Table 2.14).

Table 2.14: *Photophysical properties of Pt(pquin)L$^{1-3}$. Emission was run in degassed DCM at a concentration of 10^{-6} M and 77 K spectra were run in butyronitrile glass.*

Complex	298 K								77 K	
	λ_{abs} (nm)	λ_{em} (nm)	τ_{deg} (μs)	τ_{aer} (ns)	φ (%)	k_r (10^4 s^{-1})	k_{nr} (10^5 s^{-1})	k_q (O_2) (10^8 M^{-1} s^{-1})	λ_{em} (nm)	τ (μs)
Pt(pquin)L^1	299 (91057), 340 (26610), 361 (23992), 412 (16762).	618	1.3	500	3.4	2.6	7.4	5.7	566, 612, 664(sh).	15
Pt(pquin)L^2	277 (26554), 299 (24929), 343 (8180), 361 (8275), 418 (5003).	618	1.5	520	3.7	2.5	6.4	5.7	566, 612, 664(sh).	14
Pt(pquin)L^3	298 (126192), 339 (37889), 359 (34493), 410 (23839).	618	1.1	450	3.5	3.2	8.8	6.0	564, 608, 664(sh).	14

2.3.2.2 Cationic heteroleptic complexes

Synthesis

Bipyridine complexes

Complexes $[Pt(bpy)L^{1-3}]PF_6$ were synthesised via initial formation of $Pt(bpy)Cl_2$. This was then refluxed in DCM with the selected triazole ligand and AgOTf was present to strip the chloride ions from $Pt(bpy)Cl_2$. Ion exchange was performed with KPF_6 to obtain the more organic soluble PF_6^- salt as opposed to the Cl^- salt and complexes were purified by subsequent water washes (Scheme 2.11). Yields of the purified complexes varied from 27 to 75 %.

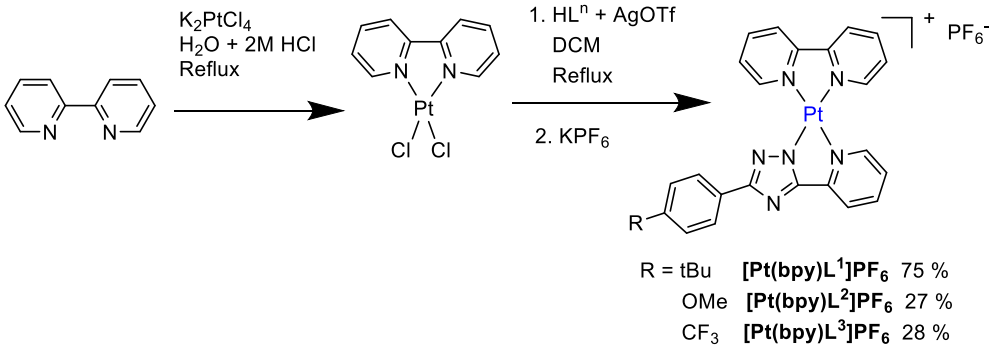

Scheme 2.11: *Synthesis of $[Pt(bpy)L^{1-3}]PF_6$ complexes.*

Phenanthroline complexes

Complexes $[Pt(phen)L^{1-3}]PF_6$ were synthesised in the same way as for $[Pt(bpy)L^{1-3}]PF_6$ discussed previously, but via initial formation of $Pt(phen)Cl_2$ as the intermediate (Scheme 2.12). Yields of the purified complexes varied from 12 to 60 %. $[Pt(phen)L^3]^+$ was insoluble for photophysical study, however, was characterised by NMR in d_6-DMSO at elevated temperature.

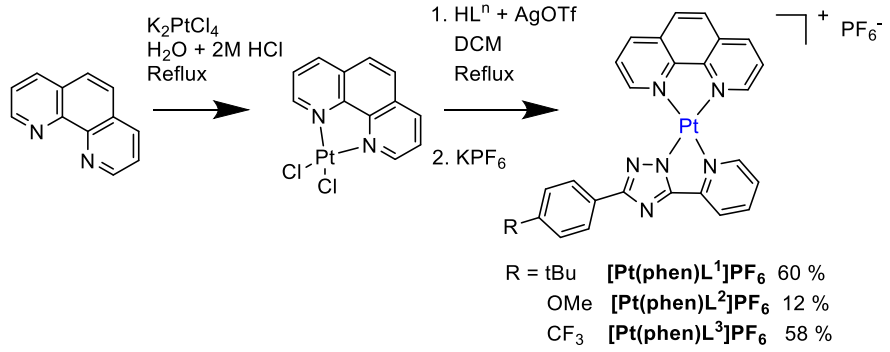

Scheme 2.12: *Synthesis of $[Pt(phen)L^{1-3}]PF_6$ complexes.*

Characterisation

Bipyridine complexes

Crystals of $[Pt(bpy)L^2]PF_6$ suitable for X-ray diffraction were obtained by slow cooling from hot DMSO solution (Fig. 2.40). The cations form off-centred stacks and the closest Pt···Pt distance is 3.429 Å. The Pt1—N5 bond distance is seen to be slightly longer than that of Pt1—N6 (2.036 vs. 1.993 Å) due to the stronger *trans* influence exerted by the N^- atom on the triazole ring compared to the neutral N on the pyridine ring of the triazole ligand (Table 2.15).

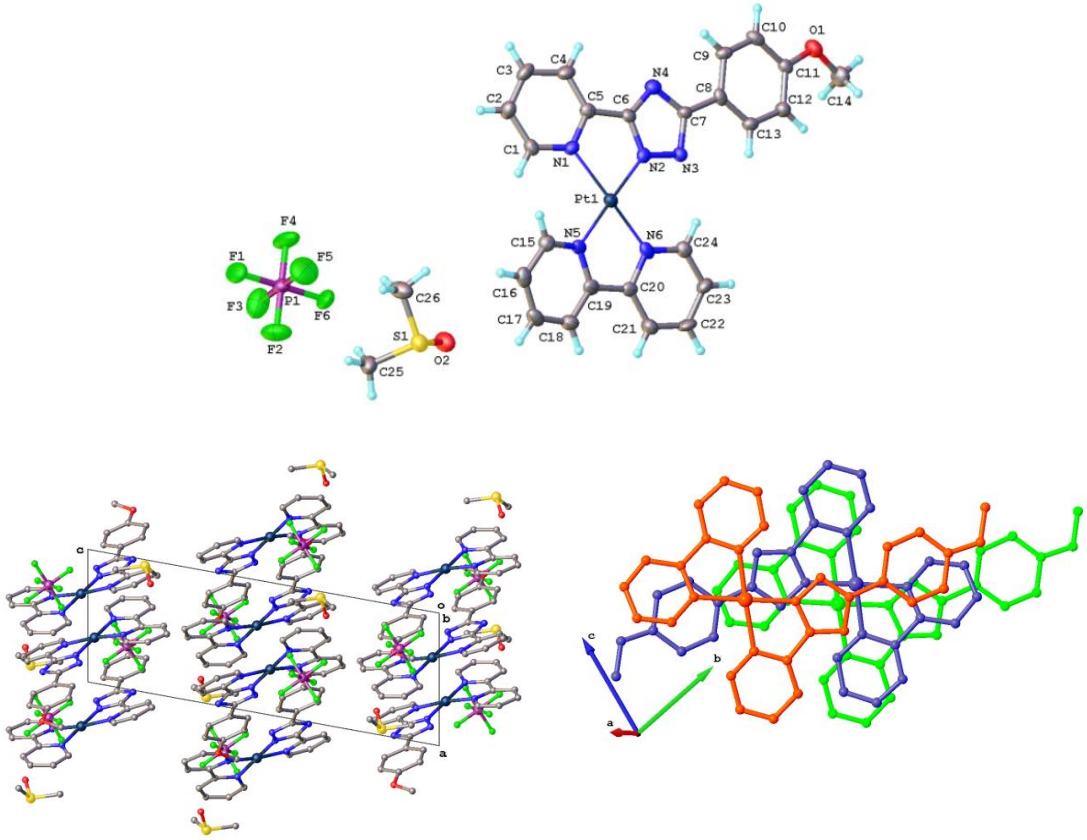

Figure 2.40: *Crystal structure and packing for* $[Pt(bpy)L^2]PF_6$.

Table 2.15: *Selected bond lengths and angles for* $[Pt(bpy)L^2]PF_6$.

Bond Lengths/ Å		*Bond Angles / °*	
Pt1—N1	2.082(5)	N2-Pt1-N1	78.4(2)
Pt1—N2	1.996(6)	N2-Pt1-N5	178.4(2)
Pt1—N5	2.036(5)	N5-Pt1-N1	102.8(2)
Pt1—N6	1.993(6)	N6-Pt1-N1	173.6(2)
		N6-Pt1-N2	99.0(2)
		N6-Pt1-N5	79.9(2)

Phenanthroline complexes

^{1}H NMR spectroscopy was used to confirm the identity of the phenanthroline complexes (Fig. 2.41). The *ortho* positions on the phenanthroline ligand (H^{9} and H^{2}) displayed the highest ppm values. All signals in $[Pt(phen)L^{1}]^{+}$ were shifted downfield compared to those in $[Pt(phen)L^{3}]^{+}$ (e.g. H^{9} at 10.11 vs. 9.83 ppm) except signals $H^{b'}$ and $H^{c'}$. These protons exhibited a de-shielding effect from the inductively electron-withdrawing CF_3 group and as a result had slightly higher ppm values than for the same signals in $[Pt(phen)L^{1}]^{+}$ which contained a ^{t}Bu group instead of the CF_3 group.

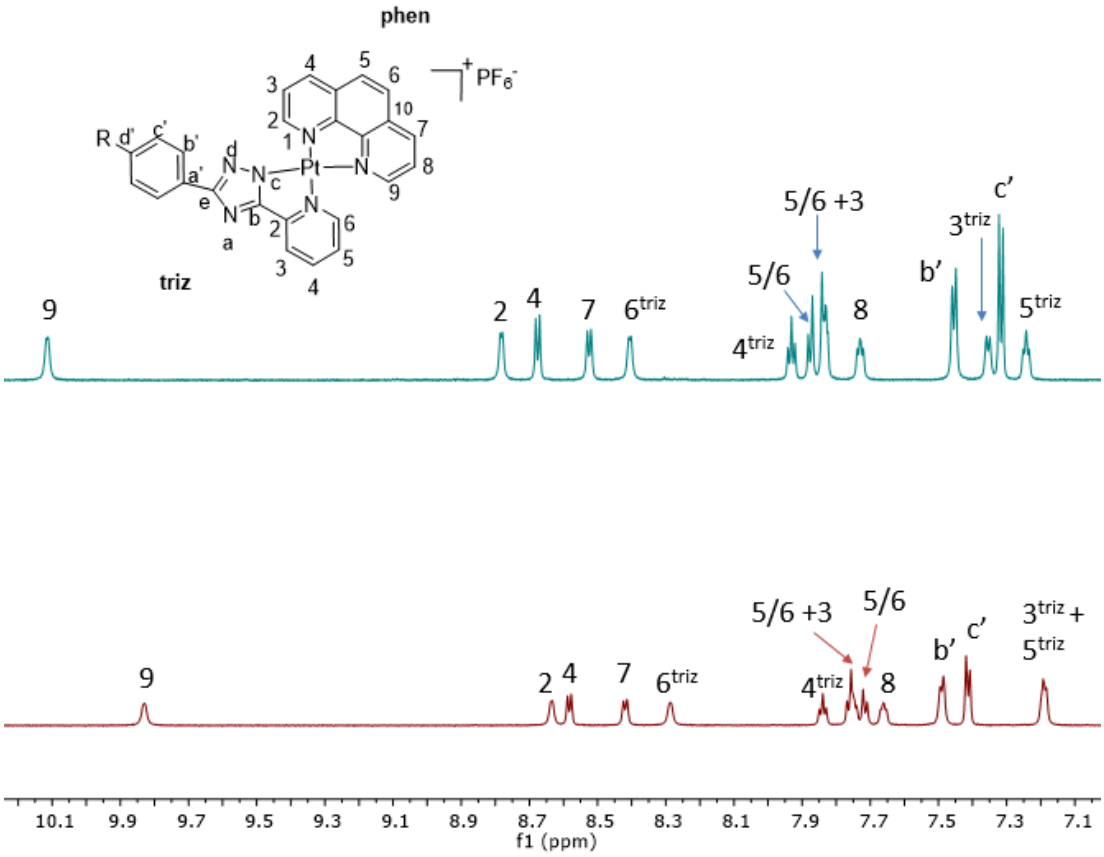

Figure 2.41: *Pt(phen)L^{1} (top) and Pt(phen)L^{3} (bottom) 700 MHz NMR in DMSO-d$_6$.*

Photophysical properties

Bipyridine complexes

The absorption spectra of complexes $[Pt(bpy)L^{1\text{-}3}]^{+}$ in MeCN solution show bands with high extinction coefficients at low energy between 250 and 305 nm which can be described as spin-allowed and LC in nature, involving mainly the triazole ligand (π→π*) (Fig. 2.42). The bands at 320 to 355 nm could be the result of a different transition with largely LC character but also some metal contribution. The bands at 385 nm for $[Pt(bpy)L^{3}]^{+}$ and at 410 nm for $[Pt(bpy)L^{1\text{-}2}]^{+}$ are assigned as MLCT in character owing to their low intensity at longer wavelengths.

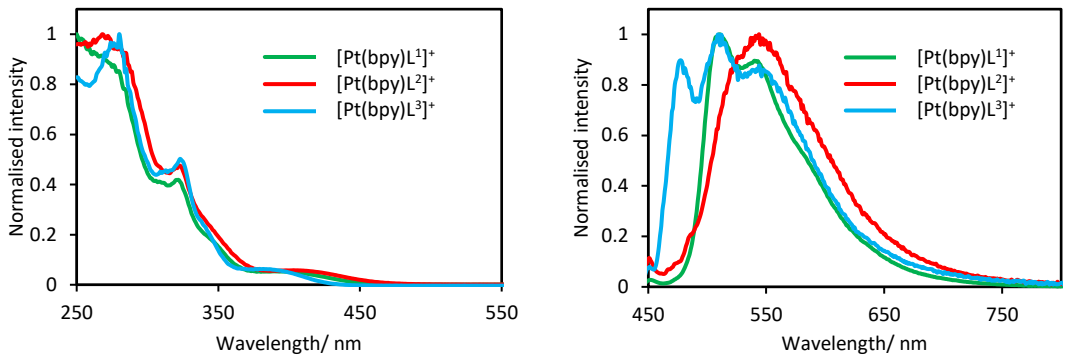

Figure 2.42: *[Pt(bpy)L$^{1\text{-}3}$]$^+$ absorption in MeCN solution at RT (left) and 77 K emission in butyronitrile glass (right).*

Complexes [Pt(bpy)L$^{1\text{-}3}$]$^+$ were non-emissive in degassed MeCN at RT however, at 77 K in butyronitrile glass they showed intense emission (Fig. 2.42). This suggests that non-radiative decay is high in these complexes at RT and is majorly suppressed at lower temperatures. On increasing the concentration in butyronitrile at 77 K, all three complexes show evidence of excimeric/aggregate emission. Indeed, for [Pt(bpy)L^2]$^+$ purely monomeric emission was only seen when the concentration of the sample was very low. As a result, the monomer emission was extremely weak and barely observable. Instead, intense, red-shifted emission was present at the same concentrations used for [Pt(bpy)L^1]$^+$ and [Pt(bpy)L^3]$^+$.

Table 2.16: *Photophysical data of complexes [Pt(bpy)L$^{1\text{-}3}$]$^+$ in butyronitrile glass at 77 K.*

Complex	*298 K*	*77 K*	
	λ_{abs} (nm)	*λ_{em} (nm)*	*τ (μs)*
[Pt(bpy)L^1]$^+$	65(24971), 310(10883), 322(11384), 344(5461), 398(1584).	511, 542, 582(sh)	17
[Pt(bpy)L^2]$^+$	268(10711), 321 (5242), 405(609).	532	20
[Pt(bpy)L^3]$^+$	279(24468) 313(11447), 324(12593), 385(1892).	478, 510, 545	15

Phenanthroline complexes

The absorption spectra for [Pt(phen)L^1]$^+$ and [Pt(phen)L^2]$^+$ are very similar to one another with high intensity bands between 200 and 300 nm (Fig. 2.43) which are assigned as LC $\pi\rightarrow\pi^*$ transitions owing to their resemblance to the absorption of phenanthroline as described in the literature.[120] The lower energy bands of lower intensity are assigned as MLCT transitions owing to contribution from the Pt centre. The solubility of [Pt(phen)L^3]$^+$ was too low to show any absorption in all common organic solvents.

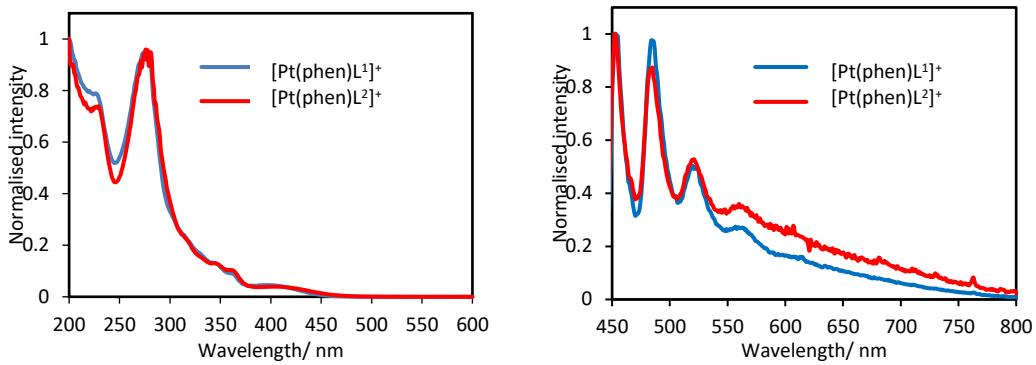

Figure 2.43: *Absorption of [Pt(phenL$^{1\text{-}2}$]$^+$ in MeCN solution (left) and emission in butyronitrile glass at 77 K (right).*

All complexes were too weak to show any emissive properties at RT and were only slightly emissive at 77 K. The 77 K emission was run in butyronitrile glass and shows structured emission at similar wavelengths for both complexes (Fig. 2.43). The 77 K emission lifetimes were extremely long, ranging from 140 to 150 µs and this feature is discussed in more detail in the next section (Table 2.17).

Table 2.17: *Photophysical data of complexes [Pt(phen)L$^{1\text{-}2}$]$^+$ in butyronitrile glass at 77 K.*

Complex	*298 K*	*77 K*	
	λ_{abs} (nm)	*λ_{em} (nm)*	*τ (µs)*
[Pt(phen)L^1]$^+$	274 (59393), 345 (9128), 401 (3191).	453, 485, 518, 560, 610(sh)	150
[Pt(phen)L^2]$^+$	275 (58680), 345 (9098), 400 (3254).	452, 483, 520, 560, 610(sh)	140

2.3.3 DFT studies on selected triazole complexes

To better understand the nature of the electronic transitions occurring in these complexes, DFT calculations and time-dependent DFT (TD-DFT) were performed using the B3LYP method and LANL2DZ basis set for all atoms, with the Gaussian09 program. TD-DFT calculated the main contributions from specific orbitals to the $S_0 \rightarrow S_1$ transition and these orbitals are shown in Table 2.18. For the majority of complexes, the transition was largely HOMO→LUMO based, excluding [Pt(phen)L^1]$^+$ which was calculated as having a HOMO→LUMO+1 transition (Table 2.19).

In all neutral complexes, the HOMO is largely situated on the triazole and conjugated aromatic rings, with a large contribution from the Pt centre. For the homoleptic complexes, the LUMO is based on the pyridyl rings with contribution from the phenyl rings on the 4-position of the pyridine in the case of PtL$^7_2$. In contrast, for both heteroleptic thienyl pyridine complexes Pt(thpy)L^1 and Pt(thpy)L^7 the LUMO resides on the thienyl group whilst the phenyl rings on the 4-position of the pyridyl group were seen to play no part in the

transition. This could explain the similarity in the two groups of thienyl pyridine complexes for which the emission spectra, quantum yields and lifetimes were almost identical (as discussed earlier). Similarly, for Pt(pquin)L^1 the LUMO is based on the quinoline moiety instead of the pyridyl ring and some metal character was retained. In terms of these neutral complexes, the transitions were thus ascribed as mixed with metal and ligand contributions i.e. $d_{Pt}/\pi_{triz} \rightarrow \pi^*$.

For the charged complexes $[Pt(bpy)L^1]^+$ and $[Pt(phen)L^1]^+$, the HOMO and LUMO/LUMO+1 orbitals are less defined and are spread more diffusely across the molecule. In $[Pt(bpy)L^1]^+$ the HOMO is more centred on the bipyridine and the LUMO on the pyridyl ring of the triazole ligand. In $[Pt(phen)L^1]^+$ however, both the HOMO and the LUMO+1 are based mainly on the phenanthroline ligand and the triazole ring is seen to have little to no contribution to the main orbitals, hence these transitions are described as having much weaker MLCT character. This could explain the poor photophysical properties displayed by these complexes, particularly for $[Pt(phen)L^1]^+$.

Colour tuning of the homoleptic complexes was achieved by changes to the pyridyl and aromatic groups. Indeed, upon going from PtL^1_2 with no pyridyl substitution to PtL^7_2 with phenyl ring incorporation on the 4-position of the pyridine, a noticeable decrease in the energy of the excited state was observed from 489 nm to 499 nm which resulted in a red-shift in the emission, as shown earlier. This can be explained by the apparent contribution of the substituted phenyl rings to stabilising the LUMO. Moreover, this is extended to complex PtL^9_2 which incorporated CF_3-substituted phenyl groups to reduce the HOMO-LUMO gap, giving a further red-shift of emission. This demonstrates the effective conjugation, owing to the planarity of the structure, whereby the CF_3 group has a strongly stabilising effect on the LUMO (Fig. 2.44).

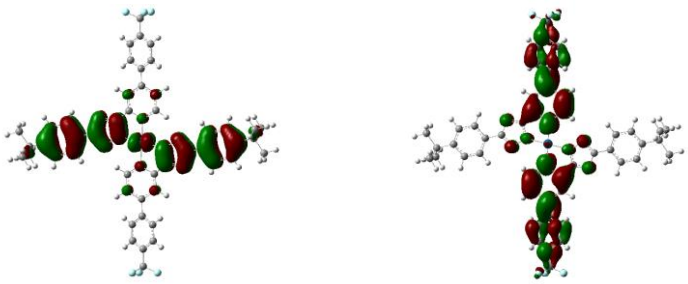

Figure 2.44: *HOMO and LUMO orbitals of* PtL^9_2.

Table 2.18: *Major contributions to the $S_0 \rightarrow S_1$ transitions in selected triazole complexes as calculated by TD-DFT.*

Complex	**PtL^1_2**	**PtL^7_2**	**$Pt(thpy)L^1$**	**$Pt(thpy)L^7$**	**$Pt(pquin)L^1$**	**$[Pt(bpy)L^1]^+$**	**$[Pt(phen)L^1]^+$**
Energy (eV/ nm)	2.53 /489	2.49 /498.81	1.3196 / 939.59	1.3179 / 940.76	2.5428 / 487.59	0.9492 / 1306.16	0.6616 / 1873.90
Oscillator Strength	0.0296	0.0453	0.0001	0.0001	0.0298	0.0721	0.0129
Main contribution (%)	HOMO→LUMO (70) HOMO-4→LUMO+1 (10)	HOMO→LUMO (70)	HOMO→LUMO (55) HOMO-1→LUMO (43)	HOMO→LUMO (56) HOMO-1→LUMO (43)	HOMO→LUMO (64)	HOMO→LUMO (99)	HOMO→ LUMO+1 (86)
Assignment	Mixed MLCT/ILCT	Mixed MLCT/ILCT	Mixed MLCT/LLCT	Mixed MLCT/LLCT	Mixed MLCT/LLCT	Mixed MLCT/LLCT	Mixed MLCT/LLCT

Table 2.19: *HOMO and LUMO orbital plots for selected triazole complexes using B3LYP/LANL2DZ. * Indicates the LUMO+1 is shown for $[Pt(phen)L^1]^+$ instead of the LUMO.*

Complex	*PtL^1_2*	*PtL^7_2*	*$Pt(thpy)L^1$*	*$Pt(thpy)L^7$*	*$Pt(pquin)L^1$*	*$[Pt(bpy)L^1]^+$*	*$[Pt(phen)L^1]^+$*
HOMO	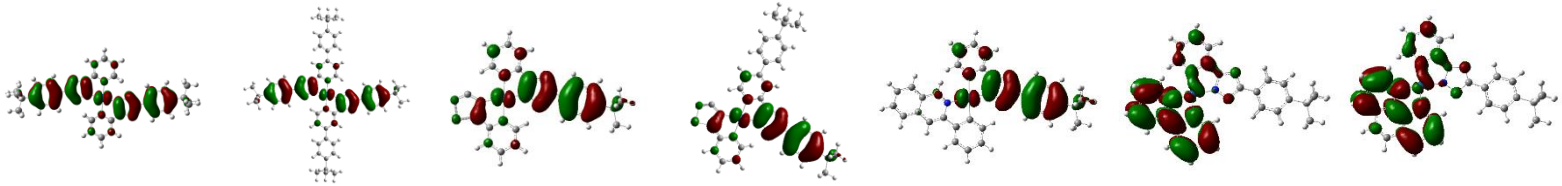						
LUMO	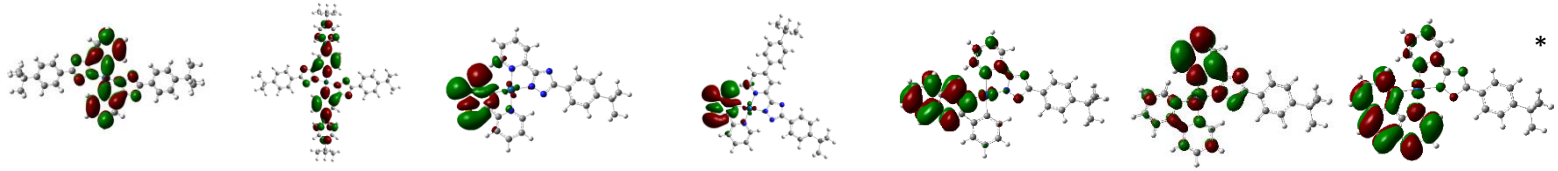						*

2.4 Results and discussion: Pt complexes containing bidentate tetrazole ligands

With similar structures to the 1,2,4-triazoles discussed previously, the synthesis of tetrazole ligands for complexation with Pt was investigated. Many of the tetrazole complexes that were synthesised were insoluble due to their square planar conformation and lack of possible functionalisation of the saturated tetrazole group. This contrasts with the triazole complexes which allowed functionalisation on the 5-position of the triazole ring to accommodate substituted aryl groups and improve solubility. Consequently, although many complexes were synthesised, only a couple were able to be studied in depth.

2.4.1 Synthesis

The synthesis of two types of tetrazole complex was attempted:

1. Homoleptic bidentate complexes containing CF_3-functionalised pyridyl rings (Group A, Scheme 2.13)
2. Homoleptic bidentate complexes containing substituted phenyl ring- functionalised pyridyl rings (Group B, Scheme 2.14)

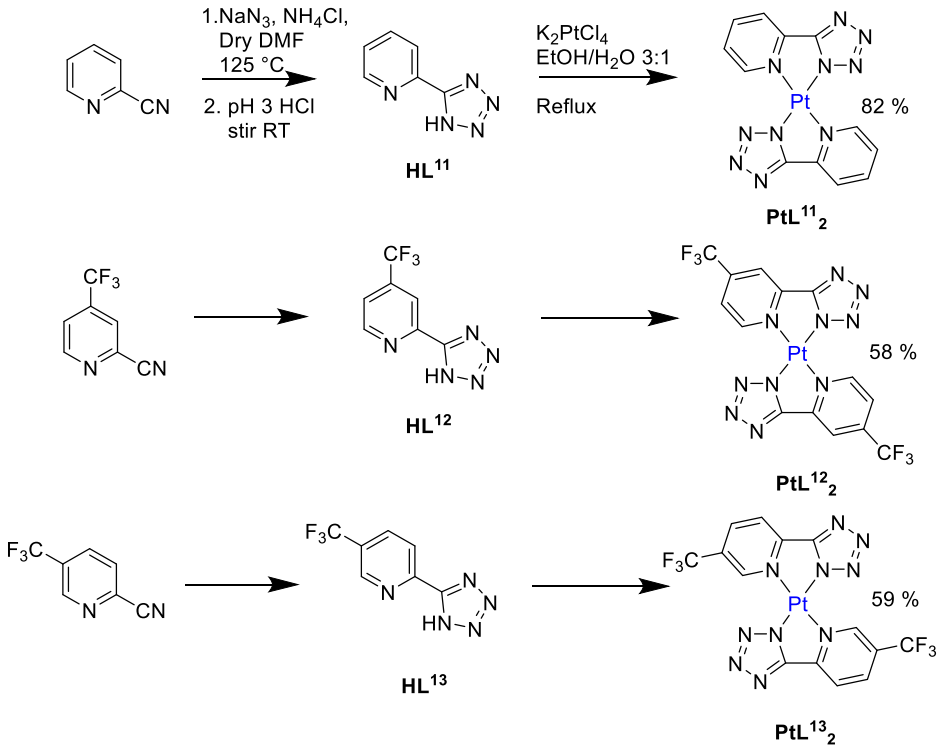

***Scheme 2.13**: Synthesis of group A tetrazole complexes.*

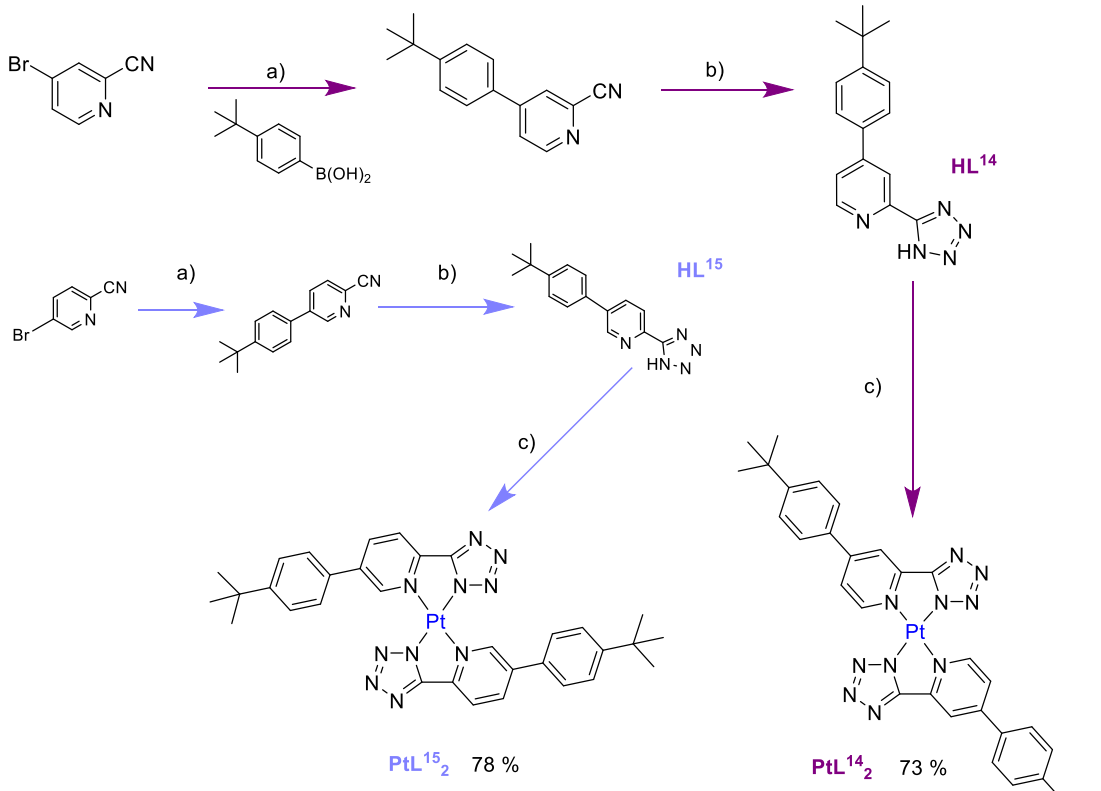

a) Na_2CO_3, $Pd(PPh_3)_4$, DME/H_2O, Reflux.
b) NaN_3, NH_4Cl, Dry DMF, 125 °C.
c) K_2PtCl_4, EtOH/H_2O 3:1, Reflux.

Scheme 2.14: *Synthesis of group B tetrazole complexes.*

The tetrazole ligands in each group were synthesised by 1,3-dipolar cycloaddition of a substituted cyanopyridine with NaN_3 in the presence of NH_4Cl in refluxing DMF, followed by addition of HCl to precipitate the protonated tetrazole according to the procedure devised by Sharpless et al.[92] Group A tetrazoles were obtained by reaction of commercial cyanopyridines with the subsequent reagents mentioned whilst group B tetrazoles were obtained by prior Suzuki cross-coupling of the appropriate bromo-substituted cyanopyridine with 4-*tert*-butyl boronic acid, as was the case for the triazole precursors discussed in the previous section. Complexations were performed by reaction of 2 equivalents of the tetrazole ligands with 1.1 equivalent of K_2PtCl_4 in a 3:1 mixture of EtOH/H_2O, refluxing for 24 hours. Complexes were purified by washes in H_2O, MeOH and diethyl ether (Et_2O). Yields for the group A complexes varied from 58 to 82 % whilst those for group B complexes were similar at 73 % for $PtL^{14}{}_2$ and 78 % for $PtL^{15}{}_2$.

2.4.2 Photophysical properties

The incorporation of CF_3 groups in group A complexes was chosen initially to see if the molecular orientation of the compound in films could be changed, depending upon the position of substitution on the pyridyl ring. This has been known to have large effects in the

photophysical properties of complexes due to a change in the molecular dipole as briefly discussed in the general introduction. Unfortunately, these group A complexes were only able to be characterised by high temperature NMR due to their limited solubility and thus were unable to be studied for their photoluminescence properties. Therefore, future complexes of this sort would need to include other groups to aid solubility for further research.

Complexes PtL^{14}_2 and PtL^{15}_2 in group B were soluble enough for complete photophysical analysis to be performed. PtL^{14}_2 was readily soluble in DCM whereas PtL^{15}_2 was only slightly soluble in this medium which prevented concentration-dependent studies from being performed. The photophysical properties of each complex are outlined in Table 2.22. The absorption spectra of the ligands and of the complexes were compared to assign the different transitions occurring. The PtL^{14}_2 absorption spectrum showed LC transitions occurring between 250 and 320 nm and the absorption with a peak maximum of 345 nm was much greater in intensity, suggesting intra-ligand charge transfer (ILCT) as opposed to MLCT character. For PtL^{15}_2 more absorption peaks were present and, again the peaks between 250 and 365 nm were assigned as ILCT, whilst the peak at longer wavelengths (370 nm) was assigned as MLCT (Fig. 2.45).

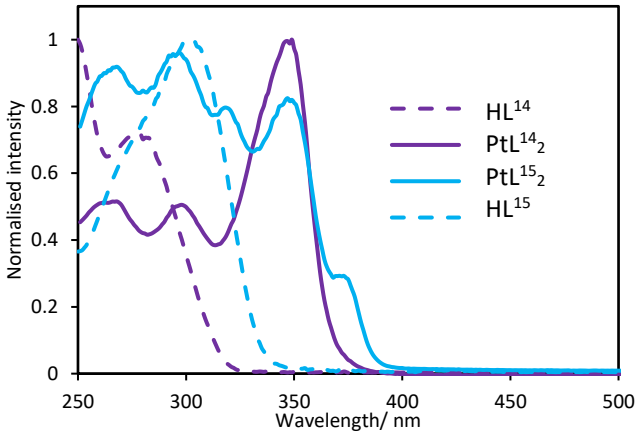

Figure 2.45: *Absorption spectra of ligands HL^{14} and HL^{15}, and their corresponding complexes PtL^{14}_2 and PtL^{15}_2 in DCM.*

Emission studies for PtL^{14}_2 were run in degassed DCM solution and in the solid-state as a 10 wt. % doped PMMA film and as a powder. When PtL^{14}_2 was excited at 350 nm in degassed DCM solution, structured monomeric emission was observed. In contrast, when excited at 420 nm broad, red-shifted emission was observed. To identify the nature of the active species involved, concentration-dependent absorption and emission studies were performed. The concentration-dependent absorption revealed the development of a new

absorption band at 450 nm for concentrations over 2.66 x 10 $^{-4}$ M (Fig 2.46 inset). The concentration-dependent emission (excited at 350 nm) showed structured monomeric emission which increased in intensity between 2.66 x 10^{-7} and 2.66 x 10^{-5} M but which then drastically decreased above this concentration. This implied that on increasing the concentration above 2.66 x 10^{-5} M, a new species was forming (as supported by the concentration-dependent absorption) which quenches the emission intensity, and which is therefore likely to be aggregate in character.

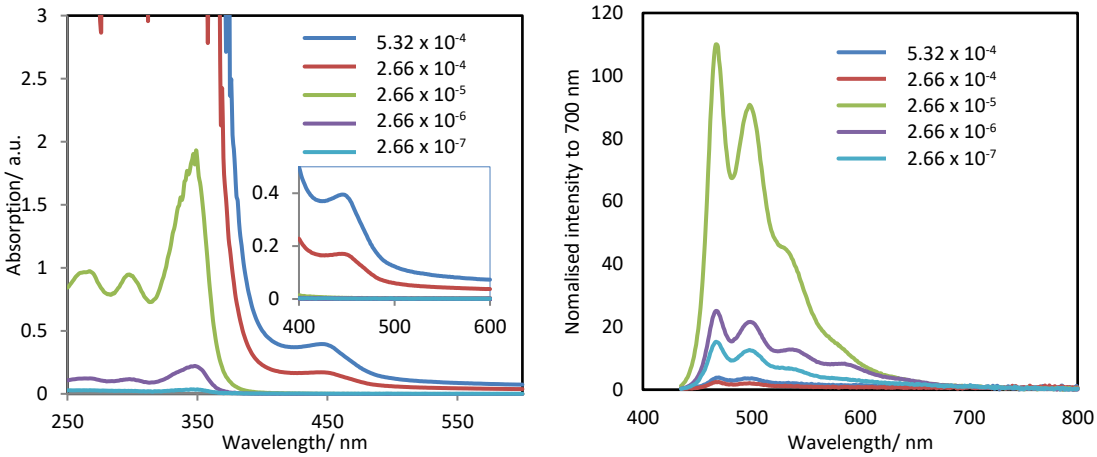

Figure 2.46: *Concentration-dependent absorption (λ^{ex} at 350 nm) with inset showing the introduction of a new longer wavelength band at increased concentrations (left) and emission (right) of PtL^{14}_2 in DCM solution. Concentrations are quoted in mol dm^{-3}.*

In the film the emission peak maximum for PtL^{14}_2 was largely unstructured and centred at 560 nm with some evidence of monomer emission present. In solution at 420 nm excitation, the peak maximum was at 613 nm and thus considerably red-shifted in comparison to the emission peak maximum in solution when excited at 350 nm. As can be seen from Figure 2.47 below, the broad and structureless red emission is from the excitation at 420 nm whilst the highly structured emission at shorter wavelength results from excitation at 350 nm. In the powder form, no monomer emission was present, and the emission had a narrow bandwidth centred 610 nm. The 77 K spectrum of PtL^{14}_2 in dilute butyronitrile glass, and excited at 350 nm, showed a structured emission profile similar to the RT emission.

PtL$^{14}_2$

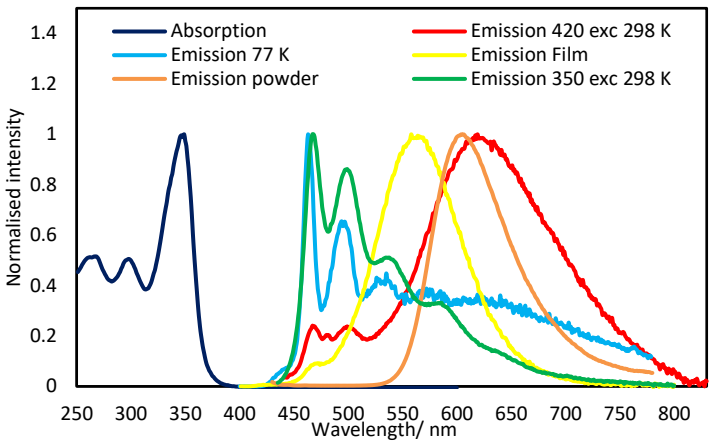

PtL$^{15}_2$

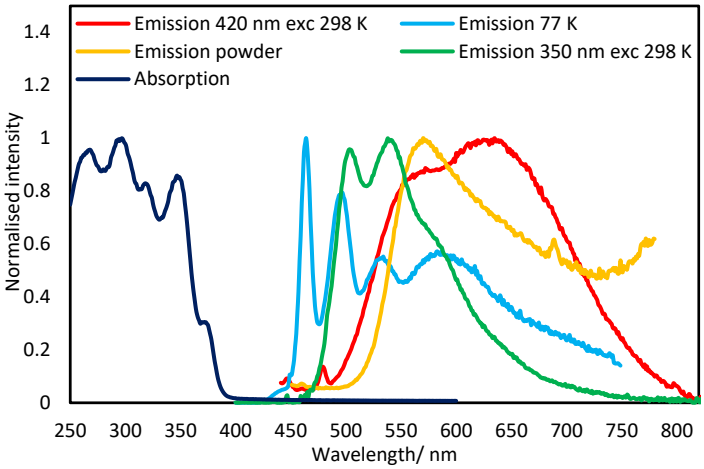

Figure 2.47: *Normalised absorption and emission spectra of PtL$^{14}_2$ and PtL$^{15}_2$. The PtL$^{15}_2$ film was spin-coated at 10 wt. % in PMMA. All solution-state absorption and emission spectra were run in degassed DCM at RT.*

As PtL$^{15}_2$ was only partially soluble in DCM, concentration-dependent studies could not be performed on this complex. When PtL$^{15}_2$ was excited at 350 nm, the RT emission displayed a structured spectrum with vibrational progression and peak maxima of 502, 539 and 574(sh) nm which are red-shifted in comparison to PtL$^{14}_2$ (Table 2.22). At 77 K the emission spectrum of PtL$^{15}_2$ was blue-shifted and showed higher resolution of the structure relative to the RT emission in solution. Only the lifetime of PtL$^{15}_2$ was able to be measured due to the use of the 404 nm laser which could not detect emission for PtL$^{14}_2$ and this was found to be 6.5 µs.

PtL$^{15}_2$ and PtL$^{14}_2$ exhibited similar quantum yields in degassed DCM solution (1.6 and 0.7 %). On the contrary, in the solid-state, the PtL$^{14}_2$ powder gave a higher quantum yield than PtL$^{15}_2$ by an order of magnitude (Table 2.22). Moreover, in the film a PLQY of 24 % was obtained for PtL$^{14}_2$ which reveals its superior solid-state photoluminescence properties

through the formation of aggregates, in comparison to the monomer in solution. The aggregate species in solution for PtL^{14}_2 and PtL^{15}_2 showed emission maxima of 613 and 633 nm respectively and PLQYs for these species were measured as 0.3 and 0.6 %.

2.4.3 DFT studies on tetrazole complexes

From TD-DFT calculations the main contributions to the $S_0 \rightarrow S_1$ transition were shown as emanating from the HOMO-1→LUMO orbitals in PtL^{14}_2 and the HOMO→LUMO orbitals in PtL^{15}_2 (Table 2.20). From the orbital plots shown in Figure 2.21, the HOMO-1 orbital in PtL^{14}_2 is seen to be largely based on the tetrazole rings with the LUMO being more centred on the pyridyl rings and no metal character is observed. The transition is thus assigned as being mixed MLCT in character. For PtL^{15}_2, the HOMO is spread across the whole molecule and the LUMO is centred on the pyridyl rings with some metal character being retained and again this is assigned as having mixed MLCT character. The higher energy of the transition in PtL^{14}_2 is matched with the blue-shifted emission observed in comparison to PtL^{15}_2.

Table 2.20: *Major contributions to the $S_0 \rightarrow S_1$ transitions in PtL^{14}_2 and PtL^{15}_2 as calculated by TD-DFT.*

Complex	*PtL^{14}_2*	*PtL^{15}_2*
Energy (eV/nm)	3.2557/ 380.83	3.1678/ 391.39
Oscillator Strength	0.002	0.2113
Main contribution (%)	HOMO-1→LUMO (56)	HOMO→LUMO (64)
Assignment	Mixed MLCT	Mixed MLCT

Table 2.21: *HOMO-1 and LUMO of PtL^{14}_2 (left) and HOMO and LUMO orbital diagrams of PtL^{15}_2 (right).*

Complex	*PtL^{14}_2*		*PtL^{15}_2*
HOMO-1	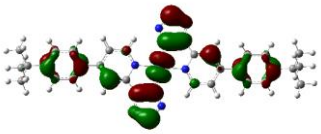	*HOMO*	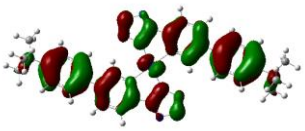
LUMO	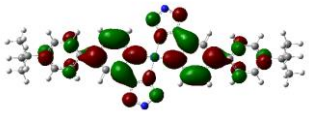	*LUMO*	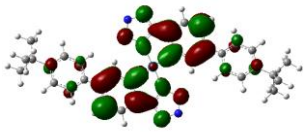

Table 2.22: *Photophysical properties of $PtL^{14}{}_2$ and $PtL^{15}{}_2$ in DCM solutions. Quinine sulfate was used as the reference for PLQY calculations.*[121] *All values are for excitation at 350 nm except those with square brackets which are values for excitations at 420 nm i.e. aggregate species. PLQYs and lifetimes are for the monomer in degassed DCM solutions.*

Complex	*Solution*				*77 K*		*Solid-state*			
	λ_{abs} *(nm)*	λ_{em} *(nm)*	φ *(%)*	τ *(μs)*	λ_{max} *(nm)*	τ *(μs)*	*Powder*		*PMMA film*	
							λ_{max} *(nm)*	φ *(%)*	λ_{max} *(nm)*	φ *(%)*
$PtL^{14}{}_2$	260 (26272), 296 (26418), 345 (52861).	469, 500, 537, 587, 639 [613]	0.7 [0.3]	*unable to obtain lifetime data as too weak for 404 nm laser	463, 495, 532, 569, 622 (sh).	44	597	9.9	560	24
$PtL^{15}{}_2$	295 (27424), 349 (20411), 364 (9792).	502, 539, 574 (sh) [553, 633]	1.6 [0.6]	6.5	463, 493, 528, 582.	12	556	0.35	-	-

2.4.4 OLED testing

The tetrazole complexes could not be sublimed and as a result were not suitable for VTE OLEDs. PtL^{14}_2 was tested for incorporation into a solution-processed OLED, but the lower solubility of PtL^{15}_2 excluded it from being tested in this way. Two solution-processed devices were tested with different doping concentrations of PtL^{14}_2 with the device architecture: ITO | HIL 1.3N (45 nm) | PVK : OXD7 (50 : 50) co. x % **PtL^{14}_2** (60 nm)| TPBi (50 nm) | LiF (0.8 nm) | Al (100 nm). The device properties are summarised in Table 2.23 and Figure 2.48 below.

Table 2.23: *Properties of tetrazole devices with PtL^{14}_2 as the dopant.*

Device	*Complex (wt. %)*	*EL λ_{max} (nm)*	*Current density (mA cm^{-2})*	*Brightness (cd m^{-2})*	*EQE (%)*
1	*PtL^{14}_2 (5)*	560	29.0	940.5	2.6
2	*PtL^{14}_2 (10)*	560	15.3	913.4	3.8

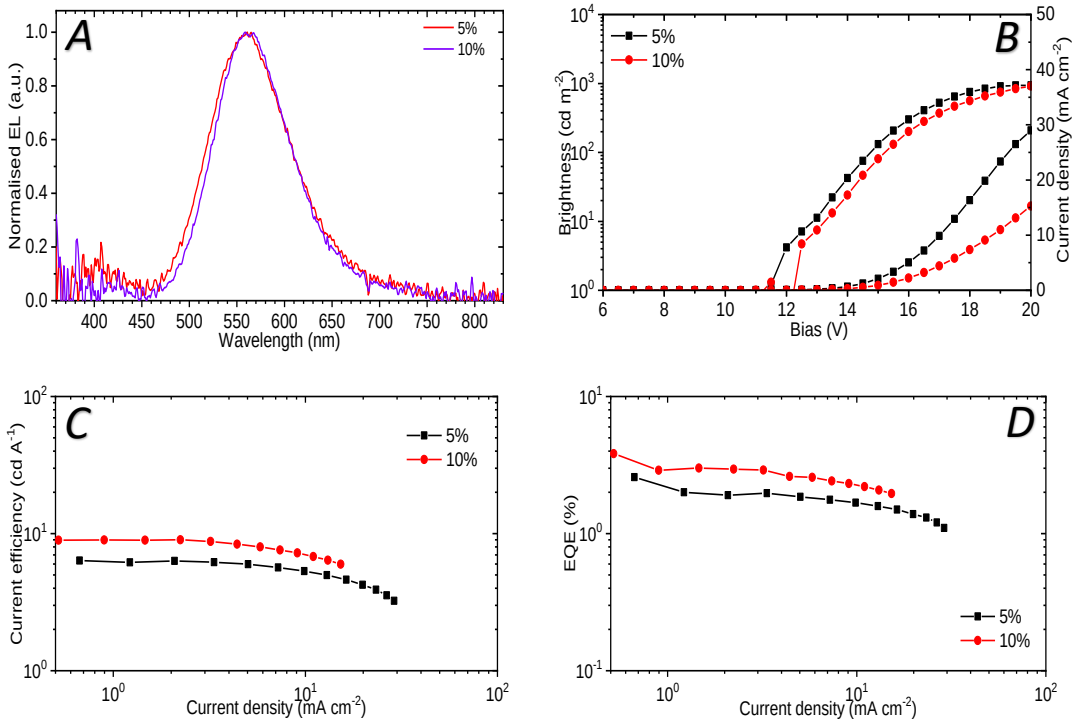

Figure 2.48: *Device 1 and 2 properties where A= EL spectra, B= voltage vs. brightness and current density, C= current efficiency at different current densities and D= EQE.*

Device 2 showed a superior EQE value of 3.8 % in comparison to device 1 (2.6 %) which suggests that the higher doping concentration of 10 % leads to more efficient aggregate formation. The EL spectra of each device were almost identical with λ_{max} of 560 nm. This is in accordance with the thin-film photoluminescence spectra carried out in PMMA at 10 wt. % as shown earlier. Despite the much lower EQEs in comparison to the triazole

devices reported earlier, these values are in line with those of other tetrazole complexes in the literature of which there are not many examples (Table 2.1).

2.5 Chapter 2 Summary

In summary, heteroleptic and homoleptic 1,2,4-triazole complexes and homoleptic tetrazole complexes have been studied which have demonstrated photophysical properties suitable for incorporation into both VTE and solution-processed OLED devices.

The neutral homoleptic triazole complexes and heteroleptic thienyl pyridine triazole complexes displayed impressive photophysical properties with quantum yields ranging from 21 to 48 %. Concentration-dependent emission studies of these complexes revealed the formation of excimers which substantially red-shifted the emission and demonstrated colour tuning possibilities.

Neutral heteroleptic pquin complexes, as well as charged bpy and phen complexes, containing 1,2,4-triazole ligands displayed less impressive photophysical properties and this was thought to be due to the weaker MLCT transitions brought about by the more diffuse orbital arrangement as evidenced by DFT.

On comparing the tetrazole complex PtL^{14}_2 with the triazole analogue PtL^{7}_2, it is clear that the triazole complex displays more impressive photophysical properties where the PLQY value for PtL^{14}_2 at 0.6 % fades in comparison to 48 % for PtL^{7}_2. Moreover, the versatility of the triazole complex was displayed through incorporation into both VTE and solution-processed devices with good efficiency, whilst the tetrazole complex was limited by thermal instability to degradation which prevented sublimation for a VTE device to be prepared. The tetrazole complexes in general were also seen to have more limited solubility in comparison to the triazole complexes, mainly due to the lack of possible functionalisation of the N_4 tetrazole ring. This poor solubility also led to the formation of aggregates in solution at RT which were seen to quench the emission, in comparison to the formation of excimers for the triazole complexes which were emissive in their own right.

This work in particular has evidenced the promising potential of Pt complexes containing bidentate 1,2,4-triazole ligands in solution-processed OLED devices.

3. Mononuclear Pt and Ir complexes containing tridentate ligands

3.1 Overview

This section will be divided into three main parts:

1. Mononuclear Pt^{II} complexes containing tridentate N^C^N ligands and their oxidation to Pt^{IV} complexes
2. Mononuclear Ir^{III} complexes containing tridentate N^C^N ligands
3. Comparison between isoelectronic Pt^{IV} and Ir^{III} complexes containing N^C^N tridentate ligands

3.2 Mononuclear Pt^{II} complexes containing N^C^N ligands and their oxidation to Pt^{IV} complexes

3.2.1 Introduction

3.2.1.1 Pt^{II} complexes containing tridentate ligands

Pt^{II} complexes with tridentate ligands are of great interest for their luminescence properties. Some common tridentate ligands and their binding modes to transition metals are shown below and include N^N^N, N^N^C, N^C^N and C^N^C-coordinating ligands (Fig. 3.1). Their complexes sometimes exhibit improved quantum yields in comparison to those of bidentate analogues owing to their enhanced rigidity which can help to minimise non-radiative decay of the excited state. For example, Pt(*C^N*-ppy)$_2$ is virtually non-emissive in degassed solution at RT[21] whilst Pt(*N^C^N*-dpyb)Cl displays a quantum yield of 0.6.[20]

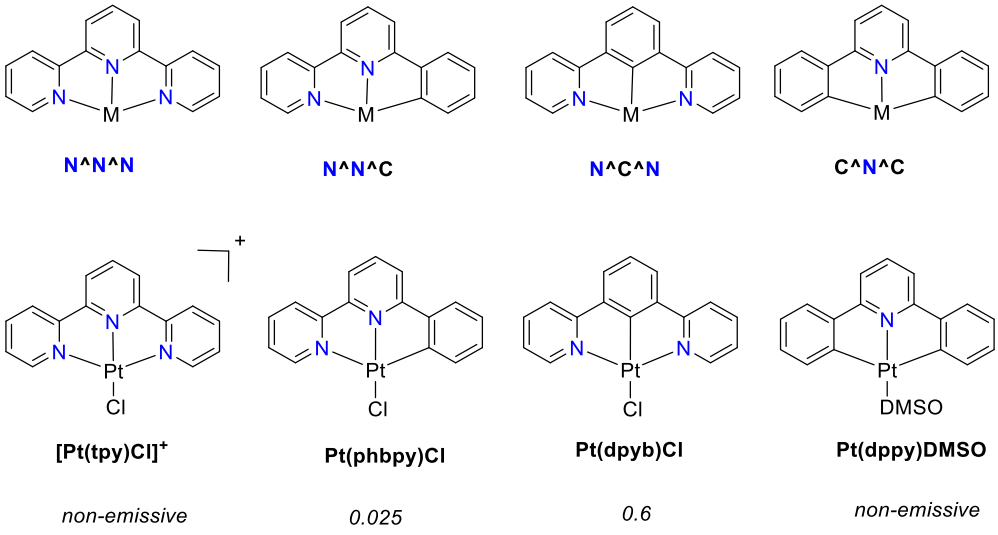

Figure 3.1: *Structures and binding modes of tridentate ligands in metal complexes where M denotes any transition metal (top) and structures of representative Pt^{II} complexes with their respective PLQY values in degassed solution at RT (bottom).*

Within these classes of complexes it can be seen that the PLQY increases upon introduction of a cyclometallating carbon atom from N^N^N to N^N^C or N^C^N. $[Pt(tpy)Cl]^+$ is non-emissive in solution at RT whilst Pt(phbpy)Cl is weakly emissive with a PLQY of 0.025 and Pt(dpyb)Cl displays impressive luminescence. There are, however, other factors to consider regarding the PLQY values for these complexes and not just the number of cyclometallating carbon atoms. The fact that the N^C^N complexes display improved luminescence properties in comparison to the N^N^C complexes, despite the fact they have the same number of cyclometallating carbons, proves this. Moreover, some C^N^C complexes with two cyclometallating carbons, are non-emissive in solution at RT. These phenomena have been investigated by Tong *et al.* in a comprehensive theoretical study regarding the excited states of different tridentate cyclometallated Pt complexes.[122] They attribute the lower PLQY for Pt(N^N^C)Cl largely to structural distortion of the first triplet excited state where, from TD-DFT calculations, it can be seen that the lateral aryl rings of its cyclometalated ligand flip up which results in a smaller d-d splitting making metal-centred excited states more thermally accessible to quench emission (Fig. 3.2). Even greater structural distortion was observed for Pt(C^N^C) complexes in comparison to Pt(N^C^N) complexes.

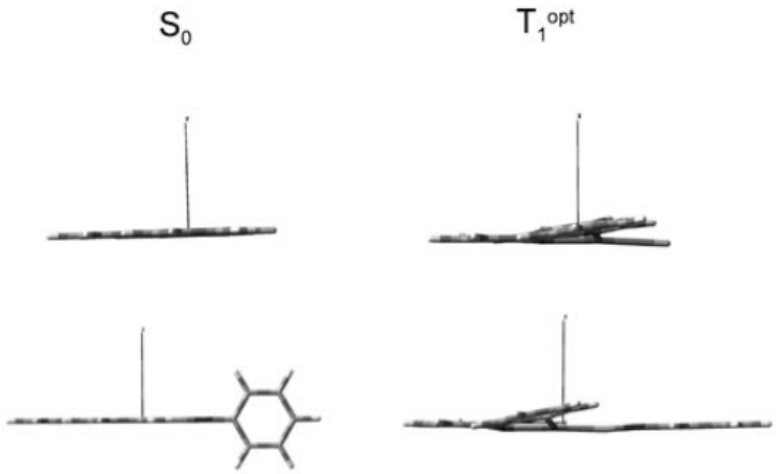

Figure 3.2: *Optimised geometries of the singlet ground state and first excited triplet state for Pt(N^N^C) (top) and Pt(C^N^C) (bottom) complexes as calculated by TD-DFT. Reproduced from Tong et al. by permission of John Wiley and Sons.*[122]

3.2.1.2 Pt^{II} (C^N^C) Complexes

The first examples of [Pt(C^N^C)L] complexes were described in 1988 by Cornioley-Deuschel *et al.* with L= py and Et_2S.[123] A more straightforward synthesis route to these [Pt(C^N^C)L] complexes with high yields was devised by Cave *et al.*, where 2,6-diphenylpyridine (dppyH) is metallated twice by K_2PtCl_4 in acetic acid to give a dinuclear species.[124] This species can then be reacted in DMSO to give the resulting complex Pt(C^N^C)DMSO (obtained in 98 % yield) which can be further modified by changing the ligand L to give complexes **33** and **34** (Scheme 3.1). The luminescence of these complexes was not studied but this facile synthesis method has since been adopted by many other groups who have investigated the Pt(C^N^C)L complexes further.

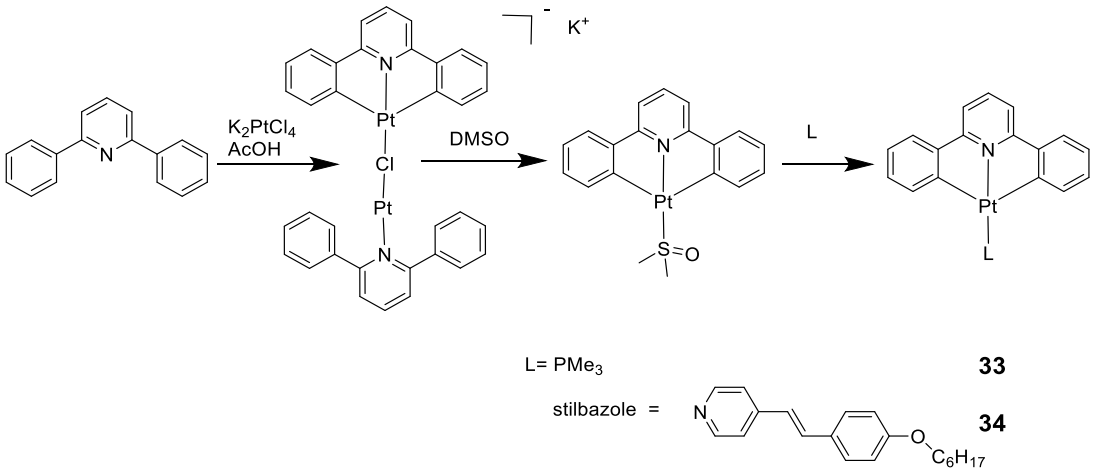

Scheme 3.1: *Synthesis of Pt(C^N^C)L complexes **33** and **34**.*

Lu *et al.* have reported on the photophysical characteristics of these types of complexes.[125] Amongst others, they synthesised the Pt(C^N^C)L complex bearing L as 4-*tert*-butylpyridine (**35**, Fig. 3.3). This had lowest-energy UV-vis absorption bands which are proposed to be an admixture of triplet Pt(d)→π*(C^N^C) and π→π* transitions. It was non-emissive in DCM at RT, although it did show emission in the solid-state and in alcohols at 77 K. The 77 K emission was seen to be concentration-dependent and broad, red-shifted emission was observed at concentrations above 5 x 10^{-7} M which was tentatively assigned as excimeric in nature (Fig. 3.3).

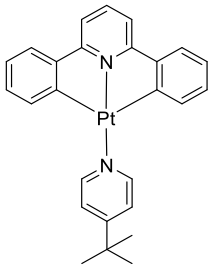

35

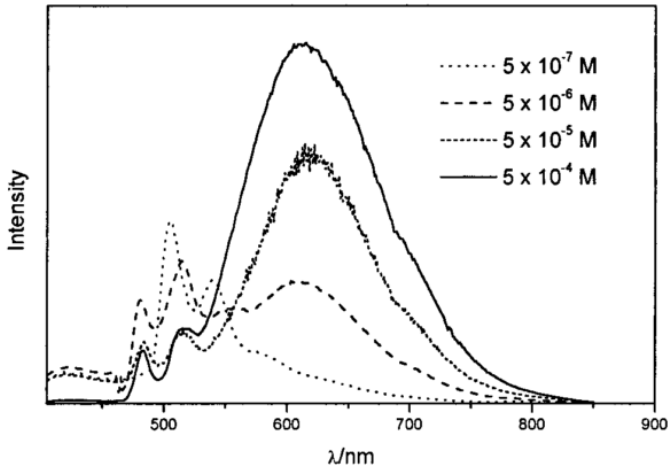

Figure 3.3: *Structure of [Pt(C^N^C)L] complex **35** and its concentration-dependent emission at 77 K in MeOH/EtOH/DMF (5:5:1) glass. Reprinted with permission from Lu et al.*[125] *Copyright 2001 American Chemical Society.*

Since then Kui *et al.* have made significant progress in the field of Pt(C^N^C)L complex synthesis including one with a highest PLQY of 0.26 for complex **36** (Fig. 3.4) which had an isocyanide group as the ancillary ligand. This complex was also incorporated into an OLED with an EQE of 12.6 %.[126] A series of compounds were made which had different C^N^C and L ligands and it was found that thiophene units on the C^N^C ligand gave the best emission in solution. In addition to this, it was found that by swapping L from DMSO to isocyanide, the PLQY doubled from 13 to 26 %.

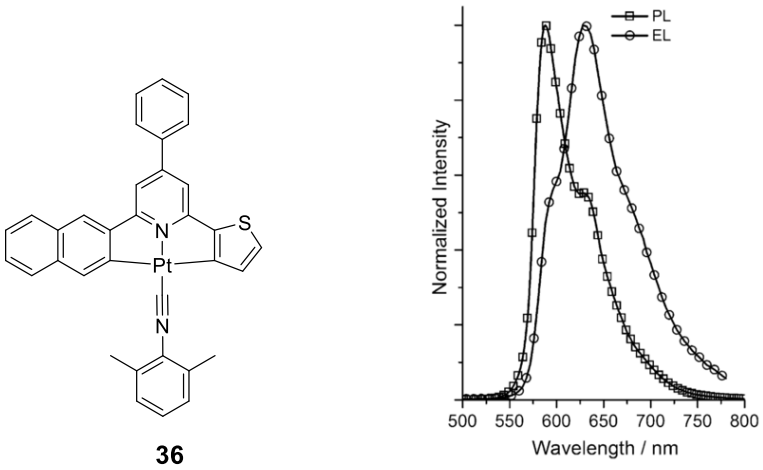

Figure 3.4: *Structure of complex* ***36*** *and its PL and EL emission spectra. Reproduced from Kui et al. by permission of John Wiley and Sons.*[126]

Therefore, although significant progress has been made for Pt(C^N^C) complexes there is still a long way to go for them to rival the likes of similar complexes with tridentate ligands, such as those based on Pt(N^C^N) systems.

3.2.1.3 Pt^{II} (N^C^N) Complexes

Far more work has subsequently been done on Pt(N^C^N) complexes. The most common N^C^N ligand for platinum complexes that has been studied is dipyridylbenzene (dpybH). Its platinum complex Pt(dpyb)Cl has been studied by the Williams group owing to its intensely luminescent nature in solution at RT as mentioned previously.[20] This is attributed to its cyclometallating carbon atom which provides good σ-donating ability through the short C—Pt bond and helps increase the ligand field strength in synergy with the π-accepting pyridyl groups.

Tuning of the substituents on the dpybH backbone can allow good control over the photophysical properties of the complex. By changing substituents at the 4-position of the central phenyl ring, absorption and emission maxima can be influenced allowing versatile colour-tuning. The introduction of aryl groups shifts the emission increasingly to the red according to their electron-donating ability, e.g. λ_{max} increases in the order R=CO_2Me <H< mesityl < Me < 2-pyridyl < 4-tolyl < 4-biphenylyl < 3,4-dimethoxyphenyl < 2-thienyl (Fig. 3.5).[127]

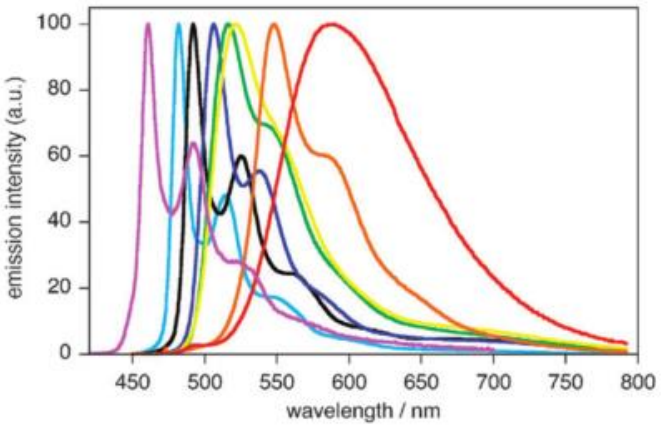

Figure 3.5: *Normalised emission spectra of the various Pt(dpyb)Cl complexes with different substituents. Reproduced from Williams et al. by permission of the Royal Society of Chemistry.*[127]

Rossi *et al.* investigated the effect of chloride metathesis by synthesis of two new Pt(N^C^N) acetylide complexes, **37** and **38**, in an effort to further improve their efficiencies.[128] The incorporation of a strong-field acetylide ligand in place of the weak-field chloride helps to raise the energies of otherwise deactivating d–d states, making them less thermally inaccessible and thus reducing non-radiative decay pathways. Synthesis of the complexes [Pt(L^n)-C≡C-$C_6H_3F_2$], where (-C≡C-$C_6H_3F_2$) is 3,5-difluorophenylacetylide, was achieved by reaction of 1-ethynyl-3,5-difluorobenzene with sodium methoxide (NaOMe) to remove the alkyne proton, followed by addition of a solution of the Pt(N^C^N)Cl complex in MeOH /DCM (1:4). Complexes **37** and **38** were achieved in almost quantitative yields after stirring for 1 day at ambient temperature (Scheme 3.2).

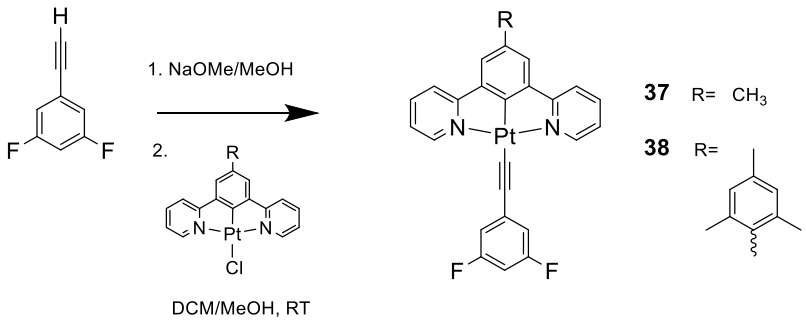

Scheme 3.2: *Synthesis of Pt(N^C^N) acetylide complexes **37** and **38**.*

The parent complexes of **37** and **38**, which contained chloride ligands as opposed to acetylide ligands, were previously reported to display quantum yields of 0.68[20] and 0.62[129] respectively. By metathesis of the chloride ligands with the acetylide ligands these values were seen to increase to 0.77 and 0.66. Moreover, they displayed vibrationally resolved

spectra, with the 0–0 band at around 510 nm and, like their parent complexes, they formed excimers at elevated concentration in solution which had λ_{max} values at around 700 nm. OLED devices were subsequently fabricated with both complexes and the corresponding EL spectra and EQE plots for each device are shown below in Fig. 3.6.

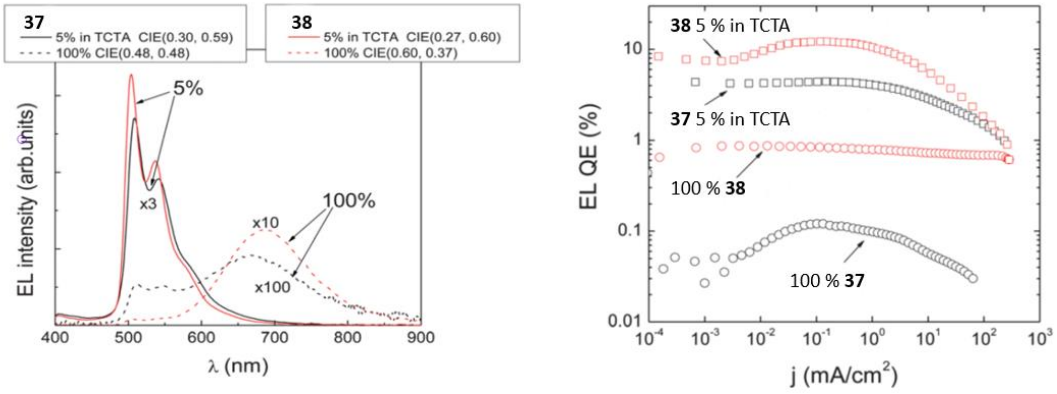

Figure 3.6: *EL spectra of complexes **37** and **38** either as a dopant at 5 wt. % in TCTA, or as the neat emitting layer (left) and EQEs versus electric current density for the four OLEDs (right). Reproduced from Rossi et al. by permission of the Royal Society of Chemistry.*[128]

OLEDs were prepared with 5 wt. % dopant in a TCTA host, as well as 100 % neat films of each complex. It is evident from the EL spectra that both complexes show excimeric/aggregate emission in the neat films, whilst structured emission similar to that observed in the PL is retained for the 5 wt. % doping concentrations in TCTA. The EQE values for the 5 wt. % films are 5 and 12 % for complexes **37** and **38** respectively, showing the mesityl group to have a positive influence on the efficiency of the luminescence. This is also reflected in the neat films where the device EQE for complex **38** is an order of magnitude higher than for complex **37**. It was postulated that the mesityl groups favour a head-to-tail arrangement of molecules, whilst the methyl-substituted complexes prefer a head-to-head arrangement. Changing the arrangements of these molecules with respect to one another in the EML may, therefore, be associated with aggregation that can cause quenching.

As one can see, there has been a substantial amount of work done on mononuclear Pt^{II} complexes with tridentate ligands, particularly with N^C^N ligands, owing to their impressive photophysical properties. These may emit across most of the visible region and recently research which incorporates these types of complexes into dinuclear/bimetallic complexes for NIR emission is becoming of interest and will be discussed in the next chapter.

3.2.1.4 Oxidation of cyclometallated complexes from Pt^{II} to Pt^{IV}

The oxidation of Pt^{II} complexes to Pt^{IV} complexes is an area which has received less attention. Pt^{IV} is isoelectronic with Ir^{III}. In degassed DCM at 298 K, $Ir(ppy)_3$ shows an emission maximum at λ_{em} = 510 nm and a luminescence lifetime of τ = 1.9 µs with a quantum yield measured to be ϕ = 0.97.[15] These impressive photophysical properties for Ir^{III} complexes suggest good potential for luminescence in Pt^{IV} complexes. In comparison to Pt^{II} complexes however, there has been little research on Pt^{IV} complexes. This is likely to be due to the high charge on the metal centre. This may act to reduce the energy of the metal d orbitals and lead to a lower metal character in the excited state and ultimately to lower values of k_r. Moreover, Pt^{IV} has very low reactivity in comparison to Pt^{II}. It has a low-spin d^6 configuration and is thus very chemically inert whilst Pt^{II} has a d^8 configuration and is more reactive.

As seen in the previous chapter, Pt^{II} complexes commonly display square planar geometry which can lead to the formation of excimers and aggregates. Sometimes this is advantageous in terms of the red-shifted emission that can be observed, but in other cases it can lead to emission quenching. Like Ir^{III} complexes, Pt^{IV} complexes display octahedral geometry. Specifically in Pt^{IV} complexes, this reduces many of the intermolecular interactions which could diminish luminescence efficiency. From the literature there are examples of oxidation of cyclometallated Pt^{II} complexes to Pt^{IV} but this is largely only for bidentate C^N ligands and not for tri- or tetradentate ligands. Here, a few examples of complexes containing bidentate ligands will be discussed in terms of their synthesis and luminescence properties, which could impact on the development of Pt^{IV} complexes containing tridentate ligands.

The use of hydrogen peroxide (H_2O_2) to achieve oxidation of Pt^{II} to Pt^{IV} has been used by Newman *et al*.[130] The oxidations were performed typically with pendant ppy complex (Pt(ppy*F*)(Hppy*F*)Cl, Scheme 3.3) in d_6-acetone so that NMR could be used as a monitoring tool. Excess H_2O_2 (30 % in H_2O) was added at RT and in the presence of air. In addition, potassium chloride (KCl) was added to ensure sufficient chloride was present to convert any potential platinum hydroxides to chlorides. Reactions were fast with all the initial Pt^{II} material (Pt(ppy*F*)(Hppy*F*)Cl) being consumed in less than an hour. On the downside, the reaction did not proceed cleanly, and several complexes were reported thought to be isomers and hydroxide complexes. The final reported products **39a** and **39b** are shown in Scheme 3.3.

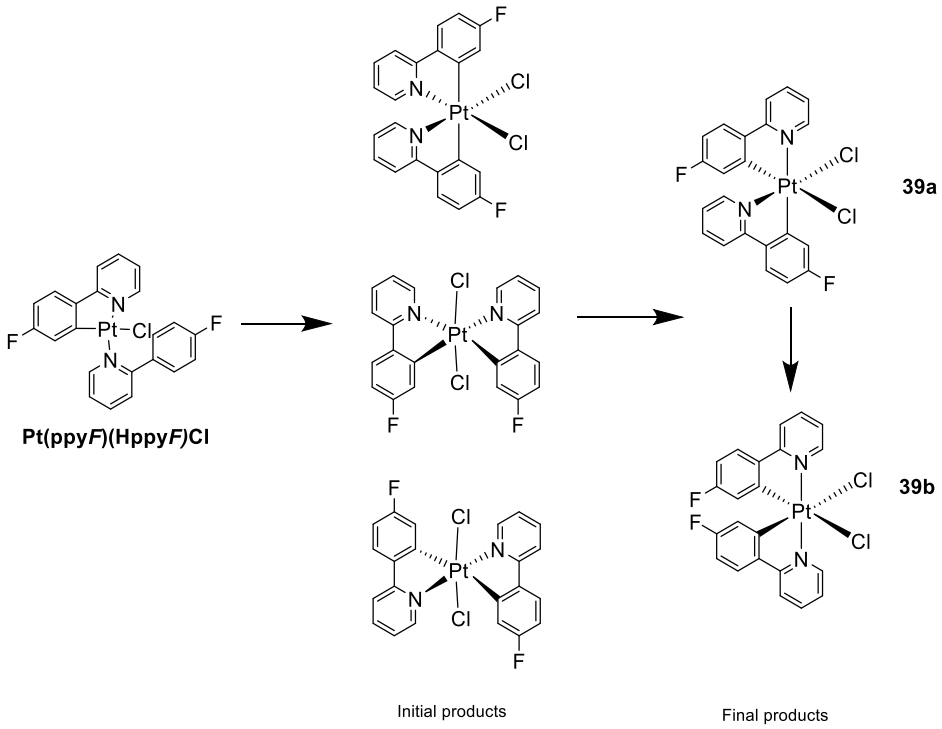

Scheme 3.3: *Different isomeric products formed by the oxidation of* Pt^{II} *complexes with* H_2O_2.

Mamtora *et al*.[131] used iodobenzenedichloride ($PhICl_2$) as an oxidising agent for a similar process. Isomeric products **40a** and **40b** were observed in the reaction of Pt(ppy*F*)(py)Cl with $PhICl_2$ in acetone (Scheme 3.4), but in chloroform a clean reaction took place. An S_N2-type attack on the $PhICl_2$ is proposed as the mechanism of the reaction in acetone which would result in a five-coordinate cationic intermediate of the type $[Pt(ppyF)(py)Cl_2]^+$ (Scheme 3.4). It is thought that this cationic intermediate exists as a tight ion-pair and when the liberated chloride combines with the platinum centre, it will approach from the same side as the initial attack. This would force one of the existing ligands to move to the vacant coordination site, rather than fill it directly, resulting in two products. In chloroform, however, only one product is observed. Chloroform is known to be able to solubilise chloride anions via a hydrogen bond type of interaction.[32] This would allow the liberated chloride to move more freely in solution and subsequently allow it to come around to the other side of the platinum centre. This would mean it would bond directly in the vacant site, forming only the thermodynamic product **40a**.

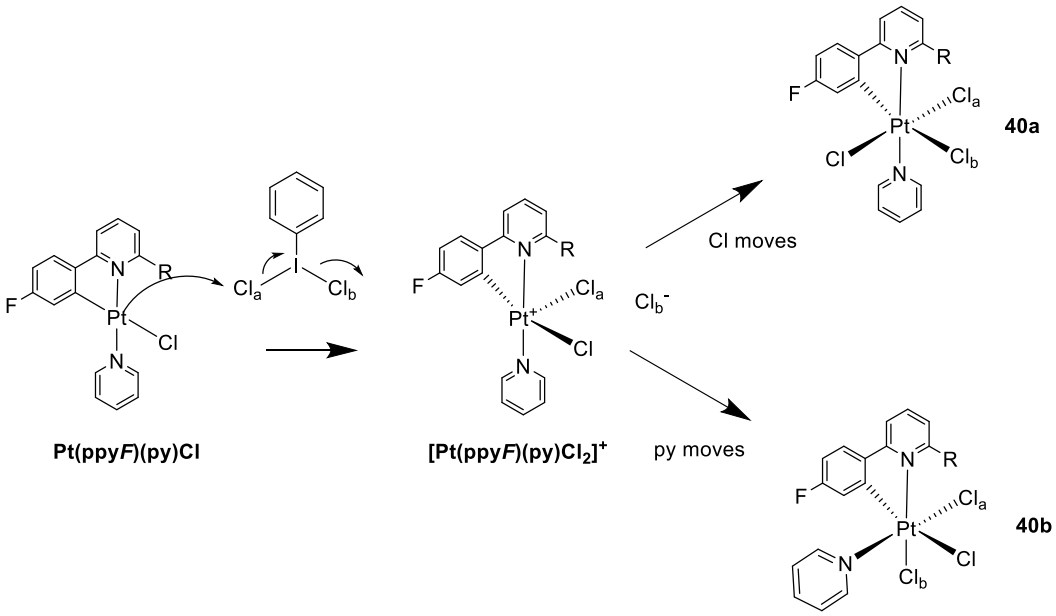

Scheme 3.4: *Oxidation of Pt(ppyF)(py)Cl in acetone with $PhICl_2$ to form* ***40a*** *and* ***40b****.*

The luminescence properties of these complexes were not investigated, but since then, there have been a few groups who have synthesised similar Pt^{IV} complexes with bidentate ligands which display respectable PLQYs including Jenkins in 2010[132] and Juliá in 2014.[133]

Jenkins adopted the method developed by Mamtora utilising $PhICl_2$ as an oxidising agent to synthesise complexes of the type $[Pt(C^N)_2(N^N)][PF_6]_2$ and the synthesis of complex **41,** where C^N is ppy and N^N is bpy**,** is shown in Scheme 3.5. Initially the neutral $Pt(N^C)_2Cl_2$ complex is formed which is then reacted with bipyridine in the presence of AgOTf as a chloride scavenger to afford the final charged complexes. They synthesised a range of complexes by varying the substituents on the C^N and N^N ligands to probe structure-property relations.

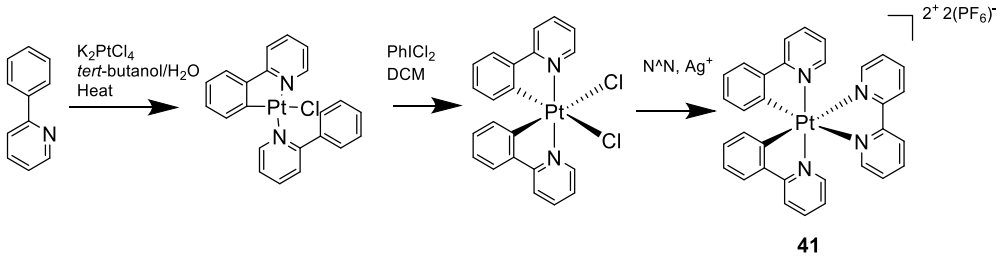

Scheme 3.5: *Synthesis of $[Pt(C^N)_2(N^N)][PF_6]_2$ complex* ***41****.*

42 C^N = Ph-mppy N^N = bpy

43 C^N = Ph-mppy N^N = dMeObpy

Figure 3.7: *The corresponding C^N and N^N structures for* $[Pt(C^N)_2(N^N)][PF_6]_2$ *complexes* ***42*** *and* ***43****.*

It was found that the complexes containing the C^N ligands as ppy exhibited blue, structured luminescence. The emission maxima were also seen to be highly blue-shifted in comparison to their Ir analogues e.g. 482 nm for **41** versus 582 nm for $[Ir(ppy)_2(bpy)](PF_6)$. A range of PLQY values from 0.05 - 1.1 % was observed with lifetimes ranging from 1.1 to 15 µs for complexes containing ppy ligands and substituted bpy ligands. They expanded this series of complexes to derivatives with the C^N ligand 5-methyl-2-(biphen-4-yl)pyridine (Ph-mppyH) for its extended π-system with the aim of increasing quantum yield and influencing the emission colour (Fig. 3.7).

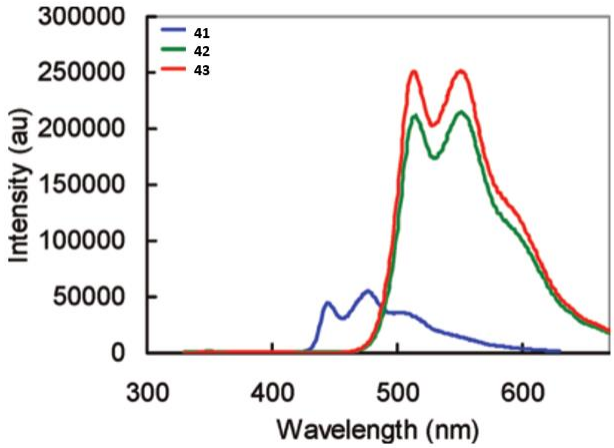

Figure 3.8: *Emission spectra and relative intensities of* $[Pt(C^N)_2(N^N)](PF_6)_2$ *complexes* ***41****-****43****. Reprinted with permission from Jenkins et al.*[132] *Copyright 2010 American Chemical Society.*

Subsequently a shift of emission energies of 70 nm and an 11-fold increase in quantum yield compared to **41** was attained in the Ph-mppy derivatives **42** and **43** (Fig. 3.8). Furthermore, longer lived excited-state lifetimes as high as 260 µs were observed which demonstrated a high sensitivity to oxygen quenching. All of which show good potential for Pt^{IV} complexes with luminescent properties, in this case particularly for oxygen sensing applications.

Juliá *et al.* developed this work with the same synthetic route using $PhICl_2$ to afford similar bidentate Pt^{IV} complexes. Initially they synthesised meridional and facial isomers of tris-cyclometalated Pt^{IV} complexes, $[Pt(C^N)_3]OTf$, where C^N is a phenylpyridine-based ligand or 1-phenylpyrazole (Scheme 3.6). They assigned the emission as coming from a ^3LC excited state and also reported significantly blue-shifted emission in comparison to isoelectronic Ir^{III} analogues. They reported the highest known Pt^{IV} quantum yield of 0.49 at the time in degassed solution at RT for *fac*-$[Pt(ppy)_3]OTf$ (**44**) and also revealed high promise for these complexes for use as oxygen sensors owing to the long lifetimes of over 200 µs. They have since developed this work to afford Pt^{IV} complexes with PLQYs of up to 81 % for complex **45** (Scheme 3.6) and similar long lifetimes.[134]

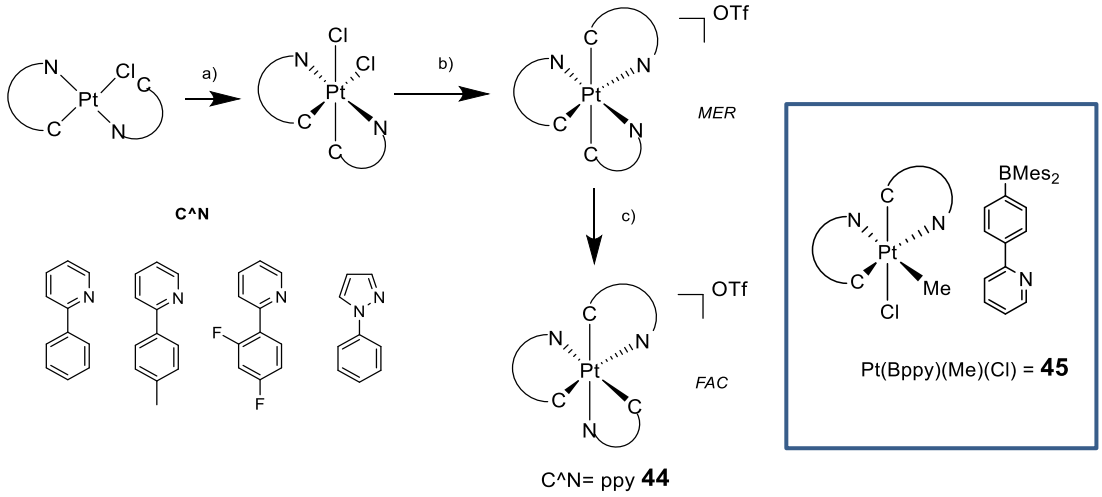

Scheme 3.6: *Synthesis of fac and mer Pt^{IV} complexes where a) $PhICl_2$ and DCM, b) AgOTf, N^CH, dichloroethane, 90 °C and c) hv, MeCN (left) and complex **45** (right).*

3.2.2 Objectives

Most Pt^{IV} complexes that have been reported in the literature appear to feature bidentate ligands and they have made huge progress in terms of luminescence efficiency in the last few years. The main objectives of the present work are to investigate the synthesis of Pt^{IV} complexes containing tridentate N^C^N ligands. The preliminary investigation into this work was started by a previous Ph. D student in our group, Gemma Freeman,[135] and this will be the basis for the development of Pt^{IV} compounds containing tridentate ligands in this work.

3.2.3 Results and Discussion

3.2.3.1 Synthesis

Pt(dpyb)Cl

The dpybH ligand was synthesised via the Suzuki-Miyaura cross-coupling procedure with Na_2CO_3 as the base and $Pd(PPh_3)_4$ as the catalyst (Scheme 3.7) as previously employed in past research.[18] All reagents were initially degassed and placed under an atmosphere of argon, before addition of the catalyst. The mixture was then heated under nitrogen at 85 °C for two days, before purification by column chromatography on silica. Yields of approximately 70 % were obtained from this one-step process.

Cyclometallation to give the Pt^{II} complex Pt(dpyb)Cl was then achieved via one of two methods. The first was the reaction of dpybH with K_2PtCl_4 in acetic acid (15 mL) at reflux for 60 hours (Scheme 3.7). The second was the microwave reaction of the same reagents at a higher concentration (1.5 mL solvent) at 160 °C for 30 minutes. This microwave synthesis has been employed by the group in previous work and was adapted from the method developed by Wang *et al*.[136] The yield of the first method was approximately 50 % whilst the microwave method gave a yield closer to 70 % in less than 1 % of the time.

$Pt(dpyb)Cl_3$

The main method that was used to oxidise the Pt^{II} complex, Pt(dpyb)Cl, through to the Pt^{IV} complex, $Pt(dpyb)Cl_3$, was via a procedure developed by Lisa Murphy[137] for related N^C^N-coordinated Pt^{II} complexes. The oxidation was achieved by taking up the Pt^{II} complex in a small volume of chloroform and bubbling chlorine gas through the solution for 30 minutes, with the exclusion of light. The chlorine gas was generated by reacting concentrated HCl with potassium permanganate ($KMnO_4$) in a separate vessel. Upon reaction, the solution became paler in colour after just a couple of minutes, indicating that oxidation had taken place. The steady supply of Cl_2 was maintained for approximately 30 minutes to ensure

complete conversion, but care was taken not to exceed this time frame owing to potential degradation of the complex for example through chlorination of the ligand. The solvent was also then removed quickly under reduced pressure to prevent possible photo-activated decomposition back to Pt^{II} in the presence of light.

$[Pt(dpyb)L^1Cl]^+$

$Pt(dpyb)Cl_3$ and the bidentate triazole ligand HL^1 (see chapter 2) were reacted in refluxing toluene under argon with AgOTf as a chloride scavenger (Scheme 3.7). This was followed by anion exchange with saturated aqueous KPF_6 and resulted in the formation of $[Pt(dpyb)L^1Cl]PF_6$. The complex was purified by recrystallization from a DCM/Hexane solution in a 7 % yield. This is one of the very few examples of a Pt^{IV} 3+2+1 complex, where 3+2+1 describes the denticity of the three ligands bound to the Pt centre and which will also be discussed in terms of Ir^{III} complexes in the next section.

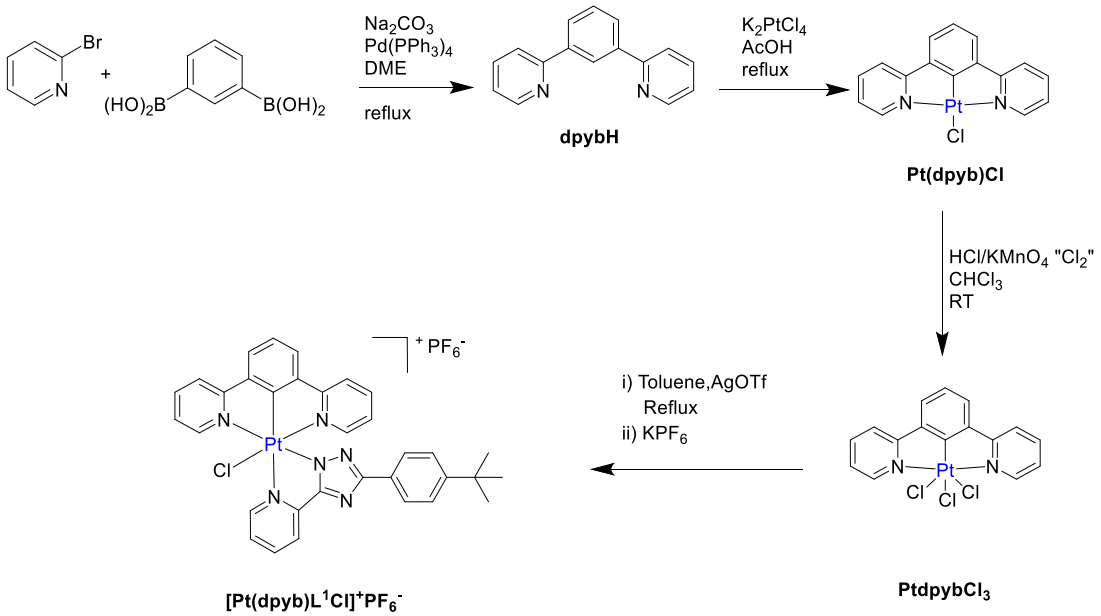

Scheme 3.7: *Synthesis of Pt(dpyb)Cl, its oxidation to $Pt(dpyb)Cl_3$ and subsequent reaction with a pyridyl triazole to form $[Pt(dpyb)L^1Cl]PF_6$.*

Crystals of $[Pt(dpyb)L^1Cl]PF_6$ suitable for X-ray diffraction were obtained by slow evaporation from an acetone solution (Fig. 3.9). The crystal structure confirmed the oxidation state of Pt to be +4 showing the binding mode of the N^N ligand to be via the deprotonated N with the presence of only one counter PF_6^- ion to balance the charge. Two independent ionic pairs were revealed which differ only by the orientation of the phenyl group on the triazole ligand. The complex co-crystallised with a molecule of acetone.

The longest bond length was for Pt—Cl at 2.29 Å whilst the shortest bond length to Pt was Pt—C7 at 1.95 Å (Table 3.1). This reflects the weaker bond between Pt and Cl in comparison

to the cyclometallated bond between Pt and the C⁻ atom which is the case in many other cyclometallated complexes such as Pt(dpyb)Cl.[20] The Pt1—N3 bond length which is *trans* to Pt1—C7 displayed the longest bond length for the Pt to any of the nitrogen atoms and this is due to the high *trans* influence of the cyclometallating carbon. Subsequently it can be seen that the N⁻ atom has a weaker *trans* influence than the C⁻ of the cyclometallating ligand. The bond angle of N3-Pt1-C7 is close to linear at 177 ° whilst those for N4-Pt1-Cl1 and N1-Pt1-N2 are 170.6 °and 161.3 ° respectively.

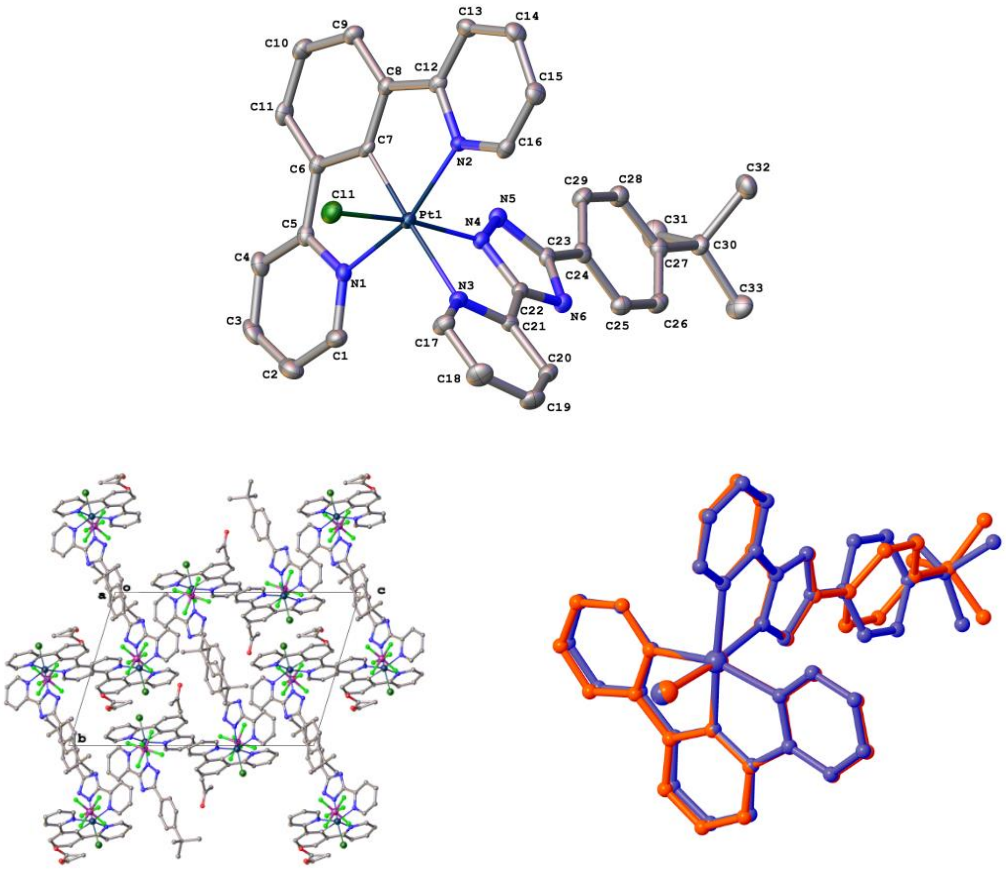

Figure 3.9: *Molecular structure of the cation [Pt(dpyb)L¹Cl]⁺, crystal packing in its PF_6^- salt and the structure of two independent ionic pairs in the crystal lattice.*

Table 3.1: *Selected bond lengths and angles for [Pt(dpyb)L¹Cl]⁺.*

Bond Lengths/ Å		*Bond Angles / °*	
Pt1—N1	2.056(3)	N1-Pt1-N2	161.33(11)
Pt1—N2	2.051(3)	N3-Pt1-C7	177.24(11)
Pt1—N3	2.171(3)	N4-Pt1-Cl1	170.64(11)
Pt1—N4	2.010(3)		
Pt1—C7	1.952(3)		
Pt1—Cl1	2.2919(9)		

[Pt(dpyb)(L^{16})]$^+$

The other Pt^{IV} complex that was successfully synthesised was the bis-tridentate [Pt(dpyb)L^{16}]$^+$ complex which is similar to [Pt(dpyb)L^1Cl]$^+$, but contains the tridentate triazole ligand L^{16} in place of both the bidentate triazole ligand and chloride ligand (Scheme 3.8). The tridentate triazole ligand H_2L^{16} was one of a series of ligands synthesised according to an adapted procedure by De Cola *et al.*[91] in the same manner as for the bidentate triazole ligands discussed in Chapter 2, but starting from 2,6-dicyanopyridine. This synthesis is outlined in more detail in the next section in relation to analogous Ir complexes (see Scheme 3.9).

The introduction of L^{16} into the Pt^{IV}(N^C^N) coordination sphere was initially attempted by reaction of Pt(dpyb)Cl_3 with triazole ligand H_2L^{16} in MeCN but this was not successful, probably due to the low solubility of the triazole. To try to improve solubility, ethylene glycol was then used as a higher boiling-point solvent at a temperature of 195 °C. The reaction was run for 3 days under argon to give the complex which was evident by MS (ES$^+$). The reaction mixture was then cooled to RT and water was added to precipitate out a solid which was thought to be the chloride/triflate salt of the final product. This was dissolved in MeOH and then saturated KPF_6 aqueous solution was added for anion exchange. The hexafluorophosphate salt of the pure product was isolated by filtration, extraction into DCM and three DCM/hexane recrystallizations. The yield of the complex was 20 % and it is the first example of a Pt^{IV} bis-tridentate complex as far as we are aware.

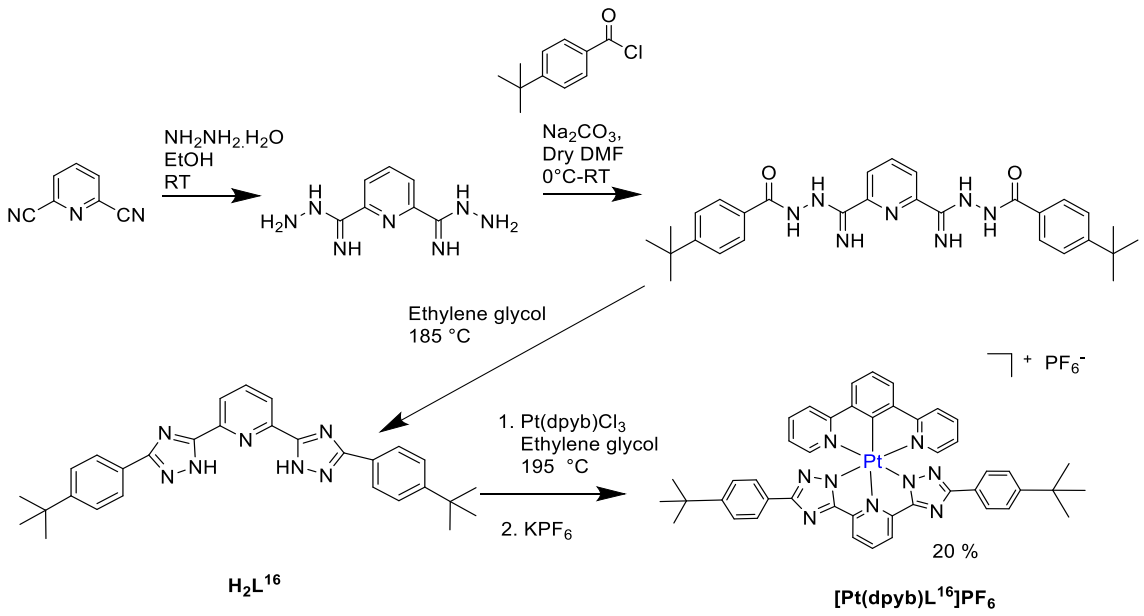

Scheme 3.8: *Synthesis of the bis-tridentate Pt^{IV} complex via the ligand H_2L^{16}.*

3.2.3.2 Photophysical properties

$[Pt(dpyb)L^1Cl]^+$

The photophysical properties of the 3+2+1 Pt^{IV} complex $[Pt(dpyb)L^1Cl]^+$ are summarised in Figure 3.10. $[Pt(dpyb)L^1Cl]^+$ showed high energy absorption between 250 and 350 nm in DCM solution and these are assigned as LC π→π* transitions. Weak absorption extended to longer wavelengths of up to 450 nm, showing a red-shifted absorption in comparison to the triazole ligand and similar observations have previously been made for other Pt^{IV} complexes.[138] This absorption is regarded as a mixture of the LC absorption with introduced metal character. The emission spectrum at RT in degassed DCM solution showed a relatively broad and unstructured band with λ_{max} at 505 nm, a lifetime of 3.1 µs and PLQY of 5.9 %, whilst at 77 K the emission was highly structured and displayed a blue-shifted λ_{max} to 480 nm with an increased lifetime of 230 µs. This suggests emission originates from either a ^{3}LC or ^{3}MLCT state owing to long lifetimes and the rigidochromism which is observed on going to 77 K.[139] It is interesting also to compare this compound with an Ir^{III} analogue and this will be discussed in the following section in this chapter.

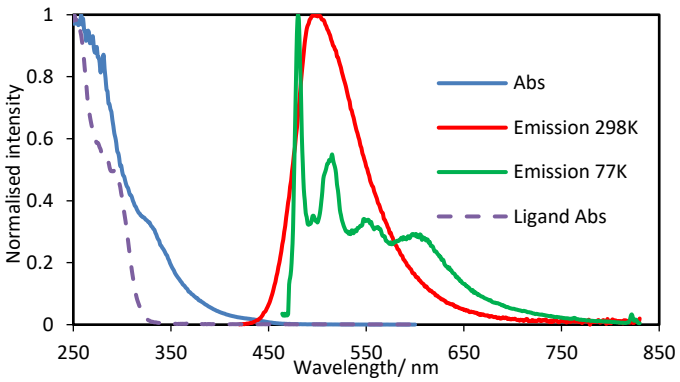

ϕ = 5.9 %
τ_{deg} = 3.1 µs
τ_{aer} = 590 ns
τ_{77K} =230 µs
k_r = 1.9 x 10^4 s^{-1}
k_{nr} = 3.0 x 10^5 s^{-1}
$k_q(O_2)$ = 6.3 x 10^8 $mol^{-1}dm^3 s^{-1}$

Figure 3.10: *RT absorption and degassed emission spectra of $[Pt(dpyb)L^1Cl]^+$ in DCM and 77 K spectrum in EPA.*

$[Pt(dpyb)L^{16}]^+$

The photophysical properties of the bis-tridentate complex $[Pt(dpyb)L^{16}]^+$ are summarised in Figure 3.11. $[Pt(dpyb)L^{16}]^+$ showed absorption from 250 to 350 nm assigned as LC π→π* and the absorption band between 350 and 420 nm of lower intensity was assigned to a MLCT transition or charge-transfer state with enhanced metal character. This MLCT band in the absorption was not noticeable for $[Pt(dpyb)L^1Cl]^+$ which suggests that there is more metal character in the absorption for this $[Pt(dpyb)L^{16}]^+$ complex. The degassed RT emission in DCM shows a highly structured spectrum with a sharp 0-0 transition centred at 480 nm. The emission at 77 K is seen to be slightly blue-shifted from the RT emission with evidence of more vibrational bands. This compound exhibits an impressive PLQY of 28 % in degassed

DCM solution at RT with a lifetime of 11 µs. The k_{nr} value is seen to be lower than that of $[Pt(dpyb)L^1Cl]^+$ (6.4×10^4 vs. 3.0×10^5 s^{-1}) which is a sign of enhanced rigidity and which is reflected by the more structured emission for $[Pt(dpyb)L^{16}]^+$, in addition to the higher PLQY. In this case it seems as though the bis-tridentate structure (containing two tridentate ligands) confers more rigidity to the structure in comparison to the 3+2+1 $[Pt(dpyb)L^1Cl]^+$ complex (containing 1 tridentate ligand).

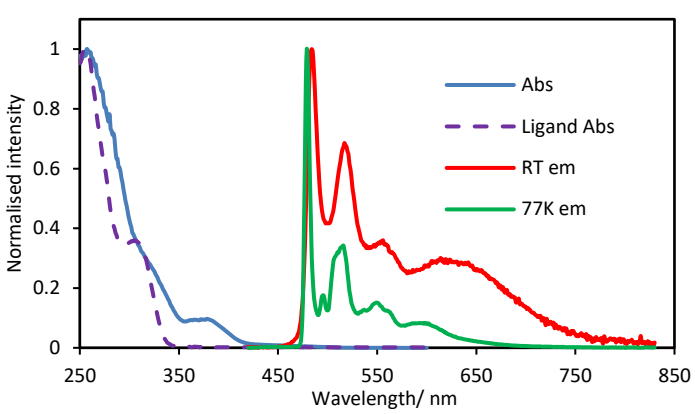

ϕ = 28 %
τ_{deg} = 11 µs
τ_{aer} = 2.1 µs
τ_{77K} = 14 µs
$k_r = 2.5 \times 10^4$ s^{-1}
$k_{nr} = 6.4 \times 10^4$ s^{-1}
$k_q(O_2) = 1.8 \times 10^8$ $mol^{-1}dm^3 s^{-1}$

Figure 3.11: *Absorption and emission spectra of $[Pt(dpyb)L^{16}]^+$ in DCM and 77 K spectrum in EPA.*

3.2.3.3 DFT studies on Pt^{IV} complexes

DFT calculations were performed for these Pt^{IV} complexes in order to try to identify the nature of the excited state transitions in each case. The HOMO→LUMO transitions in both $[Pt(dpyb)L^1Cl]^+$ and $[Pt(dpyb)L^{16}]^+$ are assigned in Table 3.2. The orbital plots for the 3+2+1 Pt complex show that there is a large contribution to the HOMO from the triazole ring and phenyl group on the triazole ligand, as well as a much smaller contribution from the metal centre (Fig. 3.12). The LUMO is delocalised over the N^C^N ligand, the chloride ligand and the triazole ring, with a large contribution from the metal centre and thus the HOMO→LUMO transition can be thought of as having mixed LMCT/LLCT character.

For the bis-tridentate Pt complex, the HOMO has a large contribution from the triazole ligand and a smaller contribution from the metal centre. The LUMO is based mainly on the triazole rings of the N^-^C^N^- ligand and the pyridine of the N^C^N ligand with a large contribution from the metal centre giving good overlap between the HOMO and LUMO orbitals. This could help to explain the relatively high PLQY value for this complex. The HOMO→LUMO transition can thus be thought of as having predominantly LMCT/LLCT character.

Table 3.2: *Summary of transitions for [Pt(dpyb)L^{1}Cl]$^{+}$ and [Pt(dpyb)L^{16}]$^{+}$.*

Complex	*[Pt(dpyb)L^{1}Cl]$^{+}$*	*[Pt(dpyb)L^{16}]$^{+}$*
Transition	HOMO→LUMO	HOMO→LUMO
Assignment	Mixed LMCT/LLCT	Mixed LMCT/LLCT

Complex	*HOMO*	*LUMO*
[Pt(dpyb)L^{1}Cl]$^{+}$	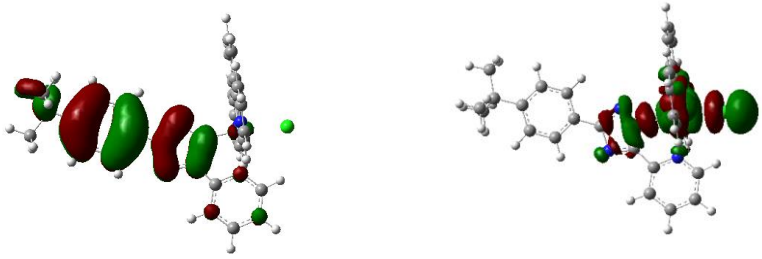	
[Pt(dpyb)L^{16}]$^{+}$	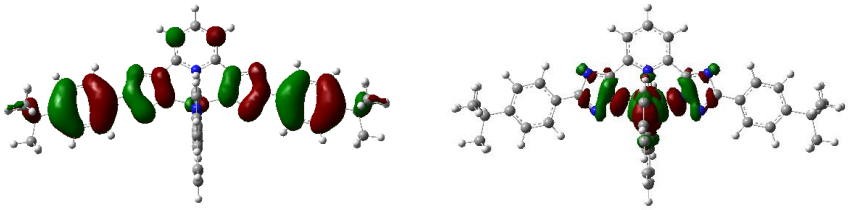	

Figure 3.12: *Orbital plots of the HOMO and LUMO for [Pt(dpyb)L^{1}Cl]$^{+}$ and [Pt(dpyb)L^{16}]$^{+}$ as calculated by DFT.*

3.3 Mononuclear Ir^{III} complexes containing tridentate N^C^N ligands

This next section discusses Ir^{III} complexes which are isoelectronic with Pt^{IV} complexes and which can display analogous structures based on their octahedral complex geometries. Table 3.3 at the end of this introductory section summarises the photophysical properties of selected Ir complexes.

3.3.1 Introduction

The most commonly reported luminescent Ir complexes are of the form $Ir(N^C)_3$ bearing three bidentate mono-anionic ligands to form a neutral Ir complex in which the metal is in its +3 oxidation state. These have been widely recognised for their intense luminescence. Indeed, Ir^{III} complexes such as tris(2-phenylpyridine)iridium $[Ir(ppy)_3]$, tris(1-phenylisoquinoline)iridium $[Ir(piq)_3]$ and bis([4,6-di-fluorophenyl]-pyridinato-$N,C^{2'}$)(picolinato)Ir^{III}, FIrpic, are well known red, green and blue emitters with quantum yields of 0.97[15], 0.53[140] and 0.89[141] in solution respectively. Since then, other Ir complexes with different ligand binding modes have been investigated including bis-tridentate and '3+2+1' conformations which contain a combination of one tridentate, one bidentate and one monodentate ligand as was seen for $[Pt(dpyb)L^1Cl]^+$ (Fig. 3.13).

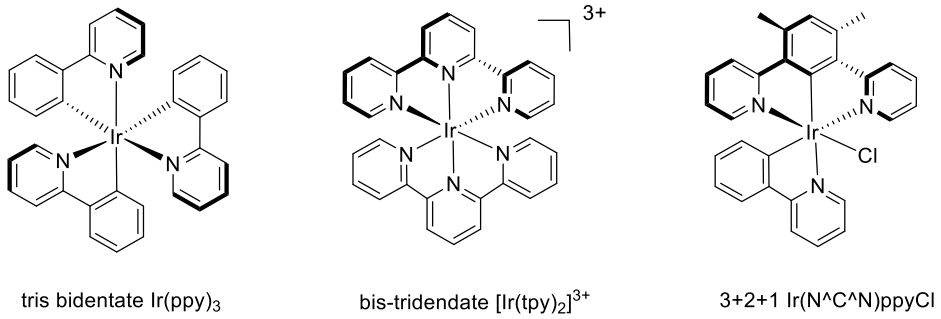

Figure 3.13: *Examples of the binding modes of Ir^{III} complexes.*

In terms of bis-tridentate complexes, historically Ir bis-terpyridine $[Ir(tpy)_2]^{3+}$ was the focus of much attention after optimisation of the synthesis procedure was achieved by Collin *et al.* in 1999.[142] $IrCl_3.3H_2O$ and tpy were reacted in ethylene glycol at 160 °C to afford $Ir(tpy)Cl_3$ which was subsequently refluxed with a second amount of tpy at higher temperatures (from 196 to 198 °C). Purification was achieved by ion-exchange to the hexafluorophosphate salt, which offers greater solubility in polar organic solvents, followed by column chromatography on either silica or alumina. $[Ir(tpy)_2]^{3+}$ showed structured emission with peak maxima at 458, 491 and 523 nm, and PLQY values ranging between 0.02 and 0.06, depending on the counter anion and solvent. Lifetimes were reported in the range of 0.7 to 1.2 µs in air- equilibrated solution at RT.[143]

This research soon extended to other charged bis-tridentate Ir complexes where Haga's group synthesised complexes containing tridentate ligands that ligate through benzimidazole nitrogen atoms.[144] The homoleptic complex $[Ir(Mebip)_2]^{3+}$ (**46**) was prepared in a similar manner to $[Ir(tpy)_2]^{3+}$ where the dimethylated ligand, 2,6-bis(1-methyl-benzimidazol-2-yl)pyridine (Mebip) was reacted with $IrCl_3 \cdot nH_2O$ in a 1:1 ratio at 100 °C, to give $[Ir(Mebip)Cl_3]$ as a red precipitate, followed by reaction with a second equivalent of the ligand in refluxing ethylene glycol. They also prepared the dicationic complex containing 1,3-bis(1-methyl-benzimidazol-2-yl)benzene (Mebib) and Mebip, **47**. The comparison of the emission spectra of **46** and **47** is shown below. **46** had emission peak maxima of 550 and 592 nm with a quantum yield of 3.7 % at RT whilst **47** displayed red-shifted emission. This work also included the synthesis of a 3+2+1 complex $[Ir(Mebip)(bpy)Cl]^{2+}$ (**48**) which showed the highest PLQY of 19 % and emission peak maxima of 547 and 582 nm (Fig. 3.14).

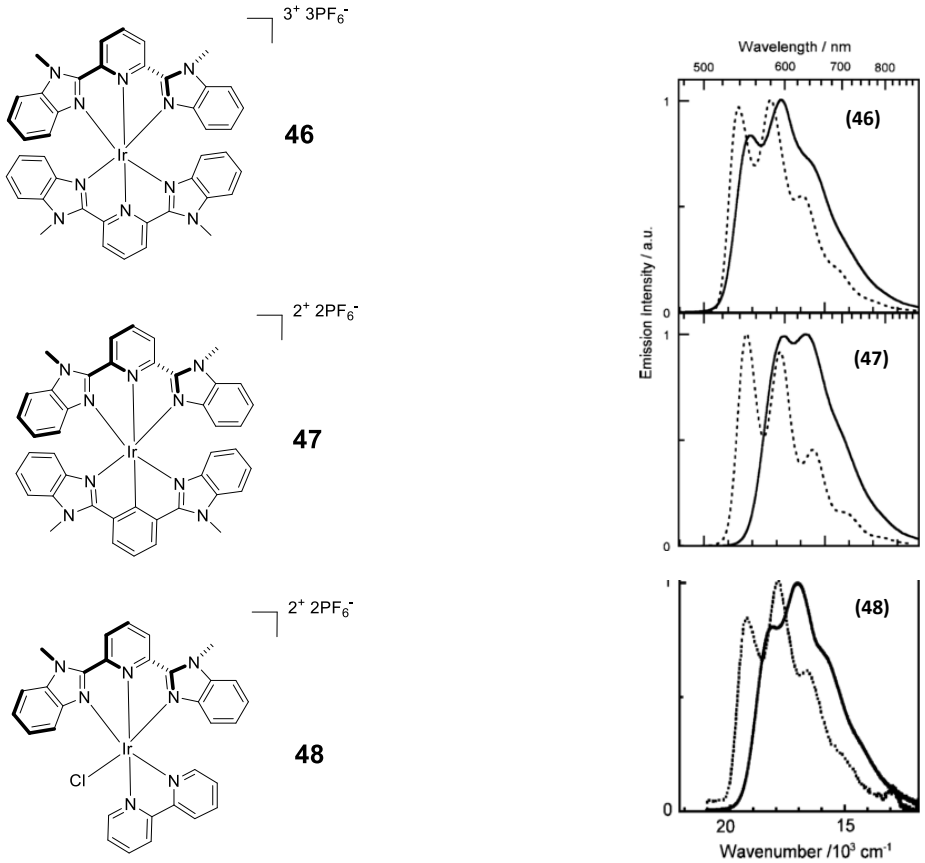

Figure 3.14: *Structures of complexes **46**, **47** and **48** along with their emission spectra where solid lines are at RT (in MeCN), and dotted lines are at 77 K in DMF-MeOH-EtOH [1:5:5(v/v)]. Reprinted with permission from Haga et al.*[144] *Copyright 2005 American Chemical Society.*

The fact that these complexes are ionic limits their use in many applications such as OLEDs where vacuum sublimation is required. Thus, a move towards mono-anionic ligands, as opposed to tpy, to give charge neutral complexes was investigated.

Williams *et al*. demonstrated the synthesis of a neutral bis-tridentate Ir^{III} complex Ir(dpyx)(dppy) (**49**) where dpyxH = 1,3-di(2-pyridyl)-4,6-dimethylbenzene in their 2004 communication.[145] Initial attempts to coordinate dipyridylbenzene to Ir^{III} in an N^C^N fashion failed owing to the adoption of binding mode II as shown below (Fig. 3.15). Methyl groups were subsequently incorporated on the 4 and 6 positions of the central ring to block this binding mode and favour N^C^N binding. The desired product **50** was then obtained as an orange solid by heating the chloro-bridged dimer $[Ir(dpyx)Cl(\mu\text{-}Cl)]_2$ with AgOTf in molten $dppyH_2$ at 110 °C, followed by column chromatography purification. The complex was found to be highly luminescent with a λ_{max} of 585 nm and quantum yield of 21 % with a lifetime of 3.9 μs in degassed MeCN solution at RT.

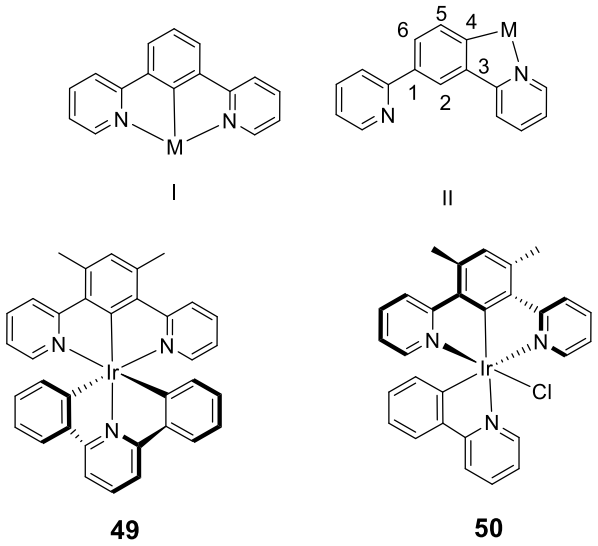

Figure 3.15: *Different possible binding modes of dipyridylbenzene (I and II, top) and structures of the bis-tridentate complex* ***49*** *and 3+2+1 complex* ***50*** *(bottom).*

The downside to this bis-tridentate complex was its instability under prolonged irradiation in polar solvents. It was observed by ^1H NMR that after irradiation in MeCN, a new product was formed that contained dppy bound asymmetrically as a C^N^- coordinating ligand with the second phenyl group unbound. This indicated a cleavage of one of the mutually *trans* Ir—C bonds. This instability was only observed in solution but raises concern as to its likely stability in a device, as well as rendering its synthesis and purification very difficult.

They also demonstrated the 3+2+1 arrangement adopted by the charge-neutral complex [Ir(dpyx)(ppy)Cl] (**50**, Fig. 3.15), containing a tridentate, bidentate and monodentate ligand.[146] This complex was synthesised via reaction of the chloro-bridged dimer $[Ir(dpyx)Cl(\mu\text{-}Cl)]_2$ with 2-phenylpyridine (ppyH) in the presence of AgOTf.

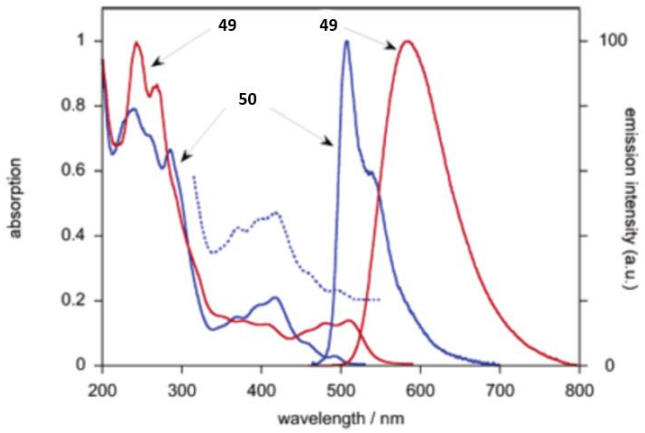

Figure 3.16: *Absorption and emission spectra of **49** and **50**. The low-energy portion of the excitation spectrum of **49**, registered at 507 nm under the same conditions, is also shown (blue dotted line). Reproduced with permission from Williams et al.*[146] *Copyright 2006 American Chemical Society.*

Complex **50** was seen to be highly emissive in solution with a PLQY of 0.76 in degassed MeCN solution. The emission spectra of both **49** and **50** are shown in Fig. 3.16. Complex **50** shows a structured, blue-shifted emission in comparison to the bis-tridentate complex **49**. The blue-shift in emission is explained by the lowering of the HOMO energy upon substitution of the strong-field cyclometallating carbon by a chloride ligand, without significantly affecting the dpyx-based LUMO. Moreover, the more structured spectrum is suggestive of an increase in LC character, therefore, the emission is assigned to a heavily mixed π-(dpyx)/d(Ir)→π*(dpyx) (LC/MLCT) excited state.

Other examples of the 3+2+1 arrangement have also been reported by Haga's group who synthesised a series of neutral Ir^{III} complexes with the formula [Ir(N^C^N)(ppy)X] where (N^C^N) represents Mebib and X = CN or Cl.[147] The reaction of Mebib with $IrCl_3.4H_2O$ in methanol gave an insoluble yellow precipitate which was then reacted with ppy under microwave conditions in glycerol to afford the Cl-containing product. The chloride could be metathesized to cyanide upon treatment with KCN in ethylene glycol. The phosphorescence of [Ir(Mebib)(ppy)X] was observed at 555 nm for X = Cl (**51**) and 526 nm for X = CN (**52**), with high quantum yields in the range of 0.77 to 0.86 at RT (Fig. 3.17).

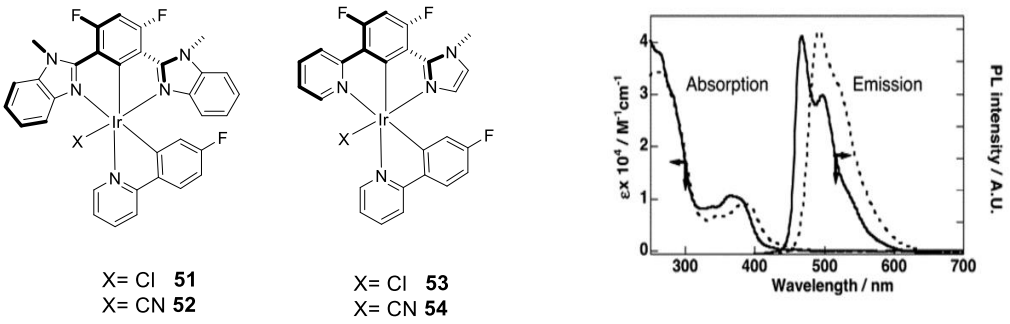

Figure 3.17: *Structure of Haga Ir complexes* ***51-54*** *(left) and absorption and emission spectra of complexes* ***53*** *and* ***54*** *where the dotted line represents complex* ***53*** *and the solid line is* ***54*** *(right). Reproduced from Haga et al. by permission of the Royal Society of Chemistry.*[148]

Moreover, they later reported the synthesis of iridium complexes bearing asymmetric tridentate N-methylimidazole derivatives which could be separated into pairs of optically pure enantiomers (**53** and **54**, Fig. 3.17).[148] In the absorption spectrum, upon the substitution of a chlorine atom by CN, a shorter wavelength shift of both the π→π* and MLCT (or LLCT) bands was observed. The weak absorption band around 450 to 460 nm was attributed to the ^{3}LC transitions mixed with ^{3}MLCT. The complex **54** exhibited a strong emission band with vibrational structure at 468 nm, a lifetime of 1.4 μs and quantum yield of 0.63 at RT. Determination of the lifetime and quantum yield for **53** was not possible due to photochemical dissociation of **53** in DCM. The two enantiomers of this complex were resolved on a chiral HPLC column and CD spectra confirmed their successful separation.

It is evident from these examples that significant developments in luminescent Ir^{III} complexes, away from the archetypal $Ir(L)_3$ structure, have been made. The 3+2+1 Ir complexes display unprecedently high quantum yields. However, Ir complexes with tridentate ligands were not investigated for incorporation into devices prior to 2012.

In 2012, in collaboration with Haga, Kuwabara *et al*. made the first steps to incorporating these types of 3+2+1 and bis-tridentate complexes into OLEDs.[149] They reported the synthesis of Ir complexes composed of benzothiazole-based pincer ligands with 1,3-bis(2-benzothiazolyl)-4,6-dimethylbenzene (bbtxH). The reaction of the chloro-bridged dimer $[Ir(bbtx)(\mu\text{-}Cl)Cl]_2$ with ppyH was carried out by applying microwave radiation for 4 minutes and resulted in the neutral 3+2+1 complex, Ir(bbtx)(ppy)Cl (**55**), in 76 % yield. Complex **55** displayed an extremely high quantum yield of 89 % in degassed DCM at RT and had an emission lifetime of 1.1 μs. The performance of this complex was then investigated in an

OLED owing to its impressive photophysical properties and the resulting EQE of the device was 10.5 % (Fig. 3.18).

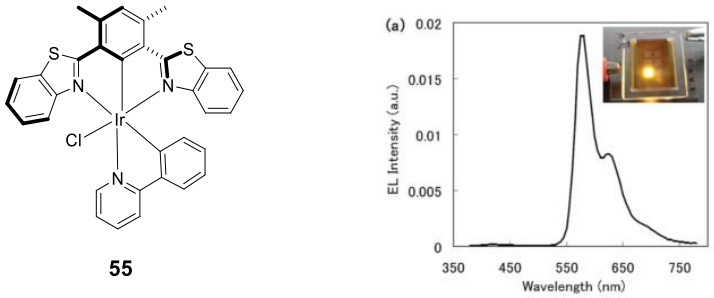

55

Figure 3.18: *Structure of* ***55*** *and EL spectrum of the device (inset: photograph of EL of the device at 3 V). Reproduced from Kuwabara et al. by permission of the Royal Society of Chemistry.*[149]

Since then, Yun Chi's group have reported a number of charge-neutral bis-tridentate complexes with high luminescence quantum yields and facile synthesis procedures for incorporation into OLED devices.[150,151,152] In 2015, they synthesised six charge-neutral bis-tridentate Ir^{III} complexes containing 2-pyrazol-3-yl-6-phenylpyridine functional groups.[152] The synthesis of complexes **56**-**61** (Fig. 3.19) was conducted at lower temperatures than those needed with dppy-containing ligands, by reaction of Ir^{III} dimers with the pyrazolo ligands in decalin and in the presence of sodium acetate (NaOAc). The presence of NaOAc acting as a base was proven invaluable in the synthesis for quick reaction times and high yields of between 52 and 72 %.

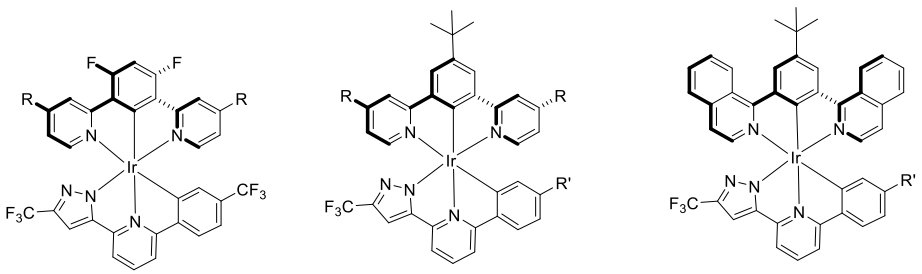

56 R = H
57 R = tBu

58 R' = CF_3
59 R' = ^{t}Bu

60 R' = CF_3
61 R' = ^{t}Bu

Figure 3.19*: Structures of bis-tridentate complexes* ***56***-***61****.*

Complexes **56** and **60** were chosen as representative green and red emitters for the fabrication of OLEDs owing to their high PLQY values of 72 and 63 % respectively in degassed DCM solution at RT. A maximum EQE of 13.2 %, luminance efficiency of

41.4 cd A^{-1} and power efficiency of 35.5 lm W^{-1} were obtained for the green OLED (complex **56**), as opposed to 15.4 %, 21.0 cd A^{-1} and 16.3 lm W^{-1} for the red emitting device (complex **60**).

By incorporating imidazole-based carbene units, Chi's group has since managed to increase the PLQY values of charge-neutral bis-tridentate Ir complexes to near unitary efficiency and subsequently give EQE values of well over 20 %.[153,151] They are striving towards deep blue emission and have produced a multitude of complexes containing bis(imidazolylidene) benzenes, acting as NHCs, in combination with both 2-pyrazolyl-6-ppy and 6-pyrazolyl-2-phenoxylpyridine ligands (**62**-**64**, Fig. 3.20). The OLED derived from the complex **62** gave a maximum EQE of 27 % but CIE coordinates of (0.18, 0.40) which is less good than OLEDs fabricated from FIrpic.[153] As a result they moved on to the complexes containing 6-pyrazolyl-2-phenoxylpyridine ligands as opposed to 2-pyrazolyl-6-ppy, complexes **63** and **64**. Complex **64** was seen to have much improved CIE coordinates of (0.15, 0.17) despite a lower, but still extremely high, maximum EQE of 20.7 %.[151]

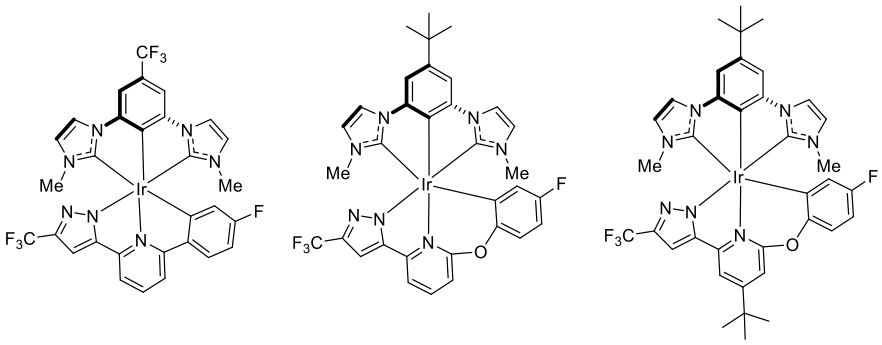

Figure 3.20: *Structures of bis-tridentate complexes* ***62***-***64****.*

Table 3.3: *PL (in degassed solution) and EL properties of literature Ir^{III} complexes where the EL performance records the maximum values obtained. Please refer to the list of abbreviations for the device architecture column.*

Compound no./Ref	*Device Architecture*	*PL performance*			*EL performance*				
		λ_{max} (nm)	*PLQY (%)*	*Lifetime (μs)*	*λ_{max}(nm)*	*CE (cd A^{-1})*	*PE (lm W^{-1})*	*Brightness (cd m^{-2})*	*EQE (%)*
55 [149]	Al (200 nm)/ LiF (0.5 nm) / 4,7-diphenyl-1,10-phenanthroline (4 nm)/ arylanthracene (35 nm) / CBP + **55**/ NBP (30 nm) / Triarylamine (30 nm) / ITO (100 nm).	572, 675	89	1.1	572, 675	-	-	-	10.5
	Al (200 nm)/ LiF (0.5 nm) / 4,7-diphenyl-1,10-phenanthroline (4 nm) / arylanthracene (35 nm) / $BAlq_2$ + **55**/ NBP (30 nm) / Triarylamine (30 nm)/ ITO (100 nm).				-	-	-	-	14
56[152]	ITO / TAPC (40 nm) / mCP with 8 wt% **56** (30 nm) / BP4mPy (50 nm) / LiF (0.8 nm) /Al (150 nm).	490, 526, 570	72	1.8	490, 526, 570	37.8	30.3	9696	12.1
	ITO / TAPC (40 nm) / mCP with 8 wt% **56** (30 nm) / TmPyPB (50 nm) / LiF (0.8 nm) / Al (150 nm).					41.4	35.5	15781	13.2
60[152]	ITO/TAPC (40 nm) / mCP with 8 wt% **60** (30 nm) / BP4mPy (50 nm) / LiF (0.8 nm) /Al (150 nm).	594, 641	63	1.8	594, 641	21.0	16.3	19085	15.4
	ITO / TAPC (40 nm)/ mCP with 8 wt% **60** (30 nm) / TmPyPB (50 nm) / LiF (0.8 nm) / Al (150 nm).					21.7	20.1	29749	15.0
63[151]	ITO / MoO_3 (1 nm) / TAPC (40 nm) / mCP (10 nm) / DPEPO + 12 wt. % **63** (20 nm) / 3TPYMB (50 nm) / LiF (1 nm) / Al (100 nm).	-	-	-	476	33.5	26.3	-	19.7
64[151]	ITO/MoO_3 (1 nm) / TAPC (40 nm) / mCP (10 nm) / DPEPO + 12 wt. % **64** (20 nm) / 3TPYMB (50 nm) / LiF (1 nm) / Al (100 nm).	-	-	-	467	28.8	22.6	-	20.7

3.3.2 Objectives

We aim to investigate the synthesis and photophysical properties of Ir^{III} complexes containing tridentate N^C^N ligands, in combination with both bidentate and tridentate triazole ligands.

The main set of complexes that will be studied are bis-tridentate Ir^{III} complexes which incorporate cyclometallating N^C^N ligands and pseudo-cyclometallating triazole ligands. Primarily, we seek to prepare Ir(N^C^N)(N^-^N^N^-) complexes in place of the Ir(N^C^N)(C^N^C) complexes which were found to be unstable in solution as discussed earlier.

Already we have seen the lower *trans* influence of the N^- atom in the bidentate triazole ligand L^1 compared to the cyclometallating C^- atom of dpyb displayed in complex $[Pt(dpyb)L^1Cl]^+$. Subsequently, here we aim to answer the question of: is the *trans* effect in these bis-tridentate complexes lower for those containing N^-^N^N^- or C^N^C ligands?

In addition to this, the synthesis of complexes with the 3+2+1 conformation which incorporate bidentate triazole ligands will be attempted. It is also the aim to confirm the binding mode of the N^N ligand in these cases, i.e. is the binding mode in this case N^N, with a neutral coordinating nitrogen atom to form a charged Ir complex, or N^N^- with a negatively charged nitrogen atom to form a neutral Ir complex?

3.3.3 Results and discussion

3.3.3.1 Bis-tridentate Ir^{III} triazole complexes

Synthesis

Tridentate triazole ligands H_2L^n where n = 16-18 were synthesised according to an adapted procedure by de Cola *et al.*[91] in the same manner as for the bidentate triazole ligands discussed in Chapter 2, but starting from 2,6-dicyanopyridine (Scheme 3.9). Yields for each step were above 80 % except when the OMe substituent was present. This electron-donating group was also seen to have a reducing impact on the yield of the bidentate triazole ligands from chapter 2. This may be due, in the case of intermediate 2 ($I2^l$) formation, to the fact that the electron donating group makes the δ^+ charge on the carbonyl less positive and hence not as susceptible to attack from intermediate 1 ($I1^h$). In the formation of the triazole itself this could also be the case whereby the elimination of water for the ring closure in this step favours a more δ^+ site on the carbonyl for attack.

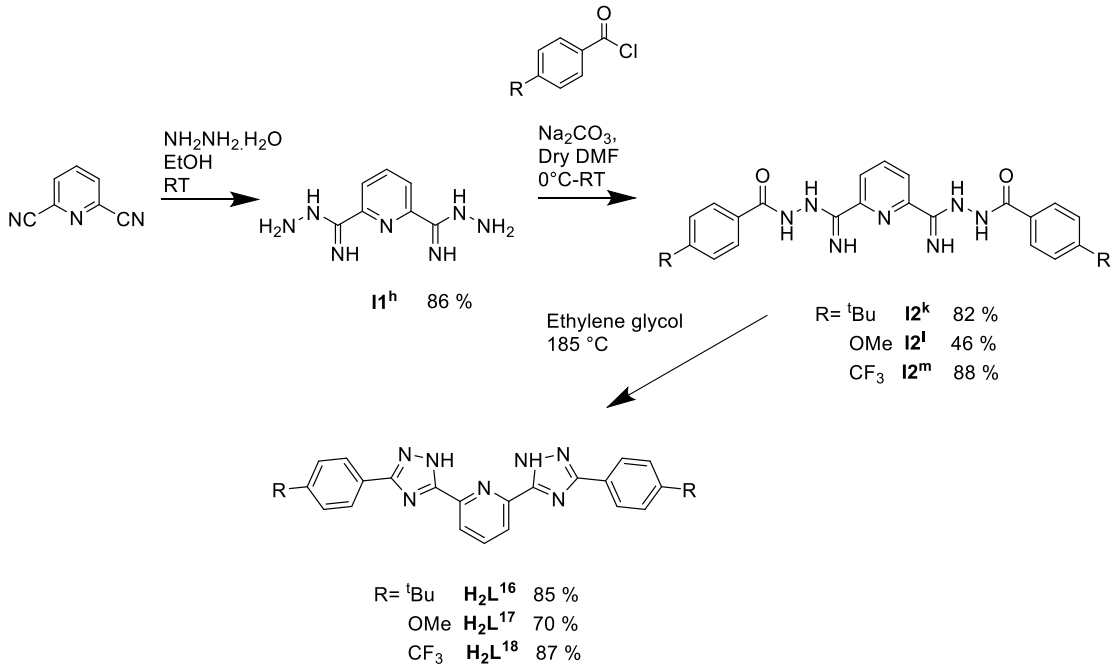

Scheme 3.9: *Synthesis of tridentate triazole ligand intermediates and resulting ligands $H_2L^{16\text{-}18}$.*

The iridium complexes Ir(dpybX)($L^{16\text{-}18}$), where X= 3,5-difluoro (*F_2*), 3,5-dimethyl (*Me_2*) and 4-OMe (*OMe*) on the phenyl ring (Scheme 3.10), were synthesised via cleavage of the corresponding $[Ir(dpybX)Cl(\mu\text{-}Cl)]_2$ chloro-bridged dimers[154] with $H_2L^{16\text{-}18}$ in the presence of AgOTf as a chloride scavenger. The reactions failed to proceed in toluene but use of the higher boiling-point solvent ethylene glycol allowed the desired compounds to be formed in

good yields. Purification was achieved by precipitation from H_2O followed by washing with H_2O, MeOH and Et_2O and finally a short column on silica in DCM/MeOH (90:10). Yields of the final complexes ranged from 45 to 74 %. The fact that these complexes were stable on the column and in solution for long periods of time suggests that the *trans* effect is weaker in these complexes containing two N^- atoms and one cyclometallating C^- atom, compared to analogous Ir(N^C^N)(C^N^C) complexes containing 3 cyclometallating C^- atoms which were unstable under similar conditions as discussed earlier.

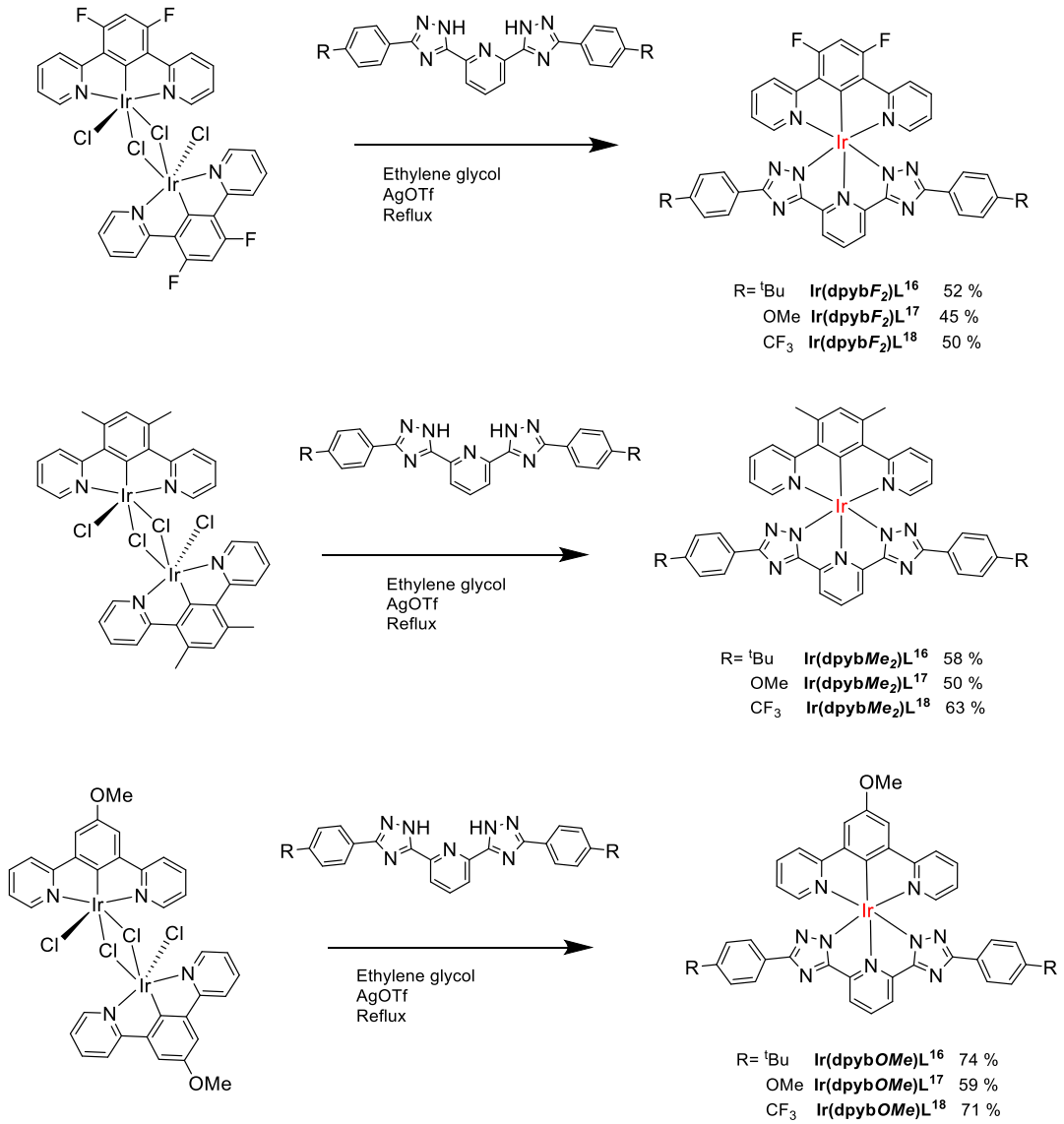

Scheme 3.10: *Synthesis of bis-tridentate Ir^{III} triazole complexes starting from the Ir chloro-bridged dimers.*

X-ray diffraction analysis of single crystals grown from slow diffusion of hexane into a DCM solution confirmed the bis-tridentate nature of the complexes Ir(dpyb*Me*$_2$)L^{16} and

Ir(dpybF_2)L[16] with mutually orthogonal chelates (Figs. 3.21 and 3.22). Tables 3.4 and 3.5 give the selected bond lengths and bond angles for complexes Ir(dpybMe_2)L[16] and Ir(dpybF_2)L[16] respectively. The Ir1—C7 bond is shorter than the corresponding Ir—N6 bond lengths in each complex which is in line with the *trans* influence seen in many cyclometallated complexes owing to the strong σ donation from C^- atoms. Ir—N7 and Ir—N3 bond lengths in each complex are also seen to be of similar length (ca. 2.0 Å) which demonstrates the slightly weaker *trans* influence of the pseudocylometallating N^- atoms compared to the cyclometallating C^- atoms for which the Ir—C7 bond length is ca. 1.9 Å. The C7-Ir1-N6 angle in Ir(dpybMe_2)L[16] is essentially linear at 177. 4° whilst the angles for N1-Ir1-N2 and N7-Ir-N3 are 160.9 and 150.9° respectively. The crystal structure of Ir(dpybMe_2)L[16] has disordered ^{t}Bu groups and for Ir(dpybF_2)L[16] there are two DMF solvent molecules per unit of crystallization.

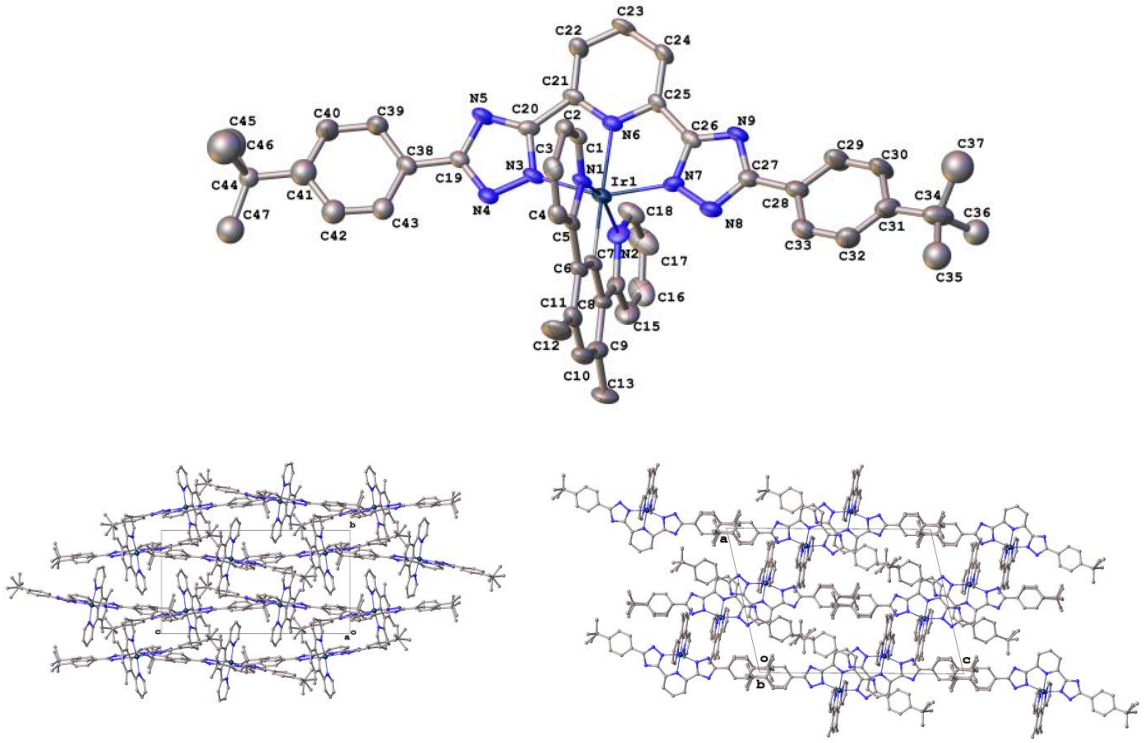

Figure 3.21: *Molecular structure and crystal packing of Ir(dpybMe$_2$)L[16], hydrogen atoms are omitted for clarity.*

Table 3.4: *Selected bond lengths and angles of Ir(dpybMe$_2$)L[16].*

Bond Lengths/ Å		*Bond Angles / °*	
Ir1—N1	2.030(5)	N1-Ir1-N2	160.90(19)
Ir1—N2	2.065(5)	N7-Ir1-N3	154.54(19)
Ir1—N3	2.039(5)	C7-Ir1-N6	177.4(2)
Ir1—N6	2.081(5)		
Ir1—N7	2.028(5)		
Ir1—C7	1.954(6)		

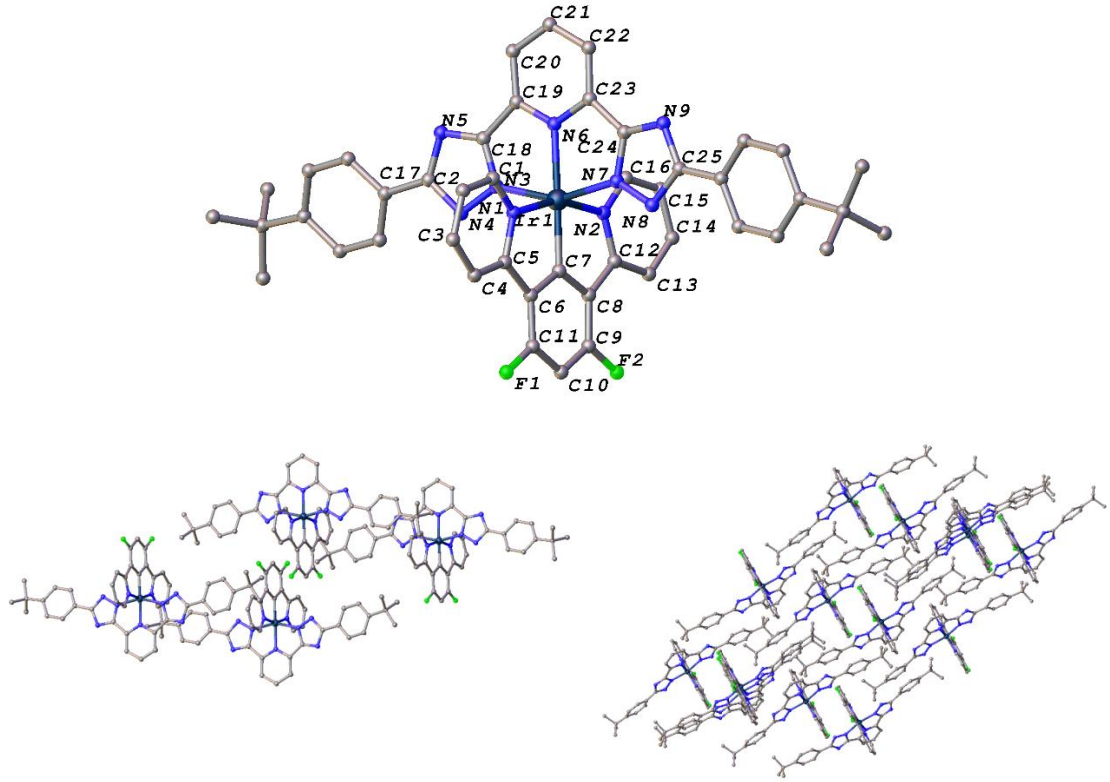

Figure 3.22: *Molecular structure and crystal packing of Ir(dpybF$_2$)L^{16}, hydrogen atoms are omitted for clarity.*

Table 3.5: *Selected bond lengths and angles of Ir(dpybF$_2$)L^{16}.*

Bond Lengths/ Å		*Bond Angles / °*	
Ir1—N1	2.049(3)	N1-Ir1-N2	160.02(12)
Ir1—N2	2.050(3)	N7-Ir1-N3	155.05(12)
Ir1—N3	2.032(3)	C7-Ir1-N6	178.95(14)
Ir1—N6	2.066(3)		
Ir1—N7	2.033(3)		
Ir1—C7	1.937(4)		

Photophysical Properties

The effect on the spectral properties of changing the N⁻^N^N⁻ ligand (L$^{16\text{-}18}$) in each complex was seen to be negligible. Consequently, for clarity, the Ir complexes have been subdivided into 3 sets for comparison, keeping L^n constant in each of the absorption/emission spectra shown below (Fig. 3.23) and only changing the N^C^N ligand dpybX. Set 1 contains the ligand L^{16} (^{t}Bu), set 2 contains L^{17} (OMe) and set 3 contains L^{18} (CF_3).

The absorption of the complexes in each group is seen to red-shift in the order of X= *OMe* > *Me₂* > *F₂* for the different substituents on the N^C^N ligand. This is anticipated due to the destabilising effect of electron-donating or accepting groups on the HOMO of the N^C^N ligand (phenyl group). Within each set of compounds, all complexes show strong absorption bands below 350 nm due to $^{1}\pi\rightarrow\pi^{*}$ transitions localised on both tridentate ligands, together with less intense bands in the region >400 nm, which are attributed to MLCT transitions from the Ir^{III} metal ion to the tridentate ligands.

Set 1

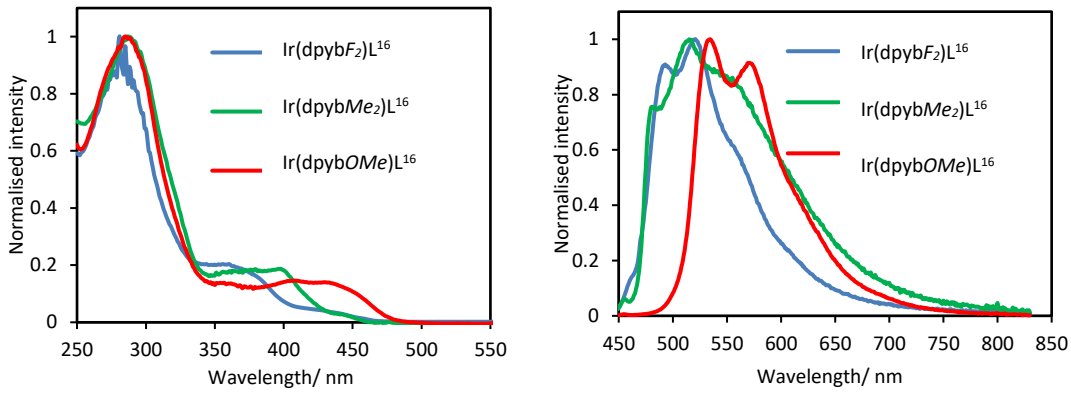

Set 2

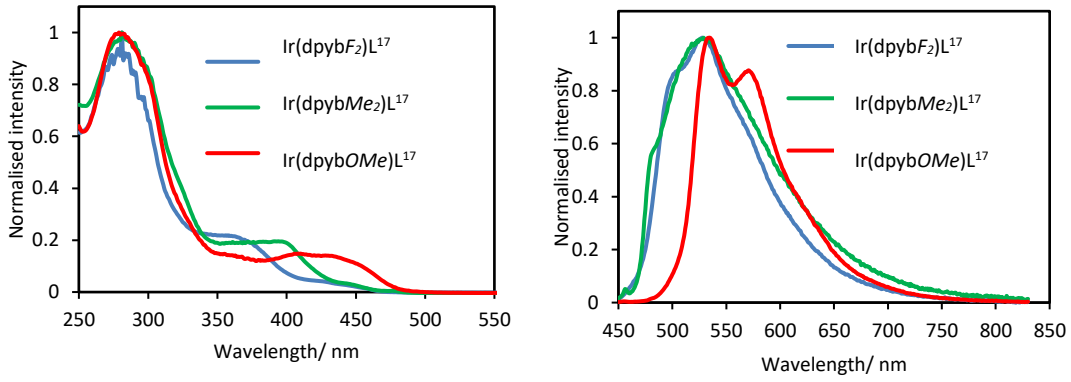

Set 3

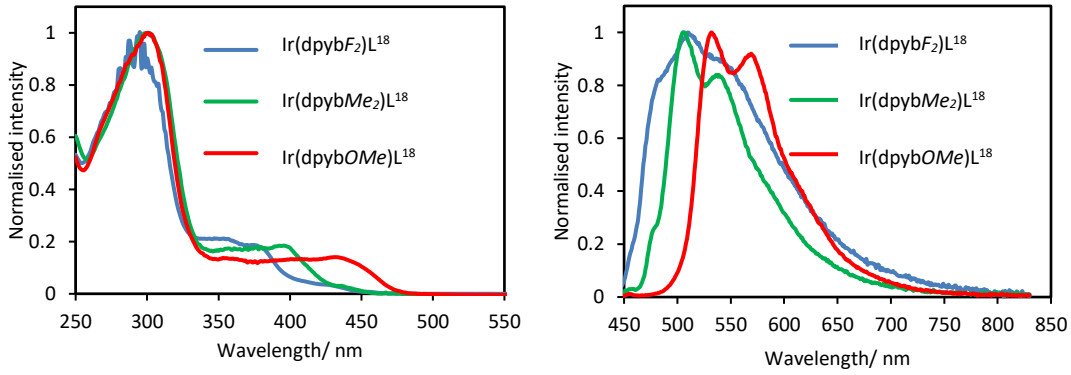

Figure 3.23: *Absorption (left) and emission (right) of bis-tridentate Ir complexes in DCM at RT.*

These complexes were weakly emissive in degassed DCM solution with quantum yields ranging from 0.35 to 1.8 % (Table 3.6). These values are significantly lower than those of some other bis-tridentate complexes in the literature discussed previously where, for example, Ir(dpyb*Me*$_2$)(C^N^C) exhibited a PLQY of 21 %.[145] In each set of complexes, the onset of emission is seen to red-shift significantly for those with X = OMe on the N^C^N ligand. The 77 K spectra of all complexes display pronounced vibrational structure (Fig. 3.24).

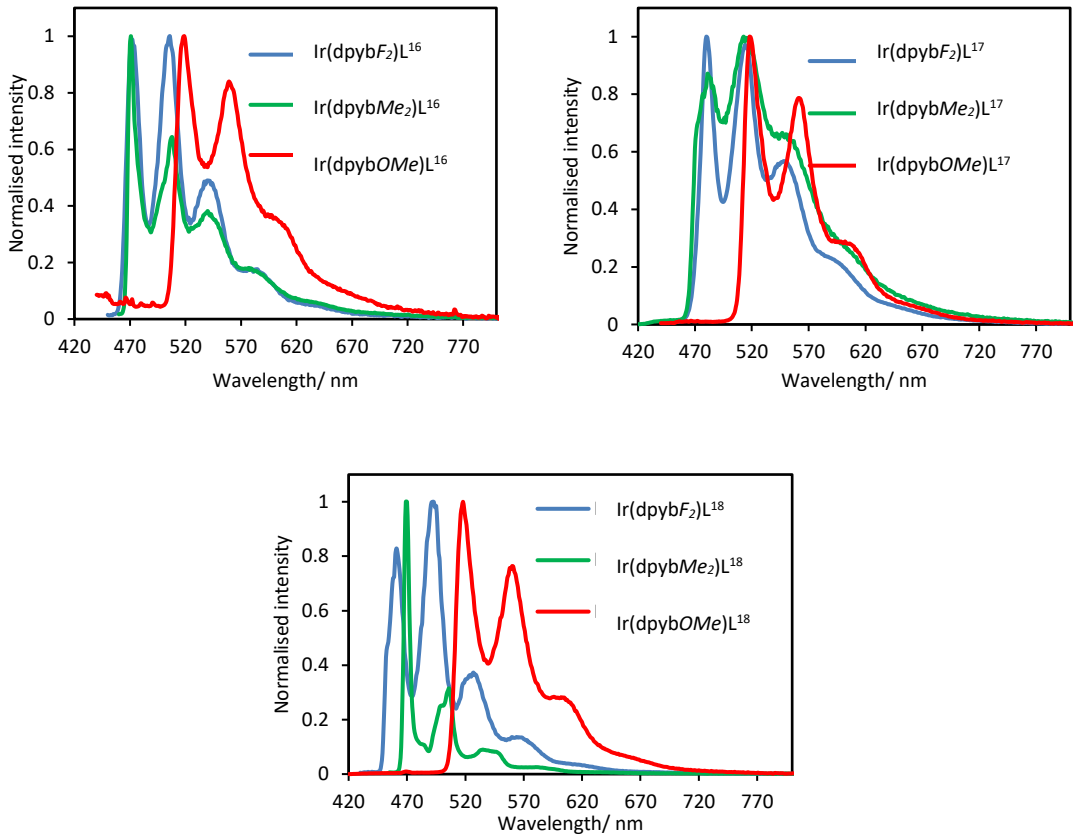

Figure 3.24: *77 K emission of Ir complexes in butyronitrile glass.*

The strength of the σ-donation from the triazole N$^-$ atoms is called into question when taking all of the photophysical properties of these complexes into consideration. Indeed, as alluded to earlier, the previously reported Ir(N^C^N)(C^N^C) complex with three cyclometallating carbon atoms displays impressive photophysical properties but is unstable with respect to cleavage of one of the *trans*-related Ir—C bonds.[145] In contrast, it has also been reported that an [Ir(N^N^N)(N^C^N)]$^{2+}$ complex containing only one cyclometallating carbon shows a low PLQY value of 0.5 %, but does not suffer from the same instability.[155] This suggests that the number of cyclometallating carbon atoms has a significant impact on both the luminescence efficiency and the stability of the complex where the greater the

number of C^- atoms, the greater the PLQY, but the more unstable the complex with respect to bond cleavage. This is seen to be true in the case of these Ir(N^-^N^N^-)(C^N^C) complexes which technically also only contain one cyclometallating carbon and which are also stable like $[Ir(N^N^N)(N^C^N)]^{2+}$. When referring back to the bond lengths for each of the crystal structures obtained, it is apparent that the Ir—N6 bond lengths (2.081 and 2.066 Å) are very similar to the Ir—N^- bond lengths (between 2.028 and 2.039 Å). This demonstrates a similar magnitude of *trans* influence for the N^- atoms on the triazole as for the N atoms on the pyridine. This could explain the very similar photophysical properties for these Ir(N^C^N)(N^-^N^N^-) to the previously reported $[Ir(N^N^N)(N^C^N)]^{2+}$complex, whereby the N^- atoms on the triazole do not display particularly strong σ-donation in these tridentate 1,2,4-triazole ligands and are in fact more akin to tpy ligands in terms of their electronic behaviour.

Table 3.6: *Photophysical properties of the Ir^{III} bis tridentate and 3+2+1 complexes. All solution-state measurements were conducted in degassed DCM solution unless otherwise stated, whilst 77 K measurements were conducted in either butyronitrile or EPA glass.*

	298 K							77 K	
Complex	ε (mol^{-1} dm^3 cm^{-1})	λ_{em} (nm)	τ_{deg} (μs)	τ_{aer} (μs)	φ (%)	k_r (10^2 s^{-1})	k_{nr} (10^4 s^{-1})	k_q [O_2] (10^5 M^{-1} s^{-1})	λ_{em} (nm)	τ (μs)
Ir(dpybF$_2$)L^{16}	275 (101140), 352 (24349), 422 (5760).	496, 523	12	12	0.63	5.1	8.1	9.8	474, 507, 545, 586	11
Ir(dpybF$_2$)L^{17}	285 (72409), 299 (55837), 361 (18778).	506, 533	11	11	1.6	14	8.9	/	482, 516, 552, 594	14
Ir(dpybF$_2$)L^{18}	293 (36958), 348 (7636), 373 (6367), 420 (1323).	484, 512, 597	12	12	0.35	2.9	8.3	5.1	462, 494, 525, 569	12
Ir(dpybMe$_2$)L^{16}	281 (94577), 300 (93241), 396 (21678).	482, 517, 547	12	11	0.38	3.1	8.1	51	470, 509, 544, 581	12
Ir(dpybMe$_2$)L^{17}	280 (35489), 394 (16548), 440 (3472).	484, 531	12	13	0.38	3.3	8.6	/	484, 514, 552, 599 (sh)	12
Ir(dpybMe$_2$)L^{18}	283 (34,783), 298 (50,759), 359 (9854), 393 (11209).	509, 541	11	13	0.45	4.0	8.7	/	470, 501, 539	11
Ir(dpybOMe)L^{16}	288 (18092), 299 (16684), 360 (2748), 406 (3115), 434 (2889).	537, 574	12	12	0.87	7.3	8.2	2.9	520, 562, 604	17
Ir(dpybOMe)L^{17}	282 (36127), 296 (37384), 361 (7464), 404 (8446).	537, 574	12	12	1.8	15	8.2	2.2	520, 564, 603	14
Ir(dpybOMe)L^{18}	286 (29037), 299 (52943), 351 (7942), 438 (9040).	535, 571	12	13	0.73	5.9	8.0	/	518, 561, 604	17
Ir(dpybMe$_2$)L^{1}Cl	264(38403), 286 (34172), 392 (7299).	-	-	-	-	-	-	-	470, 499, 507, 538, 581	12
Ir(dpybMe$_2$)L^{2}Cl	265(37657), 292(27546), 361(6548)	-	-	-	-	-	-	-	470, 486, 508, 547	12
Ir(dpybMe$_2$)L^{3}Cl	275(36540), 379(6450)	-	-	-	-	-	-	-	470, 478, 483, 504, 537	13

3.3.3.2 Ir(N^C^N)(N^N)Cl triazole complexes of the 3+2+1-type

Investigation into novel 3+2+1 complexes containing N^C^N, N^N or N^N$^-$ triazole and Cl ligands was also carried out to see the differences in their photophysical properties in comparison to the bis-tridentate complexes. These types of complex have two potential structures owing to the nature of the triazole where binding could occur through the deprotonated N$^-$ atom (I, Fig. 3.25) or the non-protonated N atom (II, Fig. 3.25) as shown below. Characterisation of the complexes will aim to elucidate the correct structure in this case. As discussed earlier, although there isn't a large literature precedent for 3+2+1-type Ir complexes, those that have been reported do have impressive photophysical properties.

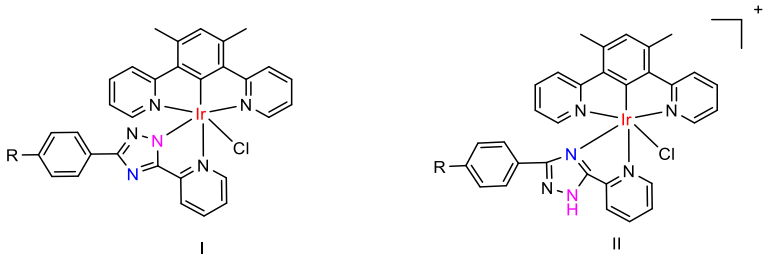

***Figure 3.25**: Different possible binding modes I and II of the 1,2,4-triazole ligand in 3+2+1 Ir complexes.*

Synthesis

The synthesis of complexes with the general structure Ir(dpybX)L$^{1\text{-}3}$Cl was attempted where dpybX has X= 3,5-dimethyl on the phenyl ring and where L^n = 4-(*tert*-butyl)phenyltriazolylpyridine (L^1), 4-(methoxy)phenyltriazolylpyridine (L^2) and 4-(trifluoromethyl)phenyltriazolylpyridine (L^3) (Scheme 3.11). The synthesis of these HL^n ligands are discussed in Chapter 2. Reaction of the chloro-bridged dimer [Ir(dpybX)(μ-Cl)Cl]$_2$ with the bidentate triazole ligand (HL^n) and 2.5 equivalents of AgOTf in refluxing toluene was attempted for each complex. Purification was achieved by removal of the solvent and recrystallization from MeOH/Et$_2$O, giving the complexes in 82, 14 and 18 % yields for Ir(dpyb*Me$_2$*)L^{1}Cl, Ir(dpyb*Me$_2$*)L^{2}Cl and Ir(dpyb*Me$_2$*)L^{3}Cl respectively. The lower yields for Ir(dpyb*Me$_2$*)L^{2}Cl and Ir(dpyb*Me$_2$*)L^{3}Cl were due to the formation of many unknown side products which meant that multiple recrystallization attempts were needed until the pure product was obtained.

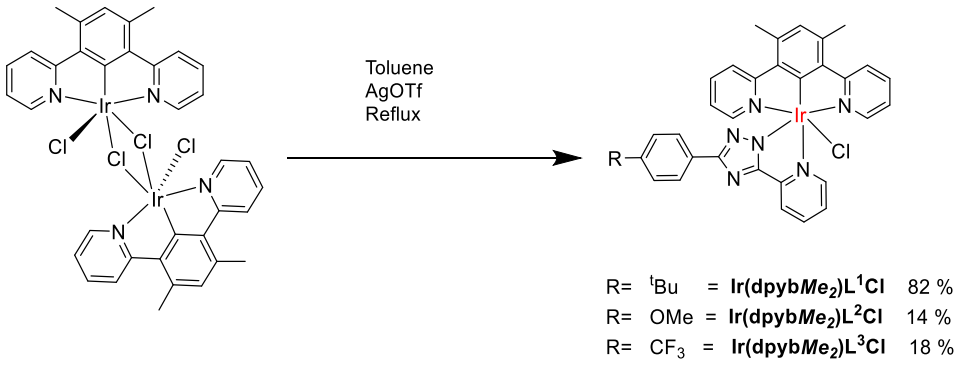

Scheme 3.11: *Synthesis of Ir(dpybMe$_2$)L$^{1-3}$Cl complexes.*

Unfortunately, no crystal structure was obtained to confirm the nature of the triazole binding mode. Moreover, other results such as MS, CHN and NMR remain inconclusive. If analogous to the isoelectronic Pt^{IV} complex for which the crystal structure was shown in the last section, it would bind through the deprotonated N to form a neutral complex. This is the likely conformation owing to the preference of the triazole ligand to bind through the N$^-$ atom rather than the non-protonated N atom as seen in all previous complexes containing triazole ligands of both bidentate and tridentate nature.

Photophysical characterisation

The absorption of the complexes is shown in the figure below and shows high energy bands between 250 and 330 nm which are representative of LC π→π* transitions, whilst the lower intensity bands at 390 nm show absorption with more MLCT character (Fig. 3.26). All complexes were found to be very weakly emissive with PLQYs of less than 10^{-3} when measured in degassed DCM solution. When measured in an EPA glass at 77 K they all showed high intensity structured emission with sharp 0-0 transitions centred at 470 nm. Ir(dpyb*Me$_2$*)L^{3}Cl showed higher intensity vibronic bands and a blue-shifted cut-off for the emission in comparison to the other complexes. The complexes were too weak to obtain lifetimes at RT, but at 77 K the recorded lifetimes ranged from 12 to 13 µs (Table 3.6).

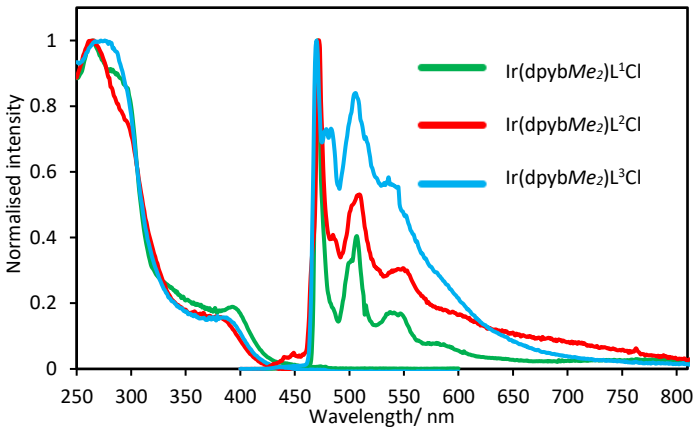

Figure 3.26: *RT absorption in DCM and 77 K spectra in EPA of Ir(dpybMe$_2$)L$^{1\text{-}3}$Cl.*

3.3.3.3 DFT Calculations for bis-tridentate and 3+2+1 Ir complexes

TD-DFT calculations showed that the largest contribution to the first excited states in the Ir complexes emanate from a HOMO→LUMO transition (Table 3.7). For the bis-tridentate complexes it is evident from the orbital plots calculated by DFT that the HOMO and LUMO orbitals are localised primarily on the triazole and N^C^N ligands respectively (Fig. 3.27). This is in accordance with other reported bis-tridentate Ir^{III} complexes as mentioned in the introduction.[152] The fact, however, that there is little or no overlap between the HOMO and LUMO differs from the complexes previously reported in the literature (such as the pyrazol-3-yl-6-ppy-containing bis tridentate Ir complexes **56**-**61** discussed in the introduction) and can help to explain the low radiative rate constants for these molecules which have a negative impact on the resulting PLQY values. It has been previously reported that this low overlap between frontier molecular orbitals results in a decreased oscillator strength for the transitions in many compounds including organic molecules and metal complexes.[156]

In stark contrast to the bis-tridentate complex, the overlap between the HOMO and LUMO for the 3+2+1 analogue Ir(dpyb*Me$_2$*)L^{n}Cl is much greater when the triazole ligand is considered as binding through the deprotonated N atom (Fig. 3.27). The main contributors to the HOMO are seen to be the Cl ligand and the triazole ring and phenyl group of the triazole ligand, with weak contribution from the metal centre. The LUMO is very delocalised with orbitals spread across the entire N^C^N ligand, the Ir centre and the pyridine of the triazole ligand. In this case the HOMO→LUMO transition is thought of as having a mix of weak LLCT and stronger ILCT. This could help explain why the Ir complexes were non-emissive at RT. The nature of the binding mode of the triazole ligand is not unequivocally confirmed so one cannot state this with absolute certainty.

Table 3.7: *Summary of main orbitals involved in first excited state transitions for Ir(dpybMe$_2$)L^{16} and Ir(dpybMe$_2$)L^{1}Cl as calculated by TD-DFT.*

Complex	*Ir(dpybMe$_2$)L^{16}*	*Ir(dpybMe$_2$)L^{1}Cl*
Energy (eV/nm)	2.5047/495.01	2.8482/435.31
Oscillator Strength	0.0552	0.0446
Main contribution (%)	HOMO→LUMO (70)	HOMO→LUMO (65)
Assignment	Mixed LLCT/MLCT	Mixed ILCT/LLCT

Complex	*HOMO*	*LUMO*
Ir(dpybMe$_2$)L^{16}	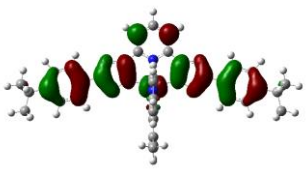	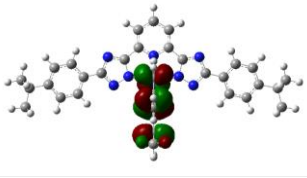
Ir(dpybMe$_2$)L^{1}Cl	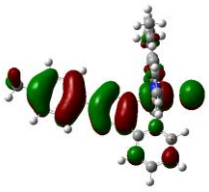	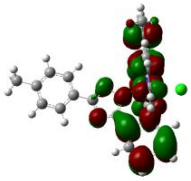

Figure 3.27: *Orbital diagrams of the HOMO and LUMO for Ir(dpybMe$_2$)L^{16} and Ir(dpybMe$_2$)L^{1}Cl complexes as calculated by DFT.*

To summarise, a range of Ir complexes containing tridentate N^C^N ligands have been synthesised. The bis-tridentate complexes of the form Ir(N^C^N)(N$^-$^N^N$^-$) were seen to be weakly emissive in degassed DCM solution with quantum yields ranging from 0.35 to 1.75 %. Compared to other Ir bis-tridentate complexes in the literature, these quantum yields are much lower, mainly owing to the poor overlap of the HOMO and LUMO as evidenced by DFT. The *trans* effect in these complexes is seen to be lower than for analogous Ir(N^C^N)(C^N^C) complexes owing to the weaker *trans* influence of the N$^-$ atoms when compared to cyclometallating C$^-$ atoms, and this helps confer enhanced stability when in solution.

The 3+2+1 complexes were synthesised via a facile synthetic procedure and purification. All complexes were highly emissive at 77 K, showing structured phosphorescence, but they showed only weak or no luminescence at RT in degassed solution. This may be due to a combination of factors including the weak-field chloride ligand that allows thermal population of the quenching d-d states. Moreover, DFT analysis shows the emission to be of weak ILCT/LLCT character, but one must also consider the possibility of different binding

modes for these types of complexes which have not yet been fully confirmed. As a result of their poor solution-state photoluminescence properties, neither type of Ir complex was not chosen for incorporation into OLEDs.

3.4 Comparison of Pt^{IV} complexes with Ir^{III} complexes analogues

By investigating both types of Pt^{IV} and Ir^{III} complexes containing N^C^N ligands we hope to compare their photophysical properties. As discussed throughout the chapter, Pt^{IV} and Ir^{III} are isoelectronic and their complexes might thus be expected to display similar properties to one another. Figure 3.28 below shows the complexes that will be compared, limited by the synthesis of only two Pt^{IV} complexes. The Ir analogues have methyl groups on the phenyl ring of the N^C^N ligand which are needed to force the tridentate N^C^N binding conformation of the ligand as opposed to a bidentate N^C^- conformation (refer back to Fig. 3.15 in section 3.3.1 of this chapter). Photophysical studies show that these methyl groups do not significantly affect the photophysical properties of the Pt complex in comparison to the parent complex Pt(dpyb)Cl (see Appendix, Fig. A1). The comparison of the methyl group containing Ir complexes with the Pt complexes that contain methyl-free N^C^N groups is thus justified.

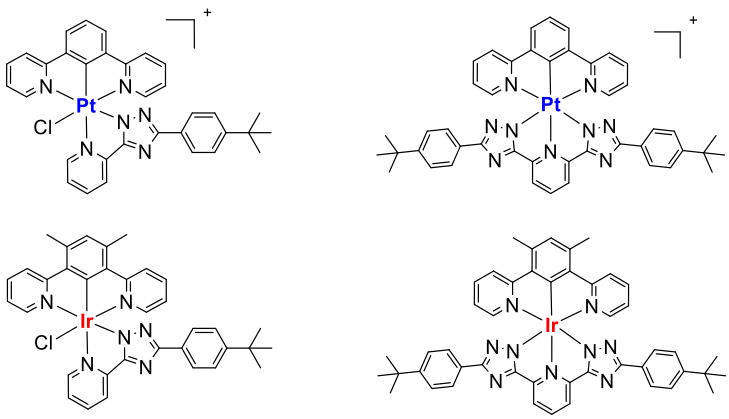

Figure 3.28: *Structures of Pt^{IV} complexes and their Ir^{III} analogues for comparison.*

Table 3.8 displays the absorption and emission spectra of the Pt^{IV} and Ir^{III} complexes which have been discussed independently in previous sections. From the absorption spectra, it is noticeable that the Ir^{III} complexes display more metal character at the longer wavelength absorptions than the Pt^{IV} complexes. The absorption cut-off for all complexes is very similar ending at 450 nm.

RT emission comparison was only possible for the bis-tridentate complexes as complex Ir(dpybMe_2)L^1Cl was non-emissive in degassed DCM solution. $[Pt(dpyb)L^{16}]^+$ was seen to have much more structured emission in comparison to the Ir analogue. It has a sharp 0-0 transition at 480 nm, whilst the Ir complex displays a weaker 0-0 transition and broader spectrum, suggestive of excited-state structural distortion. This is supported by the 77 K emission for the Ir bis-tridentate complex which displays structured emission that is

actually blue-shifted relative to the equivalent Pt spectrum. This is owing to the increased rigidity observed at low temperature for the Ir complexes (λ_{max} of 480 nm at RT and 470 nm at 77 K), whilst the Pt analogue maintains the same λ_{max} of 480 nm, independent of temperature.

The k_r value of the bis-tridentate Pt complex is seen to be much larger than that of the Ir analogue (2.5×10^4 vs. 3.1×10^2 s^{-1}) which is unexpected owing to the high charge on the Pt centre which would normally perhaps be expected to reduce the energy of deactivating d-d states to make them more thermally accessible. This low k_r value for the bis-tridentate Ir complex is in line with the poor luminescence efficiency observed (ϕ = 0.38 %) relative to the Pt complex (ϕ = 28 %). Moreover, it is also reflected by the observed structural distortion in emission at RT for the Ir complex.

For the 3+2+1 complexes, the 77 K emission profiles are very similar for both Pt and Ir and, like the bis-tridentate complexes, they show blue-shifted emission for the Ir complexes owing to the rigidification of the structure on cooling. The 77 K lifetime of the Pt complex was extremely long in comparison to the Ir complex (τ_{77K} = 226 and 12 µs respectively).

Figure 3.29 shows a comparison of the molecular orbitals as calculated by DFT for 3+2+1 and bis-tridentate Ir and Pt analogues. As discussed earlier the 3+2+1 Pt complex HOMO→LUMO transition was of mixed LMCT/LLCT character whilst Ir(dpyb*Me*$_2$)L^1Cl showed a mix of weak LLCT and stronger ILCT for the HOMO→LUMO transition. This could help explain why the Ir complexes were non-emissive at RT as the contribution of the metal in $[Pt(dpyb)L^1Cl]^+$ plays a greater role in the emission.

For the bis-tridentate complexes the Ir complex showed little or no overlap between the HOMO and LUMO with a small metal contribution to the emission, hence PLQY values were very low. In $[Pt(dpyb)L^{16}]^+$, however, the HOMO→ LUMO transition was seen to be predominantly LMCT in character with a good overlap between HOMO and LUMO orbitals on the metal centre.

Complex	*HOMO*	*LUMO*
[Pt(dpyb)L^{1}Cl]$^{+}$	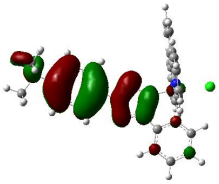	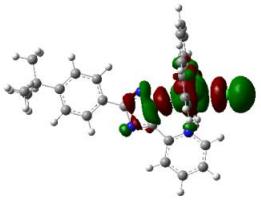
Ir(dpybMe$_2$)L^{1}Cl	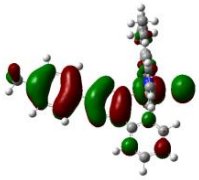	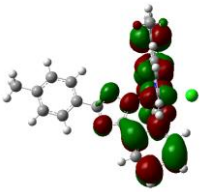
[Pt(dpyb)L^{16}]$^{+}$	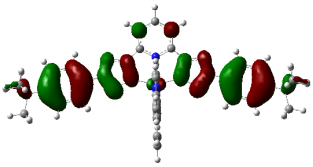	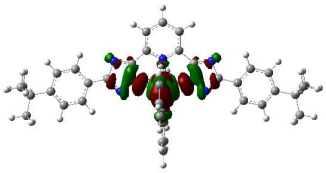
Ir(dpybMe$_2$)L^{16}	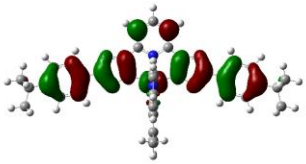	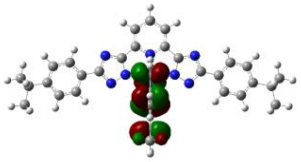

Figure 3.29: *Orbital diagrams of the HOMO and LUMOs for Ir and Pt complexes as calculated by DFT.*

Table 3.8: *Absorption and degassed RT emission in DCM and 77 K emission in EPA/butyronitrile of Pt^{IV} and Ir^{III} analogues. Note that no RT emission comparison is shown for $Ir(dpybMe_2)L^1Cl$ with $[Pt(dpyb)L^1Cl]^+$ as the Ir complex was not luminescent at RT.*

Complexes	*Absorption*	*RT degassed Emission*	*77 K Emission*
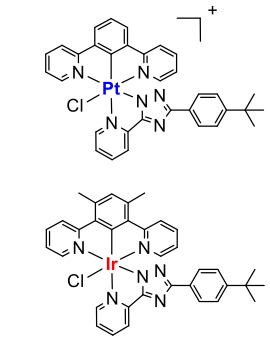	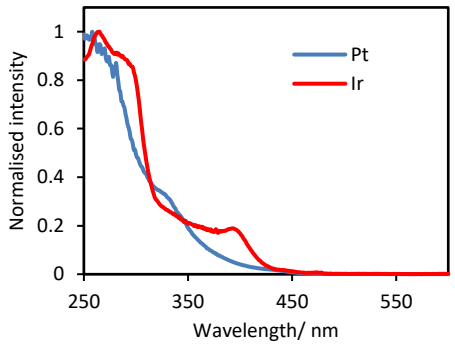	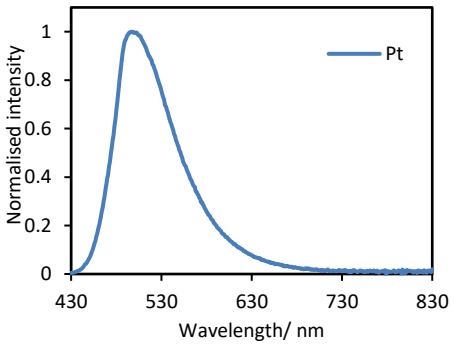	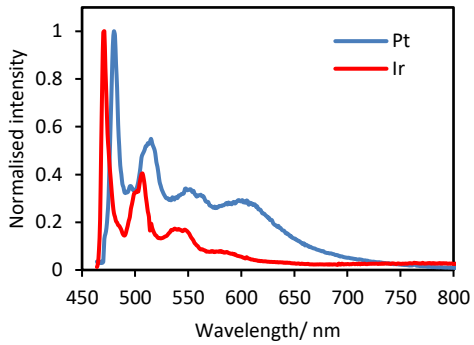
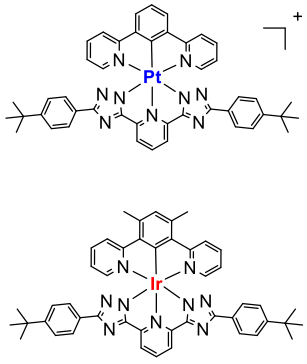	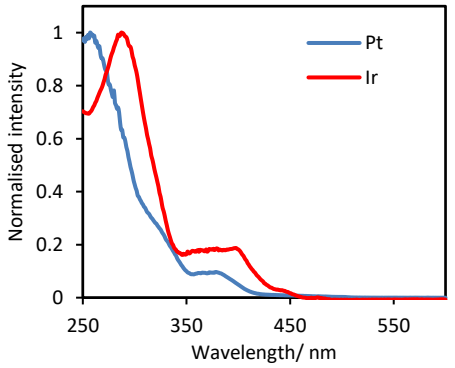	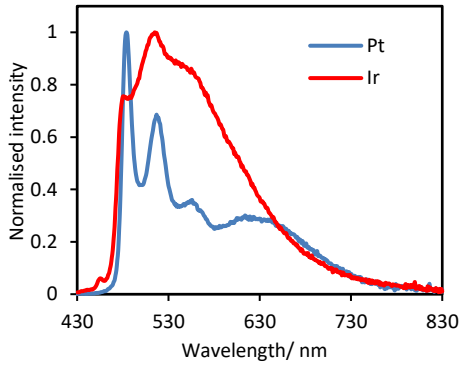	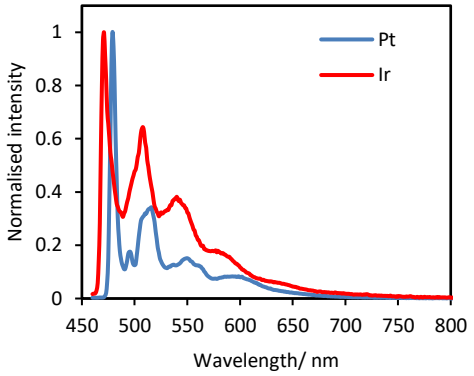

3.5 Chapter 3 summary

A range of Pt^{IV} and Ir^{III} complexes has been synthesised, all of which contain variations of the N^C^N ligand dpybX and 1,2,4-triazole ligands with different denticities (either bidentate or tridentate). Two novel Pt^{IV} complexes were synthesised of bis-tridentate and 3+2+1 structure. The 3+2+1 Pt complex, which included the bidentate triazole ligand L^1 and an ancillary chloride ligand, displayed modest photophysical properties with a PLQY of 5.9 % and lifetime of 3.1 µs at λ_{max} of 490 nm. A large improvement to this was observed on going to the bis-tridentate complex which had a high PLQY of 28 % and long lifetime of 11 µs at λ_{max} of 480 nm. This highlighted the increased rigidity in the bis-tridentate complex as a result of the two tridentate ligands surrounding the metal centre. The Pt^{IV} complexes generally displayed better photophysical properties compared to their isoelectronic Ir^{III} counterparts.

The bis-tridentate Ir complexes which have been synthesised showed relatively low luminescence efficiencies with PLQY values ranging from 0.38 to 1.8 %. They were seen to undergo a large degree of rigidification upon cooling to 77 K as was shown by the enhanced vibrational structure in their low-temperature emission spectra. The relative magnitudes for k_{nr} ranging from 8.0 to 8.9 x 10^4 s^{-1} were also much higher than those for k_r which ranged from 2.9 to 15 x 10^2 s^{-1}. The orbital overlap of the HOMO and LUMO from DFT calculations was minor and this could also help explain the poor luminescence efficiencies relative to the Pt^{IV} analogue that was compared, but also to similar bis-tridentate structures in the literature. Moreover, the *trans* influence of the N^- atoms on the triazole ring in the tridenate 1,2,4-triazole ligands is suggested to be lower than for cyclometallating C^- atoms and thus ligands $L^{16\text{-}18}$ can perhaps be thought of as similar to tpy in these Ir complexes.

In terms of the 3+2+1 Ir complexes, like the Pt^{IV} analogue, they too experienced a decrease in luminescence efficiency, but to the extent that they were non-emissive in degassed solution at RT and only emissive at 77 K. They exhibited very similar structured emission and lifetimes on the order of 12 to 13 µs at 77 K. It is still unclear the exact binding mode of these Ir 3+2+1 structures and as a result, the photophysical properties cannot be definitively assigned.

Overall, the significance of tridentate ligands in conferring rigidity to Pt and Ir complexes has been shown. This has been coupled with the effective demonstration of complex

manipulation to afford analogous Ir^{III} and Pt^{IV} complexes with 3+2+1 and bis-tridentate structures, revealing some marked differences in their photophysical properties. The Pt^{IV} complexes show great promise and should be investigated for their performance in applications such as light-emitting electrochemical cells (LEECs) owing to their charged structures.

4. Pt and Pd complexes containing tetradentate ligands

4.1 Introduction

From previous chapters it has been demonstrated that, upon going from bidentate to tridentate compounds, there can be an increase in complex rigidity which may lead to improved quantum yields. The extension of this rigidity to tetradentate compounds can, in principle, lead to further improved results. There are numerous examples of tetradentate cyclometallated complexes which are based upon the archetypal *cis*-Pt(ppy)$_2$ (Fig. 4.1). In comparison to *cis*-Pt(ppy)$_2$, which is non-emissive in solution at RT, the effect of the tetradentate ligand in conferring enhanced rigidity is striking. Many such complexes have high quantum yields, some of which approach unity, as will be discussed in this introductory section.

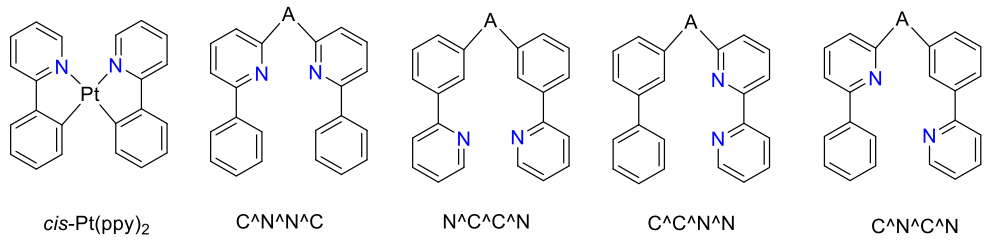

Figure 4.1: *Tetradentate cyclometallating ligands with different coordination geometries where A is a linking atom such as N, O or C, compared to cis-Pt(ppy)$_2$.*

The examples shown here in Figure 4.1 illustrate potentially cyclometallating versions of tetradentate ligands. This section will focus on some of the best performing Pt complexes containing tetradentate ligands and will also discuss the development of analogous Pd complexes, of which there are far fewer. Table 4.1 at the end of this introductory section summarises the PL and EL properties of selected complexes.

4.1.1 Platinum Complexes

4.1.1.1 C^N^N^C/N^C^C^N Complexes

Vezzu *et al.* synthesised bis-cyclometallated platinum complexes with general coordination patterns of (C^N^N^C)-Pt and (N^C^C^N)-Pt.[22] The structures of the C^N^N^C and N^C^C^N complexes are shown below (Fig. 4.2) and one can see the similarity with Pt(C^N)$_2$ complexes that contain bidentate ligands. The tetradentate structure of the

ligands was achieved by linkage of the two phenyl pyridine groups through an amine nitrogen atom.

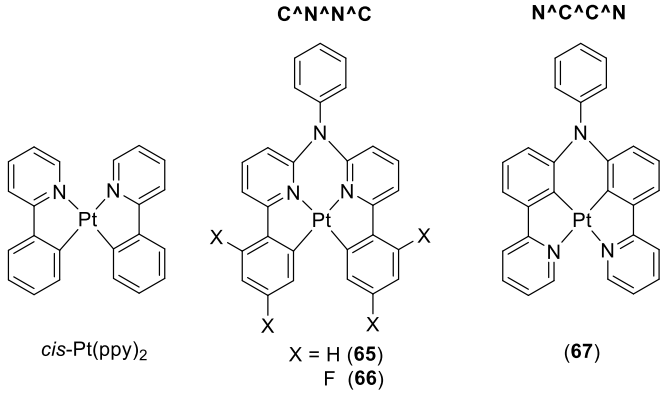

Figure 4.2: *Comparison of cis-Pt(ppy)$_2$, C^N^N^C platinum complexes (**65** and **66**) and the N^C^C^N complex (**67**).*

All complexes were emissive at RT in degassed 2-methyltetrahydrofuran (2-MeTHF) solution. Complex **65** displayed an emission maximum of 512 nm, a quantum yield of 0.74 and a lifetime of 7.2 µs, whilst the addition of fluorine substituents in complex **66** slightly changed these photophysical properties (Fig. 4.3). This resulted in a red-shift of the emission to give a λ_{max} of 488 nm, a lifetime of 11.4 µs and a quantum yield of 0.75. Both complexes **65** and **66** were seen to display excimeric emission centred at around 710 nm. The assignment of these emission bands as excimeric was supported by the linear dependence of the decay rate upon concentration when fitted to the Stern-Volmer equation.

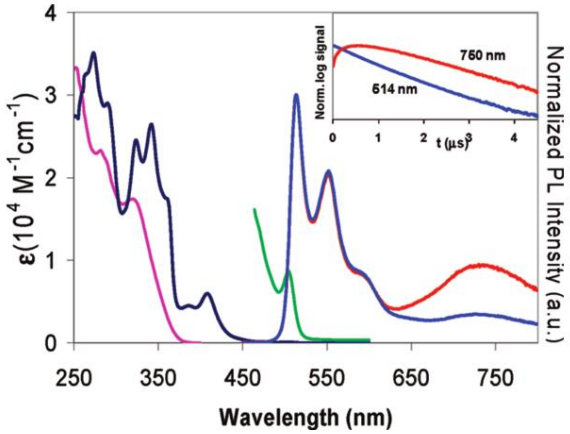

Figure 4.3: *Absorption (Ligand: pink; **65**: black), lowest energy absorption (**65**, green), and normalized emission (**65**: blue 5.13 x 10^{-5} M; red 1.54 x 10^{-4} M) spectra (365 nm excitation) and phosphorescence decay of **65** (inset, 4.62 x 10^{-4} M) in 2-MeTHF at RT. Reprinted with permission from Vezzu et al.[22] Copyright 2010 American Chemical Society.*

Upon changing the coordination sphere to the N^C^C^N arrangement, the emission was seen to red-shift significantly and complex **67** displayed a λ_{max} of 613 nm and a quantum yield of 0.14 which may be reflective of the lower efficiencies normally encountered for longer wavelength emission. The lifetime was very similar to complex **65** at 7.6 μs. Complex **65** was incorporated into an OLED device as an emitter at 4 wt. % in the mixed host of TCTA and TPBI. This demonstrated high performance with a maximum EQE of 14.7 % and showed the high efficiency that Pt^{II} complexes containing tetradentate ligands can have in luminescent applications.

In 2014, Li and co-workers reported on a series of Pt^{II} complexes containing carbazole-based tetradentate ligands that all displayed narrow emission spectral bandwidths in the blue region (**68**-**71**, Fig. 4.4).[157] All complexes had PLQY values above 0.7 in PMMA thin-films with λ_{max} values centred at ca. 450 nm. It was found that the incorporation of a bulky ^{t}Bu group on the pyridine ring of the tetradentate ligand improved the colour purity of the emission by narrowing the bandwidth. This spectral narrowing was attributed to 'increasing the energy of the ^{1}MLCT/^{3}MLCT and ^{3}LC states of the carbazole pyridine moiety'. This was then thought to result in a larger energy-separation, minimising the influence of the carbazole pyridine on the RT emission.

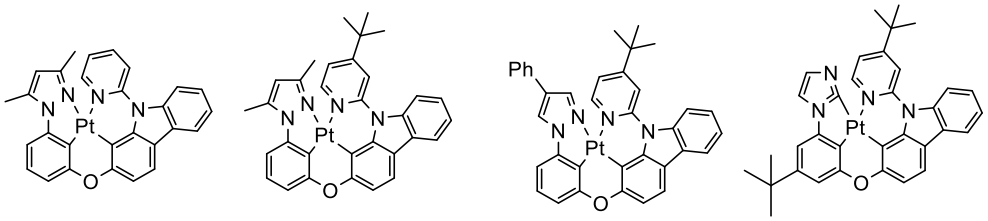

68 **69** **70** **71**

Figure 4.4: *Structures of complexes containing tetradentate carbazole-based ligands* ***68***-***71****.*

OLED devices employing complexes **69**-**71** as emitting materials were fabricated showing EL spectra similar to the PL emission. The best device performance data was obtained for complex **71** bearing an NHC ligand (Fig. 4.5). At 2 wt. % the EQE of the device was 17.2 %, but upon increasing the doping concentration to 6 wt. % and employing TAPC in conjunction with a higher bandgap electron-transporting material (PO15) at a 1:1 ratio as a co-host, an impressive peak EQE of 24.8 % was achieved without significantly affecting colour purity.

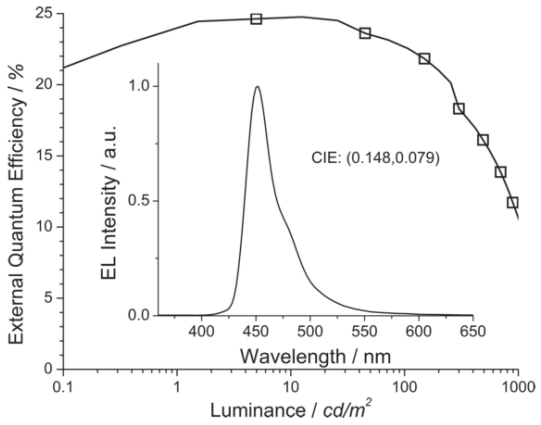

Figure 4.5: *EQE vs. luminance for complex* ***71.*** *The EL Spectra and CIE coordinates are given in the inset. Reproduced from Li et al. by permission of John Wiley and Sons.*[157]

These Pt complexes containing tetradentate ligands can emit across the entire UV-Vis-NIR spectrum depending upon changes to the ligands by incorporation of different functional groups. In an effort to produce pure white OLEDs or WOLEDs, Norby *et al.* utilised complex **68** as a blue emitter, in combination with two complexes also previously synthesised by the group which emit in the green and red (Fig. 4.6).[158]

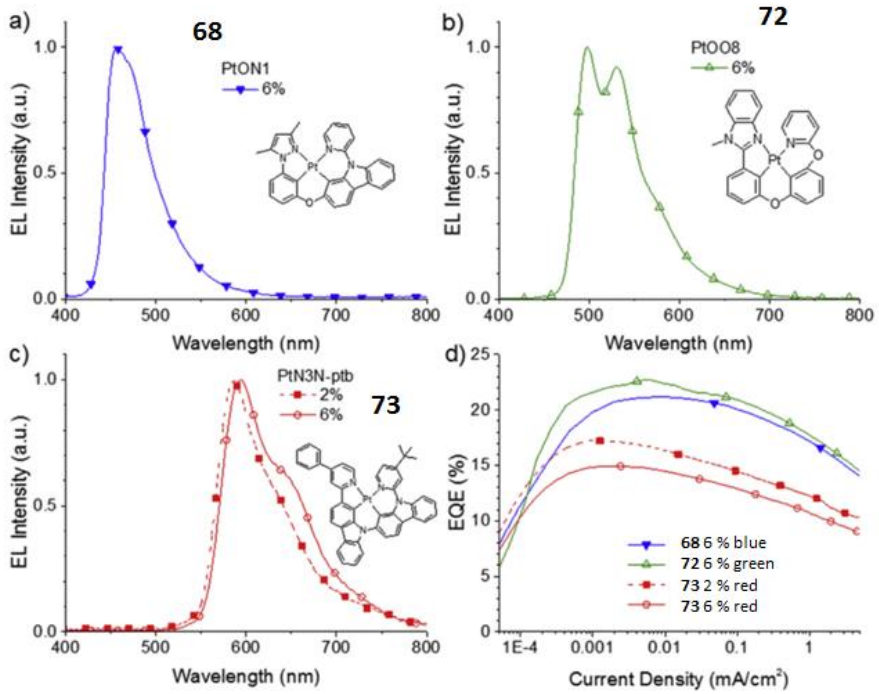

Figure 4.6: *a)-c) EL spectra for the complexes* ***68, 72*** *and* ***73*** *respectively and d) plots of EQE vs. current density for the OLEDs of the 3 individual emitters. Reproduced from Norby et al. by permission of Elsevier.*[158]

After different OLED testing, the final device with best efficiency was chosen with the stacking order: 6 % **73**: 26mCPy/ 6 % **68**: 26mCPy / 6 % **72**: 26mCPy to give red, blue and green components of emission respectively. Moreover, by separating the **72-** and **73-** containing emissive layers with a thick **68**-doped blue emissive layer, a large amount of energy transfer was inhibited and a peak EQE of 21.0 % was observed. CIE coordinates of (0.33, 0.33) are considered "pure white" and a colour rendering index (CRI) value as close to 100 as possible is desired. This device displayed promising attributes with a CRI value of 80 and CIE coordinates of (0.35, 0.35).

More recently, Wang and co-workers reported a series of seven novel Pt(N^C^C^N) complexes with either an oxygen, methylene or carbonyl to link the C^C unit and which contained 1,2,3-triazoles substituted with different R groups (**74**-**78**, Fig. 4.7). They also synthesised complexes **79** and **80** in which the two triazolyl rings were connected by a dodecamethylene chain and a 3,6,9-trioxaundecamethylene chain, respectively.[159] The synthesis of the Pt^{II} complexes was performed by reaction of the tetradentate ligand with tetra-n-butylammonium bromide (NBu_4Br) and K_2PtCl_4 at 25 °C in glacial acetic acid for one day, followed by heating at 140 °C for four days. The final Pt^{II} compounds were obtained in yields varying from 11 to 52 %.

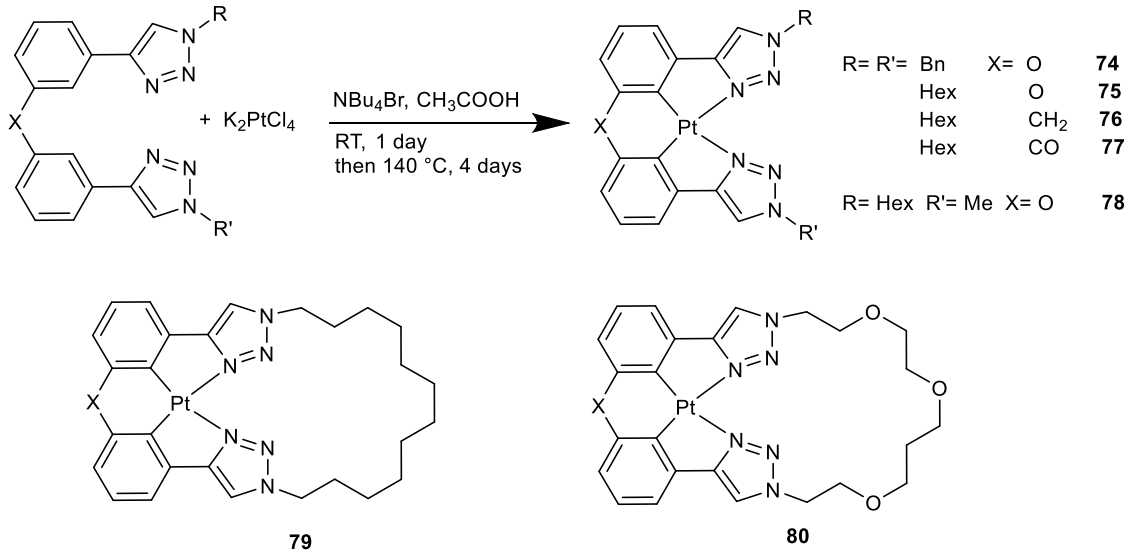

Figure 4.7: *Synthesis and structure of complexes **74**-**80**.*

All complexes (except complex **77** with a carbonyl linker) were seen to display blue emission in solution and in PMMA film with λ_{max} values at 450 nm. Complex **76** showed blue-shifted emission and a lower PLQY value (0.14) in comparison to the other complexes (PLQYs between 0.39 and 0.62). This was thought to be due to the methylene linker which

disrupts the conjugation and which also results in a puckered confirmation of the complex as shown by the crystal structure which increases k_{nr} (Fig. 4.8).

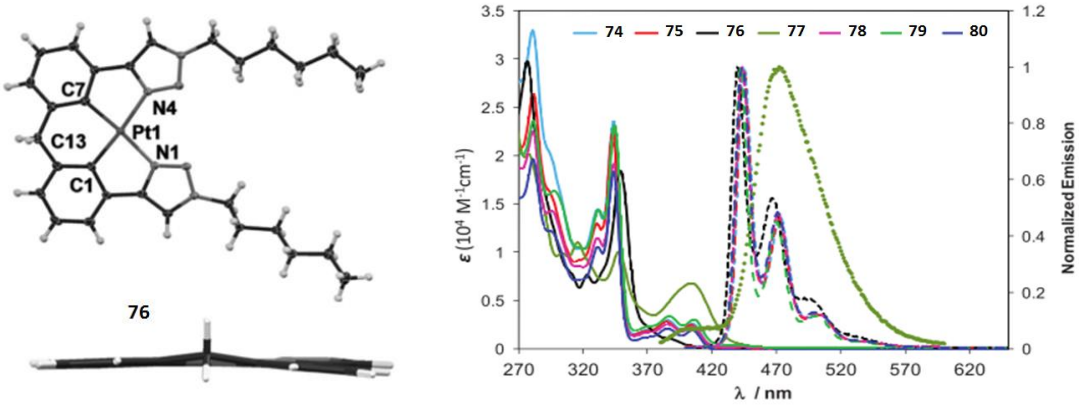

Figure 4.8: *Crystal structure of complex **76** with side view to show the puckering of the methylene linker (left) and absorption and emission spectra for complexes **74**-**80** in degassed DCM at RT (right). Reproduced from Wang et al. by permission of John Wiley and Sons.*[159]

Complex **77** differs from all other complexes as its emission is broad, featureless and significantly red-shifted by 20-30 nm. This was tentatively explained by greater MLCT character in the excited state of **77**, facilitated by the electron-withdrawing carbonyl linking group that stabilizes the LUMO, thus decreasing the emission energy.

The effect of the macrocyclic chelate was also investigated in complexes **79** and **80** which displayed significantly higher solution-state PLQY values (0.58 and 0.62, respectively) in comparison to the related non-macrocyclic compound **75** (0.42). This was attributed to the greater structural rigidity imposed by the macrocyclic ligands. Moreover, in 10 wt. %-doped PMMA films, compound **79** had the highest PLQY of 0.95, whilst **75** and **80** were much lower (0.62 and 0.48, respectively). From the PL performances displayed, complex **79** was chosen as a representative for OLED testing owing to its high PLQY and purer colour coordinates. The best device featured a dopant concentration of 10 % in a 9,9'-(4,4'-(phenylphosphoryl)bis-(4,1-phenylene))bis(9H-carbazole) (BCPO) host, giving an EQE of 15.4 %, with CIE coordinates of (0.15, 0.17).

Liao *et al.* synthesised a range of tetradentate chelates using spiro-arranged fluorene and acridine linking to pyrid-2-yl triazole and pyrazole units which were then complexed with Pt to give interesting photophysical properties (**81**-**85**, Fig. 4.9).[160] A detailed synthesis of the

ligands is outlined in their paper and subsequent complexes were then formed by reacting these ligands with $Pt(DMSO)_2Cl_2$ in DME with an excess of base.

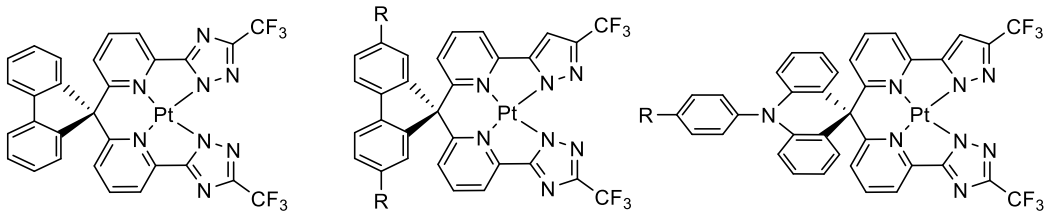

81 **82** R=H, **83** R=^{t}Bu **84** R=H, **85** R=^{t}Bu

Figure 4.9: *Structures of complexes **81**-**85** containing tetradentate ligands with spiro-arranged fluorene and acridine groups.*

The crystal structures of complexes **81** and **83** are shown below and demonstrate the dimer-like packing motif in the crystal lattice where the spiro-bridged fluorene unit is tilted away from the second molecule in order to avoid steric hindrance (Fig. 4.10). The nearest Pt···Pt interactions were found to be 3.759 Å for **81** and 3.455 Å for complex **83**.

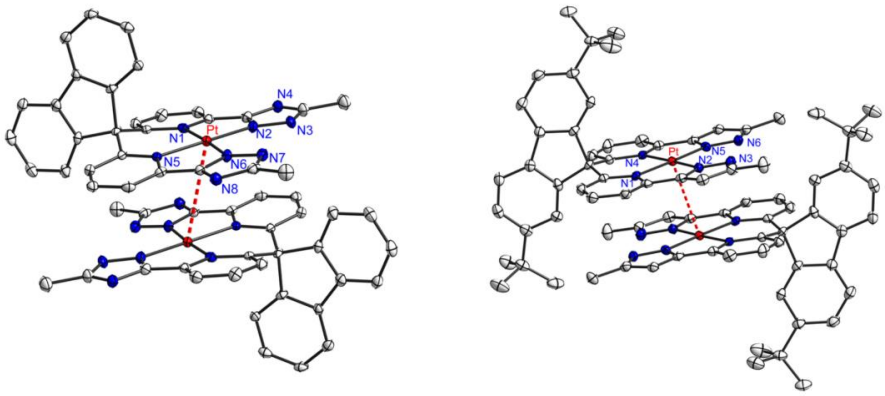

Figure 4.10: *Crystal structures for complexes **81** (left) and **83** (right) where fluorine atoms of CF_3 fragments were removed for clarity. Reprinted with permission from Liao et al.*[160]

Copyright 2015 American Chemical Society.

All complexes showed structured emission in degassed DCM solution and of particular interest was complex **85** which showed a high degree of solvatochromism. In cyclohexane it had a PLQY of 0.13 and a k_r of 6.3×10^3 s^{-1} whilst in DCM it gave dramatically improved results of 0.88 and 3.0×10^5 s^{-1} (Fig. 4.11). The increased k_r values and disappearance of the vibronic fine structures in DCM compared to cyclohexane were ascribed, in part, to a switch of emission from LC π→π*/MLCT to ILCT/MLCT based upon observations from another group for a series of Pt^{II} alkynyl complexes with distinctive tridentate pincer ligands.[161] Complexes **83** and **85** were chosen for OLED testing owing to their high PLQYs (0.82 and

0.88 respectively) and they exhibited bright blue stable EL with maximum EQEs of 12.3 and 15.3 % respectively.

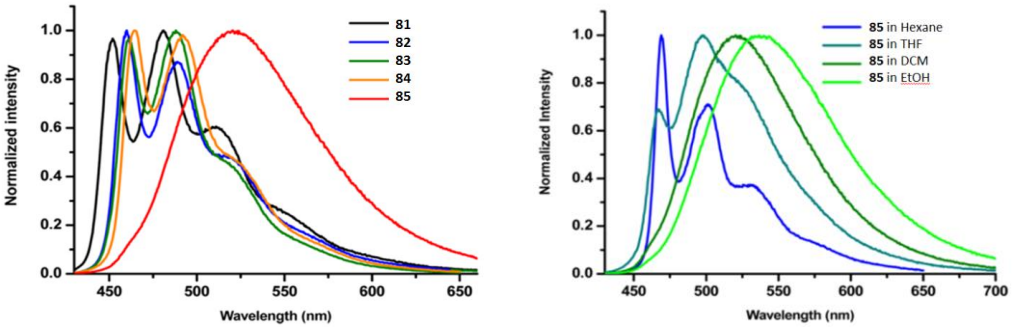

Figure 4.11: *Emission spectra for complexes **81**-**85** in DCM (left) and emission spectra for complex **85** in varying solvents (right). Reprinted with permission from Liao et al.*[160] *Copyright 2015 American Chemical Society.*

4.1.2 Palladium Complexes

Up until recently there have been significantly fewer examples of Pd tetradentate complexes which show strong luminescence applicable to OLED applications. Many Pd complexes that have been reported typically show lower-lying deactivating d-d states, which are more thermally accessible in comparison to the ones held by their Pt analogues, owing to the weaker field splitting of Pd. As a result, a lot of focus has been concentrated on Pt complexes like the ones discussed previously, but recent investigations have prevailed in achieving high efficiency Pd complexes.

Pd complexes with lower denticity ligands (particularly bidentate) commonly suffer from high distortion and subsequently are only weakly emissive in solution, if at all.[162,163] The need for a tetradentate ligand to achieve high efficiency is almost certainly a necessity to achieve the highest possible efficiencies in Pd compounds and is thus a good place to start in terms of molecular design.

Chow *et al.* reported Pd^{II} complexes containing tetradentate O^N^C^N ligands in 2013.[164] They synthesised two types of Pd(O^N^C^N) complexes as shown below in Figure 4.12, as well as the Pt analogue for the type 2 compounds.

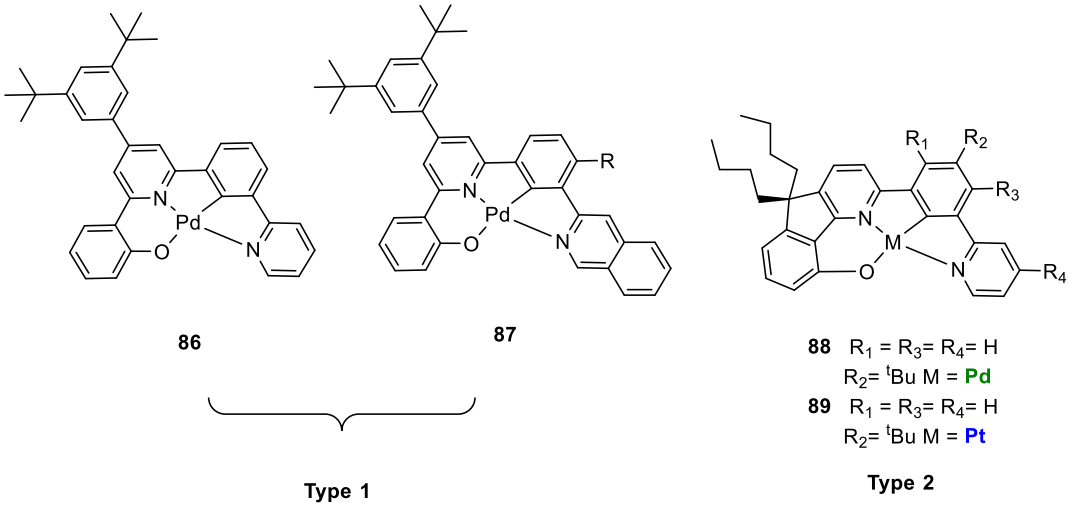

Figure 4.12: *Structures of type 1 and 2 Pt and Pd complexes.*

It was found that all type 1 compounds were weakly-emissive at RT in solution and had relatively short lifetimes (λ_{max} of 535-543 nm, $\phi \approx 0.002$ and τ=0.2-0.4 µs). In stark contrast, type 2 complexes displayed intense emission with PLQY values ranging from 0.14 to 0.22 with significantly longer lifetimes ranging from 83 to 120 µs. They attributed the much higher efficiencies for the type 2 complexes to the relatively higher k_r and lower k_{nr} values. TD-DFT showed large structural distortion on going from the S_0 state to the T_1 state in type 1 compounds, whilst in type 2 compounds; both S_0 and T_1 states remained coplanar with no obvious distortion (Fig. 4.13). Moreover, calculations revealed the origin of emission to be a ^{3}LLCT($\pi_{phol} \rightarrow \pi^*_{N^C^N}$) transition in type 1 complexes and N^C^N-localised ^{3}IL($\pi \rightarrow \pi^*$) transition in type 2 complexes with very little ^{3}MLCT($d\pi \rightarrow \pi^*$) contribution (calculated as <10 % for each). The type 2 platinum analogue, **89**, had a PLQY of 0.79 with lifetime of 10 µs which is obviously still much higher, but the type 2 Pd complex is impressive in its own right. The type 2 complex **88** was subsequently tested in an OLED which had an EQE of 7.4 % for the simple device structure ITO / NPB (40 nm) /6 wt. % **88**: mCP (30 nm) / BAlq (40 nm) / LiF (0.5 nm) / Al (80 nm.

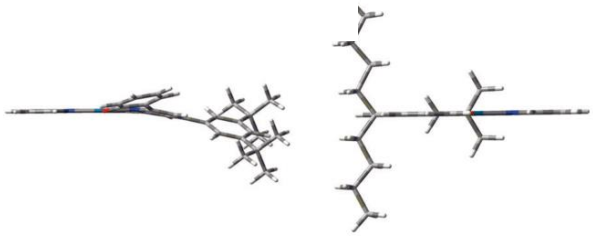

Figure 4.13: *Optimised structures of the T_1 excited state for type 1 complex **86** (left) and type 2 complex **88** (right). Reproduced from Chow et al. by permission of John Wiley and Sons.*[164]

Jian Li's group have since contributed considerable research efforts dedicated to Pd complexes containing tetradentate ligands where devices with EQEs of over 20 % have been reached.[165,166] Of most interest, however, is an example which displays efficient excimer emission that can be incorporated into devices. The compound **90** was synthesised and its photophysical properties were studied both in a doped 1 wt. % 26mCPy film and also in degassed DCM solution at RT.[167] In the film only monomer emission was observed at the 1 wt. % doping concentration, whilst in dilute DCM solution strong evidence of excimer emission was observed (Fig. 4.14).

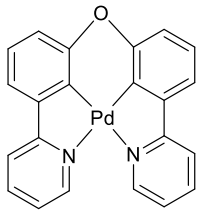

90

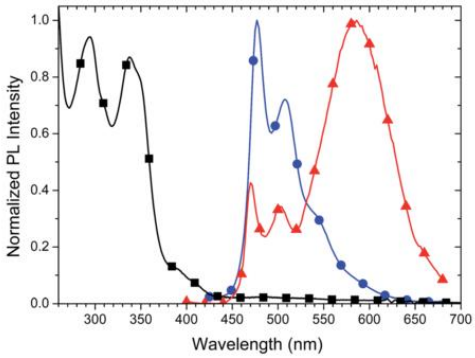

Figure 4.14: *The structure of **90** and its absorption and emission in a 1 wt. % 26mCPy film (blue) and in degassed DCM solution (red). Reproduced from Fleetham et al. by permission of the Royal Society of Chemistry.*[167]

The PLQY of **90** in a doped PMMA film at RT was found to be 87 % with a luminescent lifetime of 120 µs and thus the complex showed impressive photophysical properties amenable to OLED incorporation. Because of the broad spectrum of emission originating from both the monomer and excimer, application into a WOLED was subsequently investigated. The device with the best properties was found to give an EQE of over 27 % which is the best recorded example of an OLED containing a Pd complex in the EML and beats many Pt devices also containing tetradentate ligands. This highlights the potential for Pd complexes in OLEDs despite them having been very much overshadowed by their Pt counterparts over the years.

Table 4.1: *PL and EL data for Pt and Pd literature complexes. EL data reflects the maximum values obtained for devices. Please refer to the list of abbreviations for the device architecture column.*

Compound no. and reference	*Device Architecture*	*PL performance*			*EL performance*				
		λ_{max} (nm) [soln/film]	*PLQY [soln/film]*	*Lifetime (µs) [soln/film]*	*λ_{max}(nm)*	*CE (cd A^{-1})*	*PE (lm W^{-1})*	*Brightness (cd m^{-2})*	*EQE (%)*
Platinum									
65[22]	ITO / CF_x (1 nm) / NBP (65 nm)/ TCTA (10nm) / TPBI : (30 wt. % TCTA + 4 wt. % **65**) (35nm) / TPBI (10nm) / Alq (40 nm) / Mg:Ag (220 nm)	514 / -	0.74 / -	7.6 / -	512	50	-	5	14.7
69[157]	ITO / HATCN (10 nm) / NPD (40 nm) / TAPC (10 nm) / 2 wt. % **69** : 26mCPy (25 nm) /DPPS (10nm) / BmPyPB (40 nm) / LiF / Al	446 / -	- / 0.70		451	-	13	-	17.2
	ITO / HATCN (10 nm) / NPD (40 nm) / TAPC (10 nm) / 6 wt.% **69** : 47% TAPC : 47% PO15 (25 nm) / PO15 (10 nm) / BmPyPB (30 nm) / LiF / Al				451	-	21	-	24.8
WOLED- ***68,72*** *and* ***73***[158]	ITO / HATCN / NPD / TAPC / 6% **73**: 26mCPy (3 nm) / 6 wt. % **68** : 26mCPy (20 nm) / 6% **72** : 26mCPy (2.5 nm) / DPPS / PmPyPB / LiF / Al	-	-	-	455, 500, 595	-	41	-	21
79[159]	(ITO)/ (NPB) (50 nm) / (mCP) (10 nm)/ (BCPO) : 10 wt. % **79** (20nm) / (DPEPO) (10 nm)/ (TPBi) (30 nm) / LiF (1 nm) / Al (100 nm)	448 / 447	0.58 / 0.95	-	451	19	14	13	15.4
83[160]	ITO / TAPC (40 nm) / mCP : 8 wt. % of **83**/**85** (17 nm) / DPEPO : 8 wt. % of **83**/**85** (3 nm) / DPEPO (3 nm) / TmPyPB (50 nm) / LiF (0.8 nm) / Al (150 nm)	461, 487, 521 / -	0.82 / -	7.8 / -	461, 487, 521	27	27	1924	12.3
85[160]		520 / -	0.88 / -	2.9 / -	470, 500, 520	36	38	4121	15.3
Palladium									
88[164]	ITO / NPB (40 nm) / 6 wt. % **88** : mCP (30 nm) / BAlq (40 nm) / LiF (0.5 nm) / Al (80 nm)	498 / -	0.20 / -	120 / -	500, 535, 589	20	14	-	7.4
90[167]	ITO / HATCN (10 nm) / NPD (40 nm) / TrisPCz (10 nm) / 20 wt. % **90** : 26mCPy (10 nm) / 6 wt. % **90**: 26mCPy (20 nm) / BAlq (10 nm) / BPyTP (40 nm) / LiF (1 nm) / Al	582 / 477, 507	- / 0.87	- / 120	472, 575	-	81	7280	27.3

4.2 Objectives

Previously in the group, a former Ph.D. student Mickaële Bonneau investigated a series of tetradentate Pt^{II} and Pd^{II} complexes of the form M(C^N^N^C) based on the work of Vezzu *et al.* discussed earlier.[22] The synthesis and photophysical properties of these Pt^{II} and Pd^{II} complexes were studied, as well as the oxidation to their $M^{IV}Cl_2$ counterparts.[168] These results sparked off interest in the group to continue their investigation, primarily due to their potential for excimer formation which could result in NIR emission.

The main objectives of this work, as a continuation of the previously studied complexes, were to:

- Synthesise Pt^{II} and Pd^{II} (C^N^N^C) complexes previously studied which have the potential to show excimeric emission and investigate their concentration-dependent photophysical properties.
- Synthesise novel Pt/Pd(C^N^N^C) complexes and investigate their photophysical properties.
- Study the electroluminescence of a few selected compounds for incorporation into OLEDs.
- Attempt the oxidation of the Pt^{II}(C^N^N^C) complexes to the Pt^{IV} complexes.

4.3 Results and Discussion

4.3.1 Pt and Pd C^N^N^C complexes

4.3.1.1 Synthesis

Many of the ligands presented here were synthesised according to a method adapted by Vezzu *et al.*[22] The first step is a Buchwald-Hartwig amination of a primary aryl amine with two equivalents of 2,6-dibromopyridine to afford the precursor P^6 (Scheme 4.1). Depending upon the type of substituent, the resulting ligands H_2L^n were obtained via either a Suzuki or Stille Pd-catalysed cross-coupling reaction. The ligands $H_2L^{19\text{-}20}$ were obtained using the Suzuki method, whilst $H_2L^{21\text{-}22}$ were obtained using the Stille method. The Suzuki method typically involves palladium-catalysed cross-coupling between organoboronic acids and aryl halides whereby the boronic acid is initially activated by base.[169] Different types of catalysts, solvents and bases have proven successful for this reaction but in this work, we employed a mix of DME/H_2O (1:1) with $Pd(PPh_3)_4$ as the catalyst and Na_2CO_3 as the base to afford the ligands with yields in the range of 43 to 76 %.

The Stille reaction also utilises a Pd catalyst to couple organotin reagents with aryl halides.[170] In this method we used $Pd(PPh_3)_2Cl_2$ as the catalyst with LiCl, and toluene as the solvent. LiCl was added owing to its properties in accelerating reaction rates in low-polarity solvents where it aids dissociation of the halide on the aryl reactant.[171] Yields for the resulting ligands H_2L^{21} and H_2L^{22} were 72 % and 26 % respectively. The main drawback with the Stille reaction is the toxicity of the organotin reagents, however for these thienyl-containing ligands an alternative to the Suzuki reaction was necessary owing to the competitive deboronation reaction which can occur and significantly reduce the yield.[172]

The complexes were then synthesised by reaction of the ligands with either K_2PtCl_4 or $Pd(OAc)_2$ in acetic acid at reflux, under inert argon atmosphere. These conditions are the typical conditions needed for cyclometallation reactions to occur and are like those employed by Vezzu *et al.*

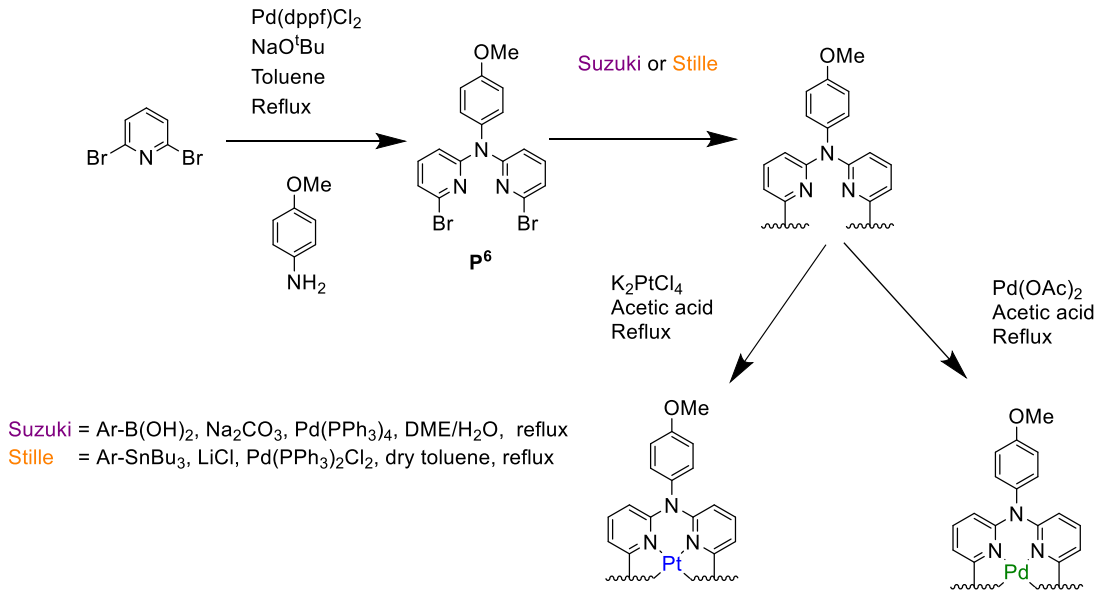

H₂Lⁿ				
n =	***19***	***20***	***21***	***22***
Yield (%)	*76*	*43*	*72*	*26*
PtLⁿ	*58*	*63*	*89*	*20**
PdLⁿ	*42*	*80*	*85*	*35*

Scheme 4.1: *Synthesis of H_2L^n and their corresponding complexes ML^n with yields. *PtL^{25} was only synthesised by Mickaële Bonneau.*

Mickaële Bonneau previously synthesised complexes PtL^{19}, PtL^{21} & $PtL^{22}$and PdL^{19}, PdL^{20} & PdL^{21}, obtaining unambiguous characterisation though in quantity sufficient for only partial photophysical characterisation.[168] These complexes were synthesised again on a larger scale and were investigated for the potential formation of excimers, in addition to the new complexes PtL^{20} and PdL^{22}.

The change in the ^{1}H NMR signals upon complexation to Pt for H_2L^{19} is shown below (Fig. 4.15). The complexation was confirmed by the lack of two protons in the NMR of the complex compared to that of the ligand, in addition to the presence of Pt satellites for signal 2'' in the complex. The complex is seen to be symmetrical about the N-OMe axis owing to the presence of 9 aromatic signals. The most significant shifts in ppm are observed for signals 2'' and 3' in the complex. Signal 2'' (called 3'' in the ligand) undergoes a downfield shift from 7.90 to 8.44 ppm whilst signal 3' undergoes an upfield shift from 7.06 to 6.55 ppm. The shift for signal 3' can be explained by the ring current effect[173] of the

anisyl ring which is seen to be perpendicular to the rest of the molecule in the complex crystal structure (discussed later on) and which subsequently shields the proton in this position, whilst in the ligand it is freely rotating and does not have the same influence. Similar shifts in the peaks were observed for the Pd analogue, PdL[19].

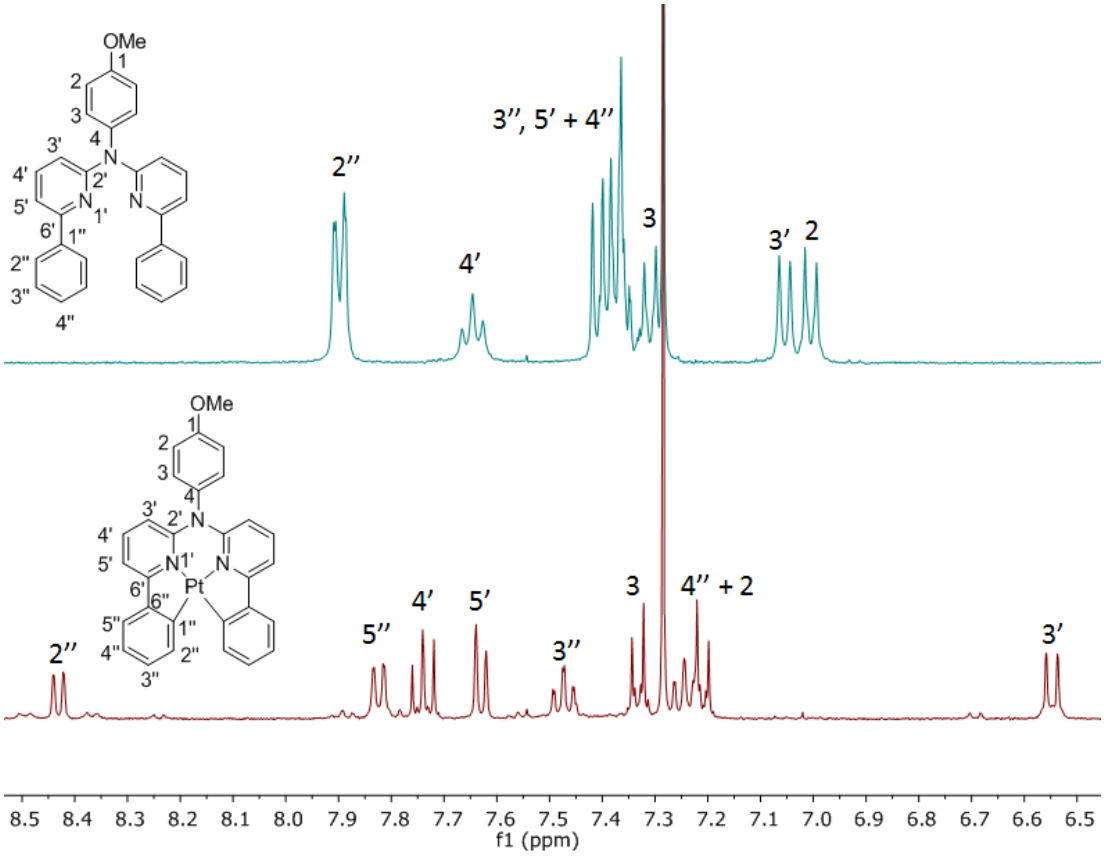

Figure 4.15: *400 MHz NMR in $CDCl_3$ comparison for H_2L[19] and PtL[19].*

The shift for the proton labelled 2'' in the complex can be explained by the loss of electron density upon binding to the Pt^{II} centre which is observed in many complexes containing ligands coordinated to transition metal centres.[174]

Crystal structures were previously obtained for complexes PtL[19], PtL[21], PtL[22], PdL[19], PdL[20] and PdL[21].[168] These revealed the perpendicular nature of the anisyl ring with respect to the rest of the complex. Moreover, the torsion angles of these complexes between the two C^N-coordinating units of the tetradentate ligand were measured for each complex, in addition to PtL[20] and PdL[22], and the results are shown in Table 4.2. It is apparent that ML[21] complexes have the smallest torsion angles (3.16 and 2.95 ° for PtL[21] and PdL[21] respectively) whilst ML[22] complexes have the largest torsion angles (14.82 and 15.78 °).

Table 4.2: *Comparison of torsion angles between the two planes defined as M-C-C-C-N for Pt and Pd complexes.*

Complex	*PtL*[19]	*PtL*[20]	*PtL*[21]	*PtL*[22]	*PdL*[19]	*PdL*[20]	*PdL*[21]	*PdL*[22]
Torsion Angle/ °	11.68	9.17	3.16	14.82	12.32	10.99	2.95	15.78

In each case, M—N bonds were slightly longer than M—C bonds owing to the higher *trans* influence of the cyclometallating carbon which is typical for cyclometallated complexes, for example in *cis*-Pt(ppy)$_2$ the Pt—C bond length is 1.993 Å whilst the Pt—N bond is 2.127 Å.[21] M—C bonds in these complexes were measured as having an average of 2.000 Å whilst M—N bonds had an average of 2.051 Å. In comparison to the analogous complexes synthesised by Vezzu *et al.*, where the average of the Pt—C bond lengths is 2.004 Å and the average of the Pt—N bonds is 2.051 Å, the corresponding bond lengths for these complexes are identical within the error. In this work, crystals of PtL[20] and PdL[22] were obtained and compared to those discussed above. Crystals for PtL[20] were obtained by slow diffusion of hexane into a DCM solution of the complex, whilst for PdL[22], crystals were obtained by slow cooling from a hot DMF solution (Figs. 4.16 and 4.17). Very similar bond lengths were observed in PtL[20] and PdL[22] as for the other crystal structures where M—C bond lengths are slightly shorter than M—N bond lengths (Tables 4.3 and 4.4).

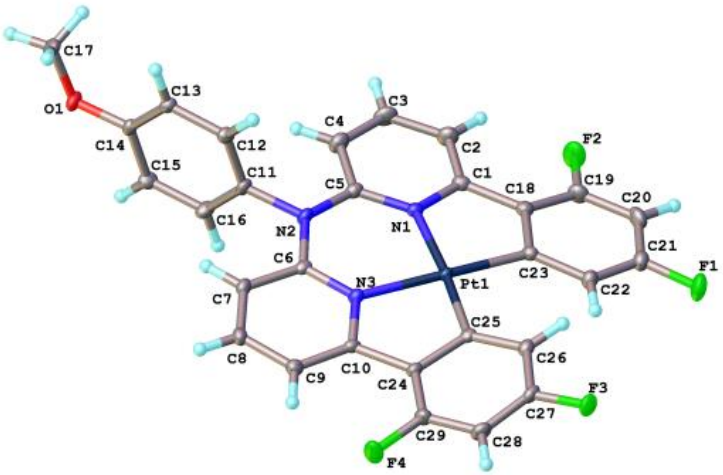

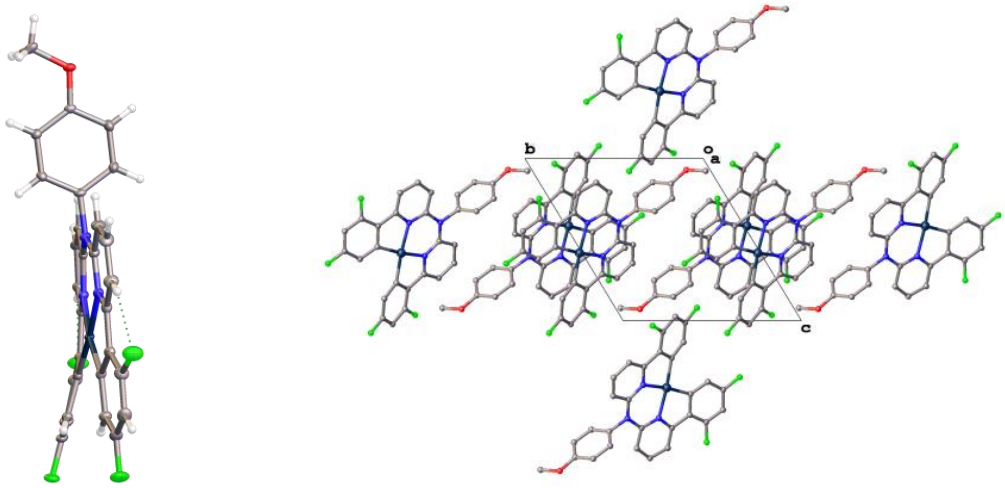

Figure 4.16: *Molecular structure and crystal packing of PtL[20].*

Table 4.3: *Selected bond lengths and angles for PtL[20].*

Bond Lengths/ Å		*Bond Angles / ˚*	
Pt1—N1	2.0429(19)	N1-Pt1-N3	93.36(7)
Pt1—N3	2.0465(18)	C23-Pt1-N1	81.95(8)
Pt1—C23	2.007(2)	C23-Pt1-N3	173.10(8)
Pt1—C25	1.991(2)	C25-Pt1-N1	174.64(7)
		C25-Pt1-N3	81.69(8)
		C25-Pt1-C23	101.16(9)

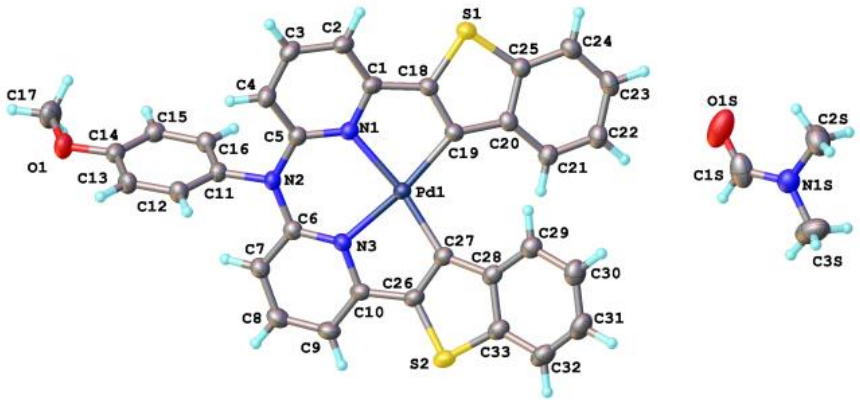

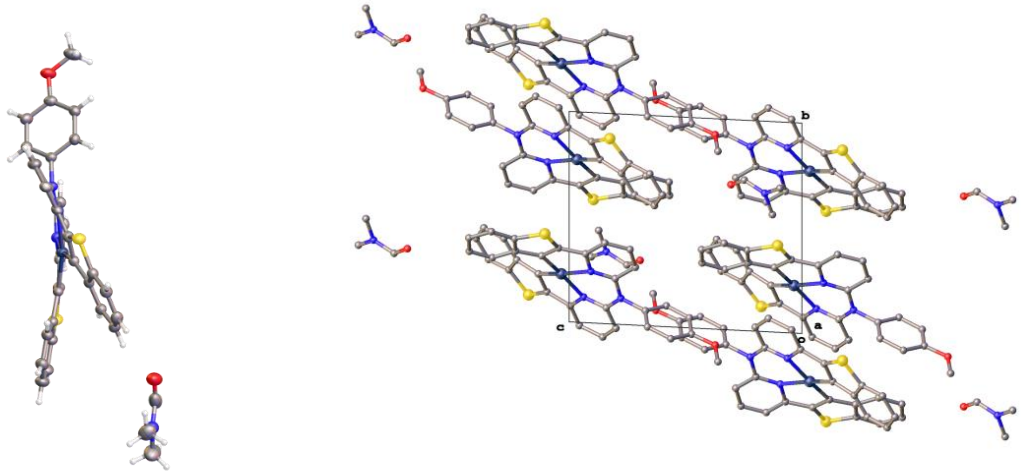

Figure 4.17: *Molecular structure and crystal packing of PdL[22].*

Table 4.4: *Selected bond lengths and angles for PdL[22].*

Bond Lengths/ Å		*Bond Angles / °*	
Pd1—N1	2.0541(17)	N1-Pd1-N3	89.52(7)
Pd1—N3	2.0612(17)	C19-Pd1-N1	83.07(8)
Pd1—C19	2.010(2)	C19-Pd1-N3	168.77(7)
Pd1—C27	2.000(2)	C27-Pd1-N1	167.46(8)
		C27-Pd1-N3	83.07(8)
		C27-Pd1-C19	105.65(8)

Interestingly, the PtL[20] crystal structure showed the presence of intramolecular hydrogen bonding between the fluorine atoms on the phenyl ring and hydrogen atoms on the pyridine ring and this was also the case for the PdL[20] structure previously reported. The closest M···M distances in each complex were found to be 4.179 Å for PtL[23] and 7.356 Å for PdL[22] which suggests there are no M···M interactions in the ground state. PdL[22] shows more steric hindrance in contrast to PtL[20] owing to the bulkiness of the benzothiophene group.

4.3.1.2 Photophysical properties

Absorption and emission measurements on the Pt complexes PtL[19], PtL[21] and PtL[22] in solution were carried out previously. Previous photophysical studies on the Pd compounds PdL[19], PdL[20] and PdL[21] were also carried out, but were not conclusive owing to the very limited amounts of sample available and doubts about purity. As a result, the photophysical properties of all the Pd complexes were repeated on new samples. In addition to this, PtL[20] and PdL[22] were also investigated.

The absorption spectra of the Pt and Pd complexes are shown below in Figure 4.18. The absorption spectra of PtL[21] and PtL[22] were noticeably red-shifted in comparison to PtL[19] and

PtL^{20} and the same trend is true of the Pd analogues. For PtL^{19} and PtL^{20}, intense absorptions were observed between 250 and 375 nm which are assigned to LC π→π* transitions, in addition to weaker bands between 375 and 420 nm which are more characteristic of MLCT transitions. PtL^{21} and PtL^{22} also show LC π→π* absorptions between 250 and 400 nm. The MLCT transition of $S_0 \rightarrow S_1$ is observed for PtL^{21} and PtL^{22} at 425 and 450 nm respectively and the low intensity bands at 475 nm in PtL^{21} and 485 nm in PtL^{22} are ascribed to the direct absorption of $S_0 \rightarrow T_1$. The Pd complexes show more structured absorption in comparison to the Pt complexes and are generally blue-shifted relative to the Pt complexes, for example the absorption cut-off for PtL^{21} is at ≈ 495 nm whilst for PdL^{21} it has tailed off by ≈ 450 nm. The general blue-shift for Pd complex absorption compared to Pt complex absorption has been investigated on a theoretical level by Georgieva *et al.* in some glyoxilic acid oxime complexes and showed that the HOMO-LUMO gap was larger for the Pd complexes.[175]

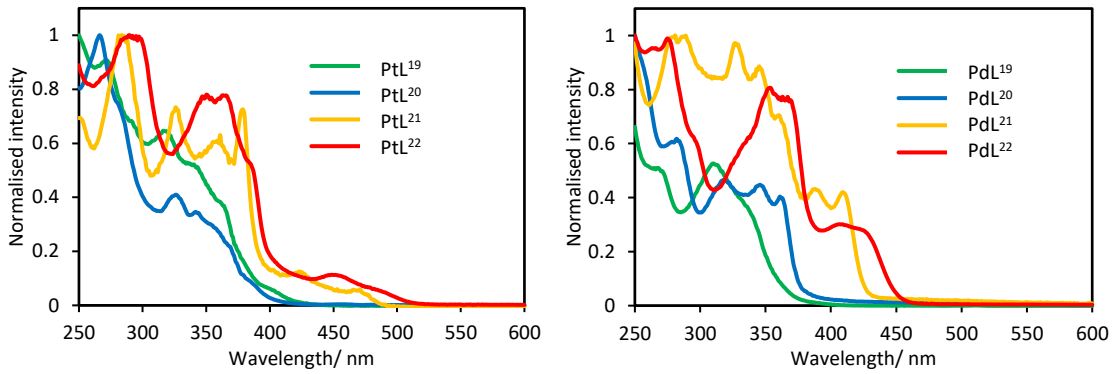

Figure 4.18: *Absorption spectra of complexes in DCM (except PdL^{22} which is in DMSO owing to low solubility).*

All complexes were emissive in degassed solution with quantum yields ranging from 4 to 78 % for the PtL^n complexes, and PLQY values of 0.7 and 15 % were obtained for PdL^{21} and PdL^{22} respectively. The PdL^{19} and PdL^{20} emission spectra were more complicated owing to the formation of an unknown new species in solution and will be discussed later. The solution-state emission of the Pt complexes shows structured emission bands with emission emanating from a ^{3}MLCT state (Fig. 4.19). The emission was found to be red-shifted in the order of PtL^{22}> PtL^{21}> PtL^{19} > PtL^{20} which is explained by the extended conjugation in the benzothiophene and thiophene rings, in comparison to the unsubstituted phenyl ring and the electron-withdrawing groups on the HOMO of the difluorophenyl ring which blue-shift the emission in comparison. This trend is also observed in the Pd analogues.

As for the absorption spectra, the emission of the PtL^n complexes is red-shifted in comparison to the Pd analogues for PtL^{21} and PtL^{22}. This is the expected trend and is supported by TD-DFT calculations (see Table 4.7) but such a trend is not observed for ML^{19} and ML^{20}. The λ_{max} values of PtL^{19} and PtL^{20} are seen to be 510 and 490 nm respectively whereas the corresponding Pd complex values are 535 and 530 nm. This reveals a red-shift of the Pd complex emission relative to the Pt complex emission in the phenyl and difluorophenyl complexes which is unexpected and is discussed later on.

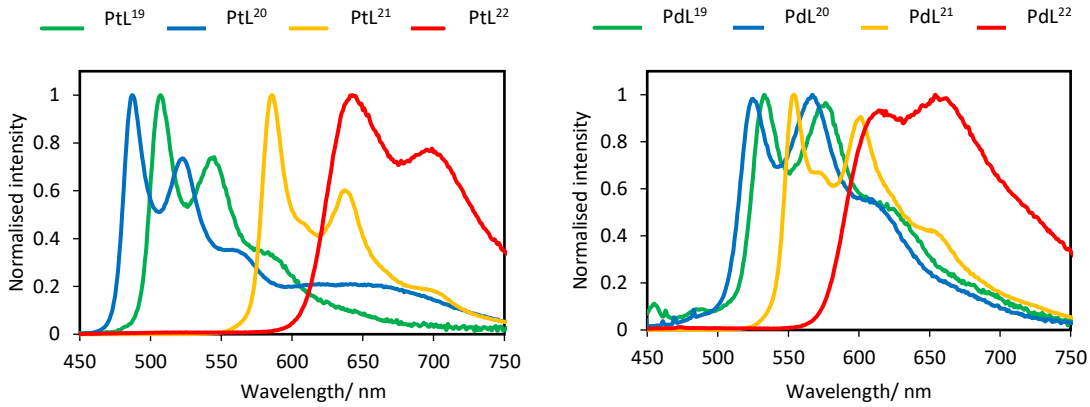

Figure 4.19: *Degassed RT emission spectra of complexes in DCM (except PdL^{22} which is in DMSO). The emission spectra of PdL^{19} and PdL^{20} should be treated with caution (see section 4.3.1.3)*

The 77 K emission spectra of all complexes were run in EPA and show intense, structured emission for each complex (Fig. 4.20). The same trend in the red-shift of the emission- benzothiophene > thiophene > phenyl > difluorophenyl- is observed in each set of complexes. Each Pd complex is seen to be blue-shifted relative to its Pt analogue, in-line with the expected results from TD-DFT. The 77 K lifetimes of the Pd complexes are extremely long at between 140 and 640 µs (Table 4.6) in comparison to their Pt analogues whose values do not differ much from their RT lifetimes and which range from 12 to 17 µs.

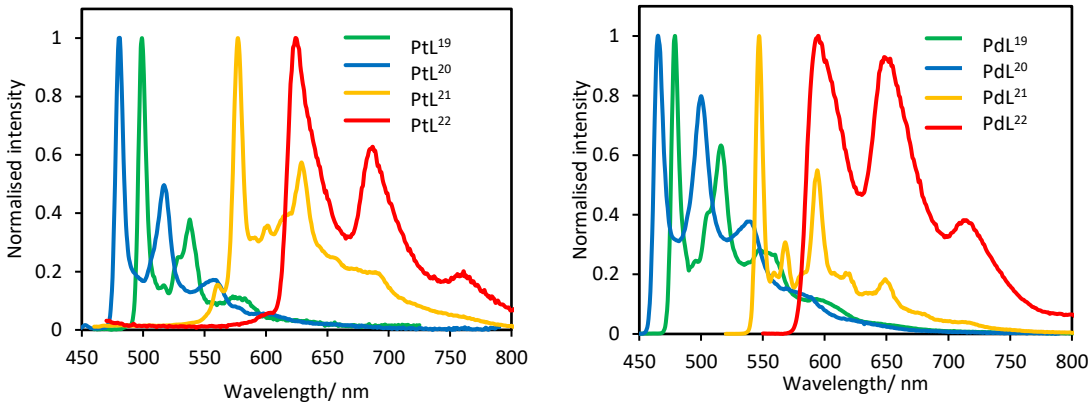

Figure 4.20: *77 K spectra for complexes ML[19-22] in EPA glass.*

Concentration-dependent emission was not studied in any detail for these complexes previously. A range of concentrations for each Pt and Pd complex were, therefore, investigated in this work and probed for the formation of excimers (Fig. 4.21). All thiophene and benzothiophene complexes show no evidence of excimer formation whereas the phenyl and difluorophenyl analogues display some excimeric emission at higher concentrations. PtL^{19} and PtL^{20} decay rates were seen to fit the Stern-Volmer equation and gave k_{sq} values of 1.26 and 2.34 x 10^9 M^{-1} s^{-1} respectively (Fig. 4.22). PtL^{20} shows the brightest excimer emission relative to the monomer, out of all the complexes studied, and its high value for k_{sq} supports the notion that this complex has the highest propensity to excimer formation. PtL^{19} also shows some evidence of excimer formation but the excimer emission relative to the monomer is weak in comparison to PtL^{20}.

The concentration-dependent emission observed for PdL^{19} and PdL^{20} was recorded but, as discussed later on, may not be representative of the actual complex emission and instead could be arising from a different species in solution. Interestingly, as for PtL^{19} and PtL^{20}, the concentration-dependent emission of the Pd analogues also show the development of excimeric emission, as shown by the increase in the relative intensity of the emission shoulder with $\lambda_{max} \approx 625$ and 610 nm in PdL^{19} and PdL^{20} respectively.

The lack of excimeric emission displayed by ML^{21} and ML^{22} could be due to the 5-membered thiophene groups which are electron-donating and thus push up the energy of the HOMO in each case. This could prevent the interaction of the metal centres in each case and stop any MMLCT emission. The k_{sq} value was determined for PdL^{21} to be 8.68 x 10^7 M^{-1} s^{-1} which is seen to be much smaller than for PtL^{19-20} (Table 4.6). Furthermore, the changes in the

lifetime for PtL[21-22] and PdL[22] are not significant as shown below, all of which supports a lack of excimer formation in these thiophene-containing complexes.

PtL[19]

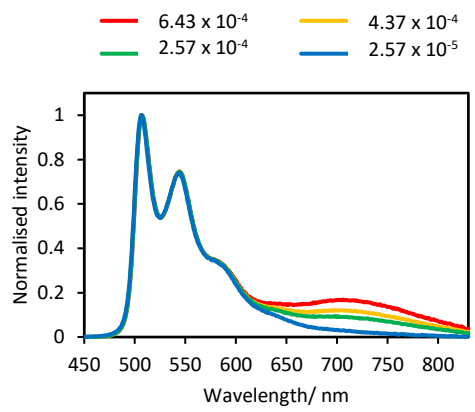

PtL[20]

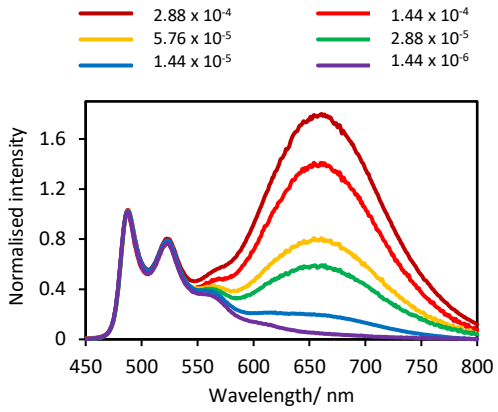

PtL[21]

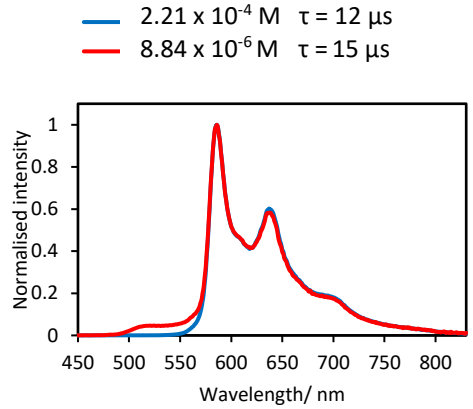

PtL[22]

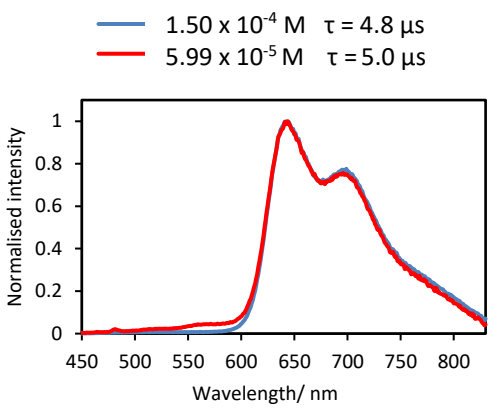

PdL[19] *

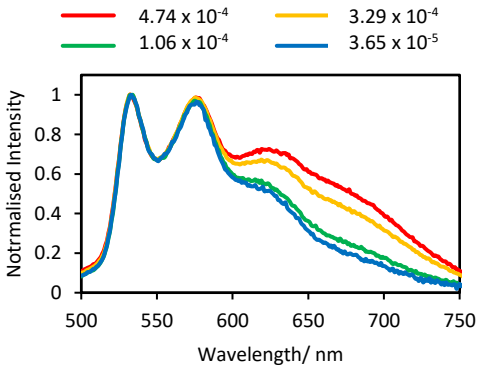

PdL[20] *

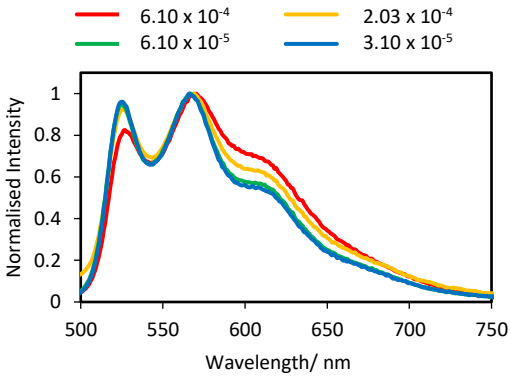

PdL[21] **PdL[22]**

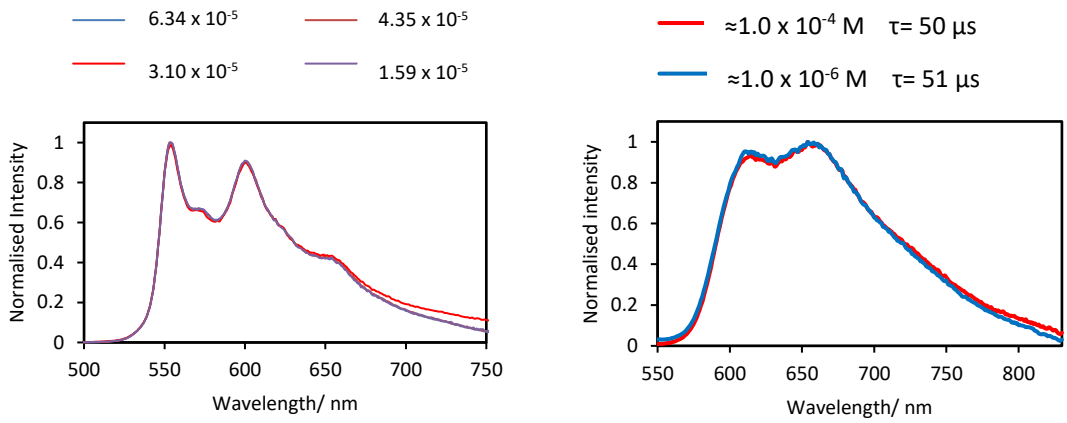

Figure 4.21: *Concentration-dependent spectra for Pt and Pd complexes ML[19-22]. *Emission shown for PdL[19] and PdL[20] may represent a new species forming in solution.*

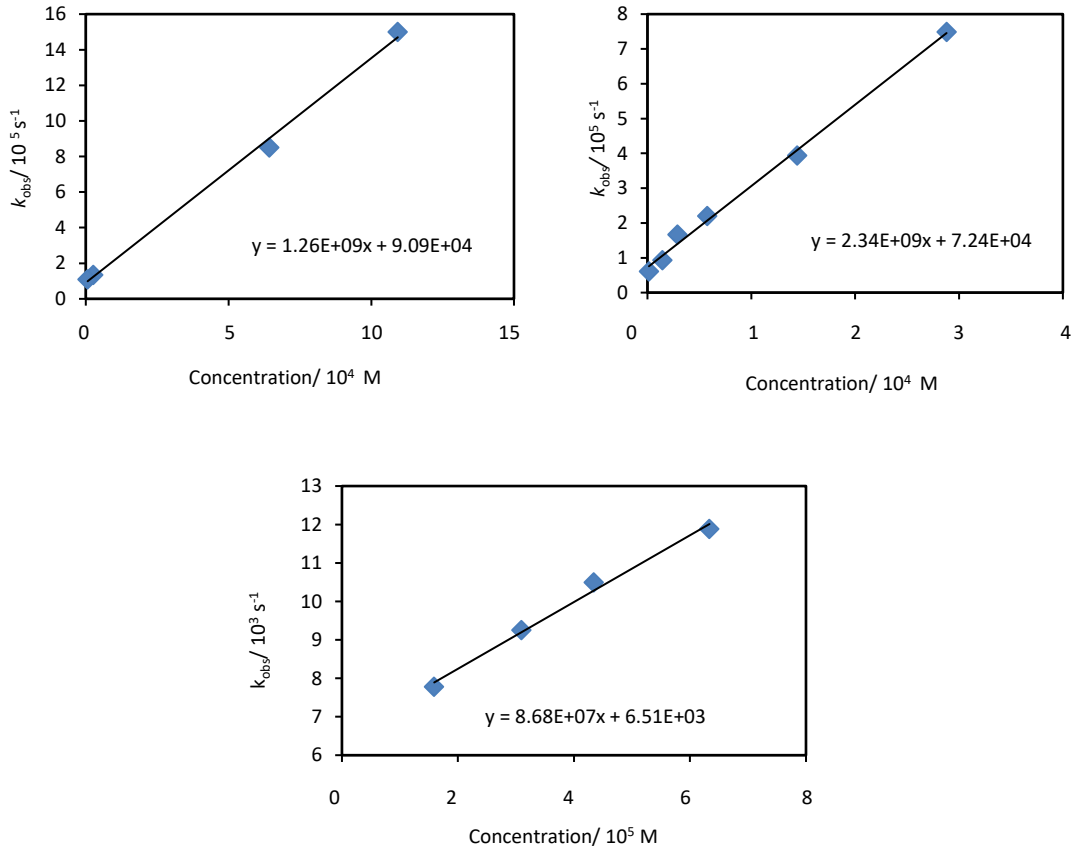

Figure 4.22: *Stern-Volmer plots for complexes PtL[19] (top left), PtL[20] (top right) and PdL[21] (bottom).*

4.3.1.3 PdL[19] and PdL[20] emission

Owing to the unexpected emission results displayed by PdL[19] and PdL[20] at RT in solution, further investigation into their photophysical properties was undertaken. Both complexes PdL[19] and PdL[20] showed high purity according to their NMR spectra, however, were recrystallized to obtain single crystals confirmed by X-ray diffraction with enhanced sample purity. After recrystallization, and in degassed DCM solution at RT, PdL[19] showed an intense emission peak with λ_{max} at 485 nm in addition to the peak at 535 nm that was also observed for the non-recrystallized sample. This is suggestive of two independent species in solution that are both emissive (Fig. 4.23). Upon cooling to 77 K, the emission is purely representative of one species with λ_{max} of ≈ 480 nm. This is thought to be the target compound as it is blue-shifted relative to the Pt analogue (λ_{max} of 499 nm at 77 K, Table 4.6).

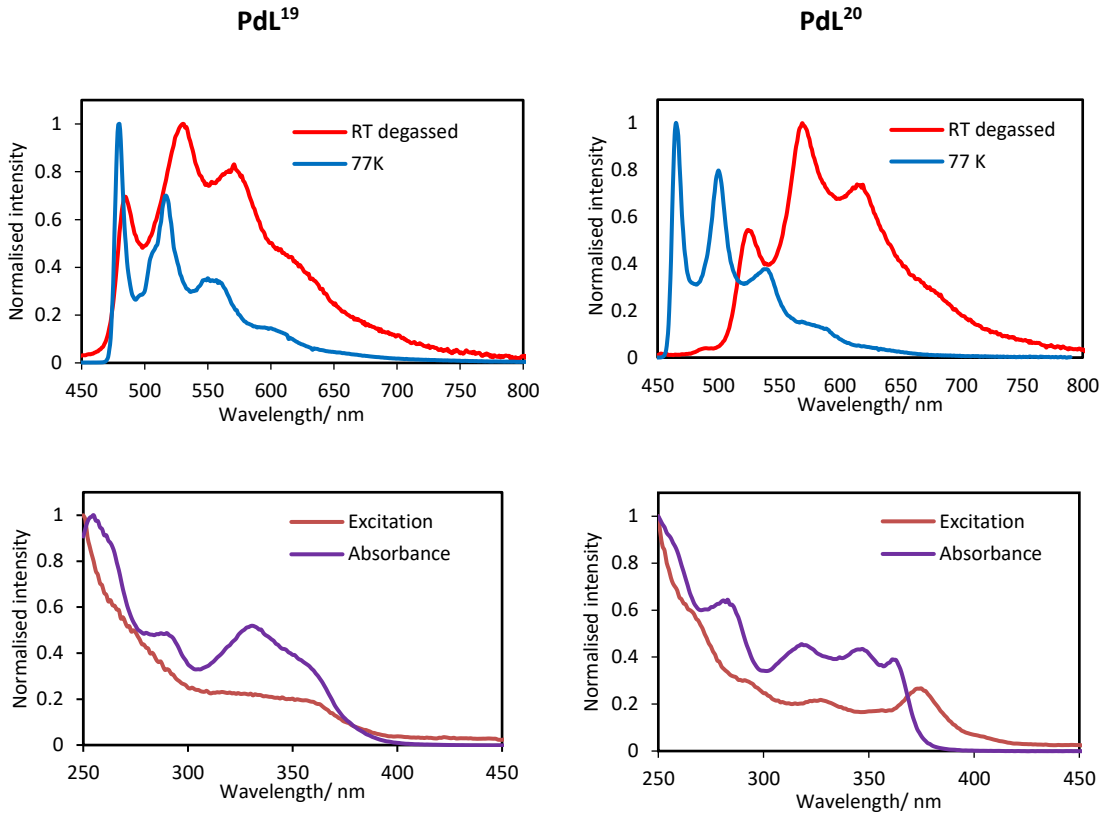

Figure 4.23: *Emission of the single crystals of PdL[19-20] at RT in DCM and at 77 K in EPA (top) and excitation vs. absorbance spectra for PdL[19-20] (bottom).*

For PdL[20], a λ_{max} of ≈ 530 nm was observed in the degassed RT emission spectrum that was also present in the non-recrystallized sample. Alongside this was another band of higher intensity with λ_{max} of ≈ 575 nm (Fig. 4.23). On cooling to 77 K, similarly with PdL[19], the

spectrum shows solely the emission of one species with λ_{max} of 465 nm that is thought to be the target compound owing to its blue-shifted emission relative to the Pt analogue (λ_{max} of 481 nm).

The excitation spectra were then run for PdL^{19} and PdL^{20} and both appear noticeably different to their corresponding absorption spectra (Fig. 4.23). This supports the formation of new emissive species in solution at RT in both cases. As a result, the RT emission is dominated by red-shifted spectra which could be masking that of the target compound, whilst at 77 K the target compounds are highly emissive.

Overall, these findings suggest that that the true emission of PdL^{19} and PdL^{20} does originate from the peaks which are blue-shifted relative to the Pt analogues i.e. with λ_{max} of 480 nm for PdL^{19} and 465 nm for PdL^{2} at RT in degassed solution. The evidence to support this lies in the following reasons;

- Crystals of both complexes were obtained and confirmed the correct structures.
- The absorption spectra of each complex are blue-shifted relative to their Pt analogues.
- The emission for PdL^{19} and PdL^{20} at 77 K in EPA showed purely the blue-shifted emission.

The formation of new species in solution is thus expected to be the cause of the other red-shifted emission in each case where PdL^{20} is more susceptible to this phenomenon. The long lifetimes and the structured emission with vibrational progression of the red-shifted emission suggest that these new species contain Pd, however, it has not yet been elucidated what these species are.

4.3.2 Complexes with tetradentate indole-containing ligands

4.3.2.1 Synthesis

Another set of complexations with Pt and Pd was attempted starting from a tetradentate indole-containing ligand. This indole ligand was similar in structure to the types of carbazole ligands that have been investigated by Jian Li's group and which show good photophysical properties when incorporated into Pt and Pd complexes.[23,26]

As for the previous set of complexes, the precursor P^{7} was synthesised via a Buchwald-Hartwig amination (Scheme 4.2). P^{7} was then reacted in a consecutive Buchwald-Hartwig amination step to obtain the tetradentate ligand H_2L^{23} in good yield. Complexation to afford

both Pt and Pd complexes was attempted but was only successful to form PtL^{23} via the typical cyclometallation reaction conditions as discussed previously (Scheme 4.2). When the complexation was attempted with a range of Pd sources ($Pd(COD)Cl_2$, $Pd(OAc)_2$ and K_2PdCl_4), solvents (acetic acid, $MeCN/H_2O$ and toluene) and temperatures, in each case largely the ligand was recovered. The reaction turned black potentially forming many unwanted side products of Pd-catalysed reactions with the indole of which there are many examples in the literature.[176]

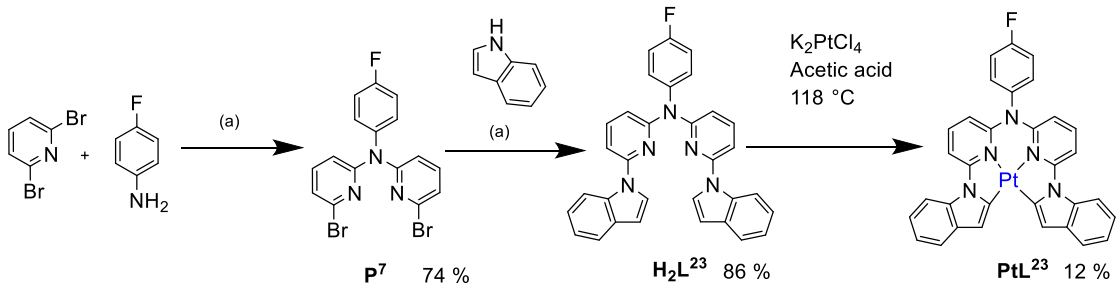

P[7] 74 % **H_2L^{23}** 86 % **PtL^{23}** 12 %

Scheme 4.2: *Synthesis of H_2L^{23} with conditions a= $Pd(dba)_2$, dppf, $HP(tBu)_3BF_4$, NaO^tBu, Dry toluene, 90 °C and subsequent complexation to form PtL^{23}.*

As with the previous set of complexes, PtL^{23} shows an upfield shift of the proton labelled 3' due to the ring current effect of the anisyl ring (Fig. 4.24). Moreover, in the free ligand signal 3'' is a doublet with a chemical shift of 6.64 ppm. Upon complexation, this signal experiences a downfield shift to 6.76 ppm and transformation into a singlet peak which helps to confirm the successful complexation.

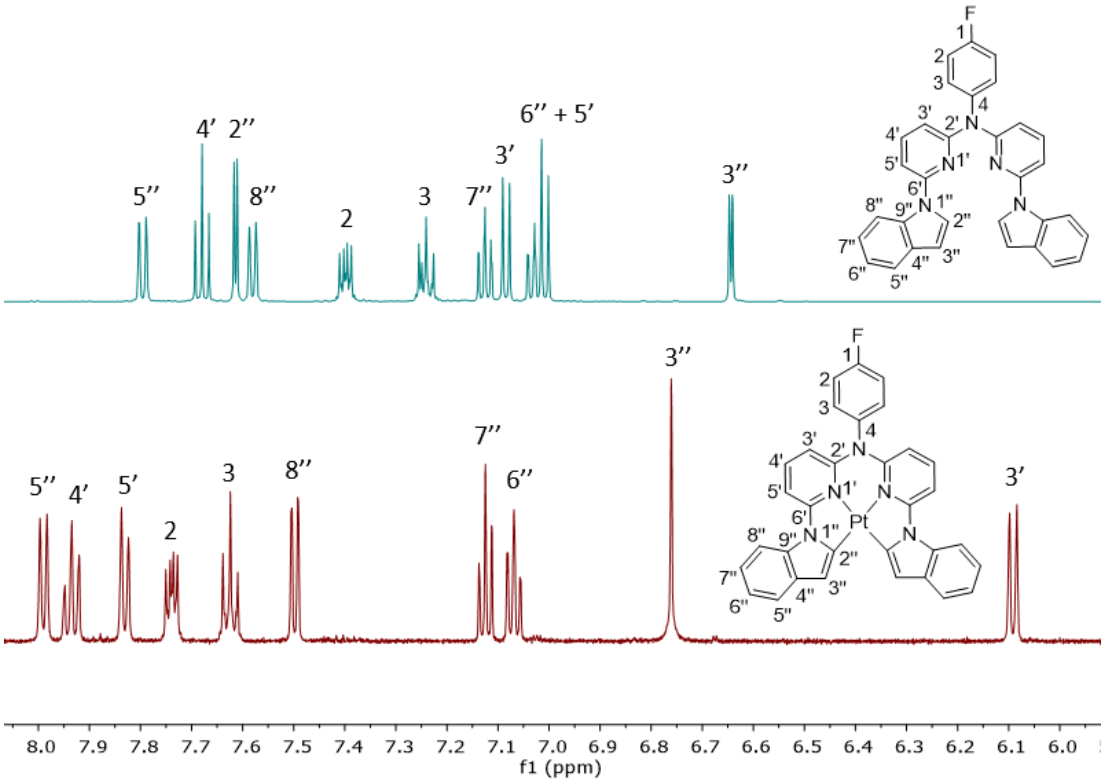

Figure 4.24: *NMR spectrum of H_2L^{23} and PtL^{23} in d_6-DMSO at 600 MHz.*

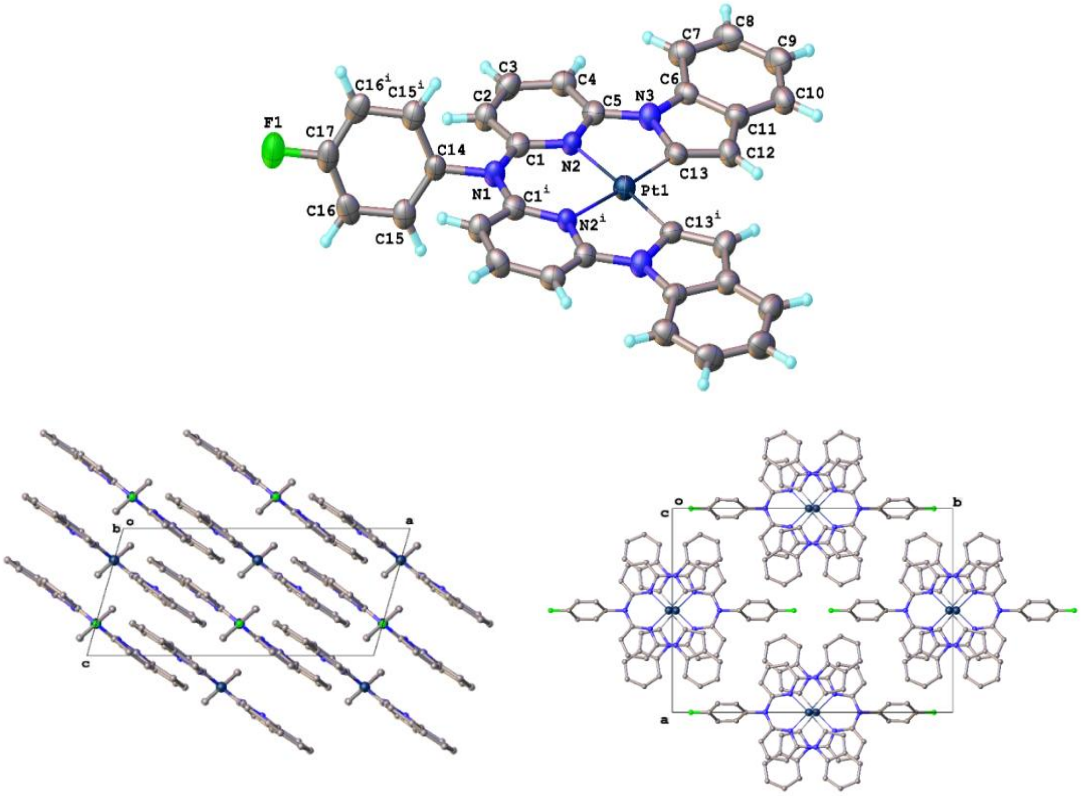

Figure 4.25: *Molecular structure and crystal packing of PtL^{23}.*

Table 4.5: *Selected bond lengths and angles for PtL[23].*

Bond Lengths/ Å		*Bond Angles / °*	
Pt1—N2	2.027 (5)	N2-Pt1-N2[1]	94.1 (3)
Pt1—N2[1]	2.028 (5)	C13[1]-Pt1-N2	175.9 (2)
Pt1—C13[1]	1.976 (7)	C13[1]-Pt1-N2[1]	81.8 (3)
Pt1—C13	1.976 (7)	C13-Pt1-N2[1]	175.9 (2)
		C13-Pt1-N2	81.8 (3)
		C13[1]-Pt1-C13	102.3(4)

Crystals suitable for X-ray diffraction were obtained by slow cooling from a hot DMSO solution (Fig. 4.25). The crystal structure confirmed the binding of the ligand in a tetradentate manner and showed head-to-tail packing of the complexes, similar to the other Pt and Pd(C^N^N^C) complexes as discussed earlier. Moreover, the anisyl ring was also seen to be perpendicular to the rest of the complex and in this case the torsion angle between the N^C planes was negligible at 0.39 °. The closest Pt···Pt distances were shown to be 3.678 Å.

4.3.2.2 Photophysical properties

All spectra for PtL[23] were recorded in DMSO due to a limited solubility of the complex in all common organic solvents (Fig. 4.26). The absorption spectrum showed bands at between 300 and 330 nm which were assigned as LC π→π*, owing to the match with the ligand absorption. The band at 330 to 440 nm was assigned as a mix of MLCT and ILCT as supported by the DFT discussed later on.

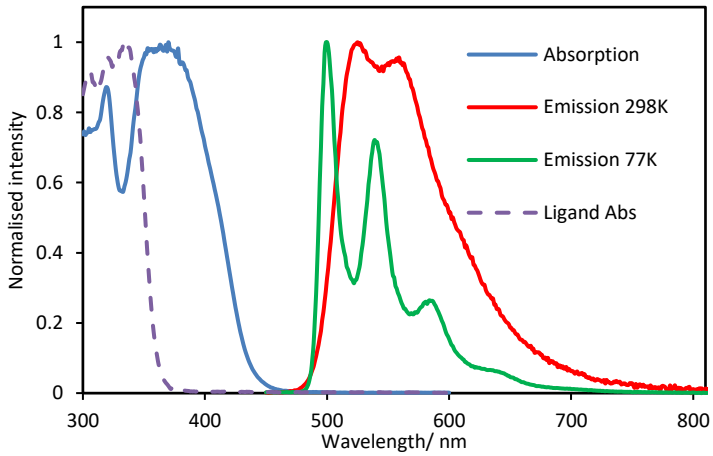

Figure 4.26: *Absorption and emission spectra of PtL[23] in DMSO at RT and 77 K emission spectrum in butyronitrile glass.*

The complex exhibited an impressive quantum yield of 33 % in degassed DMSO solution and a long lifetime of 19 μs (Table 4.6). The emission spectrum at RT showed a slightly structured band with λ_{max} at 520 and 548 nm and, on cooling to 77 K, this emission was

seen to slightly blue-shift and more vibrational progression was observed. DMSO is known to quench emission in some complexes[177] and so making a more soluble derivative of this compound would be useful to see if the emission efficiency could be enhanced. Concentration-dependent studies were not possible owing to the limited solubility of the complex.

Table 4.6: *Photophysical properties of ML^n complexes containing tetradentate ligands. 298 K quantum yields and lifetimes are in degassed DCM solutions unless otherwise stated. 77 K measurements are in EPA or butyronitrile. *Results were run in DMSO.*

Complex	298 K										77 K	
	λ_{abs} (nm)	λ_{em} (nm)	τ_{deg} (μs)	τ_{aer} (ns)	τ_0 (μs)	φ	k_r (10^2 s^{-1})	k_{nr} (10^4 s^{-1})	k_q (O_2) (10^8 M^{-1} s^{-1})	k_{sq} (mono) (10^8 M^{-1} s^{-1})	λ_{em} (nm)	τ (μs)
PtL[19]	272 (72400), 289 (57500), 323 (34600), 337 (38900), 363 (24500), 399 (7580).	506, 541, 588sh	8.3	300	11	0.78	940	2.7	14	13	499, 512, 524, 541, 572	12
PtL[20]	230 (15990), 267 (16300), 330 (8250), 343 (2060).	488, 523, 559, 662	11	490	14	0.46	410	4.8	9.0	23	481, 518, 559	15
PtL[21]	252 (45700), 283 (74100), 325 (38900), 359 (34600), 378 (40700), 424 (6700), 468 (3800).	587, 640, 699sh	15	330	/	0.74	490	1.7	13	/	559, 585, 598, 616, 628, 651, 685	17
PtL[22]	267 (27802), 291 (31881), 349 (26930), 363 (25300), 382 (18362), 452 (3636), 481 (2020).	647, 703	5.9	390	/	0.04	68	17	11	/	623, 684, 756	12
PdL[19]	298 K data not given for these complexes owing to the formation of other species in solution at RT.										479, 515, 553, 596, 653	350
PdL[20]											465, 500, 539, 580	640
PdL[21]	233 (30800), 279 (22100), 325 (22100), 342 (20100), 364 (15000), 386 (9700), 407 (9400).	553, 572, 600, 652	110	590	150	0.15	14	0.79	7.7	0.87	547, 566, 592, 611, 644	350
PdL[22] *	264 (19156), 275 (19441), 295 (12271), 354 (19181), 369 (18440), 407 (7159).	615, 658, 733sh	85	620	/	0.007	0.83	1.2	7.3	/	595, 649, 714, 797sh	140
PtL[23]*	303 (14560), 312 (17964), 369 (20349)	520, 548	19	520	/	0.33	1.8	3.6	8.4	/	498, 537, 580, 630	21

4.3.3 DFT of Pt complexes containing tetradentate ligands

Ground state DFT was carried out using the B3LYP/LANL2DZ level of theory to obtain the frontier orbital plots for each Pt and Pd complex studied (Fig. 4.27). TD-DFT confirmed the nature of the $S_0 \rightarrow S_1$ transition in each case to be mainly HOMO→LUMO in character and the energies of the first excited state absorptions are shown in Table 4.7. Generally, it was found that the HOMO of each complex was based on the phenyl rings (or the indole in PtL[23]) and the metal centre, whilst the LUMOs were spread out across the pyridyl and phenyl/indole rings of the molecule but based mainly on the pyridyl rings. As a result, most of the excited state transitions are described as being a mixture of MLCT and ILCT (Table 4.7). This is similar to the PtL[19] analogue synthesised by Vezzu *et al.* which differs only by the removal of the OMe group on the anisyl ring.[22]

On closer inspection, PtL[21] and PtL[22] LUMOs contain a large amount of metal contribution. PtL[21] and PtL[22] also show contributions to the excited state from HOMO-3 and HOMO-5 levels respectively (see Appendix, Fig. A2). The PtL[23] LUMO on the other hand, has a large contribution from the anisyl ring as well as the pyridyl ring and the HOMO and LUMO in this molecule are very clearly separated in comparison to the other Pt complexes. The excited state transition is therefore assigned as having more ILCT character in this case.

For the Pd complexes, PdL[19] and PdL[20] show largely metal character in the HOMO compared to the phenyl ring contribution in the Pt analogues and the transitions are assigned mainly to MLCT. This could give some insight to the unusual photophysical behaviour of PdL[19-20] where the increased metal contribution on the HOMO of the complexes could make them more prone to oxidation and be the result of the potential new emissive species observed at RT in solution.

PdL[21] and PdL[22] seem to show the same distribution of the HOMO as their Pt analogues, whilst the LUMOs of PdL[21] and PdL[22] show no visible contribution from the metal centre which differs to their Pt equivalents, hence the excited state transitions are described as mixed MLCT/ILCT.

TD-DFT confirmed the blue-shift of the Pd complex absorption relative to the Pt complex absorption and the trend in absorption energies in each group of complexes from benzothiophene < thiophene < phenyl < difluorophenyl.

Table 4.7: *Calculated S_1 excited state energies for ML^n complexes using TD-DFT B3LYP/LANL2DZ.*

Complex	*PtL^{19}*	*PtL^{20}*	*PtL^{21}*	*PtL^{22}*	*PtL^{23}*	*PdL^{19}*	*PdL^{20}*	*PdL^{21}*	*PdL^{22}*
Energy (eV/nm)	2.6824/ 462.21	2.9128/ 425.65	2.4973/ 496.48	2.4642/ 503.14	2.5754/ 481.42	2.9430/ 421.29	3.1918/ 388.44	2.8889/ 429.18	2.8071/ 441.68
Oscillator Strength	0.0015	0.0005	0.0208	0.0228	0.0002	0.0051	0.0054	0.0566	0.0441
Main contribution (%)	HOMO→ LUMO (70)	HOMO→ LUMO (70)	HOMO→ LUMO (69) HOMO-3→ LUMO (12)	HOMO→ LUMO (69) HOMO-5→ LUMO (11)	HOMO→ LUMO (68)	HOMO→ LUMO (70)	HOMO→ LUMO (70)	HOMO→ LUMO (68) HOMO-3→ LUMO (18)	HOMO→ LUMO (69) HOMO-5→ LUMO (18)
Assignment	Mixed MLCT/ILCT	Mixed MLCT/ILCT	Mixed MLCT/ILCT	Mixed MLCT/ILCT	Mixed ILCT/MLCT	MLCT	MLCT	Mixed MLCT/ILCT	Mixed MLCT/ILCT

Complex	*PtL^{19}*	*PtL^{20}*	*PtL^{21}*	*PtL^{22}*	*PtL^{23}*	*PdL^{19}*	*PdL^{20}*	*PdL^{21}*	*PdL^{22}*
HOMO	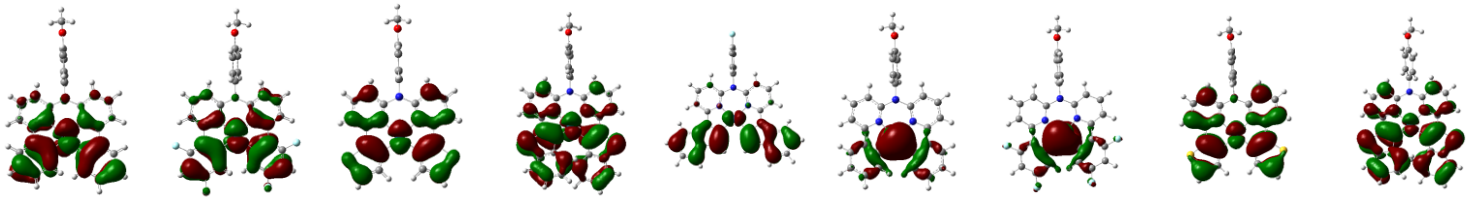								
LUMO	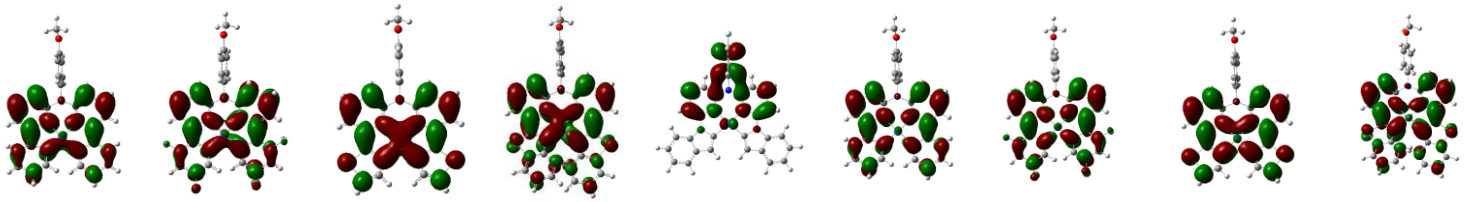								

Figure 4.27: *Frontier orbital plots for ML^n complexes calculated using B3LYP/LANL2DZ.*

4.3.4 Pd complex solid-state investigation and OLED devices

Owing to the lack of Pd relative to Pt complex devices in the literature, investigation into the incorporation of the Pd complexes PdL[19-21] into OLEDs was made. PdL[22] was not chosen due to the limited amount of complex synthesised. Initially complex PdL[21] was selected due to its high quantum yield of 15 % in degassed DCM solution. The sample was sublimed and incorporated into an evaporated thin film of mCBP at 6 wt. % which increased the PLQY to 45 % and the lifetime from 110 to 220 µs. The solution-state emission was essentially the same as for the film emission; however, there was a slight change in absorption profile (Fig. 4.28).

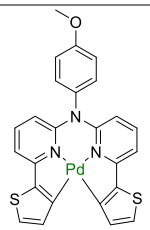

ϕ DCM (%)	15
τ DCM (µs)	110
ϕ mCBP film (%)	45
τ mCBP film (µs)	220

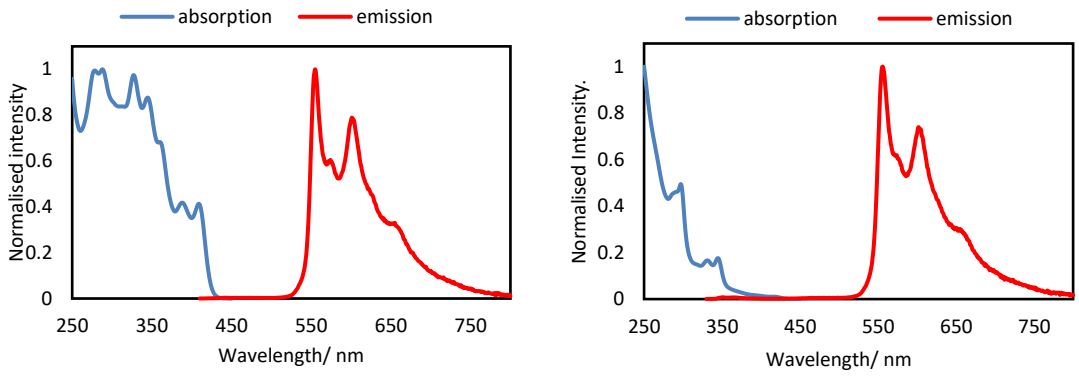

Figure 4.28: *Photophysical properties of PdL[21] in degassed DCM solution and in the film (top) and absorption and emission of PdL[21] complex in degassed DCM solution (bottom left) and mCBP film (bottom right).*

The temperature-dependence of the emission and lifetime of PdL[21] in the film was also measured from 30 K to 350 K by streak camera (Fig. 4.29). This revealled essentially no change in the emission lifetime of the complex. The only change observed was in the emission intensity which slightly increased on cooling.

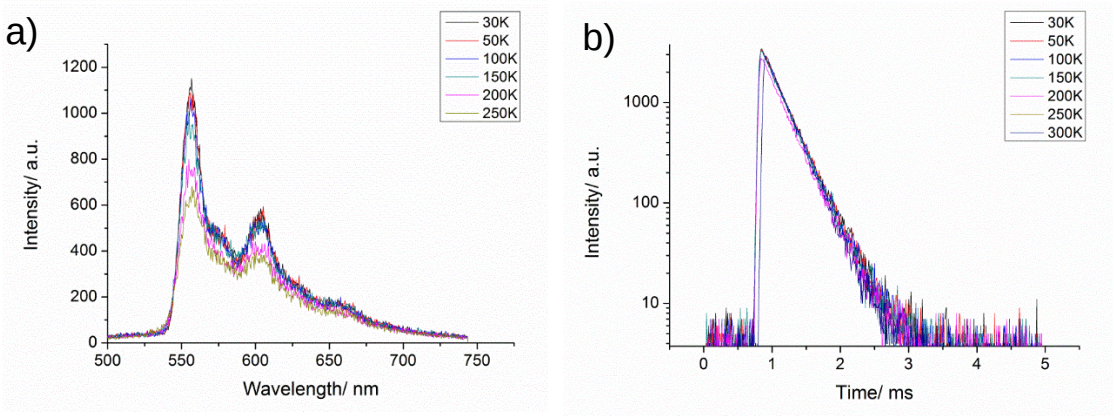

Figure 4.29: *Streak camera temperature-dependence of PdL[21] for a) emission and b) lifetime.*

This lack of change in the phosphoresence lifetime at different temperatures suggests that the complex is very rigid even at RT and consequently does not undergo a lot of rearrangement on cooling, which could explain the high quantum yield for this complex relative to the other Pd complexes. Indeed, the k_{nr} value of this complex was the lowest of all the tetradentate complexes synthesised (including the Pt analogues) at 0.79 x 10^4 s^{-1} (Table 4.6).

Due to the large amounts of complex required for VTE-processed OLEDs (ca. 50 mg for 1 device), solution-processed OLEDs were then attempted for complexes PdL[19-21] where PdL[21] set a precedent for good efficiency, at least in the solid-state film. Again PdL[22] was not chosen due to small amounts of compound but also due to inferior solubility needed for solution-processing. Solution-processed devices were fabricated by Piotr Pander (Durham Univeristy Physics Department) with the general device structure: ITO | HIL 1.3N (45 nm) | Host co. x% Pd complex (60 nm) | TPBi (50 nm) | LiF (0.8 nm) | Al (100 nm) and the properties of each device are shown below in Table 4.8 and Figure 4.30.

Table 4.8: *Maximum device properties for OLEDs of PdL[19], PdL[20] and PdL[21].*

Device no.	*Complex (wt. %)*	*EML Host*	*EL λ_{max} (nm)*	*Current density (mA cm^{-2})*	*Brightness (cd m^{-2})*	*EQE (%)*
1	PdL[19] (3)	PVK:OXD7	490, 535, 572	24.7	132.0	0.65
2	PdL[20] (5)	PVK:PBD	535, 575	72.1	451.8	2.70
3	PdL[20] (5)	PVK:OXD7	535, 575	21.3	257.3	1.40
4	PdL[20] (10)	PVK:PBD	535, 575	66.3	727.8	3.51
5	PdL[20] (10)	PVK:OXD7	535, 575	18.6	297.0	3.24
6	PdL[21] (5)	PVK:PBD	560, 605	11.4	141.5	2.25
7	PdL[21] (5)	PVK:OXD7	560, 605	16.4	346.6	3.17

EQEs of the devices ranged from 0.65 to 3.51 % and the highest EQE was displayed by PdL^{20} in device 4 containing 10 wt. % of the complex in a PVK : PBD host. Device 4 also displayed the highest brightness at 727.8 cd m^{-2}. Interestingly, both PdL^{19} and PdL^{20} display the red-shifted emission as the major component in their EL spectra that was observed in their PL spectra in degassed solution. Owing to the relatively high EQE obtained for device 4, again it suggests that this new Pd species that is forming is highly emissive. PdL^{21} displayed EL which was very similar to its PL and, when incorporated into device 7 at 5 wt. %, showed good properties with an EQE of 3.17 % and brightness of 346.6 cd m^{-2}. In general, for complexes containing tetradentate ligands, these values may not appear to be extremely high. When considering that these are solution-processed devices containing Pd complexes, however, these results are reflective of the lower efficiencies that Pd complexes typically display in comparison to Pt complexes. In no case was there any evidence of excimeric emission over the concentration range investigated, and so investigation into devices with higher doping concentrations or even neat films would be interesting to see if any excimeric emission emerges.

PdL[19]

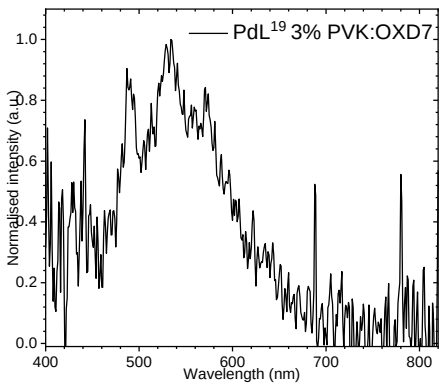
PdL19 3% PVK:OXD7
Normalised intensity (a.u)
Wavelength (nm)

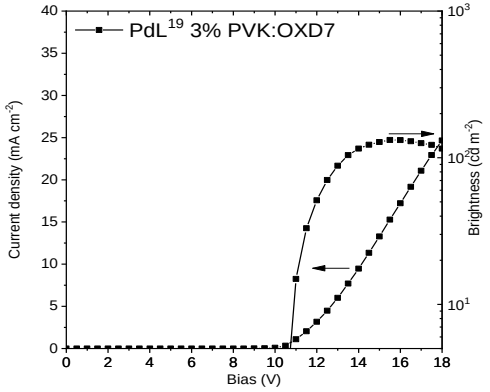
PdL19 3% PVK:OXD7
Current density (mA cm-2)
Brightness (cd m-2)
Bias (V)

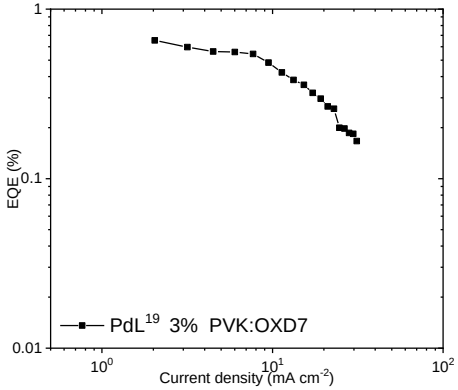
PdL19 3% PVK:OXD7
EQE (%)
Current density (mA cm-2)

PdL[20]

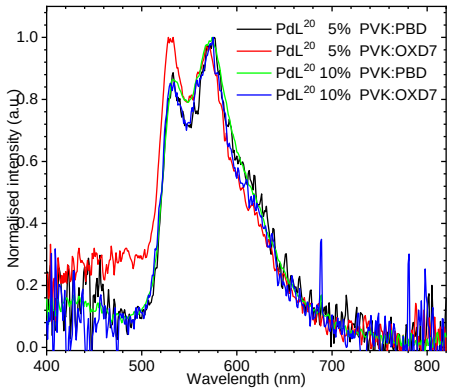
PdL20 5% PVK:PBD
PdL20 5% PVK:OXD7
PdL20 10% PVK:PBD
PdL20 10% PVK:OXD7
Normalised intensity (a.u)
Wavelength (nm)

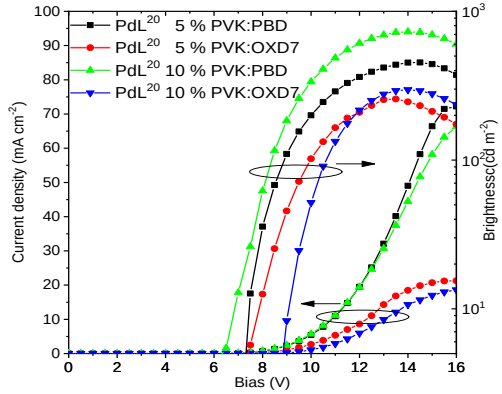
PdL20 5 % PVK:PBD
PdL20 5 % PVK:OXD7
PdL20 10 % PVK:PBD
PdL20 10 % PVK:OXD7
Current density (mA cm-2)
Brightnessc(cd m-2)
Bias (V)

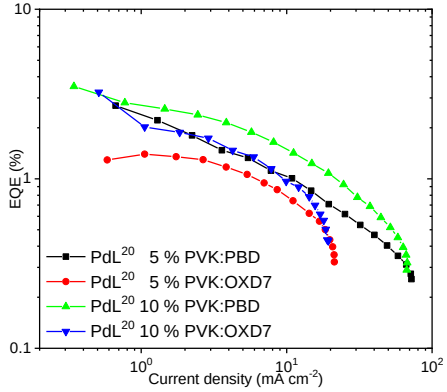
PdL20 5 % PVK:PBD
PdL20 5 % PVK:OXD7
PdL20 10 % PVK:PBD
PdL20 10 % PVK:OXD7
EQE (%)
Current density (mA cm-2)

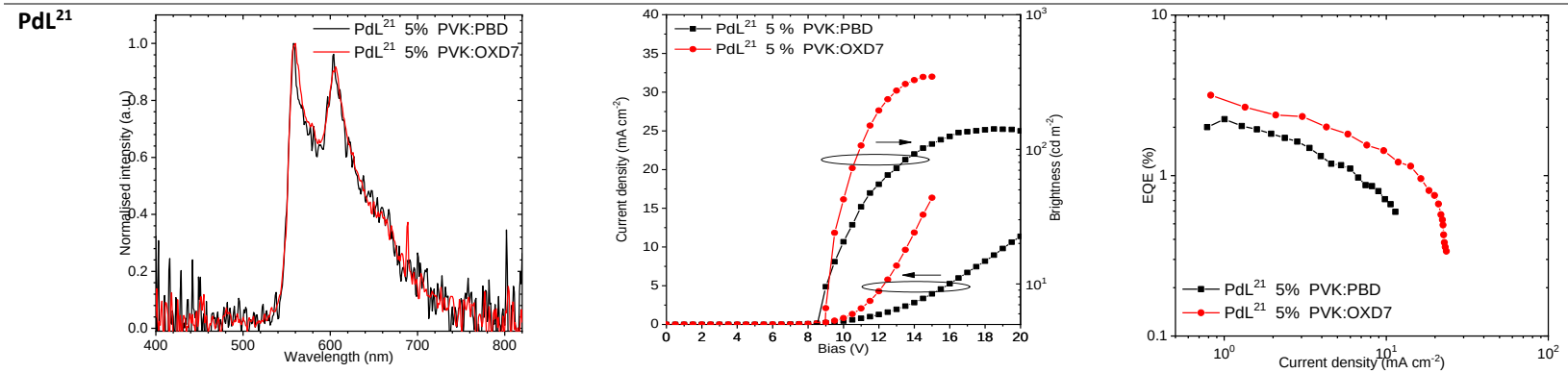

Figure 4.30: *OLED devices of complexes PdL[19], PdL[20] and PdL[21] with device structure: ITO | HIL 1.3N (45 nm) | Host co x% Pd complex (60 nm) | TPBi (50 nm) | LiF (0.8 nm) | Al (100 nm).*

4.3.5 Oxidation of Pt^{II} to Pt^{IV} complexes

As mentioned in chapter 3, most Pt^{IV} complexes in the literature contain bidentate ligands and there are not many examples of those containing tridentate or tetradentate ligands. We attempted the synthesis of the $Pt^{IV}L^{n}$ complexes by some of the different methods that were described in the introduction to chapter 3.

4.3.5.1 Synthesis

Oxidation via addition of Cl_2 gas to the reaction mixture has been employed as a standard method in our group previously.[53] Alongside this has been used the irradiation of Pt^{II} complexes suspended in chloroform with UV light. Both methods of Cl_2 addition proved to be successful in the case of the Pt(N^C^N) complexes and in some Pt(C^N^N^C) complexes.[51] For example, Mickaële Bonneau successfully synthesised $PtL^{19}Cl_2$, $PtL^{21}Cl_2$ and $PtL^{22}Cl_2$ using the method of UV light irradiation in $CHCl_3$. An investigation into clean and synthetically less-challenging oxidation strategies for tetradentate complexes has been made here. Firstly, oxidation via addition of Cl_2 gas was attempted for the tetradentate Pt thiophene complex PtL^{21} to show its amenability to oxidation. As is shown by Figure 4.31, the addition of Cl_2 gas to the tetradentate thiophene Pt^{II} complex in chloroform led to destruction of the aromatic region ^1H signals over time.

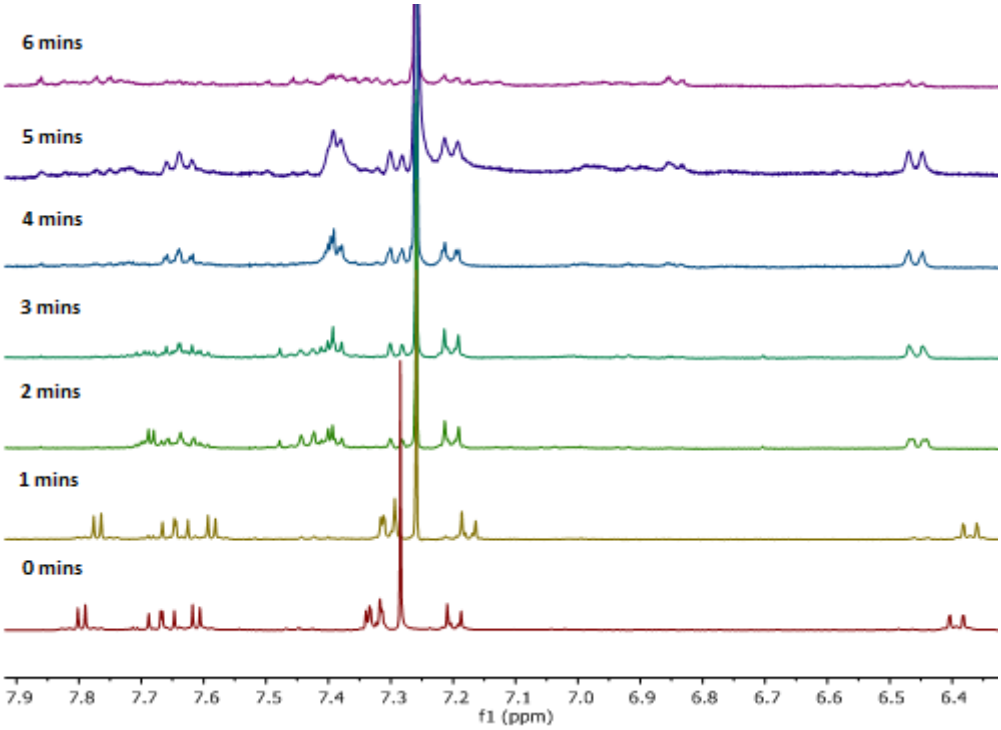

***Figure 4.31**: 400 MHz $CDCl_3$ NMR evolution of PtL^{21} with chlorine addition over varying time intervals.*

This suggests a decomposition of the complex and could be due to the reactivity of the electron-rich thiophene group with Cl_2. It is known that thiophene itself reacts vigorously with Cl_2 in aqueous solution (Fig. 4.32).[178] As a result, an electrophilic attack by the thiophene group may be the cause of the destruction of the aromatic region in this case. Integration to show removal of 2 protons would show evidence of this, although the complete destruction of the aromatic region made it difficult to assign. It is, however, noticeable that the signal at 6.4 ppm for PtL^{21} is shifted to a higher frequency after Cl_2 addition which is indicative of oxidation.

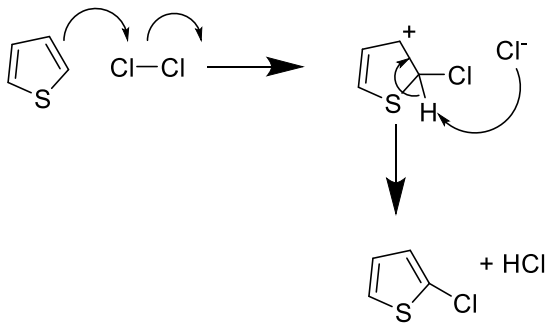

Figure 4.32: *Mechanism for the chlorination of thiophene.*

The use of $PhICl_2$ was then attempted to see if it was effective in oxidising the PtL^{21} complex. $PhICl_2$ was added to PtL^{21} and left to stir at RT for 24 hours with the exclusion of light (Scheme 4.3). The reaction was attempted with DCM and $CHCl_3$ as solvents and in both cases the desired product was formed in solution.

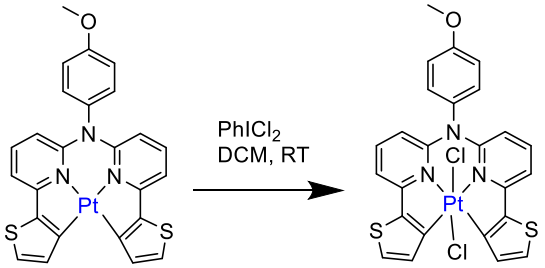

PtL^{21} **$PtL^{21}Cl_2$**

Scheme 4.3: *Oxidation of PtL^{21} to $PtL^{21}Cl_2$.*

Mass spectrometry showed clear evidence of product formation (ES^+); $[M\text{-}2Cl]^+$, $[M\text{-}Cl]^+$ and $[M+H]^+$. The NMR results are given below (Fig. 4.33) and show that the protons at position 4'' and 5'' are shifted to higher frequency in the $PtL^{21}Cl_2$ complex compared to the PtL^{21} complex. This may be due to the effect of the chloride additions which would be likely to take an axial conformation and interact with those protons on the thiophene ring to cause

significant de-shielding. The protons on the anisyl ring seem largely unaffected. This may be due to the distance of the anisyl ring from the chloride additions.

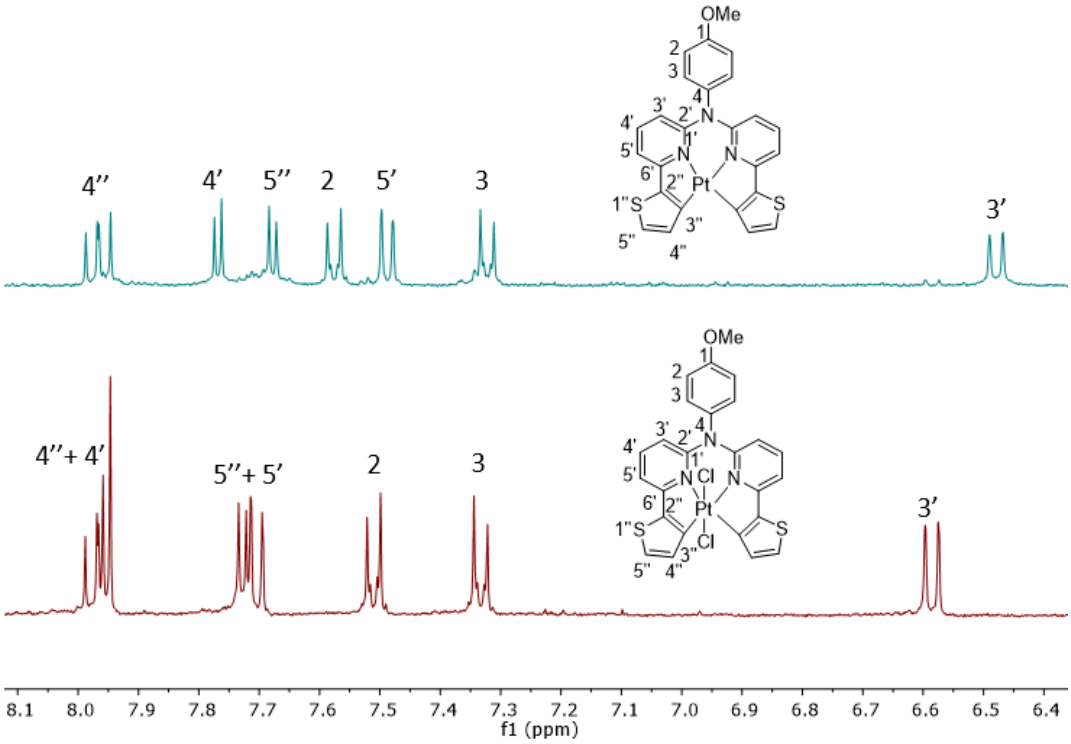

Figure 4.33: *Comparison of ^{1}H NMR results of PtL^{21} (top) and PtL^{21}Cl$_2$ (bottom) in d_6-DMSO, 400 MHz.*

PtL^{19} is an example of a Pt(C^N^N^C) complex previously oxidised by the addition of two chlorides. In an attempt to achieve an easier synthetic route to the oxidised product, the oxidation of PtL^{19} was attempted with I_2. This route proved facile, stirring solid I_2 with PtL^{19} at RT in acetone for 2 hours (Scheme 4.4). The oxidised product was obtained in a 70 % yield.

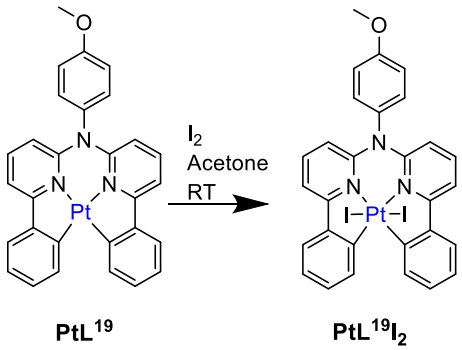

Scheme 4.4: *Oxidation of PtL^{19} to PtL^{19}I$_2$.*

The NMR results (Fig. 4.34) show an upfield shift for the proton labelled 2'' which is closest to the Pt centre. This suggests that the addition of the I atoms serves to shield the protons in the 2'' position. Furthermore, the proton labelled 3' is seen to experience a downfield shift upon oxidation. This suggests it is being affected by a de-shielding influence potentially because it is located on the pyridine ring which serves to withdraw more electron density than in the Pt^{II} complex owing to the added I atoms.

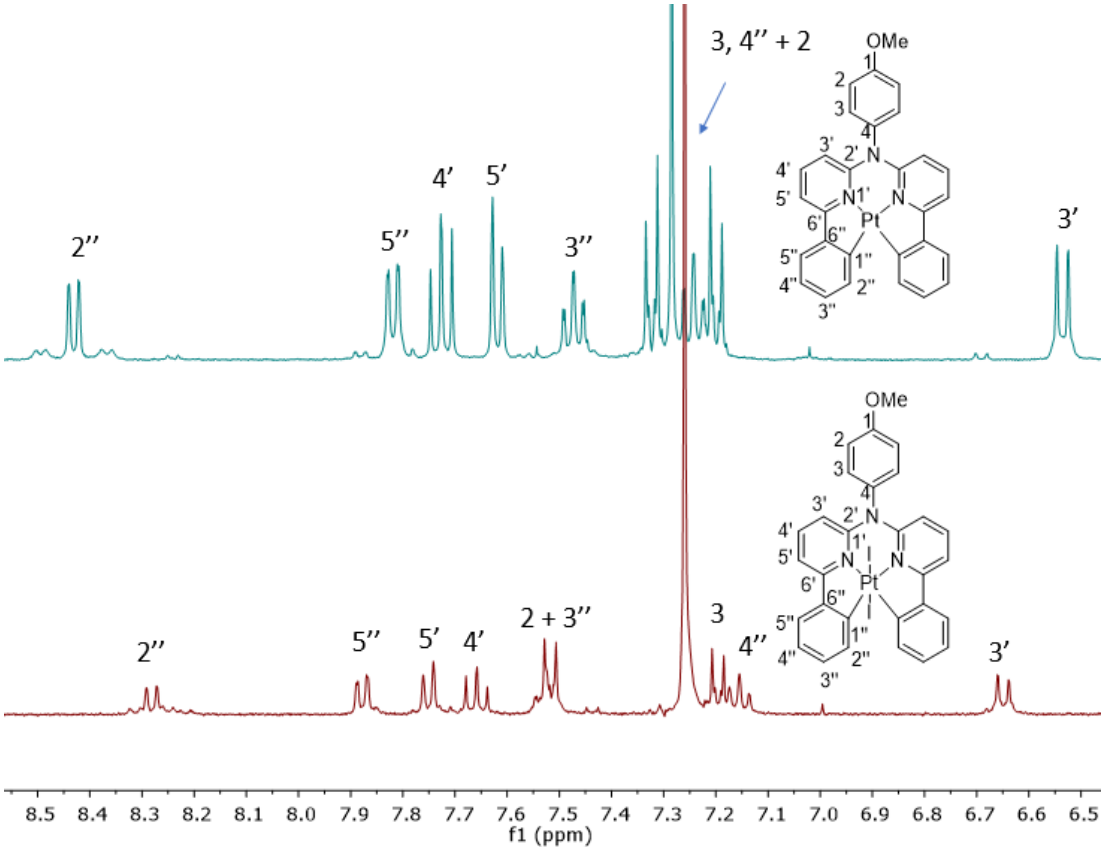

Figure 4.34: *Comparison of PtL^{19} and $PtL^{19}I_2$ ^1H NMR spectra in $CDCl_3$ at 400 MHz.*

The emission of these Pt^{IV} complexes was not investigated in this work, however Mickaële Bonneau found the Pt^{IV} complexes she synthesised to be non-emissive at RT and only emissive at 77 K. The goal with these Pt^{IV} complexes would therefore be to metathesise the chloride ligands for higher field strength ligands such as alkyne groups which could push up the d-d states to give potentially improved emission.

4.4 Chapter 4 Summary

The synthesis of previously studied Pt^{II} and Pd^{II} complexes with tetradentate ligands has been repeated, alongside the synthesis of new derivatives of these complexes. Their photophysical properties, focusing on the concentration-dependent emission for potential excimer formation, have been investigated.

It was found that thiophene and benzothiophene-containing complexes did not display any excimeric emission, thought to be due to the 5-membered thiophene groups which are electron-donating and thus push up the energy of the HOMO in each case. This could prevent the close interaction of the metals in each case which could sometimes otherwise result in MMLCT transitions. Conversely, the phenyl and difluorophenyl complexes were seen to exhibit certain degrees of excimeric emission where PtL^{20} had the highest propensity towards excimer formation.

PdL^{19} and PdL^{20} were seen to exhibit unusual photophysical behaviour, different to the other complexes. This was displayed by the formation of red-shifted emission bands that were highly structured and indicative of Pd complexes with a different structure to those anticipated. It is still unclear as to what these different species are.

Devices of selected Pd complexes have also been fabricated and revealed a maximum EQE of 3.51 % for a 10 wt. % PdL^{20}-containing device and 3.17 % for a 5 wt. % PdL^{3}-containing device. The emission displayed in the PdL^{20} device was red-shifted to that expected and thus is indicative of a different Pd species.

A new Pt^{II} complex containing a tetradentate indole-based ligand was also synthesised which gave impressive photophysical properties despite its poor solubility and this gives potential for more investigation into this type of compound and work towards Pd complexes of the same sort.

Finally, oxidation of Pt^{II} complexes containing tetradentate ligands has been achieved to form the corresponding Pt^{IV} species of composition $PtL^{n}X_2$ (where X=halogen) using $PhICl_2$ and I_2 as oxidants. This gives a good basis for possible future metathesis of weak-field I and Cl ancillary ligands for strong-field ligands such as alkyne groups.

5. Dinuclear Pt^{II} complexes containing tridentate ligands

5.1 Introduction

The basis for the work in this chapter surrounds Pt^{II}(N^C^N) complexes joined together through specific linking groups to form dinuclear complexes containing two Pt^{II}(N^C^N) sites. The importance of these dinuclear complexes comes to light with regard to efficient deep red and NIR emission that is normally hard to achieve. One way in which this emission can be accessed is through the formation of square planar Pt^{II} complex excimers. These excimers can form via *inter*molecular interactions between separate Pt moieties and/or *intra*molecular interactions when two Pt sites are present. Moreover, NIR emission can also be achieved by extending the conjugation in monomeric complexes. The following examples highlight some of the best performing NIR Pt emitters, including both mononuclear and dinuclear/bimetallic complexes. Table 5.1 at the end of this introductory section summarises the photophysical properties of selected complexes.

5.1.1 Mononuclear Pt complexes

One of the earlier noteworthy examples of a NIR-emitting OLED featuring a Pt^{II} complex came from Cocchi *et al.* in 2007.[179] Three different OLEDs were fabricated by vacuum sublimation and each contained a neat film of the mononuclear complex based on Pt(dpyb)Cl as the EML (Fig. 5.1). Peak electroluminescence emission was centred at 720, 715 and 705 nm for **91**, **92** and **93** respectively, originating from the formation of excimers through intermolecular Pt interactions. Complexes **91** and **92** gave the highest EQEs of 10.5 % each which remains a highly respectable value for NIR emission in OLED devices.

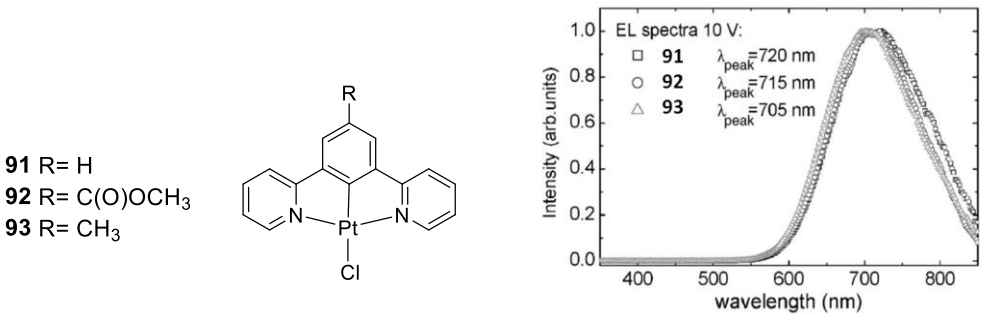

Figure 5.1: *Structures of complexes **91**-**93** incorporated into OLED devices and their corresponding EL spectra. Reproduced from Cocchi et al. by permission of AIP.*[179]

In the same year, an OLED incorporating a Pt^{II} tetraphenyltetrabenzoporphyrin (Pt(TPBP), **94**) was fabricated by Sun et al.[180] This displayed emission in the NIR owing to the extended conjugation offered by the TPBP ligand, and had a peak electroluminescence emission of 772 nm with an EQE of 8.5 % for a 4 wt. % **94** : Alq_3 EML. As can be seen from Figure 5.2 the emission bandwidth centred at 772 nm is very narrow, suggestive of potential high colour purity.

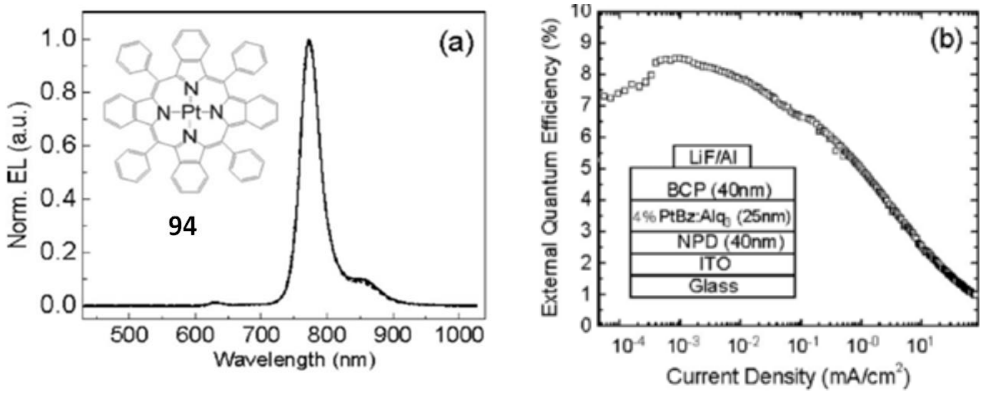

Figure 5.2: *a) Normalised electroluminescence intensity and b) EQE & device architecture of* ***94****. Reproduced from Sun et al. by permission of AIP.*[180]

More recently, Pt porphyrin derivative OLEDs have been revisited owing to these promising performances in the NIR. Huang *et al*.[181] synthesised three compounds (**95**-**97**, Fig. 5.3) according to a method previously reported by Borisov[182] which involved reaction of the porphyrin ligand with $Pt(C_6H_5CN)_2Cl_2$ in diphenylether at 160 °C. The replacement of the *meso* carbon atoms in the porphyrin ring with nitrogen was seen to shift the EL emission peak nearly 80 nm further into the infrared region which shows an effective colour-tuning strategy. For the VTE OLEDs, the parent complex **95** displayed an EL emission peak at 770 nm with an EQE of 8 %. The EQEs of the other devices decreased to 2.8 % for **96** and 1.5 % for **97**, but the emission peak maxima increased to 848 nm and 846 nm respectively and consequently they show promise for infrared device development.

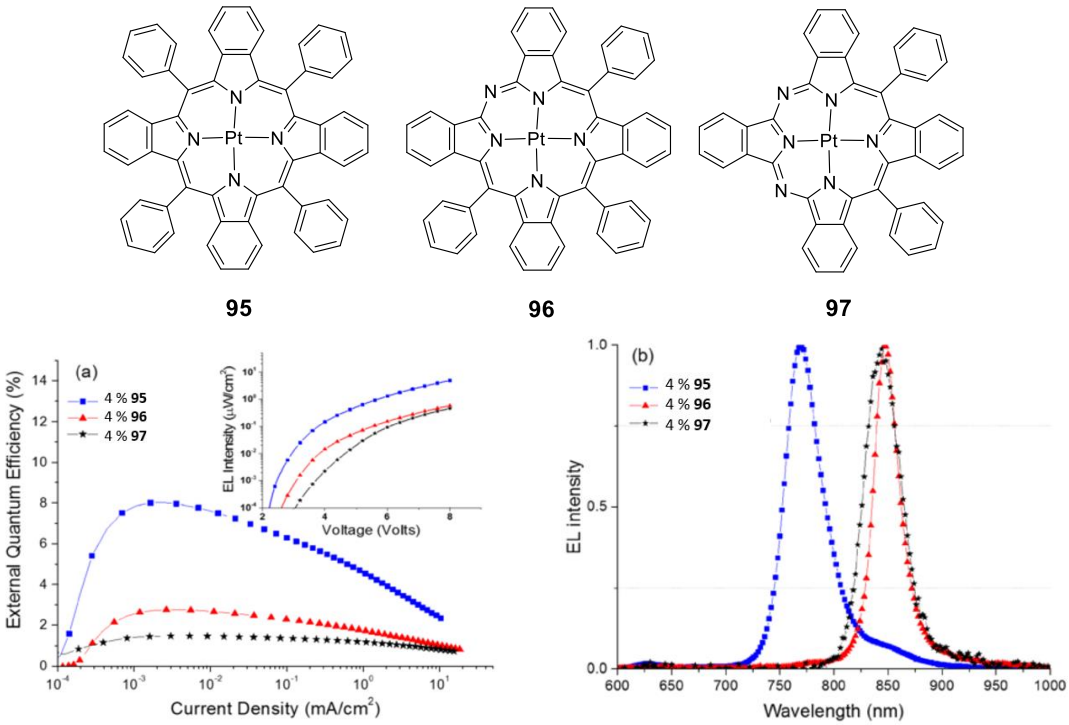

Figure 5.3: *a) EQE and b) EL of **95**, **96** and **97**. Reproduced from Huang et al. by permission of AIP.*[181]

In 2017, Zhang *et al*. described the use of Pt complexes with tetradentate salen-like ligands and their performance as red/NIR emitters in OLEDs.[183] They took inspiration from NIR-emitting organic and polymeric fluorescent dyes such as those reported by Wang *et al.* which were based on electron-donating (D) and electron-accepting (A) units separated by π spacers, and which displayed emission of λ > 1000 nm.[184] The Pt^{II} complexes synthesised by Zhang thus included D-A groups appended onto a central salophen ligand (Fig. 5.4). It was hoped that the two salophen complexes initially synthesised (**98** and **99**) would show NIR emission and also that the appendage of the donor-acceptor groups to either the head or the waist of the salophen unit as shown in Figure 5.4 might have some impact on the nature of this emission as well. It was found that complex **99** gave the most red-shifted emission when the donor-acceptor groups were appended to the head of the complex with a peak emission of EL at 695 nm, very close to the NIR. This work was extended to shift the emission directly into the NIR by synthesis of a similar salophen complex (**100**), this time changing the D-A unit to contain thiadiazole groups, resulting in emission with a peak EL of 703 nm and a device EQE of 0.88 %.[185]

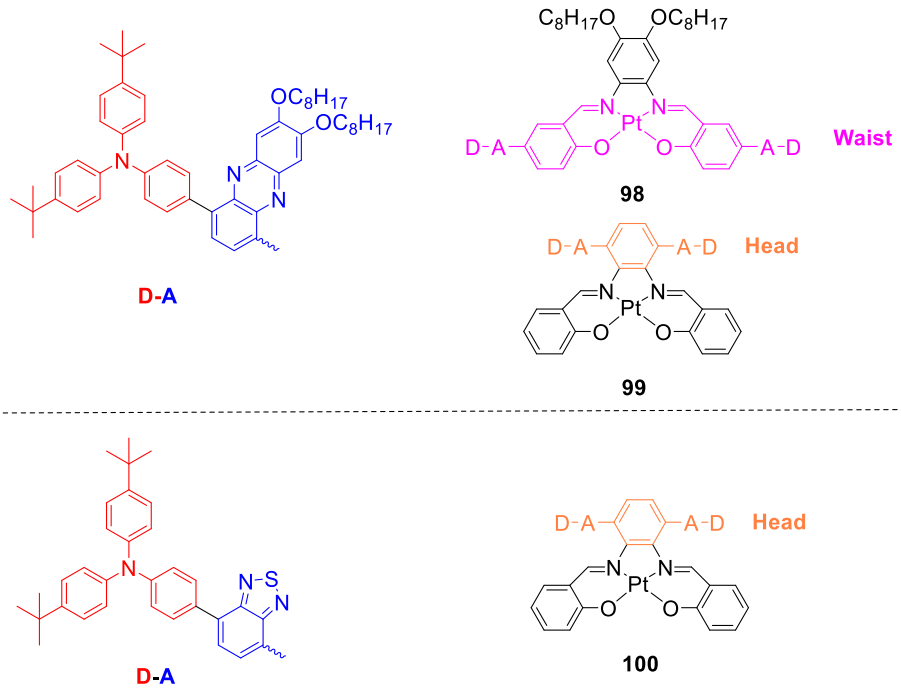

Figure 5.4: *Structures of Pt^{II} tetradentate salophen complexes:* ***98, 99*** *and* ***100****.*

As was discussed in Chapter 2, the homoleptic Pt complex containing bidentate pyrazole ligands (**26**) displayed the most impressive EQE for NIR emission of 24 % that remains unbeaten, with a peak maximum of 740 nm.[108] It is therefore of great interest to investigate all potential avenues for NIR emission, looking at the balance between intermolecular interactions which can form excimers with red-shifted emission versus those which can result in self-quenching through processes such as triplet-triplet annihilation (TTA). Another recent area of interest is in bimetallic and dinuclear complexes and how potential intramolecular interactions, dependent upon the molecular conformation, could promote this NIR emission.

5.1.2 Dinuclear/bimetallic Pt complexes

These intramolecular interactions have been previously studied by Develay in 2008 with the synthesis of a dinuclear complex in which two N^C^N-coordinated Pt^{II} ions were linked via a xanthene bridge.[186] Synthesis of the complex **101** was achieved by reaction of a N^C^N boronic acid with the xanthene derivative to form the ditopic ligand. This ligand was then added to a MeCN/H_2O (3:1) mixture with K_2PtCl_4 and stirred at reflux for 3 days to obtain the mononuclear product, and for 11 days to achieve the binuclear product (Scheme 5.1).

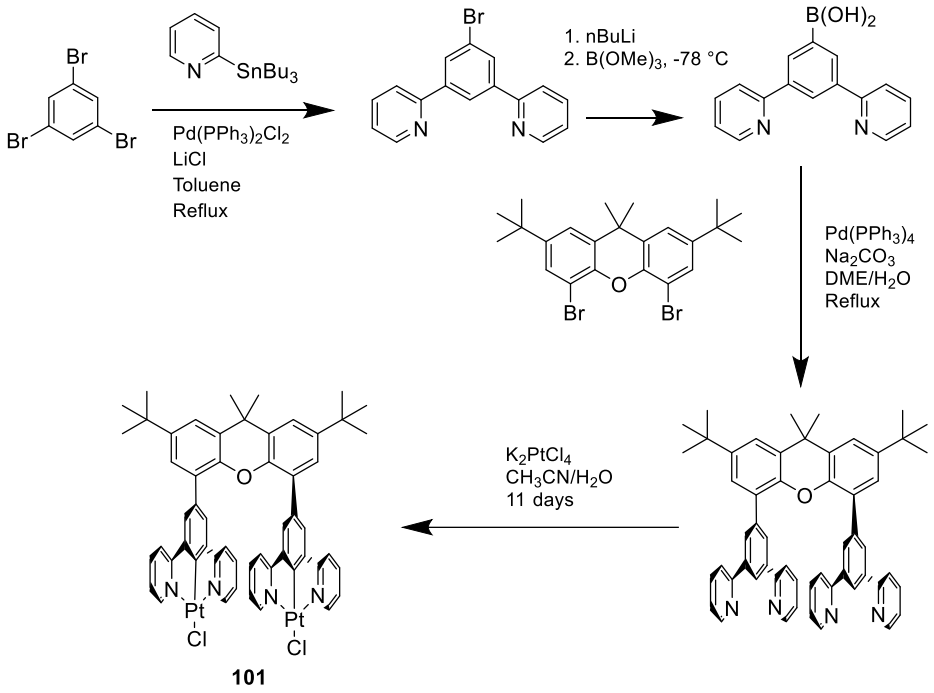

Scheme 5.1: *Synthesis of dinuclear complex* ***101****.*

Inspiration for this work was taken from Tanaka *et al*. who successfully linked two metal terpyridyl complexes together to form a dinuclear complex existing in a face-to-face conformation.[187] This face-to-face conformation has proved beneficial in promoting excimer formation, necessary for deep red emission, through intramolecular interactions. Complex **101** was found to have an emission maximum in the deep red at 690 nm with a quantum yield of 20 %. It was compared to its parent compound Pt(dpyb)Cl and it showed excimer-like emission throughout all concentrations that were measured (2×10^{-7}– 5×10^{-4} M) whilst Pt(dpyb)Cl only displayed excimeric emission at elevated concentrations and monomeric emission was also always evident (Fig. 5.5).

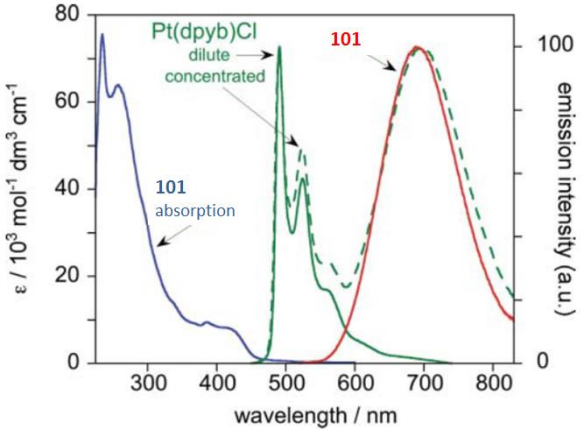

Figure 5.5: *Absorption and emission of* ***101*** *and emission of the parent compound Pt(dpyb)Cl in both dilute and concentrated solutions. Reproduced from Develay et al. by permission of the Royal Society of Chemistry.*[186]

Chan and colleagues also made use of a xanthene backbone in order to link Pt(salphen) units to dibenzofuran and biphenylene resulting in complexes **102**, **103** and **104** respectively (Fig. 5.6).[188]

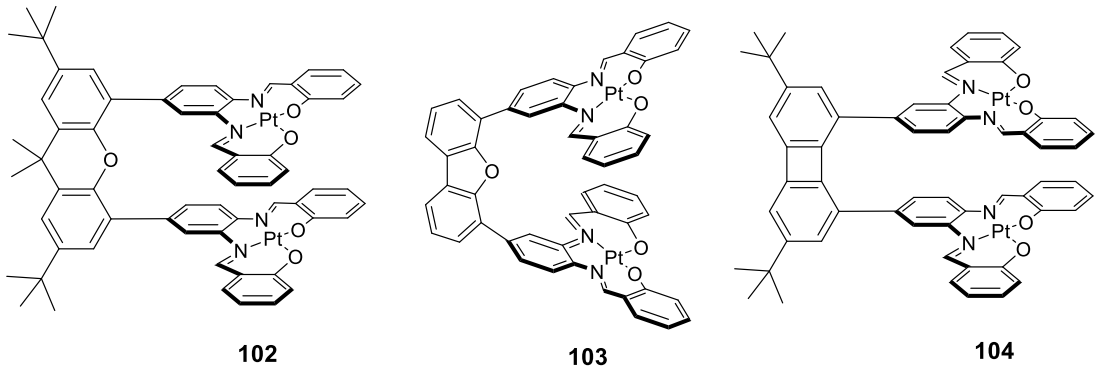

Figure 5.6*: Structures of dinuclear complexes **102**, **103** and **104**.*

Crystal structures of **102** and **104** showed that the Pt(salphen) units are twisted relative to the plane of the bridging aromatic unit (torsion angles of 43° and 36° respectively). In complex **102**, despite the intramolecular interplanar separation (defined as the mean separation between Pt and the adjacent N_2O_2 plane) being only 3.22 Å, the twist leads to the Pt atoms being displaced relative to one another, leading to a much longer Pt···Pt distance of 5.012(2) Å. In complex **104**, on the other hand, the Pt atoms are held closer to one another, with an intramolecular Pt···Pt distance of 3.359 Å. Though shorter, this is only short enough for weak Pt···Pt interaction. No crystal data was available for complex **103**, but a larger inter-planar distance was expected, given the shape of the dibenzofuran bridge. All three complexes were found to emit at similar energies in solution at RT (around 635 nm) but there was no evidence of MMLCT excited states. The respective quantum yields were 0.007, 0.080 and 0.009 for **102**, **103** and **104**. The higher PLQY of complex **103** is attributed to π-π quenching processes in **102** and **104**, facilitated by the closer separations of the Pt(N_2O_2) units.

There is also a literature precedent for bimetallic and dinuclear platinum complexes containing strong-field alkyne groups linked by the same xanthene core as for complexes **101** and **102**.[189] Muñoz-Rodríguez *et al.* synthesised a series of bimetallic and dinuclear complexes with tridentate, cyclometallating N^N^C- and C^N^C-coordinating ligands for Pt^{II} and Au^{III} respectively. In this way, new dinuclear Pt complexes containing Pt(N^C^N) units linked to a xanthene core by acetylide groups were synthesised. The complex **105,** containing *n*Bu groups at the 4-position on the pyridyl ring (Fig. 5.7), displayed an emission

maximum at 817 nm and a quantum yield of 0.0026 %. It was postulated that a ground state intramolecular interaction of the Pt units resulted in an MMLCT character of emission and gave rise to its broad, red-shifted emission.

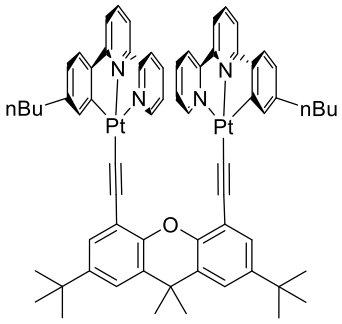

105

Figure 5.7: *Homo-dinuclear Pt complex **105** with N^N^C coordinating ligand.*

None of the aforementioned bimetallic/dinuclear complexes displaying NIR emission have been tested in OLED devices, primarily owing to poor PLQY values. Complexes such as **101** with a quantum yield of 20 % do, however, have the potential for improved EL properties and have sparked off interest into these types of complexes owing to more efficient NIR emission through potential intramolecular interactions.

Table 5.1: *PL and EL data of complexes with red/NIR emission. All EL data presented represents the maximum values obtained. *Also discussed in Chapter 2.*

Compound no. and reference	*Device Architecture*	*PL performance*			*EL performance*	
		λ_{max} (nm) [soln/film]	*PLQY (%) [soln/film]*	*Lifetime (µs) [soln/film]*	*λ_{max} (nm) [mono/exc]*	*EQE (%)*
91[179]	ITO/ TPD:PC (70 nm) / CBP (20 nm) / **91**/**92**/**93** / OXA (30 nm) /Ca.	- / 680	- / 24	- / 0.98	- / 720	10.5
92[179]		-	- / 35	- / 1.10	- / 715	10.5
93 [179]		-	- / 31	- / 1.10	- / 705	10.0
94[180]	NPD (40 nm) / (4 wt. % **94**, TPBD) : Alq_3 (40 nm) / Alq_3 (50 nm) / LiF (1nm) / Al (110 nm).	-	-	- / 45	- / 772	8.5
95 [181]	ITO/ PEDOT:PSS / NPD (30nm) / TAPC (10nm) / Alq_3 : 4 wt. % **95**/**96**/**97** (25 nm) / BCP (40 nm) / LiF / Al	770 / -	51 / -	47 / -	- / 770	8.0
96 [181]		842 / -	22 / -	0.4 / -	- / 848	2.8
97 [181]		840 / -	17 / -	0.2 / -	- / 846	1.5
98[183]	PVK:OXD-7 host and **98**/**99** dopant	646 / 628			- / 653	0.1
99 [183]		670 / 693			- / 695	1.36
100[185]	ITO /PEDOT / PVK : OXD-7 : **100** (50 nm) / TPBI (30 nm) / Ba (4 nm) / Al (100 nm)	697,730	1.2 / -	0.88 / -	- / 703	0.88
101 [186]	-	690 / -	20 / -	1.7 / -	-	-
105 [189]	-	817/ -	26 / -	26 ns / -	-	-
26 [108]*	ITO (100 nm) / HATCN (10 nm) / NPB (50 nm)/ mCP (15 nm)/ **26** (20 nm)/ TPBi (60 nm) / Liq (2 nm) / Al (100 nm)	- / 740	- / 81	- / 310	- / 740	24

5.2 Objectives

We aimed to prepare a larger quantity of **101** (called $L^{24}(PtCl)_2$ in this work, Scheme 5.4) in order to test it in an OLED. We also sought to explore other new dinuclear Pt complexes incorporating a xanthene linker that have the potential to form intramolecular excimers displaying efficient, red-shifted emission nearing the NIR. The distinction between intra- and intermolecular excimers in these dinuclear complexes is shown in Figure 5.8. These complexes will be studied for their photophysical properties and hopefully performance in OLED devices.

Two classes of complexes have been investigated. The first class is based on the work by Develay which link Pt moieties to the xanthene core via the phenyl ring of the N^C^N group (class 1) and the second set have the same xanthene core but appended with acetylide groups to bind directly to the Pt centres after exchange of the chloride ancillary ligand (class 2) (Fig. 5.8).

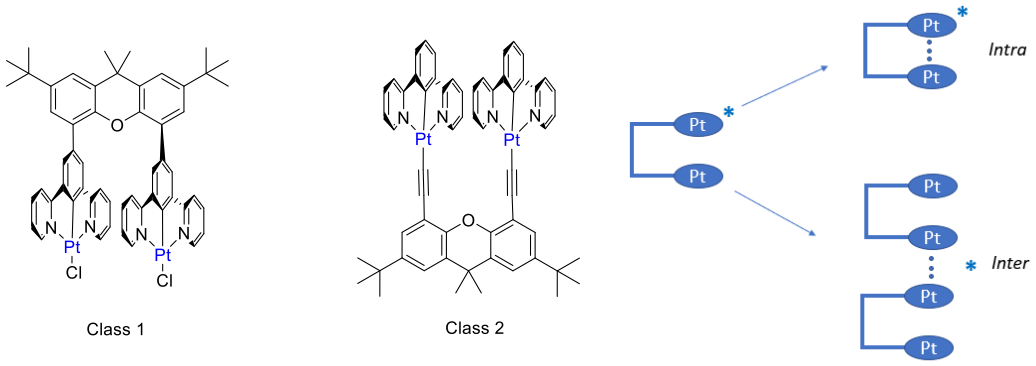

Figure 5.8: *Structures of parent class 1 and class 2 dinuclear Pt complexes (left) and the representation of intra- and intermolecular excimers in these dinuclear complexes.*

5.3 Results and Discussion

5.3.1 Class 1 complexes

5.3.1.1 Synthesis

In the synthesis of the class 1 complexes, the parent complex $L^{24}(PtCl)_2$ was synthesised in the same way as reported by Develay, but it was found that complexation of the Pt ions could be achieved by refluxing in acetic acid and water (3:1) for 3 days instead of MeCN/H_2O (3:1) for 11 days.

An analogue incorporating CF_3 substituents in the 4-position of the phenyl rings, $L^{25}(PtCl)_2$, was also synthesised for comparison. The first step in this synthesis was a Miyaura borylation reaction, first reported in 1995 for reaction between any aryl halide and bis(pinacolato)diboron (b_2pin_2) to form boronates.[190] This enabled the formation of the CF_3 substituted N^C^N boronate which was then Suzuki cross-coupled with the dibromo xanthene derivative to form the resulting CF_3 substituted N^C^N ligand (Scheme 5.2).

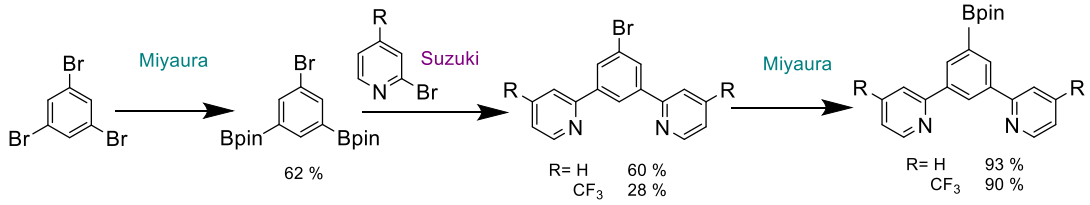

Miyaura = $Pd(dppf)Cl_2$, B_2pin_2, KOAc, Dioxane, Reflux, 18 h

Suzuki = $Pd(PPh_3)_4$, Na_2CO_3, DME/H_2O, Reflux, 24 h

Scheme 5.2: *Synthesis of N^C^N boronates.*

Attempts were made to synthesise the parent ligand H_2L^{24} in the same manner as the CF_3 substituted compound but the Suzuki reaction between the xanthene derivative and the N^C^N boronate was not successful in this case (Scheme 5.3).

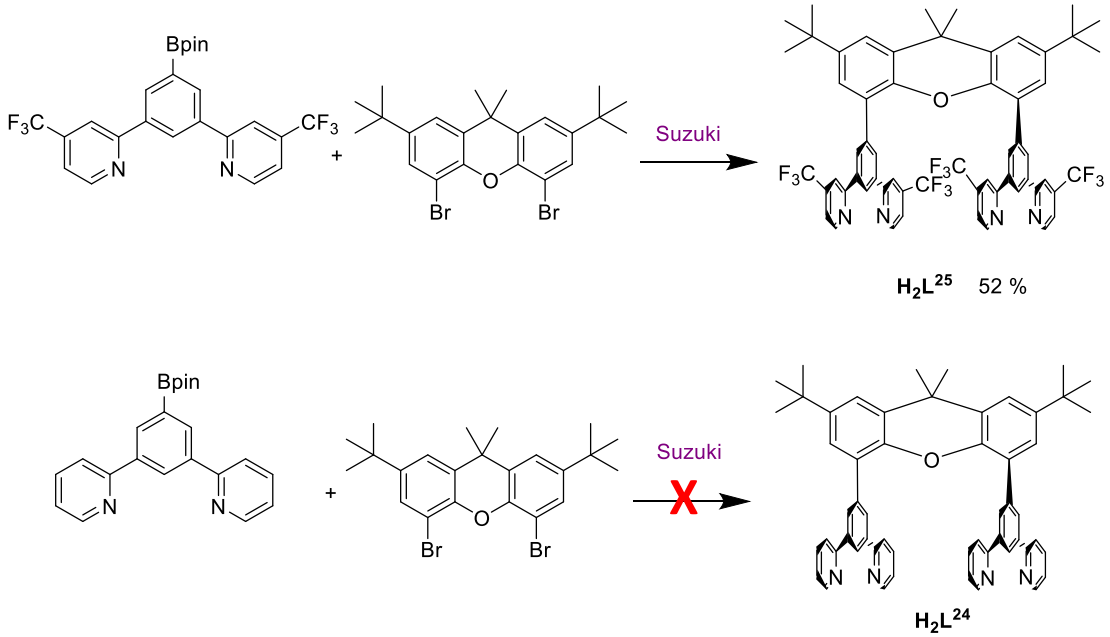

H_2L^{25} 52 %

H_2L^{24}

Scheme 5.3: *Synthesis of H_2L^{25} and the attempted synthesis of H_2L^{24} via the boronate Suzuki method.*

Complexation was carried out in the same manner for both $L^{24}(PtCl)_2$ and $L^{25}(PtCl)_2$ under argon, by refluxing the ligand with K_2PtCl_4 in an acetic acid/H_2O (3:1) solvent mixture for 3 days (Scheme 5.4).

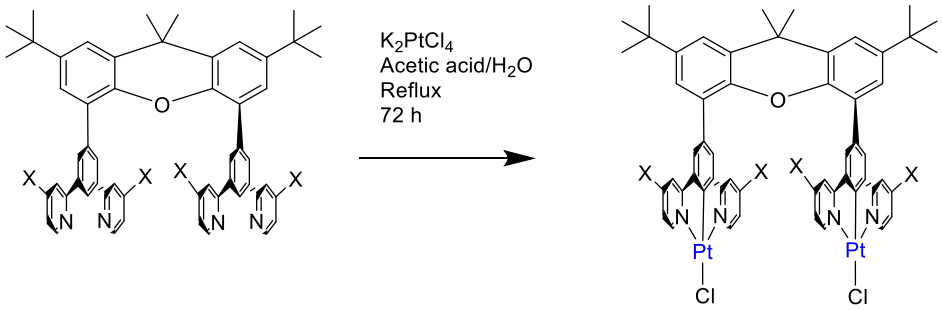

Scheme 5.4: *Synthesis of $L^{24}(PtCl)_2$ and $L^{25}(PtCl)_2$.*

Complexes $L^{24}(PtCl)_2$ and $L^{25}(PtCl)_2$ were obtained in yields of 4 % and 66 % respectively. It was not possible to obtain a pure sample of the N^C^N boronic acid and this resulted in crude H_2L^{24} which was reacted on to give a poor yield for complexation.

5.3.1.2 Photophysical Properties

All photophysical properties for the complexes discussed in this chapter are summarised in Table 5.5. The absorption spectra of $L^{24}(PtCl)_2$ and $L^{25}(PtCl)_2$ show similar profiles to one another with the latter being slightly red-shifted. Bands in the region of 350 to 450 nm are attributed to charge-transfer transitions involving the metal and halide co-ligand (Fig. 5.9). Absorbances at shorter wavelengths have higher extinction coefficients owing to π→π* transitions associated with the xanthene moiety. A very weak absorption band centred at 496 nm is also present for the parent compound $L^{24}(PtCl)_2$ (Fig. 5.9 inset) and is suggestive of ground-state Pt···Pt interactions (i.e. MMLCT), but this is not present in $L^{25}(PtCl)_2$.

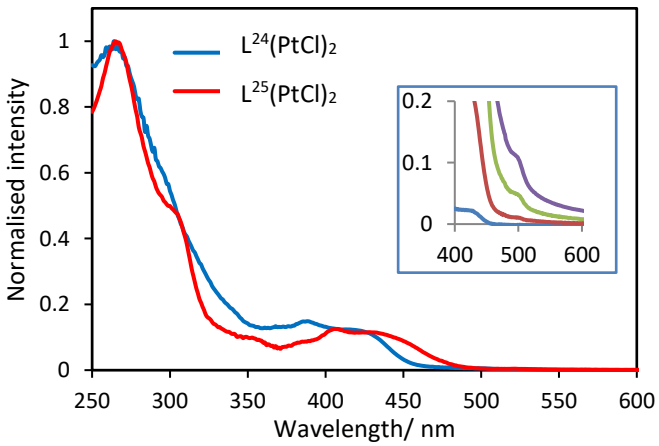

Figure 5.9*: Normalised absorption spectra of $L^{24}(PtCl)_2$ and $L^{25}(PtCl)_2$ and concentration-dependent absorption of $L^{24}(PtCl)_2$ (inset).*

The emission of $L^{24}(PtCl)_2$ is virtually all excimer-like with a λ_{max} of 690 nm, independent of concentration in the range investigated (2×10^{-7} to 5×10^{-4} M), and trace monomer-likeemission is observed at lower concentrations (Fig. 5.10). This proves the high propensity of $L^{24}(PtCl)_2$ to form excimers, probably owing to a locked face-to-face conformation of the two Pt centres. The interactions responsible for excimer formation were therefore assigned as intramolecular. As was communicated in the Develay paper, this compound exhibits a high quantum yield for red emission, found here to be 15 % with a long lifetime of 5.4 µs.

In contrast, the emission of $L^{25}(PtCl)_2$ showed both monomer and excimer emission over a range of concentrations from 10^{-7} to 10^{-4} M (Fig. 5.10). This suggests that, although excimer formation is still occurring, it is inhibited by the presence of the CF_3 groups, perhaps due to steric interference preventing close interactions. Neither purely monomeric nor purely excimeric emission was observed in the concentration range investigated which could suggest that inter- as well as intramolecular interactions assist in excimer formation here.

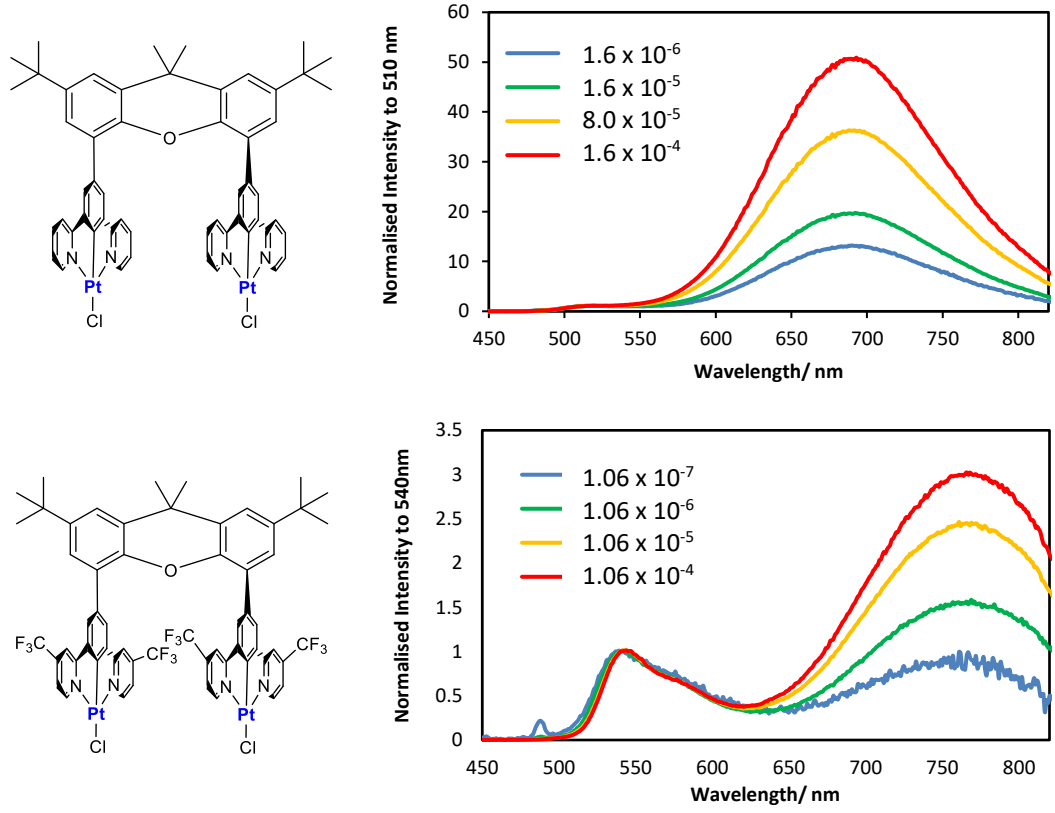

***Figure 5.10**: Concentration-dependent emission of $L^{24}(PtCl)_2$ and $L^{25}(PtCl)_2$. Concentrations are given in mol dm^{-3}.*

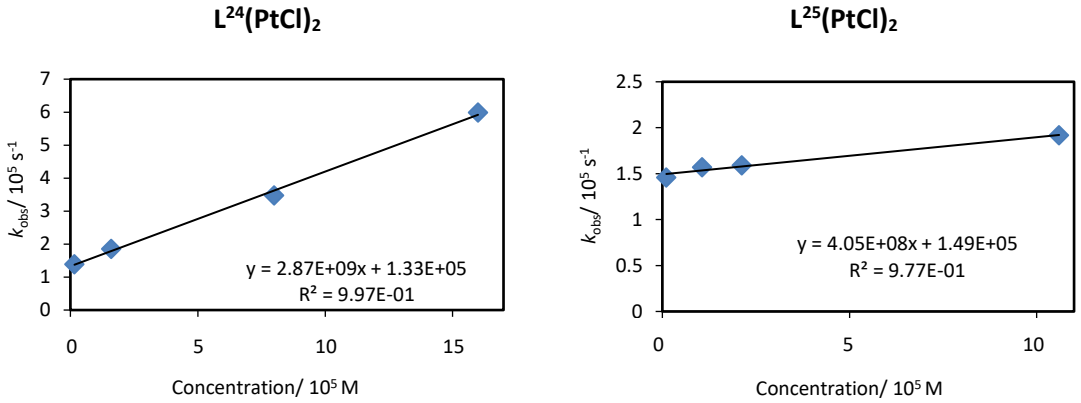

Figure 5.11: *Stern-Volmer plots for class 1 complexes showing self-quenching parameters.*

By probing the monomer emission at 510 and 540 nm for $L^{24}(PtCl)_2$ and $L^{25}(PtCl)_2$ respectively, the change in decay rates as a function of concentration were fitted to a Stern-Volmer equation and a linear dependence was observed in each case (Fig. 5.11). This supports some contribution to excimer formation from intermolecular interactions.

From the Develay paper, it was observed that, at 77 K, the emission of $L^{24}(PtCl)_2$ showed only the monomer form and this was reproduced here. For $L^{25}(PtCl)_2$ the 77 K emission showed a strong monomer contribution but also some excimer, even in very dilute butyronitrile glass (Fig. 5.12).

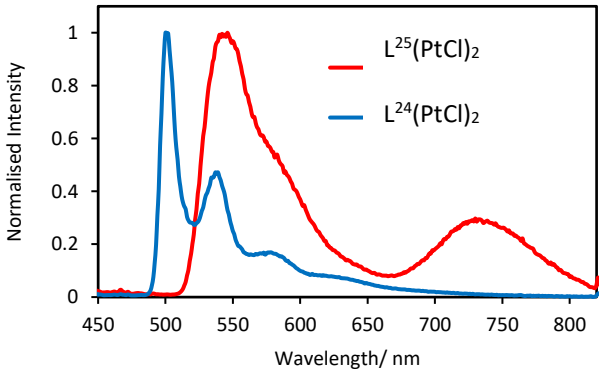

Figure 5.12: *77 K spectra of $L^{24}(PtCl)_2$ and $L^{25}(PtCl)_2$ in butyronitrile glass.*

It was previously postulated for $L^{24}(PtCl)_2$ that the strong monomeric emission at 77 K was due to a lack of thermal activation which is needed for the formation of the excimeric state centred at 690 nm. In this case there would need to be some motion of the two Pt(N^C^N)Cl units relative to one another. The fact that $L^{25}(PtCl)_2$ displays excimeric emission at 77 K may not follow the same trend and in fact the Pt(N^C^N)Cl units may

already be positioned in the favourable orientation in the ground state and at low temperatures for excimers to form.

5.3.1.3 Comparison with parent complexes

In order to try and gain a deeper understanding of the photophysical properties that these dinuclear complexes display, it is important to compare them with their mononuclear derivatives. In this case, the mononuclear derivatives are Pt(dpyb)Cl and Pt(dpybX)Cl, where X= 2 x CF_3 on the 4-pyridyl position. The emission of Pt(dpyb)Cl shows the evolution of high-intensity excimer emission with increasing concentration, but which does not exceed the relative intensity of monomer emission at the highest concentration measured (1.6 x 10^{-4} M) (Fig. 5.13). In $L^{24}(PtCl)_2$ the concentration-dependent emission is purely excimeric, independent of concentration, and thus is in stark contrast to the mononuclear derivative. The PLQY is higher for the mononuclear complex Pt(dpyb)Cl at a concentration displaying purely monomeric emission, in comparison to the dinuclear complex (0.6 vs. 0.15) which is understandable in terms of the red-shift for the excimeric emission of $L^{24}(PtCl)_2$ which is likely to suffer from enhanced k_{nr} due to the energy gap law.

Pt(dpyb)Cl[20]

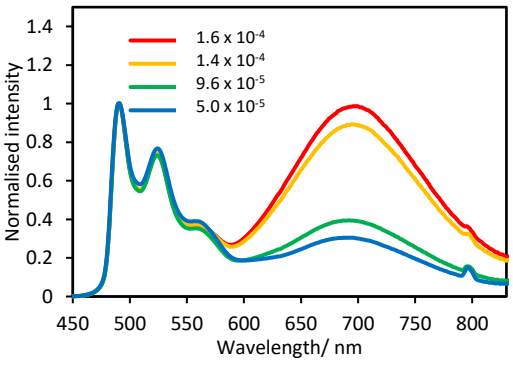

ϕ = 0.60

λ_{max} = 491, 524, 562 (683) nm

τ_0 = 7.2 µs

k_{sq}= 5.3 x 10^9 $M^{-1}s^{-1}$

Pt(dpybX)Cl[i]

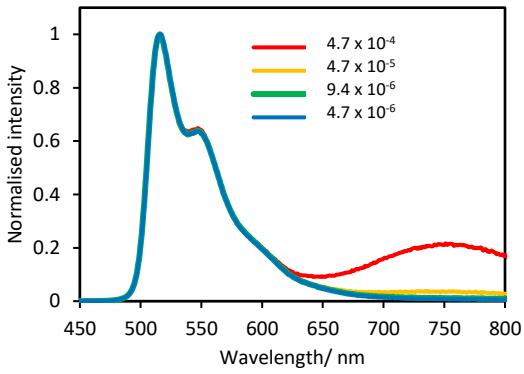

ϕ = 0.21

λ_{max} = 517, 545 (754) nm

τ_0 = 5.1 µs

k_{sq} = 3.1 x 10^9 $M^{-1}s^{-1}$

Figure 5.13: *Concentration-dependent emission of Pt(dpyb)Cl and Pt(dpybX)Cl (X = 2 x CF_3 on the 4-pyridyl position) and their photophysical properties where λ_{max} values for the excimer are quoted in the parentheses.*

[i] This complex was synthesised by Chris Harris (MChem student) and the photophysical data carried out by me.

For Pt(dpybX), purely monomeric emission is displayed at concentrations below 4.68 x 10^{-5} M, whilst in the dinuclear complex $L^{25}(PtCl)_2$ a mixture of monomeric and excimeric emission is maintained throughout the concentration range investigated (1.06 x 10^{-7} – 1.06 x 10^{-4} M) and the k_{sq} values of each complex are 3.1 and 0.4 x 10^9 $M^{-1}s^{-1}$ respectively. This differs from $L^{24}(PtCl)_2$ where excimeric emission was dominant at all concentrations, suggesting that the incorporation of CF_3 groups causes some steric interference to excimer formation. The emissive behaviour of $L^{25}(PtCl)_2$ supports some contribution from intramolecular interactions to the formation of the excimer, however, this may be much less pronounced in comparison to $L^{24}(PtCl)_2$. Indeed, intermolecular interactions may also have a large contribution to the formation of excimers in $L^{25}(PtCl)_2$, like those seen in the mononuclear complex Pt(dpybX)Cl. The PLQY values of 0.21 for Pt(dpybX) and 0.05 for $L^{25}(PtCl)_2$ are lower than those for Pt(dpyb)Cl and $L^{24}(PtCl)_2$, probably owing to the incorporation of CF_3 groups on the pyridyl rings which could increase non-radiative decay through vibrational relaxation.

5.3.2 Class 2 complexes

5.3.2.1 Synthesis

A range of complexes were synthesised containing different substituents on the N^C^N ligand of the form $L^{26}(Pt(dpybX))_2$, where X = A, B, C, D and E that are outlined in Scheme 5.5. The mononuclear starting complexes of the form Pt(dpybX)Cl were synthesised by reaction of the dpybX ligand with K_2PtCl_4 in refluxing acetic acid.[ii] The synthesis method that was adopted to make the xanthene bis-acetylide bridge (H_2L^{26}) followed the work of Muñoz-Rodríguez *et al*. which is also shown in Scheme 5.5. Complexation was then achieved by reacting two equivalents of the Pt(dpybX)Cl complex with H_2L^{26} in MeOH/DCM in the presence of NaOMe to act as a base for the deprotonation of the alkyne units. The reaction was done in the presence of air offering a facile synthesis route to these dinuclear complexes, giving scope for many other derivatives. There was no evidence of complex formation containing only one Pt unit linked to the xanthene core. Yields varied from 16 % to 73 % with $L^{26}(Pt(dpybC))_2$ giving the highest yield. This may be due to the increased solubility of the starting mononuclear complex Pt(dpyb*C*)Cl which contains the ^{t}Bu group.

[ii] Mononuclear Pt(dpybX)Cl complexes were synthesised by either Chris Harris or Rebecca Salthouse (MChem students in our group).

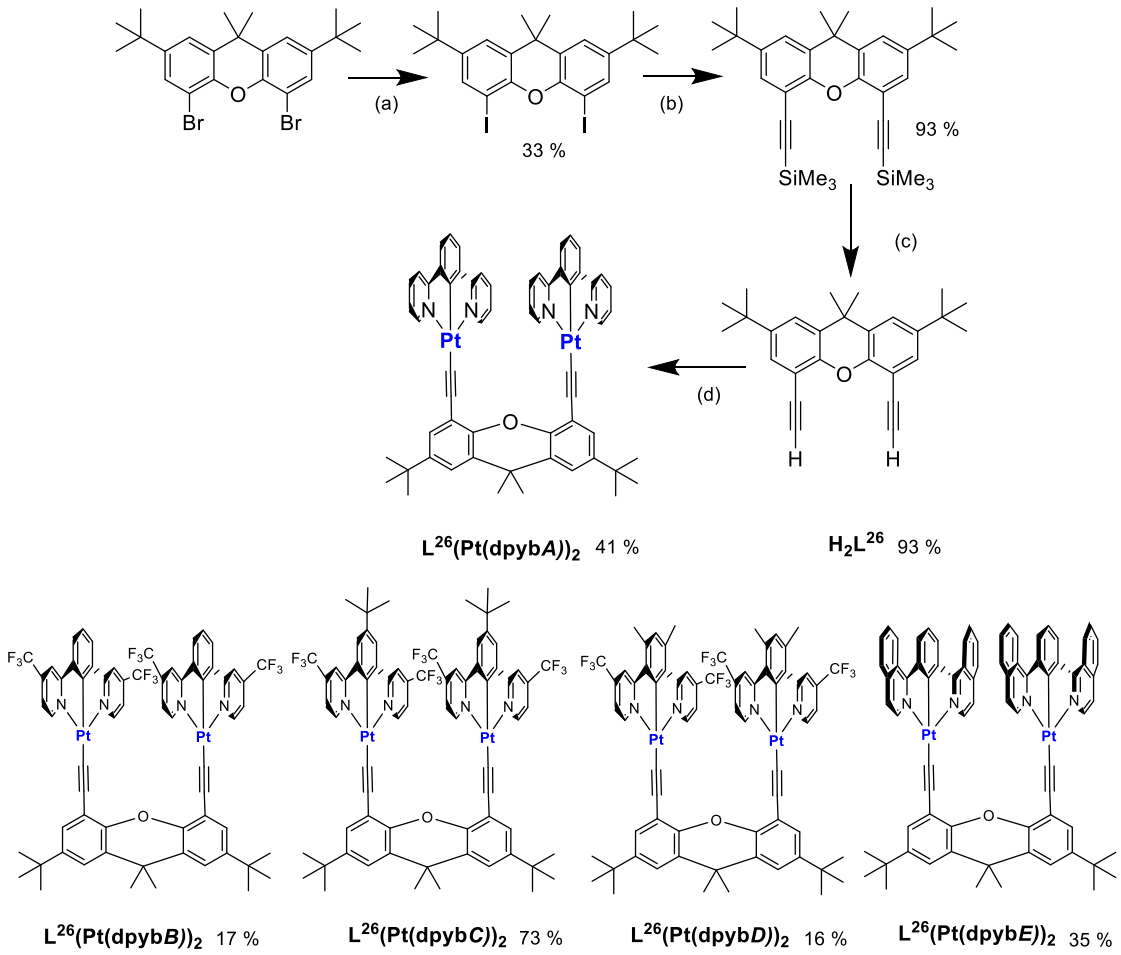

Scheme 5.5: *Synthesis of group 2 dinuclear Pt compounds. (a) THF dry, nBuLi in hexanes, I_2 , -20˚C to RT, (b) $Pd(PPh_3)_2Cl_2$, CuI, trimethylsilylacetylene, NEt_3, 60 °C, 24h, (c) K_2CO_3, MeOH/DCM, RT, 12h, (d) PtL^XCl, NaOMe, MeOH/DCM, 50 °C, 48h.*

Crystals of L^{26}(Pt(dpyb*A*))$_2$ suitable for X-ray diffraction were obtained by slow evaporation of a solution in chloroform. The crystal structure revealed two independent molecules in the unit cell which differed only by the orientation of the ^{t}Bu group (Fig. 5.14). The crystals revealed long intramolecular and intermolecular Pt···Pt distances of 4.660 Å and 8.538 Å respectively. The Pt atoms are off-centred and, by taking the Pt(N^C^N) unit as a plane, torsion angles between the planes of the Pt(N^C^N) units and the xanthene linker were 125.3 and 129.6 °. Bond lengths were seen to be very similar to Pt(dpyb)Cl, for instance, Pt1—C7 and Pt2—C50 were 1.94 and 1.96 Å (cf. the cyclometallated carbon-Pt bond in Pt(dpyb)Cl of 1.90 Å[20]). Interestingly, bond lengths between Pt atoms and acetylide carbons were slightly longer (2.06 and 2.07 Å for Pt1—C17 and Pt2—C43 respectively) (Table 5.2).

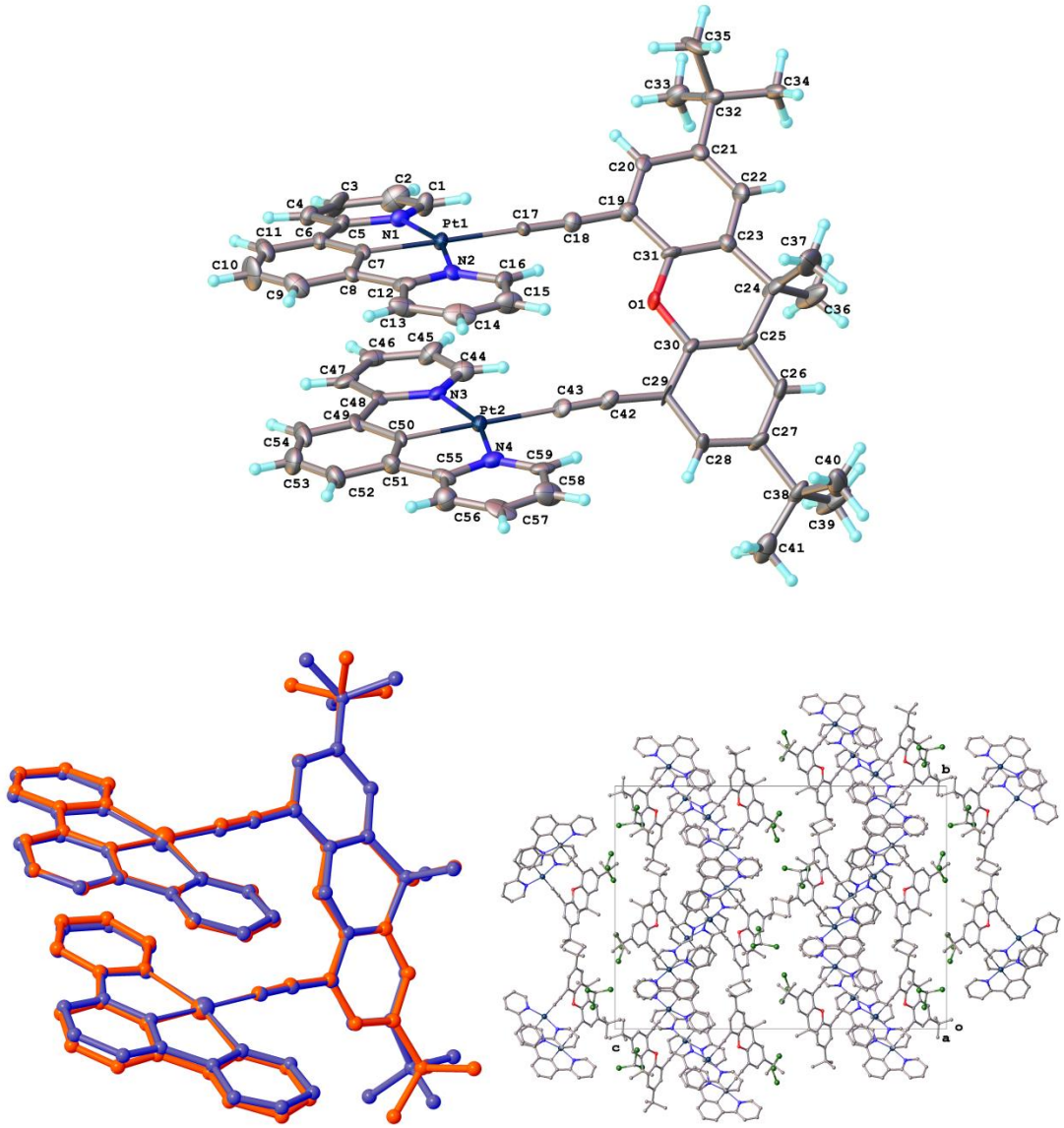

Figure 5.14: *Crystal structure and packing for $L^{26}(Pt(dpybA))_2$.*

Table 5.2: *Selected bond lengths and angles for $L^{26}(Pt(dpybA))_2$.*

Bond Lengths/ Å		*Bond Angles / °*	
Pt1—N1	2.042(9)	N1-Pt1-C17	100.2(4)
Pt1—N2	2.038(10)	N2-Pt1-N1	151.3(4)
Pt1—C7	1.941(11)	N2-Pt1-C17	100.3(4)
Pt1—C17	2.055(11)	C7-Pt1-N1	79.7(5)
Pt2—N3	2.046(10)	C7-Pt1-N2	79.9(4)
Pt2—N4	2.029(11)	C7-Pt1-C17	179.4(5)
Pt2—C43	2.068(11)	N3-Pt2-C43	99.6(4)
Pt2—C50	1.959(11)	N4-Pt2-N3	159.7(4)
		N4-Pt2-C43	100.7(4)
		C50-Pt2-N3	79.3(5)
		C50-Pt2-N4	80.5(2)
		C50-Pt2-C43	178.4(5)

Crystals of $L^{26}(Pt(dpybD))_2$ suitable for X-ray diffraction were also obtained by slow evaporation of a solution in chloroform. The crystals revealed long intramolecular and intermolecular Pt···Pt distances of approximately 5.0 Å for each (Fig. 5.15). The torsion angles between the planes of the Pt(N^C^N) units with the xanthene linker were calculated as 136.5 and 137.4° which are greater than those found in the crystal structure of $L^{26}(Pt(dpybA))_2$ possibly due to the CF_3 groups posing a greater steric hindrance. Bond lengths were seen to be very similar to those found in the crystal structure of $L^{26}(Pt(dpybA))_2$ (Table 5.3).

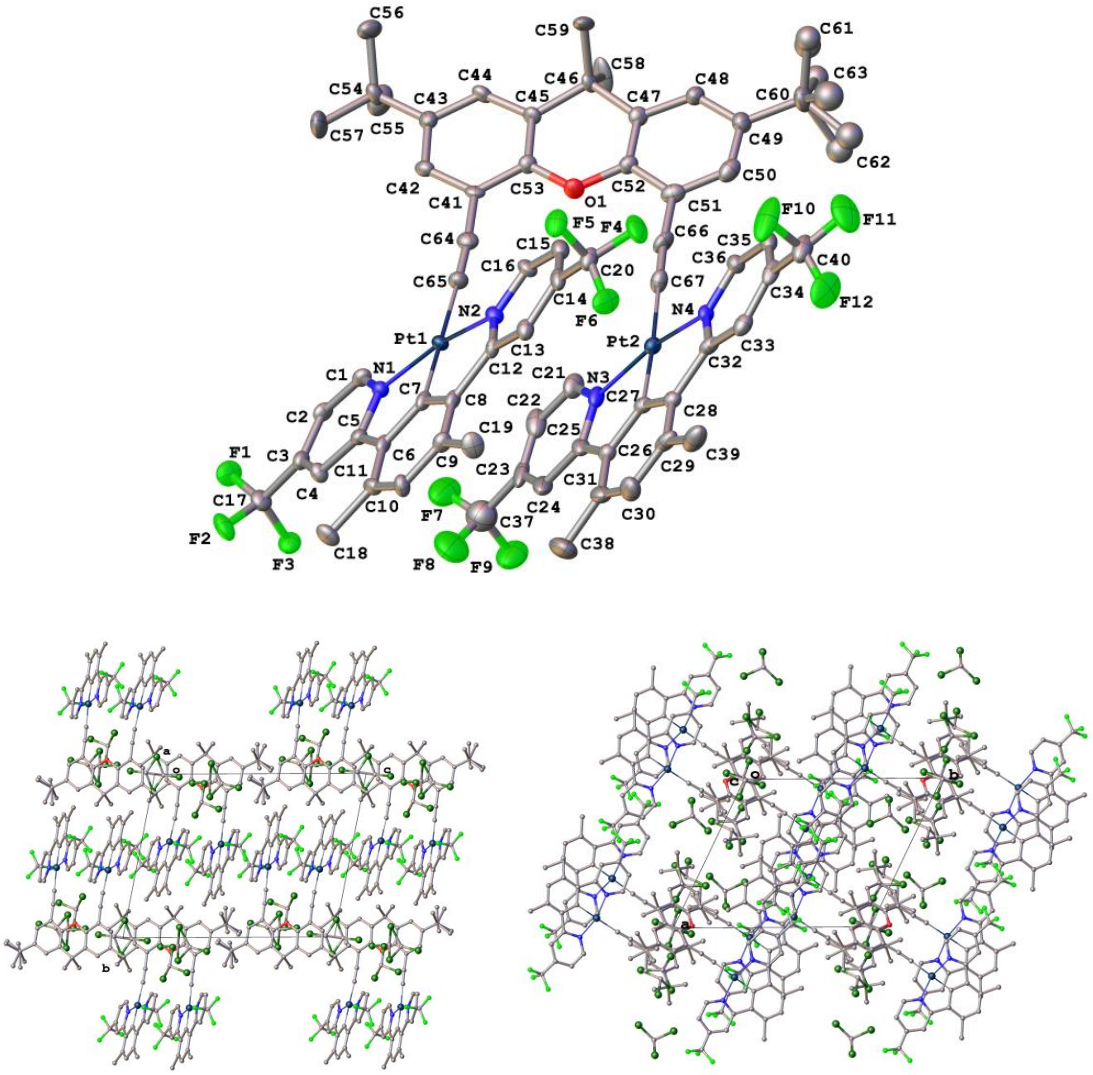

Figure 5.15: *Crystal structure and packing for* $L^{26}(Pt(dpybD))_2$.

Table 5.3: *Selected bond lengths and angles for $L^{26}(Pt(dpybD))_2$.*

Bond Lengths/ Å		*Bond Angles / °*	
Pt1—N1	2.017(6)	N1-Pt1-N2	161.9(2)
Pt1—N2	2.2024(6)	N1-Pt1-C65	99.9(3)
Pt1—C7	1.926(3)	N2-Pt1-C65	98.2(3)
Pt1—C65	2.057(7)	C7-Pt1-N1	80.8(2)
Pt2—N3	2.005(6)	C7-Pt1-N2	81.2(2)
Pt2—N4	2.023(5)	C7-Pt1-C65	179.2(2)
Pt2—C27	1.910(3)	N3-Pt2-N4	161.4(3)
Pt2—C67	2.036(8)	N3-Pt2-C67	99.1(3)
		N4-Pt2-C67	99.5(3)
		C27-Pt2-N3	79.8(2)
		C27-Pt2-N4	81.6(2)
		C27-Pt2-C67	177.1(2)

Crystals of $L^{26}(Pt(dpyb\mathit{E}))_2$ suitable for X-ray diffraction were obtained by slow diffusion of hexane into a DCM solution (Fig. 5.16). The crystals revealed much shorter Pt···Pt interactions than for $L^{26}(Pt(dpyb\mathit{A}))_2$ and $L^{26}(Pt(dpyb\mathit{D}))_2$ where the intramolecular Pt···Pt distances were 3.976 Å. The Pt atoms are off-centred in the complex and torsion angles between the planes of the Pt(N^C^N) units and the xanthene linker were much smaller than for those seen in the previous complex crystal structures at 61.34 and 60.15 °. Indeed, it is noticeable that the acetylide bonds point inwards in these molecules, facilitating the closer intramolecular Pt···Pt interactions compared to $L^{26}(Pt(dpyb\mathit{A}))_2$ and $L^{26}(Pt(dpyb\mathit{D}))_2$ where the acetylide bonds appear to point outwards. The complex is seen to pack in a head-to-tail manner and the closest intermolecular Pt···Pt distances were 5.260 Å.

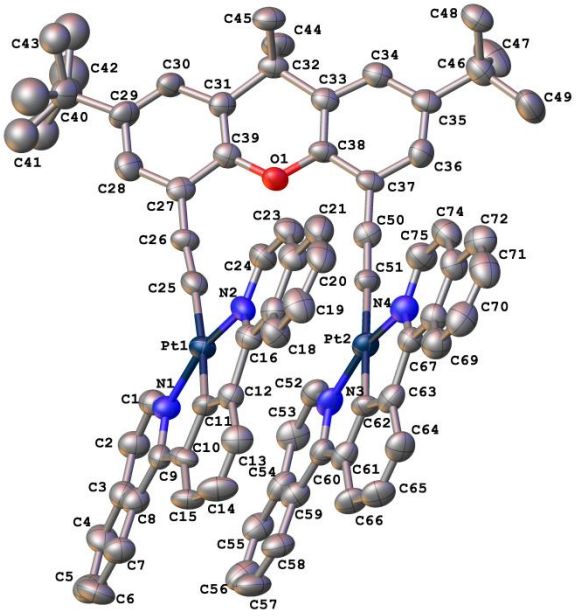

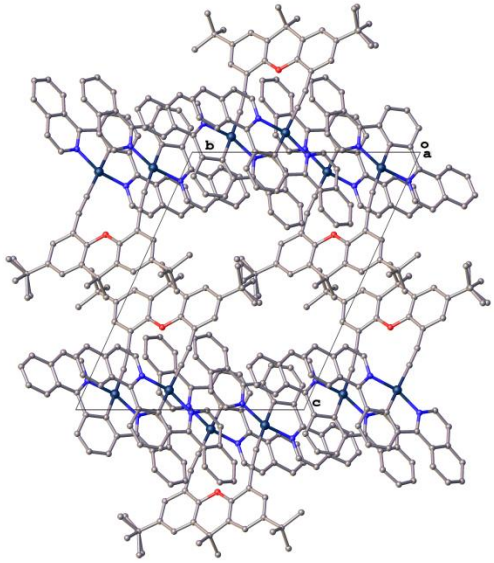

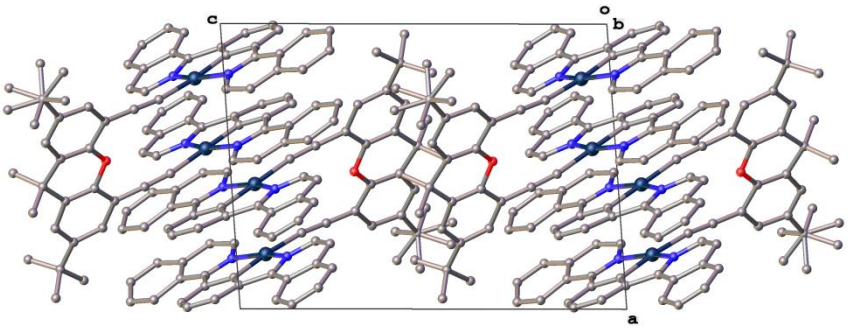

Figure 5.16: *Crystal structure and packing for $L^{26}(Pt(dpybE))_2$.*

Table 5.4: *Selected bond lengths and angles for $L^{26}(Pt(dpybE))_2$.*

Bond Lengths/ Å		*Bond Angles / °*	
Pt1—N1	2.0068(8)	N1-Pt1-N2	160.2(4)
Pt1—N2	2.016(10)	N1-Pt1-C25	101.5(4)
Pt1—C11	1.895(11)	C11-Pt1-N1	79.5(5)
Pt1—C25	2.014(13)	C11-Pt1-N2	80.8(5)
Pt2—N3	1.985(11)	C11-Pt1-C25	175.0(4)
Pt2—N4	2.049(11)	C25-Pt1-N2	98.3(4)
Pt2—C51	1.983(12)	N3-Pt2-N4	160.3(4)
Pt2—C62	1.888(10)	C51-Pt2-N3	102.2(4)
		C51-Pt2-N4	97.4(4)
		C62-Pt2-N3	78.5(4)
		C62-Pt2-N4	81.8(5)
		C62-Pt2-C51	179.0(4)

5.3.2.2 Photophysical properties

The absorption spectra of the class 2 complexes have a similar profile to the class 1 complexes with red-shifted absorption for the charge transfer transitions centred at 450 nm and additional absorptions extending to 550 nm are also apparent. Complex $L^{26}(Pt(dpyb\mathit{E}))_2$ has a higher intensity for these lower energy transitions in comparison to the other complexes, likely due to the extended conjugation in the isoquinoline ring (Fig. 5.17).

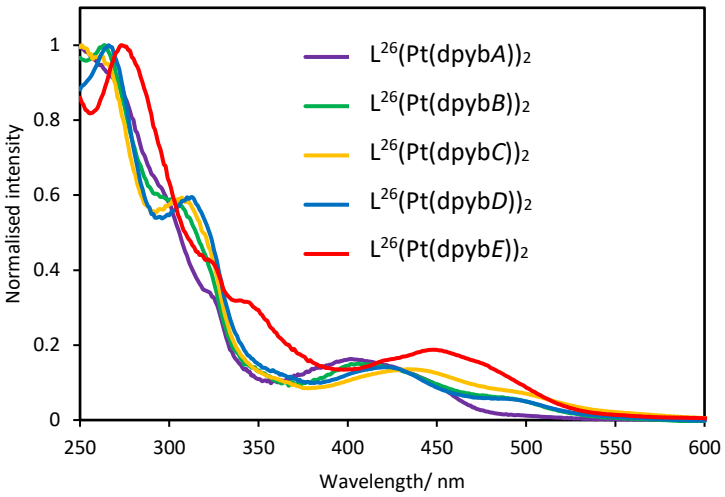

Figure 5.17: *Absorption spectra of class 2 complexes in DCM solution.*

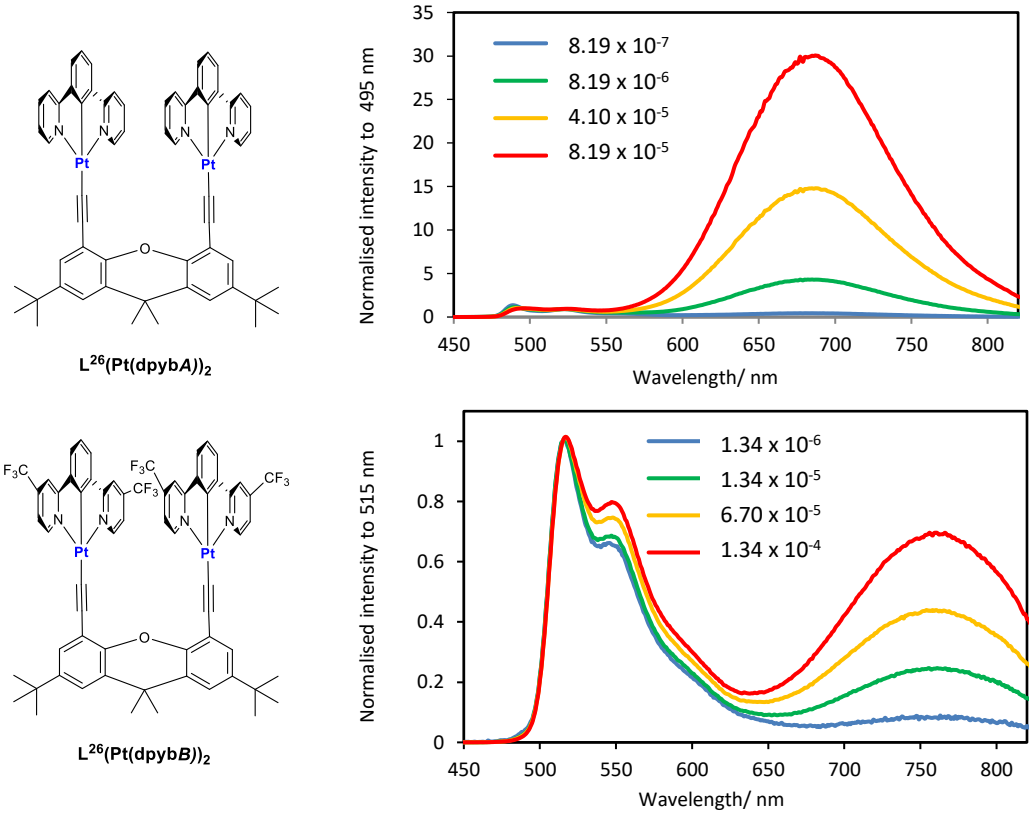

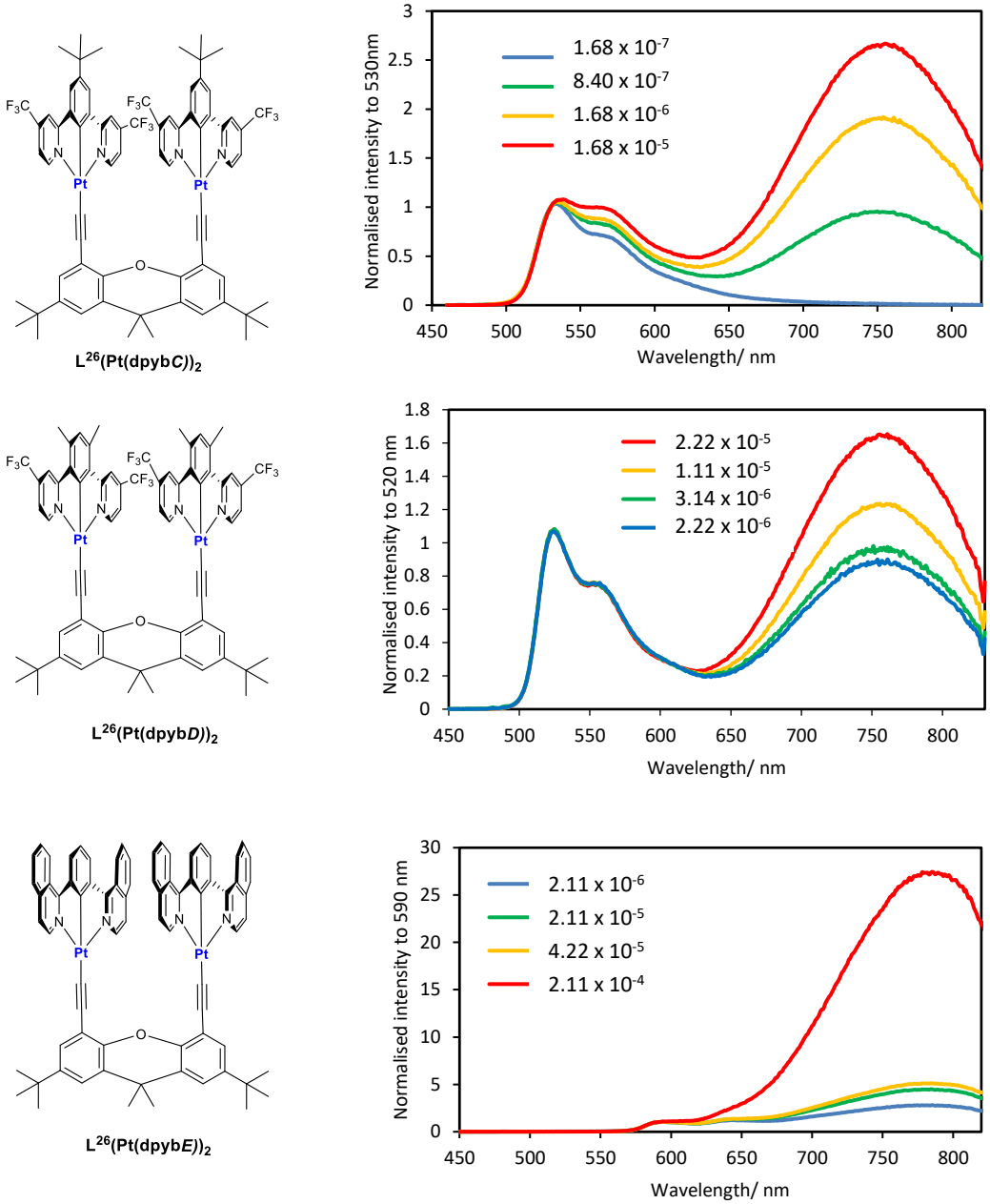

Figure 5.18: *Normalised concentration-dependent emission spectra of class 2 complexes.*

Like the class 1 complex $L^{24}(PtCl)_2$, complexes $L^{26}(Pt(dpyb\mathit{A}))_2$ and $L^{26}(Pt(dpyb\mathit{E}))_2$ show only a trace amount of monomer emission and a high propensity for excimer formation in solution (Fig. 5.18). In comparison to the class 2 complexes which contain CF_3 groups, the excimeric emission in $L^{26}(Pt(dpyb\mathit{A}))_2$ and $L^{26}(Pt(dpyb\mathit{E}))_2$ is much more prevalent and again suggests that CF_3 groups on the pyridyl rings of the N^C^N components may sterically inhibit the approach of two Pt units face-to-face in the excited state. The crystal structures obtained for $L^{26}(Pt(dpyb\mathit{A}))_2$ and $L^{26}(Pt(dpyb\mathit{E}))_2$ support these observations where $L^{26}(Pt(dpyb\mathit{A}))_2$ and $L^{26}(Pt(dpyb\mathit{E}))_2$ displayed shorter intramolecular Pt···Pt interactions in comparison to the CF_3-containing complex $L^{26}(Pt(dpyb\mathit{D}))_2$.

At the lowest concentration of 1.68 x 10^{-7} M, complex C displayed purely monomeric emission. This contrasts to the class 1 complex $L^{25}(PtCl)_2$ which displays both monomeric and excimeric emission, even at 1.06 x 10^{-7} M concentration. In this case, the arrangement of complex C in solution may not be as rigidly fixed due to the bulky and flexible ^{t}Bu group which enables only monomer emission to be observed at low concentrations. This may also suggest a greater degree of intermolecular interactions which assist in excimer formation in this complex.

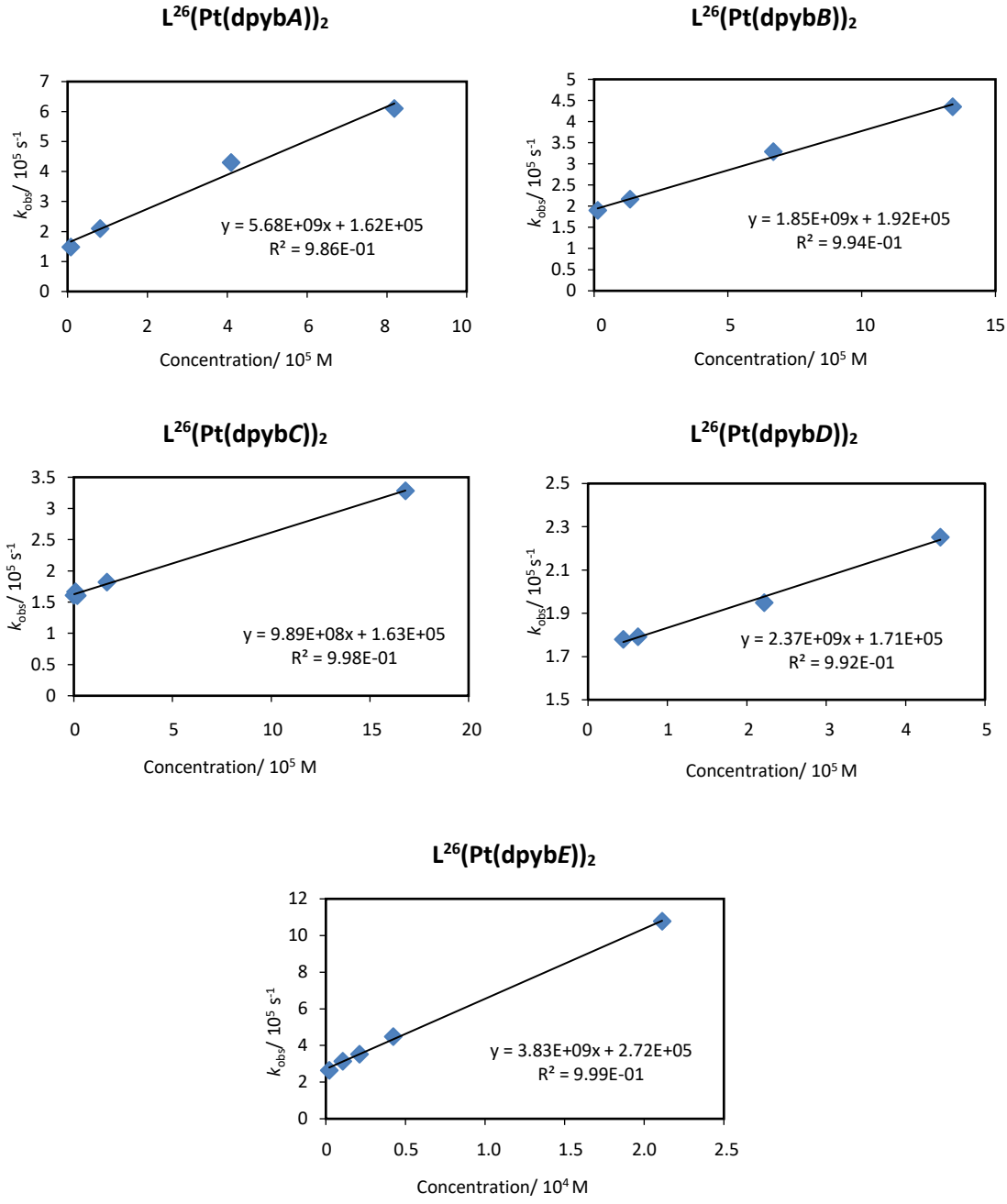

Figure 5.19: *Stern-Volmer plots for class 2 complexes showing self-quenching parameters.*

By probing the monomer emission, all complexes investigated were seen to follow a linear trend with respect to concentration versus the inverse of the lifetime, whilst excimer lifetimes were seen to stay constant independent of concentration (Fig. 5.19 and Table 5.5). Degassed excimer lifetimes ranged from 410 ns to 1.7 µs at 298 K and at 77 K ranged from 2.4 µs to 3.0 µs.

Complex $L^{26}(Pt(dpyb\mathit{A}))_2$ had the highest quantum yield of 35 % with a degassed lifetime of 4.8 µs and a λ_{max} of 690 nm. In comparison to the homo-dinuclear N^N^C complex **105** in the Muñoz-Rodríguez paper which had a lifetime of 26 ns, a 0.0026 % PLQY and a λ_{max} of 817 nm, this shows the great potential for these types of compounds which could be incorporated into NIR OLEDs. Moreover, this demonstrates first-hand the superior efficiency of luminescence that can be achieved by the N^C^N arrangement in the tridentate dpybX ligand compared to the N^N^C arrangement.

The 77 K emission was also investigated for the class 2 complexes (Fig. 5.20). Similarly, with the class 1 parent complex $L^{24}(PtCl)_2$, compound $L^{26}(Pt(dpyb\mathit{A}))_2$ showed more structured monomeric emission at low temperature in comparison to the CF_3-substituted complexes. Moreover, as the number of substituents increased on the Pt units, the amount of monomer emission was seen to decrease whilst the amount of excimer emission increased (the reverse phenomenon for the emission observed at RT for these complexes). This is demonstrated by complex $L^{26}(Pt(dpyb\mathit{C}))_2$ which had the largest excimeric emission at 77 K, but which also displayed purely monomeric emission at 10^{-7} M at RT.

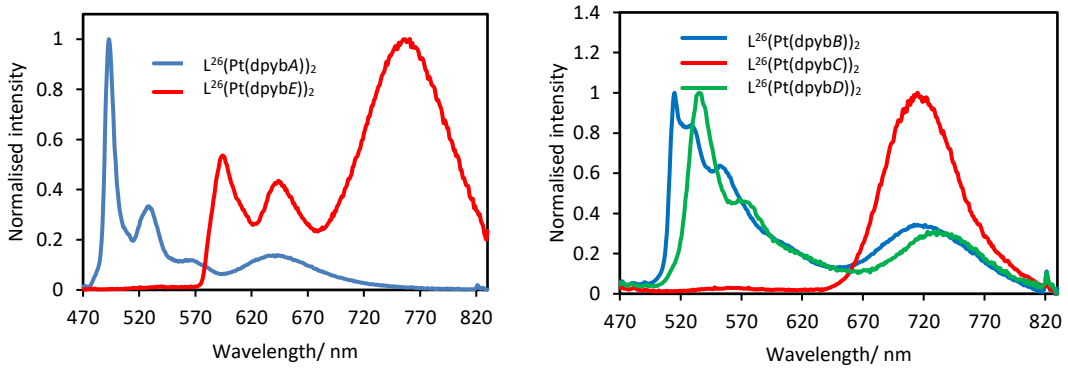

Figure 5.20: *77 K spectra of complexes* $L^{26}(Pt(dpyb\mathit{X}))_2$ *in butyronitrile glass split into complexes with no* CF_3 *substituents (left) and complexes with* CF_3 *substituents (right).*

5.3.2.3 Comparison with mononuclear analogues

The comparison with mononuclear analogues containing an acetylide instead of a chloride as an ancillary ligand was not possible owing to the fact they have not been synthesised. In lieu of this, comparisons with Pt(dpybX)Cl complexes, which were the starting materials in the syntheses of these dinuclear complexes, are made. The concentration-dependent emission for two of these Pt(dpybX)Cl complexes, namely where X= 2 x CF_3 (*B*) and H (*A*), are shown earlier on for their comparison with class 1 complexes (Fig. 5.13).

Class 2 complexes $L^{26}(Pt(dpyb\mathit{A}))_2$ and $L^{26}(Pt(dpyb\mathit{B}))_2$ display similar behaviour to their respective class 1 compounds $L^{24}(PtCl)_2$ and $L^{25}(PtCl)_2$ (discussed previously) when comparing their emission to their mononuclear analogues. Complex $L^{26}(Pt(dpyb\mathit{A}))_2$ has a slightly larger k_{sq} value in comparison to Pt(dpyb)Cl (5.7 vs. 5.3 x 10^9 M^{-1} s^{-1}) and lower quantum yield of 35 % compared to 60 % for Pt(dpyb)Cl. $L^{26}(Pt(dpyb\mathit{B}))_2$ on the other hand has a slightly larger k_{sq} value in comparison to Pt(dpyb*B*)Cl (1.9 vs. 3.1 x 10^9 M^{-1} s^{-1}) and the quantum yield is seen to be exactly the same for each at 21 %. The relative intensity of excimer formation in complex $L^{26}(Pt(dpyb\mathit{A}))_2$ is seen to be higher than Pt(dpyb)Cl but lower than that of $L^{25}(PtCl)_2$ which suggests that the class 1 compounds could have an excited state geometry for which intramolecular excimer formation is more accessible compared to the class 2 compounds.

$L^{26}(Pt(dpyb\mathit{C}))_2$has been highlighted as displaying intriguing photophysical behaviour. At very low concentrations and at RT, it displays properties which are very similar to the mononuclear complex Pt(dpyb*C*)Cl, where X= 2 x CF_3 and 1 x ^{t}Bu (Fig. 5.21). In contrast to this, the extent of excimer formation is still much greater for $L^{26}(Pt(dpyb\mathit{C}))_2$ than for Pt(dpyb*C*)Cl at equivalent concentrations.

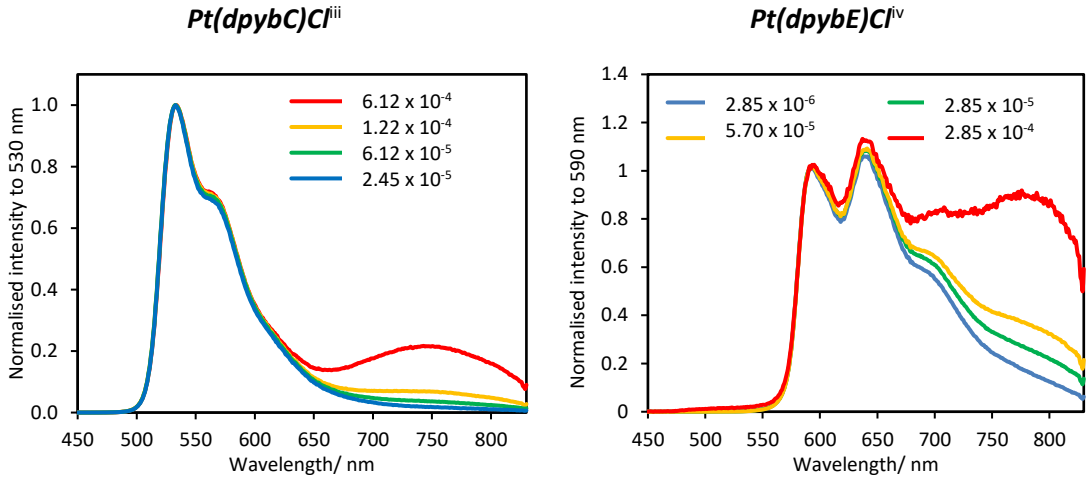

ϕ = 0.48

λ_{max} = 533, 562 (747) nm

τ_0 = 5.8 µs

k_{sq} = 1.2 x 10^9 $M^{-1}s^{-1}$

ϕ = 0.12

λ_{max} = 592, 641, 695sh (785) nm

τ_0 = 3.3 µs

k_{sq} = 5.2 x 10^9 $M^{-1}s^{-1}$

Figure 5.21: *Concentration-dependent emission of Pt(dpybX)Cl complexes and photophysical properties of complexes λ_{max} values for the excimer are quoted in the parentheses.*

On comparing the emission spectra of the mononuclear complex Pt(dpyb*E*)Cl (Fig. 5.21) and the dinuclear complex L^{26}(Pt(dpyb*E*))$_2$ (Fig. 5.18), there is a stark contrast in the amount of excimer formation between the two. At the highest concentrations investigated (between 2 and 3 x 10^{-4} M for each complex), Pt(dpyb*E*)Cl showed a relativley small amount of excimer formation. This is also likely to be accentuated due to the fluorimeter correction accounting for weaker detection of the lamp in the red and NIR regions, particularly for weakly-emitting samples such as this one. On the contrary, the emission of L^{26}(Pt(dpyb*E*))$_2$ was dominated by excimeric emission with λ_{max} of 780 nm. This high propensity for excimer formation thus reflects the behaviour of complex L^{26}(Pt(dpyb*A*))$_2$ and its mononuclear derivative Pt(dpyb)Cl.

[iii] This complex was synthesised by Chris Harris (MChem student) and photophysical data was carried out by Professor J. A. Gareth Williams.

[iv] This complex was synthesised by Rebecca Salthouse (MChem student) and photophysical data was carried out by me.

Table 5.5: *Photophysical properties of class 1 and 2 complexes in DCM solution at 298 K and in butyronitrile glass at 77 K. Excimer results are shown in red. *A triexponential lifetime which had a large error associated with the fit was obtained so is not recorded here.*

Complex	298 K										77 K	
	λ_{abs} (nm)	λ_{em} (nm)	τ_{deg} (ns)	τ_{aer} (ns)	τ_0 (μs)	φ (%)	k_r (10^3 s^{-1})	k_{nr} (10^5 s^{-1})	k_q (O_2) (10^7 M^{-1} s^{-1})	k_{sq} (mono) (10^9 M^{-1} s^{-1})	λ_{em} (nm)	τ (μs)
$L^{24}(PtCl)_2$	386 (14650), 412 (9940), 495sh (350).	690	5400 (1400)	990 (260)	7.5	15	28	1.56	37	2.9	500, 538, 578, 614	7.3 /
$L^{25}(PtCl)_2$	262 (55721), 301 (30431), 353 (6741), 384 (5403), 405 (7217), 429 (6189).	540, 770	6400 (440)	1100 (290)	6.7	5	7.8	1.5	34	0.40	544, 573, 731	5.6 (2.6)
$L^{26}(Pt(dpybA))_2$	268 (34359), 321 (12885), 374 (4813), 400 (6119)	690	4800 (1700)	3100 (740)	6.2	35	73	1.4	5.1	5.7	493, 527, 565, 638	5.4 (3.0)
$L^{26}(Pt(dpybB))_2$	268 (65245), 287 (46005), 302 (42998), 404 (14832), 484 (3495).	515, 550, 765	4600 (660)	1000 (360)	5.2	21	45	1.7	36	1.9	514, 525, 548, 586, 715	5.0 (2.6)
$L^{21}(Pt(dpybC))_2$	260 (99509), 308 (61357), 435 (13748), 482 (8575).	530, 566, 760	5500 (690)	790 (340)	6.2	5	9.1	1.7	49	0.99	715	/ (2.4)
$L^{26}(Pt(dpybD))_2$	268 (80915), 316 (48318), 422 (12407), 495 (5073).	526, 555, 757	5600 (690)	1100 (400)	5.8	16	29	1.5	35	2.4	533, 567, 729	13 (*)
$L^{26}(Pt(dpybE))_2$	276 (141563), 323(63832), 345(46716), 449(28262)	590, 780	3200 (410)	540 (260)	3.7	5	16	3.0	70	3.8	593, 644, 758	5.3 (2.4)

5.3.3 Solid-state photophysical properties of Class 1 and 2 complexes

Complexes $L^{24}(PtCl)_2$, $L^{25}(PtCl)_2$, $L^{26}(Pt(dpyb\mathit{A}))_2$, $L^{26}(Pt(dpyb\mathit{C}))_2$ and $L^{26}(Pt(dpyb\mathit{E}))_2$ were also tested for their photophysical properties in the solid-state by doping into thin films of polystyrene (PS) at concentrations of 1, 5 and 20 wt. % and as neat films. Complexes $L^{26}(Pt(dpyb\mathit{B}))_2$ and $L^{26}(Pt(dpyb\mathit{D}))_2$ were not studied due to their inferior solubility needed for spin-coating the films. Class 1 complexes were seen to show mainly monomer emission at concentrations of 1-20 wt. % doping in PS, but in the neat film $L^{24}(PtCl)_2$ emission was dominated by excimer formation and $L^{25}(PtCl)_2$ had a large proportion of excimer emission whilst retaining some monomer emission (Fig. 5.22). Class 2 complexes, on the other hand, showed largely excimeric emission at all concentrations tested.

$L^{24}(PtCl)_2$

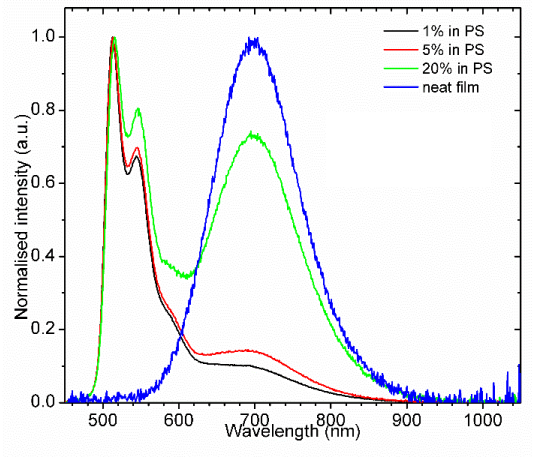

$L^{25}(PtCl)_2$

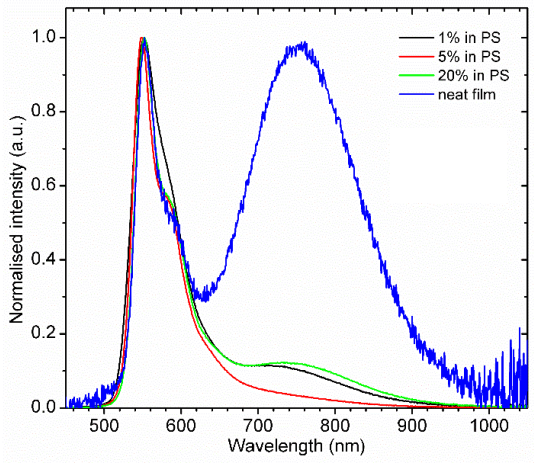

$L^{26}(Pt(dpyb\mathit{A}))_2$

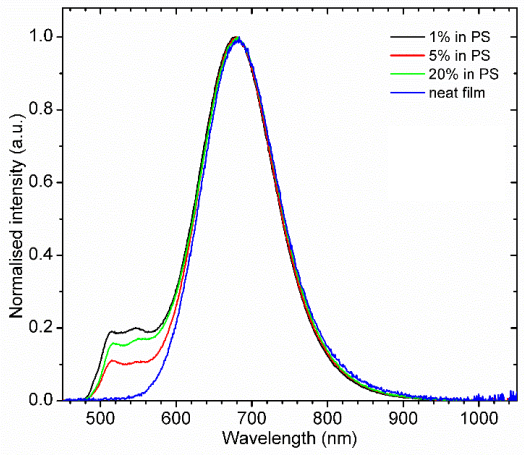

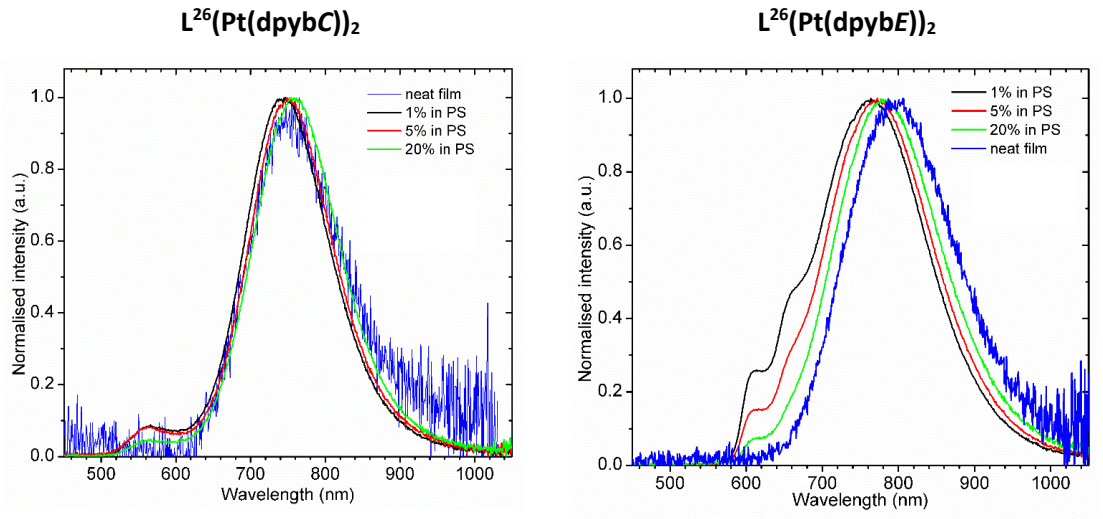

Figure 5.22: *Solid-state emission spectra for the dinuclear complexes at different concentrations in polystyrene (PS).*[v]

Table 5.6: *PLQY values of class 2 complexes in the solid-state.*

Film/Complex	*L^{26}(Pt(dpybA))$_2$*	*L^{26}(Pt(dpybC))$_2$*	*L^{26}(Pt(dpybE))$_2$*
1 % in PS	0.57	0.17	0.13
5 % in PS	0.38	0.09	0.11
20 % in PS	0.36	0.10	0.07
Neat film	0.22	0.02	0.04

In the case of class 1 compounds, intermolecular interactions with the PS matrix (e.g. π-π stacking between phenyl rings in PS and on the N^C^N groups of the dinuclear complexes) could prevent intramolecular excimer formation at low concentrations and hence may explain why only monomer emission is observed. Meanwhile at higher concentrations, these intermolecular interactions with PS could be weakened by the preference to form intramolecular excimers. This is definitely not the case in class 2 compounds where excimer formation of either an intermolecular or intramolecular nature dominates at all concentrations.

The PLQY values were determined for the class 2 compounds (Table 5.6) and L^{26}(Pt(dpyb*A*))$_2$ in particular showed impressive results with ϕ = 0.57 at a 1 wt. % doping concentration in PS. At this concentration, although there is still some monomer emission present, the vast majority of emission is centred deep into the red with λ_{max} = 680 nm. The PLQY values for L^{26}(Pt(dpyb*E*))$_2$ in different films are lower than those for L^{26}(Pt(dpyb*A*))$_2$ where ϕ = 0.13 at a 1 wt. % doping concentration in PS, but the emission maximum is

[v] Solid-state emission carried out by Piotr Pander (Durham University Physics department).

centred well into the NIR at ca. 780 nm in this case.

Consequently, the behaviour in the solid-state identifies the class 2 compounds as the most promising in terms of incorporation into NIR OLEDs. Complex $L^{26}(Pt(dpyb\mathit{E}))_2$ displays impressive photophysical properties with emission at λ_{max} of 780 nm in PS doped films up to 20 wt. % and a λ_{max} of 800 nm in a neat film, making it the most red-shifted out of all the compounds investigated.

5.4 Chapter 5 Summary

A range of dinuclear Pt^{II} complexes containing tridentate N^C^N ligands have been synthesised with high PLQY values for red and NIR emitting complexes between 5 and 35 %. Investigation into class 1 compounds introduced the dramatic impact that substituents on the N^C^N group can have in affecting complex emission and posed the question of whether excimer formation occurs through intra/inter molecular interactions, or a mixture of both.

Class 2 compounds were seen to display similar trends in terms of photophysical behaviour to class 1 compounds where CF_3 substituents on the N^C^N ring appeared to reduce the amount of excimer formation in both cases. Complex $L^{26}(Pt(dpyb\mathit{C}))_2$ was highlighted as displaying unusual behaviour owing to its purely monomeric emission in low concentration solution at RT versus its purely excimeric emission at 77 K. Complex $L^{26}(Pt(dpyb\mathit{E}))_2$ was seen to display emission well into the NIR in the solid-state with λ_{max} at ca. 800 nm and this was nearly all excimeric. All of which demonstrates the high potential these complexes possess for incorporation into NIR OLEDs.

This work was undertaken right at the end of the period of study and the question that still remains is the extent to which the emission that is observed in these class 1 and 2 complexes is intra-/intermolecular in origin.

Evidence for intra-/intermolecular excimers:

Intra

- Class 1 complex $L^{24}(PtCl)_2$ shows almost exclusively excimer emission at all concentrations investigated in solution-state emission.
- Class 1 complex $L^{25}(PtCl)_2$ shows presence of both monomer and excimer emission at all concentrations investigated and never solely monomer emission
- The 77 K emission for all complexes except $L^{24}(PtCl)_2$ shows either all excimer or a mix of excimer and monomer emission

- The crystal structure of $L^{26}(Pt(dpyb\textit{E}))_2$ shows shorter intramolecular Pt···Pt distances of 3.98 Å compared to $L^{26}(Pt(dpyb\textit{D}))_2$, which could reflect the possibility of even closer distances upon rearrangement in the excited state (i.e. < 3.5 Å).
- The solid-state emission in PS films of class 2 compounds shows largely excimeric emission.

Inter

- Stern-Volmer plots follow a linear trend for both class 1 and class 2 complexes i.e. as the concentration increases, monomer lifetimes decrease owing to the formation of excimers. If purely intramolecular in nature, then the lifetimes would not be concentration dependent as they would always reflect the excimer lifetime.
- Class 2 complex $L^{26}(Pt(dpyb\textit{C}))_2$ shows purely monomeric emission at the lowest concentration investigated.
- The 77 K emission for complex $L^{24}(PtCl)_2$ shows purely monomeric emission.
- The crystal structure of $L^{26}(Pt(dpyb\textit{D}))_2$ has the longest intramolecular Pt···Pt distances of 5.00 Å.

The photophysical properties of these molecules need further investigation to deduce exactly which interactions are present in the excited state, however, possible explanations for the above observations are as follows;

- $L^{24}(PtCl)_2$ has enough energy to orient itself in a face-to-face conformation at RT to show intramolecular excimers but at 77 K exists in a state which does not allow face-to-face conformation.
- The presence of CF_3 groups in $L^{25}(PtCl)_2$, $L^{26}(Pt(dpyb\textit{B}))_2$, $L^{26}(Pt(dpyb\textit{C}))_2$ and $L^{26}(Pt(dpyb\textit{D}))_2$ makes it harder for the complexes to adopt a face-to-face conformation at RT owing to steric hindrance and so a mix of intra- and intermolecular excimers are displayed and the crystal structures obtained help prove this as the Pt···Pt distances are not short enough to support intramolecular Pt···Pt interactions
- Complexes $L^{26}(Pt(dpyb\textit{A}))_2$ and $L^{26}(Pt(dpyb\textit{E}))_2$ are similar to $L^{24}(PtCl)_2$ owing to the lack of CF_3 substituents, but the presence of the alkyne group on the linker gives more flexibility to the molecule so that the face-to-face conformation is not locked at RT and so a mix of intra- and intermolecular interactions is observed, although intramolecular interactions dominate.

Despite the uncertainty in the origin of the excimeric emission in these dinuclear Pt complexes containing N^C^N ligands, the fact stands that they show efficient NIR emission and have good solubility for potential use in solution-processable NIR OLEDs. Indeed, future work on this area would first and foremost aim to determine the origin of excimeric emission as intra/intermolecular or as a mixture of both. This would hopefully be determined by detailed investigation into the kinetics of excimer formation. These complexes are also currently under investigation for incorporation into OLED devices and these results will be very informative as to which compounds would give the best performance in a scaled-up device. Moreover, the synthesis of other derivatives of these dinuclear complexes should be attempted to try to eliminate any visible emission, trace amounts of which are still noticeable in both the solid and solution-state spectra, in order to obtain pure NIR emission. There is a lot of promise in this area of work which will hopefully be continued.

6. Concluding remarks and future work

A range of complexes based on the transition metals Pt, Pd and Ir has been synthesised. Investigation into ligands offering bidentate, tridentate or tetradentate coordination modes to the metal centres has led to complexes with interesting photophysical properties. Moreover, the incorporation of more than one metal centre to generate dinuclear complexes has presented intriguing results which could be the basis of substantial further research. Incorporation of selected complexes into both thermally-evaporated and solution-processed OLEDs has also shown impressive results for some complexes.

Pt^{II} complexes containing 1,2,4-triazole and tetrazole ligands were synthesised and probed for their excimeric emission. The homoleptic triazole complexes PtL^{1}_{2} and PtL^{7}_{2} exhibited impressive photophysical properties with PLQY values of 21 and 48 % respectively in degassed DCM solutions. These were incorporated into solution-processed devices that displayed red emission with maximum EQEs of 12.5 and 11.2 % respectively. At higher doping concentrations, the emission became increasingly red-shifted owing to the increased excimeric contribution. A VTE device of PtL^{1}_{2} at 30 wt. % in mCP was also fabricated. It showed increased efficiency with maximum EQE of 14.9 %. Other complexes containing the bidentate triazole ligands that showed impressive solution-state photophysical properties included the heteroleptic $Pt(thpy)L^{n}$ complexes with PLQY values ranging from 30 to 37 %. These also showed a concentration-dependence of their emission and would be interesting to incorporate into OLED devices. The tetrazole complexes that were synthesised were largely difficult to study owing to their limited solubility. The exception was complex PtL^{14}_{2} which was soluble enough for incorporation into a solution-processed OLED at 10 wt. % in a PVK : OXD7 (50 : 50) host and which showed a 3.8 % EQE.

In order to study more of these tetrazole complexes in the future, more soluble derivatives should be made, possibly by incorporating bulky hydrocarbon substituents on the 4-pyridyl substituted phenyl rings such as adamantyl groups (Scheme 6.1).

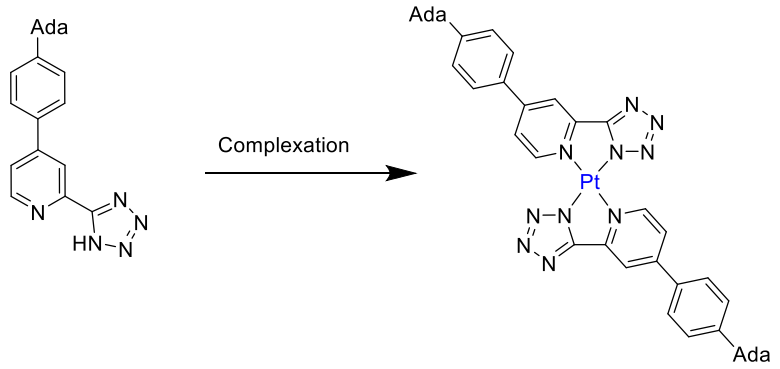

Scheme 6.1: *Synthesis of tetrazole Pt complex with adamantyl substituents.*

Pt^{IV} complexes with '3+2+1' and bis-tridentate conformations displayed impressive photophysical properties. The 3+2+1 complex $[Pt(dpyb)L^{1}Cl]^{+}$ had a PLQY of 5.9 % and a lifetime of 3.1 µs. On increasing the denticity of the triazole ligand from bidentate to tridentate, a PLQY of 28 % and a lifetime of 11 µs were shown for $[Pt(dpyb)L^{16}]^{+}$, which appears to be the first reported example of a Pt^{IV} bis-tridentate complex. Different series of Ir complexes with similar bis-tridentate and 3+2+1 structures were also synthesised and showed lower efficiencies overall. PLQY values ranging from 0.35 to 1.8 % were displayed for the bis-tridentate Ir(dpyb*X*)($L^{16\text{-}18}$) complexes, whilst the 3+2+1 Ir(dpybMe_2)($L^{1\text{-}3}$)Cl complexes were found to be non-emissive at RT and only emissive at 77 K. In comparison with their isoelectronic Ir^{III} analogues, the Pt^{IV} complexes displayed more impressive properties which should be investigated further through the synthesis of different derivatives for potential future incorporation into devices such as LEECs. Moreover, it would be interesting to see the effect on the photophysical properties by metathesising the ancillary chloride ligand with a strong field ligand such as an acetylide in the case of $[Pt(dpyb)L^{n}Cl]^{+}$ complexes (Scheme 6.2).

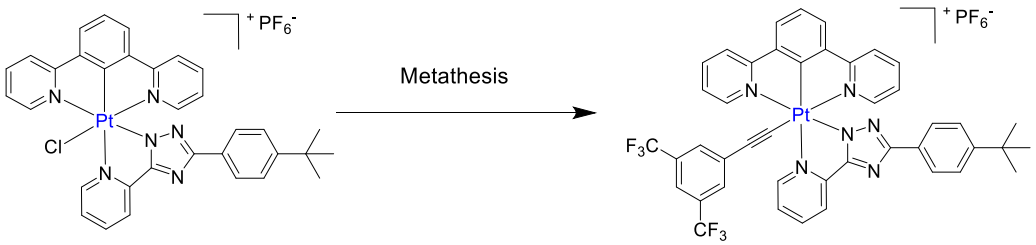

$[Pt(dpyb)L^{1}Cl]^{+}PF_6^{-}$

Scheme 6.2: *Metathesis of the ancillary chloride ligand in $[Pt(dpyb)L^{1}Cl]^{+}$for an acetylide using 1-ethynyl-3,5-bis(trifluoromethyl)benzene as the reagent in this case.*

A range of Pt and Pd complexes containing tetradentate ligands were discussed based on the work of former Ph.D. student Mickaële Bonneau. The complexes were investigated for their concentration-dependent photophysical properties. PtL[20], containing the difluorophenyl ligand, showed the highest propensity for excimer formation whereas ML[21] and ML[22] (where M = Pt and Pd) showed no evidence of excimer formation but had improved photophysical properties in comparison to the others in the series. For this reason, the thiophene ligand-containing complex PdL[21] was studied for its solid-state photophysical properties and was also incorporated into a solution-processed OLED which had an EQE of 3.17 %. It would, therefore, be interesting to investigate further these Pd complexes for their excimeric emission, by studying more concentrated films of these complexes and derivatives. Complex PtL[23] was also synthesised which contained an indole-based tetradentate ligand. It had a PLQY of 33 % in DMSO and it would be interesting to see the performance of more soluble derivatives in OLED devicesMoreover, although the attempted synthesis of a Pd analogue of PtL[23] was unsuccessful, extended efforts to achieve another derivative could be attempted to see if high luminescence efficiencies in Pd analogues could be obtained (Fig. 6.1).

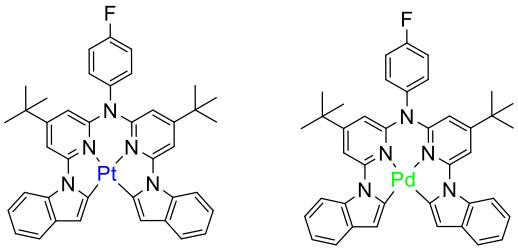

Figure 6.1: *Structures of Pt and Pd complexes containing indole-based tetradentate ligands that could potentially be synthesised to achieve higher solubility of the complexes.*

Finally, dinuclear complexes containing Pt(N^C^N) units rigidly linked in a face-to-face conformation by a xanthene core were synthesised and displayed intriguing photophysical properties. Both monomeric and excimeric emission were shown by these complexes with PLQY values ranging from 5 to 35 % in degassed solution and up to 57 % in thin films. The excimeric emission extended well into the NIR region and the complex L[26](Ptdpyb*E*)$_2$ was seen to display the most promising properties with mostly excimeric emission (λ_{max} of 780 nm in solution and 800 nm in a neat film). The emissive properties of these dinuclear complexes were seen to differ significantly from the mononuclear derivatives; however, the exact nature of the excimeric emission is still unclear. As this work was done at the very end of this project, more investigation will be required in the future in order to gain a clearer

understanding of the mechanism of emission in each case. A very interesting basis to build on has thus been developed where high efficiency NIR OLEDs could be in reach. Overall, a diverse range of luminescent metal complexes has been synthesised and more work, particularly to synthesise more soluble derivatives of certain complexes for OLED incorporation, would be extremely insightful.

7. Experimental

7.1 General Experimental

7.1.1 Materials

Reagents were obtained from commercial sources and used without further purification unless stated otherwise. All solvents used in preparative work were at least Analar grade and water was purified using the Purite$_{STILL}$ plus^{TM} system. Dry solvents were obtained from HPLC grade solvent that had been passed through a Pure Solv 400 solvent purification system and stored over activated 3 or 4 Å molecular sieves. For procedures involving dry solvent, glassware was oven-dried for at least 8 hours prior to use. Dedicated oxygen-free argon cylinders (BOC, UK) were used to provide an inert atmosphere.

7.1.2 Physical Measurements

NMR spectra were recorded on a Bruker Avance-400 (400 MHz ^{1}H and 100 MHz ^{13}C) spectrometer. Two-dimensional NMR (COSY, NOESY, HSQC and HMBC) were acquired by the solution state NMR service at Durham University on Varian VNMRS-600 (600 MHz) or VNMRS-700 (700 MHz) instruments. Chemical shifts (δ) are in ppm, referenced to residual protio-solvent resonances, and coupling constants are given in Hertz.

ES-MS data were obtained on a Waters TQD mass spectrometer interfaced with an Acquity UPLC system with acetonitrile as the carrier solvent. ASAP experiments were performed on Waters Xevo QToF mass spectrometer.

Thin-layer chromatography (TLC) was carried out using silica plates (MerckArt 5554) for all ligands and alumina plates (Merck 60 neutral) for all complexes, which are fluorescent upon irradiation at 254 nm. Column chromatography was carried out using silica (Merck 60, 230-400 mesh) for all ligands and alumina (Merck aluminium oxide 90, standard) for all complexes.

Melting points were measured on a Gallenkamp melting point apparatus.

Elemental analysis was performed by Dr. Emily Unsworth using an Exeter CE-440 Elemental Analyser device (University of Durham elemental analysis service).

UV/Vis-Electronic spectra were recorded on a Biotek Instruments UVIKON XS spectrometer operating with LabPower software.

Solution-based emission spectra were acquired on a Jobin Yvon Spex Fluoromax-2 spectrometer. All samples were contained within quartz cuvettes of 1 cm path length. Samples that were to be measured in the absence of air were degassed within the cuvette by three freeze-pump-thaw (FPT) cycles. Emission was recorded at 90° to the excitation source, and appropriate filters were used when required to remove second-order peaks. All emission spectra were corrected after acquisition for dark count and for the spectral response of the detector. The quantum yields were determined relative to a reference of an aqueous solution of $[Ru(bpy)_3]Cl_3$. The quantum yield of this complex is well established in air-equilibrated H_2O to be 0.028.[191] To measure the quantum yield, a sample of the complex was prepared so that the absorbance at the excitation wavelength was below 0.1 and a solution of $[Ru(bpy)_3]Cl_3$ with a similar intensity was prepared. The emission spectra of the complex and reference were measured under identical conditions and the quantum yield was determined by equation

$$\varphi = \varphi_{st} \times \frac{I}{I_{st}} \times \frac{A_{st}}{A} \times \frac{n^2}{n_{st}^2} \quad (9)$$

φ represents the quantum yield, I the overall integrated intensity, A the absorbance at the excitation wavelength and n^2 the refractive index of the solvent, the subscript *st* denotes the standard and all other values the sample.

Lifetimes were determined using an Edinburgh Instruments OB920 fluorimeter. Luminescence lifetimes of the complexes up to approximately 10 µs were measured by time-correlated single-photon counting method, using an EPL405 pulsed-diode laser as excitation source (405 nm excitation, pulse length of 60 ps). The laser repetition rate was selected so that the pulse period was at least 5-10 times longer than the complex lifetime. The emission was detected at 90° to the excitation source, after passage through a monochromator, using a Peltier-cooled R928. Lifetimes in excess of 10 µs were measured by multichannel scaling, and a xenon microsecond flash lamp was used as the excitation source (excitation wavelength matched to a suitable absorption band of the complex). The lifetimes were obtained by least-squares fitting to a mono-exponential decay and goodness-of-fit was assessed from the residuals. Low temperature (77 K) experiments were performed using a glass vacuum cold finger apparatus built in house. A small amount of sample was dissolved in either a 2:2:1 solvent mix of ether/isopentane/ethanol (EPA) or butyronitrile and placed into a glass tube. The cold finger was filled with liquid nitrogen and the tube containing the sample was inserted.

7.1.3 OLED Fabrication

All solution-processed OLEDs were fabricated by Piotr Pander (Durham Univeristy Physics Department) according to the following procedure:

OLEDs were fabricated by spin-coating / evaporation hybrid methods. The hole injection layer (Heraeus Clevios HIL 1.3N) and EML (mCP : OXD-7 or mCP:PO-T2T + dopant) were spin-coated, whereas the ETL (TPBi or PO-T2T) and cathode (LiF/Al) were evaporated. Devices of 4 x 2 mm pixel size were fabricated. PO-T2T (sublimed, LUMTEC), mCP (sublimed, LUMTEC), OXD-7 (sublimed, LUMTEC), TPBi (sublimed, LUMTEC), LiF (99.995%, Sigma Aldrich), and aluminium wire (99.9995%, Alfa Aesar) were purchased from the companies indicated in parentheses. OLED devices were fabricated using pre-cleaned ITO coated glass substrates after ozone plasma treatment with a sheet resistance of 20 Ω cm^{-2} and ITO thickness of 100 nm. Heraeus Clevios HIL 1.3N was spin-coated and annealed onto a hotplate at 200 ˚C for 3 min to give a 45 nm film. The EML was spin-coated from a chloroform : chlorobenzene (95:5 v/v) solution of mCP:OXD-7 (80:20 w/w) or mCP:PO-T2T (70:30 w/w) with the total concentration of host + dopant kept at 20 mg/mL. The dopant was dissolved in the host solution in order to obtain the final 5-30 % (w/w) concentration in the EML. The solution was spin-coated onto the HIL 1.3N layer and then annealed at 50 ˚C for 5 min giving a 60 ± 5 nm (mCP : OXD-7) and 70 ± 5nm (mCP : PO-T2T) film. All solutions were filtrated directly before application using a syringe filter with 0.45 µm pore size. All other organic and cathode layers were thermally evaporated using Kurt J. Lesker Spectros II deposition system at 10^{-6} mbar. All organic materials and aluminum were deposited at a rate of 1 Å s^{-1} and the LiF layer was deposited at 0.1-0.2 Å s^{-1}. Characterisation of OLED devices was conducted in 10 inch integrating sphere (Labsphere) connected to a Source Measure Unit.

VTE devices of PtL^1_2 were fabricated by me under the supervision of Kazuya Jinnai at the Adachi Laboratory, Kyushu University, Japan.

7.1.4 Crystallography

Single-crystal X-ray data were collected on a Bruker D8Venture diffractometer (IµS microfocus sources, focusing mirrors, CMOS Photon100 detector) using MoKα (λ = 0.71073 Å) radiation, equipped with Cryostream (Oxford Cryosystems) open-flow nitrogen cryostats, the temperature on the crystals was maintained at 120.0 K. Smaller crystals were taken to the synchotron Diamond light source using λ = 0.6889 Å radiation and a temperature of 100 K. All structures were solved by direct methods and refined by full-

matrix least squares on F2 for all data using SHELXTL190 and OLEX2191 software by Dr. D. S. Yufit (University of Durham).

7.1.5 Density Functional Theory

DFT geometry optimisations, frequency, stability and TD-DFT excitation calculations were performed using Gaussian 09. The geometry optimizations of the complexes were performed at the B3LYP[192,193,194] level of theory and LANL2DZ basis set for all atoms.

7.2 Synthesis Procedures

The following synthesis procedures were used frequently throughout this work, featuring in the synthesis of many ligands and will be referred to in the main experimental chapter.

7.2.1 Suzuki cross-coupling

An aryl halide, a boronic acid derivative and Na_2CO_3 were dissolved in a mixture of dimethoxyethane (DME) and water (1:1). The reaction mixture was degassed by 3 x FPT cycles and put under an argon atmosphere. The catalyst, tetrakis(triphenylphosphine) palladium, $Pd(PPh_3)_4$ was then added to the solution and the mixture was heated at 85 °C for 24 h. After cooling to RT, the solution was poured into water and the organic layer was extracted with DCM (typically 2 × 10 mL) and washed with water (2 × 10 mL). The organic layer was dried over $MgSO_4$, filtered, and the solvent was removed *in vacuo*. The crude product was purified by column chromatography on silica gel.

7.2.2 Stille cross-coupling

Toluene was added to a mixture of an aryl halide, a stannane derivative and LiCl. The mixture was degassed by 3 FPT cycles and the catalyst bis(triphenylphosphine) palladium dichloride $Pd(PPh_3)_2Cl_2$ was then added to the mixture. The reaction was heated at 110 °C for 48 h under argon. After cooling to RT, saturated aqueous potassium fluoride (KF) solution (ca. 5 mL) was added and left to stir for a further 30 mins. The solution was then filtered and an insoluble grey powder was removed by filtration and washed with toluene. The combined toluene washings were removed under reduced pressure giving a brown/orange oil. This was extracted into 100 mL of DCM and washed with aqueous sodium hydrogen carbonate ($NaHCO_3$) (5 % by mass, 2 x 100 mL). The organic layer was dried over $MgSO_4$, filtered and the solvent was removed *in vacuo*. The crude product was purified by column chromatography on silica gel.

7.3 Chapter 2 Synthesis

7.3.1 1,2,4-Triazoles

7.3.1.1. Intermediate and ligand general procedures

Step 1 intermediates ($I1^x$)

Hydrazine monohydrate was added to 2-cyanopyridine or derivative thereof in ethanol. The reaction mixture was stirred at RT overnight, yielding a suspension. The precipitate was filtered off, washed with cold ethanol, and dried *in vacuo*.

Step 2 intermediates ($I2^x$)

An oven-dried, nitrogen-purged Schlenk tube was loaded with **$I1^x$** and Na_2CO_3, then evacuated, gently heated, and refilled with nitrogen after being cooled to RT. Dry DMF was added and the suspension was cooled to 0 °C. In a separately prepared Schlenk tube, a solution of a benzoyl chloride in dry DMF was prepared in the same way. This solution was then slowly added to the cooled suspension under vigorous stirring. The reaction mixture was warmed to RT and then water was added to yield more precipitate. This suspension was stirred vigorously for another 1.5 hours, filtered and washed with water thoroughly before being dried *in vacuo*.

Triazole ligand (HL^n)

$I2^x$ was suspended in ethylene glycol in a 100 mg/mL ratio in an open round-bottom flask. This suspension was heated to 180 °C, eliminating water. Once the solution turned clear, the reaction mixture was heated under reflux for another hour. After the reaction mixture was cooled to RT, the product was precipitated with water and stirred vigorously for a further hour. The solid was filtered through a Whatman membrane filter (0.2 µm, nylon), washed with water, and dried *in vacuo*.

7.3.1.2 1,2,4-Triazoles with no substitution on the pyridyl ring

Step 1 intermediates

Compound I1[a]

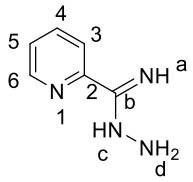

2-Cyanopyridine (500 mg, 4.80 mmol) and hydrazine monohydrate (2.5 mL, 48.02 mmol) in EtOH (25 mL). A pale yellow solid was obtained (680 mg, 67 %). The experimental data obtained were in good agreement with the literature.[195]

Compound I1[b]

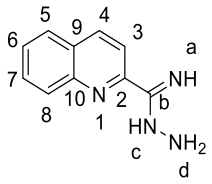

Quinoline-2-carbonitrile (1 g, 6.49 mmol) and hydrazine monohydrate (3.2 mL, 64.9 mmol) in EtOH (50 mL). A yellow solid was obtained (976 mg, 81 %); ^{1}H NMR (599 MHz, Chloroform-*d*) δ 8.13 – 8.11 (m, 2H, H^{3} and H^{4}), 8.05 (ddt, *J* = 8.4, 1.2, 0.7 Hz, 1H, H^{8}), 7.80 (ddd, *J* = 8.1, 1.5, 0.6 Hz, 1H, H^{5}), 7.69 (ddd, *J* = 8.4, 6.9, 1.4 Hz, 1H, H^{7}), 7.52 (ddd, *J* = 8.1, 6.9, 1.2 Hz, 1H, H^{6}), 5.39 (s, 2H, H^{d}), 4.75 (s, 2H, H^{a} and H^{c}); ^{13}C NMR (151 MHz, Chloroform-*d*) δ 150.5 (C^{2}), 148.6 (C^{b}), 146.8 (C^{10}), 136.1 ($C^{3/4}$), 129.5 (C^{7}), 129.3 (C^{8}), 128.3 (C^{9}), 127.5 (C^{5}), 126.7 (C^{6}), 117.5 ($C^{3/4}$); ES^{+}) *m/z* = 187.6 $[M + H]^{+}$; HRMS (ES^{+}) *m/z* = 187.0967 $[M + H]^{+}$; calculated for $[C_{10}H_{11}N_{4}]^{+}$ 187.0984.

Compound I1[c]

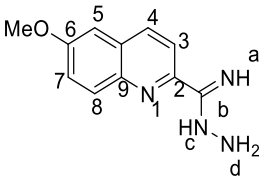

6-methoxy-2-quinoline carbonitrile (500 mg, 2.71 mmol) and hydrazine monohydrate (2.64 mL, 54.20 mmol) in ethanol (25 mL). A pale yellow solid was obtained after recrystallization in hot EtOH (186 mg, 32 %); ^{1}H NMR (700 MHz, Chloroform-*d*) δ 8.08 (d, *J* = 8.7 Hz, 1H, H^{8}),

8.01 (d, *J* = 8.7 Hz, 1H, H^7), 7.95 (d, *J* = 9.1 Hz, 1H, H^3), 7.34 (dd, *J* = 9.2, 2.8 Hz, 1H, H^4), 7.07 (d, *J* = 2.8 Hz, 1H, H^5), 5.36 (s, 2H, H^d), 4.69 (s, 2H, H^a and H^c), 3.93 (s, 3H, H^{OMe}); ^{13}C NMR (176 MHz, Chloroform-*d*) δ 158.0 (C^b), 148.9 (C^2), 148.4 (C^6), 142.7 (C^{10}), 134.9 (C^7), 130.7 (C^3), 129.4 (C^9), 122.1 (C^4), 117.8 (C^8), 105.3 (C^5), 55.5 (C^{OMe}); MS (ES^+) *m/z* = 218.0 $[M + H]^+$.

Step 2 intermediates

Compound I2[a]

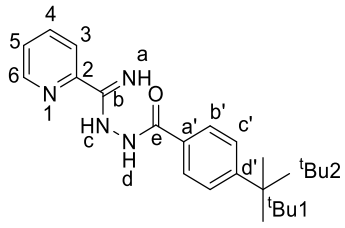

I1[a] (200 mg, 1.47 mmol), Na_2CO_3 (187 mg, 1.76 mmol), and dry DMF (6.4 mL) in one Schlenk. 4-^{t}Bu benzoyl chloride (289 mg, 1.47 mmol) and dry DMF (2.4 mL) in the second Schlenk. A yellow solid was obtained (217 mg, 50 %); ^{1}H NMR (700 MHz, DMSO-d_6) δ 10.11 (s, 1H, H^c), 8.57 (d, *J* = 4.5 Hz, 1H, H^6), 8.15 (d, *J* = 8.0 Hz, 1H, H^3), 7.88 (td, *J* = 7.8, 1.7 Hz, 1H, H^4), 7.79 (d, *J* = 8.0 Hz, 2H, $H^{b'}$), 7.49 – 7.43 (m, 3H, H^5 and $H^{c'}$), 6.89 (s, 2H, H^a and H^d), 1.29 (s, 9H, H^{tBu2}); ^{13}C NMR (176 MHz, DMSO-d_6) 233.2 (C^b), 163.6 (C^e), 154.2 ($C^{d'}$), 151.1 (C^2), 148.5 (C^6), 137.3 (C^4), 132.4 ($C^{a'}$), 127.9 ($C^{b'}$), 125.4 ($C^{c'}$), 125.1 (C^5), 121.1 (C^3), 31.4 (C^{tBu2}), 35.1 (C^{tBu1}); (ES^+) *m/z* = 296.9 $[M + H]^+$; HRMS (ES^+) m/z = 297.1716 $[M + H]^+$; calculated for $[C_{17}H_{21}N_4O]^+$ 297.1715.

Compound I2[b]

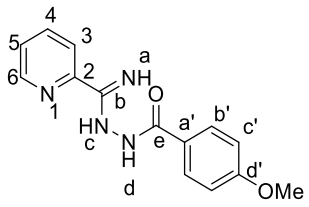

I1[a] (500mg, 3.67 mmol), Na_2CO_3 (857 mg, 8.08 mmol) with dry DMF (16 mL) in one Schlenk. 4-methoxybenzoyl chloride (689 mg, 4.04 mmol) and dry DMF (6 mL) in the second Schlenk. An off-white powder was obtained (852 mg; 86 %); ^{1}H NMR (600 MHz, DMSO-d_6) δ 10.02 (s, 1H, H^c), 8.57 (d, *J* = 4.5 Hz, 1H, H^6), 8.14 (d, *J* = 8.0 Hz, 1H, H^3), 7.92-7.80 (m, 3H, H^4 and $H^{b'}$), 7.45 (t, *J* = 6.2 Hz, 1H, H^5), 6.99 (d, *J* = 8.8 Hz, 2H, $H^{c'}$), 6.87 (s, 2H, H^a and H^d), 3.80 (s, 3H,

H^{OMe}); ^{13}C NMR (151 MHz, DMSO-d_6) δ 163.0 (C^{e}), 161.9 (C^{2}), 151.4 ($C^{a'}$), 148.5 (C^{6}), 147.8 (C^{b}), 137.3 (C^{5}), 129.9 ($C^{b'}$), 125.1 (C^{4}), 121.1 (C^{3}), 113.8 ($C^{c'}$), 110.0 ($C^{d'}$), 55.8 (C^{OMe}); (ES^{+}) *m/z* = 271.4 $[M + H]^{+}$; HRMS (ES^{+}) m/z = $[M + H]^{+}$; 271.1199 calculated for $[C_{14}H_{15}N_4O_2]^{+}$ 271.1195.

Compound I2^{c}

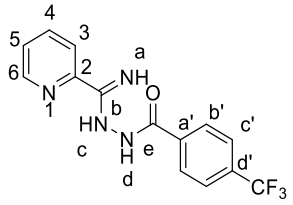

I1^{a} (250 mg, 1.84 mmol), Na_2CO_3 (214 mg, 2.02 mmol) with dry DMF (8 mL) in one Schlenk. 4-Trifluoromethylbenzoyl chloride (0.27 mL, 1.84 mmol) and dry DMF (3 mL) in the second Schlenk. An off-white powder was obtained (308 mg, 43 %); ^{1}H NMR (700 MHz, DMSO-d_6) δ 10.34 (s, 1H, H^{c}), 8.59 (d, *J* = 4.4 Hz, 1H, H^{6}), 8.16 (d, *J* = 8.0 Hz, 1H, H^{3}), 8.06 (d, *J* = 8.0 Hz, 2H, $H^{c'}$), 7.89 (td, *J* = 7.7, 1.7 Hz, 1H, H^{4}), 7.84 (d, *J* = 8.1 Hz, 2H, $H^{b'}$), 7.51 – 7.48 (d, *J* = 5.6 Hz, 1H, H^{5}), 6.97 (s, 2H, H^{a} and H^{d}); ^{13}C NMR (176 MHz, DMSO-d_6) δ 162.4 ($C^{a'}$), 150.9 (C^{2}), 149.3 ($C^{b'}$), 148.6 (C^{6}), 138.9 ($C^{e'}$), 137.4 (C^{4}), 131.4 (C^{CF3}), 129.1 ($C^{c'}$), 125.6 ($C^{b'}$), 125.4 (C^{5}), 123.7 ($C^{d'}$), 121.3 (C^{3}); ^{19}F NMR (376 MHz, Chloroform-*d*) δ -62.79; (ES^{+}) *m/z* = 309.1 $[M + H]^{+}$; HRMS (ES^{+}) *m/z* = 309.0966 $[M + H]^{+}$; calculated for $[C_{14}H_{12}F_3N_4O]^{+}$ 309.0963.

Compound I2^{d}

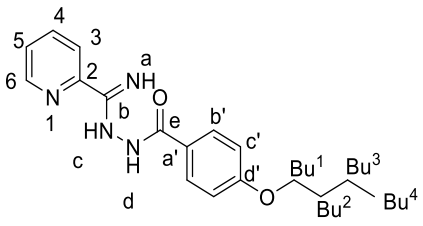

I1^{a} (1.52 g, 11.2 mmol), Na_2CO_3 (1.3 g, 12.3 mmol) and dry DMF (60 mL). 4-n-Butoxybenzoylchloride (2.13 mL, 11.2 mmol) and dry DMF (25 mL) in the second Schlenk. A white solid was obtained (2.9 g, 95 %); ^{1}H NMR (700 MHz, DMSO-d_6) δ 10.03 (s, 1H, H^{a}), 8.57 (d, *J* = 4.8 Hz, 1H, H^{6}), 8.15 (d, *J* = 8.0 Hz, 1H, H^{3}), 7.87 (t, *J* = 7.5 Hz, 1H, H^{4}), 7.84 (d, *J* = 8.3 Hz, 2H, $H^{b'}$), 7.45 (t, *J* = 6.2 Hz, 1H, H^{5}), 6.98 (d, 2H, *J* = 8.8 Hz, $H^{c'}$), 6.89 (s, 2H, H^{c} and H^{d}), 4.02 (t, *J* = 6.5 Hz, 2H, H^{Bu1}), 1.70-1.68 (m, 2H, H^{Bu2}), 1.49 – 1.32 (m, 2H, H^{Bu3}), 0.92 (t, *J* = 7.4 Hz, 3H, H^{Bu4}); ^{13}C NMR (176 MHz, DMSO-d_6) δ 163.0 (C^{e}), 161.4 ($C^{d'}$), 151.2

(C^2), 148.5 (C^6), 147.7 (C^b), 137.3 (C^4), 129.9 ($C^{c'}$), 127.0 ($C^{a'}$), 125.0 (C^5), 121.1 (C^3), 114.3 ($C^{b'}$), 67.8 (C^{Bu1}), 31.1 (C^{Bu2}), 19.1 (C^{Bu3}), 14.1 (C^{Bu4}); ES^+) *m/z* = 313.8 $[M + H]^+$; HRMS (ES^+) *m/z* = 313.1649 $[M + H]^+$; calculated for $[C_{17}H_{21}N_4O_2]^+$ 313.1665.

Compound I2[e]

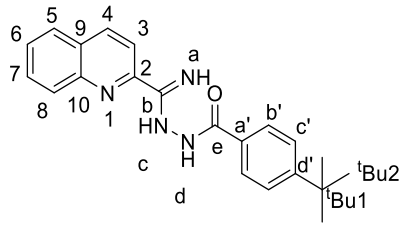

I1[b] (800 mg, 4.3 mmol), Na_2CO_3 (456 mg, 5.16 mmol) and dry DMF (26 mL) in one Schlenk. 4-*tert*-butylbenzoylchloride (0.84 mL, 4.3 mmol) and dry DMF (10 mL) in the second Schlenk. A cream-coloured solid was obtained (1.3 g, 85 %); ^{1}H NMR (599 MHz, DMSO-d_6) δ 10.24 (s, 1H, H^d), 8.41 (d, *J* = 8.7 Hz, 1H, H^3), 8.30 (d, *J* = 8.7 Hz, 1H, H^4), 8.06 (d, *J* = 8.4 Hz, 1H, H^8), 8.01 (d, *J* = 8.0 Hz, 1H, H^5), 7.84 – 7.76 (m, 3H, $H^{b'}$and H^7), 7.63 (t, *J* = 7.5 Hz, 1H, H^6), 7.50 (d, *J* = 8.0 Hz, 2H, $H^{c'}$), 7.03 (s, 2H, H^a and H^c), 1.30 (s, 9H, H^{tBu2}); ^{13}C NMR (151 MHz, DMSO-d_6) δ 163.7 (C^e), 154.4 ($C^{d'}$), 151.3, 147.3 (C^2), 146.6, 137.0 (C^3), 132.3 ($C^{a'}$), 130.5 (C^7), 129.2 (C^8), 128.6, 128.4 (C^5), 128.0 ($C^{2''}$), 127.7 (C^6), 125.4 ($C^{3''}$), 118.8 (C^4), 35.1 (C^{tBu1}), 31.4 (C^{tBu2}); ESI^+) *m/z* = 348.8 $[M + H]^+$; HRMS (ES^+) *m/z* = 347.1872 $[M + H]^+$; calculated for $[C_{21}H_{23}N_4O]^+$ 347.1872.

Compound I2[f]

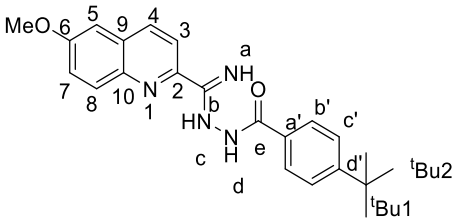

I1[c] (186 mg, 0.86 mmol), Na_2CO_3 (100 mg, 0.95 mmol) with dry DMF (5.3 mL) in one Schlenk. 4-*tert*-butylbenzoyl chloride (0.17 mL, 0.86 mmol) and dry DMF (2 mL) in the second Schlenk. A white powder was obtained after recrystallization in hot EtOH (56 mg, 17 %); ^{1}H NMR (700 MHz, DMSO-d_6) δ 10.19 (s, 1H, H^c), 8.29 (d, *J* = 8.7 Hz, 1H, H^8), 8.24 (d, *J* = 8.6 Hz, 1H, H^7), 7.95 (d, *J* = 9.0 Hz, 1H, H^3), 7.80 (d, *J* = 8.1 Hz, 2H, $H^{b'}$), 7.50 (d, *J* = 8.1 Hz, 2H, $H^{c'}$), 7.43 (dd, *J* = 9.0, 2.8 Hz, 1H, H^d), 7.41 (d, *J* = 2.8 Hz, 1H, H^5), 6.96 (s, 2H, H^a and H^d), 3.90 (s, 3H, H^{OMe}), 1.30 (s, 9H, H^{tBu2}); ^{13}C NMR (176 MHz, DMSO-d_6) δ 163.6 (C^e), 158.3 (C^6), 154.2 ($C^{d'}$), 148.9 (C^b), 147.6 (C^2), 142.4 (C^{10}), 135.7 (C^7), 132.2 ($C^{a'}$), 130.7 (C^3), 129.8 (C^9),

127.9 ($C^{b'}$), 125.4 ($C^{c'}$), 122.7 (C^4), 119.0 (C^8), 106.4 (C^5), 56.1 (C^{OMe}), 35.1 (C^{tBu1}), 31.4 (C^{tBu2}); (ES^+) *m/z* = 377.2 $[M + H]^+$; HRMS (ES^+) *m/z* = 377.1980 $[M + H]^+$; calculated for $[C_{14}H_{10}F_3N_4]^+$ 377.1978.

HL^n Triazoles

Compound HL¹

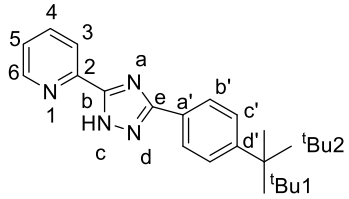

I2[a] (500 mg, 1.69 mmol) suspended in ethylene glycol (5 mL). A white solid was obtained; (347 mg, 74 %); ^{1}H NMR (600 MHz, Chloroform-*d*) δ 8.73 (d, *J* = 10.3 Hz, 1H, H^6), 8.31 (dd, *J* = 8.0, 5.0 Hz, 1H, H^3), 8.12 (d, *J* = 8.3 Hz, 2H, $H^{b'}$), 7.88 (dd, *J* = 7.9, 2.2 Hz, 1H, H^4), 7.50 (d, *J* = 8.5 Hz, 2H, $H^{c'}$), 7.40 (ddt, *J* = 7.6, 4.8, 1.4 Hz, 1H, H^5), 1.36 (s, 9H, H^{tBu2}); ^{13}C NMR (151 MHz, Chloroform-*d*) 163.1 (C^e), 152.8 ($C^{d'}$), 149.3 (C^6), 146.3 (C^2), 137.4 (C^4), 127.8 ($C^{a'}$), 126.2 ($C^{b'}$), 125.4 ($C^{c'}$), 124.7 (C^5), 121.8 (C^3), 34.8 (C^{tBu1}), 31.3 (C^{tBu2}); (ESI^+) *m/z* = 279.8 $[M + H]^+$; HRMS (ES^+) m/z = 279.1611 $[M + H]^+$; calculated for $[C_{17}H_{19}N_4]^+$ 279.1610.

Compound HL²

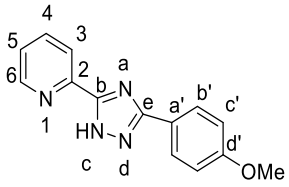

I2[b] (500 mg, 1.85 mmol) was suspended in ethylene glycol (5 mL). An off-white powder was obtained (405 mg, 87 %); ^{1}H NMR (400 MHz, Chloroform-*d*) δ 12.74 (s, 1H, H^c), 8.80 (ddd, *J* = 4.9, 1.8, 0.9 Hz, 1H, H^6), 8.35 (dt, *J* = 7.9, 1.1 Hz, 1H, H^3), 8.18 (d, *J* = 8.8 Hz, 1H, $H^{b'}$), 7.92 (td, *J* = 7.7, 1.7 Hz, 1H, H^4), 7.45 (ddd, *J* = 7.6, 4.9, 1.2 Hz, 1H, H^5), 7.03 (d, *J* = 8.8 Hz, 1H, $H^{C'}$), 3.90 (s, 3H, H^{OMe}); ^{13}C NMR (176 MHz; $(CD_3)_2SO$) 160.6 (C^e), 149.6 (C^6), 146.4 (C^2), 137.5 (C^4), 129.1 (C^b), 128.0 ($C^{c'}$), 124.9 (C^5), 123.6 ($C^{d'}$), 121.7 (C^3), 114.5 ($C^{a'}$), 114.0 ($C^{b'}$), 55.3 (C^{OMe}); (ES^+) *m/z* = 253.4 $[M + H]^+$; HRMS (ES^+) *m/z* =253.1088 $[M + H]^+$; calculated for $[C_{14}H_{13}N_4O]^+$ 253.1089.

Compound HL[3]

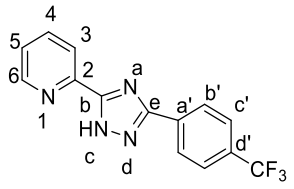

I2[c] (200 mg, 0.65 mmol) was suspended in ethylene glycol (2.5 mL). An off-white powder was obtained (153 mg, 29 %); ^{1}H NMR (700 MHz, DMSO-d_6) δ 8.72 (dt, *J* = 4.7, 1.4 Hz, 1H, H^{6}), 8.28 (d, *J* = 8.0 Hz, 2H, $H^{c'}$), 8.17 (dt, *J* = 7.8, 1.1 Hz, 1H, H^{3}), 8.01 (td, *J* = 7.7, 1.8 Hz, 1H, H^{4}), 7.85 (d, *J* = 8.1 Hz, 2H, $H^{b'}$), 7.54 (dd, *J* = 7.6, 4.9 Hz, 1H, H^{5}); ^{13}C NMR (176 MHz, DMSO-d_6) δ 150.1 (C^{6}), 146.5 (C^{b}), 138.2 (C^{4}), 135.3 (C^{CF3}), 129.8 ($C^{a'}$), 127.4 (C^{2}), 127.0 ($C^{c'}$), 126.2 ($C^{b'}$), 125.8 (C^{5}), 125.4 ($C^{d'}$), 123.9 (C^{e}), 121.9 (C^{3}); ^{19}F NMR (376 MHz, Chloroform-*d*) δ -62.62; MS (ES^+) *m/z* = 291.1 $[M + H]^+$; HRMS (ES^+) *m/z* = 291.0865 $[M + H]^+$; calculated for $[C_{14}H_{10}F_3N_4]^+$ 291.0858.

Compound HL[4]

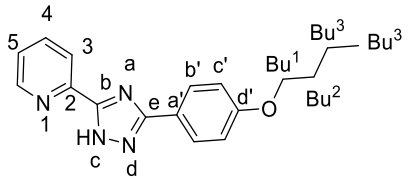

I2[d] (3.00 g, 11.1 mmol) was suspended in ethylene glycol (30 mL). An off-white powder was obtained (2.56 g, 74 %); ^{1}H NMR (599 MHz, Chloroform-*d*) δ 8.81 (ddd, *J* = 4.9, 1.8, 1.0 Hz, 1H, H^{6}), 8.34 (dt, *J* = 7.8, 1.1 Hz, 1H, H^{3}), 8.14 (d, *J* = 8.9 Hz, 2H, $H^{b'}$), 7.89 (td, *J* = 7.7, 1.7 Hz, 1H, H^{4}), 7.42 (ddd, *J* = 7.6, 4.8, 1.2 Hz, 1H, H^{5}), 6.99 (d, *J* = 8.9 Hz, 2H, $H^{c'}$), 4.02 (t, *J* = 6.5 Hz, 2H, $H^{1'''}$), 1.80 (ddt, *J* = 9.1, 7.8, 6.5 Hz, 2H, $H^{2'''}$), 1.61 – 1.43 (m, 2H, $H^{3'''}$), 0.99 (t, *J* = 7.4 Hz, 3H, $H^{4'''}$); ^{13}C NMR (151 MHz, Chloroform-*d*) δ 160.3 ($C^{4''}$), 149.5 (C^{6}), 146.6 (C^{2}), 137.6 (C^{5}), 129.1 ($C^{2'}$), 128.0 ($C^{2''}$), 124.8 (C^{4}), 123.2 ($C^{1''}$), 121.9 (C^{3}), 114.9 ($C^{4'}$), 114.6 ($C^{3''}$), 67.8 ($C^{1'''}$), 31.3 ($C^{2'''}$), 19.3 ($C^{3'''}$), 13.9 ($C^{4'''}$); MS (ES^+) *m/z* = 295.1 $[M + H]^+$; HRMS (ES^+) *m/z* = 295.1553 $[M + H]^+$; calculated for $[C_{17}H_9N_4O]^+$ 295.1559.

Compound HL[5]

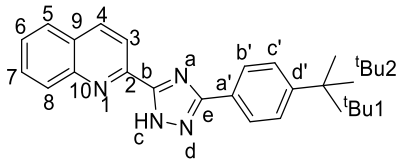

I2[e] (1.20 g, 3.47 mmol) was suspended in ethylene glycol (14 mL). An off-white powder was obtained after recrystallization in hot EtOH (497 mg, 44 %); ^{1}H NMR (599 MHz, DMSO-d_6) δ 8.54 (s, 1H, H^3), 8.29 (d, J = 8.5 Hz, 1H, H^4), 8.13 (d, J = 8.4 Hz, 1H, H^8), 8.07 – 8.00 (m, 3H, $H^{b'}$ and H^5), 7.83 (t, J = 7.8 Hz, 1H, H^7), 7.66 (t, J = 7.6 Hz, 1H, H^6), 7.53 (d, J = 7.9 Hz, 2H, $H^{c'}$), 1.30 (s, 9H, H^{tBu2}); ^{13}C NMR (151 MHz, DMSO-d_6) δ 152.7 ($C^{d'}$), 147.7 (C^3), 130.9 (C^7), 129.3 (C^8), 128.6 ($C^{b'/5}$), 127.7 (C^6), 126.3 ($C^{b'/5}$), 126.1 ($C^{3''}$), 119.7 (C^4), 35.0 (C^{tBu1}), 31.5 (C^{tBu2}); MS (ES^+) *m/z* = 329.2 $[M + H]^+$; HRMS (ES^+) *m/z* = 329.1761 $[M + H]^+$; calculated for $[C_{21}H_{21}N_4]^+$ 329.1766.

Compound HL[6]

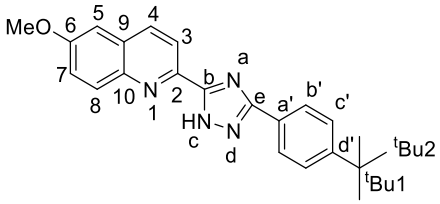

I2[f] (50 mg, 0.13 mmol) was suspended in ethylene glycol (0.7 mL). A beige powder was obtained (35 mg, 75 %); ^{1}H NMR (400 MHz, DMSO-d_6) δ 14.80 (s, 1H, H^c), 8.45 (d, J = 8.6 Hz, 1H, H^8), 8.26 (d, J = 8.6 Hz, 1H, H^7), 8.09-8.03 (m, 3H, H^3 and H^5), 7.56 (d, J = 8.0 Hz, 1H, $H^{b'}$), 7.53 – 7.45 (m, 2H, $H^{c'}$), 3.95 (s, 3H, H^{OMe}), 1.34 (s, 9H, H^{tBu2}); (ES^+) *m/z* = 359.2 $[M + H]^+$; HRMS (ES^+) *m/z* = 359.1877 $[M + H]^+$; calculated for $[C_{22}H_{23}N_4O]^+$ 359.1872.

7.3.1.3 1,2,4-Triazole ligands with 4-pyridyl substitution

Precursors

General procedure for pyridyl-substituted carbonitrile precursors (P^n)

A substituted-2-carbonitrile (1 eq), 4-substituted phenylboronic acid (1.2 eq) and Na_2CO_3 (5 eq) were added to a Schlenk with DME and H_2O (1:1) and reacted according to the general Suzuki cross-coupling method given earlier.

Compound P¹

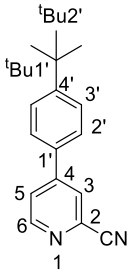

4-Bromopyridine-2-carbonitrile (1.00 g, 5.46 mmol), 4-*tert*-butyl phenylboronic acid (1.07 g, 6.01 mmol) and Na_2CO_3 (4.6g, 43.7 mmol) with $Pd(PPh_3)_4$ (789 mg, 0.68 mmol) in DME (15 mL) and H_2O (15 mL). A white powder was obtained (1.17 g, 91 %); ^{1}H NMR (700 MHz, Chloroform-*d*) δ 8.71 (dd, *J* = 5.2, 0.8 Hz, 1H, H^6), 7.90 (dd, *J* = 1.8, 0.8 Hz, 1H, H^3), 7.70 (dd, *J* = 5.2, 1.8 Hz, 1H, H^5), 7.58 (d, *J* = 8.4 Hz, 2H, $H^{2'}$), 7.54 (d, *J* = 8.4 Hz 2H, $H^{3'}$), 1.36 (s, 9H, $H^{tBu2'}$); ^{13}C NMR (176 MHz, Chloroform-*d*) δ 153.8 ($C^{4'}$), 151.4 (C^6), 149.6 (C^4), 134.5 (C^2), 132.9 ($C^{1'}$), 126.7 ($C^{2'}$), 126.5 ($C^{3'}$), 126.2 (C^3), 124.3 (C^5), 117.4 (C^{CN}), 34.8 ($C^{tBu1'}$), 31.2 ($C^{tBu2'}$); MS (ES^+) *m/z* = 237.3 $[M+H]^+$; HRMS (ES+) *m/z* = 237.1394 $[M+H]^+$; calculated for $[C_{16}H_{17}N_2]^+$ 237.1392;

Compound P²

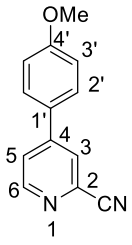

4-Bromopyridine-2-carbonitrile (657 mg, 3.60 mmol), 4-methoxy phenylboronic acid (600 mg, 3.95 mmol) and Na_2CO_3 (3.04 g, 28.7 mmol) with $Pd(PPh_3)_4$ (207 mg, 0.18 mmol) in DME (10 mL) and H_2O (10 mL). A white powder was obtained (700 mg, 93 %); ^{1}H NMR

(700 MHz, Chloroform-*d*) δ 8.67 (d, *J* = 5.5 Hz, 1H, H^6), 7.85 (dd, *J* = 1.9, 0.8 Hz, 1H, H^3), 7.65 (dd, *J* = 5.2, 1.9 Hz, 1H, H^5), 7.58 (d, *J* = 8.9 Hz, 2H, $H^{2'}$), 7.02 (d, *J* = 8.9 Hz, 2H, $H^{3'}$), 3.86 (s, 3H, H^{OMe}); ^{13}C NMR (176 MHz, Chloroform-*d*) δ 161.4 ($C^{4'}$), 151.3 (C^6), 149.2 (C^4), 134.4 (C^2), 128.2 ($C^{2'}$), 128.0 ($C^{1'}$), 125.8 (C^3), 123.8 (C^5), 117.4 (C^{CN}), 114.9 ($C^{3'}$), 53.4 (C^{OMe}); MS (ES^+) *m/z* = 211.1 $[M + H]^+$; HRMS (ES^+) *m/z* = 211.0860 $[M + H]^+$; calculated for $[C_{14}H_{10}F_3N_4]^+$ 211.0871.

Compound P³

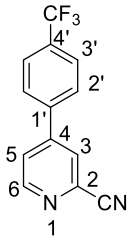

4-Bromopyridine-2-carbonitrile (1.00 g, 5.46 mmol), 4-trifluoromethylphenylboronic acid (1.14 g, 6.01 mmol) and Na_2CO_3 (4.63 g, 43.68 mmol) with $Pd(PPh_3)_4$ (789 mg, 0.68 mmol) in DME (15 mL) and H_2O (15 mL). A white solid was obtained (925 mg, 68 %); ^{1}H NMR (700 MHz, Chloroform-*d*) δ 8.81 (dd, *J* = 5.1, 0.8 Hz, 1H, H^6), 7.91 (dd, *J* = 1.8, 0.8 Hz, 1H, H^3), 7.80 (d, *J* = 8.09 Hz, 2H, $H^{2'}$), 7.74 (d, *J* = 8.09 Hz, 2H, $H^{3'}$), 7.72 (dd, *J* = 5.1, 1.8 Hz, 1H, H^5); ^{13}C NMR (176 MHz, Chloroform-*d*) δ 151.7 (C^6), 148.4 (C^4), 139.6 ($C^{4'}$), 139.5 ($C^{1'}$), 134.9 (C^2), 132.1 (C^{CF3}), 127.5 ($C^{3'}$), 126.5 ($C^{2'}$), 126.4 (C^3), 124.7 (C^5), 117.0 (C^{CN}); ^{19}F NMR (376 MHz, Chloroform-*d*) δ -62.84; MS (ES^+) *m/z* = 249.1 $[M+H]^+$; MS (ES^+) *m/z* = 249.1 $[M + H]^+$; HRMS (ES^+) *m/z* = 249.0630 $[M + H]^+$; calculated for $[C_{13}H_8F_3N_2]^+$ 249.0640.

Compound P⁴

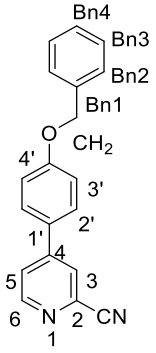

4-Bromopyridine-2-carbonitrile (700 mg, 4.00 mmol), 4-benzyloxyphenylboronic acid (1.00 g, 4.39 mmol) and Na_2CO_3 (2.90 g, 27.90 mmol) with $Pd(PPh_3)_4$ (230 mg, 0.20 mmol) in

DME (15 mL) and H_2O (15 mL). A white solid was obtained (1.1 g, 97 %); ^{1}H NMR (400 MHz, Chloroform-*d*) δ 8.72 (dd, *J* = 5.2, 0.8 Hz, 1H, H^6), 7.89 (dd, *J* = 1.9, 0.8 Hz, 1H, H^3), 7.69 (dd, *J* = 5.2, 1.9 Hz, 1H, H^5), 7.62 (d, *J* = 8.9 Hz, 2H, $H^{2'}$), 7.51 – 7.37 (m, 5H, H^{Bn2}, H^{Bn3} and H^{Bn4}), 7.14 (d, *J* = 8.9 Hz, 2H, $H^{3'}$), 5.17 (s, 2H, H^{CH2}); MS (ES^+) *m/z* = 287.2 $[M + H]^+$; HRMS (ES^+) *m/z* = 287.1188 $[M + H]^+$; calculated for $[C_{19}H_{15}N_2O]^+$ 287.1184.

Step 1 intermediates

Compound I1[d]

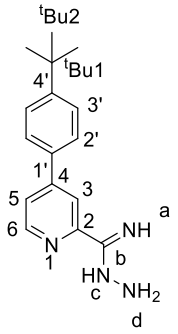

P[1] (1.00 g, 4.23 mmol) and hydrazine monohydrate (2.06 mL, 42.35 mmol) in EtOH (40 mL). A white powder was obtained (1.09 g, 96 %); ^{1}H NMR (700 MHz, Chloroform-*d*) δ 8.52 (dd, *J* = 5.2, 0.8 Hz, 1H, H^6), 8.26 (s, 1H, H^3), 7.64 (d, *J* = 8.2 Hz, 2H, $H^{2'}$), 7.50 – 7.46 (m, 3H, H^5 and $H^{3'}$), 5.31 (s, 2H, H^a and H^c), 4.58 (s, 2H, H^d), 1.35 (s, 9H, H^{tBu2}); ^{13}C NMR (176 MHz, Chloroform-*d*) δ 152.4 ($C^{4'}$), 151.2 (C^2), 148.6 (C^4), 148.3 (C^6), 134.9 ($C^{1'}$), 126.7 ($C^{2'}$), 126.0 ($C^{3'}$), 121.6 (C^5), 117.2 (C^3), 34.7 (C^{tBu1}), 31.3 (C^{tBu2}); MS (ES^+) *m/z* = 269.2 $[M + H]^+$; HRMS (ES^+) *m/z* = 269.1774 $[M + H]^+$; calculated for $[C_{14}H_{10}F_3N_4]^+$ 269.1766.

Compound I1[e]

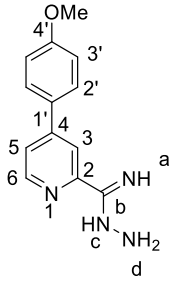

P[2] (250 mg, 1.19 mmol) and hydrazine monohydrate (0.58 mL, 11.90 mmol) in EtOH (10 mL). A white powder was obtained (218 mg, 76 %); ^{1}H NMR (700 MHz, Chloroform-*d*) δ 8.50 (d, *J* = 5.3, 1H, H^6), 8.21 (s, 1H, H^3), 7.64 (d, *J* = 8.8, 2H, $H^{2'}$), 7.45 (dd, *J* = 5.2, 1.9 Hz, 1H, H^5), 6.98 (m, *J* = 8.8, 2H, $H^{3'}$), 5.31 (s, 2H, H^d), 4.58 (s, 2H, H^a and H^c), 3.85 (s, 3H, H^{OMe}); ^{13}C

NMR (176 MHz, Chloroform-*d*) δ 160.5 ($C^{4'}$), 151.2 (C^{2}), 149.0 (C^{4}), 148.3 (C^{6}), 130.2 ($C^{1'}$), 128.2 ($C^{2'}$), 121.2 (C^{5}), 116.8 (C^{3}), 114.4 ($C^{3'}$), 58.4 (C^{b}), 55.4 (C^{OMe}); MS (ES^{+}) *m/z* = 243.1 [M + H]$^{+}$; HRMS (ES^{+}) *m/z* = 243.1255 [M + H]$^{+}$; calculated for $[C_{13}H_{15}N_4O]^{+}$ 243.1246.

Compound I1^{f}

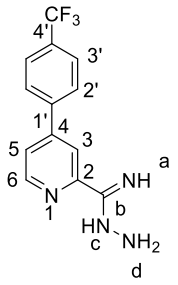

P^{3} (370 mg, 1.49 mmol) and hydrazine monohydrate (0.73 mL, 14.90 mmol) in EtOH (20 mL). A yellow powder was obtained (342 mg, 82 %);^{1}H NMR (700 MHz, Chloroform-*d*) δ 8.59 (dd, *J* = 5.1, 0.9 Hz, 1H, H^{6}), 8.26 (dd, *J* = 1.9, 0.8 Hz, 1H, H^{3}), 7.78 (d, *J* = 8.1 Hz, 2H, $H^{2'}$), 7.72 (d, *J* = 8.1 Hz, 2H, $H^{3'}$), 7.48 (dd, *J* = 5.1, 1.8 Hz, 1H, H^{5}), 5.31 (s, 2H, H^{d}), 4.61 (s, 2H, H^{a} and H^{c}); ^{13}C NMR (176 MHz, Chloroform-*d*) δ 151.6 (C^{2}), 148.6 (C^{6}), 148.4 (C^{b}), 147.3 (C^{4}), 141.6 ($C^{4'}$), 127.5 ($C^{2'}$), 126.0 ($C^{3'}$), 124.7 (C^{CF3}), 123.2 ($C^{1'}$), 121.7 (C^{5}), 117.6 (C^{3}); ^{19}F NMR (376 MHz, Chloroform-*d*) δ -62.68; MS (ES^{+}) *m/z* = 281.1 [M + H]$^{+}$; HRMS (ES^{+}) *m/z* = 281.1016 [M + H]$^{+}$; calculated for $[C_{13}H_{12}F_3N_4]^{+}$ 281.1014.

Compound I1^{g}

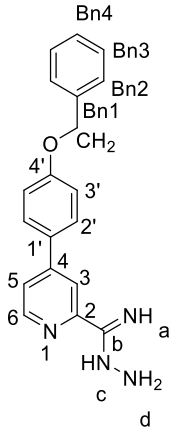

P^{4} (1.00 g, 3.5 mmol) and hydrazine monohydrate (1.7 mL, 35 mmol) in EtOH (50 mL). A white powder was obtained (556 mg, 50 %); ^{1}H NMR (700 MHz, Chloroform-*d*) δ 8.50 (dd, *J* = 5.2, 0.9 Hz, 1H, H^{6}), 8.24 (s, 1H, H^{3}), 7.65 (d, *J* = 8.9 Hz, 2H, $H^{2'}$), 7.47 – 7.43 (m, 3H, H^{5} and H^{Bn2}), 7.39 (t, *J* = 7.3 Hz, 2H, H^{Bn3}), 7.34 (t, *J* = 7.5 Hz, 1H, H^{Bn4}), 7.06 (d, *J* = 8.9 Hz, 2H, $H^{3'}$), 5.34 (s, 2H, H^{CH2}), 5.11 (s, 2H, H^{d}), 4.64 (s, 2H, H^{a} and H^{c}); ^{13}C NMR (176 MHz, Chloroform-*d*)

δ 159.7 ($C^{4'}$), 151.1 (C^{2}), 148.3 (C^{6}), 148.2 (C^{4}), 136.6 (C^{Bn1}), 130.4 ($C^{1'}$), 128.6 (C^{Bn3}), 128.3 ($C^{2'}$), 128.1 (C^{Bn4}), 127.5 (C^{Bn2}), 121.3 (C^{5}), 116.9 (C^{3}), 115.3 ($C^{3'}$), 70.1 (C^{CH2}); MS (ASAP$^+$) *m/z* = 319.2 $[M + H]^+$; HRMS (ASAP$^+$) *m/z* = 319.1553 $[M + H]^+$; calculated for $[C_{19}H_{19}N_4O]^+$ 319.1559.

Step 2 intermediates

Compound I2^g

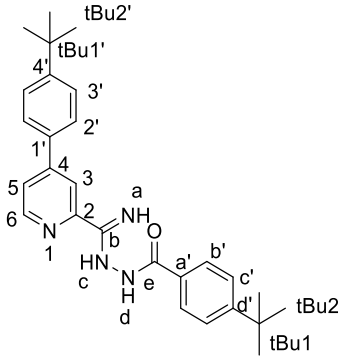

I1^d (418 mg, 1.56 mmol), Na_2CO_3 (198 mg, 1.87 mmol) with dry DMF (15 mL) in one Schlenk. 4-*tert* butylbenzoyl chloride (0.34 mL, 1.56 mmol) in dry DMF (5 mL) in the second Schlenk. A white powder was obtained (600 mg, 90 %); ^{1}H NMR (599 MHz, DMSO-d_6) δ 10.15 (s, 1H, H^{d}), 8.62 (d, J = 5.2 Hz, 1H, H^{6}), 8.39 (s, 1H, H^{3}), 7.79 (d, J = 8.0 Hz, 2H, $H^{b'}$), 7.76 (d, J = 5.1 Hz, 1H, H^{5}), 7.73 (d, J = 8.0 Hz, 2H, $H^{2'}$), 7.56 (d, J = 8.1 Hz, 2H, $H^{3'}$), 7.48 (d, J = 8.1 Hz, 2H, $H^{c'}$), 6.93 (s, 2H, H^{a} and H^{c}), 1.31 (s, 9H, $H^{tBu2'}$), 1.29 (s, 9H, H^{tBu2}); ^{13}C NMR (151 MHz, DMSO-d_6) δ 154.1, 152.6, 149.1 (C^{6}), 134.6, 127.9 ($C^{b'}$), 127.0 ($C^{2'}$), 126.6 ($C^{3'}$), 125.3 ($C^{c'}$), 122.4 (C^{5}), 117.9 (C^{3}), 35.1 (C^{tBu1}), 34.9 ($C^{tBu1'}$), 31.5-31.4 ($C^{tBu2'}$ and C^{tBu2}); MS (ES$^+$) *m/z* = 429.8 $[M+H]^+$; HRMS (ES+) *m/z* = 429.2651 $[M+H]^+$; calculated for $[C_{16}H_{17}N_2]^+$ 429.2654.

Compound I2^h

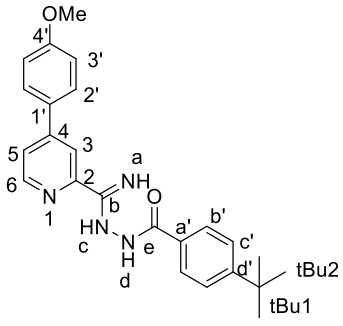

I1^e (400 mg, 1.51 mmol), Na_2CO_3 (199 mg, 1.88 mmol) with dry DMF (13 mL) in one Schlenk. 4-*tert* butylbenzoyl chloride (0.31 mL, 1.51 mmol) in dry DMF (5 mL) in the second Schlenk.

A white powder was obtained (500 mg, 80 %); ^{1}H NMR (599 MHz, DMSO-d_6) δ 10.13 (s, 1H, H^{d}), 8.58 (d, *J* = 5.2 Hz, 1H, H^{6}), 8.35 (s, 1H, H^{3}), 7.81-7.72 (m, 4H, H^{5}, $H^{b'}$ and $H^{2'}$), 7.48 (d, *J* = 8.0 Hz, 2H, $H^{3'/5'}$), 7.09 (dd, *J* = 8.8, 4.7 Hz, 2H, $H^{c'}$), 6.92 (s, 2H, H^{a} and H^{c}), 3.81 (d, *J* = 1.1 Hz, 3H, H^{OMe}), 1.29 (s, 9H, H^{tBu2}); ^{13}C NMR (151 MHz, DMSO-d_6) δ 163.6 (C^{e}), 149.1 (C^{6}), 128.6, 127.9, 125.4, 122.1 (C^{5}), 117.4 (C^{3}), 115.2, 55.8 (C^{OMe}), 55.4, 40.5, 39.7, 35.1 (C^{tBu1}), 31.4 (C^{tBu2}); MS (ES$^+$) *m/z* = 403.3 [M + H]$^+$; HRMS (ES$^+$) *m/z* = 403.2137 [M + H]$^+$; calculated for $[C_{24}H_{27}N_4O_2]^+$ 403.2134.

Compound I2^{i}

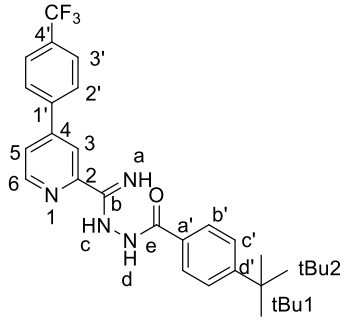

I1^{f} (500 mg, 1.78 mmol), Na_2CO_3 (208 mg, 1.96 mmol) with dry DMF (16 mL) in one Schlenk. 4-*tert* butylbenzoyl chloride (0.35 mL, 1.78 mmol) in dry DMF (6 mL) in the second Schlenk. A white powder was obtained (680 mg, 87 %); ^{1}H NMR (599 MHz, DMSO-d_6) δ 10.17 (s, 1H, H^{d}), 8.70 (d, *J* = 5.2 Hz, 1H, H^{6}), 8.45 (s, 1H, H^{3}), 8.03 (d, *J* = 8.0 Hz, 2H, $H^{2'}$), 7.90 (d, *J* = 8.1 Hz, 2H, $H^{3'}$), 7.85 (d, *J* = 4.7 Hz, 1H, H^{5}), 7.79 (d, *J* = 8.2 Hz, 2H, $H^{b'}$), 7.48 (d, *J* = 8.1 Hz, 2H, $H^{c'}$), 6.98 (s, 2H, H^{a} and H^{c}), 1.29 (s, 9H, H^{tBu2}); ^{13}C NMR (151 MHz, DMSO-d_6) δ 163.6 (C^{e}), 154.4 ($C^{d'}$), 152.2 (C^{b}), 149.5 (C^{6}), 146.8 (C^{4}), 141.0 ($C^{1'}$), 132.3 ($C^{a'}$), 130.1 ($C^{4'}$), 128.4 ($C^{2'}$), 127.9 ($C^{b'}$), 126.6 ($C^{3'}$), 125.4 ($C^{c'}$), 123.0 (C^{5}), 122.9 (C^{2}), 118.6 (C^{3}), 35.1 (C^{tBu1}), 31.4 (C^{tBu2}); ^{19}F NMR (376 MHz, Chloroform-*d*) δ -62.72; MS (ES$^+$) *m/z* = 441.2 [M + H]$^+$; HRMS (ES$^+$) *m/z* = 441.1913 [M + H]$^+$; calculated for $[C_{24}H_{24}F_3N_4O]^+$ 441.1902.

Compound I2[j]

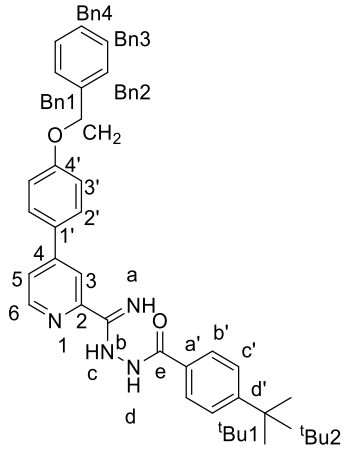

I1[g] (400 mg, 1.26 mmol), Na_2CO_3 (147 mg, 1.38 mmol) with dry DMF (15 mL) in one Schlenk. 4-*tert* butylbenzoyl chloride (0.25 mL, 1.26 mmol) in dry DMF (5 mL) in the second Schlenk. A shiny silver powder was obtained and used without purification for the next step (434 mg, 72%); (ES^+) *m/z* = 479.4 $[M + H]^+$; HRMS (ES^+) *m/z* = 479.2454 $[M + H]^+$; calculated for $[C_{30}H_{31}N_4O_2]^+$ 479.2447.

HL[n] Triazoles

Compound HL[7]

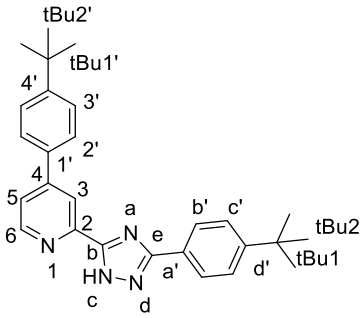

I2[g] (570 mg, 1.33 mmol) and ethylene glycol (6 mL). A beige powder was obtained (414 mg, 76 %); ^1H NMR (700 MHz, Chloroform-*d*) δ 8.79 (dd, *J* = 5.2, 0.8 Hz, 1H, H^6), 8.60 (dd, *J* = 1.9, 0.8 Hz, 1H, H^3), 8.16 (d, *J* = 8.4 Hz, 2H, $H^{b'}$), 7.74 (d, *J* = 8.4 Hz, 2H, $H^{2'}$), 7.64 (dd, *J* = 5.2, 1.9 Hz, 1H, H^5), 7.55 (d, *J* = 8.4 Hz, 2H, $H^{3'}$), 7.50 (d, *J* = 8.4 Hz, 2H, $H^{c'}$), 1.38 (s, 9H, $H^{tBu2'}$), 1.36 (s, 9H, H^{tBu2}); ^{13}C NMR (176 MHz, Chloroform-*d*) δ 153.1 ($C^{4'}$), 152.6 ($C^{d'}$), 150.3 (C^4), 149.4 (C^6), 146.7 (C^2), 134.2 ($C^{1'}$), 127.8 ($C^{a'}$), 126.9 ($C^{2'}$), 126.4 ($C^{b'}$), 126.2 ($C^{3'}$), 125.6 ($C^{c'}$), 122.4 (C^3), 119.6 (C^5), 34.8-34.7 ($C^{tBu1'}$ and C^{tBu1}), 31.3 (C^{tBu2}), 31.2 ($C^{tBu2'}$); MS (ES^+) *m/z* = 411.0 $[M + H]^+$; HRMS (ES^+) *m/z* = 411.2543 $[M + H]^+$; calculated for $[C_{27}H_{30}N_4]^+$ 411.2544.

Compound HL[8]

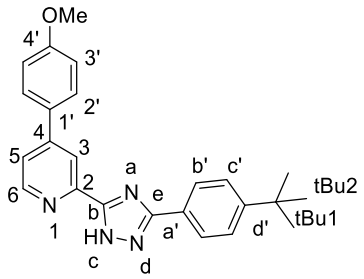

I2[h] (500 mg, 1.24 mmol) and ethylene glycol (5 mL). A beige powder was obtained (300 mg, 63 %); ^{1}H NMR (700 MHz, DMSO-d_6) δ 8.70 (d, *J* = 5.2 Hz, 1H, H^{6}), 8.33 (s, 1H, H^{3}), 8.02 (d, *J* = 8.3 Hz, 2H, $C^{2'}$), 7.85 (d, *J* = 8.4 Hz, 2H, $H^{b'}$), 7.78 (s, 1H, H^{5}), 7.51 (d, *J* = 8.0 Hz, 2H, $H^{3'}$), 7.10 (d, *J* = 8.9 Hz, 2H, $H^{c'}$), 3.82 (s, 3H, H^{OMe}), 1.30 (s, 9H, H^{tBu2}); ^{13}C NMR (176 MHz, DMSO-d_6) δ 161.0 ($C^{4'}$), 152.1 ($C^{d'}$), 150.6 (C^{6}), 148.6 (C^{4}), 129.2 ($C^{1'}$), 128.7 ($C^{b'}$), 126.2 ($C^{2'}$), 126.0 ($C^{3'}$), 122.0 (C^{2}), 115.2 ($C^{c'}$), 55.8 (C^{OMe}), 35.0 (C^{tBu1}), 31.5 (C^{tBu2}); MS (ES^{+}) *m/z* = 385.2 $[M + H]^{+}$; HRMS (ES^{+}) *m/z* = 385.2029 $[M + H]^{+}$; calculated for $[C_{13}H_{12}F_3N_4]^{+}$ 385.2028.

Compound HL[9]

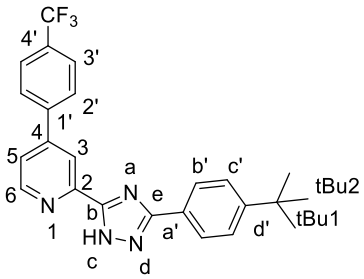

I2[i] (680 mg, 1.54 mmol) and ethylene glycol (7 mL). A beige powder was obtained (568 mg, 87 %); ^{1}H NMR (400 MHz, DMSO-d_6) δ 8.84 (d, *J* = 5.3 Hz, 1H, H^{6}), 8.44 (s, 1H, H^{3}), 8.14 (d, *J* = 8.1 Hz, 2H, $H^{2'}$), 8.05 (d, *J* = 8.5 Hz, 2H, $H^{b'}$), 7.94 (d, *J* = 8.1 Hz, 2H, $H^{3'}$), 7.58 – 7.49 (m, 3H, H^{5} and $H^{c'}$), 1.33 (s, 9H, H^{tBu2}); ^{19}F NMR (376 MHz, DMSO-d_6) δ -61.14; MS (ES^{+}) *m/z* = 423.2 $[M + H]^{+}$; HRMS (ES^{+}) *m/z* = 423.1806 $[M + H]^{+}$; calculated for $[C_{24}H_{22}F_3N_4]^{+}$ 423.1797.

Compound HL[10]

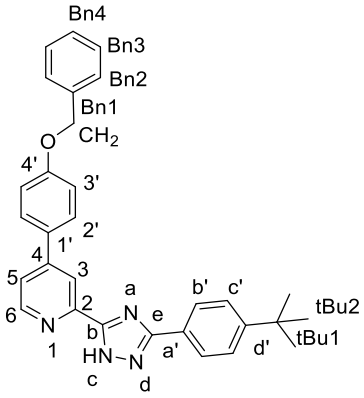

I2[j] (400 mg, 0.84 mmol) and ethylene glycol (6 mL). A beige powder was obtained (200 mg, 52 %); ^{1}H NMR (700 MHz, DMSO-d_6) δ 8.69 (d, J = 5.1 Hz, 1H, H^{6}), 8.34 (s, 1H, H^{3}), 8.03 (d, J = 8.3 Hz, 2H, $H^{b'}$), 7.84 (d, J = 8.6 Hz, 2H, $H^{3'}$), 7.78 (s, 1H, H^{5}), 7.51 (d, J = 8.0 Hz, 2H, $H^{c'}$), 7.46 (d, J = 6.8 Hz, 2H, H^{Bn2}), 7.40 (d, J = 7.3 Hz, 2H, H^{Bn3}), 7.33 (d, J = 7.4 Hz, 1H, H^{Bn4}), 7.18 (d, J = 8.8 Hz, 2H, $H^{2'}$), 5.18 (s, 2H, H^{CH2}), 1.30 (s, 9H, H^{tBu2}); ^{13}C NMR (176 MHz, DMSO-d_6) δ 160.1 ($C^{4'}$), 152.2 ($C^{d'}$), 150.6 (C^{6}), 148.4 (C^{4}), 137.3 (C^{Bn1}), 129.5 ($C^{1'}$), 128.9 (C^{Bn3}), 128.8, 128.7 ($C^{3'}$), 128.4 (C^{Bn4}), 128.1 (C^{Bn2}), 126.2 ($C^{b'}$), 126.0 ($C^{c'}$), 121.9 (C^{5}), 118.3 (C^{3}), 116.1 ($C^{2'}$), 116.0, 69.8 (C^{CH2}), 35.0 (C^{tBu1}), 31.5 (C^{tBu2}); MS (ES^{+}) m/z = 461.4.

7.3.2 Homoleptic Pt triazole complexes

7.3.2.1. Complexes with no pyridyl substitution on the triazole ligand

General Procedure

HL^{n} (2.2 eq) was added to a Schlenk with K_2PtCl_4 (1 eq) in H_2O and EtOH (1:3). This was degassed via 3 x FPT and set to heat at 80 °C overnight. Upon reaction completion the mixture was cooled to RT and the solid was then isolated by centrifuge and washed with small amounts of MeOH. The complexes were recrystallized by cooling from a hot DMF solution.

PtL$^{1}_{2}$

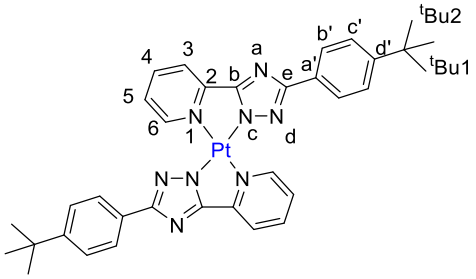

HL[1] (100 mg, 0.36 mmol), K_2PtCl_4 (68 mg, 0.16 mmol) with H_2O (1 mL) and EtOH (3 mL). An orange solid was obtained (80 mg, 67 %); ^{1}H NMR (600 MHz, Chloroform-*d*) δ 9.61 (s, 2H, H^6), 7.83 (d, *J* = 7.7 Hz, 4H, $H^{b'}$), 7.54 (d, *J* = 6.9 Hz, 4H, H^3), 7.44 (d, *J* = 7.8 Hz, 4H, $H^{c'}$), 7.15 (d, *J* = 6.5 Hz, 2H, H^4), 6.71 (t, *J* = 6.4 Hz, 2H, H^5), 1.41 (s, 18H H^{tBu2}); ^{13}C NMR (151 MHz, Chloroform-*d*) δ 213.8 (C^6), 172.1, 167.4, 151.0, 139.1 (C^5) 134.8, 126.0 ($C^{b'}$), 125.2 ($C^{c'}$), 124.0 (C^4) 120.2, 119.5 (C^3), 34.7 (C^{tBu1}), 31.4 (C^{tBu2}); (ESI$^+$) *m/z* = 750.7 $[M + H]^+$; HRMS (ES$^+$) *m/z* =749.2593 $[M + H]^+$; calculated for $[C_{34}H_{35}N_8{}^{194}Pt]^+$ 749.2611; Mp. >250 °C.

PtL[2]$_2$

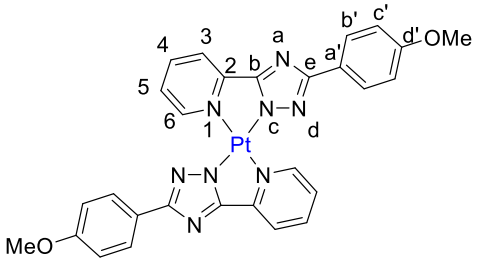

HL[2] (150 mg, 0.59 mmol) and K_2PtCl_4 (113 mg, 0.27mmol) with H_2O (1.5 mL) and EtOH (4.5 mL). An orange powder was obtained (65 mg, 35%); ^{1}H NMR (700 MHz, Chloroform-*d*) δ 9.59 (s, 2H, H^6), 7.84 (d, *J* = 8.2 Hz, 4H, $H^{b'}$), 7.59 (d, *J* = 7.3 Hz, 2H, H^3), 7.23 (d, *J* = 7.1 Hz, 2H, H^4), 6.97 (d, *J* = 8.2 Hz, 4H, $H^{c'}$), 6.77 (t, *J* = 6.8 Hz, 2H, H^5), 3.92 (s, 6H, H^{OMe}); (ES$^+$) *m/z* = 698.3 $[M + H]^+$; HRMS (ES$^+$) *m/z* = 697.1559 $[M + H]^+$; calculated for $[C_{14}H_{13}N_4O]^+$ 697.1571; Mp. >250 °C.

PtL[3]$_2$

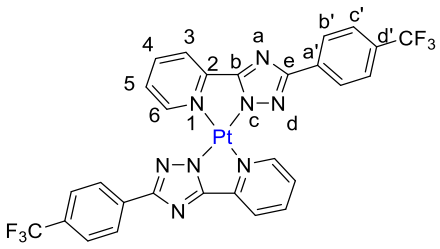

HL[3] (100 mg, 0.34 mmol) and K_2PtCl_4 (65 mg, 0.16 mmol) with H_2O (1 mL) and EtOH (3 mL). An orange powder was obtained (30 mg, 24 %) that was insoluble in all common organic solvents; MS (ASAP$^+$) *m/z* = 774.1 $[M+H]^+$; HRMS (ASAP$^+$) *m/z* = 772.1020 $[M+H]^+$; calculated for $[C_{28}H_{17}F_6N_8{}^{194}Pt]^+$ 772.1029; Anal. Calcd for $C_{28}H_{16}F_6N_8Pt$: C, 43.47; H, 2.08; F, 14.74; N, 14.49; Found: C, 43.91; H, 1.96; F, 14.62; N, 14.76.

PtL$^4_2$

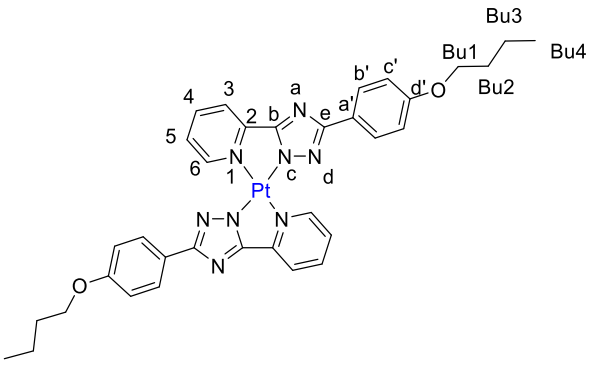

HL^4 (300 mg, 1.02 mmol), K_2PtCl_4 (233 mg, 0.56 mmol) with H_2O (6 mL) and EtOH (18mL). A yellow solid was obtained (76 mg, 18 %); ^{1}H NMR (599 MHz, Chloroform-*d*) δ 10.45 (dt, *J* = 5.7, 1.1 Hz, 1H, H^6), 8.55 – 8.45 (m, 2H, H^3 and H^4), 8.03 (d, *J* = 8.9 Hz, 2H, $H^{c'}$), 7.96 (ddd, *J* = 6.6, 5.7, 2.7 Hz, 1H, H^5), 7.14 (d, *J* = 8.9 Hz, 2H, $H^{b'}$), 4.13 (t, *J* = 6.6 Hz, 2H, H^{Bu1}), 1.94 – 1.79 (m, 2H, H^{Bu2}), 1.62 – 1.48 (m, 2H, H^{Bu3}), 1.02 (t, *J* = 7.4 Hz, 3H, H^{Bu4}); ^{13}C NMR (151 MHz, Chloroform-*d*) δ 162.8 ($C^{d'}$), 153.4 (C^6), 143.7 (C^2), 143.3 ($C^{3/4}$), 128.7 ($C^{c'}$), 128.2 (C^5), 124.01 ($C^{3/4}$), 115.8 ($C^{b'}$), 115.3, 68.6 (C^{Bu1}), 30.9 (C^{Bu2}), 19.0 (C^{Bu3}), 13.5 (C^{Bu4}); MS (ES^+) *m/z* = 782.3 $[M + H]^+$; HRMS (ES^+) *m/z* = 779.2466 $[M + H]^+$; calculated for $[C_{34}H_{35}N_8O_2{}^{192}Pt]^+$ 779.2493; Mp. >250 °C.

7.3.2.2 Complexes with 4-pyridyl substitution on the triazole ligand

General procedure

HL^n (2.2 eq) was added to a Schlenk with K_2PtCl_4 (1 eq) in H_2O and MeCN (1:3). This was degassed via 3 x FPT and set to heat at 80 °C overnight. Upon reaction completion the reaction mixture was cooled to RT and the solid was then isolated by centrifuge and washed with H_2O, MeOH and Et_2O and then further purified by column chromatography on alumina (DCM/MeOH, 100:0 to 98:2).

PtL$^{7}_{2}$

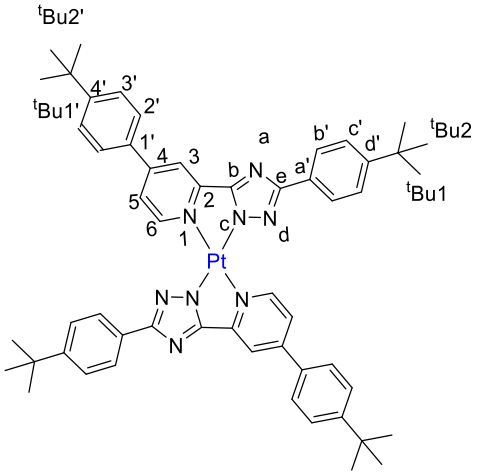

HL^{7} (100 mg, 0.24 mmol), K_2PtCl_4 (56 mg, 0.13 mmol) with H_2O (1 mL) and MeCN (3 mL). A red powder was obtained after column and recrystallization (30 mg, 22 %); R_f= 0.9 (alumina, 100 % DCM); ^{1}H NMR (700 MHz, Chloroform-*d*) δ 9.70 (s(broad), 2H, H^6), 7.90 (d, *J* = 7.6 Hz, 4H, H$^{b'}$), 7.49 (d, *J* = 7.6 Hz, 4H, H$^{2'}$), 7.44 (d, *J* = 7.6 Hz, 4H, H$^{3'}$), 7.32 (d, *J* = 7.6 Hz, 4H, H$^{c'}$), 7.25 (s, 2H, H^3), 7.12 (d, *J* = 5.7 Hz, 2H, H^5), 1.40 (s, 18H, H$^{tBu2'}$), 1.37 (s, 18H, H^{tBu2}); ^{13}C NMR (176 MHz, Chloroform-*d*) δ 127.4, 126.3, 126.2, 125.4, 34.9 (C$^{tBu1'}$), 34.7 (C^{tBu1}), 31.4 (C^{tBu2}), 31.3 (C$^{tBu2'}$); (ASAP$^+$) *m/z* = 1014.4 [M + H]$^+$; HRMS (ES$^+$) *m/z* =1013.4474 [M + H]$^+$; calculated for [$C_{54}H_{59}N_8{}^{194}Pt$]$^+$ 1013.4489.

PtL$^{8}_{2}$

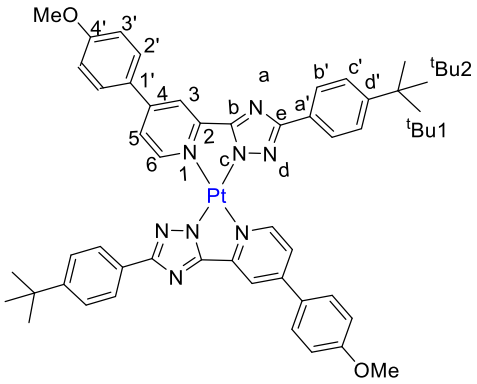

HL^{8} (50 mg, 0.13 mmol), K_2PtCl_4 (30 mg, 0.07 mmol) with H_2O (2 mL) and MeCN (6 mL). An orange powder was obtained after column and recrystallization (20 mg, 29 %); R_f= 0.9 (alumina, 100 % DCM)^{1}H NMR (700 MHz, Chloroform-*d*) δ 9.72 (d, *J* = 6.0 Hz, 2H, H^6), 8.69 (d, *J* = 2.2 Hz, 2H, H^3), 7.79 (dd, *J* = 6.1, 2.2 Hz, 2H, H^5), 7.73 (d, *J* = 8.2 Hz, 4H, H$^{3'}$), 7.58 (d, *J*

= 8.6 Hz, 4H, $H^{c'}$), 7.33 (d, *J* = 8.2 Hz, 4H, $H^{2'}$), 6.91 (d, *J* = 8.6 Hz, 4H, $H^{b'}$), 3.92 (s, 6H, H^{OMe}), 1.30 (s, 18H, H^{tBu2}); ^{13}C NMR (176 MHz, Chloroform-*d*) δ 163.5 ($C^{4'}$), 157.2 (C^{2}), 156.8 ($C^{d'}$), 155.5 ($C^{a'}$), 153.6 ($C^{1'}$), 151.5 (C^{6}), 143.1 (C^{b}), 128.9 ($C^{3'}$), 126.5 ($C^{c'}$), 126.2 ($C^{b'}$), 124.6 (C^{4}), 123.1 (C^{5}), 119.9 (C^{3}), 119.8 (C^{e}), 115.3 ($C^{2'}$), 55.5 (C^{OMe}), 35.0 (C^{tBu1}), 30.8 (C^{tBu2}); (ASAP$^+$) *m/z* = 962.3 $[M + H]^+$.

PtL$^9_2$

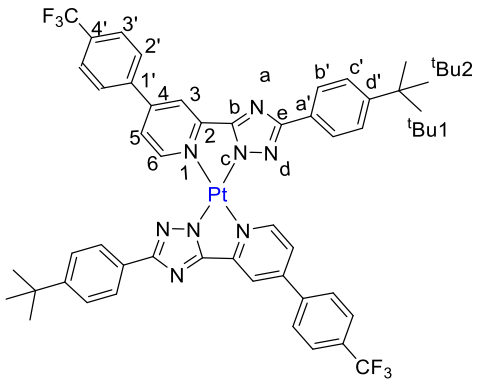

HL^9 (150 mg, 0.36 mmol), K_2PtCl_4 (81 mg, 0.19 mmol) with H_2O (1 mL) and MeCN (3 mL). A red powder was obtained after column and recrystallization (14 mg, 7 %); R_f= 0.9 (alumina, 100 % DCM); ^{1}H NMR (700 MHz, Chloroform-*d*) δ 10.34 (d, *J* = 6.0 Hz, 2H, H^{6}), 8.87 (d, *J* = 2.0 Hz, 2H, H^{3}), 8.10 (dd, *J* = 6.1, 2.0 Hz, 2H, H^{5}), 8.02 (d, *J* = 8.0 Hz, 4H, $H^{2'}$), 7.92 (d, *J* = 7.9 Hz, 4H, $H^{b'}$), 7.85 (d, *J* = 8.0 Hz, 4H, $H^{c'}$), 7.58 (d, *J* = 8.0 Hz, 4H, $H^{3'}$), 1.36 (s, 18H, H^{tBu2}); ^{19}F NMR (376 MHz, Chloroform-*d*) δ -62.42; (ASAP$^+$) *m/z* = 1037.3 $[M + H]^+$; HRMS (ES$^+$) *m/z* =1037.2968 $[M + H]^+$; calculated for $[C_{48}H_{41}N_8{}^{194}PtF_6]^+$ 1037.2985.

7.3.3 Heteroleptic Pt triazole complexes

7.3.3.1 Neutral complexes

Dimers

[Pt(thpy)(μ-Cl)]₂

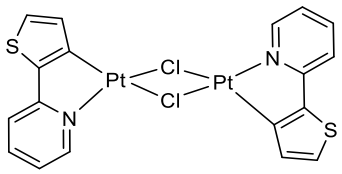

2-(2-Thienyl)pyridine (50 mg, 0.31 mmol), K_2PtCl_4 (129 mg, 0.31 mmol) with H_2O (1 mL) and ethoxyethanol (3 mL). A light green solid was obtained (90 mg, 37 %) and used without further purification. The experimental data obtained were in good agreement with the literature.[196]

[Pt(pquin)(μ-Cl)]₂

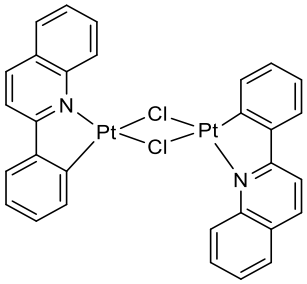

2-phenylquinoline (74 mg, 0.36 mmol), K_2PtCl_4 (150 mg, 0.36 mmol) with H_2O (1.5 mL) and ethoxyethanol (4.5 mL). A pale green solid was obtained (83 mg, 27 %) and used without any further purification. The experimental data obtained were in good agreement with the literature.[197]

Thienyl Pyridine Complexes

General procedure

$[Pt(thpy)(\mu\text{-}Cl)]_2$ (1 eq) and HL^n (2 eq) were added to a Schlenk with a DCM/MeOH mixture (1:1). This was degassed via 3 x FPT then set to reflux at 50 °C for 24 h. Once cooled to RT the solvent was removed and the residue was columned on alumina and then recrystallized in DCM/Hexane.

Pt(thpy)L¹

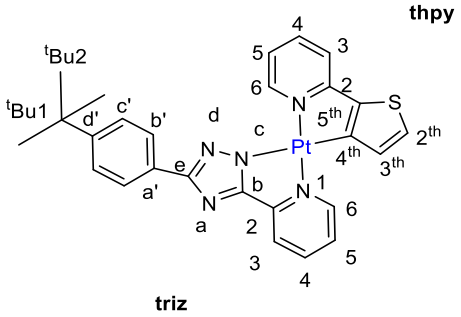

[Pt(thpy)(μ-Cl)]$_2$ (30 mg, 0.04 mmol), **HL¹** (21 mg, 0.08 mmol) in DCM (1 mL) and MeOH (1 mL). A red solid was obtained (12 mg, 49 %); ^{1}H NMR (600 MHz, Chloroform-*d*) δ 10.54 (d, *J* = (^{195}Pt 39.9), 5.9 Hz, 1H, H^{6triz}), 9.29 (d, *J* = (^{195}Pt 48.1), 5.8 Hz, 1H, H^6), 8.18 (d, *J* = 8.5 Hz, 2H, H$^{b'}$), 8.15 (dt, *J* = 7.7, 1.3 Hz, 1H, H^{2th}), 7.97 (td, *J* = 7.6, 1.4 Hz, 1H, H^4), 7.72 (td, *J* = 7.7, 1.4 Hz, 1H, H^{4triz}), 7.52 – 7.48 (m, 3H, H^5 and H$^{c'}$), 7.34 (dd, *J* = 7.9, 1.2 Hz, 1H H^{3triz}), 7.25 – 7.23 (m, 2H, H^3 and H^{3th}), 7.05 (ddd, *J* = 7.3, 5.8, 1.4 Hz, 1H, H^{5triz}), 1.39 (s, 9H, H^{tBu2}); ^{13}C NMR (151 MHz, Chloroform-*d*) δ 163.3 (C$^{a'}$), 163.0 (C^b), 162.7 (C^{2triz}), 152.8 (C^{6triz}), 152.2 (C^2), 151.6 (C^9), 151.1 (C$^{d'}$), 148.2 (C^{4th}), 142.9 (C^{5th}), 139.3 (C^4), 139.3 (C^{4triz}), 130.9 (C^{3th}), 130.2 (C^e), 127.4 (C^5), 126.0 (C$^{b'}$), 125.3 (C$^{c'}$), 123.5 (C^3), 120.9 (C^{2th}), 120.0 (C$^{5'}$), 116.8 (C^{3triz}), 34.7 (C^{tBu1}), 31.4 (C^{tBu2}); MS (ES$^+$) *m/z* = 633.0 [M+H]$^+$; HRMS (ES+) *m/z* = 632.1379 [M+H]$^+$; calculated for [$C_{26}H_{24}N_5S^{194}Pt$]$^+$ 632.1379.

Pt(thpy)L²

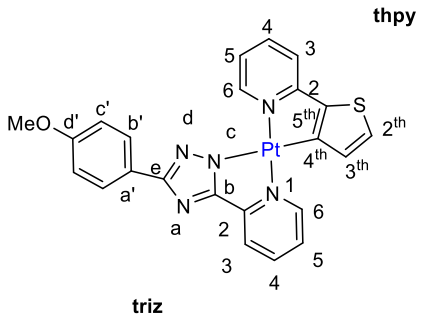

[Pt(thpy)(μ-Cl)]$_2$ (30 mg, 0.04 mmol), **HL²** (19 mg, 0.08 mmol), DCM (1 mL) and MeOH (1 mL). A red solid was obtained (5 mg, 22 %); ^{1}H NMR (700 MHz, Chloroform-*d*) δ 10.45 (d, *J* = 5.3 Hz, 1H, H^{6triz}), 9.24 (d, *J* = 5.8 Hz, 1H, H^6), 8.20 (d, *J* = 8.8 Hz 2H, H$^{b'}$), 8.17 (d, *J* = 5.8 Hz, 1H, H^3), 7.95 (td, *J* = 7.6, 1.4 Hz, 1H, H^4), 7.70 (td, *J* = 7.6, 1.5 Hz, 1H, H^{4triz}), 7.48 (d, *J* = 4.7 Hz, 1H, H^{2th}), 7.31 (d, *J* = 7.8 Hz, 1H, H^{3triz}), 7.22 (ddd, *J* = 7.3, 5.7, 1.5 Hz, 1H, H^5), 7.20 (d,

J = 4.8 Hz, 1H, H^{3th}), 7.03 (t, *J* = 6.2 Hz, 1H, H^{5triz}), 7.01(d, *J* = 8.8 Hz, 2H, $H^{c'}$), 3.89 (s, 3H, H^{OMe}); ^{13}C NMR (176 MHz, Chloroform-*d*) δ 162.6 (C^{2triz}), 159.9 ($C^{a'}$), 152.7 (C^{6triz}), 151.6 (C^{6}), 147.9 (C^{4th}), 142.9 (C^{5th}), 139.4 (C^{4}), 139.3 (C^{4triz}), 130.8 (C^{3th}), 127.7 ($C^{b'}$), 127.3 (C^{2th}), 125.4 ($C^{d'}$), 123.6 (C^{5}), 121.0 (C^{3}), 121.0 (C^{2}), 120.0 (C^{5triz}), 116.8 (C^{3triz}), 113.9 ($C^{c'}$), 55.3 (C^{OMe}); MS (ES^+) *m/z* = 607.0 $[M+H]^+$; HRMS (ES+) *m/z* = 606.0872 $[M+H]^+$; calculated for $[C_{23}H_{18}N_5OS^{194}Pt]^+$ 606.0859.

Pt(thpy)L³

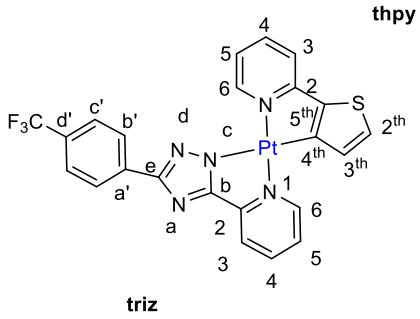

$[Pt(thpy)(\mu\text{-}Cl)]_2$ (30 mg, 0.04 mmol), **HL³** (22 mg, 0.08 mmol) in DCM (1 mL) and MeOH (1 mL). A red solid was obtained (9 mg, 37 %); ^1H NMR (700 MHz, Chloroform-*d*) δ 10.32 (d, *J* = 5.7 Hz, 1H, H^{6triz}), 9.16 (d, *J* = 5.7 Hz, 1H, H^{6}), 8.32 (d, *J* = 8.0 Hz, 2H, $H^{b'}$), 8.04 (d, *J* = 8.0 Hz, 1H, H^{3}), 7.90 (td, *J* = 7.6, 1.4 Hz, 1H, H^{4}), 7.71 (d, *J* = 8.0 Hz, 2H, $H^{c'}$), 7.65 (td, *J* = 7.6, 1.4 Hz, 1H, H^{4triz}), 7.43 (d, *J* = 4.7 Hz, 1H, H^{2th}), 7.26 (d, *J* = 6.3 Hz, 1H, H^{3triz}), 7.16 (ddd, *J* = 7.2, 5.6, 1.6 Hz, 1H, H^{5}), 7.11 (d, *J* = 4.8 Hz, 1H, H^{3th}), 6.96 (ddd, *J* = 7.3, 5.7, 1.4 Hz, 1H, H^{5triz}); ^{13}C NMR (176 MHz, Chloroform-*d*) δ 163.6 (C^{4th}), 162.6 (C^{2triz}), 161.3 ($C^{a'}$), 152.5 (C^{6triz}), 151.6 (C^{2}), 151.5 (C^{6}), 147.8 (C^{5th}), 142.7, 139.2 (C^{4}), 139.2 (C^{4triz}), 136.3 ($C^{d'}$), 130.7 (C^{3th}), 129.8 (C^{c}), 127.2 (C^{2th}), 126.3 ($C^{b'}$), 125.4 ($C^{c'}$), 125.3 (C^{CF3}), 123.7 (C^{5}), 120.8 (C^{3}), 119.9 (C^{5triz}), 116.8 (C^{3triz}); ^{19}F NMR (376 MHz, Chloroform-*d*) δ -62.76; MS (ES^+) *m/z* = 645.8 $[M+H]^+$; HRMS (ES+) *m/z* = 644.0631 $[M+H]^+$; calculated for $[C_{23}H_{15}F_3N_5S^{194}Pt]^+$ 644.0627.

Pt(thpy)L[7]

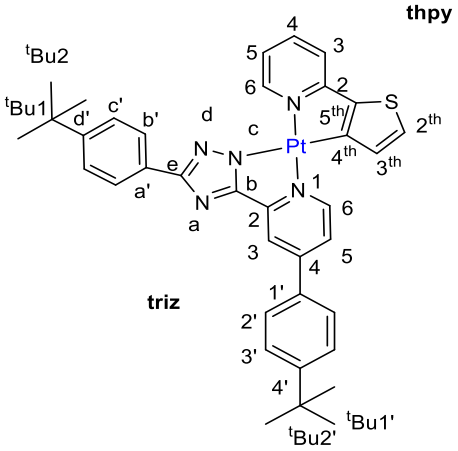

[Pt(thpy)(μ-Cl)]$_2$ (27 mg, 0.04 mmol), **HL[7]** (30 mg, 0.07 mmol) in DCM (1 mL) and MeOH (1 mL). An orange solid was obtained (21 mg, 69 %); ^{1}H NMR (599 MHz, Chloroform-*d*) δ 10.49 (d, *J* = 5.7 Hz, 1H, H^6), 9.16 (d, *J* = 6.1 Hz, 1H, H^{6triz}), 8.30 (d, *J* = 2.1 Hz, 1H, H^{3triz}), 8.19 (d, *J* = 8.3 Hz, 2H, H$^{b'}$), 7.73 (d, *J* = 8.4 Hz, 2H, H$^{2'}$), 7.67 (td, *J* = 7.6, 1.4 Hz, 1H, H^4), 7.55 (d, *J* = 8.4 Hz, 2H, H$^{3'}$), 7.50 (dd, *J* = 8.2, 1.4 Hz, 2H, H$^{c'}$), 7.47 (dd, *J* = 4.8, 1.2 Hz, 1H, H^{2th}), 7.40 – 7.37 (m, 1H, H^{5triz}), 7.28 (d, *J* = 8.0 Hz, 1H, H^3), 7.23 (d, *J* = 4.8 Hz, 1H, H^{3th}), 6.98 (ddd, *J* = 7.3, 5.9, 1.4 Hz, 1H, H^5), 1.41-1.39 (m, 18H, H^{tBu2} and H$^{tBu2'}$); ^{13}C NMR (151 MHz, Chloroform-*d*) δ 162.9 (C$^{a'}$), 154.0 (C$^{4'}$), 152.8 (C^6), 152.0 (C^{2triz}), 151.4 (C^{6triz}), 151.1 (C^{4triz}), 151.0 (C$^{d'}$), 148.5 (C^{4th}), 142.7 (C^{5th}), 139.0 (C^4), 133.0 (C$^{1'}$), 131.0 (C^{3th}), 130.3 (C$^{3''}$), 127.1 (C^{2th}), 126.9 (C$^{2'}$), 126.3 (C$^{3'}$), 126.0 (C$^{b'}$), 125.3 (C$^{c'}$), 120.6 (C^{5triz}), 119.8 (C^5), 117.8 (C^{3triz}), 116.7 (C^3), 34.9 (C^{tBu1}), 34.7 (C$^{tBu1'}$), 31.4 (C^{tBu2}), 31.2 (C$^{tBu2'}$); MS (ES$^+$) *m/z* = 765.6 [M + H]$^+$; HRMS (ES$^+$) *m/z* = 764.2346 [M + H]$^+$; calculated for [$C_{36}H_{36}N_5S^{194}Pt$]$^+$ 764.2318; Anal. Calcd for $C_{36}H_{35}N_5SPt$: C, 56.53; H, 4.61; N, 9.16; Found: C, 55.89; H, 4.54, N, 8.78.

Pt(thpy)L[8]

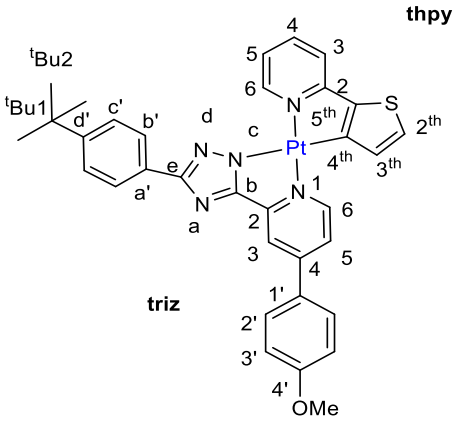

$[Pt(thpy)(\mu\text{-}Cl)]_2$ (14 mg, 0.02 mmol), **HL[8]** (15 mg, 0.04 mmol) in DCM (1 mL) and MeOH (1 mL). An orange solid was obtained (20 mg, 90 %); ^{1}H NMR (700 MHz, Chloroform-*d*) δ 10.48 (dd, *J* = 6.0, 1.3 Hz, 1H, H^{6}), 9.11 (d, *J* = 6.1 Hz, 1H, H^{6triz}), 8.25 (d, *J* = 2.2 Hz, 1H, H^{3triz}), 8.17 (d, *J* = 8.4 Hz, 2H, $H^{b'}$), 7.73 (d, *J* = 8.6 Hz, 2H, $H^{3'}$), 7.66 (td, *J* = 7.6, 1.4 Hz, 1H, H^{4}), 7.48 (d, *J* = 8.6 Hz, 2H, $H^{c'}$), 7.46 (d, *J* = 4.8 Hz, 1H, H^{2th}), 7.32 (dd, *J* = 6.1, 2.3 Hz, 1H, H^{5triz}), 7.27 (d, *J* = 7.6 Hz, 1H, H^{3}), 7.21 (d, *J* = 4.8 Hz, 1H, H^{3th}), 7.01 (d, *J* = 8.8 Hz, 2H, $H^{2'}$), 6.98 (ddd, *J* = 7.3, 5.7, 1.4 Hz, 1H, H^{5}), 3.89 (s, 3H, H^{OMe}), 1.39 (s, 9H, H^{tBu2}); ^{13}C NMR (176 MHz, Chloroform-*d*) δ 161.6 ($C^{4'}$), 152.8 (C^{6}), 151.9 (C^{2triz}), 151.3 (C^{6triz}), 150.9 ($C^{d'}$), 150.7 (C^{4triz}), 142.6 (C^{3th}), 139.0 (C^{4}), 131.1 (C^{4th}), 130.3 ($C^{a'}$), 128.6 ($C^{3'}$), 128.0 ($C^{1'}$), 127.1 (C^{2th}), 126.0 ($C^{b'}$), 125.3 ($C^{c'}$), 120.0 (C^{5triz}), 119.9 (C^{5}), 117.3 (C^{3triz}), 116.7 (C^{3}), 114.7 ($C^{2'}$), 55.4 (C^{OMe}), 34.7 (C^{tBu1}), 31.4 (C^{tBu2}); MS (ES^{+}) *m/z* = 738.2 $[M+H]^{+}$; HRMS (ES+) *m/z* = 738.1793 $[M+H]^{+}$; calculated for $[C_{33}H_{30}N_5OS^{194}Pt]^{+}$ 738.1798.

Pt(thpy)L[9]

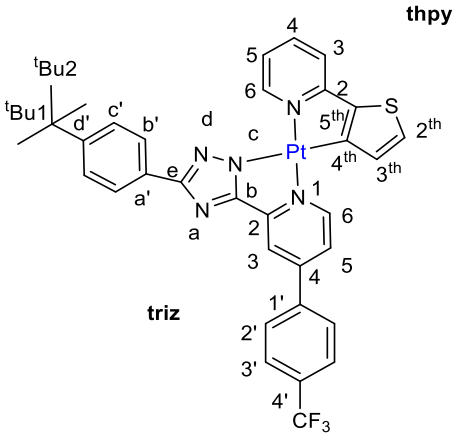

$[Pt(thpy)(\mu\text{-}Cl)]_2$ (26 mg, 0.03 mmol), **HL[9]** (30 mg, 0.07 mmol), DCM (1 mL) and MeOH (1 mL). An orange solid was obtained (22 mg, 94 %); ^{1}H NMR (700 MHz, Chloroform-*d*) δ 10.33 (d, *J* = 5.1 Hz, 1H, H^{6}), 9.09 (d, *J* = 6.0 Hz, 1H, H^{6triz}), 8.21 (s, 1H, H^{3triz}), 8.12 (d, *J* = 8.4 Hz, 2H, $H^{3'}$), 7.78 (d, *J* = 7.9 Hz, 2H, $H^{b'}$), 7.71 (d, *J* = 8.0 Hz, 2H, $H^{c'}$), 7.61 (td, *J* = 7.5, 1.4 Hz, 1H, H^{4}), 7.47 (d, *J* = 8.3 Hz, 2H, $H^{2'}$), 7.40 (d, *J* = 4.7 Hz, 1H, H^{2th}), 7.23 (dd, *J* = 6.0, 2.2 Hz, 1H, H^{5triz}), 7.21 (d, *J* = 7.8 Hz, 1H, H^{3}), 7.13 (d, *J* = 4.8 Hz, 1H, H^{3th}), 6.91 (t, *J* = 6.5 Hz, 1H, H^{5}), 1.39 (s, 9H, H^{tBu2}); ^{13}C NMR (176 MHz, Chloroform-*d*) δ 152.6 (C^{6}), 151.9 (C^{6triz}), 139.0 (C^{4}), 130.9 (C^{3th}), 127.5 (C^{b}), 127.1 (C^{2th}), 126.1 ($C^{c'}$), 126.0 ($C^{3'}$), 125.2 ($C^{2'}$), 120.9 (C^{5triz}), 119.7 (C^{5}), 118.2 (C^{3triz}), 116.6 (C^{3}), 34.7 (C^{tBu1}), 31.4 (C^{tBu2}); ^{19}F NMR (376 MHz, Chloroform-*d*) δ -62.76; MS (ES^{+}) *m/z* = 776.16 $[M+H]^{+}$; HRMS (ES+) *m/z* = 776.1575 $[M+H]^{+}$; calculated for $[C_{33}H_{27}F_3N_5S^{194}Pt]^{+}$ 776.1566.

Pt(thpy)L[10]

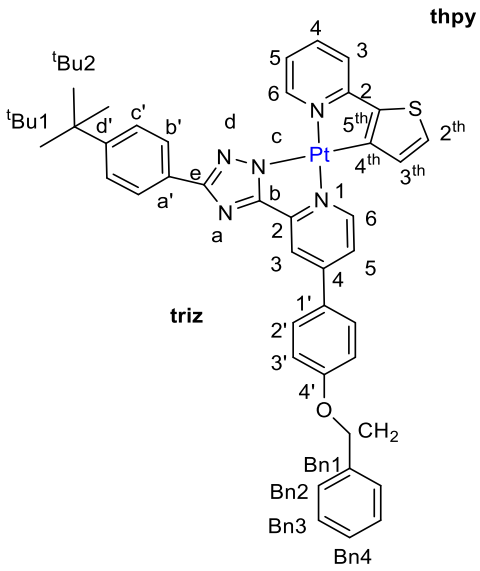

[Pt(thpy)(μ-Cl)]$_2$ (25 mg, 0.03 mmol), **HL[10]** (33 mg, 0.07 mmol) in DCM (1 mL) and MeOH (1 mL). An orange solid was obtained (25 mg, 96 %); ^{1}H NMR (400 MHz, Chloroform-*d*) δ 10.53 (d, *J* = 5.7 Hz, 1H, H^6), 9.17 (d, *J* = 6.2 Hz, 1H, H^{6triz}), 8.31 (d, *J* = 2.2 Hz, 1H, H^{3triz}), 8.22 (d, *J* = 8.2 Hz, 2H, H$^{3'}$), 7.78 (d, *J* = 8.2 Hz, 2H, H$^{b'}$), 7.71 (td, *J* = 7.7, 1.5 Hz, 1H, H^4), 7.56 – 7.49 (m, 5H, H$^{c'}$, H^{2th} and H^{Bn2}), 7.47-7.30 (m, 4H, H^{5triz}, H^{3th}, H^3 and H^{Bn4}), 7.27 (d, *J* = 5.0 Hz, 2H, H^{Bn3}), 7.13 (d, *J* = 8.9 Hz, 2H, H$^{2'}$), 7.04 (td, *J* = 6.6, 1.6 Hz, 1H, H^5), 5.18 (s, 2H, H^{CH2}), 1.42 (s, 9H, H^{tBu2}); MS (ES$^+$) *m/z* = 815.2 [M+H]$^+$; HRMS (ES+) *m/z* = 814.2111 [M+H]$^+$; calculated for [$C_{39}H_{34}N_5OS^{194}Pt$]$^+$ 814.2096.

Phenylquinoline complexes

General procedure

$[Pt(pquin)(\mu\text{-}Cl)]_2$ (1 eq) and **HL^n** (2.2 eq) were added to a Schlenk containing DCM and MeOH (5:4) and degassed via 3 x FPT. This was set to reflux under argon at 50 °C for 24 h and then cooled to RT. Purification was then performed by column chromatography (DCM/MeOH 98:2 on silica) followed by recrystallization in DCM/Hexane.

Pt(pquin)L^1

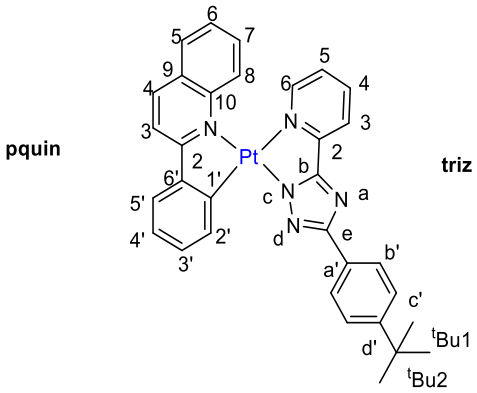

$[Pt(pquin)(\mu\text{-}Cl)]_2$ (25 mg, 0.03 mmol), **HL^1** (18 mg, 0.06 mmol) with DCM (1 mL) and MeOH (0.8 mmol). An orange solid was obtained (14 mg, 71 %); ^{1}H NMR (600 MHz, Chloroform-*d*) δ 9.37 (dd, *J* = 7.9, 1.1 Hz, 1H, H^{6triz}), 8.61 (d, *J* = 8.1 Hz, 1H, $H^{2'}$), 8.38 (d, *J* = 8.7 Hz, 1H, $H^{5'}$), 8.29 (d, *J* = 8.4 Hz, 2H, $H^{b'}$), 8.24 (d, *J* = 7.6 Hz, 1H, H^{8}), 8.11 (d, *J* = 5.6 Hz, 1H, H^{5}), 7.97 – 7.89 (m, 3H, $H^{3/4}$, $H^{3'}$and $H^{6/7}$), 7.69 (d, *J* = 7.6 Hz, 1H, H^{3triz}), 7.66 – 7.57 (m, 2H, $H^{3/4}$ and $H^{4'}$), 7.51 (d, *J* = 8.4 Hz, 2H, $H^{c'}$), 7.41 (td, *J* = 7.7, 1.4 Hz, 1H, H^{5triz}), 7.24 (d, *J* = 7.8 Hz, 1H, H^{4triz}), 7.15 – 7.09 (m, 1H, $H^{6/7}$), 1.39 (s, 9H, H^{tBu2}); ^{13}C NMR (151 MHz, Chloroform-*d*) δ 168.7 (C^{1}), 163.6 (C^{e}), 151.0 ($C^{d'}$), 150.5 (C^{5}), 146.7 (C^{2}), 145.9 (C^{2triz}), 143.4 (C^{b}), 139.2 ($C^{3/4}$, $C^{6/7}$or $C^{3'}$), 138.9 ($C^{5'}$), 135.7 (C^{5}), 130.4 (C^{5triz}) 130.3 ($C^{3/4}$ and $C^{4'}$), 128.5 ($C^{3/4}$, $C^{6/7}$ or $C^{3'}$), 127.90 ($C^{9/10}$), 127.1 ($C^{3/4}$ and $C^{4'}$), 127.0 ($C^{6'}$), 126.1 ($C^{b'}$), 126.0 ($C^{2'}$), 125.3 ($C^{c'}$), 124.9 (C^{3triz}), 124.4 (C^{4triz}), 122.7 ($C^{6/7}$), 120.4 (C^{8}), 117.3 ($C^{3/4}$, $C^{6/7}$ or $C^{3'}$), 34.7 (C^{tBu1}), 31.4 (C^{tBu2}); MS (ES$^+$) *m/z* = 677.0 $[M+H]^+$; HRMS (ES+) *m/z* = 676.1971 $[M+H]^+$; calculated for $[C_{32}H_{28}N_5{}^{194}Pt]^+$ 676.1972.

Pt(pquin)L²

pquin 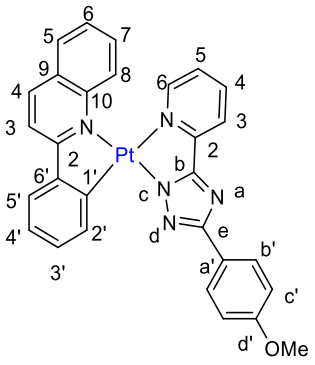 triz

[Pt(pquin)(μ-Cl)]$_2$ (25 mg, 0.03 mmol), **HL²** (16 mg, 0.06 mmol) with DCM (1 mL) and MeOH (0.8 mL). An orange crystalline solid was obtained (15 mg, 77 %); ^{1}H NMR (600 MHz, Chloroform-*d*) δ 9.33 (d, *J* = 8.2 Hz, 1H, H^{6triz}), 8.57 (d, J = 8.2 Hz, 1H, H$^{2'}$), 8.35 (d, J = 8.6 Hz, 1H, H$^{5'}$), 8.30 (d, J = 8.1 Hz, 2H, H$^{b'}$), 8.20 (d, *J* = 7.8 Hz, 1H, H^{8}), 8.07 (d, *J* = 5.6 Hz, 1H, H^{5}), 7.94 – 7.85 (m, 3H, H$^{3/4}$, H$^{3'}$ and H$^{6/7}$), 7.67 (d, *J* = 7.6 Hz, 1H, H^{3triz}), 7.63-7.56 (m, 2H, H$^{3/4}$ and H$^{4'}$), 7.40 (t, *J* = 7.3 Hz, 1H, H^{5triz}), 7.23 (t, *J* = 7.9 Hz, 1H, H^{4triz}), 7.10 (t, *J* = 6.4 Hz, 1H, H$^{6/7}$), 7.03 (d, *J* = 8.4 Hz, 2H, H$^{c'}$), 3.89 (t, *J* = 1.2 Hz, 3H, H^{OMe}); ^{13}C NMR (151 MHz, Chloroform-*d*) δ 168.7 (C$^{1'}$), 164.2 (C$^{6'}$), 163.5 (C^{e}), 159.7 (C$^{4''}$), 150.9 (C$^{9/10}$), 150.5 (C^{5}), 146.4 (C^{2}), 145.9 (C^{2triz}), 143.3 (C^{b}), 139.2 (C$^{3'}$ or C$^{6/7}$), 139.1 (C$^{5'}$), 135.6 (C^{6triz}), 130.3 (C^{5triz}), 130.2 (C$^{3/4}$ and C$^{4'}$), 128.5 (C$^{3'}$ or C$^{6/7}$), 127.9 (C^{2}), 127.7 (C$^{b'}$), 127.1 (C$^{3/4}$and C$^{4'}$), 126.0 (C$^{2'}$), 124.9 (C^{3triz}), 124.4 (C^{4triz}), 122.8 (C$^{6/7}$), 120.3 (C^{8}), 117.3 (C$^{3'}$ or C$^{6/7}$), 113.8 (C$^{c'}$), 55.3 (C^{OMe}); MS (ES$^+$) *m/z* = 651.0 [M+H]$^+$; HRMS (ES+) *m/z* = 650.1453 [M+H]$^+$; calculated for [$C_{29}H_{22}N_5O^{194}Pt$]$^+$ 650.1451.

Pt(pquin)L³

pquin 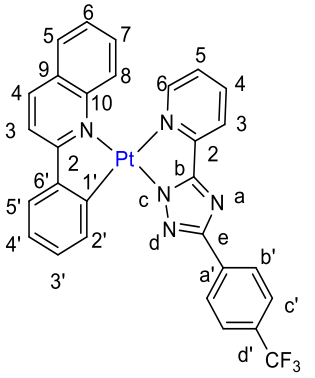 triz

[Pt(pquin)(μ-Cl)]$_2$ (25 mg, 0.03 mmol), **HL^3** (18 mg, 0.06 mmol) with DCM (1 mL) and MeOH (0.8 mL). An orange solid was obtained (12 mg, 60 %); ^{1}H NMR (700 MHz, Chloroform-*d*) δ 9.28 (dd, *J* = 7.8, 0.9 Hz, 1H, H^{6triz}), 8.58 (d, *J* = 8.1 Hz, 1H, H$^{2'}$), 8.48 (d, *J* = 8.1 Hz, 2H, H$^{b'}$), 8.38 (d, *J* = 8.6 Hz, 1H, H$^{5'}$), 8.23 (ddd, *J* = 7.8, 1.4, 0.8 Hz, 1H, H^8), 8.11 (d, *J* = 5.6 Hz, 1H, H^5), 7.96 (td, *J* = 7.8, 1.4 Hz, 1H, H^7), 7.93 – 7.90 (m, 2H, H$^{4'}$ and H^4), 7.73 (d, *J* = 8.1 Hz, 2H, H$^{c'}$), 7.69 (d, *J* = 7.6 Hz, 1H, H^{3triz}), 7.64 – 7.58 (m, 2H, H$^{3'}$ and H^3), 7.41 (ddd, *J* = 7.7, 7.1, 1.3 Hz, 1H, H$^{5triz/4triz}$), 7.26 (td, *J* = 8.6, 1.4 Hz, 1H, H$^{5triz/4triz}$), 7.15 (ddd, *J* = 7.2, 5.6, 1.4 Hz, 1H, H^6); ^{13}C NMR (176 MHz, Chloroform-*d*) δ 168.7 (C$^{1'}$), 164.8 (C^9), 162.4 (C^e), 150.6 (C^5), 146.4 (C^2), 145.9 (C^{2triz}), 143.0 (C^b), 139.3 (C^7), 139.2 (C$^{5'}$), 136.3 (C$^{a'}$), 135.3 (C^{6triz}), 130.4 (C$^{4triz/5triz}$), 130.3 (C$^{3'}$), 129.7 (C$^{d'}$), 128.5 (C$^{4/4'}$), 127.9 (C^{10}), 127.2 (C$^{3/3'}$), 126.4 (C$^{b'}$), 125.9 (C$^{2'}$), 125.4 (C$^{c'}$), 125.3 (C$^{a'}$), 125.0 (C^{3triz}), 124.5 (C$^{4triz//5triz}$), 123.1 (C^6), 120.5 (C^8), 117.3 (C$^{4/4'}$); ^{19}F NMR (376 MHz, Chloroform-*d*) δ -62.65; MS (ES$^+$) *m/z* = 690.0 [M+H]$^+$; HRMS (ES+) *m/z* = 688.1210 [M+H]$^+$; calculated for [$C_{29}H_{19}N_5F_3{}^{194}Pt$]$^+$ 688.1219.

7.3.3.2 Cationic complexes

General procedures

Pt(N^N)Cl$_2$ starting materials

K_2PtCl_4 (1 eq) and 2,2'-bipyridine or 1,10-phenanthroline reagents (10 eq) were added to a round bottom flask with H_2O and stirred. 2M HCl was added dropwise to this solution which was then refluxed for 1 hr. On cooling to RT, the suspension was filtered and washed with water. The resulting solid was then dried *in vacuo* and used without further purification.

Pt(bpy)Cl$_2$

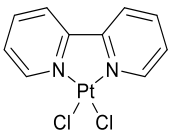

K_2PtCl_4 (200 mg, 0.48 mmol) and 2,2'-bipyridine (752 mg, 4.81 mmol) with H_2O (120 mL) and 2M HCl (4 mL). A yellow solid resulted and was dried under vacuum (200 mg, 99 %). The experimental data obtained were in good agreement with the literature.[198]

Pt(phen)Cl$_2$

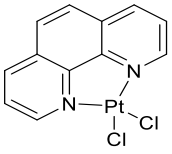

K_2PtCl_4 (116 mg, 0.28 mmol) and 1,10-phenanthroline (500 mg, 2.77 mmol) with H_2O (60 mL) and 2M HCl (2 mL). A yellow solid resulted and was dried *in vacuo* (116 mg, 93 %). The experimental data obtained were in good agreement with the literature.[199]

Pt(N^N)(triazole) complexes

$Pt(N^N)Cl_2$ (1 eq) and AgOTf (2 eq) were added to a Schlenk with DCM. This was degassed via 3 x FPT and then stirred at RT for 1 hr under argon. **HL^n** (1 eq) was then added under argon and the mixture was heated at reflux overnight. After cooling to RT, the product was then extracted into MeOH. Following this, an ion exchange with PF_6^- was performed by dissolving in the minimum amount of DMSO and then precipitating out with saturated aqueous KPF_6 solution. This was washed with H_2O (3 x 5 mL) and dried *in vacuo*.

Bipyridyl complexes

[Pt(bpy)L^1]PF$_6$

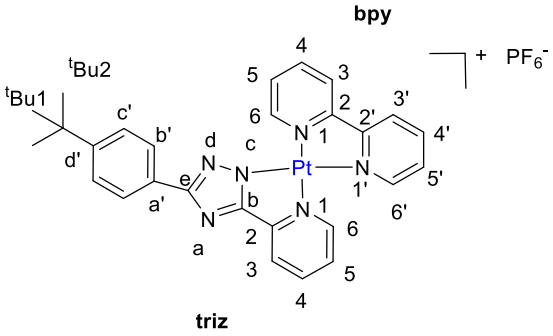

$Pt(bpy)Cl_2$ (32 mg, 0.08 mmol) and AgOTf (39 mg, 0.15 mmol) were added to a Schlenk with DCM (2 mL) and **HL^1** (21 mg, 0.08 mmol). A yellow solid was obtained (36 mg, 76 %); ^{1}H NMR (700 MHz, DMSO-d_6) δ 10.36 (d, *J* = 5.7 Hz, 1H, H^6), 8.76 (d, *J* = 5.7 Hz, 1H, H^{6bpy}), 8.61 (d, *J* = 5.7 Hz, 1H, H^{6triz}), 8.47-8.42 (m, 2H, H^{3bpy} and $H^{3'}$), 8.35 (t, *J* = 7.7 Hz, 1H, H^{4bpy}), 8.28 (t, *J* = 7.7 Hz, 1H, $H^{4'}$), 8.16 (t, *J* = 7.5 Hz, 1H, H^{4triz}), 7.83-7.79 (m, 2H, $H^{5'}$ and H^{3triz}), 7.76 – 7.75 (m, 3H, H^{5bpy} and $H^{b'}$), 7.55 (t, *J* = 6.4 Hz, 1H, H^{5triz}), 7.37 (d, *J* = 8.1 Hz, 2H, $H^{c'}$), 1.34 (s, 9H, H^{tBu2}); ^{13}C NMR (176 MHz, DMSO-d_6) δ 163.2 ($C^{a'}$), 161.2 (C^e), 156.4 (C^{2bpy}), 156.1 ($C^{2'}$), 152.0 ($C^{6'}$), 151.9 ($C^{d'}$), 151.2 (C^{6bpy}), 151.0 (C^{6triz}), 148.8 (C^b), 143.0 (C^{4triz}), 142.2 ($C^{4'}$), 142.2 (C^{4bpy}), 128.8 (C^{5bpy}), 128.7 (C^{3triz}), 128.3 (C^{2triz}), 126.0 (C^{5triz}), 125.8 ($C^{b'}$), 125.7 ($C^{c'}$), 124.9 (C^{3bpy}), 124.5 ($C^{3'}$), 121.3 ($C^{5'}$), 34.9 (C^{tBu1}), 31.6 (C^{tBu2}); MS (ES$^+$) *m/z* = 628.6 $[M]^+$; HRMS (ES+) *m/z* = 627.1767 $[M]^+$; calculated for $[C_{27}H_{25}N_6{}^{194}Pt]^+$ 627.1767.

[Pt(bpy)L²]PF₆

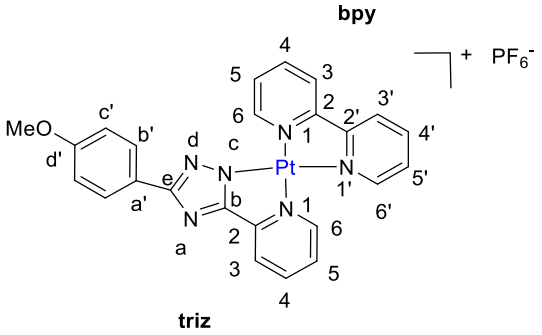

Pt(bpy)Cl_2 (50 mg, 0.12 mmol), **HL²** (30 mg, 0.12 mmol), AgOTf (61 mg, 0.24 mmol) and DCM (3 mL). A yellow solid was obtained (19 mg, 27 %); ^{1}H NMR (600 MHz, DMSO-d_6) δ 10.39 (d, *J* = 5.7 Hz, 1H, $H^{6'}$), 8.78 (d, *J* = 5.6 Hz, 1H, H^{6bpy}), 8.65 (d, *J* = 5.7 Hz, 1H, H^{6triz}), 8.52-8.49 (m, 2H, H^{3bpy} and $H^{3'}$), 8.39 (t, *J* = 7.7 Hz, 1H, H^{4bpy}), 8.33 (t, *J* = 7.8 Hz, 1H, $H^{4'}$), 8.21 (t, *J* = 7.7 Hz, 1H, H^{4triz}), 7.85-7.79 (m, 5H, $H^{5'}$, H^{3triz}, $H^{b'}$ and H^{5bpy}), 7.59 (t, *J* = 6.8 Hz, 1H, H^{5triz}), 6.93 (d, *J* = 8.3 Hz, 2H, $H^{c'}$), 3.83 (s, 3H, H^{OMe}); ^{13}C NMR (151 MHz, DMSO-d_6) δ 163.1 (C^{6triz}), 161.1 (C^{e}), 160.3 ($C^{d'}$), 156.5 (C^{2bpy}), 156.1 ($C^{2'}$), 152.1 ($C^{6'}$), 151.1 (C^{6bpy}), 151.0 (C^{6triz}), 148.9 (C^{b}), 142.9 (C^{4triz}), 142.2 ($C^{4'}$), 142.1 (C^{4bpy}), 128.8 (C^{5bpy}), 128.3 ($C^{5'}$), 127.5 ($C^{b'}$), 126.0 (C^{5triz}), 125.0 (C^{3bpy}), 124.6 ($C^{3'}$), 124.2 ($C^{a'}$), 121.3 (C^{3triz}), 114.4 ($C^{c'}$), 55.7 (C^{OMe}); MS (ES⁺) *m/z* = 602.5 $[M]^+$; HRMS (ES+) *m/z* = 601.1231 $[M]^+$; calculated for $[C_{24}H_{19}N_6O^{194}Pt]^+$ 601.1247.

[Pt(bpy)L³]PF₆

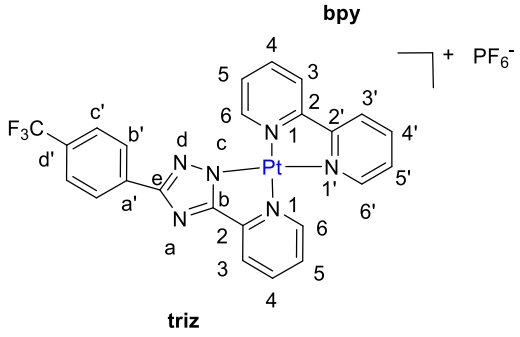

Pt(bpy)Cl_2 (76 mg, 0.17 mmol), **HL³** (72 mg, 0.17 mmol), AgOTf (81 mg, 0.34 mmol) and DCM (4 mL). A yellow solid was obtained (30 mg, 28 %); ^{1}H NMR (400 MHz, DMSO-d_6) δ 10.10 (dd, *J* = 6.0, 1.3 Hz, 1H, $H^{6'}$), 8.62 (d, *J* = 5.7 Hz, 1H, H^{6bpy}), 8.51 (d, *J* = 5.8 Hz, 1H, H^{6triz}), 8.39 – 8.28 (m, 3H, H^{3bpy}, $H^{3'}$ and H^{4bpy}), 8.22 (td, *J* = 7.8, 1.4 Hz, 1H, $H^{4'}$), 8.12 (td, *J* = 7.7, 1.2 Hz, 1H, H^{4triz}), 7.91 (d, *J* = 8.0 Hz, 2H, $H^{b'}$), 7.76 – 7.66 (m, 3H, $H^{5'}$, H^{5bpy} and H^{3triz}), 7.66 – 7.62 (d, *J* = 8.0 Hz, 2H, $H^{c'}$), 7.50 (ddd, *J* = 7.5, 5.8, 1.6 Hz, 1H, H^{5triz}); ^{19}F NMR (376 MHz, DMSO-d_6)

δ -60.97; MS (ES^+) *m/z* = 639.2 $[M]^+$; HRMS (ES+) *m/z* = 639.1028 $[M]^+$; calculated for $[C_{24}H_{16}N_6F_3{}^{194}Pt]^+$ 639.1015.

Phenanthroline complexes

[Pt(phen)L¹]PF₆

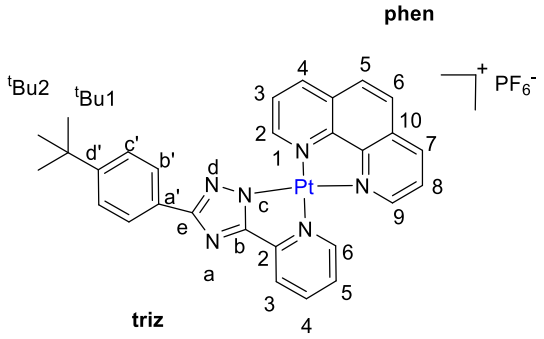

HL¹ (500 mg, 0.18 mmol), Pt(phen)Cl_2 (80 mg, 0.18 mmol) and AgOTf (93 mg, 0.36 mmol) with DCM (4 mL). A yellow solid was obtained (70 mg, 60 %); ^{1}H NMR (700 MHz, DMSO-*d₆*) δ 10.11 (s, 1H, H^9), 8.78 (d, J = 4.8 Hz, 1H, H^2), 8.68 (d, J = 7.8 Hz, 1H, H^4), 8.52 (d, J = 7.8 Hz, 1H, H^7), 8.40 (d, J = 5.2 Hz, 1H, H^{6triz}), 7.93 (t, J = 7.3 Hz, 1H, H^{4triz}), 7.88 (d, J = 8.5 Hz, 1H, $H^{5/6}$), 7.85-7.82 (m, 2H, $H^{5/6}$ and H^3), 7.73 (t, J = 6.2 Hz, 1H, H^8), 7.45 (d, J = 7.5 Hz, 2H, $H^{b'}$), 7.35 (d, J = 7.4 Hz, 1H, H^{3triz}), 7.32 (d, J = 7.8 Hz, 2H, $H^{c'}$), 7.24 (t, J = 6.4 Hz, 1H, H^{5triz}), 1.38 (s, 9H, H^{tBu2}); ^{13}C NMR (176 MHz, DMSO-*d₆*) δ 162.3, 160.7 (C^e), 152.2 (C^9), 151.9 ($C^{d'}$), 151.5 (C^2), 150.3 (C^{6triz}), 147.9 ($C^{a'}$), 145.8 (C^{10}), 142.7 (C^{4triz}), 141.3 (C^4), 140.9 (C^7), 130.6 (C), 130.2 (C^{11}), 128.2 ($C^{5/6}$), 128.1 ($C^{5/6}$), 126.6 (C^3), 126.2 (C^8), 125.8 (C^{5triz}), 125.7 ($C^{b'}$), 125.6 ($C^{c'}$), 121.1 (C^{3triz}), 35.0 (C^{tBu1}), 31.6 (C^{tBu2}); MS (ES^+) *m/z* = 653.1 $[M]^+$; HRMS (ES+) *m/z* = 651.1785 $[M]^+$; calculated for $[C_{29}H_{25}N_6{}^{194}Pt]^+$ 651.1767.

[Pt(phen)L²]PF₆

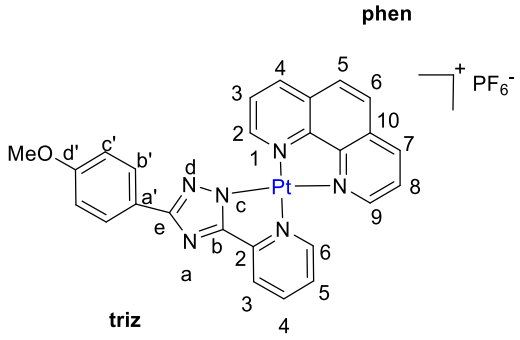

HL² (20 mg, 0.08mmol), AgOTf (41 mg, 0.16 mmol) and Pt(phen)Cl_2 (35 mg, 0.08 mmol) were added to a Schlenk with DCM (4 mL). The solid was then recrystallized in DMF and ether and dried *in vacuo* (6 mg, 12 %); ^{1}H NMR (400 MHz, Chloroform-*d*) δ 9.36 (dd, *J* = 7.9, 1.1 Hz, 1H, H^9), 8.62 (d, *J* = 8.8 Hz, 1H, H^2), 8.40 (d, *J* = 8.7 Hz, 1H, H^4), 8.33 (d, *J* = 8.8 Hz, 1H, $H^{b'}$), 8.25 (ddd, *J* = 7.9, 1.5, 0.9 Hz, 1H, H^7), 8.12 (d, *J* = 5.6 Hz, 1H, H^{6triz}), 7.99 – 7.88 (m, 3H, H^{4triz}, H^5 and H^6), 7.71 (d, *J* = 8.1 Hz, 1H, H^3), 7.69 – 7.59 (m, 2H, H^8 and H^{3triz}), 7.43 (td, *J* = 7.4, 1.4 Hz, 1H, H^{5triz}), 7.06 (d, *J* = 8.8 Hz, 1H, $H^{c'}$), 3.91 (s, 3H, H^{OMe}); MS (ES^+) *m/z* = 650.1 $[M]^+$; HRMS (ES+) *m/z* = 650.1453 $[M]^+$; calculated for $[C_{29}H_{22}N_5O^{194}Pt]^+$ 650.1451.

[Pt(phen)L³]PF₆

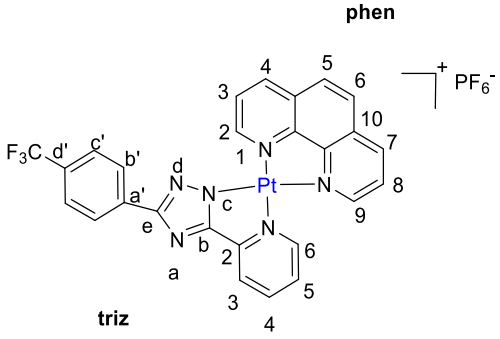

HL³ (30 mg, 0.103 mmol), Pt(phen)Cl_2 (46 mg, 0.103 mmol) and AgOTf (53 mg, 0.206 mmol) with DCM (4 mL). A yellow solid was obtained (40 mg, 58 %); ^{1}H NMR (700 MHz, DMSO-d_6) δ 9.83 (s, 1H, H^9), 8.63 (s, 1H, H^2), 8.58 (d, *J* = 7.7 Hz, 1H, H^4), 8.42 (d, *J* = 7.6 Hz, 1H, H^7), 8.29 (s, 1H, H^{6triz}), 7.84 (t, *J* = 7.1 Hz, 1H, H^{4triz}), 7.79-7.73 (m, 2H, $H^{5/6}$ and H^3), 7.72 (t, *J* = 6.0 Hz, 1H, $H^{5/6}$), 7.66 (d, *J* = 6.9 Hz, 1H, H^8), 7.49 (d, *J* = 7.3 Hz, 2H, $H^{b'}$), 7.41 (d, *J* = 7.5 Hz, 2H, $H^{c'}$), 7.22-7.17 (m, 2H, H^{3triz} and H^{5triz}); ^{13}C NMR (176 MHz, DMSO-d_6) δ 162.6, 159.3, 152.3 (C^9), 151.4 (C^2), 150.3 (C^{6triz}), 145.3, 142.9 (C^{4triz}), 141.4 (C^4), 140.9 (C^7), 128.1 (C^3), 128.0 ($C^{5/6}$), 126.7 ($C^{5/6}$), 126.2 (C^8), 126.1 (C^{3triz}), 125.9 ($C^{b'}$), 125.6 ($C^{c'}$), 121.3 (C^{5triz}), 40.9 (C^{CF3}); ^{19}F NMR (376 MHz, Chloroform-*d*) δ -60.72; MS (ES^+) *m/z* = 664.1 $[M]^+$; HRMS (ES+) *m/z* = 663.1000 $[M]^+$; calculated for $[C_{26}H_{16}N_6F_3{}^{194}Pt]^+$ 663.1015.

7.3.4 Tetrazoles

7.3.4.1 Precursors

Compound P[1]

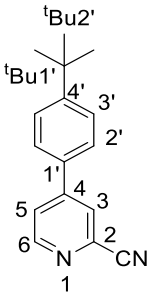

As for the 1,2,4-triazole precursor **P[1]**.

Compound P[5]

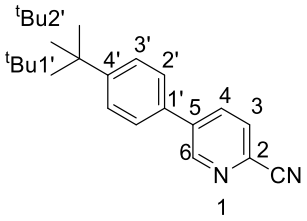

5-bromopyridine-2-carbonitrile (171 mg, 0.94 mmol), 4-*tert*-butyl phenylboronic acid (200 mg, 1.21 mmol) and Na_2CO_3 (496 mg, 4.68 mmol) with $Pd(PPh_3)_4$ (135 mg, 0.12 mmol) in DME (3 mL) and H_2O (3 mL). A white solid was obtained (118 mg, 53 %); ^{1}H NMR (700 MHz, Chloroform-*d*) δ 8.93 (dd, *J* = 2.2, 0.9 Hz, 1H, H^6), 7.98 (dd, *J* = 8.1, 2.3 Hz, 1H, H^4), 7.74 (dd, *J* = 8.0, 0.9 Hz, 1H, H^3), 7.55-7.54 (m, 4H, $H^{2'}$ and $H^{3'}$), 1.36 (s, 9H, $H^{tBu2'}$); ^{13}C NMR (176 MHz, Chloroform-*d*) δ 152.9 ($C^{4'}$), 149.5 (C^6), 139.7 ($C^{1'}$), 134.5 (C^4), 132.9, 131.9 (C^5), 128.4 (C^3), 127.0 ($C^{2'}$), 126.4 ($C^{3'}$), 117.4 (C^2), 114.7 (C^{CN}), 31.5 ($C^{tBu1'}$), 31.2 ($C^{tBu2'}$); MS (ES^+) *m/z* = 237.5 $[M+H]^+$; HRMS (ES+) *m/z* = 237.1385 $[M+H]^+$; calculated for $[C_{16}H_{17}N_2]^+$ 237.1392.

7.3.4.2 HL[n] Tetrazole ligands

General procedure

The cyano precursor (1 eq), NaN_3 (5 eq) and NH_4Cl (5 eq) were added to a Schlenk and placed under argon. Dry DMF was then added and the mixture was degassed via 3 x FPT. This was set to heat to reflux at 125 °C for 24 h. On leaving to cool to RT, the mixture was filtered and to the filtrate 0.1 M HCl aq. solution was added to precipitate out a white solid. This was stirred at RT for 1 hour, refrigerated and then re-filtered. The solid was then dried *in vacuo*.

Compound HL[11]

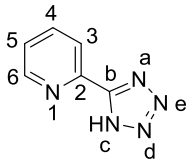

2-cyanopyridine (1.00 g, 9.6 mmol), NaN_3 (1.56 g, 24.0 mmol) and NH_4Cl (1.28 g, 24.0 mmol) in dry DMF (20 mL). A white powder was obtained (837 mg, 59 %); The experimental data obtained were in good agreement with the literature.[200]

Compound HL[12]

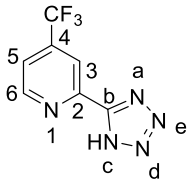

4-Trifluoromethyl-2-cyanopyridine (200 mg, 1.16 mmol), NaN_3 (189 mg, 2.91 mmol) and NH_4Cl (156 mg, 2.91 mmol) in dry DMF (6 mL). A white powder was obtained (125 mg, 50 %); ^{1}H NMR (400 MHz, DMSO-d_6) δ 9.10 (d, J = 5.1 Hz, 1H, H^6), 8.44 (s, 1H, H^3), 8.06 (dd, J = 5.2, 1.7 Hz, 1H, H^5); MS (ES$^+$) m/z = 216.1 [M+H]$^+$; HRMS (ES+) m/z = 216.1341[M+H]$^+$; calculated for $[C_7H_5F_3N_5]^+$ 216.1362.

Compound HL[13]

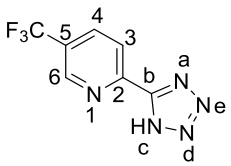

5-Trifluoromethyl-2-cyanopyridine (1.00 g, 5.81 mmol), NaN_3 (943 mg, 14.5 mmol) and NH_4Cl (769 mg, 14.5 mmol) in dry DMF (20 mL). A white powder was obtained (199 mg, 16 %); ^{1}H NMR (400 MHz, DMSO-d_6) δ 9.22 (s, 1H, H^6), 8.52 (dd, J = 8.3, 2.3 Hz, 1H, H^4), 8.44 (d, J = 8.3 Hz, 1H, H^3); MS (ES$^+$) m/z = 216.1 [M+H]$^+$; HRMS (ES+) m/z = 216.1231[M+H]$^+$; calculated for $[C_7H_5F_3N_5]^+$ 216.1200.

Compound HL[14]

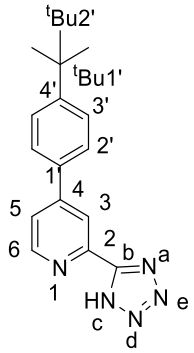

P[1] (1.01 g, 4.23 mmol), NaN_3 (688 mg, 10.59 mmol) and NH_4Cl (566mg, 10.59 mmol) with dry DMF (20 mL). A white solid was obtained (1.01 g, 86 %); ^{1}H NMR (600 MHz, DMSO-d_6) δ 8.79 (dd, J = 5.2, 1.5 Hz, 1H, H^6), 8.42 (s, 1H, H^c), 7.93 (s, 1H, H^3), 7.88 (dd, J = 5.0, 2.2 Hz, 1H, H^5), 7.82 (dd, J = 8.3, 1.7 Hz, 2H, $H^{3'}$), 7.60 – 7.54 (m, 2H, $H^{2'}$), 1.31 (d, J = 1.7 Hz, 9H, H^{tBu2}); ^{13}C NMR (151 MHz, DMSO-d_6) δ 162.8 (C^3), 156.0 (C^c), 153.0 ($C^{1'}$), 151.0 (C^6), 149.1 (C^4), 145.6 (C^2), 133.9 ($C^{4'}$), 127.2 ($C^{3'}$), 126.7 ($C^{2'}$), 123.2 (C^5), 35.0 ($C^{tBu1'}$), 31.4 ($C^{tBu2'}$); MS (ES^+) *m/z* =280.1 $[M+H]^+$.

Compound HL[15]

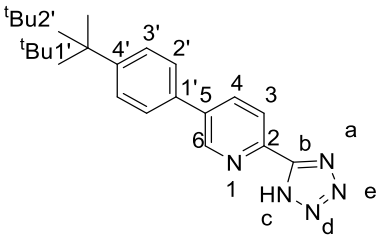

P[5] (100 mg, 0.43 mmol), NaN_3 (69 mg, 1.06 mmol) and NH_4Cl (57 mg, 1.06 mmol) with dry DMF (2 mL). A white solid was obtained (73 mg, 61%); ^{1}H NMR (600 MHz, DMSO-d_6) δ 9.06 (d, *J* = 1.8 Hz, 1H, H^6), 8.31 (dd, *J* = 8.2, 2.3 Hz, 1H, H^4), 8.25 (dd, *J* = 8.2, 0.9 Hz, 1H, H^3), 7.75 (d, *J* = 8.5 Hz, 1H, $H^{3'}$), 7.54 (d, *J* = 8.5 Hz, 1H, $H^{2'}$), 1.31 (s, 9H, $H^{tBu2'}$); ^{13}C NMR (151 MHz, DMSO-d_6) δ 151.9 ($C^{4'}$), 148.3 (C^6), 137.6 ($C^{1'}$), 136.0 (C^4), 133.6 (C^5), 127.3 ($C^{3'}$), 126.5 ($C^{2'}$), 123.0 (C^3), 110.0 (C^2), 34.9 ($C^{tBu1'}$) and 31.5 ($C^{tBu2'}$); MS (ES^+) *m/z* =280.2 $[M+H]^+$; HRMS (ES^+) *m/z* = 280.1559 $[M+H]^+$; calculated for $[C_{16}H_{18}N_5]^+$ 280.1562.

7.3.4.3 Homoleptic Pt complexes

General procedure

HL$^{11\text{-}15}$ and K_2PtCl_4 were added to a Schlenk with H_2O and EtOH (1:3). The mixture was degassed via 3 x FPT and then refluxed at 80 °C for 24 h. This was cooled to RT and the solid was isolated by centrifuge and washed with H_2O (2 x 5 mL), MeOH (2 x 5 mL) and Et_2O (2 x 5 mL). The solid was then dried *in vacuo.*

PtL$^{11}_2$

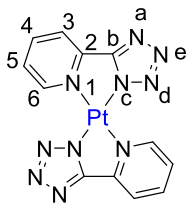

HL^{11} (50 mg, 0.34 mmol), K_2PtCl_4 (71 mg, 0.17 mmol) with H_2O (1 mL) and EtOH (3 mL). A yellow powder that was insoluble in all common organic solvents was obtained (68 mg, 82 %); MS (ASAP$^+$) *m/z* =488.1 $[M+H]^+$; HRMS (ASAP$^+$) *m/z* = 485.0626 $[M+H]^+$; calculated for $[C_{12}H_9N_{10}{}^{195}Pt]^+$ 485.0622; Anal. Calcd for $C_{12}H_8N_{10}Pt$ C, 29.57; H, 1.65; N, 28.74. Found: C, 29.09; H, 1.71; N, 28.62.

PtL$^{12}_2$

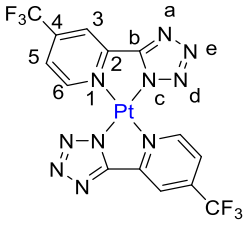

HL^{12} (330 mg, 1.53 mmol), K_2PtCl_4 (350 mg, 0.84 mmol) with H_2O (1 mL) and EtOH (3 mL). An orange powder that was insoluble in all common organic solvents was obtained (306 mg, 58 %); MS (ASAP$^+$) *m/z* =624.0 $[M+H]^+$; HRMS (ASAP$^+$) *m/z* = 624.0145 $[M+H]^+$; calculated for $[C_{14}H_7F_6N_{10}{}^{195}Pt]^+$ 624.0139; Anal. Calcd for $C_{14}H_6F_6N_{10}Pt$: C, 26.98; H, 0.97; F, 18.29; N, 22.47. Found: C, 28.01; H, 1.63; F, 17.93; N, 23.12.

PtL$^{13}_2$

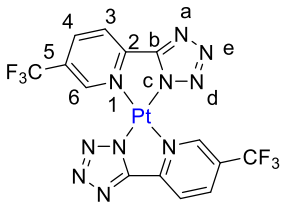

HL^{13} (190 mg, 0.88 mmol), K_2PtCl_4 (202 mg, 0.49 mmol) with H_2O (1 mL) and EtOH (3 mL). An orange powder that was insoluble in all common organic solvents was obtained (181 mg, 59 %); MS (ASAP$^+$) *m/z* =624.0 $[M+H]^+$; HRMS (ASAP$^+$) *m/z* = 624.1256 $[M+H]^+$ $]^+$; calculated for $[C_{14}H_7F_6N_{10}{}^{195}Pt]^+$ 624.1286.

PtL$^{14}_2$

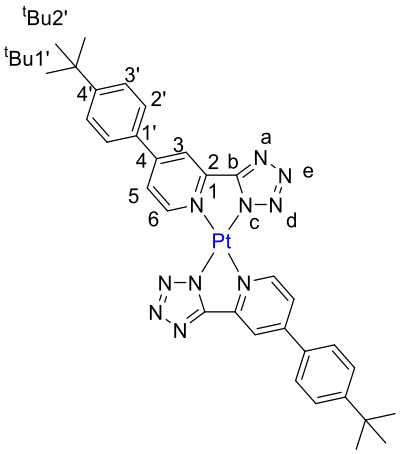

HL^{14} (50 mg, 0.17 mmol), K_2PtCl_4 (39 mg, 0.10 mmol) in H_2O (1 mL) and EtOH (3 mL). An orange solid was obtained (51 mg, 69 %); ^{1}H NMR (600 MHz, Chloroform-*d*) δ 9.82 (d, *J* = 6.1 Hz, 2H, H^6), 8.26 (d, *J* = 2.1 Hz, 2H, H^3), 7.75 (d, *J* = 8.5, 4H), 7.64-7.60 (m, 6H, H^5 and H^3), 1.42 (s, 18H, $H^{tBu2'}$); ^{13}C NMR (151 MHz, Chloroform-*d*) δ 155.2 ($C^{1'}$), 153.6 ($C^{4'}$), 153.0 (C^6), 146.6 (C^b), 132.0 (C^2), 127.3 ($C^{2'}$), 126.8 ($C^{3'/5}$), 123.4 ($C^{3'/5}$), 119.2 (C^3), 35.1 ($C^{tBu1'}$), 31.2 ($C^{tBu2'}$); MS (ES$^+$) *m/z* = 752.3 $[M+H]^+$; HRMS (ES+) *m/z* = 749.2511 $[M+H]^+$; calculated for $[C_{32}H_{33}N_{10}{}^{192}Pt]^+$ 749.2500.

PtL$^{15}_2$

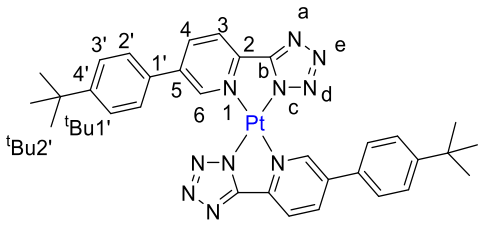

HL^{15} (30 mg, 0.11 mmol), K_2PtCl_4 (20 mg, 0.05 mmol), H_2O (0.5 mL) and EtOH (1.5 mL). An orange solid was obtained (27 mg, 73 %); ^{1}H NMR (600 MHz, Chloroform-*d*) δ 10.45 (s, 2H, H^6), 8.32 (d, J = 8.0 Hz, 2H, H^4), 8.17 (d, J = 8.1 Hz, 2H, H^3), 7.74 (d, J = 8.4 Hz, 4H, $H^{2'}$), 7.62 (d, J = 8.4 Hz, 4H, $H^{3'}$), 1.41 (s, 18H, $H^{tBu2'}$); ^{13}C NMR (151 MHz, Chloroform-*d*) δ 153.60 ($C^{4'}$), 151.92 (C^6), 144.53 (C^2), 139.98 (C^5) 138.24 (C^4), 130.96 ($C^{1'}$), 126.86 ($C^{3'}$), 126.82 ($C^{2'}$), 121.96 (C^3), 34.89 ($C^{tBu1'}$), 31.23 ($C^{tBu2'}$); MS (ES$^+$) *m/z* = 752.2 $[M+H]^+$; HRMS (ES+) *m/z* = 749.2511 $[M+H]^+$; calculated for $[C_{32}H_{33}N_{10}{}^{192}Pt]^+$ 749.2500.

7.4 Chapter 3 Synthesis

7.4.1 Pt(dpyb) complexes

dpybH

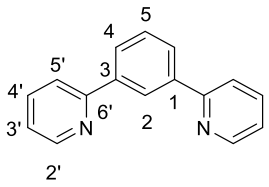

Benzene-1,3-diboronic acid (150 mg, 0.91 mmol), 2-bromopyridine (286 mg, 1.81 mmol) and Na_2CO_3 (7.5 mL, 1 M) were added with DME (7.5 mL) to a Schlenk and degassed by 3 x FPT. $Pd(PPh_3)_4$ (52 mg, 0.044 mmol) was then added under a flow of argon and the mixture was heated at reflux overnight. Water (5 mL) was then added and the product was extracted into DCM (3 x 30 mL) before drying over potassium carbonate (K_2CO_3). The solution was filtered, and the solvent removed under reduced pressure before drying *in vacuo*, giving a yellow oil. The product was purified by column chromatography on silica (hexane / ethyl acetate gradient, 100:0 to 70:30) to give the product as a yellow oily solid (141 mg, 67%). The experimental data obtained were in good agreement with the literature.[201]

Pt(dpyb)Cl

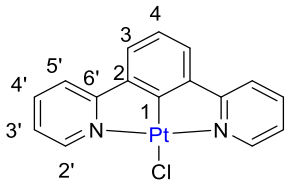

Method 1

dpybH (121 mg, 0.52 mmol), K_2PtCl_4 (239 mg, 0.58 mmol) and acetic acid (15 mL) were placed in a clean, dry Schlenk and degassed by 3 x FPT cycles. The mixture was then heated at reflux for 72 h under nitrogen before cooling to RT. The crude, solid product was removed from the solvent by separation on the centrifuge then washed with water (4 mL), methanol (4 mL) and diethyl ether (4 mL). The product was then extracted into DCM and the solvent removed under reduced pressure to give Pt(dpyb)Cl as a yellow solid (115 mg, 48 %).

Method 2

dpybH (109 mg, 0.47 mmol), K_2PtCl_4 (200 mg, 0.48 mmol), acetic acid (1.2 mL) and water (0.3 mL) were placed in a sealed microwave vial and degassed by 3 x FPT cycles. The

mixture was heated at 160 °C for 30 min in the microwave and then left to cool to RT. The solid was isolated by centrifuge and washed with H_2O (2 x 5 mL), MeOH (5 mL) and Et_2O (5 mL) before extraction into DCM. The solvent was removed under reduced pressure and the complex dried *in vacuo* to give the pure product (217 mg, 68 %).

The experimental data obtained for both methods were in good agreement with the literature.[201]

Pt(dpyb)Cl₃

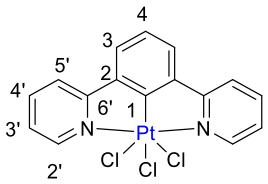

Pt(dpyb)Cl (83 mg, 0.18 mmol) was suspended in chloroform ($CHCl_3$) (83 mL) and chlorine gas (generated in a separate flask by addition of concentrated HCl, 37 %, to $KMnO_4$) was bubbled through the solution for 30 min. The solvent was removed *in vacuo* and the product was dried *in vacuo* to give a pale yellow solid (86 mg, 90 %); ^{1}H NMR (400 MHz, DMSO-d_6) δ 9.24 (dd, *J* = 6.0, 1.4 Hz, 2H, $H^{2'}$), 8.51 (dd, *J* = 8.1, 1.5 Hz, 2H, $H^{5'}$), 8.36 (td, *J* = 7.8, 1.6 Hz, 2H, $H^{4'}$), 8.18 (d, *J* = 7.7 Hz, 2H, H^3), 7.81 (ddd, *J* = 7.5, 5.9, 1.6 Hz, 2H, $H^{3'}$), 7.58 (t, *J* = 7.7 Hz, 1H, H^4); MS (ASAP$^+$) *m/z* =497.0 [M-Cl]$^+$; HRMS (ASAP+) *m/z* = 494.9922 [M-Cl]$^+$; calculated for $[C_{16}H_{11}N_2Cl_2{}^{194}Pt]^+$ 494.9926.

[Pt(dpyb)L¹Cl]PF₆

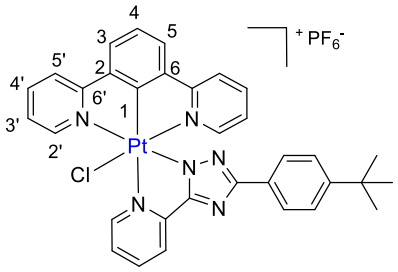

Pt(dpyb)Cl₃ (20 mg, 0.04 mmol) was suspended in dry toluene (3 mL) with AgOTf (21 mg, 0.08 mmol) and **HL¹** (13 mg, 0.05 mmol). The mixture was heated at reflux, under nitrogen, with the exclusion of light for 24 h. After cooling to RT, the precipitated solid was isolated on the centrifuge and washed with toluene (2 × 3 mL). The crude product was extracted into acetone (3 × 5 mL) and the solvent removed under reduced pressure. The product was then dissolved in the minimum volume of acetone and the PF_6^- salt was obtained by pipetting a saturated aqueous solution of KPF_6 (5 mL) to precipitate the product. The solid

was isolated by centrifugation and then washed with H_2O (5 × 3 mL). The solid was then recrystallized by slow evaporation from acetone to yield a yellow crystalline solid before drying *in vacuo* (2 mg, 7 %); MS (ASAP$^+$) *m/z* = 737.5 $[M]^+$; HRMS (ASAP+) *m/z* = 737.1677 $[M]^+$; calculated for $[C_{33}H_{28}N_6Cl^{194}Pt]^+$ 737.1691.

[Pt(dpyb)L^{16}]PF$_6$

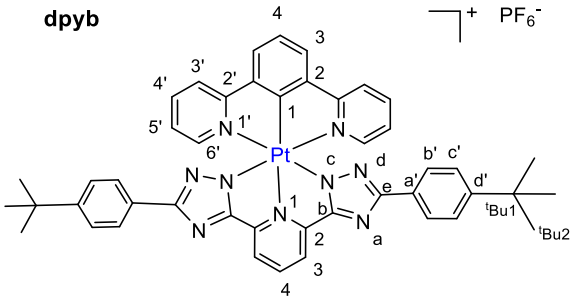

Pt(dpyb)Cl$_3$ (20 mg, 0.04 mmol), **H$_2$L^{16}** (18 mg, 0.038 mmol) and AgOTf (48 mg, 0.19 mmol) were added to a Schlenk and suspended in ethylene glycol (2 mL). The mixture degassed via 3 x FPT and then set to reflux for 3 days. After cooling to RT, water (5 mL) was added and the precipitated solid was isolated via centrifuge. The crude product was dissolved in the minimum volume of MeOH and the PF_6^- salt was obtained by pipetting a saturated aqueous solution of KPF_6 (5 mL) to precipitate the product. The solid was isolated by centrifugation and then washed with water (5 × 3 mL). The solid was then purified by 3 x DCM/Hexane recrystallizations to afford a yellow crystalline solid (7 mg, 20 %); ^{1}H NMR (400 MHz, DMSO-d_6) δ 9.19 – 9.10 (m, 1H, H^{4triz}), 9.01 (d, *J* = 8.0 Hz, 2H, $H^{6'}$), 8.39 (d, *J* = 8.5 Hz, 4H, $H^{b'}$), 7.85 (d, *J* = 5.7 Hz, 2H, H^{3triz}), 7.70 (d, *J* = 7.7 Hz, 4H, $H^{c'}$), 7.59 (t, *J* = 7.8 Hz, 2H, $H^{5'}$), 6.99 – 6.83 (m, 2H, $H^{4'}$), 6.72 – 6.52 (m, 2H, $H^{3'}$), 6.36 (d, *J* = 7.8 Hz, 2H, H^{3dpyb}), 5.68 (t, *J* = 7.7 Hz, 1H, H^{4dpyb}), 1.10 (s, 18H); MS (ASAP$^+$) *m/z* = 901.3 $[M]^+$.

7.4.2 Ir(dpyb) complexes

7.4.2.1 Step 1 intermediate

Compound I1^h

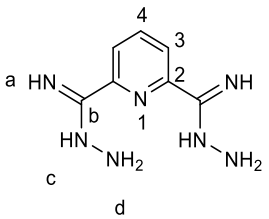

To a solution of 2,6-pyridinedicarbonitrile (500 mg, 3.87 mmol) in ethanol (25 mL) was added hydrazine monohydrate (3.76 mL, 77.45 mmol). The reaction mixture was stirred at RT overnight, yielding a pale-yellow precipitate in a yellow solution. The precipitate was filtered off, washed with cold ethanol, and dried *in vacuo*. A pale-yellow solid was obtained (582 mg, 78 %). The experimental data obtained were in good agreement with the literature.[91]

7.4.2.2 Step 2 intermediates

General procedure

An oven-dried, nitrogen-purged Schlenk tube was loaded with **I1^{h}** (1 eq) and Na_2CO_3 (2.2 eq), evacuated, gently heated, and refilled with nitrogen after being cooled to RT. Next, dry DMF was added and the suspension was cooled to 0 °C. In a separately prepared Schlenk tube, a solution of the acyl chloride (2 eq) in dry DMF was prepared the same way as above. This solution was then slowly added to the cooled suspension under vigorous stirring and the reaction mixture was allowed to warm to RT overnight. Then the reaction volume was doubled by the addition of water, yielding a suspension. This suspension was stirred strongly for another 1.5 h and then filtered and washed with water thoroughly. The solid was then dried *in vacuo*.

Compound I2^{k}

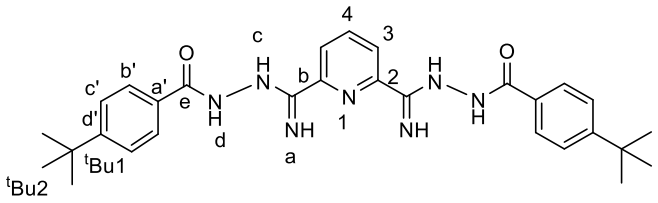

I1^{h} (500 mg, 2.59 mmol) and Na_2CO_3 (603 mg, 5.70 mmol) in 16 mL DMF and 4-*tert*-butylbenzoyl chloride (1.01 mL, 5.18 mmol) in 6 mL DMF were reacted according to the general procedure outlined above. A cream-coloured solid was obtained (151 mg, 46 %); ^{1}H NMR (400 MHz, DMSO-d_6) δ 10.12 (s, 2H, H^{c}), 8.25 (d, *J* = 7.8 Hz, 2H, H^{3}), 7.99 (t, *J* = 6.5 Hz, 1H, H^{4}), 7.82 (d, *J* = 8.2, 4H, H$^{b'}$), 7.53 (d, *J* = 8.2, 4H, H$^{c'}$), 7.28-7.19 (m, 4H, H^{a} and H^{d}), 1.33 (s, 18H, H^{tBu2}); MS (ESI^{+}) *m/z* = 514.3 [M+H]$^{+}$; HRMS (ESI+) *m/z* = 514.2921 [M+H]$^{+}$; calculated for $[C_{29}H_{36}N_7O_2]^{+}$ 514.2930.

Compound I2^{l}

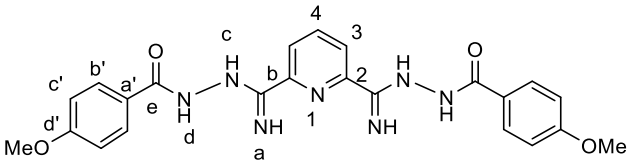

I1^{h} (300 mg, 1.55 mmol) and Na_2CO_3 (362 mg, 3.42 mmol) in 10 mL DMF and 4-methoxybenzoyl chloride (530 mg, 3.11 mmol) in 4 mL DMF were reacted according to the general procedure outlined above. A cream-coloured solid was obtained (326 mg, 46 %); ^{1}H NMR (400 MHz, DMSO-d_6) δ 10.11 (s, 2H, H^{c}), 8.24 (d, *J* = 7.9 Hz, 2H, H^{3}), 7.96 (t, *J* = 6.9 Hz, 1H, H^{4}), 7.91 (d, *J* = 8.3 Hz, 4H, H$^{b'}$), 7.37-7.13 (m, 4H, H^{a} and H^{d}), 7.04 (d, *J* = 8.3 Hz, 4H, H$^{c'}$), 3.84 (s, 6H, H^{OMe}); MS (ESI$^+$) *m/z* = 462.2 [M+H]$^+$; HRMS (ESI+) *m/z* = 462.1880 [M+H]$^+$; calculated for $[C_{23}H_{24}N_7O_4]^+$ 462.1890.

Compound I2^{m}

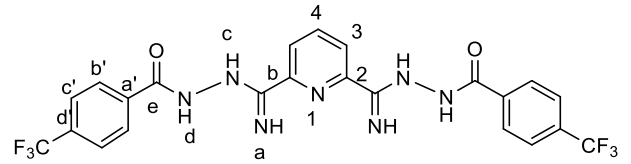

I1^{h} (700 mg, 3.60 mmol) and Na_2CO_3 (840 mg, 7.92 mmol) in 22 mL DMF and 4-trifluoromethylbenzoyl chloride (1.08 mL, 7.25 mmol) in 8 mL DMF were reacted according to the general procedure outlined above. A cream-coloured solid was obtained (1.7 g, 87 %); ^{1}H NMR (400 MHz, DMSO-d_6) δ 10.44 (s, 2H, H^{c}), 8.28 (d, *J* = 7.9 Hz, 2H, H^{3}), 8.12 (d, *J* = 8.3 Hz, 4H, H$^{b'}$), 8.00 (t, *J* = 6.6 Hz, 1H, H^{4}), 7.89 (d, *J* = 8.3 Hz, 4H, H$^{c'}$), 7.41-7.23 (m, 4H, H^{a} and H^{d}); ^{19}F NMR (376 MHz, DMSO-d_6) δ -61.21; MS (ESI$^+$) *m/z* = 538.1 [M+H]$^+$; HRMS (ESI$^+$) *m/z* = 538.1418 [M+H]$^+$; calculated for $[C_{23}H_{18}N_7O_2F_6]^+$ 538.1426.

7.4.2.3 H_2L^n Triazoles

General procedure

I2^{x} was suspended in ethylene glycol in a 100 mg/mL ratio in an open round-bottom flask. This suspension was heated to 180 °C, eliminating water. Once the solution was clear, the reaction mixture was heated under reflux for another hour. After the reaction mixture was cooled to RT, the product was precipitated with water and stirred vigorously for a further hour. The solid was filtered through a Whatman membrane filter (0.2 µm, nylon), washed with water, and dried *in vacuo*.

Compound H_2L^{16}

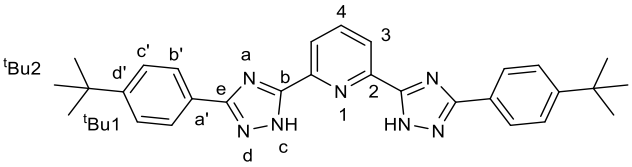

I2^{k} (4 g, 7.79 mmol) was suspended in ethylene glycol (40 mL) and reacted according to the general procedure as outlined above. A white solid was obtained (2.9 g, 78 %); ^{1}H NMR (400 MHz, DMSO-d_6) δ 14.50 (s, 2H, H^{c}), 8.24-8.19 (m, 3H, H^{3} and H^{4}), 8.07 (d, *J* = 8.5 Hz, 4H, H$^{b'}$), 7.56 (d, *J* = 8.5 Hz, 4H, H$^{c'}$), 1.34 (s, 18H, H^{tBu2}); ^{13}C NMR (176 MHz, DMSO-d_6) δ 126.2 (C$^{b'}$), 126.0 (C$^{c'}$), 121.8 (C^{3} and C^{4}), 35.0 (C^{tBu1}), 31.5 (C^{tBu2}); MS (ESI^{+}) *m/z* = 478.2 [M+H]$^{+}$; HRMS (ESI+) *m/z* = 478.4569 [M+H]$^{+}$; calculated for $[C_{29}H_{32}N_7]^{+}$ 478.4876.

Compound H_2L^{17}

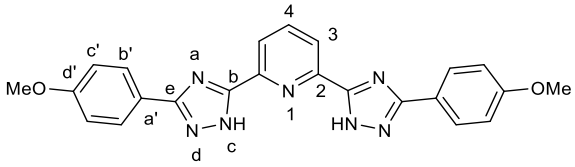

I2^{l} (320 mg, 0.69 mmol) was suspended in ethylene glycol (3.5 mL) and reacted according to the general procedure as outlined above. A white solid was obtained (261 mg, 89 %); ^{1}H NMR (400 MHz, DMSO-d_6) δ 8.25-8.16 (m, 3H, H^{3} and H^{4}), 8.07 (d, *J* = 8.8 Hz, 4H, H$^{b'}$), 7.11 (d, *J* = 8.8 Hz, 4H, H$^{c'}$), 3.85 (s, 6H, H^{OMe}); MS (ESI^{+}) *m/z* = 426.2 [M+H]$^{+}$; HRMS (ESI+) *m/z* = 426.1679 [M+H]$^{+}$; calculated for $[C_{23}H_{19}N_7O_2]^{+}$ 426.1678.

Compound H_2L^{18}

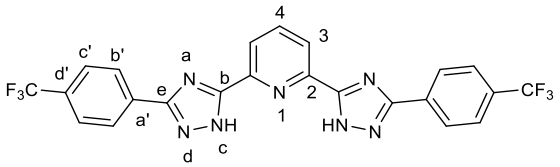

I2^{m} (1.6 g, 2.99 mmol) was suspended in ethylene glycol (16 mL) and reacted according to the general procedure as outlined above. A white solid was obtained (1.2 g, 80 %); ^{1}H NMR (400 MHz, DMSO-d_6) δ 8.36 (d, *J* = 8.2 Hz, 4H, H$^{b'}$), 8.28 – 8.19 (m, 3H, H^{3} and H^{4}), 7.91 (d, *J*

= 8.2 Hz, 4H, $H^{c'}$); ^{19}F NMR (376 MHz, DMSO-d_6) δ -61.10; MS (ESI^+) *m/z* = 502.5 $[M+H]^+$; HRMS (ESI+) *m/z* = 502.1207 $[M+H]^+$; calculated for $[C_{23}H_{13}N_7F_6]^+$ 502.1215.

7.4.2.4 Ir(dpyb)(L^n) complexes

General procedure

All chloro-bridged Ir dimers, $[Ir(dpybX)(\mu\text{-}Cl)Cl]_2$, were synthesised according to literature procedure (Nonoyama route) by reaction of the ligand with $IrCl_3.H_2O$ in ethoxyethanol/H_2O reflux for 24 h.[202] $[Ir(dpybX)(\mu\text{-}Cl)Cl]_2$ (1 eq) was added to a Schlenk with **H_2L^n** (2 eq) and ethylene glycol. The mixture was degassed via 3 x FPT cycles and then set to reflux at 185 °C for 24 h. The mixture was then allowed to cool to RT. The suspension was filtered and washed with water. This was then columned over a slow gradient of DCM/MeOH from 100:0 to 95:5 on alumina.

Ir(dpybMe$_2$)L^{16}

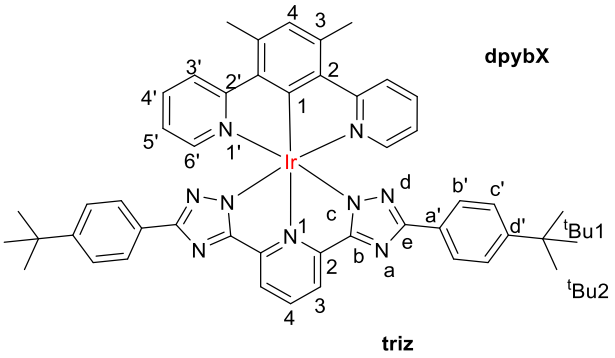

$[Ir(dpyb\mathit{Me_2})(\mu\text{-}Cl)Cl]_2$ (32 mg, 0.03 mmol), **H_2L^{16}** (29 mg, 0.06 mmol) and ethylene glycol (2 mL). A yellow powder was obtained (15 mg, 52 %); R_f = 0.45 (95:5 DCM/MeOH, alumina); ^1H NMR (700 MHz, DMSO-d_6) δ 8.37 (t, *J* = 7.8 Hz, 1H, H^{4triz}), 8.21 (d, *J* = 8.2 Hz, 2H, $H^{6'}$), 8.19 (d, *J* = 7.7 Hz, 2H, H^{3triz}), 7.80 (t, *J* = 8.0 Hz, 2H, $H^{5'}$), 7.61 (d, *J* = 8.7 Hz, 4H, $H^{b'}$), 7.40 (d, *J* = 5.8 Hz, 2H, $H^{3'}$), 7.25 (d, *J* = 8.7 Hz, 4H, $H^{c'}$), 7.18 (s, 1H, H^4), 7.04 (d, *J* = 6.8 Hz, 2H, $H^{4'}$), 2.90 (s, 6H, H^{Me}), 1.18 (s, 18H, H^{tBu2}); MS (ES^+) *m/z* = 928.3 $[M+H]^+$; HRMS (ES+) *m/z* = 926.3439 $[M+H]^+$; calculated for $[C_{47}H_{45}N_9{}^{191}Ir]^+$ 926.3404.

Ir(dpybMe$_2$)L^{17}

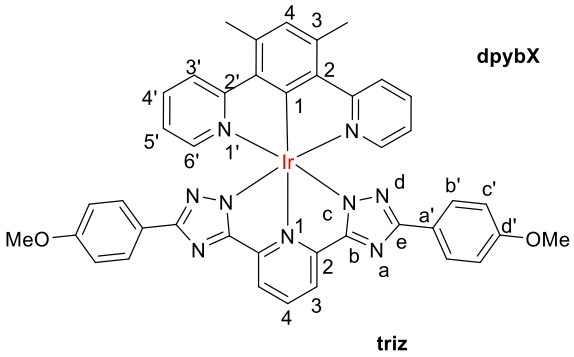

[Ir(dpyb*Me$_2$*)(μ-Cl)Cl]$_2$ (24 mg, 0.02 mmol), **H$_2$L^{17}** (20 mg, 0.05 mmol) and ethylene glycol (1 mL). A yellow powder was obtained (5 mg, 25 %); R_f = 0.27 (90:10 DCM/MeOH, alumina); MS (ES$^+$) *m/z* = 876.2 [M+H]$^+$; HRMS (ES+) *m/z* = 874.2365 [M+H]$^+$; calculated for [$C_{41}H_{33}N_9O_2{}^{191}Ir$]$^+$ 874.2363. This compound was insoluble in all common organic solvents, so no NMR data was obtained; Anal. Calcd for $C_{41}H_{33}N_9O_2Ir$: C, 56.28; H, 3.69; N, 14.41; Found: C, 55.76; H, 3.09; N, 14.78.

Ir(dpyb(Me)$_2$)L^{18}

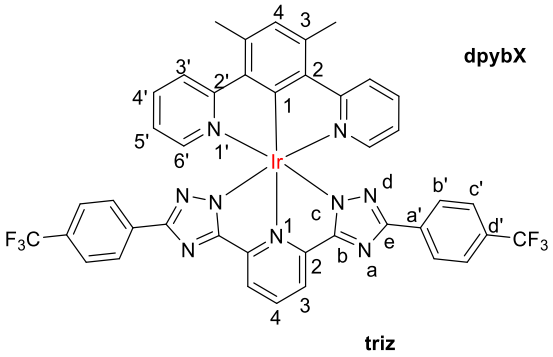

[Ir(dpyb*Me$_2$*)(μ-Cl)Cl]$_2$ (50 mg, 0.05 mmol), **H$_2$L^{18}** (48 mg, 0.10 mmol) and ethylene glycol (3 mL). A yellow powder was obtained (30 mg, 63 %); R_f = 0.32 (95:5 DCM/MeOH, alumina); ^{1}H NMR (700 MHz, DMSO-*d$_6$*) δ 8.42 (t, *J* = 7.7 Hz, 1H, H^{4triz}), 8.27 (d, *J* = 8.0 Hz, 2H, H^{3triz}), 8.22 (d, *J* = 8.5 Hz, 2H, H$^{6'}$), 7.90 (d, *J* = 8.2 Hz, 4H, H$^{c'}$), 7.81 (t, *J* = 7.7 Hz, 2H, H$^{5'}$), 7.60 (d, *J* = 8.3 Hz, 4H, H$^{b'}$), 7.42 (d, *J* = 5.8 Hz, 2H, H$^{3'}$), 7.18 (s, 1H, H^4), 7.04 (t, *J* = 6.6 Hz, 2H, H$^{4'}$), 2.90 (s, 6H, H^{Me}); ^{19}F NMR (376 MHz, Chloroform-*d*) δ -62.47; MS (ES$^+$) *m/z* = 951.8 [M+H]$^+$; HRMS (ES+) *m/z* = 950.1907 [M+H]$^+$; calculated for [$C_{41}H_{27}N_9F_6{}^{191}Ir$]$^+$ 950.1900.

Ir(dpybF$_2$)L^{16}

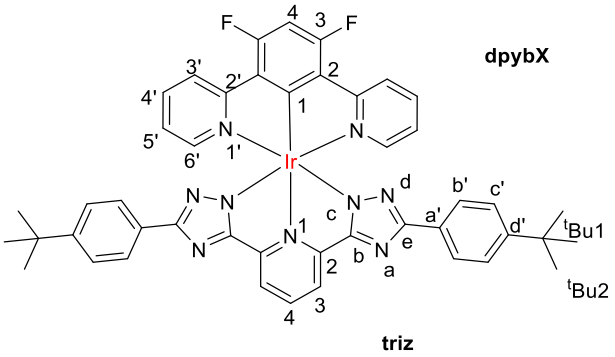

[Ir(dpyb*F$_2$*)(μ-Cl)Cl]$_2$ (100 mg, 0.09 mmol), **H$_2$L^{16}** (90 mg, 0.19 mmol) and ethylene glycol (3 mL). A yellow powder was obtained (46 mg, 52 %); R_f 0.51 (95:5 DCM/MeOH, alumina); ^{1}H NMR (400 MHz, DMSO-*d*$_6$) δ 8.44 (dd, *J* = 8.4, 7.5 Hz, 1H, H^{4triz}), 8.26 (d, *J* = 7.9 Hz, 2H, H$^{6'}$), 8.22 (d, *J* = 8.2 Hz, 2H, H^{3triz}), 7.94 (dd, *J* = 7.9, 1.4 Hz, 2H, H$^{5'}$), 7.67 (d, *J* = 8.6 Hz, 4H, H$^{b'}$), 7.54 – 7.46 (m, 3H, H^4 and H$^{4'}$), 7.30 (d, *J* = 8.6 Hz, 4H, H$^{c'}$), 7.17 (ddd, *J* = 7.4, 5.7, 1.4 Hz, 2H, H$^{3'}$), 1.22 (s, 18H, H^{tBu}); ^{19}F NMR (376 MHz, DMSO-*d*$_6$) δ -107.48 (d, *J* = 14.2 Hz); MS (ES$^+$) *m/z* =936.3 [M+H]$^+$; HRMS (ES+) *m/z* = 934.2894 [M+H]$^+$; calculated for [C$_{45}$H$_{39}$N$_9$F$_2$^{191}Ir]$^+$ 934.2903.

Ir(dpybF$_2$)L^{17}

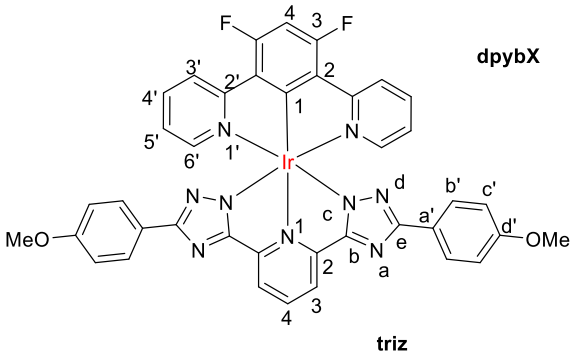

[Ir(dpyb*F$_2$*)(μ-Cl)Cl]$_2$ (125 mg, 0.12 mmol), **H$_2$L^{17}** (100mg, 0.24 mmol) and ethylene glycol (2 mL). A yellow powder was obtained (24 mg, 23 %); R_f=0.4 (95:5 DCM/MeOH, alumina); ^{1}H NMR (700 MHz, DMSO-*d*$_6$) δ 8.40 (t, *J* = 8.0 Hz, 1H, H^{4triz}), 8.20-8.17 (m, 4H, H^{3triz} and H$^{6'}$), 7.90 (td, *J* = 7.9, 1.6 Hz, 2H, H$^{5'}$), 7.64 (d, *J* = 8.9 Hz, 4H, H$^{b'}$), 7.47 (d, *J* = 5.6 Hz, 2H, H$^{3'}$), 7.44 (t, *J* = 11.6 Hz, 1H, H^4), 7.14 (ddd, *J* = 7.4, 5.8, 1.4 Hz, 2H, H$^{4'}$), 6.80 (d, *J* = 8.9 Hz, 4H, H$^{c'}$), 3.68 (s, 6H, H^{OMe}); ^{19}F NMR (376 MHz, DMSO-*d*$_6$) δ -107.49 (d, *J* = 12.0 Hz); MS (ES$^+$) *m/z* =884.1 [M+H]$^+$; HRMS (ES+) *m/z* =882.1857 [M+H]$^+$; calculated for [C$_{39}$H$_{27}$N$_9$O$_2$F$_2$^{191}Ir]$^+$; 882.1862.

Ir(dpybF$_2$)L^{18}

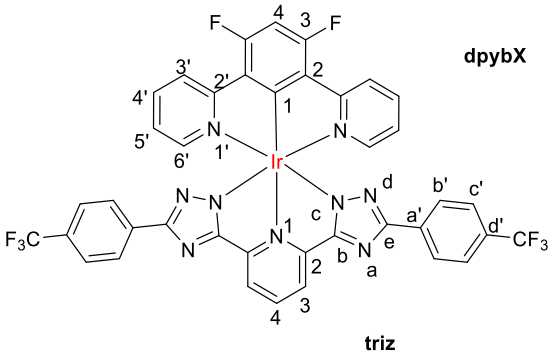

[Ir(dpyb*F$_2$*))(μ-Cl)Cl]$_2$ (100 mg, 0.09 mmol), **H$_2$L^{18}** (95 mg, 0.19 mmol) and ethylene glycol (2 mL). A yellow powder was obtained (35 mg, 39 %); ^{1}H NMR (700 MHz, DMSO-*d*$_6$) δ 8.47 (t, *J* = 8.1 Hz, 1H, H^{4triz}), 8.30 (d, *J* = 7.9 Hz, 2H, H^{3triz}), 8.19 (d, *J* = 8.2 Hz, 2H, H$^{6'}$), 7.93 (d, *J* = 8.4 Hz, 4H, H$^{c'}$), 7.91 (d, *J* = 7.7 Hz, 2H, H$^{5'}$), 7.61 (d, *J* = 8.4 Hz, 4H, H$^{b'}$), 7.51 (d, *J* = 6.0 Hz, 2H, H$^{3'}$), 7.46 (t, *J* = 11.6 Hz, 1H, H^4), 7.14 (ddd, *J* = 7.4, 5.9, 1.4 Hz, 2H, H$^{4'}$); ^{19}F NMR (376 MHz, DMSO-*d*$_6$) δ -60.99, -107.30 (d, *J* = 13.1 Hz); MS (ES$^+$) *m/z* = 960.0 [M+H]$^+$; HRMS (ES+) *m/z* = 958.1384 [M+H]$^+$; calculated for [C$_{39}$H$_{21}$N$_9$F$_8$^{191}Ir]$^+$ 958.1398.

Ir(dpybOMe)L^{16}

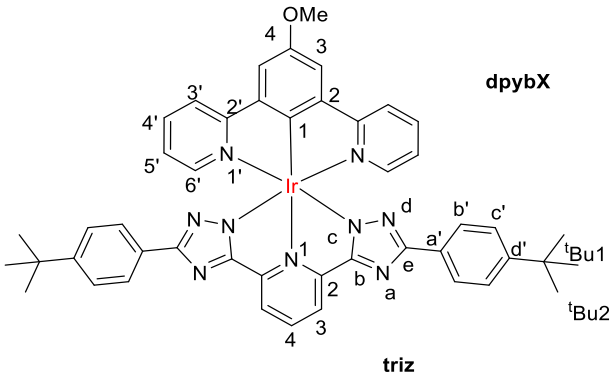

[Ir(dpyb*OMe*)(μ-Cl)Cl]$_2$ (50 mg, 0.05mmol), **H$_2$L^{16}** (46 mg, 0.10 mmol) and ethylene glycol (3 mL). A yellow/orange powder was obtained (33 mg, 74 %); MS (ES$^+$) *m/z* = 930.2 [M+H]$^+$; HRMS (ES+) *m/z* = 928.3202 [M+H]$^+$; calculated for [C$_{46}$H$_{43}$N$_9$O^{191}Ir]$^+$ 928.3197; Anal. Calcd for C$_{46}$H$_{42}$N$_9$OIr: C, 59.47; H, 4.56; N, 13.57; Found: C, 59.23; H, 4.48; N, 12.93.

Ir(dpybOMe)L[17]

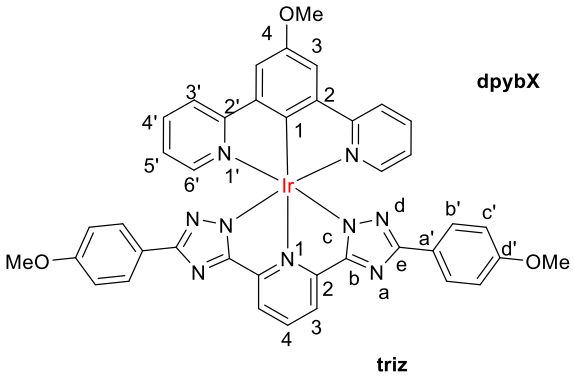

[Ir(dpyb*OMe*)(μ-Cl)Cl]$_2$ (50 mg, 0.05mmol), **H_2L^{17}** (41 mg, 0.10 mmol) and ethylene glycol (3 mL). A yellow/orange powder was obtained (25 mg, 59 %); R_f=0.2 (95:5 DCM/MeOH, alumina); ^{1}H NMR (700 MHz, DMSO-d_6) δ 8.36 – 8.33 (m, 3H, H^{4triz} and $H^{6'}$), 8.15 (d, *J* = 7.9 Hz, 2H, H^{3triz}), 7.96 (s, 2H, H^3), 7.84 (ddd, *J* = 8.1, 7.4, 1.5 Hz, 2H, $H^{5'}$), 7.61 (d, *J* = 9.0 Hz, 4H, $H^{b'}$), 7.38 (d, *J* = 5.9 Hz, 2H, $H^{3'}$), 7.04 (ddd, *J* = 7.3, 5.8, 1.4 Hz, 2H $H^{4'}$), 6.78 (d, *J* = 9.0 Hz, 4H, $H^{c'}$), 4.06 (s, 3H, $H^{OMe(NCN)}$), 3.67 (s, 6H, $H^{OMe(triz)}$); MS (ES$^+$) *m/z* = 878.1 [M+H]$^+$; HRMS (ES+) *m/z* = 876.2155 [M+H]$^+$; calculated for [$C_{40}H_{30}N_9O_3{}^{191}Ir$]$^+$ 876.2156.

Ir(dpybOMe)L[18]

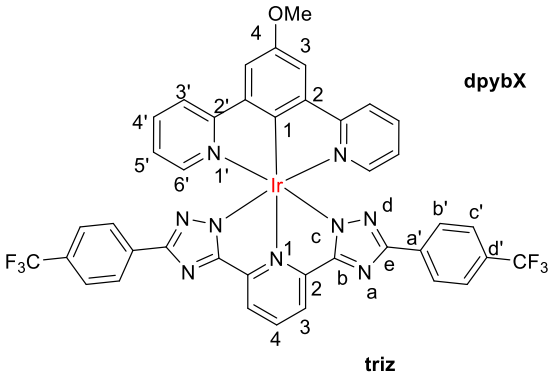

[Ir(dpyb*OMe*)(μ-Cl)Cl]$_2$ (50 mg, 0.05mmol), **H_2L^{18}** (48 mg, 0.10 mmol) and ethylene glycol (3 mL). A yellow/orange powder was obtained (34 mg, 71 %); R_f=0.26 (95:5 DCM/MeOH); ^{1}H NMR (700 MHz, DMSO-d_6) δ 8.42 (t, *J* = 7.9 Hz, 1H, H^{4triz}), 8.36 (d, *J* = 8.1 Hz, 2H, $H^{6'}$), 8.27 (d, *J* = 7.9 Hz, 2H, H^{3triz}), 7.98 (s, 2H, H^3), 7.91 (d, *J* = 8.2 Hz, 4H, $H^{c'}$), 7.85 (t, *J* = 7.7 Hz, 2H, $H^{5'}$), 7.59 (d, *J* = 8.4 Hz, 4H, $H^{b'}$), 7.42 (d, *J* = 5.8 Hz, 2H, $H^{3'}$), 7.05 (t, *J* = 6.5 Hz, 2H, $H^{4'}$), 4.07 (s, 3H, H^{OMe}); ^{19}F NMR (376 MHz, DMSO-d_6) δ -60.96; MS (ES$^+$) *m/z* = 953.9 [M+H]$^+$; HRMS (ES+) *m/z* = 952.1714 [M+H]$^+$; calculated for [$C_{40}H_{24}N_9O_1F_6{}^{191}Ir$]$^+$ 952.1692.

7.4.2.5 Ir(dpybMe$_2$)(L$^{1-3}$)Cl complexes

General procedure

[Ir(dpyb*Me$_2$*)(μ-Cl)Cl]$_2$ (1 eq) and **HL^n** (2 eq) were added to a Schlenk with AgOTf (4.5 eq) and suspended in toluene (3 mL). The mixture was degassed via 3 x FPT cycles and set to heat at reflux for 24 h. The mixture was cooled to RT and the solvent was removed *in vacuo.* The solid was extracted into DCM and then recrystallized in MeOH/hexane.

Ir(dpybMe$_2$)L^{1}Cl

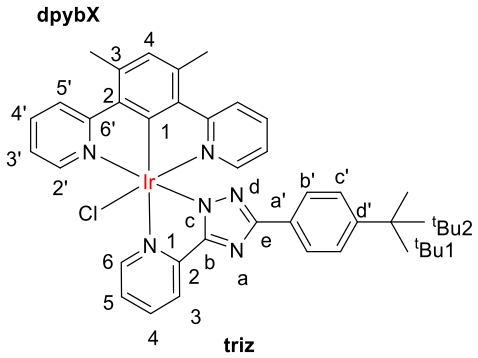

[Ir(dpyb*Me$_2$*)(μ-Cl)Cl]$_2$ (50 mg, 0.05 mmol) and **HL^1** (27 mg, 0.10 mmol) with AgOTf (56 mg, 0.22 mmol) and toluene (3 mL). A yellow powder was obtained (30 mg, 82 %); ^{1}H NMR (400 MHz, Methanol-*d$_4$*) δ 8.41 (d, *J* = 8.3 Hz, 2H, H$^{2'}$), 8.27-8.20 (m, 3H, H^{6triz} and H$^{b'}$), 7.89 (d, *J* = 5.6 Hz, 2H, H$^{3'}$), 7.83 – 7.70 (m, 3H, H$^{5'}$ and H^{3triz}), 7.47 (d, *J* = 8.2 Hz, 2H, H$^{c'}$), 7.23 (d, *J* = 5.8 Hz, 1H, H^{4triz}), 7.15 (s, 1H, H^{4dpyb}), 7.01 (td, *J* = 6.9, 1.67 Hz, 1H, H^{5triz}), 6.98-6.90 (m, 2H, H$^{4'}$), 2.91 (s, 6H, H^{Me}), 1.37 (s, 9H, H^{tBu2}); MS (ES$^+$) *m/z* = 763.0 [M+H]$^+$; HRMS (ES+) *m/z* = 763.2071 [M+H]$^+$; calculated for [C$_{35}$H$_{33}$N$_6$Cl^{191}Ir]$^+$ 763.2061.

Ir(dpybMe$_2$)L^{2}Cl

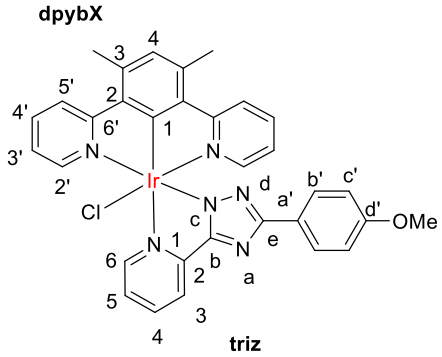

[Ir(dpyb*Me$_2$*)(μ-Cl)Cl]$_2$ (50 mg, 0.05 mmol) and **HL^2** (24 mg, 0.10 mmol) with AgOTf (56 mg, 0.22 mmol) and toluene (3 mL). A yellow powder was obtained (5 mg, 14 %); ^{1}H NMR (700 MHz, DMSO-*d$_6$*) δ 9.55 (d, *J* = 5.4, 1H, H^{6triz}), 8.63 (d, *J* = 7.9, 1H, H^{3triz}), 8.30 (t, *J* = 7.9,

1H, H^{5triz}), 8.14-7.99 (m, 3H, H^{4triz} and $H^{2'}$), 7.85 (t, *J* = 8.0 Hz, 2H, $H^{3'}$), 7.55 (d, *J* = 5.2 Hz, 2H, $H^{5'}$), 7.29 (d, *J* = 7.7 Hz, 2H, $H^{c'}$), 7.14 (t, *J* = 7.1, 2H, $H^{4'}$), 6.40 (s, 1H, H^{4dpyb}), 6.35 (d, *J* = 7.7 Hz, 2H, $H^{b'}$), 3.68 (s, 6H, H^{OMe}), 2.51 (s, 6H, H^{Me}); MS (ES^+) *m/z* = 737.1 $[M+H]^+$; HRMS (ES+) *m/z* = 737.1580 $[M+H]^+$; calculated for $[C_{32}H_{27}N_6OCl^{191}Ir]^+$ 737.1541.

Ir(dpybMe$_2$)L^{3}Cl

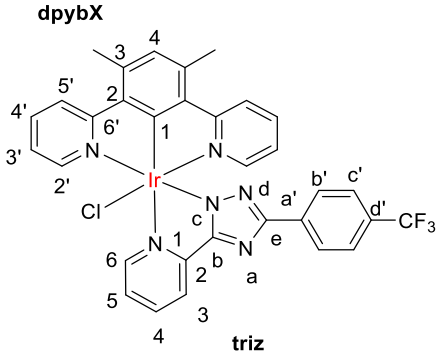

[Ir(dpyb*Me$_2$*)(μ-Cl)Cl]$_2$ (50 mg, 0.05 mmol) and **HL^3** (28 mg, 0.10 mmol) with AgOTf (56 mg, 0.22 mmol) and toluene (3 mL). A yellow powder was obtained (7 mg, 18 %); ^{1}H NMR (700 MHz, DMSO-d_6) δ 9.57 (dt, *J* = 5.2, 1.3 Hz, 1H, H^{6triz}), 8.48 (dt, *J* = 7.9, 1.2 Hz, 1H, H^{3triz}), 8.42 (td, *J* = 7.9, 1.6 Hz, 1H, H^{5triz}), 8.05-8.00 (m, 3H, H^{4triz} and $H^{2'}$), 7.85 (ddd, *J* = 8.5, 7.4, 1.7 Hz, 2H, $H^{3'}$), 7.58 (d, *J* = 5.7 Hz, 2H, $H^{5'}$), 7.22 (d, *J* = 7.8 Hz, 2H, $H^{c'}$), 7.14 (ddd, *J* = 7.2, 5.6, 1.3 Hz, 2H, $H^{4'}$), 6.46 (s, 1H, H^{4dpyb}), 6.35 (d, *J* = 7.7 Hz, 2H, $H^{b'}$), 2.53 (s, 6H, H^{Me}); ^{13}C NMR (176 MHz, DMSO-d_6) δ 169.1 ($C^{6'}$), 163.3 ($C^{b/e}$), 162.8 ($C^{b/e}$), 161.9 ($C^{a'}$), 151.8 ($C^{5'}$), 148.9 ($C^{d'}$), 148.6 (C^{6triz}), 140.5 (C^{5triz}), 139.3 ($C^{3'}$), 138.0 (C^{3dpyb}), 137.0 (C^{2dpyb}), 130.8 (C^{4dpyb}), 129.1 ($C^{b'}$), 127.1 (C^{4triz}), 124.1 ($C^{c'}$), 123.4 ($C^{2'}$), 123.2 ($C^{4'}$), 121.9 (C^{3triz}), 22.0 (C^{Me}); ^{19}F NMR (376 MHz, DMSO-d_6) δ -61.84; MS (ES^+) *m/z* = 775.1 $[M+H]^+$; HRMS (ES+) *m/z* = 775.1348 $[M+H]^+$; calculated for $[C_{32}H_{24}N_6F_3Cl^{191}Ir]^+$ 775.1309.

7.5 Chapter 4 Synthesis

7.5.1 Precursors

Compound P[6]

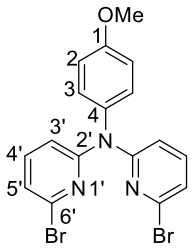

Toluene (40 mL) was added to a mixture of *p*-anisidine (490 mg, 4 mmol), 2,6-dibromopyridine (2.37 g, 10 mmol), NaO^{t}Bu (960 mg, 10 mmol) and 1,1'-bis(diphenylphosphino)ferrocene (dppf) (89 mg, 0.16 mmol). The mixture was degassed by 3 x FPT cycles and then the catalyst bis(dibenzylideneacetone)palladium(0) ($Pd(dba)_2$) (46 mg, 0.08 mmol) was added. The reaction mixture was refluxed for 48 h under argon. After cooling to RT, water (10 mL) was added to the reaction mixture. The organic phase was extracted with ethyl acetate (3 x 20 mL) and washed with water (3 x 20 mL). The organic layer was dried with $MgSO_4$ and the solvent was removed *in vacuo*. The crude oil was purified with column chromatography on silica gel (hexane/ethyl acetate 100:0 to 80:20) to obtain a white crystalline powder (520 mg, 30 %); R_f =0.57 (silica, 70:30, hexane/ethyl acetate); ^{1}H NMR (400 MHz, Chloroform-*d*) δ 7.39 (t, *J* = 7.6 Hz, 2H, $H^{4'}$), 7.16 (d, *J* = 8.9 Hz, 2H H^2), 7.09 (dd, *J* = 7.6, 0.7 Hz, 2H, $H^{3'}$), 7.01 – 6.90 (m, 4H, H^3 and $H^{5'}$), 3.87 (s, 3H, H^{OMe}); ^{13}C NMR (400 MHz; $CDCl_3$) 157.5 (C^1), 156.3 ($C^{2'}$), 138.6 ($C^{6'}$), 138.4 ($C^{4'}$), 135.1 (C^4), 128.8 (C^2), 120.7 ($C^{3'}$), 114.3 (C^3), 113.4 ($C^{5'}$), 54.6 (C^{OMe}); MS (ES^+) *m/z* = 433.94 $[M+H]^+$; HRMS (AP+) *m/z* = 433.9509 $[M+H]^+$; calculated for $[C_{17}H_{14}Br_2N_3O]^+$ 433.9504; Mp. = 125 °C.

***Compound* P[7]**

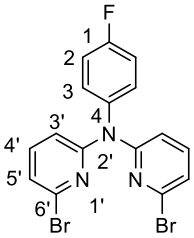

Dibromopyridine (2.00 g, 8.44 mmol), 4-fluoroaniline (426.43 mg, 3.83 mmol), dppf (106 mg, 0.19 mmol), NaO^{t}Bu (3.31 g, 34.47 mmol) and $Pd(dba)_2$ (110 mg, 0.19 mmol) were added to a Schlenk with dry toluene (90 mL). This mixture was degassed via 3 x FPT cycles and set to reflux for 3 days. The crude oil was purified with column chromatography on silica gel (hexane/DCM 1:1) to obtain a yellow oil (1.19 g, 74 %); Rf= 0.60 (80:20

hexane:ethyl acetate); ^{1}H NMR (400 MHz, Chloroform-d) δ 7.42 (d, J = 8.2 Hz, 2H, H^{3}), 7.24 – 7.18 (m, 2H, $H^{4'}$), 7.17 – 7.10 (m, 4H, $H^{3'}$ and $H^{5'}$), 6.96 (dd, J = 8.1 Hz, 2H, H^{2}); MS (ES^{+}) m/z = 424.1 $[M+H]^{+}$; HRMS (ES^{+}) m/z = 421.9324 $[M+H]^{+}$; calculated for $[C_{16}H_{10}Br_2N_3F]^{+}$ 421.9304.

7.5.2 H_2L^n tetradentate ligands

Compound H_2L^{19}

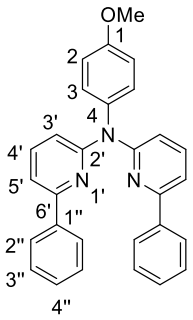

The ligand was prepared via the Suzuki cross-coupling methodology. **P^{6}** (325.70 mg, 0.7523 mmol), phenylboronic acid (275 mg, 2.26 mmol) and Na_2CO_3 (797 mg, 7.52 mmol) with DME (6 mL) and H_2O (6 mL). $Pd(PPh_3)_4$ (70 mg, 0.06 mmol) was added after 3 x FPT cycles. The compound was purified by column chromatography on silica (hexane/ethyl acetate 70:30). A white powder was obtained (322 mg, 49 %); R_f= 0.79 (silica, 70:30, hexane/ethyl acetate); ^{1}H NMR (400 MHz, Chloroform-*d*) δ 7.91 (dd, *J* = 8.2, 1.4 Hz, 4H, $H^{2''}$), 7.64 (t, *J* = 7.9 Hz, 2H, $H^{4'}$), 7.43 – 7.35 (m, 8H, $H^{3''}$ and $H^{5'}$ and $H^{4''}$), 7.31 (d, *J* = 8.9 Hz, 2H, H^{3}), 7.07 (dd, *J* = 8.2, 0.7 Hz, 2H, $H^{3'}$), 7.01 (d, *J* = 8.9 Hz, 2H, H^{2}), 3.90 (s, 3H, H^{OMe}); ^{13}C NMR (400 MHz; $CDCl_3$) 157.8 ($C^{2'}$), 157.7 ($C^{6'}$), 155.3 ($C^{1''}$), 139.4 (C^{4}), 137.9 ($C^{4'}$), 129.9 (C^{3}), 128.8 ($C^{4''}$), 128.7 ($C^{3''}$), 126.8 ($C^{2''}$), 114.9 (C^{2}), 114.7 ($C^{3'}$), 113.7 ($C^{5'}$), 55.7 (C^{Me}); MS (ES^{+}) *m/z* = 430.2 $[M+H]^{+}$; HRMS (ES+) *m/z* = 430.1907 $[M+H]^{+}$; calculated for $[C_{29}H_{24}N_3O]^{+}$ 430.1919; Mp. = 188 °C.

Compound H_2L^{20}

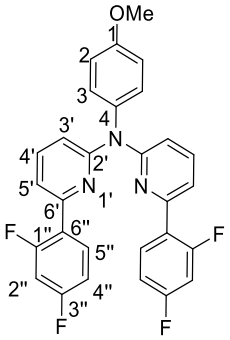

The ligand was prepared via the Suzuki cross-coupling methodology. **P^{6}** (305 mg, 0.70 mmol), Na_2CO_3 (748 mg, 7.06 mmol) and 2,4-difluorophenylboronic acid (280 mg,

1.77 mmol) with DME (5 mL) and water (5 mL). $Pd(PPh_3)_4$ (66 mg, 0.06mmol) was added after 3 x FPT cycles. The crude product was purified by column chromatography on silica (100:0 to 50:50 hexane/ethyl acetate). A white powder was obtained (85 mg, 24 %); ^{1}H NMR (700 MHz, Chloroform-*d*) δ 7.78 (td, *J* = 9.0, 6.8 Hz, 2H, $H^{4''}$), 7.60 (t, *J* = 7.9 Hz, 2H, $H^{4'}$), 7.43 (dd, *J* = 7.6, 2.0 Hz, 2H, $H^{5'}$), 7.24 (d, *J* = 9.1 Hz, 2H, H^{3}), 7.00 (d, *J* = 8.2 Hz, 2H, $H^{3'}$), 6.96 (d, *J* = 9.1 Hz, 2H, H^{2}), 6.87 – 6.79 (m, 4H, $H^{2''}$ and $H^{5''}$), 3.85 (s, 3H, H^{OMe}); ^{13}C NMR (176 MHz, Chloroform-*d*) δ 161.5 ($C^{1''}$), 160.1 ($C^{3''}$), 157.8 (C^{1}), 157.4 ($C^{2'}$), 150.0 ($C^{6'}$), 137.8 ($C^{4'}$), 132.0 ($C^{4''}$), 129.6 (C^{3}), 123.3 ($C^{6''}$), 117.7 ($C^{2'}$), 114.9 ($C^{3'}$), 114.8 (C^{2}), 111.6 ($C^{5''}$), 104.1 ($C^{2''}$), 55.5 (C^{OMe}); ^{19}F NMR (376 MHz, Chloroform-*d*) δ -109.90, -111.70 (dd, *J* = 21.6, 10.4 Hz); MS (ESI+) *m/z*= 502.7 $[M+H]^+$; HRMS (ES+) *m/z* = 502.1530 $[M+H]^+$ calculated for for $[C_{29}H_{20}F_4N_3O]^+$ *m/z* = 502.1543; Mp. = 127 °C.

Compound H_2L^{21}

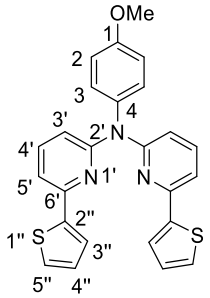

This ligand was prepared via the Stille cross-coupling methodology. **P^6** (207 mg, 0.48 mmol), 2-tri-n-butylstannylthiophene (453 mg, 1.21 mmol) and LiCl (162 mg, 3.82 mmol) with toluene (10 mL). $Pd(PPh_3)_2Cl_2$ (23 mg, 0.03 mmol) was added after 3 x FPT. The reaction was refluxed for 48 h. The crude product was purified by column chromatography on silica (70:30, hexane/ethyl acetate). A white powder was obtained (145mg, 69 %); R_f =0.8 (silica, 80:20 hexane/ethyl acetate); ^{1}H NMR (700 MHz, Chloroform-*d*) δ 7.56 (dd, *J* = 8.3, 7.5 Hz, 2H, $H^{4'}$), 7.49 (dd, *J* = 3.7, 1.1 Hz, 2H, $H^{3''}$), 7.31-7.27 (m, 4H, H^3 and $H^{5'}$), 7.26 (dd, *J* = 7.6, 0.7 Hz, 2H, $H^{5''}$), 7.09 – 7.03 (m, 4H, $H^{4''}$ and $H^{3'}$), 7.01 (d, *J* = 9.0 Hz, 2H, H^2), 3.90 (s, 3H, H^{OMe}); ^{13}C NMR (176 MHz, Chloroform-*d*) δ 158.1 (C^1), 157.0 ($C^{6'}$), 150.5 ($C^{2'}$), 145.7 ($C^{2''}$), 137.7 ($C^{4'}$), 137.1 (C^4), 130.5 ($C^{5''}$), 127.9 ($C^{3'}$), 127.2 (C^3), 124.2 ($C^{3''}$), 114.8 (C^2), 114.1 ($C^{4''}$), 111.9 ($C^{5'}$), 55.6 (C^{Me}); MS (ES^+) *m/z* = 442.1 $[M+H]^+$; HRMS (ES^+) *m/z* = 442.1033 $[M+H]^+$; calculated for $[C_{25}H_{20}N_3OS_2]^+$ 442.1040; Mp. = 137 °C.

Compound H_2L^{22}

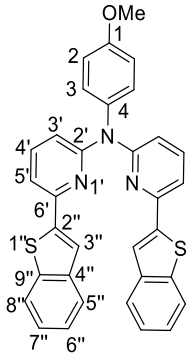

This ligand was prepared via the Stille cross-coupling methodology. **P[6]** (213 mg, 0.49 mmol) with LiCl (166 mg, 3.92 mmol) and 2-tri-n-butylstannyl benzothiophene (520 mg, 1.29 mmol) and dry toluene (8 mL). $Pd(PPh_3)_2Cl_2$ (28 mg, 0.04 mmol) was added after 3 x FPT cycles. The reaction was refluxed for 48 h. The crude product was columned on silica (90:10, hexane/ethyl acetate). A white powder was obtained (68 mg, 26 %); R_f =0.27; ^{1}H NMR (700 MHz, Chloroform-*d*) δ 7.78 (d, *J* = 8.1 Hz, 2H, $H^{5''}$), 7.74 (d, *J* = 7.7 Hz, 2H, $H^{8''}$), 7.72 (s, 2H, $H^{3''}$), 7.62 (dd, *J* = 8.3, 7.5 Hz, 2H, $H^{4'}$), 7.40 (dd, *J* = 7.5, 0.7 Hz, 2H, $H^{3'}$), 7.32 – 7.26 (m, 6H, H^3, $H^{6''}$ and $H^{7''}$), 7.13 (dd, *J* = 8.2, 0.7 Hz, 2H, $H^{5'}$), 7.04 (d, *J* = 8.9 Hz, 2H, H^2), 3.90 (s, 3H, H^{OMe}); ^{13}C NMR (176 MHz, Chloroform-*d*) δ 156.8 ($C^{2'}$), 150.2 ($C^{6'}$), 140.7 ($C^{4''}$), 140.5 ($C^{9''}$), 137.5 ($C^{4'}$), 130.4 (C^3), 124.6 ($C^{6''}$), 124.2 ($C^{7''}$), 123.9 ($C^{8''}$), 122.4 ($C^{5''}$), 120.5 ($C^{3''}$), 114.8 (C^2), 114.7 ($C^{3'}$), 112.8 ($C^{5'}$), 55.5 (C^{OMe}); (ESI$^+$) *m/z* = 542.2 $[M+H]^+$; HRMS (ES$^+$) *m/z* = 542.1359 $[M+H]^+$; calculated for $[C_{33}H_{24}N_3OS_2]^+$ 542.1361; Mp. = 201 °C.

Compound H_2L^{23}

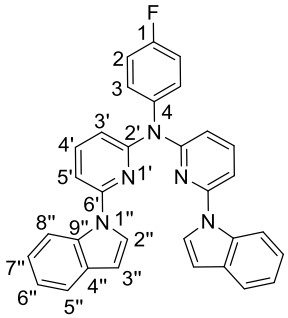

P[7] (500 mg, 1.18 mmol), indole (306 mg, 2.61 mmol) and NaO^tBu (1.02 g, 10.62 mmol) were added to a Schlenk with dry toluene (70 mL). In a separate Schlenk, tri-*tert*-butylphosphonium tetrafluoroborate ($HP(^tBu)_3^+BF_4^-$) (52 mg, 0.18 mmol) was added

to $Pd(dba)_2$ (33.9 mg, 0.06 mmol) with toluene (20 mL). The Schlenk containing the catalyst was added to the other Schlenk dropwise via cannular under an argon atmosphere. This was stirred at reflux for 24 hours and left to cool to RT. Water was added and the product was extracted with ethyl acetate and then reduced *in vacuo*. The crude product was columned on silica (100:0 to 80:20, hexane/ethyl acetate) to obtain a white powder (403 mg, 69 %); R_f =0.57 (80:20. hexane/ethyl acetate); ^{1}H NMR (599 MHz, Chloroform-*d*) δ 7.80 (dq, *J* = 8.4, 0.9 Hz, 2H, $H^{5''}$), 7.68 (t, *J* = 8.0 Hz, 2H, $H^{4'}$), 7.61 (d, *J* = 3.5 Hz, 2H, $H^{2''}$), 7.58 (d, *J* = 7.9 Hz, 2H, $H^{8''}$), 7.44 – 7.37 (m, 2H, H^2), 7.27 – 7.20 (m, 2H, H^3), 7.13 (ddd, *J* = 7.9, 7.0, 1.0 Hz, 2H, $H^{7''}$), 7.08 (dd, *J* = 8.0, 0.6 Hz, 2H, $H^{3'}$), 7.05 – 6.99 (m, 4H, $H^{6''}$ and $H^{5'}$), 6.64 (dd, *J* = 3.5, 0.8 Hz, 2H, $H^{3''}$); ^{13}C NMR (151 MHz, Chloroform-*d*) δ 162.1 (C^1), 160.5 (C^4), 156.5 ($C^{2'}$), 151.3 ($C^{6'}$), 139.6 (d, *J* = 2.1 Hz) ($C^{4'}$), 135.0 ($C^{4''}$), 130.9 (d, *J* = 8.4 Hz) (C^2), 130.3 ($C^{9''}$), 125.3 (d, *J* = 1.5 Hz) ($C^{2''}$), 122.8 ($C^{6''}$), 121.2 ($C^{7''}$), 120.7 ($C^{8''}$), 116.8 (d, *J* = 22.6 Hz) (C^3), 114.3 ($C^{5''}$), 111.2 ($C^{5'}$), 106.6 (d, *J* = 1.5 Hz) ($C^{3'}$), 105.8 ($C^{3''}$); ^{19}F NMR (376 MHz, Chloroform-*d*) δ -115.37; (ESI^+) *m/z* = 496.3 $[M+H]^+$; HRMS (ES^+) *m/z* = 496.1916 $[M+H]^+$; calculated for $[C_{32}H_{23}FN_5]^+$ 496.1937.

7.5.3 Pt and Pd Complexes

7.5.3.1. Pt^{II} Complexes

H_2L^n (0.66 mmol, 1eq), K_2PtCl_4 (0.72 mmol, 1.1 eq), and acetic acid (3 mL) were added to a Schlenk. The reaction mixture was degassed by 3 x FPT cycles and heated at refluxed for 48 hours. Water (5 mL) was added to the reaction mixture and the precipitate was collected via centrifugation. The precipitate was then washed with H_2O (1 x 5 mL) EtOH (1 x 5 mL) and Et_2O (2 x 5 mL) before being dried *in vacuo*.

PtL^{19}

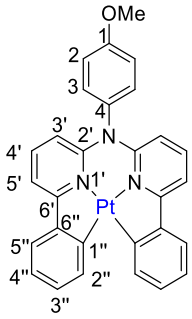

H_2L^{19}(100 mg, 0.233 mmol), acetic acid (3 mL) and K_2PtCl_4 (106 mg, 0.26 mmol). A yellow solid was obtained (84 mg; 58 %); ^{1}H NMR (700 MHz, Chloroform-*d*) δ 8.40 (d, *J* = (^{195}Pt 50.4), 7.6 Hz, 2H, $H^{2''}$), 7.79 (d, *J* = 7.5 Hz, 2H, $H^{5''}$), 7.71 (dd, *J* = 8.6, 7.6 Hz, 2H, $H^{4'}$), 7.60 (d, *J*

= 7.6 Hz, 2H, $H^{5'}$), 7.43 (t, *J* = 7.7 Hz, 2H, $H^{3''}$), 7.30 (d, *J* = 8.7 Hz, 2H, H^{3}), 7.21 (t, *J* = 7.4 Hz, 2H, $H^{4''}$), 7.18 (d, *J* = 8.7 Hz, 2H, H^{2}), 6.52 (d, *J* = 8.7 Hz, 2H, $H^{3'}$), 3.95 (s, 3H, H^{OMe}); ^{13}C NMR (176 MHz, Chloroform-*d*) δ 164.3 ($C^{6'}$), 160.1 (C^{1}), 149.0 ($C^{2'}$), 148.6 ($C^{1''}$), 147.0 ($C^{6''}$), 142.8 (C^{4}), 136.7 ($C^{4'}$), 136.0 ($C^{2''}$), 131.3 (C^{3}), 129.4 ($C^{3''}$), 123.7 ($C^{5''}$), 123.2 ($C^{4''}$), 116.6 (C^{2}), 113.7 ($C^{3'}$), 111.7 ($C^{5'}$), 55.7 (C^{OMe}); (ESI$^+$) *m/z* = 623.4 $[M+H]^+$; HRMS (ES$^+$) *m/z* = 622.1397 $[M+H]^+$; calculated for $[C_{29}H_{22}N_3O^{194}Pt]^+$ 622.1390.

***PtL*^{20}**

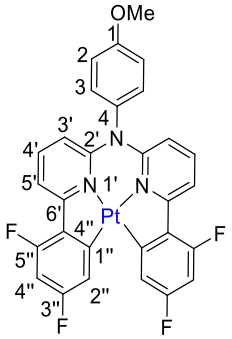

H_2L^{20} (50 mg, 0.10 mmol), K_2PtCl_4 (46 mg, 0.11 mmol) and acetic acid (3 mL) set to refluxed for 3 nights at 118 °C. A yellow solid resulted (5 mg; 7 %); Isomers obtained in NMR and so all characterisation done on a crystal; (ES$^+$) *m/z* = 695.1 $[M+H]^+$; HRMS (ES$^+$) *m/z* = 694.1003 $[M+H]^+$; calculated for $[694.1013]^+$.

***PtL*^{21}**

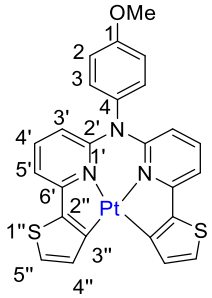

H_2L^{21} (100 mg, 0.23 mmol), K_2PtCl_4 (103 mg, 0.25 mmol) and acetic acid (3 mL). A pale green powder was obtained (128 mg, 89 %); ^{1}H NMR (700 MHz, Chloroform-*d*) δ 7.76 (d, *J* = (^{195}Pt 20.4), 4.7 Hz, 2H, $H^{4''}$), 7.64 (dd, *J* = 8.7, 7.5 Hz, 2H, $H^{4'}$), 7.58 (d, *J* = 4.7 Hz, 2H, $H^{5''}$), 7.31 – 7.27 (m, 4H, $H^{5'}$ and H^{2}), 7.17 (d, *J* = 8.8 Hz, 2H, H^{3}), 6.36 (dd, *J* = 8.7, 0.8 Hz, 2H, $H^{3'}$), 3.95 (s, 3H, H^{OMe}); ^{13}C NMR (176 MHz, Chloroform-*d*) δ 160.2 (C^{1}), 158.9 ($C^{2'}$), 152.1 ($C^{3''}$), 148.2 ($C^{6'}$), 142.5 ($C^{2''}$), 137.1 ($C^{4'}$), 135.4 ($C^{4''}$), 135.3 (C^{4}), 131.3 ($C^{5'/2}$), 128.2 ($C^{5''}$), 116.4 (C^{3}), 111.8 ($C^{3'}$),

110.7 ($C^{5'/2}$); MS (ASAP$^+$) *m/z* = 635.1 $[M+H]^+$; HRMS (AP$^+$) *m/z* = 634.0526 $[M+H]^+$; calculated for $[C_{25}H_{18}N_3OPtS_2]^+$ 634.0534.

PtL[23]

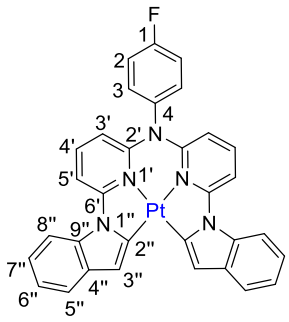

H_2L^{23} (50 mg, 0.101 mmol), K_2PtCl_4 (46 mg, 0.111 mmol) and MeCN/H_2O (6 mL, 2:1). A yellow powder was obtained which was recrystallized in hot DMF to afford the pure product (5 mg, 7 %); ^{1}H NMR (599 MHz, DMSO-d_6) δ 7.99 (d, *J* = 8.1 Hz, 2H, $H^{5''}$), 7.93 (t, *J* = 8.6 Hz, 2H, $H^{4'}$), 7.83 (d, *J* = 7.9 Hz, 2H, $H^{5'}$), 7.74 (dd, *J* = 8.8, 4.9 Hz, 2H, H^2), 7.62 (t, *J* = 8.7 Hz, 2H, H^3), 7.50 (d, *J* = 7.7 Hz, 2H, $H^{8''}$), 7.12 (td, *J* = 7.4, 0.8 Hz, 2H, $H^{7''}$), 7.07 (ddd, *J* = 8.3, 7.1, 1.4 Hz, 2H, $H^{6''}$), 6.76 (d, s, 2H, $H^{3''}$), 6.09 (d, *J* = 8.6 Hz, 2H,$H^{3'}$); ^{19}F NMR (376 MHz, DMSO-d_6) δ -110.81.

7.5.3.2 Pd^{II} Complexes

H_2L^n (0.20 mmol, 1eq), $Pd(OAc)_2$ (0.22 mmol, 1.1 eq), and acetic acid (3 mL) were added to a Schlenk. The reaction mixture was degassed by 3 x FPT cycles and heated at 90 °C for 48 h. The reaction was quenched with water (5 mL) and the precipitate was collected via centrifugation. The precipitate was then washed with H_2O (1 x 5 mL) EtOH (1 x 5 mL) and Et_2O (2 x 5 mL) before being dried *in vacuo*.

PdL[19]

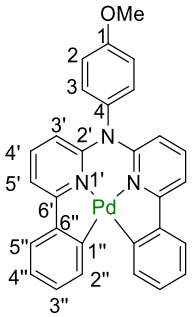

H_2L^{19} (40 mg, 0.093 mmol) and $Pd(OAc)_2$ (23 mg, 0.10 mmol) in acetic acid (3 mL). A yellow solid was obtained (22 mg, 42 %); ^{1}H NMR (400 MHz, DMSO-d_6) δ 8.06 (d, *J* = 7.6 Hz, 2H, $H^{2''}$), 7.96 – 7.83 (m, 6H), 7.54 (d, *J* = 8.3 Hz, 2H, $H^{5''}$), 7.31 (t, *J* = 6.6 Hz, 4H), 7.18 (t, *J* = 7.5

Hz, 2H, H), 6.53 – 6.41 (m, 2H, $H^{3'}$), 3.92 (s, 3H, H^{OMe}); MS (ESI^+) *m/z* = 532.1 $[M+H]^+$; HRMS (ES^+) *m/z* = 532.0803 $[M+H]^+$; calculated for $[C_{29}H_{21}N_3OPd]^+$ 532.0803.

PdL[20]

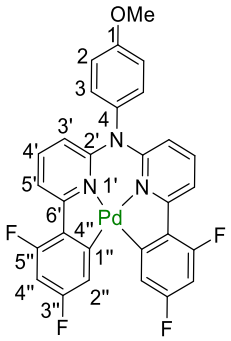

H_2L^{20} (70 mg, 0.14 mmol) and $Pd(OAc)_2$ (35 mg, 0.15 mmol) in acetic acid (4 mL). A green powder was obtained which was then recrystallized to obtain a yellow crystalline solid (67 mg, 79 %); ^{1}H NMR (400 MHz, Chloroform-*d*) δ 7.90 (dt, *J* = 8.1, 1.0 Hz, 2H, $H^{5'}$), 7.64 (t, *J* = 8.3 Hz, 2H, $H^{4'}$), 7.58 (dd, *J* = 8.3, 2.4 Hz, 2H, $H^{2''}$), 7.27 (d, *J* = 8.8 Hz, 2H, H^3), 7.19 (d, *J* = 8.8 Hz, 2H, H^2), 6.66 (ddd, *J* = 12.8, 8.8, 2.3 Hz, 2H, $H^{4''}$), 6.44 (d, *J* = 8.7 Hz, 2H, H^3), 3.97 (s, 3H, H^{OMe}); ^{19}F NMR (376 MHz, Chloroform-*d*) δ -108.44 (dd, *J* = 18.4, 8.9 Hz), -109.10 – -109.42 (m); MS ($ASAP^+$) *m/z* = 603.1 $[M+H]^+$; HRMS ($ASAP^+$) *m/z* = 603.0366 $[M+H]^+$; calculated for $[C_{29}H_{21}N_3OPd]^+$ 603.0348.

PdL[21]

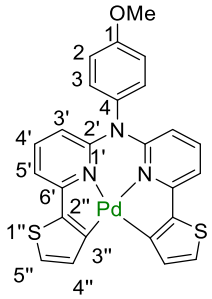

H_2L^{21} (300 mg, 0.68 mmol) and $Pd(OAc)_2$ (168 mg, 0.75 mmol) in acetic acid (6 mL). A green powder was obtained (300 mg, 81 %); ^{1}H NMR (400 MHz, DMSO-d_6) δ 7.83 (dd, *J* = 8.8, 7.6 Hz, 2H), 7.70 (d, *J* = 4.7 Hz, 2H), 7.61 (d, *J* = 4.8 Hz, 2H), 7.57 – 7.49 (m, 2H), 7.40 (dd, *J* = 7.6, 0.8 Hz, 2H), 7.33 – 7.24 (m, 2H), 6.30 (dd, *J* = 8.8, 0.7 Hz, 2H), 3.92 (s, 3H); MS ($ASAP^+$) *m/z* = 546.0 $[M+H]^+$; HRMS ($ASAP^+$) *m/z* = 546.001 $[M+H]^+$; calculated for $[C_{25}H_{18}N_3OPdS_2]^+$ 546.004.

PdL[22]

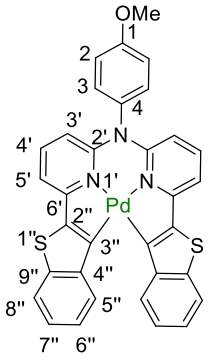

H_2L^{22} (60 mg, 0.1108 mmol), $Pd(OAc)_2$ (27 mg, 0.12 mmol) and acetic acid (3 mL). A green solid was obtained (25 mg, 35 %); ^{1}H NMR (700 MHz, DMSO-d_6) δ 8.00 (d, *J* = 8.0 Hz, 2H, $H^{5''}$), 7.95 (dd, *J* = 8.8, 7.6 Hz, 2H, $H^{4'}$), 7.79 (d, *J* = 8.0 Hz, 2H, $H^{8''}$), 7.59 – 7.50 (m, 4H, H^2 and $H^{5'}$), 7.36 – 7.27 (m, 4H, H^3 and $H^{6'}$), 7.08 (ddd, *J* = 8.2, 7.1, 1.1 Hz, 2H, $H^{7''}$), 6.42 (dd, *J* = 8.8, 0.8 Hz, 2H, $H^{3'}$), 3.92 (s, 3H, H^{OMe}); MS (ASAP$^+$) *m/z* = 646.0 $[M+H]^+$; HRMS (ASAP$^+$) *m/z* = 644.0214 $[M+H]^+$; calculated for $[C_{33}H_{22}N_3OS_2{}^{104}Pd]^+$ 644.0245.

7.5.3.3 Pt^{IV} Complexes

$PtL^{21}Cl_2$

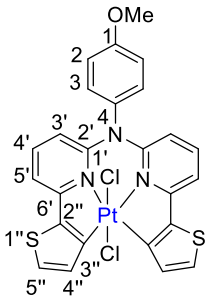

PtL^{21} (46 mg, 0.07 mmol) was added to a solution of $PhICl_2$ (20 mg, 0.07 mmol) in DCM (4 mL) and left to stir at room temperature for 24 h with the exclusion of light. The reaction solution was isolated from a precipitated orange solid by centrifuge. This solid was then washed with DCM (2 x 5 mL). The DCM washings were combined with the reaction solution and then evaporated to dryness to leave behind an orange solid. This was recrystallized with DCM and washed with hexane to obtain an orange solid powder (10 mg, 16 %); ^{1}H NMR (700 MHz, DMSO-d_6) δ 7.95 – 7.91 (m, 4H, $H^{4'}$ and $H^{4''}$), 7.70 (d, *J* = 5.0 Hz, 2H, $H^{5'}$), 7.67 (d, *J* = 7.5 Hz, 2H, $H^{5''}$), 7.48 (d, *J* = 8.8 Hz, 2H, H^2), 7.30 (d, *J* = 8.8 Hz, 2H, H^3), 6.56 (d, *J* = 8.7 Hz, 2H, $H^{3'}$), 3.89 (s, 3H, H^{OMe}); ^{13}C NMR (176 MHz, DMSO-d_6) δ 160.4 (C^1), 155.9 ($C^{2''}$), 149.5 ($C^{2'}$), 141.9 ($C^{4'}$), 137.9 ($C^{3''}$), 134.9 (C^4), 133.3 ($C^{6'}$), 131.7 (C^2), 131.2 ($C^{5'}$), 130.5 ($C^{4''}$),

117.4 (C^{3}), 113.7 ($C^{5''}$), 113.4 ($C^{3'}$), 56.1 (C^{OMe}); MS (ES^{+}) *m/z* = 670.0 $[M\text{-}Cl]^{+}$; HRMS (ES^{+}) *m/z* = 669.0256 $[M\text{-}Cl]^{-}$; calculated for $[C_{25}H_{17}N_3O^{194}PtS_2Cl]^{+}$ 669.0128.

PtL^{19}I$_2$

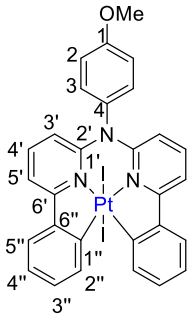

PtL^{19} (10 mg, 0.016 mmol) was added to 1.5 mL of H_2O. To this yellow suspension was added a solution of I_2 (4 mg, 0.016 mmol) in acetone (1.5 mL) dropwise. On addition, the yellow suspension turned orange, over further addition, a brown suspension resulted. This was stirred for 3 hours at RT. The orange solid was isolated by centrifugation and then dried *in vacuo* (10 mg; 71%); ^{1}H NMR (700 MHz, DMSO-d_6) δ 8.14 – 8.07 (m, 6H, $H^{5'}$, $H^{3''}$ and $H^{2''}$), 7.94 (dd, *J* = 8.6, 7.7 Hz, 2H, $H^{4'}$), 7.58 (d, *J* = 8.9 Hz, 2H, H^{2}), 7.47 (td, *J* = 7.6, 7.1, 1.5 Hz, 2H, $H^{4''}$), 7.29 (d, *J* = 8.9 Hz, 2H, H^{3}), 7.13 (d, *J* = 7.4 Hz, 2H, $H^{5''}$), 6.78 (d, *J* = 8.9 Hz, 2H, $H^{3'}$), 3.87 (s, 3H, H^{OMe}); ^{13}C NMR (176 MHz; DMSO) 161.9 ($C^{6'}$), 160.2 (C^{4}), 150.8 ($C^{2'}$), 144.7 ($C^{1''}$), 141.1 ($C^{4'}$), 136.2 (C^{1}), 134.7 ($C^{3''}$), 132.1 (C^{2}), 130.9 ($C^{4''}$), 125.9 ($C^{6''}$), 125.5 ($C^{5''}$), 125.4 ($C^{2''}$), 117.3 (C^{3}), 115.3 ($C^{3'}$ and $C^{5'}$), 56.1 (C^{OMe}); (ESI^{+}) *m/z* = 749.3 $[M\text{-}I]^{+}$; HRMS (ES^{+}) *m/z* = 748.0372 $[M\text{-}I]^{+}$; calculated for $[C_{29}H_{21}N_3O^{194}Pt^{127}I]^{+}$ 748.0356.

7.6 Chapter 5 Synthesis

7.6.1 Class 1 compounds

7.6.1.1. General

Miyaura borylation[190]

The aryl halide (1 eq), B_2pin_2 (2 eq), KOAc (6 eq) and $Pd(dppf)Cl_2$ (0.1 eq) were added to a Schlenk which was evacuated and heated, before adding dry dioxane under argon. This mixture was set to reflux for 18 h before cooling to RT. The solvent was then removed *in vacuo* the product was extracted into DCM, dried over $MgSO_4$ and the solvent removed *in vacuo*. The resulting residue was purified by column chromatography on silica.

7.6.1.2 Compound synthesis

dypbBr

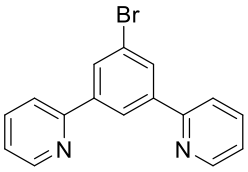

Tribromobenzene (1.86 g, 9.10 mmol), 2-tri-n-butylstannyl pyridine (7.12 µL, 20.06 mmol), $Pd(PPh_3)_2Cl_2$ (382 mg, 0.54 mmol) and LiCl (3.12 g, 73.4 mmol) reacted in refluxing dry toluene (30 mL) according to the outlined Stille procedure for 48 h. A yellow oil was obtained (220 mg, 58 %). The experimental data obtained were in good agreement with the literature.[203]

dpybB(OH)$_2$

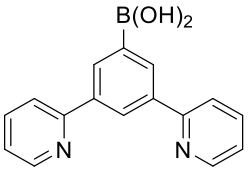

dypbBr (400 mg, 1.29 mmol) was added to a Schlenk, heated and evacuated before being filled with argon. Dry THF (10 mL) was added to the Schlenk and the mixture was cooled to -78 °C, nBuLi (2.5M in hexanes, 0.8 mL, 1.55 mmol) was added and the mixture was stirred at -78 °C under argon for 30 mins. In a separately prepared Schlenk, $B(OMe)_3$ (173 µL, 1.55 mmol) was added to 5 mL of dry THF and this was added to the other Schlenk. This was mixture was allowed to warm to RT and stirred for a further 18h at RT. H_2O (10 mL) was then added and the organic layer was extracted with ethyl acetate and dried over $MgSO_4$.

The crude product (350 mg) was used for the next step. The experimental data obtained were in good agreement with the literature.[186]

Compound H_2L^{24}

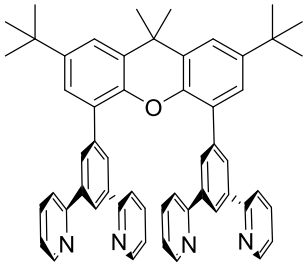

dpybH-B(OH)$_2$ (300mg, 1.08 mmol), 4,5-dibromo-2,7-di-*tert*-butyl-9,9-dimethylxanthene (261 mg, 0.543 mmol), Na_2CO_3 (576 mg, 5.43 mmol) and $Pd(PPh_3)_4$ (62 mg, 0.054 mmol) were reacted in refluxing DME/H_2O (10 mL) according to the previously outlined Suzuki procedure. A white solid was obtained after column on silica (100 % ethyl acetate) which was still a crude product (54 mg) and which was used without further purification for the next step. The experimental data obtained were in good agreement with the literature.[186]

$L^{24}(PtCl)_2$

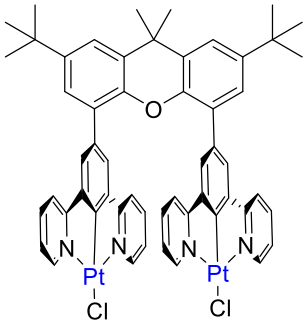

H_2L^{24} (54 mg, crude) and K_2PtCl_4 (143 mg, 0.0345 mmol) were added to a Schlenk with acetic acid/H_2O (4 mL, 3:1) and degassed via 3 x FPT cycles. This mixture was set to reflux under argon for 48 h. On cooling to RT, water (5 mL) was added and the resulting suspension was filtered and washed with H_2O, MeOH and Et_2O. The resulting yellow/brown solid was recrystallized in DCM/Hexane and a yellow solid resulted (5 mg). The experimental data obtained were in good agreement with the literature.[186]

B_2pin_2-bromobenzene

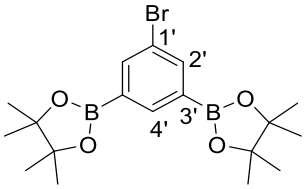

Tribromobenzene (2 g, 6.35 mmol), B_2pin_2 (3.55 g, 13.98 mmol), KOAc (3.74 g, 38.1 mmol) and Pd(dppf)Cl_2 (464 mg, 0.635 mmol) were reacted in refluxing dry dioxane (40 mL) according to the previously outlined Miyaura borylation procedure. A yellow oil was obtained (1.49g, 57 %). ^{1}H NMR (400 MHz, Chloroform-*d*) δ 8.38 (s, 1H, $H^{4'}$), 8.02 (d, *J* = 1.1 Hz, 2H, $H^{2'}$), 1.35 (s, 24H, H^{Me}).

$(CF_3)_2$dypbBr

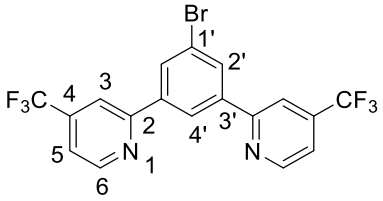

$Bpin_2$-bromobenzene (1 g, 2.45 mmol), 4-trifluoromethyl-2-bromo pyridine (0.67 mL, 5.39 mmol), Na_2CO_3 (1.3 g, 12.25 mmol) and Pd(PPh_3)$_4$ (141 mg, 0.1225 mmol) were added to a Schlenk containing DME/H_2O (30 mL) and reacted according to the previously outlined Suzuki procedure. A white solid was obtained after column on silica (100:0 to 90:10 hexane/ethyl acetate) (310 mg, 28 %); R_f = 0.5 (90:10 hexane/ethyl acetate, silica); ^{1}H NMR (599 MHz, Chloroform-*d*) δ 8.90 (d, *J* = 5.0 Hz, 2H, H^6), 8.62 (s, 1H, $H^{4'}$), 8.27 (d, *J* = 1.6 Hz, 2H, $H^{2'}$), 8.00 (s, 2H, H^3), 7.52 (d, *J* = 5.0, 2H, H^5); ^{13}C NMR (151 MHz, Chloroform-*d*) δ 156.6 ($C^{3'}$), 150.8 (C^6), 140.4 (C^2), 139.4 (d, *J* = 34.1 Hz) (C^{CF3}), 131.2 ($C^{2'}$), 124.2 ($C^{4'}$), 123.9 ($C^{1'}$), 123.7 (C^4) 118.4 (t, *J* = 3.5 Hz) (C^5), 116.2 (d, *J* = 3.6 Hz) (C^3); ^{19}F NMR (376 MHz, Chloroform-*d*) δ -64.74; MS (ASAP$^+$) *m/z* = 446.8 $[M+H]^+$; HRMS (ES+) *m/z* = 446.9937 $[M+H]^+$; calculated for $[C_{18}H_{10}N_2BrF_6N_2]^+$ 446.9932.

(CF$_3$)$_2$dypbBpin

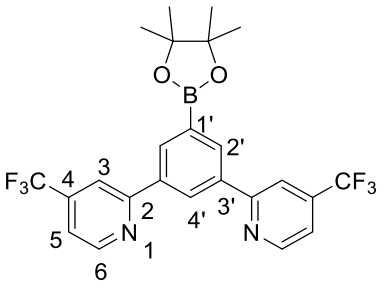

(CF$_3$)$_2$dypbBr (300 mg, 0.67 mmol), B_2pin_2 (376 mg, 1.48 mmol), KOAc (395 mg, 4.02 mmol) and Pd(dppf)Cl_2 (49 mg, 0.067 mmol) were reacted in refluxing dry dioxane (15 mL) according to the previously outlined Miyaura borylation procedure. A white crystalline solid was obtained after column on silica (100:0 to 70:30 hexane/ethyl acetate) (381 mg, 91 %); R_f = 0.78 (70:30 hexane/ethyl acetate, silica); ^{1}H NMR (400 MHz, Chloroform-*d*) δ 8.92 – 8.86 (m, 3H, H^6 and $H^{4'}$), 8.51 (d, *J* = 1.9 Hz, 2H, $H^{2'}$), 8.08 (dt, *J* = 1.7, 0.9 Hz, 2H, H^3), 7.47 (ddd, *J* = 5.0, 1.6, 0.8 Hz, 2H, H^5), 1.40 (s, 12H, H^{Me}); MS (ASAP$^+$) *m/z* = 495.2 $[M+H]^+$; HRMS (ES+) *m/z* = 494.1737 $[M+H]^+$; calculated for $[C_{24}H_{22}N_2O_2F_6{}^{10}B]^+$ 494.1715.

Compound H$_2$L^{25}

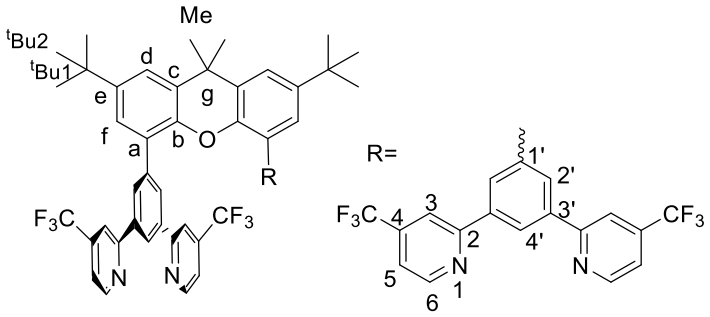

(CF$_3$)$_2$dypbBpin (300 mg, 0.61 mmol), 4,5-dibromo-2,7-di-tert-butyl-9,9-dimethylxanthene (133 mg, 0.28 mmol), Na_2CO_3 (170 mg, 1.60 mmol) and Pd(PPh_3)$_4$ (20 mg, 0.017 mmol) were reacted in refluxing DME/H_2O according to the previously outlined Suzuki procedure. A white solid was obtained after column on silica (100:0 to 70:30 hexane/ethyl acetate) (153 mg, 52 %); R_f= 0.83 (70:30 hexane/ethyl acetate, silica); ^{1}H NMR (599 MHz, Chloroform-*d*) δ 8.68 (dd, *J* = 5.0, 0.8 Hz, 4H, H^6), 8.22 (t, *J* = 1.7 Hz, 2H, $H^{4'}$), 7.97 (d, *J* = 1.7 Hz, 4H, $H^{2'}$), 7.66 (s, 4H, H^3), 7.53 (d, *J* = 2.4 Hz, 2H, H^f), 7.22 (d, *J* = 2.3 Hz, 2H, H^d), 7.11 (dd, *J* = 5.0, 1.5 Hz, 4H, H^5), 1.85 (s, 6H, H^{Me}), 1.38 (s, 18H, H^{tBu2}); ^{13}C NMR (151 MHz, Chloroform-*d*) δ 157.3 (C^2), 150.2 (C^6), 145.6 (C^a), 144.7 (C^e), 139.6 (C^c), 138.6 (C^{CF3}), 137.1 ($C^{3'}$), 129.3 ($C^{2'}$), 128.2 ($C^{1'}$), 125.9 (C^d), 123.6 ($C^{4'}$), 123.0 (C^f), 121.9 (C^4), 117.1 (C^5), 115.4 (C^3), 34.8 (C^g),

34.6 (C^{tBu1}), 33.4 (C^{Me}), 31.6 (C^{tBu2}); ^{19}F NMR (376 MHz, Chloroform-*d*) δ -64.83; MS (ASAP$^+$) *m/z* = 1055.4 [M+H]$^+$; HRMS (ES+) *m/z* = 1055.3558 [M+H]$^+$; calculated for $[C_{59}H_{47}N_4OF_{12}]^+$ 1055.3575.

L^{25}(PtCl)$_2$

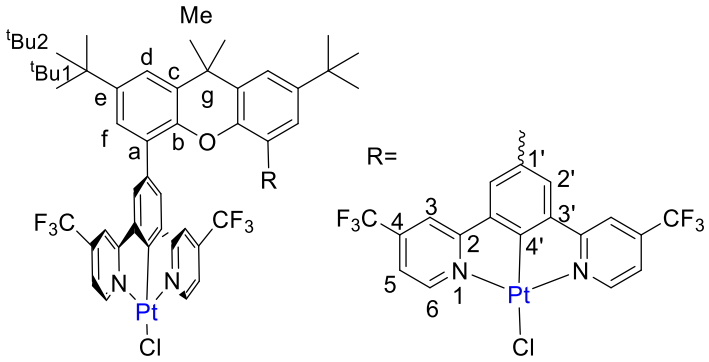

H$_2$L^{25} (22 mg, 0.021 mmol) and K_2PtCl_4 (44 mg, 0.104 mmol) were added to a Schlenk with acetic acid (4 mL) and degassed via 3 x FPT cycles. This mixture was then set to reflux under argon for 48 h. Water (5 mL) was added and the resulting suspension was filtered and the solid washed with H_2O, MeOH and Et_2O. A grey-green solid resulted and the product was extracted into DCM from washings of this solid. An orange solid was obtained after removal of the solvent *in vacuo* (18 mg, 67 %); ^{1}H NMR (700 MHz, Chloroform-*d*) δ 9.53 (d, *J* = (^{195}Pt 31.8), 5.8 Hz, 4H, H^6), 7.54 (d, *J* = 2.4 Hz, 2H, $H^{d/f}$), 7.48 (s, 4H, $H^{2'}$), 7.41 (s, 4H, H^3), 7.38 (dd, *J* = 5.8, 1.9 Hz, 4H, H^5), 7.23 (d, *J* = 2.3 Hz, 2H, $H^{d/f}$), 1.83 (s, 6H, H^{Me}), 1.41 (s, 18H, H^{tBu2}); ^{13}C NMR (176 MHz, Chloroform-*d*) δ 167.8 (C^2), 161.8 ($C^{4'}$), 153.9 (C^6), 146.1 (C^e), 144.1 (C^b), 139.3 ($C^{1'}$), 129.4 (C^c), 128.1 (C^a), 126.8 ($C^{2'}$), 125.8 ($C^{d/f}$), 123.3 ($C^{d/f}$), 119.6 (C^5), 115.0 (C^3), 34.7 (C^g), 34.6 (C^{tBu1}), 33.7 (C^{Me}), 31.6 (C^{tBu2}); ^{19}F NMR (376 MHz, Chloroform-*d*) δ -65.54; MS (ASAP$^+$) *m/z* = 1478.2 [M-Cl]$^+$; HRMS (ASAP+) *m/z* = 1478.2312 [M-Cl]$^+$; calculated for $[C_{59}H_{44}ClN_4O_1F_{12}{}^{194}Pt_2]^+$ 1478.2314.

7.6.2 Class 2 compounds

7.6.2.1 Precursors

2,7-di-tert-butyl-4,5-diiodo-9,9-dimethylxanthene

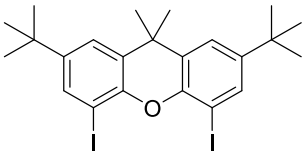

At -20 °C *n*-BuLi (2.5 M in hexanes, 1.66 mL, 4.14 mmol) was added dropwise to a stirred solution of 4,5-dibromo-2,7-di-*t*-butyl-9,9-dimethylxanthene (0.9 g, 1.87 mmol) in 20 ml of dry THF. The resulting beige suspension was stirred for 2 h. Next a solution of I_2 (0.6 g, 4.7 mmol) in 10 mL of dry THF was added and the reaction mixture was slowly warmed to RT overnight. The reaction mixture was poured out in a saturated sodium thiosulfate solution and extracted with DCM. The organic layer was washed with brine and dried over $MgSO_4$. The solvents were removed *in vacuo* and the residue was recrystallised from DCM. A white powder was obtained (350 mg, 33 %). The experimental data obtained were in good agreement with the literature.[204]

2,7-di-tert-butyl-4,5-bis((trimethylsilyl)ethynyl)-9,9-dimethylxanthene

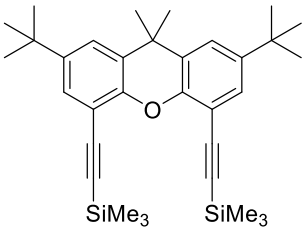

$Pd(dppf)_2Cl_2$ (74 mg, 0.10 mmol) and copper(I) iodide (32 mg, 0.17 mmol) were added successively to a solution of **2,7-di-tert-butyl-4,5-diiodo-9,9-dimethylxanthene** (300 mg, 0.52 mmol) and trimethysilylacetylene (0.24 mL, 1.58 mmol) in dry NEt_3 (3 mL) under argon at RT. The reaction mixture was stirred at 60 °C for 24 h and the NEt_3 was then removed *in vacuo*. The residue was diluted with H_2O (5 mL) and DCM (5 mL). The product was extracted into DCM (3 x 10 mL), and the combined organic phases were dried over $MgSO_4$ and evaporated. The crude produced was purified by flash column chromatography on silica gel (30:1, hexane/ethyl acetate) and a white solid was obtained (300 mg, 93 %). The experimental data obtained were in good agreement with the literature.[189]

2,7-di-tert-butyl-4,5-diethynyl-9,9-dimethylxanthene = H_2L^{26}

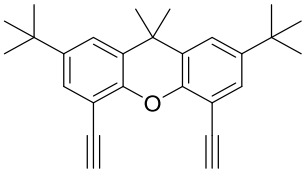

A solution of K_2CO_3 (150 mg, 1.09 mmol) in MeOH (3 mL) was added to a solution of **2,7-di-tert-butyl-4,5-bis((trimethylsilyl)ethynyl)-9,9-dimethylxanthene** (100 mg, 0.174 mmol) in DCM (3 mL). After stirring at RT for 12 h, the solvent was removed *in vacuo*. The residue was diluted with H_2O (20 mL) and DCM (20 mL). The product was extracted into DCM (3 x 10 mL), and the combined organic phases were dried over $MgSO_4$ and evaporated. The crude produced was purified by flash column chromatography on silica gel (30:1, hexane/ethyl acetate) and a white solid was obtained (69 mg, 93 %). The experimental data obtained were in good agreement with the literature.[189]

7.6.2.2 Complexes

General procedure for complexation of H_2L^{26} with Pt(dpybX)Cl

Starting complexes Pt(dpybX)Cl, where X= A, B, C, D and E as represented in each case, were synthesised by either Rebecca Salthouse or Chris Harris (MChem students in our group). **H_2L^{26}** (1 eq) was suspended in MeOH and added to this was a solution of 0.5 M NaOMe in MeOH (2.1 eq). This mixture was stirred for 30 mins at RT. Following this, Pt(dpybX)Cl (2 eq) dissolved in DCM was added to the mixture and this was set to stir at 60 °C for 48 h. On cooling to RT, the solvent was removed in *vacuo* and the resulting solid was then washed with H_2O, MeOH and Et_2O. Recrystallization in DCM/Hexane gave the pure product.

L^{26}(Pt(dpybA))$_2$

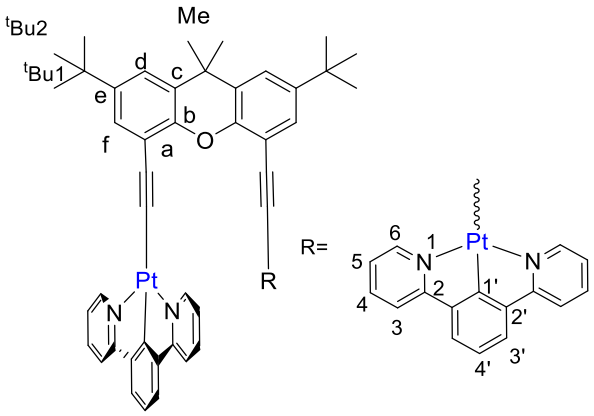

H_2L^{26} (7.5 mg, 0.02 mmol) and 0.5 M NaOMe solution (1 mL, 0.05 mmol) were stirred in MeOH (15 mL) at RT and **Pt(dpyb*A*)Cl** (18 mg, 0.04 mmol) in DCM (15 mL) was then added. The mixture was reacted according to the general procedure given above. An orange solid was obtained (10 mg, 41 %); ^{1}H NMR (700 MHz, Chloroform-*d*) δ 9.51 (d, *J* = (^{195}Pt 38.8), 5.5 Hz, 4H, H^6), 7.47 – 7.44 (m, 6H, $H^{d/f}$ and H^4), 7.24 (d, *J* = 2.4 Hz, 2H, $H^{d/f}$), 7.08 (dd, *J* = 7.8, 1.3 Hz, 4H, H^3), 6.97 – 6.93 (m, 8H, $H^{3'}$ and H^5), 6.85 (t, *J* = 7.5 Hz, 2H, $H^{4'}$), 1.70 (s, 6H, H^{Me}), 1.33 (s, 18H, H^{tBu2}); ^{13}C NMR (176 MHz, Chloroform-*d*) δ 168.8 (C^2), 156.8 (C^6), 143.9 (C^e), 142.3 ($C^{2'}$), 136.7 ($C^{d/f}$), 128.9 (C^c), 128.1 (C^4), 122.8 ($C^{3'}$), 122.7 (C^5), 121.5 ($C^{4'}$), 119.4 ($C^{d/f}$), 118.1 (C^3), 34.7 (C^g), 34.4 (C^{tBu1}), 32.6 (C^{Me}), 31.6 (C^{tBu2}); MS (ASAP$^+$) *m/z* = 1221.3 [M+H]$^+$; HRMS (ASAP+) *m/z* = 1221.3357 [M+H]$^+$; calculated for $[C_{59}H_{51}N_4O_1{}^{194}Pt_2]^+$ 1221.3331.

L^{26}(Pt(dpybB))$_2$

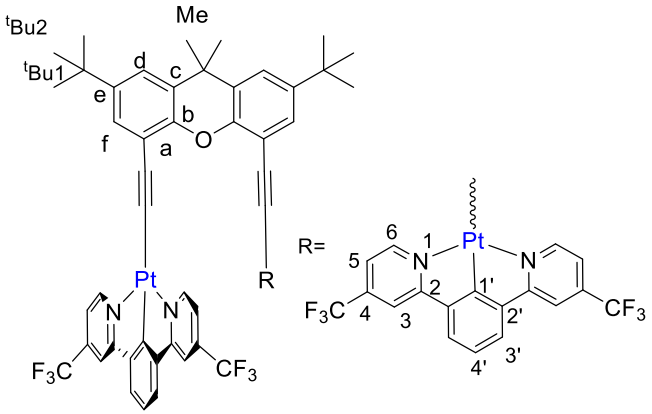

H_2L^{26} (7.5 mg, 0.02 mmol) and 0.5 M NaOMe solution (1 mL, 0.05 mmol) were stirred in MeOH (15 mL) at RT and **Pt(dpyb*B*)Cl** (24 mg, 0.04 mmol) in DCM (15 mL) was then added. The mixture was reacted according to the general procedure given previously. A dark red solid was obtained (5 mg, 17 %); ^{1}H NMR (400 MHz, Chloroform-*d*) δ 9.69 (d, *J* = (^{195}Pt 38.6), 5.8 Hz, 4H, H^6), 7.45 (d, *J* = 2.3 Hz, 2H, $H^{f/d}$), 7.34 (d, *J* = 2.4 Hz, 2H, $H^{f/d}$), 7.31 (d, *J* = 2.0 Hz, 4H, H^3), 7.25 (dd, *J* = 5.9, 2.0 Hz, 4H, H^5), 7.14 – 7.10 (m, 4H, $H^{3'}$), 7.03 (dd, *J* = 8.3, 6.8 Hz, 2H, $H^{4'}$), 1.77 (s, 6H, H^{Me}), 1.39 (s, 17H, H^{tBu2}); ^{19}F NMR (376 MHz, Chloroform-*d*) δ -65.13; MS (ASAP$^+$) *m/z* = 1493.3 [M+H]$^+$; HRMS (ASAP+) *m/z* = 1493.2853 [M+H]$^+$; calculated for $[C_{63}H_{47}N_4O_1F_{12}{}^{194}Pt_2]^+$ 1493.2933.

L[26](Pt(dpybC))₂

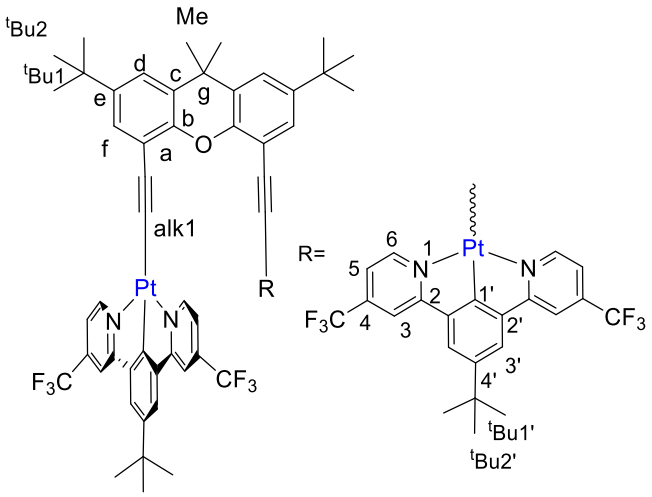

H_2L^{26} (7.5 mg, 0.02 mmol) and 0.5 M NaOMe solution (1 mL, 0.05 mmol) were stirred in MeOH (15 mL) at RT and **Pt(dpyb*C*)Cl** (28 mg, 0.04 mmol) in DCM (15 mL) was then added. The mixture was reacted according to the procedure given above. A dark red solid was obtained (24 mg, 73 %); ^{1}H NMR (700 MHz, Chloroform-*d*) δ 9.60 (d, *J* = (^{195}Pt 41.0), 5.8 Hz, 4H, H^{6}), 7.39 (d, *J* = 2.3 Hz, 2H, $H^{d/f}$), 7.30 (d, *J* = 2.3 Hz, 2H, $H^{d/f}$), 7.25 (s, 4H, H^{3}), 7.18 (d, *J* = 5.2 Hz, 4H, H^{5}), 7.11 (s, 4H, $H^{3'}$), 1.74 (s, 6H, H^{Me}), 1.40 (s, 18H, $H^{tBu2'}$), 1.35 (s, 18H, H^{tBu2}); ^{13}C NMR (176 MHz, Chloroform-*d*) δ 178.62 ($C^{1'}$), 169.90 ($C^{2'}$), 157.86 (C^{6}), 150.25 (C^{b}), 145.50($C^{4'}$), 144.47 (C^{e}), 140.70 (C^{2}), 129.35 (C^{g}), 127.13 ($C^{d/f}$), 121.88 (C^{4}), 121.43 ($C^{3'}$), 119.74 ($C^{d/f}$), 119.01 (C^{5}), 115.98 (C^{alk1}), 114.27 (C^{3}), 35.17 ($C^{tBu1'}$), 34.47 (C^{tBu1}), 31.93 (C^{Me}), 31.65 ($C^{tBu2'}$), 31.58 (C^{tBu2}); ^{19}F NMR (376 MHz, Chloroform-*d*) δ -65.01; MS (ASAP^{+}) *m/z* = 1605.4 $[M+H]^{+}$; HRMS (ASAP+) *m/z* =1605.4097 $[M+H]^{+}$; calculated for $[C_{71}H_{63}N_4O_1F_{12}{}^{194}Pt_2]^{+}$ 1605.4105.

L[26](Pt(dpybD))₂

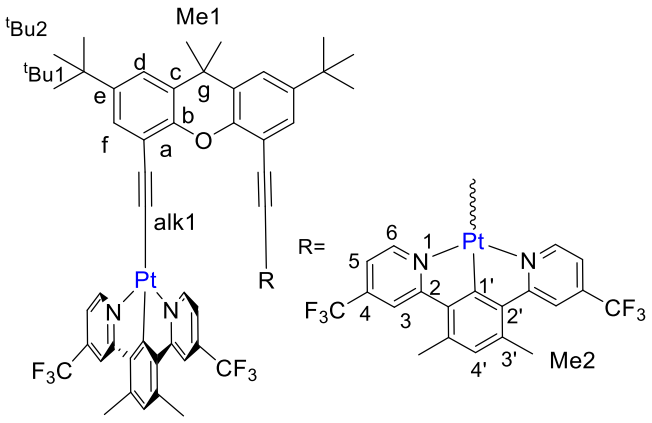

H_2L^{26} (7.5 mg, 0.02 mmol) and 0.5 M NaOMe solution (1 mL, 0.05 mmol) were stirred in MeOH (15 mL) at RT and **Pt(dpyb*D*)Cl** (27 mg, 0.04 mmol) in DCM (15 mL) was then added. The mixture was reacted according to the procedure given above. A dark red solid was obtained (5 mg, 16 %); ^{1}H NMR (400 MHz, Chloroform-*d*) δ 9.87 (d, *J* = (^{195}Pt 45.9), 5.8 Hz, 4H, H^6), 7.47 (s, 4H, H^3), 7.45 (d, *J* = 2.3 Hz, 2H, $H^{d/f}$), 7.34 (d, *J* = 2.4 Hz, 2H, $H^{d/f}$), 7.22 (d, *J* = 6.0 Hz, 4H, H^5), 6.60 (s, 2H, $H^{4'}$), 2.39 (s, 12H, H^{Me2}), 1.76 (s, 6H, H^{Me1}), 1.38 (s, 18H, H^{tBu2}); ^{19}F NMR (376 MHz, Chloroform-*d*) δ -65.15; MS (ASAP$^+$) *m/z* = 1549.4 $[M+H]^+$; HRMS (ASAP+) *m/z* = 1549.3479 $[M+H]^+$; calculated for $[C_{67}H_{55}N_4O_1F_{12}{}^{194}Pt_2]^+$ 1549.3547.

L^{26}(Pt(dpybE))$_2$

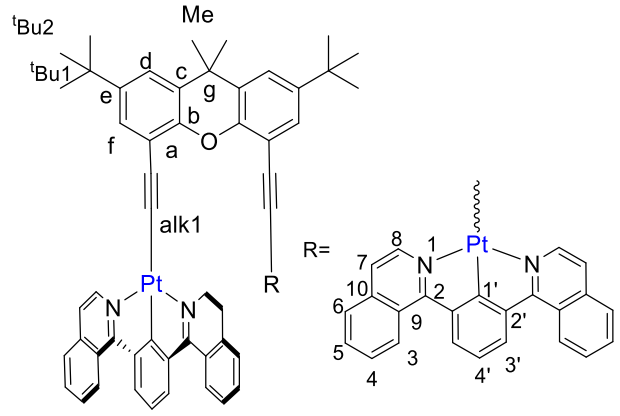

H_2L^{26} (7.5 mg, 0.02 mmol) and 0.5 M NaOMe solution (1 mL, 0.05 mmol) were stirred in MeOH (15 mL) at RT and **Pt(dpyb*E*)Cl** (22 mg, 0.04 mmol) in DCM (15 mL) was then added. The mixture was reacted according to the procedure given above. A dark red solid was obtained (10 mg, 35 %); ^{1}H NMR (700 MHz, Chloroform-*d*) δ 9.67 (d, *J* = (^{195}Pt 36.0), 6.2 Hz, 4H, H^8), 8.34 (d, *J* = 8.5 Hz, 4H, H^6), 7.68 (d, *J* = 7.8 Hz, 4H, $H^{3'}$), 7.54 (d, *J* = 2.3 Hz, 2H, $H^{d/f}$), 7.40 (d, *J* = 7.9 Hz, 4H, H^3), 7.35 (ddd, *J* = 7.9, 6.6, 1.0 Hz, 4H, H^4), 7.30 (d, *J* = 2.4 Hz, 2H, $H^{d/f}$), 7.28 (ddd, *J* = 8.1, 6.6, 1.4 Hz, 4H, H^5), 7.14 (d, *J* = 6.2 Hz, 4H, H^7), 7.00 (t, *J* = 7.7 Hz, 2H, $H^{4'}$), 1.77 (s, 6H, H^{Me}), 1.37 (s, 18H H^{tBu2}); ^{13}C NMR (176 MHz, Chloroform-*d*) δ 186.7 ($C^{1'}$), 167.6 (C^2), 148.8 (C^8), 144.0 ($C^{2'}$), 143.9 (C^e), 136.4 (C^9), 129.9 (C^4), 129.0 (C^g), 128.2 ($C^{f/d}$), 127.8 ($C^{3'}$), 127.2 (C^3), 127.0 (C^5), 126.1 (C^{10}), 125.1 (C^6), 121.2 ($C^{4'}$), 121.1 (C^7), 119.6 ($C^{d/f}$), 34.4 (C^{tBu1}), 32.7 (C^{Me}), 31.6 (C^{tBu2}).

8. References

1 J. Kalinowski, V. Fattori, M. Cocchi and J. A. G. Williams, *Coord. Chem. Rev.*, 2011, **255**, 2401–2425.

2 J.-H. Jang, J. Y. Park, H. Un Kim, H. J. Park, I.-N. Kang, J. Y. Lee and D.-H. Hwang, *J. Nanosci. Nanotechnol.*, 2018, **18**, 7047–7052.

3 S. Zhou, Q. Wang, M. Li, Z. Lu and J. Yu, *J. Lumin.*, 2014, **154**, 487–490.

4 J. Zhao, Z. Feng, D. Zhong, X. Yang, Y. Wu, G. Zhou and Z. Wu, *Chem. Mater.*, 2018, **30**, 929–946.

5 Y. L. Chang, S. Gong, X. Wang, R. White, C. Yang, S. Wang and Z. H. Lu, *Appl. Phys. Lett.*, 2014, **104**, 173303.

6 A. Zamora, G. Vigueras, V. Rodríguez, M. D. Santana and J. Ruiz, *Coord. Chem. Rev.*, 2018, **360**, 34–76.

7 N. A. M. Pereira, M. Laranjo, J. Casalta-Lopes, A. C. Serra, M. Piñeiro, J. Pina, J. S. Seixas de Melo, M. O. Senge, M. F. Botelho, L. Martelo, H. D. Burrows and T. M. V. D. Pinho e Melo, *ACS Med. Chem. Lett.*, 2017, **8**, 310–315.

8 K. V. Sudheesh, P. S. Jayaram, A. Samanta, K. S. Bejoymohandas, R. S. Jayasree and A. Ajayaghosh, *Chem. Eur. J*, 2018, **24**, 10999–11007.

9 Z. Lv, L. Zou, H. Wei, S. Liu, W. Huang and Q. Zhao, *ACS Appl. Mater. Interfaces*, 2018, **10**, 19523–19533.

10 R. E. Doherty, I. V. Sazanovich, L. K. McKenzie, A. S. Stasheuski, R. Coyle, E. Baggaley, S. Bottomley, J. A. Weinstein and H. E. Bryant, *Sci. Rep.*, 2016, **6**, 1–9.

11 E. Baggaley, J. A. Weinstein and J. A. G. Williams, *Coord. Chem. Rev.*, 2012, **256**, 1762–1785.

12 X. Jiang, J. Peng, J. Wang, X. Guo, D. Zhao and Y. Ma, *ACS Appl. Mater. Interfaces*, 2016, **8**, 3591–3600.

13 W. Wu, C. Cheng, W. Wu, H. Guo, S. Ji, P. Song, K. Han, J. Zhao, X. Zhang, Y. Wu and G. Du, *Eur. J. Inorg. Chem.*, 2010, 4683–4696.

14 Y. G. Ma, T. C. Cheung, C. M. Che and J. C. Shen, *Thin Solid Films*, 1998, **333**, 224–227.

15 T. Sajoto, P. I. Djurovich, A. B. Tamayo, J. Oxgaard, W. A. Goddard and M. E. Thompson, *J. Am. Chem. Soc.*, 2009, **131**, 9813–9822.

16 A. Jablonski, *Nature*, 1933, **131**, 839–840.

17 K. Huang and A. Rhys, *Proc. R. Soc. A*, 1950, **204**, 406.

18 K. Li, G. S. Ming Tong, Q. Wan, G. Cheng, W. Y. Tong, W. H. Ang, W. L. Kwong and C. M. Che, *Chem. Sci.*, 2016, **7**, 1653–1673.

19 A. Hofmann, L. Dahlenburg and R. van Eldik, *Inorg. Chem.*, 2003, **42**, 6528–6538.

20 J. A. G. Williams, A. Beeby, E. S. Davies, J. A. Weinstein and C. Wilson, *Inorg. Chem. Commun.*, 2003, **42**, 8609–8611.

21 M. Maestri, D. Sandrini, V. Balzani, L. Chassot, P. Jolliet and A. von Zelewsky, *Chem. Phys. Lett.*, 1985, **122**, 375–379.

22 D. A. K. Vezzu, J. C. Deaton, J. S. Jones, L. Bartolotti, C. F. Harris, A. P. Marchetti, M. Kondakova, R. D. Pike and S. Huo, *Inorg. Chem.*, 2010, **49**, 5107–5119.

23 G. Li, K. Klimes, T. Fleetham, Z. Q. Zhu and J. Li, *Appl. Phys. Lett.*, 2017, **110**, 113301.

24 T. Fleetham, G. Li, L. Wen and J. Li, *Adv. Mater.*, 2014, **26**, 7116–7121.

25 X. Q. Zhang, Y. M. Xie, Y. Zheng, F. Liang, B. Wang, J. Fan and L. S. Liao, *Org. Electron.*, 2016, **32**, 120–125.

26 G. Li, J. Ecton, B. Obrien and J. Li, *Org. Electron.*, 2014, **15**, 1862–1867.

27 P. Jolliet, M. Gianini, A. von Zelewsky, G. Bernardinelli and H. Stoeckli-Evans, *Inorg. Chem.*, 1996, **35**, 4883–4888.

28 S.-W. Lai, M. C.-W. Chan, T.-C. Cheung, S.-M. Peng and C.-M. Che, *Inorg. Chem.*, 1999, **38**, 4046–4055.

29 B. Yang, S. Huang and J. Wang, *Phys. Chem. Chem. Phys.*, 2017, **19**, 23454–23460.

30 C. Gourlaouen and C. Daniel, *Dalton Trans.*, 2014, **43**, 17806–17819.

31 P. Pinter, H. Mangold, I. Stengel, I. Münster and T. Strassner, *Organometallics*, 2016, **35**, 673–680.

32 E. V. Puttock, M. T. Walden and J. A. G. Williams, *Coord. Chem. Rev.*, 2018, **367**, 127–162.

33 C. W. Tang and S. A. Van Slyke, *Appl. Phys. Lett.*, 1987, **51**, 913.

34 N. Thejokalyani and S. J. Dhoble, *Renew. Sustain. Energy Rev.*, 2015, 44, 319–347.

35 M. Stolka, in *Organic Light Emitting Diodes (OLEDs) for General Illumination, Optoelectronics industry development association*, 2002.

36 N. Thejokalyani and S. J. Dhoble, *Defect Diffus. Forum*, 2014, **357**, 1–27.

37 B. Geffroy, P. le Roy and C. Prat, *Polym. Int.*, 2006, 55, 572–582.

38 X. T. Hao, F. R. Zhu, K. S. Ong and L. W. Tan, *Appl. Phys. B*, 2006, **83**, 67–74.

39 C. Y. Kwong, A. B. Djurišić, W. C. H. Choy, D. Li, M. H. Xie, W. K. Chan, K. W. Cheah, P. T. Lai and P. C. Chui, *Mater. Sci. Eng. B*, 2005, **116**, 75–81.

40 L. A. Lozano-Hernández, J. L. Maldonado, C. Garcias-Morales, A. Espinosa Roa, O. Barbosa-García, M. Rodríguez and E. Pérez-Gutiérrez, *Molecules*, 2018, **23**, 1–19.

41 A. P. Kulkarni, C. J. Tonzola, A. Babel and S. A. Jenekhe, *Chem. Mater.*, 2004, **16**, 4556–4573.

42 C.-T. Sun, I.-H. Chan, P.-C. Kao and S.-Y. Chu, *J. Electrochem. Soc.*, 2011, **158**, 1284–

1288.

43 M. Shukla, N. Brahme, R. S. Kher and M. S. K. Khokhar, *Indian J. Pure Appl. Phys.*, 2011, **49**, 142–145.

44 S. R. Forrest, D. D. C. Bradley and M. E. Thompson, *Adv. Mater.*, 2003, **15**, 1043–1048.

45 D. J. Gaspar and E. Polikarpov, *OLED Fundamentals: materials, devices, and processing of organic light-emitting diodes*, CRC press, Taylor and Francis Group, Boca Raton, 2015.

46 J. P. Spindler, J. W. Hamer and M. . Kondakova, *Handbook of Advanced Lighting Technology: OLED Manufacturing Equipment and Methods*, Springer, Cham, 2017.

47 H. Uoyama, K. Goushi, K. Shizu, H. Nomura and C. Adachi, *Nature*, 2012, **492**, 234–238.

48 T. T. Bui, F. Goubard, M. Ibrahim-Ouali, D. Gigmes and F. Dumur, *Beilstein J. Org. Chem.*, 2018, **14**, 282–308.

49 S. Y. Byeon, J. Kim, D. R. Lee, S. H. Han, S. R. Forrest and J. Y. Lee, *Adv. Opt. Mater.*, 2018, **6**, 1–6.

50 J. W. Sun, J. H. Lee, C. K. Moon, K. H. Kim, H. Shin and J. J. Kim, *Adv. Mater.*, 2014, **26**, 5684–5688.

51 C. F. Chang, Y. M. Cheng, Y. Chi, Y. C. Chiu, C. C. Lin, G. H. Lee, P. T. Chou, C. C. Chen, C. H. Chang and C. C. Wu, *Angew. Int. Ed.*, 2008, **47**, 4542–4545.

52 H. Fu, Y. M. Cheng, P. T. Chou and Y. Chi, *Mater. Today*, 2011, **14**, 472–479.

53 Y. Nagai, H. Sasabe, J. Takahashi, N. Onuma, T. Ito, S. Ohisa and J. Kido, *J. Mater. Chem. C*, 2017, **5**, 527–530.

54 B. Blondel, F. Delarue, M. Lopes, S. Ladeira-Mallet, F. Alary, C. Renaud and I. Sasaki, *Synth. Met.*, 2017, **227**, 106–116.

55 L. L. Wen, C. X. Zang, Y. Gao, G. G. Shan, H. Z. Sun, T. Wang, W. F. Xie and Z. M. Su, *Inorg. Chem.*, 2018, **57**, 6029–6037.

56 H. Guo, J. Zhao, Z. Tian, Y. Wu, B. Liu, F. Dang, X. Yang, G. Zhou, Z. Wu and W. Y. Wong, *J. Mater. Chem. C*, 2017, **5**, 208–219.

57 C. Fan and C. Yang, *Chem. Soc. Rev.*, 2014, **43**, 6439–6469.

58 D. Septiadi, A. Aliprandi, M. Mauro and L. De Cola, *RSC Adv.*, 2014, **4**, 25709–25718.

59 A. Colombo, F. Fiorini, D. Septiadi, C. Dragonetti, F. Nisic, A. Valore, D. Roberto, M. Mauro and L. De Cola, *Dalton Trans.*, 2015, **44**, 8478–8487.

60 H. L. Steel, S. L. Allinson, J. Andre, M. P. Coogan and J. A. Platts, *Chem. Commun.*, 2015, **51**, 11441–11444.

61 J. S. Souris, *Trends Biotechnol.*, 2002, **20**, 364–366.

62 P. Chen and T. J. Meyer, *Chem. Rev.*, 1998, **98**, 1439–1478.

63 R. Englman and J. Jortner, *Mol. Phys.*, 1970, **18**, 285–287.

64 C. Mayr, M. Taneda, C. Adachi and W. Brütting, *Org. Electron.*, 2014, **15**, 3031–3037.

65 C. K. Moon, K. H. Kim and J. J. Kim, *Nat. Commun.*, 2017, **8**, 1–10.

66 M. Taneda, T. Yasuda and C. Adachi, *Appl. Phys. Express*, 2011, **4**, 71602.

67 M. Flämmich, M. C. Gather, N. Danz, D. Michaelis, A. H. Bräuer, K. Meerholz and A. Tünnermann, *Org. Electron.*, 2010, **11**, 1039–1046.

68 K. H. Kim, J. Y. Ma, C. K. Moon, J. H. Lee, J. Y. Baek, Y. H. Kim and J. J. Kim, *Adv. Opt. Mater.*, 2015, **3**, 1191–1196.

69 T. Miwa, S. Kubo, K. Shizu, T. Komino, C. Adachi and H. Kaji, *Sci. Rep.*, 2017, **7**, 1–8.

70 M. J. Jurow, C. Mayr, T. D. Schmidt, T. Lampe, P. I. Djurovich, W. Brütting and M. E. Thompson, *Nat. Mater.*, 2016, **15**, 85–91.

71 T. U. Connell, J. M. White, T. A. Smith and P. S. Donnelly, *Inorg. Chem.*, 2016, **55**, 2776–2790.

72 B. S. Uppal, R. K. Booth, N. Ali, C. Lockwood, C. R. Rice and P. I. P. Elliott, *Dalton Trans.*, 2011, **40**, 7610–7616.

73 N. Su, G.-Z. Lu and Y. Zheng, *J. Mater. Chem. C*, 2018, **6**, 5778–5784.

74 J. L. Liao, Y. Chi, J. Y. Wang, Z. N. Chen, Z. H. Tsai, W. Y. Hung, M. R. Tseng and G. H. Lee, *Inorg. Chem.*, 2016, **55**, 6394–6404.

75 Y. Chi, B. Tong and P.-T. Chou, *Coord. Chem. Rev.*, 2014, **281**, 1–25.

76 J. A. Bladin, *Berichte der Dtsch. Chem. Gesellschaft*, 1885, **18**, 1544–1551.

77 X. Cao, C. Chen, W. Lu and S. Ke, *Pestic. Biochem. Physiol.*, 2011, **99**, 189–193.

78 G. Ren, J. Li, X. Wei, J. Zhou, B. Yan, Z. Guo, Y. Ren, X. Sun and H. Ma, *Appl. Organomet. Chem.*, 2018, **32**, 1–13.

79 J. Pernak, B. Markiewicz, B. Łegosz, F. Walkiewicz, R. Gwiazdowski and T. Praczyk, *RSC Adv.*, 2015, **5**, 9695–9702.

80 C. H. Zhou and Y. Wang, *Curr. Med. Chem.*, 2012, **19**, 239–280.

81 M. Genc, Z. Karagoz Genc, S. Tekin, S. Sandal, M. Sirajuddin, T. Ben Hadda and M. Sekerci, *Acta Chim. Slov.*, 2016, **63**, 726–737.

82 K. Dzitko, A. Paneth, T. Plech, J. Pawełczyk, L. Węglińska and P. Paneth, *Antimicrob. Agents Chemother.*, 2014, **58**, 7583–7585.

83 V. V. Rostovtsev, L. G. Green, V. V. Fokin and K. B. Sharpless, *Angew. Int. Ed.*, 2002, **41**, 2596–2599.

84 F. Himo, T. Lovell, R. Hilgraf, V. V. Rostovtsev, L. Noodleman, K. B. Sharpless and V. V. Fokin, *J. Am. Chem. Soc.*, 2005, **127**, 210–216.

85 H. C. Kolb, M. G. Finn and K. B. Sharpless, *Angew. Int. Ed.*, 2001, **40**, 2004–2021.

86 W. K. C. Lo, G. S. Huff, J. R. Cubanski, A. D. W. Kennedy, C. J. McAdam, D. A. McMorran, K. C. Gordon and J. D. Crowley, *Inorg. Chem.*, 2015, **54**, 1572–1587.

87 H.-Z. Zhang, G. Damu, G.-X. Cai and C.-H. Zhou, *Curr. Org. Chem.*, 2014, **18**, 359–406.

88 K. T. Potts, *Chem. Rev.*, 1961, **61**, 87–127.

89 G. Pellizzari, *Gazz. Chim. Ital.*, 1911, **41**, 2.

90 H. Huang, W. Guo, W. Wu, C.-J. Li and H. Jiang, *Org. Lett.*, 2015, **17**, 2894–2897.

91 M. Mydlak, M. Mauro, F. Polo, M. Felicetti, J. Leonhardt, G. Diener, L. De Cola and C. A. Strassert, *Chem. Mater.*, 2011, **23**, 3659–3667.

92 Z. P. Demko and K. B. Sharpless, *J. Org. Chem.*, 2001, **66**, 7945–7950.

93 P.-I. Kvam, M. V. Puzyk, K. P. Balashev and J. Songstad, *Acta Chem. Scand.*, 1995, **49**, 335–343.

94 M. M. Mdleleni, J. S. Bridgewater, R. J. Watts and P. C. Ford, *Inorg. Chem.*, 1995, **34**, 2334–2342.

95 J.-Y. Cho, K. Y. Suponitsky, J. Li, T. V. Timofeeva, S. Barlow and S. R. Marder, *J. Organomet. Chem.*, 2005, **690**, 4090–4093.

96 D. A. W. Ross, P. A. Scattergood, A. Babaei, A. Pertegás, H. J. Bolink and P. I. P. Elliott, *Dalton Trans.*, 2016, **45**, 7748–7757.

97 P. A. Scattergood and P. I. P. Elliott, *Dalton Trans.*, 2017, **46**, 16343–16356.

98 P. I. P. Elliott, *Organomet. Chem.*, 2014, **39**, 1–25.

99 K. J. Kilpin and J. D. Crowley, *Polyhedron*, 2010, **29**, 3111–3117.

100 M. Felici, P. Contreras-Carballada, J. M. M. Smits, R. J. M. Nolte, R. M. Williams, L. De Cola and M. C. Feiters, *Molecules*, 2010, **15**, 2039–2059.

101 H. Y. Hsieh, C. H. Lin, G. M. Tu, Y. Chi and G. H. Lee, *Inorg. Chim. Acta.*, 2009, **362**, 4734–4739.

102 S. Y. Chang, J. Kavitha, S. W. Li, C. S. Hsu, Y. Chi, Y. S. Yeh, P. T. Chou, G. H. Lee, A. J. Carty, Y. T. Tao and C. H. Chien, *Inorg. Chem.*, 2006, **45**, 137–146.

103 D. Enders, K. Breuer, U. Kallfass and T. Balensiefer, *Synthesis (Stuttg).*, 2003, **8**, 1292–1295.

104 J. Soellner and T. Strassner, *Organometallics*, 2018, **37**, 1821–1824.

105 M. Li, W. H. Chen, M. Te Lin, M. A. Omary and N. D. Shepherd, *Org. Electron.*, 2009, **10**, 863–870.

106 H. J. Park, J. N. Kim, H. Yoo, K. Wee, S. O. Kang and D. W. Cho, *J. Org. Chem.*, 2013, **78**, 8054–8064.

107 K. H. Kim, J. L. Liao, S. W. Lee, B. Sim, C. K. Moon, G. H. Lee, H. J. Kim, Y. Chi and J. J. Kim, *Adv. Mater.*, 2016, 2526–2532.

108 K. Tuong Ly, R.-W. Chen-Cheng, H.-W. Lin, Y.-J. Shiau, S.-H. Liu, P.-T. Chou, C.-S. Tsao, Y.-C. Huang and Y. Chi, *Nat. Photonics*, 2016, **11**, 63–68.

109 M. Cocchi, J. Kalinowski, D. Virgili and J. A. G. Williams, *Appl. Phys. Lett.*, 2008, **92**, 113302.

110 K. D. M. Magee, P. J. Wright, S. Muzzioli, C. M. Siedlovskas, P. Raiteri, M. V Baker, D. H. Brown, S. Stagni and M. Massi, *Dalton. Trans.*, 2013, **42**, 4233–4236.

111 P. Brulatti, V. Fattori, S. Muzzioli, S. Stagni, P. P. Mazzeo, D. Braga, L. Maini, S. Milita and M. Cocchi, *J. Mater. Chem. C*, 2013, **1**, 1823–1831.

112 M. Gómez, J. Granell and M. Martinez, *Eur. J. Inorg. Chem.*, 2000, 217–224.

113 J. M. Vila, M. Gayoso, M. T. Pereira, M. Löpez Torres, J. J. Fernández, A. Fernández and J. M. Ortigueira, *J. Organomet. Chem.*, 1996, **506**, 165–174.

114 I. R. Laskar, S. F. Hsu and T. M. Chen, *Polyhedron*, 2005, **24**, 881–888.

115 L. Chassot, E. Mueller and A. Von Zelewsky, *Inorg. Chem.*, 1984, **23**, 4249–4253.

116 S. Y. Chang, J. Kavitha, S. W. Li, C. S. Hsu, Y. Chi, Y. S. Yeh, P. T. Chou, G. H. Lee, A. J. Carty, Y. T. Tao and C. H. Chien, *Inorg. Chem.*, 2006, **45**, 137–146.

117 Y. Chi, H. Y. Tsai and Y. K. Chen, *J. Chinese Chem. Soc.*, 2017, **64**, 574–588.

118 W. B. Connick, D. Geiger and R. Eisenberg, *Inorg. Chem.*, 1999, **38**, 3264–3265.

119 C. E. McCusker, A. Chakraborty and F. N. Castellano, *J. Phys. Chem. A*, 2014, **118**, 10391–10399.

120 N. Armaroli, L. De Cola and V. Balzani, *J. Chem. Soc. Faraday Trans.*, 1992, **88**, 553–556.

121 A. M. Brouwer, *Pure Appl. Chem.*, 2011, **83**, 2213–2228.

122 G. S. M. Tong and C. M. Che, *Chem. Eur. J.*, 2009, **15**, 7225–7237.

123 C. Cornioley-Deuschel, T. Ward and A. Von Zelewsky, *Helv. Chim. Acta*, 1988, **71**, 130–133.

124 G. W. V. Cave, N. W. Alcock and J. P. Rourke, *Organometallics*, 1999, **18**, 1801–1803.

125 W. Lu, M. W. C. Chan, K. Cheung and C. Che, *Organometallics*, 2001, **20**, 2477–2486.

126 S. C. F. Kui, F. F. Hung, S. L. Lai, M. Y. Yuen, C. C. Kwok, K. H. Low, S. S. Y. Chui and C. M. Che, *Chem. Eur. J.*, 2012, **18**, 96–109.

127 J. A. G. Williams, *Chem. Soc. Rev.*, 2009, **38**, 1783–1801.

128 E. Rossi, A. Colombo, C. Dragonetti, D. Roberto, R. Ugo, A. Valore, L. Falciola, P. Brulatti, M. Cocchi and J. A. G. Williams, *J. Mater. Chem.*, 2012, **22**, 10650.

129 S. J. Farley, D. L. Rochester, A. L. Thompson, J. A. K. Howard and J. A. G. Williams, *Inorg. Chem.*, 2005, **44**, 9690–9703.

130 C. P. Newman, K. Casey-Green, G. J. Clarkson, G. W. V Cave, W. Errington and J. P.

Rourke, *Dalton Trans.*, 2007, 3170–3182.

131 J. Mamtora, S. H. Crosby, C. P. Newman, G. J. Clarkson and J. P. Rourke, *Organometallics*, 2008, **27**, 5559–5565.

132 D. M. Jenkins and S. Bernhard, *Inorg. Chem.*, 2010, **49**, 11297–11308.

133 F. Juliá, D. Bautista, J. M. Fernández-Hernández and P. González-Herrero, *Chem. Sci.*, 2014, **5**, 1875–1880.

134 F. Juliá, D. Bautista and P. González-Herrero, *Chem. Commun.*, 2016, **2**, 1657–1660.

135 G. R. Freeman, PhD Thesis, Durham University, 2014.

136 Z. Wang, E. Turner, V. Mahoney, S. Madakuni, T. Groy and J. Li, *Inorg. Chem.*, 2010, **49**, 11276–11286.

137 L. Murphy, PhD Thesis, Durham University, 2010.

138 L. Chassot, A. von Zelewsky, D. Sandrini, M. Maestri and V. Balzani, *J. Am. Chem. Soc.*, 1986, **108**, 6084–6085.

139 A. J. Lees, *Comments Inorg. Chem.*, 1995, **17**, 319–346.

140 K. Suzuki, A. Endo, T. Yoshihara, S. Tobita, M. Yahiro, D. Yokoyama and C. Adachi, *Proc. SPIE, Org. Light Emit. Mater. Devices*, 2009, **7415**, 1–8.

141 A. Endo, K. Suzuki, T. Yoshihara, S. Tobita, M. Yahiro and C. Adachi, *Chem. Phys. Lett.*, 2008, **460**, 155–157.

142 J. P. Collin, I. M. Dixon, J. P. Sauvage, J. A. G. Williams, F. Barigelletti and L. Flamigni, *J. Am. Chem. Soc*, 1999, **121**, 5009–5016.

143 Y. Chi, T. K. Chang, P. Ganesan and P. Rajakannu, *Coord. Chem. Rev.*, 2017, **346**, 91–100.

144 T. Yutaka, S. Obara, S. Ogawa, K. Nozaki, N. Ikeda, T. Ohno, Y. Ishii, K. Sakai and M. A. Haga, *Inorg. Chem.*, 2005, **44**, 4737–4746.

145 A. J. Wilkinson, A. E. Goeta, C. E. Foster and J. A. G. Williams, *Inorg. Chem.*, 2004, **43**, 6513–6515.

146 A. J. Wilkinson, H. Puschmann, J. A. K. Howard, C. E. Foster and J. A. G. Williams, *Inorg. Chem.*, 2006, **45**, 8685–8699.

147 S. Obara, M. Itabashi, F. Okuda, S. Tamaki, Y. Tanabe, Y. Ishii, K. Nozaki and M. A. Haga, *Inorg. Chem.*, 2006, **45**, 8907–8921.

148 M. Ashizawa, L. Yang, K. Kobayashi, H. Sato, A. Yamagishi, F. Okuda, T. Harada, R. Kuroda and M. A. Haga, *Dalton Trans.*, 2009, **954**, 1700–1702.

149 J. Kuwabara, T. Namekawa, M. Haga and T. Kanbara, *Dalton Trans.*, 2012, **41**, 44–46.

150 J. Lin, Y. Wang, P. Gnanasekaran, Y. C. Chiang, C. C. Yang, C. H. Chang, S. H. Liu, G. H. Lee, P. T. Chou, Y. Chi and S. W. Liu, *Adv. Funct. Mater.*, 2017, **27**, 1–10.

151 H. H. Kuo, Y. T. Chen, L. R. Devereux, C. C. Wu, M. A. Fox, C. Y. Kuei, Y. Chi and G. H.

Lee, *Adv. Mater.*, 2017, **29**, 1–7.

152 B. Tong, H. Y. Ku, I. J. Chen, Y. Chi, H. C. Kao, C. C. Yeh, C. H. Chang, S. H. Liu, G. H. Lee and P. T. Chou, *J. Mater. Chem. C*, 2015, **3**, 3460–3471.

153 C. Y. Kuei, W. L. Tsai, B. Tong, M. Jiao, W. K. Lee, Y. Chi, C. C. Wu, S. H. Liu, G. H. Lee and P. T. Chou, *Adv. Mater.*, 2016, **28**, 2795–2800.

154 P. Brulatti, PhD Thesis, Durham University, 2010.

155 A. Mamo, I. Stefio, M. F. Parisi, A. Credi, M. Venturi, C. Di Pietro and S. Campagna, *Inorg. Chem.*, 1997, **36**, 5947–5950.

156 B. Hirani, J. Li, P. I. Djurovich, M. Yousufuddin, J. Oxgaard, P. Persson, S. R. Wilson, R. Bau, W. A. Goddard and M. E. Thompson, *Inorg. Chem.*, 2007, **46**, 3865–3875.

157 T. Fleetham, G. Li, L. Wen and J. Li, *Adv. Mater.*, 2014, **26**, 7116–7121.

158 G. E. Norby, C. D. Park, B. O'Brien, G. Li, L. Huang and J. Li, *Org. Electron.*, 2016, **37**, 163–168.

159 X. Wang, T. Peng, C. Nguyen, Z. H. Lu, N. Wang, W. Wu, Q. Li and S. Wang, *Adv. Funct. Mater.*, 2017, **27**, 1604318.

160 K. Y. Liao, C. W. Hsu, Y. Chi, M. K. Hsu, S. W. Wu, C. H. Chang, S. H. Liu, G. H. Lee, P. T. Chou, Y. Hu and N. Robertson, *Inorg. Chem.*, 2015, **54**, 4029–4038.

161 W. H. Lam, E. S. H. Lam and V. W. W. Yam, *J. Am. Chem. Soc.*, 2013, **135**, 15135–15143.

162 C. Bronner, S. A. Baudron, M. W. Hosseini, C. A. Strassert, A. Guenet and L. De Cola, *Dalton Trans.*, 2010, **39**, 180–184.

163 J. Kuwabara, Y. Ogawa, A. Taketoshi and T. Kanbara, *J. Organomet. Chem.*, 2011, **696**, 1289–1293.

164 P. K. Chow, C. Ma, W. P. To, G. S. M. Tong, S. L. Lai, S. C. F. Kui, W. M. Kwok and C. M. Che, *Angew. Int. Ed.*, 2013, **52**, 11775–11779.

165 Z.-Q. Zhu, T. Fleetham, E. Turner and J. Li, *Adv. Mater.*, 2015, **27**, 2533–2537.

166 T. Fleetham, G. Li and J. Li, *Adv. Mater.*, 2017, **29**, 1–16.

167 T. Fleetham, Y. Ji, L. Huang, T. S. Fleetham and J. Li, *Chem. Sci.*, 2017, **8**, 7983–7990.

168 M. Bonneau, PhD Thesis, Durham University, 2014.

169 N. Miyaura, K. Yamada and A. Suzuki, *Tet. Lett.*, 1979, **36**, 3437–3440.

170 J. K. Stille, *Angew. Int. Ed.*, 1986, **25**, 508–524.

171 A. L. Casado, P. Espinet and A. M. Gallego, *J. Am. Chem. Soc.*, 2000, **122**, 11771–11782.

172 A. Carpita and R. Rossi, *Gazz. Chim. Ital.*, 1985, **115**, 575–583.

173 J. A. Pople, *J. Chem. Phys.*, 1956, **24**, 1111–1111.

174 S. Shanmugaraju, S. A. Joshi and P. S. Mukherjee, *Inorg. Chem.*, 2011, **50**, 11736–11745.

175 I. Georgieva, N. Trendafilova and N. I. Dodoff, *J. Photochem. Photobiol. A Chem.*, 2013, **267**, 35–48.

176 S. Cacchi and G. Fabrizi, *Chem. Rev.*, 2005, **105**, 2873–2920.

177 S. D. Cummings and R. Eisenberg, *Inorg. Chem.*, 1995, **34**, 2007–2014.

178 V. T. Dangat, S. L. Bonde, V. T. Borkar and P. D. Maske, *Res. J. Chem. Sci.*, 2012, **2**, 75–78.

179 M. Cocchi, D. Virgili, V. Fattori, J. A. G. Williams and J. Kalinowski, *Appl. Phys. Lett.*, 2007, **90**, 163508.

180 Y. Sun, C. Borek, K. Hanson, P. I. Djurovich, M. E. Thompson, J. Brooks, J. J. Brown and S. R. Forrest, *Appl. Phys. Lett.*, 2007, **90**, 213503.

181 L. Huang, C. D. Park, T. Fleetham and J. Li, *Appl. Phys. Lett.*, 2016, **109**, 233302.

182 S. M. Borisov, G. Zenkl and I. Klimant, *ACS Appl. Mater. Interfaces*, 2010, **2**, 366–374.

183 Y. Zhang, F. Meng, C. You, S. Yang, W. Xiong, Y. Wang, S. Su and W. Zhu, *Dye. Pigm.*, 2017, **138**, 100–106.

184 G. Qian, Z. Zhong, M. Luo, D. Yu, Z. Zhang, Z. Y. Wang and D. Ma, *Adv. Mater.*, 2009, **21**, 111–116.

185 Y. Zhang, Z. Yin, F. Meng, J. Yu, C. You, S. Yang, H. Tan, W. Zhu and S. Su, *Org. Electron.*, 2017, **50**, 317–324.

186 S. Develay and J. A. G. Williams, *Dalton Trans.*, 2008, **0**, 4562–4564.

187 R. Okamura, T. Wada, K. Aikawa, T. Nagata and K. Tanaka, *Inorg. Chem.*, 2004, **43**, 7210–7217.

188 Z. Guo, S. M. Yiu and M. C. W. Chan, *Chem. Eur. J.*, 2013, **19**, 8937–8947.

189 R. Muñoz-Rodríguez, E. Buñuel, J. A. G. Williams and D. J. Cárdenas, *Chem. Commun.*, 2012, **48**, 5980–5982.

190 T. Ishiyama, M. Murata and N. Miyaura, *J. Org. Chem.*, 1995, **60**, 7508–7510.

191 K. Nakamaru, *Bull. Chem. Soc. Jpn.*, 1982, **55**, 2697–2705.

192 C. Lee, W. Yang and R. G. Parr, *Phys. Rev. B*, 1988, **37**, 785–789.

193 A. D. Becke, *J. Chem. Phys.*, 1993, **98**, 5648–5652.

194 A. D. Becke, *J. Chem. Phys.*, 1986, **84**, 4524–4529.

195 S. Y. Ahn and Y. Ha, *Mol. Cryst. Liq. Cryst.*, 2010, **520**, 68–74.

196 C. Deuschel-Cornioley, R. Lüönd and A. Zelewsky, *Helv. Chim. Acta*, 1989, **72**, 377–382.

197 J. R. Berenguer, Á. -Díez, E. Lalinde, M. T. Moreno, S. Ruiz and S. Sánchez,

Organometallics, 2011, **30**, 5776–5792.

198 K. A. Mitchell and C. M. Jensen, *Inorg. Chem.*, 1995, **34**, 4441–4446.

199 N. Margiotta, P. Papadia, F. P. Fanizzi and G. Natile, *Eur. J. Inorg. Chem.*, 2003, 1136–1144.

200 A. Xie, M. Cao, Y. Liu, L. Feng, X. Hu and W. Dong, *European J. Org. Chem.*, 2014, **2014**, 436–441.

201 D. J. Cardenas, A. M. Echavarren and M. C. Ramırez de Arellano, *Organometallics*, 1999, **18**, 3337–3341.

202 M. Nonoyama, *Bull. Chem. Soc. Jpn.*, 1974, **47**, 767–768.

203 H. J. Nie, J. Yao and Y. W. Zhong, *J. Org. Chem.*, 2011, **76**, 4771–4775.

204 L. A. Van Der Veen, P. K. Keeven, P. C. J. Kamer and P. W. N. M. Van Leeuwen, *J. Chem. Soc. Dalton Trans.*, 2000, 2105–2112.

9. Appendix

9.1 Publications arising from this work

The luminescence properties of multinuclear platinum complexes.

Emma V. Puttock, Melissa T. Walden, J. A. Gareth Williams.

Coordination Chemistry Reviews, **367**, (2018), 127–162.

9.2 Luminescence data for chapter 3

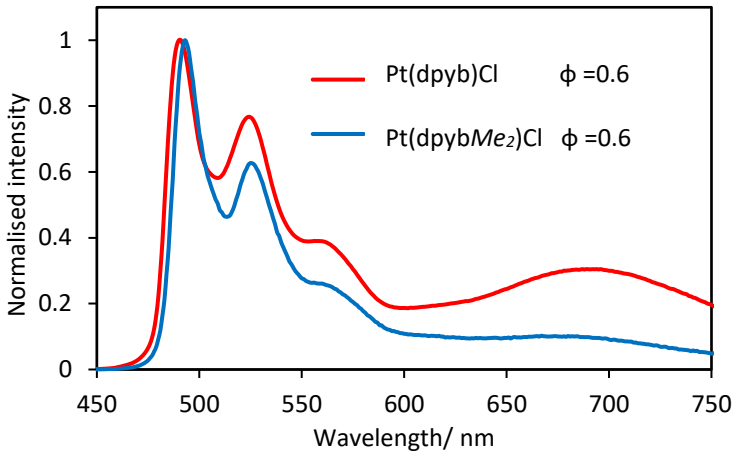

Figure A1: *Degassed emission in DCM of Pt(dpyb)Cl and Pt(dpybMe₂)Cl.*

9.3 DFT data for chapter 4

Complex	*HOMO-3*	*Complex*	*HOMO-5*
PtL[21]	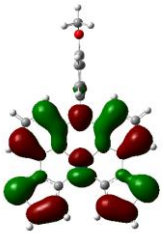	*PtL*[22]	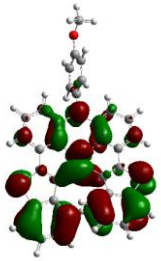
PdL[21]	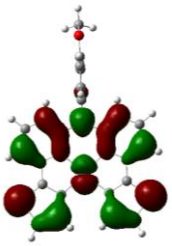	*PdL*[22]	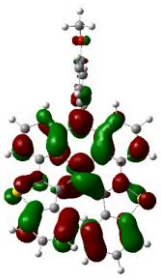

Figure A2: *Orbital diagrams of the HOMO-3 for ML*[21] *and the HOMO-5 for ML*[22].

9.4 Crystal structure information

Crystal data and structure refinement for HL[1]

Identification code	16srv384
Empirical formula	$C_{17}H_{18}N_4$
Formula weight	278.35
Temperature/K	120.0
Crystal system	monoclinic
Space group	$P2_1/n$
a/Å	5.9123(6)
b/Å	13.2287(13)
c/Å	18.6718(19)
α/°	90
β/°	98.757(4)
γ/°	90
Volume/Å^3	1443.3(3)
Z	4
ρ_{calc}g/cm^3	1.281
μ/mm^{-1}	0.079
F(000)	592.0
Crystal size/mm^3	0.21 × 0.09 × 0.08
Radiation	MoKα (λ = 0.71073)
2Θ range for data collection/°	4.414 to 55.992
Index ranges	-7 ≤ h ≤ 7, -17 ≤ k ≤ 17, -24 ≤ l ≤ 24
Reflections collected	27498
Independent reflections	3480 [R_{int} = 0.0696, R_{sigma} = 0.0465]
Data/restraints/parameters	3480/0/262
Goodness-of-fit on F^2	1.031
Final R indexes [I>=2σ (I)]	R_1 = 0.0467, wR_2 = 0.0942
Final R indexes [all data]	R_1 = 0.0790, wR_2 = 0.1057
Largest diff. peak/hole / e Å^{-3}	0.21/-0.27

Crystal data and structure refinement for HL²

Identification code	16srv386
Empirical formula	$C_{14}H_{12}N_4O$
Formula weight	252.28
Temperature/K	100.0
Crystal system	orthorhombic
Space group	Pbca
a/Å	6.9306(16)
b/Å	10.920(3)
c/Å	31.555(7)
α/°	90
β/°	90
γ/°	90
Volume/Å^3	2388.1(10)
Z	8
ρ_{calc}g/cm^3	1.403
μ/mm^{-1}	0.088
F(000)	1056.0
Crystal size/mm^3	0.03 × 0.005 × 0.005
Radiation	synchrotron (λ = 0.6889)
2Θ range for data collection/°	2.502 to 57.996
Index ranges	-9 ≤ h ≤ 9, -15 ≤ k ≤ 15, -44 ≤ l ≤ 44
Reflections collected	29429
Independent reflections	3316 [R_{int} = 0.0822, R_{sigma} = 0.0524]
Data/restraints/parameters	3316/0/177
Goodness-of-fit on F^2	1.046
Final R indexes [I>=2σ (I)]	R_1 = 0.0675, wR_2 = 0.1856
Final R indexes [all data]	R_1 = 0.0768, wR_2 = 0.1949
Largest diff. peak/hole / e Å^{-3}	0.42/-0.46

Crystal data and structure refinement for HL[6]

Identification code	MW401
Empirical formula	$C_{22}H_{22}N_4O$
Formula weight	358.43
Temperature/K	120.0
Crystal system	monoclinic
Space group	C2/c
a/Å	19.417(2)
b/Å	6.9032(7)
c/Å	27.468(3)
α/°	90
β/°	94.997(4)
γ/°	90
Volume/Å^3	3667.7(6)
Z	8
ρ_{calc}g/cm^3	1.298
μ/mm^{-1}	0.082
F(000)	1520.0
Crystal size/mm^3	0.63 × 0.19 × 0.044
Radiation	MoKα (λ = 0.71073)
2Θ range for data collection/°	4.212 to 62.226
Index ranges	-28 ≤ h ≤ 28, -10 ≤ k ≤ 10, -39 ≤ l ≤ 39
Reflections collected	39689
Independent reflections	5863 [R_{int} = 0.1350, R_{sigma} = 0.1019]
Data/restraints/parameters	5863/0/248
Goodness-of-fit on F^2	1.041
Final R indexes [I>=2σ (I)]	R_1 = 0.0674, wR_2 = 0.1288
Final R indexes [all data]	R_1 = 0.1358, wR_2 = 0.1518
Largest diff. peak/hole / e Å^{-3}	0.28/-0.29

Crystal data and structure refinement for PtL^1_2

Identification code	16srv190
Empirical formula	$C_{34}H_{38}N_8Pt$
Formula weight	753.81
Temperature/K	120.0
Crystal system	monoclinic
Space group	$P2_1/c$
a/Å	11.6673(5)
b/Å	5.5870(3)
c/Å	21.8713(10)
α/°	90
β/°	101.0279(15)
γ/°	90
Volume/Å^3	1399.36(12)
Z	2
ρ_{calc}g/cm^3	1.789
μ/mm^{-1}	5.055
F(000)	752.0
Crystal size/mm^3	0.18 × 0.15 × 0.01
Radiation	MoKα (λ = 0.71073)
2Θ range for data collection/°	4.678 to 59.998
Index ranges	-16 ≤ h ≤ 16, -7 ≤ k ≤ 7, -30 ≤ l ≤ 30
Reflections collected	21893
Independent reflections	4081 [R_{int} = 0.0489, R_{sigma} = 0.0399]
Data/restraints/parameters	4081/0/199
Goodness-of-fit on F^2	1.177
Final R indexes [I>=2σ (I)]	R_1 = 0.0382, wR_2 = 0.0799
Final R indexes [all data]	R_1 = 0.0630, wR_2 = 0.0859
Largest diff. peak/hole / e Å^{-3}	3.45/-1.15

Crystal data and structure refinement for PtL^2_2

Identification code	16srv162
Empirical formula	$C_{28}H_{22}N_8O_2Pt$ x 2 C_3H_7NO
Formula weight	843.82
Temperature/K	120.0
Crystal system	monoclinic
Space group	$P2_1/n$
a/Å	14.3162(17)
b/Å	5.8624(7)
c/Å	19.762(2)
α/°	90
β/°	102.596(4)
γ/°	90
Volume/Å^3	1618.7(3)
Z	2
ρ_{calc}g/cm^3	1.731
μ/mm^{-1}	4.391
F(000)	840.0
Crystal size/mm^3	0.21 × 0.05 × 0.01
Radiation	MoKα (λ = 0.71073)
2Θ range for data collection/°	5.832 to 55.994
Index ranges	-18 ≤ h ≤ 18, -7 ≤ k ≤ 7, -26 ≤ l ≤ 26
Reflections collected	29088
Independent reflections	3913 [R_{int} = 0.0949, R_{sigma} = 0.0665]
Data/restraints/parameters	3913/0/226
Goodness-of-fit on F^2	1.023
Final R indexes [I>=2σ (I)]	R_1 = 0.0320, wR_2 = 0.0550
Final R indexes [all data]	R_1 = 0.0750, wR_2 = 0.0628
Largest diff. peak/hole / e Å^{-3}	1.25/-1.00

Crystal data and structure refinement for PtL^4_2

Identification code	18srv220
Empirical formula	$C_{34}H_{34}N_8O_2Pt$ x 6 $C_2HF_3O_2$
Formula weight	1465.95
Temperature/K	120.0
Crystal system	triclinic
Space group	P-1
a/Å	14.6085(9)
b/Å	14.8858(9)
c/Å	15.4429(9)
α/°	117.828(2)
β/°	107.634(2)
γ/°	97.622(2)
Volume/Å^3	2676.5(3)
Z	2
ρ_{calc}g/cm^3	1.819
μ/mm^{-1}	2.757
F(000)	1448.0
Crystal size/mm^3	0.16 × 0.11 × 0.05
Radiation	MoKα (λ = 0.71073)
2Θ range for data collection/°	4.202 to 58.998
Index ranges	-20 ≤ h ≤ 20, -20 ≤ k ≤ 20, -21 ≤ l ≤ 21
Reflections collected	57254
Independent reflections	14922 [R_{int} = 0.0480, R_{sigma} = 0.0559]
Data/restraints/parameters	14922/66/780
Goodness-of-fit on F^2	1.059
Final R indexes [I>=2σ (I)]	R_1 = 0.0380, wR_2 = 0.0895
Final R indexes [all data]	R_1 = 0.0536, wR_2 = 0.0940
Largest diff. peak/hole / e Å^{-3}	1.75/-1.50

Crystal data and structure refinement for PtL^{7}_{2}

Identification code	18srv161
Empirical formula	$C_{54}H_{58}N_8Pt$
Formula weight	1014.17
Temperature/K	120.0
Crystal system	triclinic
Space group	P-1
a/Å	6.5952(3)
b/Å	10.7367(5)
c/Å	16.1585(8)
α/°	88.6300(17)
β/°	83.5014(17)
γ/°	85.8827(17)
Volume/Å^3	1133.76(9)
Z	1
ρ_{calc}g/cm^3	1.485
μ/mm^{-1}	3.141
F(000)	516.0
Crystal size/mm^3	0.13 × 0.07 × 0.01
Radiation	MoKα (λ = 0.71073)
2Θ range for data collection/°	4.538 to 55.996
Index ranges	-8 ≤ h ≤ 8, -13 ≤ k ≤ 14, -21 ≤ l ≤ 21
Reflections collected	22013
Independent reflections	5458 [R_{int} = 0.0470, R_{sigma} = 0.0512]
Data/restraints/parameters	5458/15/292
Goodness-of-fit on F^2	1.067
Final R indexes [I>=2σ (I)]	R_1 = 0.0343, wR_2 = 0.0720
Final R indexes [all data]	R_1 = 0.0360, wR_2 = 0.0729
Largest diff. peak/hole / e Å^{-3}	1.86/-1.32

Crystal data and structure refinement for Pt(pquin)L³

Identification code	MW351
Empirical formula	$C_{59}H_{38}Cl_2F_6N_{10}Pt_2$
Formula weight	1462.07
Temperature/K	120.0
Crystal system	orthorhombic
Space group	Pbca
a/Å	22.121(2)
b/Å	15.0778(17)
c/Å	29.960(3)
α/°	90
β/°	90
γ/°	90
Volume/Å^3	9992.5(19)
Z	8
ρ_{calc}g/cm^3	1.944
μ/mm^{-1}	5.777
F(000)	5648.0
Crystal size/mm^3	0.034 x 0.062 x 0.402
Radiation	MoKα (λ = 0.71073)
2Θ range for data collection/°	3.682 to 49.998
Index ranges	-31 ≤ h ≤ 31, -21 ≤ k ≤ 21, -42 ≤ l ≤ 42
Reflections collected	166359
Independent reflections	8787 [R_{int} = 0.1849, R_{sigma} = 0.1049]
Data/restraints/parameters	8787/54/709
Goodness-of-fit on F^2	1.095
Final R indexes [I>=2σ (I)]	R_1 = 0.0424, wR_2 = 0.0886
Final R indexes [all data]	R_1 = 0.0659, wR_2 = 0.1023
Largest diff. peak/hole / e Å^{-3}	2.00/-1.23

Crystal data and structure refinement for [Pt(bpy)L^2]PF$_6$

Identification code	16srv263
Empirical formula	$C_{24}H_{19}N_6OPt$ x PF_6 x C_2H_6OS
Formula weight	825.64
Temperature/K	120.0
Crystal system	monoclinic
Space group	$P2_1/c$
a/Å	7.72184(18)
b/Å	17.6396(4)
c/Å	20.8547(5)
α/°	90
β/°	100.251(2)
γ/°	90
Volume/Å^3	2795.29(12)
Z	4
ρ_{calc}g/cm^3	1.962
μ/mm^{-1}	5.230
F(000)	1608.0
Crystal size/mm^3	0.09 × 0.07 × 0.04
Radiation	MoKα (λ = 0.71073)
2Θ range for data collection/°	4.592 to 57
Index ranges	-10 ≤ h ≤ 10, -23 ≤ k ≤ 23, -27 ≤ l ≤ 27
Reflections collected	45256
Independent reflections	7094 [R_{int} = 0.1190, R_{sigma} = 0.0860]
Data/restraints/parameters	7094/0/391
Goodness-of-fit on F^2	1.018
Final R indexes [I>=2σ (I)]	R_1 = 0.0495, wR_2 = 0.0996
Final R indexes [all data]	R_1 = 0.0846, wR_2 = 0.1136
Largest diff. peak/hole / e Å^{-3}	4.83/-1.15

Crystal data and structure refinement for [Pt(dpyb)L^{1}Cl]PF$_6$

Identification code	18srv166
Empirical formula	$C_{36}H_{34}ClF_6N_6OPPt$
Formula weight	942.20
Temperature/K	120.0
Crystal system	triclinic
Space group	P-1
a/Å	13.1978(5)
b/Å	13.9099(6)
c/Å	20.8134(8)
α/°	106.4901(13)
β/°	90.4623(14)
γ/°	102.0568(13)
Volume/Å^3	3573.7(2)
Z	4
ρ_{calc}g/cm^3	1.751
μ/mm^{-1}	4.117
F(000)	1856.0
Crystal size/mm^3	0.16 × 0.12 × 0.06
Radiation	MoKα (λ = 0.71073)
2Θ range for data collection/°	4.102 to 58
Index ranges	-18 ≤ h ≤ 18, -18 ≤ k ≤ 18, -28 ≤ l ≤ 28
Reflections collected	74522
Independent reflections	18950 [R_{int} = 0.0410, R_{sigma} = 0.0433]
Data/restraints/parameters	18950/7/942
Goodness-of-fit on F^2	1.014
Final R indexes [I>=2σ (I)]	R_1 = 0.0285, wR_2 = 0.0588
Final R indexes [all data]	R_1 = 0.0486, wR_2 = 0.0643
Largest diff. peak/hole / e Å^{-3}	1.01/-1.00

Crystal data and structure refinement for Ir(dpybMe$_2$)(L^{16})

Identification code	18srv184
Empirical formula	$C_{47}H_{46}IrN_9$
Formula weight	929.13
Temperature/K	120.0
Crystal system	monoclinic
Space group	$P2_1/n$
a/Å	16.4690(10)
b/Å	12.1118(8)
c/Å	22.6956(14)
α/°	90
β/°	103.379(2)
γ/°	90
Volume/Å^3	4404.2(5)
Z	4
ρ_{calc}g/cm^3	1.401
μ/mm^{-1}	3.074
F(000)	1872.0
Crystal size/mm^3	0.22 × 0.17 × 0.02
Radiation	MoKα (λ = 0.71073)
2Θ range for data collection/°	4.832 to 55.998
Index ranges	-21 ≤ h ≤ 21, -16 ≤ k ≤ 16, -29 ≤ l ≤ 29
Reflections collected	62748
Independent reflections	10610 [R_{int} = 0.1340, R_{sigma} = 0.1205]
Data/restraints/parameters	10610/21/516
Goodness-of-fit on F^2	1.006
Final R indexes [I>=2σ (I)]	R_1 = 0.0521, wR_2 = 0.1041
Final R indexes [all data]	R_1 = 0.1088, wR_2 = 0.1200
Largest diff. peak/hole / e Å^{-3}	2.45/-1.50

Crystal data and structure refinement for Ir(dpybF$_2$)(L^{16})

Identification code	MW387.res
Empirical formula	$C_{53}H_{63}F_2IrN_{13}O_4$
Formula weight	1176.39
Temperature/K	120.0
Crystal system	triclinic
Space group	P-1
a/Å	11.4994(7)
b/Å	15.4525(10)
c/Å	16.3649(10)
α/°	117.046(2)
β/°	91.454(2)
γ/°	96.054(2)
Volume/Å^3	2566.7(3)
Z	2
ρ_{calc}g/cm^3	1.5221
μ/mm^{-1}	2.668
F(000)	1195.9
Crystal size/mm^3	0.025 x 0.096 x 0.347
Radiation	Mo Kα (λ = 0.71073)
2Θ range for data collection/°	4.36 to 60
Index ranges	-16 ≤ h ≤ 16, -22 ≤ k ≤ 22, -23 ≤ l ≤ 22
Reflections collected	57856
Independent reflections	14936 [R_{int} = 0.0736, R_{sigma} = 0.0936]
Data/restraints/parameters	14936/14/669
Goodness-of-fit on F^2	1.033
Final R indexes [I>=2σ (I)]	R_1 = 0.0472, wR_2 = 0.0865
Final R indexes [all data]	R_1 = 0.0709, wR_2 = 0.0933
Largest diff. peak/hole / e Å^{-3}	2.38/-2.04

Crystal data and structure refinement for PtL[20]

Identification code	15srv227
Empirical formula	$C_{29}H_{17}F_4N_3OPt$
Formula weight	694.55
Temperature/K	120.0
Crystal system	triclinic
Space group	P-1
a/Å	9.5160(4)
b/Å	11.7283(5)
c/Å	12.0991(5)
α/°	118.4489(12)
β/°	95.4022(14)
γ/°	104.4798(14)
Volume/Å^3	1112.91(8)
Z	2
ρ_{calc}g/cm^3	2.073
μ/mm^{-1}	6.369
F(000)	668.0
Crystal size/mm^3	0.28 × 0.19 × 0.18
Radiation	MoKα (λ = 0.71073)
2Θ range for data collection/°	4.2 to 60
Index ranges	-13 ≤ h ≤ 13, -16 ≤ k ≤ 16, -17 ≤ l ≤ 16
Reflections collected	24536
Independent reflections	6491 [R_{int} = 0.0462, R_{sigma} = 0.0364]
Data/restraints/parameters	6491/0/344
Goodness-of-fit on F^2	1.043
Final R indexes [I>=2σ (I)]	R_1 = 0.0193, wR_2 = 0.0404
Final R indexes [all data]	R_1 = 0.0221, wR_2 = 0.0413
Largest diff. peak/hole / e Å^{-3}	1.35/-1.80

Crystal data and structure refinement for PdL[22]

Identification code	15srv193
Empirical formula	$C_{33}H_{21}N_3OPdS_2$ x C_3H_7NO
Formula weight	719.14
Temperature/K	120.0
Crystal system	triclinic
Space group	P-1
a/Å	11.2231(4)
b/Å	11.5339(4)
c/Å	13.0267(5)
α/°	81.2260(10)
β/°	68.9980(10)
γ/°	72.4640(10)
Volume/Å^3	1499.20(9)
Z	2
ρ_{calc}g/cm^3	1.593
μ/mm^{-1}	0.800
F(000)	732.0
Crystal size/mm^3	0.22 × 0.18 × 0.12
Radiation	MoKα (λ = 0.71073)
2Θ range for data collection/°	3.36 to 58
Index ranges	-15 ≤ h ≤ 15, -15 ≤ k ≤ 15, -17 ≤ l ≤ 17
Reflections collected	24903
Independent reflections	7983 [R_{int} = 0.0269, R_{sigma} = 0.0278]
Data/restraints/parameters	7983/0/409
Goodness-of-fit on F^2	1.048
Final R indexes [I>=2σ (I)]	R_1 = 0.0327, wR_2 = 0.0821
Final R indexes [all data]	R_1 = 0.0388, wR_2 = 0.0864
Largest diff. peak/hole / e Å^{-3}	1.27/-0.80

Crystal data and structure refinement for PtL[23]

Identification code	17srv378
Empirical formula	$C_{32}H_{20}FN_5Pt$
Formula weight	688.62
Temperature/K	100.0
Crystal system	monoclinic
Space group	C2/c
a/Å	15.8393(11)
b/Å	20.9252(14)
c/Å	7.2775(5)
α/°	90
β/°	105.968(4)
γ/°	90
Volume/Å^3	2319.0(3)
Z	4
ρ_{calc}g/cm^3	1.972
μ/mm^{-1}	5.611
F(000)	1336.0
Crystal size/mm^3	0.085 × 0.034 × 0.012
Radiation	synchrotron (λ = 0.6889)
2Θ range for data collection/°	6.228 to 54.99
Index ranges	-19 ≤ h ≤ 21, -28 ≤ k ≤ 24, -9 ≤ l ≤ 9
Reflections collected	8305
Independent reflections	2756 [R_{int} = 0.0812, R_{sigma} = 0.1075]
Data/restraints/parameters	2756/0/179
Goodness-of-fit on F^2	1.037
Final R indexes [I>=2σ (I)]	R_1 = 0.0520, wR_2 = 0.1136
Final R indexes [all data]	R_1 = 0.0816, wR_2 = 0.1238
Largest diff. peak/hole / e Å^{-3}	3.09/-2.93

Crystal data and structure refinement for $L^{26}(Pt(dpybA)Cl)_2$

Identification code	18srv333
Empirical formula	$C_{60}H_{51}Cl_3N_4OPt_2$
Formula weight	1340.57
Temperature/K	120.0
Crystal system	monoclinic
Space group	$P2_1/c$
a/Å	11.1103(8)
b/Å	26.454(2)
c/Å	36.437(3)
α/°	90
β/°	96.037(3)
γ/°	90
Volume/Å^3	10649.9(14)
Z	8
ρ_{calc}g/cm^3	1.672
μ/mm^{-1}	5.444
F(000)	5232.0
Crystal size/mm^3	0.22 × 0.18 × 0.09
Radiation	MoKα (λ = 0.71073)
2Θ range for data collection/°	3.996 to 57.998
Index ranges	-14 ≤ h ≤ 15, -36 ≤ k ≤ 36, -49 ≤ l ≤ 49
Reflections collected	151553
Independent reflections	28121 [R_{int} = 0.0752, R_{sigma} = 0.0932]
Data/restraints/parameters	28121/48/1277
Goodness-of-fit on F^2	1.131
Final R indexes [I>=2σ (I)]	R_1 = 0.0840, wR_2 = 0.1647
Final R indexes [all data]	R_1 = 0.1280, wR_2 = 0.1788
Largest diff. peak/hole / e Å^{-3}	4.69/-3.50

Crystal data and structure refinement for $L^{26}(Pt(dpybD)Cl)_2$

Identification code	18srv276
Empirical formula	$C_{67}H_{54}F_{12}N_4OPt_2$ x 2.5 $CHCl_3$
Formula weight	1847.74
Temperature/K	120.0
Crystal system	triclinic
Space group	P-1
a/Å	13.3456(8)
b/Å	15.5621(10)
c/Å	18.5662(11)
α/°	94.442(2)
β/°	103.675(2)
γ/°	113.8416(19)
Volume/$Å^3$	3361.4(4)
Z	2
$\rho_{calc}g/cm^3$	1.826
μ/mm^{-1}	4.537
F(000)	1802.0
Crystal size/mm^3	0.12 × 0.11 × 0.01
Radiation	MoKα (λ = 0.71073)
2Θ range for data collection/°	4.384 to 57.998
Index ranges	-18 ≤ h ≤ 18, -21 ≤ k ≤ 21, -25 ≤ l ≤ 25
Reflections collected	69733
Independent reflections	17856 [R_{int} = 0.0616, R_{sigma} = 0.0741]
Data/restraints/parameters	17856/111/835
Goodness-of-fit on F^2	1.036
Final R indexes [I>=2σ (I)]	R_1 = 0.0535, wR_2 = 0.1284
Final R indexes [all data]	R_1 = 0.0948, wR_2 = 0.1457
Largest diff. peak/hole / e $Å^{-3}$	5.40/-2.95

Crystal data and structure refinement for $L^{26}(Pt(dpybE)Cl)_2$

Identification code	18srv388
Empirical formula	$C_{75}H_{58}N_4OPt_2$
Formula weight	1421.43
Temperature/K	100.0
Crystal system	triclinic
Space group	P-1
a/Å	12.3705(16)
b/Å	14.832(2)
c/Å	17.645(2)
α/°	65.796(3)
β/°	87.028(3)
γ/°	73.841(3)
Volume/Å^3	2829.0(7)
Z	2
ρ_{calc}g/cm^3	1.669
μ/mm^{-1}	4.596
F(000)	1400.0
Crystal size/mm^3	0.025 × 0.015 × 0.005
Radiation	synchrotron (λ = 0.6889)
2Θ range for data collection/°	3.022 to 53.998
Index ranges	-16 ≤ h ≤ 16, -19 ≤ k ≤ 19, -23 ≤ l ≤ 23
Reflections collected	38279
Independent reflections	13486 [R_{int} = 0.0885, R_{sigma} = 0.1630]
Data/restraints/parameters	13486/15/741
Goodness-of-fit on F^2	0.981
Final R indexes [I>=2σ (I)]	R_1 = 0.0864, wR_2 = 0.2375
Final R indexes [all data]	R_1 = 0.1245, wR_2 = 0.2684
Largest diff. peak/hole / e Å^{-3}	5.25/-0.89